OFFICE OF CIVILIAN RADIOACTIVE WASTE MANAGEMENT
ANALYSIS/MODEL COVER SHEET

Complete Only Applicable Items

1. QA: QA

2. ☒ Analysis — Check all that apply	3. ☒ Model — Check all that apply
Type of Analysis: ☐ Engineering; ☐ Performance Assessment; ☒ Scientific	Type of Model: ☒ Conceptual Model; ☐ Abstraction; ☒ Mathematical Model; ☐ System Model; ☐ Process Model
Intended Use of Analysis: ☒ Input to Calculation; ☒ Input to another Analysis or Model; ☐ Input to Technical Document; ☐ Input to Other Technical Products	Intended Use of Model: ☒ Input to Calculation; ☒ Input to another Model or Analysis; ☐ Input to Technical Document; ☐ Input to Other Technical Products
Describe use: Provide transport properties and information for other AMRs and a PMR.	Describe use: Provide conceptual and field data on subsurface transport for PA calculations and for PMRs.

4. Title:

Unsaturated Zone and Saturated Zone Transport Properties (U0100)

5. Document Identifier (including Rev. No. and Change No., if applicable):

ANL-NBS-HS-000019, Rev 00, ICN 1

6. Total Attachments: None

7. Attachment Numbers - No. of Pages in Each:

N/A

	Printed Name	Signature	Date
8. Originator	Jim Conca	SIGNATURE ON FILE	12/20/00
9. Checker	N.E. Biggar	SIGNATURE ON FILE	12/20/00
10. Lead/Supervisor	P. R. Dixon	SIGNATURE ON FILE	12/20/00
11. Responsible Manager	G. S. Bodvarsson	SIGNATURE ON FILE	12/20/00

12. Remarks:

Rev. 00, ICN 1

Those parts of this document that were not affected by ICN 1 to Rev. 01 (i.e., those parts of the document outside the change bars) were obtained from the Document Control Department in compliance with applicable procedures. These parts of the document represent the official controlled version of Rev. 00 and are not affected by ICN 1. If the user encounters legibility problems with figures in the document that are not part of ICN 1, the user is referred to the Document Control Department or the record copy of Rev. 00 (ACC: MOL.20000829.0006) for assistance.

OFFICE OF CIVILIAN RADIOACTIVE WASTE MANAGEMENT
ANALYSIS/MODEL REVISION RECORD

Complete Only Applicable Items

1. Page: 2 of: 295

2. Analysis or Model Title:

Unsaturated Zone and Saturated Zone Transport Properties (U0100)

3. Document Identifier (including Rev. No. and Change No., if applicable):

ANL-NBS-HS-000019, Rev 00, ICN 1

4. Revision/Change No.	5. Description of Revision/Change
00	INITIAL ISSUE
00/01	ICN incorporates changes to remove TBV's from cited data by replacing unqualified DTN's with qualified DTN's, correcting input status entries, or revising text to directly use only qualified information. Changes are indicated with change bars in the text. The following DTN citations in the text were affected: GS920408312321.001 replaced with MO0007MAJIONPH.011 GS920408312321.003 replaced with MO0007MAJIONPH.011 GS930308312323.001 replaced with MO0007MAJIONPH.013 GS980908312322.008 replaced with MO0007MAJIONPH.005 GS990608312133.001 replaced with MO0007MAJIONPH.003 LA9909WS831372.022 status changed to output from analysis LAIT831341AQ96.001 replaced with LA0010JC831341.002, LA0010JC831341.003, LA0010JC831341.004, LA0010JC831341.005, LA0010JC831341.006, LA0010JC831341.007 MO9907YMP99025.001 replaced with MO9906GPS98410.000 LA9909PR831231.004 replaced with MO0012PERMCHOL.000, MO0012BRLI25C2.000, MO0012MINLCHOL.000, MO0012CATECHOL.000, MO0012SORBCHOL.000, MO0012POROCHOL.000

CONTENTS

Page

1. PURPOSE 21

2. QUALITY ASSURANCE 23

3. COMPUTER SOFTWARE AND MODEL USAGE 25

4. INPUTS 29
   - 4.1 DATA AND PARAMETERS 29
   - 4.2 CRITERIA 34
   - 4.3 CODES AND STANDARDS 34

5. ASSUMPTIONS 35

6. ANALYSIS/MODEL 41
   - 6.1 INTRODUCTION 41
   - 6.2 APPROACH 41
   - 6.3 SOLUBILITY STUDIES 42
   - 6.4 SORPTION STUDIES 42
     - 6.4.1 Introduction 42
     - 6.4.2 Sorption Coefficients for Performance Assessment 42
     - 6.4.3 Hydrochemistry and Eh-pH Characteristics of the Saturated Zone 48
     - 6.4.4 Sorption Experiments 49
       - 6.4.4.1 Batch-Sorption Experiments 50
         - 6.4.4.1.1 The Distribution Coefficient 50
         - 6.4.4.1.2 Linear Versus Nonlinear Sorption 51
         - 6.4.4.1.3 Experimental Procedures 51
         - 6.4.4.1.4 Data from Batch-Sorption Tests 52
           - 6.4.4.1.4.1 Plutonium 52
           - 6.4.4.1.4.2 Neptunium 56
           - 6.4.4.1.4.3 Americium, Actinium, and Samarium 64
           - 6.4.4.1.4.4 Uranium 68
           - 6.4.4.1.4.5 Technetium 74
           - 6.4.4.1.4.6 Protactinium 74
           - 6.4.4.1.4.7 Selenium 75
           - 6.4.4.1.4.8 Carbon, Chlorine, and Iodine 76
           - 6.4.4.1.4.9 Cesium, Radium, and Strontium 76
           - 6.4.4.1.4.10 Nickel and Lead 78

CONTENTS (Continued)

Page

6.4.4.1.4.11 Thorium, Niobium, Tin, and Zirconium ... 79
6.4.4.2 Effects of Organics on Actinide Sorption ... 84
6.4.5 Adsorption of Radionuclides by Alluvium ... 86
6.4.5.1 Results and Discussion ... 86
6.4.5.1.1 Adsorption of ^{237}Np ... 86
6.4.5.1.2 Adsorption of ^{99}Tc ... 87
6.4.5.1.3 Adsorption of ^{129}I ... 87
6.4.5.2 Conclusions about Sorption onto Alluvium ... 92
6.4.6 Effects of Temperature Perturbations on Adsorption of Radionuclides ... 93
6.5 DYNAMIC TRANSPORT STUDIES ... 94
6.5.1 Crushed-Rock Columns ... 94
6.5.1.1 Approach ... 94
6.5.1.2 Results and Discussion ... 96
6.5.1.2.1 Neptunium Results ... 96
6.5.1.2.2 Plutonium and Technetium Results ... 98
6.5.2 Solid-Rock Columns ... 102
6.5.2.1 Methodology ... 102
6.5.2.1.1 Retardation ... 102
6.5.2.1.2 Hydraulic Conductivity ... 103
6.5.2.2 Results and Discussion for Vitric and Zeolitic Tuff ... 105
6.5.2.2.1 Column Breakthrough Test Results ... 105
6.5.2.2.2 Batch-Sorption Test Results ... 106
6.5.2.2.3 Conclusions ... 108
6.5.3 Radionuclide Transport Through Fractures ... 108
6.5.3.1 Overview ... 108
6.5.3.2 Experimental Procedures ... 110
6.5.3.3 Results and Discussion ... 111
6.6. DIFFUSION TRANSPORT STUDIES IN THE LABORATORY ... 116
6.6.1 Rock-Beaker Experiments ... 116
6.6.1.1 Experimental Procedure ... 116
6.6.1.2 Data Analysis ... 116
6.6.1.3 Results and Discussion ... 117
6.6.2 Diffusion-Cell Experiments ... 121
6.6.2.1 Experimental Procedures and Data Analysis ... 122
6.6.2.2 Results and Discussion ... 123
6.6.3 Distribution Parameters for Matrix Diffusion Coefficients ... 126
6.7 COLLOID-FACILITATED RADIONUCLIDE TRANSPORT ... 126
6.7.1 Review of Geochemical Controls on Colloid Stability ... 126
6.7.2 Colloid Concentrations at Yucca Mountain ... 127
6.7.3 Review of Sorption Behavior of Radionuclides on Colloids ... 127
6.8 BUSTED BUTTE UNSATURATED ZONE TRANSPORT TEST ... 129

CONTENTS (Continued)

Page

6.8.1 Overview 129
6.8.1.1 Unsaturated Zone Transport Test Location 129
6.8.1.2 Unsaturated Zone Transport Test Concept 129
6.8.1.3 Unsaturated Zone Transport Test Project Objectives 130
6.8.2 Test Design 131
6.8.2.1 Site Description 131
6.8.2.2 Experimental Design: Test Phases 131
6.8.2.2.1 Test Phase 1 131
6.8.2.2.2 Test Phase 2 132
6.8.2.3 Borehole Injection and Sampling Systems 134
6.8.2.3.1 Moisture Sensors 136
6.8.2.3.2 Phase-1 and Phase-2 Data Collection 136
6.8.2.4 Conservative and Reactive Tracers and Microspheres 137
6.8.2.4.1 Phase-1 Tracers 137
6.8.2.4.2 Phase-2 Tracers 139
6.8.2.4.3 Synthetic Pore-Water Recipe 141
6.8.2.5 Use of Numerical Simulations for Test Design 141
6.8.2.5.1 Sample Collection Analyses Simulating Performance of a Sampling Pad 141
6.8.2.5.2 Performance Measures 148
6.8.3 Geology, Mineralogy, and Hydrologic Properties 150
6.8.3.1 Geology of the Busted Butte Test Facility 150
6.8.3.1.1 Calico Hills Formation 151
6.8.3.1.2 Topopah Spring Tuff 152
6.8.3.2 Mineralogy of the Busted Butte Locality 153
6.8.3.2.1 Mineralogic Comparison with Yucca Mountain: Boreholes H-5 and SD-6 155
6.8.3.3 Hydrologic Properties 155
6.8.4 Tomographic Studies: Geophysical Techniques at the Busted Butte Unsaturated Zone Test Facility—Overview 158
6.8.4.1 Ground-Penetrating Radar Tomography 158
6.8.4.1.1 Experimental Objective and Status 158
6.8.4.1.2 Background and Experimental Approach 159
6.8.4.1.3 Equipment Description, Component Specifications, Operating Principles, and Survey Methodology 159
6.8.4.1.4 Results of Busted Butte Unsaturated Zone Transport Test Radar Data Acquisition 159
6.8.4.1.5 Conclusions 166
6.8.4.2 Electrical-Resistance Tomography 166
6.8.4.2.1 Experimental Objective 166

CONTENTS (Continued)

Page

6.8.4.2.2 Description of the Electrical-Resistance Tomography Method ... 167
6.8.4.2.3 Description of 2-D Algorithms ... 167
6.8.4.2.4 Description of the 3-D Imaging Algorithm ... 169
6.8.4.2.5 Electrical-Resistance Tomography Data-Collection and Processing Codes ... 171
6.8.4.2.6 Electrical-Resistance Tomography Data-Collection System ... 171
6.8.4.2.7 Results of Data Collections—July to Early September ... 174
6.8.4.2.8 Absolute Electrical-Resistance Tomography Images of the Block ... 176
6.8.4.2.9 Difference Electrical-Resistance Tomography Images of the Block ... 176
6.8.4.2.10 Conclusions ... 176
6.8.5 Geochemistry and Tracer Migration – Laboratory and Field Tests ... 179
6.8.5.1 Laboratory Sorption Studies ... 179
6.8.5.1.1 Preliminary Studies ... 179
6.8.5.1.2 Detailed Studies ... 180
6.8.5.1.2.1 Sample Description ... 180
6.8.5.1.2.2 Radionuclide Sorption ... 180
6.8.5.1.2.3 Tracer Sorption ... 180
6.8.5.1.2.4 Quantitative X-ray Diffraction ... 180
6.8.5.2 In-situ Pore-Water Chemistry ... 181
6.8.5.3 Field-Scale Tracer Transport ... 183
6.8.5.3.1 Phase 1A ... 183
6.8.5.3.1.1 Description ... 183
6.8.5.3.1.2 Results ... 183
6.8.5.3.2 Phase 1B ... 183
6.8.5.3.2.1 Description ... 183
6.8.5.3.2.2 Results ... 184
6.8.5.3.3 Phase 2 ... 188
6.8.5.3.3.1 Description ... 188
6.8.5.3.3.2 Status ... 189
6.8.5.4 Special Topic—Microsphere Measurements ... 190
6.8.5.5 Special Topic—Tracer Degradation ... 191
6.8.5.6 Forward Efforts ... 191
6.8.6 Phase-1A Predictions ... 192
6.8.6.1 Deterministic Model ... 192
6.8.6.1.1 Model Configuration and Parameter Set ... 192
6.8.6.1.2 Modeling Results ... 196

CONTENTS (Continued)

Page

6.8.6.1.2.1 Overview of Simulations 196
6.8.6.1.2.2 Discussion of Simulations: Base Case 198
6.8.6.1.2.3 Discussion of Simulations: Sensitivity Analyses 200
6.8.6.1.2.4 Discussion of Simulations: 2-D versus 3-D 204
6.8.6.1.3 Implications for Unsaturated Zone Transport Test Phase-2 Design and Analysis 204
6.8.6.2 Stochastic Model 205
6.8.6.2.1 Introduction 205
6.8.6.2.2 Stochastic Modeling 206
6.8.6.2.3 Phase-1A Modeling 207
6.8.6.2.4 Nonstationarity 218
6.8.6.3 Monte Carlo Flow and Transport Simulations 218
6.8.6.3.1 Introduction 218
6.8.6.3.2 Methodology 220
6.8.6.3.3 Statistical Results 221
6.8.6.3.4 Interpretations of the Monte Carlo Phase-1A Study 224
6.8.6.3.5 Forward Efforts 224
6.8.7 Initial Phase-2 Model Predictions 225
6.8.7.1 Introduction 225
6.8.7.2 Model Description 225
6.8.7.3 Predictions 230
6.8.7.4 Summary and Interpretation 237
6.8.8 Model Validation 240
6.8.9 Summary: Implications for Performance Assessment 242
6.9 C-WELLS FIELD AND LABORATORY TRANSPORT TESTING 243
6.9.1 Introduction 243
6.9.2 Summary of Field Test Results and Interpretations 246
6.9.3 Summary of Laboratory Test Results and Interpretations 257
6.9.3.1 Batch-Sorption Testing of Lithium Ion 257
6.9.3.2 Diffusion Cell Testing 257
6.9.3.3 Flowing Transport Experiments in Crushed and Fractured Tuffs 259
6.9.4 Conclusions from C-Wells Field and Laboratory Testing 260

7. CONCLUSIONS 261
7.1 RECOMMENDATIONS 264
7.2 IMPACTS 265
7.3 OUTPUT DATA 265

8. INPUTS AND REFERENCES 267
8.1 DOCUMENTS CITED 267

CONTENTS (Continued)

Page

8.2 CODES, STANDARDS, REGULATIONS, AND PROCEDURES 286
8.3 SOFTWARE 287
8.4 SOURCE DATA, LISTED BY DATA TRACKING NUMBER..... 287
8.5 OUTPUT DATA, LISTED BY DATA TRACKING NUMBER..... 294

FIGURES

Page

1. Neptunium Sorption in J-13 Well Water 58
2. pH Dependence of Neptunium Sorption onto Tuffs at 10^{-7} M 59
3. Neptunium Sorption onto Clinoptilolite-Rich Tuff 61
4. Neptunium Sorption onto Clinoptilolite 61
5. Dependence on Water for Sorption onto Tuffs 63
6. Dependence on Water for Sorption onto Minerals 63
7. Uranium Sorption onto Clinoptilolite-Rich Tuff 72
8. Uranium Sorption onto Clinoptilolite 73
9. Adsorption of ^{237}Np on Three Alluvial Samples 88
10. Kinetics of ^{237}Np Adsorption on Three Alluvial Samples 89
11. Adsorption of ^{99}Tc on Three Alluvial Samples 90
12. Kinetics of ^{99}Tc Adsorption on Three Alluvial Samples 91
13. Kinetics of ^{129}I Adsorption on Three Alluvial Samples 92
14. Plutonium through Vitric Tuff 98
15. Plutonium through Zeolitic Tuff 99
16. Plutonium in Devitrified Tuff at Various Flow Rates (J-13 Water) 100
17. Plutonium in Devitrified Tuff at Various Flow Rates (p#1) 100
18. Technetium in Devitrified Tuff 101
19. Technetium in Vitric Tuff 101
20. Technetium in Zeolitic Tuff 102
21. Selenium Breakthrough Curves 106

FIGURES (Continued)

Page

22. Unsaturated Hydraulic Conductivity 107

23. Neptunium in Fractured Tuff G1-1941 113

24. Neptunium in Fractured Tuff UZ-16 919 113

25. Neptunium and Technetium in Fractured Tuff 114

26. Technetium in Fractured Tuff 115

27. Diffusion Data 118

28. Diffusion Data Curve Fits 119

29. Calculated Diffusion Curves 120

30. Comparison of Calculated and Actual Diffusion Data 121

31. Tritium, Plutonium, and Uranium Diffusion through Devitrified Tuff 124

32. Technetium and Neptunium Diffusion through Devitrified Tuff 125

33. Tritium, Plutonium, and Uranium Diffusion through Zeolitic Tuff 125

34. Busted Butte Unsaturated Zone Transport Test 133

35. Injection and Collection System Configuration 135

36. Injection-System Transparent Packer 135

37. Phase-1A Borehole Numbers and Relative Locations 138

38. Phase-1B and Phase-2 Borehole Numbers and Relative Locations 138

39. Distributions of Saturation under Steady-State Water Flow Conditions within the Tac ... 144

40. Water Saturation as a Function of Time for a New Pad Attached to the System 145

41. Solute Resident Concentrations in Tac 146

42. Performance of a Collection Pad in Tac 147

FIGURES (Continued)

Page

43. Influence of Borehole and Pad on Solute Travel Times for Tac 148

44. Busted Butte Geologic Map 151

45. Tomography (GPR-T) Results for Well Pair 46-16, December 1998 162

46. Tomography (GPR-T) Results for Well Pair 46-16, March 1999 162

47. Tomography (GPR-T) Results for Well Pair 46-16, April 1999 163

48. Tomography (GPR-T) Results for Well Pair 46-9, December 1998 164

49. Tomography (GPR-T) Results for Well Pair 46-9, April 1999 164

50. Tomography (GPR-T) Results for Well Pair 15-13, April 1999 166

51. Flow Chart of Computer Codes Used for Electrical-Resistance Tomography Data Collection and Processing at Busted Butte 172

52. Electrical-Resistance Tomography Data-Collection System 173

53. Electrical-Resistance Tomography Layout 174

54. Electrical-Resistance Tomography Electrode Assignments 175

55. Electrical-Resistance Tomography Images of Test Block Viewed from Test Alcove: Baseline and August Differences 177

56. Electrical-Resistance Tomography Images of Test Block Viewed from Test Alcove: September Differences 178

57. Phase-1B Pad Extraction/Analysis Scheme 185

58a. Bromide Concentrations in Borehole 6 for Phase 1B 186

58b. 2,6-DFBA Concentrations in Borehole 6 for Phase 1B 186

58c. Fluorescein Concentrations in Borehole 6 for Phase 1B 187

58d. Pyridone Concentrations in Borehole 6 for Phase 1B 187

FIGURES (Continued)

Page

58e. Lithium Concentrations in Borehole 6 for Phase 1B 188

59. Schematic Layout of Phase-2 Collection Boreholes 189

60. Phase-2 Pad Extraction/Analysis Scheme 190

61. Computational Grid for UZTT Single-Borehole Simulations 193

62. 2-D Sensitivity Runs. 198

63. Tracer Concentration versus Distance for 2-D and 3-D Simulations 200

64. Time Profiles of Tracer Concentrations 201

65. Effect of Water Injection on Matrix Saturation 201

66. Tracer Concentration for Different Sensitivity Runs 202

67. Concentration versus Time at Various Distances from Injection 203

68. Differences in 2-D and 3-D Predicted Concentrations 205

69. Steady-State Profiles 209

70. Case 1. Horizontal and Vertical Profiles of Pressure Head h and Saturation S at 150 Days after Injection Started. 209

71. Case 2. The Same as Case 1 in Figure 70 but with $\lambda_f = \lambda_\alpha = 30$ cm. 210

72. Case 3. The Same as Case 1 in Figure 70 but with $L_1 = L_2 = 400$ cm. 211

73. Case 4. The Same as Case 1 in Figure 70 but with $S_o = 20\%$. 212

74. Case 5. The Same as Case 1 in Figure 70 but with $S_o = 40\%$. 213

75. Case 6. The Same as Case 1 in Figure 70 but with $S_o = 60\%$. 213

76. Case 7. The Same as Case 1 in Figure 70 but with $\phi = 0.3$. 214

77. Case 8. The Same as Case 1 in Figure 70 but with $(f) = -4.258$ and $L_1 = L_2 = 400$ cm. 214

FIGURES (Continued)

Page

78. Case 9. The Same as Case 1 in Figure 70 but with $<\alpha> = 0.02$ cm^{-1} 215

79. Case 10. The Same as Case 1 in Figure 70 but with $\sigma_\alpha = 0$ 215

80. Case 11. The Same as Case 1 in Figure 70 but with $Q = 10$ mL hr^{-1} 216

81. Case 12. The Same as Case 8 in Figure 77 but with $Q = 50$ mL hr^{-1} and $L_3 = 100$ cm 216

82. Case 13. The Same as Case 1 in Figure 70 but with $<f> = 0.314$, $L_1 = L_2 = 400$ cm, and $Q = 10$ mL hr^{-1} 217

83. Case 14. The Same as Case 13 in Figure 82 but with $Q = 50$ mL hr^{-1} and $L_3 = 100$ cm 217

84. Finite-Element Grid Used in the Monte Carlo Simulation 219

85. Permeability Distribution 220

86. Fluid Saturations and Tracer Concentrations 222

87. Three-Dimensional View of the Injection and Collection Boreholes 226

88. Top View of Finite-Element Grid and the Injection and Collection Boreholes..... 227

89. Finite-Element Grid as seen from the Test Alcove. 228

90. Finite-Element Grid as seen from the Main Adit 229

91. Phase-1B Breakthrough Predictions Using Equivalent-Continuum Model and Tptpv2 Properties..... 231

92. A Conservative Tracer Concentration Plume..... 233

93. Predicted Saturation Profiles for Phase 2 239

94. Location and Layout of the C-Wells Complex 244

95. Stratigraphy, Lithology, Matrix Porosity, Fracture Density, and Inflow from Open-Hole Flow Surveys at the C-Wells..... 245

96. Normalized Tracer Responses in the Bullfrog Tuff Multiple Tracer Test..... 247

FIGURES (Continued)

Page

97. Normalized Tracer Responses in the Prow Pass Tuff Multiple Tracer Test 248

98. Normalized PFBA Responses in Two Different Tracer Tests in the Bullfrog Tuff 249

99. Log Normalized Tracer Responses in the Prow Pass Tuff Multiple Tracer Test 251

100. Longitudinal Dispersivity versus Length Scale of C-Wells Values from Interpretations of the Prow Pass and Bullfrog Reactive Tracer Tests..... 254

101. Fitted Langmuir Sorption Isotherms for Lithium Sorption onto C-Wells Tuffs from Different Units/Lithologies 258

TABLES

Page

1a. Sorption and Sorption Modeling Studies 29

1b. Dynamic Transport Studies 30

1c. Diffusion Transport Studies in the Laboratory 31

1d. Colloid-Facilitated Radionuclide Transport 31

1e. Busted Butte Unsaturated Zone Transport Test 32

1f. C-Wells Field and Laboratory Transport Testing 33

1g. Scientific Notebooks Used 34

2a. Sorption-Coefficient Distributions for Unsaturated-Zone Units 45

2b. Sorption-Coefficient Distributions for Saturated-Zone Units 46

3. Groundwater Compositions of Wells J-13 and p#1 49

4. Plutonium Sorption Distribution Coefficients 54

5. Prediction of Neptunium Sorption on Clinoptilolite-Rich G4-1510 Tuff in J-13 Water 59

6. Neptunium Sorption onto Clinoptilolite-Rich Tuffs in J-13 Water 60

7. Uranium Sorption in J-13 Water under Oxidizing Conditions 72

8. Prediction of Uranium Sorption on Clinoptilolite-Rich G4-1510 Tuff in J-13 Water 73

9. Depth Intervals (below the surface) and Bulk Densities of Alluvial Samples 86

10. Quantitative X-ray Diffraction (QXRD) Results of Three Alluvial Samples 87

11. Comparison of Neptunium K_d Values from Batch and Column Measurements 97

12. Selenium Batch Adsorption on Nonwelded Zeolitic Tuff 107

13. Minerals Coating Fracture Walls in Yucca Mountain Tuffs 109

14. Characteristics of Fractured Devitrified-Tuff Columns 111

TABLES (Continued)

Page

15. Batch-Sorption Results for ^{237}Np in J-13 Well Water 112

16. Rock-Beaker Diffusion Results for Nonsorbing Radioisotopes and Devitrified Tuffs 119

17. Batch-Sorption Coefficients for Devitrified Tuffs 120

18. Dimensions of Diffusion Cells 122

19. Hydraulic Parameter Sets Used to Define the Material Properties for the Simulations 142

20. Descriptions of Outcrop Samples Collected from Busted Butte 153

21. Quantitative X-ray Diffraction Results for Samples from Lower Tpt Section (weight %) 154

22. Mineral Abundances (weight %) in Calico Hills Formation (Tac) and Wahmonie Formation Surface Samples from Busted Butte 154

23. Mineral Abundances (weight %) in Calico Hills Formation (Tac) Samples from Auger Hole AUG-1 in the Floor of the Busted Butte Test Alcove 155

24. Quantitative X-ray Diffraction Results (weight %) for USW H-5 Core and Drill Cuttings 156

25. Quantitative X-ray Diffraction Results (weight %) for Samples from Drill Hole USW SD-6 157

26. Preliminary Measured Sorption Coefficients 179

27. Sorption Mineralogy Samples 180

28. Summary of Radionuclide Sorption Results 180

29. Chemical Composition of Busted Butte Pore Water with J-13 Groundwater for Comparison 182

30. Tracer C_0 Values for Phase 1B Injection 184

31. Hydrologic Parameters Used for the 2-D Simulations 195

32. Hydrologic Parameters Used for the 3-D Simulations 196

TABLES (Continued)

Page

33. Predicted Transport Distances for a Given Concentration 198

34. Simulation Results at 180 Days 199

35. Case Description 208

36. Summary of Monte Carlo Cases 220

37. Statistical Results of Monte Carlo Simulations 223

38. Property Sets for the Phase-2 Test 228

39. Closest Sampling Point to the Injection Planes Within Each Collection Borehole 231

40. Fluorescein from Upper Injection Boreholes 232

41. Fluorescein from Lower Injection Boreholes 232

42. Retardation of Reactive Tracers 234

43. Lithium from Upper Injection Boreholes 235

44. Lithium from Lower Injection Boreholes 235

45. Manganese from Upper Injection Boreholes 236

46. Manganese from Lower Injection Boreholes 236

47. Nickel or Cobalt from Upper Injection Boreholes 237

48. Nickel or Cobalt from Lower Injection Boreholes 237

49. Fluorescein from Upper Injection Boreholes with Physical Heterogeneities 238

50. Fluorescein from Lower Injection Boreholes with Physical Heterogeneities 238

51. Transport Parameters Deduced from Fits of the Bullfrog Tuff Tracer Responses 253

52. Transport Parameters Deduced from Fits of the Prow Pass Tuff Tracer Responses 253

53. Comparison of Field- and Laboratory-Derived Sorption Parameters for Lithium Ion 256

TABLES (Continued)

Page

54. Ratios of Observed Tracer Arrival Times and Distances Squared for C-Wells Tracer Tests 257

55. Laboratory-Measured Matrix Diffusion Coefficients of Bromide and PFBA in Various C-Wells Tuffs 259

ACRONYMS

2-D	Two dimensional
3-D	Three dimensional
AMR	Analysis/Model Report
CEC	Cation exchange capacity
CF	Configuration file
CHv	vitric Calico Hills
CM	Configuration Management
CML	Carboxylate-modified latex
COV	Coefficient of variation
DFBA	Difluorobenzoic acid
DI	Deionized
DOE	U.S. Department of Energy
DOPA	Dihydroxyphenylalanine
DTN	Data tracking number
ECM	Equivalent continuum model
ERT	Electrical resistance tomography
ESF	Exploratory Studies Facility
FBA	Fluorinated benzoic acid
FEM	Finite-element method
FEHM	A finite-element heat- and mass-transfer numerical code
GPR	Ground-penetrating radar
GPR-T	Ground-penetrating radar tomography
HPLC	High-pressure liquid chromatography
HSAB	Hard-soft acid-base
HTO	Tritiated water
IC	Ion chromatography
ICP/AES	Inductively coupled plasma/atomic-emission spectrometry
ICP/MS	Inductively coupled plasma/mass spectrometry
IHSS	International Humic Substances Society
LA	License Application
LANL	Los Alamos National Laboratory
LBNL	Lawrence Berkeley National Laboratory

M&O	Management and Operating Contractor
Min/Pet	Mineralogy/petrology
MOP	Multiple-offset profile
NAFA	Nordic aquatic fulvic acid
N/A	Not applicable
NRC	Nuclear Regulatory Commission
NTS	Nevada Test Site
OCRWM	Office of Civilian Radioactive Waste Management
OP	Operating program
PA	Performance assessment
PFBA	Pentafluorobenzoic acid
PMR	Process Model Report
Q	Quality, such as in Q samples that were obtained in conformance with quality assurance procedures
QA	Quality assurance
QARD	Quality Assurance Requirements and Description
QXRD	Quantitative x-ray diffraction
RTA	Reactive Transport Application
SAN	Software activity number
SMF	Sample Management Facility
STN	Software tracking number
SZ	Saturated zone
TBV	To be verified
TDMS	Technical Data Management System
TDS	Total dissolved solids
TOC	Total organic carbon
TSPA	Total systems performance assessment
UFA	A method using ultracentrifuge-induced flow
USGS	U.S. Geological Survey
UV	Ultraviolet
UZ	Unsaturated zone
UZTT	Unsaturated Zone Transport Test
YMP	Yucca Mountain Site Characterization Project
ZOP	Zero-offset profile

1. PURPOSE

This Analysis/Model Report (AMR) summarizes transport properties for the lower unsaturated zone hydrogeologic units and the saturated zone at Yucca Mountain and provides a summary of data from the Busted Butte Unsaturated Zone Transport Test (UZTT). The purpose of this report is to summarize the sorption and transport knowledge relevant to flow and transport in the units below Yucca Mountain and to provide backup documentation for the sorption parameters decided upon for each rock type. Because of the complexity of processes such as sorption, and because of the lack of direct data for many conditions that may be relevant for Yucca Mountain, data from systems outside of Yucca Mountain are also included. The data reported in this AMR will be used in Total System Performance Assessment (TSPA) calculations and as general scientific support for various Process Model Reports (PMRs) requiring knowledge of the transport properties of different materials.

This report provides, but is not limited to, sorption coefficients and other relevant thermodynamic and transport properties for the radioisotopes of concern, especially neptunium (Np), plutonium (Pu), uranium (U), technetium (Tc), iodine (I), and selenium (Se). The unsaturated-zone (UZ) transport properties in the vitric Calico Hills (CHv) are discussed, as are colloidal transport data based on the Busted Butte UZTT, the saturated tuff, and alluvium. These values were determined through expert elicitation, direct measurements, and data analysis. The transport parameters include information on interactions of the fractures and matrix. In addition, core matrix permeability data from the Busted Butte UZTT are summarized by both percent alteration and dispersion. Other data from C-wells testing for use in the saturated-zone (SZ) Process Model Report (PMR) (CRWMS M&O 1999a) are also included.

The limitations of this AMR are that all conditions and properties on all rock relevant to Yucca Mountain have not, and cannot, be directly measured in the time frame of this project, and the key properties summarized in Section 6 are the best estimates based on available data, some of which are not qualified. These values are considered to be conservative and, thus, should provide conservative estimates for repository performance assessment calculations.

This report is governed by the Office of Civilian Radioactive Waste Management (OCRWM) AMR Development Plan entitled *U0100 UZ/SZ Transport Properties Data, Rev 00* (CRWMS M&O 1999b). As per this Development Plan, Tables 2a and b in Section 6.4 summarize the sorption data that will be used in flow and transport models and the TSPA. Solubility data was relegated to another AMR (CRWMS M&O 2000a). The Interim Change Notice (ICN), ICN 1, of this AMR was prepared as part of activities being conducted under Technical Work Plan (TWP), TWP-NBS-HS-000001, *Technical Work Plan for Unsaturated Zone (UZ) Flow and Transport Process Model Report* (CRWMS M&O 2000c).

Sections 6.8.6 and 6.8.7 document the use and validation of the UZTT model, which is based on a conceptual model that accounts for various radionuclide dilution and retardation mechanisms including sorption, matrix diffusion, dispersion, and colloid transport. The importance of the UZTT model to Performance Assessment (PA) is that it will be used to analyze data from the UZTT and to demonstrate and refine capability to model radionuclide transport at Yucca Mountain using the FEHM V2.00 (STN: 10031-2.00-00) code.

Sections 6.8 and 6.9 assess the applicability of laboratory-derived parameters to the prediction of transport in the saturated and unsaturated zones at the field scale. Section 6.9 summarizes the field-scale estimates of transport model parameters in the Bullfrog and Prow Pass tuffs and validates the conceptual dual-porosity transport model in the saturated zone.

The analyses and model presented in this AMR are appropriate for the intended use of this report.

2. QUALITY ASSURANCE

The activities documented in this AMR were evaluated in accordance with QAP-2-0, *Conduct of Activities*, and were determined to be subject to the requirements of the U.S. DOE Office of Civilian Radioactive Waste Management (OCRWM) *Quality Assurance Requirements and Description* (QARD) (DOE 2000). This evaluation is documented in CRWMS M&O (1999c and d) and Wemheuer 1999 (activity evaluations for work packages WP 1401213UM1 and WP 1401213SM1). The activities associated with the preparation of this ICN 1 were determined to be subject to the requirements of the QARD pursuant to the Activity Evaluation conducted in accordance with AP-2.21Q, *Quality Determinations and Planning for Scientific, Engineering, and Regulatory Compliance Activities* and documented in the TWP (CRWMS M&O 2000c). Both the initial AMR Rev. 00 and ICN 1 were prepared in accordance with procedure AP-3.10Q, *Analyses and Models*. The development plan (CRWMS M&O 1999b) was prepared in accordance with AP-2.13Q, *Technical Product Development Planning*, and the Technical Work Plan was developed in accordance with AP-2.21Q. The conclusions in this AMR do not affect the repository design or permanent items as discussed in QAP-2-3, *Classification of Permanent Items*.

This document is a compilation and synthesis of data and information collected under other activities and reported elsewhere in published literature and in Yucca Mountain Site Characterization Project (YMP) reports and technical databases. All of the YMP site characterization work or activities summarized in this report were subject to QARD requirements. The quality assurance (QA) status of the YMP data used in this report is determined by the activities under which they were generated, with the specific controls noted in scientific notebooks associated with those activities.

The work activities documented in this AMR depend on electronic media to store, maintain, retrieve, modify, update, and transmit quality-affecting information. The applicable process controls identified through AP-SV.1Q, *Control of Electronic Management of Data*, are implemented for the activities documented in this AMR through procedure LANL-YMP-QP-S5.01, *Electronic Data Management*.

INTENTIONALLY LEFT BLANK

3. COMPUTER SOFTWARE AND MODEL USAGE

The computer software codes used in this AMR are listed below. The qualification status of each code is indicated in the electronic Document Input Reference System (DIRS) database. The software was obtained from Configuration Management (CM) unless otherwise stated. Input files used with the software codes are identified in the respective discussions in Section 6; the outputs are listed in Section 7.3.

1. *Software*: FEHM Version (V) 2.00 [Software Tracking Number (STN): 10031-2.00-00], Sun Ultra Sparc, Unix System

   Used for: Transport simulations

FEHM is a finite-element heat and mass transfer numerical code (Zyvoloski et al. 1995). Version 2.00 of the FEHM application has been tested and verified for a variety of different types of transport problems, including matrix and fracture reactive transport. Detailed information about the verification can be found in the report by Dash et al. (1997). The software is appropriate for the application and was used only within a range for which it was validated.

2. *Software*: TRACRN V1.0 (STN: 10106-1.0-00), Sun Ultra 2, Unix System

   Used for: Solving flow and transport equations

The TRACRN V1.0 computer code solves the equations of transient two-phase flow and multicomponent transport in deformable, heterogeneous, sorptive, porous media. Solution is obtained by an implicit finite difference scheme for flow and a semi-implicit or implicit approach for transport. TRACRN can be used to study radioactive waste migration from repositories in unsaturated and saturated media, soil water movement, environmental restoration of chemically polluted soils and groundwaters, and the migration of volatile organic plumes. The software is appropriate for the application, and was used only within a range for which it was validated.

3. *Software*: RTA V1.1 (STN: 10032-1.1-00), Sun, Unix System

   Used for: Obtaining field and laboratory transport predictions and preliminary interpretations of transport data acquired in tracer tests in saturated media

RTA (Reactive Transport Application) is a software package that consists of two complementary computer models that can be used to predict and interpret tracer responses in laboratory or field tracer tests in dual-porosity media. The two models are the semianalytical code, RELAP, and the 2-D finite-difference code, RETRAN. The software is appropriate for the application and was used only within a range for which it was validated.

4. *Software*: LAGRIT V1.0 (STN: 10212-1.0-00), SUN Solaris, Unix System, verification in process according to AP-SI.1Q, *Software Management*

   Used for: Developing the grid for the Busted Butte Phase-1A model

The LAGRIT code has been adapted from its original application for use in generating hydrogeologic computational grids. Computational grids are generated using any of a number of mechanisms, from hand numbering, to simple automated rectilinear numbering, to LAGRIT. All grids have been tested for accuracy by running test simulations (including a linear heat gradient and steady-state flow calculations). A procedure for qualifying grids, independent of the method of generation, is currently being developed, and all grids will be fully tested to this procedure. The software is appropriate for the application and was used only within a range for which it was developed.

5. *Software*: Zombie V3.0 (STN: 10298-3.0-00), Unix System, verification in process

   Used for: Collection and processing of electrical-resistance tomography (ERT) data

Zombie V3.0 is data-acquisition-control software written in LabView V3.0. The computer codes and software routines that comprise Zombie are to be qualified in accordance with AP-SI.1Q, *Software Management*. The data-acquisition-control and data-processing software is used as part of the electrical resistance tomography (ERT) system. Electrical resistance tomography is a geophysical imaging technique that is used to map subsurface resistivity. The ERT measurements consist of a series of voltages and current measurements from buried electrodes using an automated data-collection system. The data are then processed to produce electrical resistive tomographs using state-of-the-art data inversion algorithms. These measurements are used to calculate tomographs that show the spatial distribution of changes in subsurface resistivity. The software is appropriate for the application and was used only within a range for which it was developed.

6. *Software*: STO-UNSAT V1.0 (STN: 10292-1.0LV-00), Unix System, verification in process according to AP-SI.1Q, *Software Management.*

   Used for: Stochastic method simulations for Busted Butte Phase-1A fluid flow

STO-UNSAT is a numerical code for multiphase flow using a stochastic differential equation approach. It is currently being tested and verified for a range of multiphase flow problems. The software is appropriate for the application and was used only within a range for which it was developed.

7. *Software*: CART V1.0 (STN: 10046-1.0-00), Sun, Unix System

   Used for: Collection and processing of ground-penetrating radar tomography (GPR-T) data

The GPR-T method involves the emplacement of modified surface radar into a rock formation and transmission of high-frequency electromagnetic (radar) signals through the formation to a receiving antenna. The electrical properties of the subsurface material, which are determined in part by its moisture and chemical content, greatly influence the propagation of the transmitted signal and whether it travels at a high or low velocity. The transmitted signals may be represented as multiple-ray paths crossing through a zone of interest within the block. If sufficient ray paths are recorded, a tomographic image may be obtained through computer processing using CART V1.0. The information extracted from such data consists of the transit time, which depends on the wave velocity. This information, in the form of a processed radar velocity tomogram, offers a high-resolution approach to monitoring the changes in moisture and chemical content occurring in the rock over the duration of the tracer-injection experiment at the Busted Butte underground test facility. The software is appropriate for the application and was used only within a range for which it was validated.

In addition, the following commercially available software was used in this AMR. Only built-in standard functions were used. No software routines or macros were used with this software. The software is appropriate for the application and was used only within a range for which it was developed.

1. *Software*: DeltaGraph, Version 4.0.1, Macintosh

   Used for: Plotting graphs

   The software was used for illustration purposes only. The results were not used in any subsequent analysis or modeling subject to QARD requirements.

2. *Software*: Microsoft Excel, Version 5, Macintosh

   Used for: Spreadsheet analysis of geochemical data

   Only standard Excel functions were used.

3. *Software*: Microsoft Excel 97 SR-1

   Used for: Calculating averages and standard deviations, plotting and graphing results, and performing linear regressions on specific data sets.

   Only built-in standard functions were used.

The UZTT model presented in this AMR is a three-dimensional flow and transport model in the unsaturated zone. It encompasses field-scale experiments, laboratory experiments and analyses, geophysical methods, and numerical modeling. No previously documented models are used to support the analyses or modeling activities reported in this AMR.

INTENTIONALLY LEFT BLANK

4. INPUTS

4.1 DATA AND PARAMETERS

Locations, brief descriptions, and data tracking numbers (DTN) that were used as input for this AMR are listed in Tables 1a through 1f. The qualification status of data inputs is indicated in the electronic Document Input Reference System (DIRS) database. All input data are appropriate for the intended use of this AMR. Data qualification efforts, as needed, will be conducted in accordance with AP-SIII.2Q, *Qualification of Unqualified Data and the Documentation of Rationale Accepted Data*, and documented separately from this AMR.

Input data described in Tables 1a through 1d and used in Sections 6.4 through 6.7 of this report include laboratory results of radionuclide experiments using waters either collected from Yucca Mountain or synthesized to reflect Yucca Mountain waters and materials either collected from the field or synthesized in the laboratory. Parameters used are the radionuclide and colloid type and concentration, percent sorbed onto various substrates, and attachment/detachment rates for radionuclides onto and off of various substrates.

Table 1a gives the input data for sorption and sorption modeling studies discussed in Section 6.4.

Table 1a. Sorption and Sorption Modeling Studies

Data Tracking Number	Description	Location in this AMR
LA0002JC831341.001	Depth intervals and bulk densities of alluviums	Table 9
LA0002JC831341.002	Quantitative X-ray diffraction (QXRD) results of three alluviums	Table 10
LA0010JC831341.002, LA0010JC831341.003, LA0010JC831341.004, LA0010JC831341.005, LA0010JC831341.006, LA0010JC831341.007	Batch sorption distribution coefficients for plutonium, neptunium, cesium, strontium, selenium, and uranium onto various tuffs and minerals in different groundwaters	Table 4, Figs. 1–8, Section 6.4.2, Table 11
LAIT831361AQ95.003	Transport data of H-3, Np, and Tc-95m collected to calculate retardation coefficients using J-13 and UE-25 p#1 waters	Table 3
LA0003JC831341.001*	Alluvium sorption data for ^{237}Np	Figs. 9, 10
LA0003JC831341.002*	Alluvium sorption data for ^{99}Tc	Figs. 11, 12
LA0003JC831341.003	Alluvium sorption data for ^{129}I	Fig. 13
LA0004AM831341.001	Uranium sorption coefficients for minerals and tuff under oxidizing conditions in J-13 water	Tables 7 and 8
LA0004AM831341.002	Np sorption onto clinoptilolite-rich tuff in J-13 water under atmospheric conditions with Ka, Kd, and SA	Tables 5, 6, 8
LAAM831311AQ98.005	Geochemical field measurements for UE-25 WT#17, 27-Jan-98	Sec. 6.4.3
LAAM831311AQ98.007	Flow-thru cell and static measurements at UE-25 WT#3, 22-Jun-98	Sec. 6.4.3
LAAM831311AQ98.008	Analysis of bailed sample for UE-25 WT#17, 04-Jun-98	Sec. 6.4.3

Data Tracking Number	Description	Location in this AMR
LAAM831311AQ98.010	Static measurements for US-25 WT#17, 01-Jul-98	Sec. 6.4.3
LA9907AM831234.003	Downhole Eh and pH measurements for NC-EWDP-01S, 11-Jan-99	Sec. 6.4.3
LA0004AM831234.001	Flow-through cell measurements for NC-EWDP-01S, 22-Feb-99 and 23-Feb-99	Sec. 6.4.3
LA9907AM831234.009	Flow-through cell measurements for NC-EWDP-01S, NC-EWDP-03S, NC-EWDP-09SX, 5/17/99, 5/18/99. 5/20/99	Sec. 6.4.3
LA9907AM831234.010	Flow-through cell measurements for SD6-ST1, 02-Jun-99 and 08-Jun-99	Sec. 6.4.3
LA9907AM831234.011	Flow-through cell measurements for AD-2, 10-Jun-99	Sec. 6.4.3
LA0004AM831234.002	Downhole probe measurements for NC-EWDP-03S, 23-Feb-99	Sec. 6.4.3
MO0007MAJIONPH.011	Chemical composition data and laboratory analyses for groundwater from Yucca Mountain test wells	Sec. 6.4.3
MO0007MAJIONPH.003	Major ion and pH for borehole USW-G2	Sec. 6.4.3
MO0007MAJIONPH.013	Chemical composition of groundwater and the locations of permeable zones in the Yucca Mountain area	Sec. 6.4.3
GS930908312323.003	Hydrochemical data from field tests and lab analyses of water samples collected at various field stations	Sec. 6.4.3
GS950808312322.001	Field, chemical, and isotopic data describing water samples collected in Death Valley National Monument and at various boreholes and around Yucca Mountain, Nevada, between 1992 and 1995	Sec. 6.4.3
MO0007MAJIONPH.005	Field, chemical, and isotopic data from precipitation sample collected behind service station in Area 25 and groundwater samples collected at various boreholes, 10/06/97 to 07/01/98	Sec. 6.4.3
GS990808312322.001	Field and isotopic data from groundwater samples from wells in the Amargosa Valley and NTS	Sec. 6.4.3

* used as corroborative information

Table 1b gives the input data for the dynamic transport studies discussed in Section 6.5.

Table 1b. Dynamic Transport Studies

Data Tracking Number	Description	Location in this AMR
LA000000000106.001	Np sorption column measurements	Table 11
LA0001JC831361.001	Radionuclide transport through saturated fractures	Figs. 23–26
LA0001JC831361.002*	Radionuclide transport through saturated fractures	Figs. 25, 26
LA0002JC831341.003	Selenium batch adsorption on nonwelded zeolitic tuff	Table 12
LA0002JC831361.001	Column studies using G4-268 devitrified tuff with J-13 well water and radionuclides (H-3 and Pu-239)	Fig. 16
LA0002JC831361.002	Column studies using G4-268 devitrified tuff with synthetic UE-25 p#1 water and radionuclides (H-3 and Pu-239)	Fig. 17
LA0002JC831361.003	Column studies using G4-268 devitrified tuff with J-13 well	Fig. 18

Data Tracking Number	Description	Location in this AMR
	water and radionuclides (H-3 and Tc-95m)	
LA0002JC831361.004	Column studies using GU3-1414 vitric tuff with J-13 well water and radionuclides (H-3 and Tc-95m)	Fig. 19
LA0002JC831361.005	Column studies using G4-1533 zeolitic tuff with J-13 well water and radionuclides (H-3 and Tc-95m)	Fig. 20
LA0004JC831361.001*	Preliminary retardation data for selenium transport through unsaturated tuffs	Fig. 21
LA0004JC831224.001*	Preliminary unsaturated hydraulic conductivities of tuffs from Yucca Mountain boreholes, Tunnel Bed 5 (G-Tunnel) and Bandelier tuff (Los Alamos)	Fig. 22
LA0010JC831341.007	Batch sorption distribution coefficients for neptunium onto various tuffs and minerals in different groundwaters	Table 11
LAIT831361AQ95.001	Radionuclide elution data through crushed tuff columns	Figs. 14 and 15
LAIT831361AQ95.003	Characteristics of column experiments and batch sorption values	Tables 14, 15

* used as corroborative information

Table 1c gives the input data for diffusion transport studies in the laboratory discussed in Section 6.6.

Table 1c. Diffusion Transport Studies in the Laboratory

Data Tracking Number	Description	Location in this AMR
LA000000000034.001	Diffusion of sorbing and non-sorbing radionuclides	Figs. 27–30, Table17
LA000000000034.002	Diffusion measurements data of rock beaker experiments (modeled using TRACRN), 11/25/1991 to 03/25/1992	Table 16
LAIT831362AQ95.001	Diffusion data for various radionuclides in various tuffs in different groundwaters	Figs. 31-33

Table 1d gives the input data for colloid-facilitated radionuclide transport discussed in Section 6.7.

Table 1d. Colloid-Facilitated Radionuclide Transport

Data Tracking Number	Description	Location in this AMR
LA0003NL831352.002	K_d values of ^{239}Pu on colloids of hematite, montmorillonite, and silica in natural and synthetic groundwaters	Sec. 6.7.3
LA0005NL831352.001	Sorption distribution coefficients of ^{243}Am on colloids of hematite, montmorillonite, and silica as a function of time, temperature, and concentration in natural and synthetic waters	Sec. 6.7.3
LA0002SK831352.001	Total colloidal particles concentration and size distribution in groundwaters from the Nye County early warning drilling program	Sec. 6.7.2

LA0002SK831352.002	Total colloidal particles concentration and size distribution in groundwaters around Yucca Mountain	Sec. 6.7.2
LA9910SK831341.005	Total colloidal particles concentration and size distribution in NTS-ER-20-5-1, NTS-ER-20-5-3, and J-13 groundwater	Sec. 6.7.2
LAIT831341AQ97.002	Reversibility of radionuclide sorption	Sec. 6.7.3

Input data described in Table 1e and discussed in Section 6.8 generally come from two sources: measured data from samples taken from the UZTT or data derived from model simulations of the UZTT. Measured data include: mineralogy, hydrologic parameters, sorption, solubility, tracer concentrations, and breakthroughs from collection pad analyses, etc. Simulation input data include: as-needed measured data (from the above list) and some data from other YMP sources as noted in the text. Simulation output data include: fluid distributions, tracer distribution in the rock, and tracer breakthrough times.

Table 1e. Busted Butte Unsaturated Zone Transport Test

Data Tracking Number	Description	Location in this AMR
GS990308312242.007	Physical and hydraulic properties of core samples from Busted Butte boreholes	Sec. 6.8.3.3
GS990708312242.008	Physical and hydraulic properties of core samples from Busted Butte boreholes	Sec. 6.8.3.3
GS000408312231.003, GS940508312231.006, GS950408312231.004, GS950608312231.008 GS951108312231.009, GS960808312231.001, GS960808312231.003, GS960808312231.005, GS990408312231.001	Physical and hydraulic properties of cores from Yucca Mountain boreholes	Sec. 6.8.6.1.2.1
LB970601233129.001	The site-scale unsaturated zone model of Yucca Mountain, Nevada	Sec. 6.8.6.1.2.1
LA9909WS831372.001, LA9909WS831372.002	Measurements of tracer breakthrough concentrations (bromide, 2,6-DFBA, fluorescein, pyridone, and lithium) in UZTT Borehole 6	Figs. 58a–e
LA0004WS831372.002	Radionuclide sorption of Np, Pu, and Am on rock samples from Busted Butte	Table 28
LA9909WS831372.005	Descriptions of outcrop samples collected from Busted Butte; quantitative x-ray diffraction results for samples from lower Tpt section	Table 20 Table 21
LA9909WS831372.006*	Mineral abundances in Calico Hills; surface samples from Busted Butte	Table 22
LA9909WS831372.007	Quantitative X-ray diffraction results for USW H-5 core and drill cuttings	Table 24
LA9909WS831372.010	Mineral abundances in Calico Hills Formation (Tac) samples from auger hole AUG-1 in the floor of the Busted Butte test alcove	Table 23
LA9909WS831372.011*	Preliminary measured sorption coefficients for lithium, manganese, cobalt, and nickel	Table 26
LA9909WS831372.014	Measurements and specifications of fluorescent polystyrene	Sec. 6.8.5.4

Data Tracking Number	Description	Location in this AMR
	microspheres	
LA9909WS831372.015	Chemical composition of Busted Butte pore water with UE-25 J-13 groundwater for comparison using ICPAES analysis	Table 29
LA9909WS831372.016	Chemical composition of Busted Butte pore water with UE-25 J-13 groundwater for comparison using ion chromatography	Table 29
LA9909WS831372.017	Chemical composition of Busted Butte pore water with UE-25 J-13 groundwater for comparison using pH measurements	Table 29
LA9909WS831372.018	Chemical composition of Busted Butte pore water with UE-25 J-13 groundwater for comparison using gravimetric moisture content analysis	Table 29
LA9910WS831372.008	Busted Butte transport test: Gravimetric moisture content and bromide concentration in selected Phase 1A rock samples	Sec. 6.8.5.3.1.2
LA9910WS831372.009	QXRD data for UZTT Busted Butte samples	Sec. 6.8.5.1.2.4
LASC831321AQ98.003	Quantitative X-ray diffraction results for samples from drill hole USW SD-6	Table 25
LB00032412213U.001	Ground penetrating radar (GPR) tomography data	Sec. 6.8.4.1.4, Figs. 45–50
LL990612704244.098	ERT data for Busted Butte	Sec. 6.8.4.2.7, Figs. 55, 56
MO0004GSC00167.000	Coordinate of boreholes in the test alcove and running drift, Busted Butte test facility	Sec. 6.8.4.1.4, Figs. 45-49; Sec. 6.8.7.2, Figs. 87-89

* used as corroborative information

Table 1f gives the input data for C-wells field and laboratory transport testing discussed in Section 6.9.

Table 1f. C-Wells Field and Laboratory Transport Testing

Data Tracking Number	Description	Location in this AMR
GS970708312315.001	Concentrations of 2,6 DFBA and pyridone from tracer tests conducted at the C-wells complex, 1/8/97–7/11/97	Table 54
GS981008312314.002	Pump test data collected at the C-wells complex, 1/8/97–3/31/97 (used for packer locations)	Sec. 6.9
GS981008312314.003*	Pumping test data collected at the C-wells complex, 5/7/96–12/31/96 (bottom hole coordinates)	Sec. 6.9
LA0002PR831231.001	Bullfrog reactive tracer test data	Figs. 96, 98, Table 54
LA9909PR831231.003	Transport parameters deduced from fits of the Bullfrog Tuff tracer responses	Tables 51, 53, 55, Fig. 100
LA9909PR831231.005	Transport parameters deduced from fits of the Prow Pass Tuff tracer responses	Tables 52, 53, 55 Fig. 102
LAPR831231AQ99.001	Normalized pentafluorobenzoic (PFBA) acid responses in two different tracer tests in the Bullfrog Tuff, Fig. 98; Log normalized tracer responses in the Prow Pass Tuff multiple tracer test, Fig. 99	Figs. 97-99

MO9906GPS98410.000	List of boreholes	Fig. 94
MO0012BRLI25C2.000	Br and Li data from laboratory tests	Table 53
MO0012PERMCHOL.000	Permeability data from C-holes core	Table 55
MO0012POROCHOL.000	Porosity data from C-holes core	Table 55
MO0012SORBCHOL.000	Sorbing element concentration data for C-holes	Fig. 101
MO0012CATECHOL.000	Cation exchange capacity data for C-well tuff	Sec. 6.9.3.1
MO0012MINLCHOL.000	Mineral abundance data from C-hole tuff	Sec. 6.9.3.1

* Information for which confirmation is not required.

Table 1g is a listing of the scientific notebooks used in this AMR.

Table 1g. Scientific Notebooks Used

Description of Information	Notebook Identifier	Page Number	Reference	YMP M&O SNR	Location in this AMR
Phase-2 testing	LA-EES-5-NBK-98-010	79	Bussod (1998)	SN-LANL-SCI-040-V1	Sec. 6.8.2.2.2
Phase-1A results	LA-EES-5-NBK-98-018	1-61	Soll (1997)	SN-LANL-SCI-048-V1	Sec. 5, Assumption 16, Sec. 6.8.8
Phase-1A results	LA-EES-5-NBK-98-017	1-78	Zhang (1998)	SN-LANL-SCI-047-V1	Sec. 6.8.8

4.2 CRITERIA

This AMR complies with the DOE interim guidance (Dyer 1999). Subparts of the interim guidance that apply to this analysis are those pertaining to the characterization of the Yucca Mountain site (Subpart B, Section 15), the compilation of information regarding geochemistry and mineral stability of the site in support of the License Application (Subpart B, Section 21(c)(1)(ii)), and the definition of geochemical parameters and conceptual models used in performance assessment (Subpart E, Section 114(a)).

4.3 CODES AND STANDARDS

No specific formally established codes or standards have been identified as applying to this analysis and modeling activity. This activity does not directly support License Application (LA) design.

5. ASSUMPTIONS

Assumptions used in the sorption work include the following.

Assumption 1. It is assumed that radionuclide sorption parameters measured in laboratory experiments are not significantly affected by microbial activity. The rationale for accepting this assumption is that microbial growth in the test apparatus is not expected to be significant given the short times that are typical of sorption experiments (days to a few weeks), and the presence of significant microbial activity would be marked by turbid conditions in the solutions. This assumption primarily applies to sorption data obtained for elements that have different redox states under the environmental conditions expected at Yucca Mountain and affects parts of Section 6 in which sorption data for these radionuclides are discussed (Sections 6.4, 6.5, 6.6, 6.7, 6.8.5, and 6.9.3). This assumption requires confirmation.

Assumption 2. It is assumed that sorption parameters determined in laboratory experiments using crushed tuff are applicable to transport through solid tuff matrix in the field. Experiments with solid rock columns are generally infeasible because of the long time required to elute sorbing radionuclides from such columns. To investigate the effects of crushing, results of sorption experiments on thin (2-mm) intact tuff wafers were compared to those for columns of crushed tuff for alkali and alkaline earth elements, which are simple cations (strontium, cesium, barium). The two data sets were found to be quite similar (Rundberg 1987, p. 18). Furthermore, experiments with sorption using different particle sizes of tuff material also yielded similar results for cesium, strontium, and neptunium, suggesting that sorption parameters are not a strong function of the degree of crushing (Rogers and Meijer 1993). In addition to the effect of crushing on affinity for sorption, there is also the potential for the measured sorption coefficient (K_d) to be affected by the use of a water/rock ratio in the laboratory that is much higher than that for in-situ rock. Crushed-rock column experiments involve a lower water/rock ratio than used in crushed-rock batch experiments and yield consistent results for alkali and alkaline earths, but this assumption has not been adequately tested for actinides. This assumption applies to all sorption results and affects parts of Section 6 in which sorption data are discussed (Sections 6.4, 6.5, 6.6, 6.7, 6.8.5, and 6.9.3). This assumption requires confirmation for actinide elements.

Assumption 3. It is assumed that waters from wells J-13 and p#1 bound the chemistry of groundwaters at Yucca Mountain. Sorption is a function of water chemistry and the type of tuff at Yucca Mountain. The concentrations of the major cations and anions in unsaturated-zone groundwaters at Yucca Mountain appear to be intermediate between the saturated-zone tuffaceous waters (e.g., from well J-13) and waters from the Paleozoic carbonate aquifer (from well p#1). Consequently, the assumption made for the PA recommendations was that waters from wells J-13 and p#1 bound the chemistry of groundwaters at Yucca Mountain, and these compositions were used in the sorption experiments. (The compositions of natural and synthetic J-13 or p#1 waters used in each experiment are found in the documentation associated with the DTNs for those experiments.) It was recognized that pH and Eh (i.e., redox state) of in-situ waters may lie outside of the range of the values measured for these two waters. For this reason, sorption experiments were done under a variety of pH conditions. However, Eh was not directly controlled in the sorption experiments; therefore, the potential range of in-situ Eh conditions in Yucca Mountain waters were not directly addressed by the experiments. This assumption

influences parts of Section 6 in which sorption data are discussed (Sections 6.4, 6.5, 6.6, and 6.7). This assumption requires confirmation for redox conditions for Np, Pu, Tc, U, and Se.

Assumption 4. From the perspective of transport modeling, it is assumed that hydrogeologic strata at the site can be classified into five representative rock types: iron oxides, devitrified tuff, vitric tuff, zeolitic tuff (Wilson et al. 1994, section 9.3.1), and alluvium material. For the performance assessment calculations, these rock types are assigned sorption coefficient distributions for each radionuclide of interest (Tables 2a and 2b). It is assumed that the sorption coefficient distributions for a given rock type can be determined from a limited number of batch experiments, and that the available data are adequately representative of the hydrogeologic rock types used in the transport calculations. This assumption applies to all sorption results and affects parts of Section 6 in which sorption data are discussed (Sections 6.4, 6.5, 6.6, and 6.7). The assumption requires confirmation for alluvium.

Assumption 5. It is assumed that sorption parameters measured using a single radionuclide are applicable to the case where more than one radionuclide is present, i.e., it is assumed that competitive effects are negligible. For transport in the far field, the rationale for accepting this assumption is that solutes emanating from the repository would be transported at different rates (due to different sorption characteristics) such that the groundwater in the far field would not contain multiple radionuclides at significant concentrations. However, the assumption requires confirmation for near-field sorption behavior. This assumption applies to all sorption results and affects parts of Section 6 in which sorption data are discussed (Sections 6.4, 6.5, 6.6, and 6.7).

Assumption 6. Nonlinear isotherms imply the sorption coefficient is not a constant value. It is assumed that the variability of the sorption parameter as a function of concentration can be adequately captured by lowering the minimum K_d value defined for the sorption distribution function so as to include the reduced K_d expected under high concentration conditions. This assumption does not require confirmation because radionuclide concentrations in the groundwater are not expected to reach concentrations where the non-linearity would be significant. This assumption applies to all sorption results and affects parts of Section 6 in which sorption data are discussed (Sections 6.4, 6.5, 6.6, and 6.7).

Assumption 7. It is conceivable that flow rates in the natural system may be sufficiently fast that sorption equilibrium may not be achieved during solute transport through the matrix or fractures. If so, then a smaller sorption coefficient may apply than for the case where equilibrium is assumed. It is assumed that the possible presence of non-equilibrium conditions is adequately addressed by lowering the minimum K_d value assumed in the sorption coefficient distributions for those radionuclides with slow sorption reaction kinetics (primarily, Pu). This assumption requires confirmation and could best be evaluated by a modeling analysis providing bounds for in-situ flow velocities at Yucca Mountain to be compared against estimates of the velocity limits for which adsorption kinetics for various radionuclides would be a concern (e.g., Rundberg 1987, Table XII). This assumption applies to all sorption results and affects parts of Section 6 in which sorption data are discussed (Sections 6.4, 6.5, 6.6, and 6.7).

Assumption 8. It is assumed that sorption experiments conducted under saturated conditions yield results that are also applicable to unsaturated conditions. The rationale for accepting this

assumption is that it has been verified (to a very limited extent) in experiments using Se as the sorbing ion (DTN: LA0010JC831341.004). Results for batch experiments under saturated conditions are similar to those obtained for unsaturated solid rock core (LA0010JC831341.004 and Section 6.5.2.2). However, this assumption requires confirmation for all radionuclides of concern. This assumption applies to all sorption results and affects parts of Section 6 in which sorption data are discussed (Sections 6.4, 6.5, 6.6, and 6.7).

Assumption 9. It is assumed that the characteristics of J-13 or p#1 groundwaters that influence sorption parameters can be adequately represented by solutions prepared in the laboratory to simulate these water compositions. This assumption requires confirmation. This assumption applies to all sorption results and affects parts of Section 6 in which sorption data are discussed (Sections 6.4, 6.5, 6.6, and 6.7).

Assumption 10. It is assumed that decreases in radionuclide concentrations in solution during sorption experiments—which is the basis for estimating the value of the sorption coefficient, or K_d—are due to sorption and not precipitation of the radionuclide being studied. The validity of this assumption has been tested by comparing the K_d values obtained from batch-sorption tests for consistency with those obtained from crushed-rock and solid-rock column studies (Section 6.5; Triay et al. 1997, Ch. V, Sections A and B). This assumption does not require confirmation.

Assumptions used in the UZTT are listed below (Assumptions 11 through 21). The UZTT results presented in this report are preliminary. Work that is currently being conducted on this activity directly addresses many of these assumptions.

Assumption 11. The rocks identified as Calico Hills vitric (CHv) and Topopah Spring welded (TSw) hydrogeologic units at Busted Butte are part of the same-named units that exist under the repository and are also representative of those same units under the repository. The basis for this assumption is the equivalent location of the units within the rock sequence at Busted Butte and Yucca Mountain (including the repository), as well as an understanding of the geologic processes that formed the region. Mineralogic analyses of samples from Busted Butte, compared to those collected from boreholes on Yucca Mountain, support this assumption (Section 6.8.3.2; Bussod et al. 1997, Section 2.2 and 2.3). Therefore, this assumption does not require further confirmation. This assumption is used in Section 6.8.

Assumption 12. The presence of boreholes does not unduly influence the results of the transport test. This assumption has been tested through numerical assessment of borehole influence as shown in Section 6.8.2. Figure 42 of that section shows that solute travel time is disturbed by less than 20%. This assumption does not require further confirmation. This assumption is used in Section 6.8.

Assumption 13. The principal barrier to radionuclide migration in the unsaturated zone at Yucca Mountain is the Calico Hills nonwelded hydrogeologic unit (Montazer and Wilson, 1984; Ortiz et al., 1985), and the Busted Butte test location sufficiently represents the vitric portions of this unit to produce data applicable to Yucca Mountain flow and transport models. The information in Section 6.8.3 and Bussod et al. (1997, Sections 2.2 and 2.3) documents the representativeness of the Busted Butte site with respect to lithology, mineralogy, and hydrologic properties.

Therefore, this assumption does not require further confirmation. This assumption is used in Section 6.8.

Assumption 14. The vitric units of the Calico Hills Formation play a significant role as a barrier to transport (beyond the zeolitic CH). This is a primary assumption that the UZTT was designed to test. Laboratory studies supporting this assumption are discussed in Section 6.5. However, due to the uncertainty of the scaling of laboratory studies to the natural setting, this assumption requires further confirmation. The assumption is used in all of Section 6.8 but primarily in Section 6.8.1.

Assumption 15. The test block was minimally disturbed (saturation, in situ water distribution, fractures, faults) during construction of the test and is assumed to represent natural conditions. Precautions, such as dry drilling, were taken to avoid disturbance of the test block during construction, and no unexpected disturbances have been observed during visual inspection of the integrity of the test block. On this basis, plus the assessment that the effects of an undetected disturbance on subsequent tests will be small compared to intentionally induced effects, the assumption does not require further confirmation. This assumption is used throughout Section 6.8. and particularly in Sections 6.8.2, 6.8.6, and 6.8.7.

Assumption 16. The UZTT test blocks were at a steady-state background moisture distribution before injection. The UZTT is located in an otherwise undisturbed area of the Yucca Mountain site. It is assumed that the construction of the UZTT and the test design caused minimal disturbance of the system (see previous assumption), and that any change caused by construction would quickly return to an equilibrium state within the time between tunnel excavation and beginning injection. Models indicate that any perturbations would disappear in less than 14 days (Soll 1997, p. 21, Phase 1A results), which is before injection started. Therefore, this assumption does not require verification. This assumption is used throughout Section 6.8.

Assumption 17. The different emitters in any given borehole are all injecting at the same rate. All emitters are identical. Total injection quantity is carefully monitored, and any variation can be identified and incorporated into analyses. Because each emitter is designed to be identical, this assumption does not require confirmation. This assumption is used in Section 6.8.5.

Assumption 18. In selecting the tracers, fluorescein, bromide, and FBAs were assumed to be significantly less sorbing than the metals and were referred to as nonreactive. These tracers are accepted by the hydrologic community as conservative. This assumption has been confirmed in practice, and no further confirmation is required. This assumption is used in Section 6.8.5.

Assumption 19. Hydrogeologic parameters for the same units available in the YM database are reasonable estimates for the parameters at Busted Butte. Prior to Busted Butte specific parameters being available, the best estimate is reported data from the same hydrologic unit at Yucca Mountain. This assumption does not require confirmation. This assumption is used in Sections 6.8.6 and 6.8.7.

Assumption 20. This assumption not used.

Assumption 21. The stochastic parameters contained in *Stochastic Hydrogeologic Units and Hydrogeologic Properties Development for Total-System Performance Assessments*, (Schenker et al. 1995), are representative of Busted Butte properties. The intended use of this information is for scoping and sensitivity only; therefore, these data are acceptable to use as a baseline and require no further confirmation. This assumption is used in Section 6.8.6.

Assumptions used in the C-wells work include the following.

Assumption 22. It is assumed that all tracers experience the same mean residence time and longitudinal dispersivity. The rationale for accepting this assumption as valid is that the tracers were injected simultaneously. This assumption influences the interpretation of the tracer tests and affects all of Section 6.9.2 where tracer tests are discussed. This assumption does not require confirmation.

Assumption 23. Bromide and PFBA tracers were assumed to be conservative (nonsorbing). This assumption is supported by laboratory experiments in which the K_d values for these tracers were statistically indistinguishable from zero (i.e., no sorption) (Reimus et al. 1999). This assumption influences the interpretation of the tracer tests and affects all of Section 6.9.2 where tracer tests are discussed. This assumption does not require confirmation.

Assumption 24. It is assumed that bromide and PFBA diffusion coefficients differ by a factor of 3, with the bromide coefficient being the larger of the two, and that the lithium diffusion coefficient is twice that of PFBA. This assumption is supported by laboratory experiments for bromide and PFBA diffusion coefficients (DTN: LA9909PR831231.004), and by values published for lithium (Newman 1973, p. 230). This assumption influences the interpretation of the tracer tests and affects all of Section 6.9.2 where tracer tests are discussed. This assumption does not require confirmation.

Assumption 25. The microspheres were assumed to not diffuse into the matrix (i.e., the diffusion coefficient is effectively zero). The rationale for accepting this assumption results is that the diffusion coefficient for microspheres is smaller than those for solutes by about three orders of magnitude (based on application of the Stokes-Einstein equation) (Bird et al. 1960, p. 514). Consequently, the low diffusivity for microspheres, in combination with matrix tortuosity, limits the rate and extent to which microspheres can diffuse into the matrix. This assumption influences the interpretation of the tracer tests and affects all of Section 6.9.2 where tracer tests are discussed. This assumption does not require confirmation.

INTENTIONALLY LEFT BLANK

6. ANALYSIS/MODEL

6.1 INTRODUCTION

This analysis directly supports four Principal Factors for the Post-Closure Safety Case as discussed in AP-3.15Q *Managing Technical Product Inputs*: (1) Solubility Limits of Dissolved Radionuclides, (2) Dilution of Radionuclide Concentrations in the Geologic Setting, (3) Retardation of Radionuclide Migration in the Unsaturated Zone, and (4) Retardation of Radionuclide Migration in the Saturated Zone. Therefore, this AMR is deemed to be of Level 1 importance in addressing the factors associated with the post-closure safety case.

This section summarizes field and laboratory data and interpretations that were collected or developed in laboratory activities and that are relevant to the development and testing of conceptual and numerical transport models of the saturated zone at Yucca Mountain. These data include sorption coefficients for the radionuclides of interest in various hydrologic units, transport data and modeling results from the C-Wells activity and the Busted Butte UZTT activity, measurements of hydrochemistry and Eh-pH conditions in groundwater, and parameters related to colloidal transport.

6.2 APPROACH

Radionuclide migration from a potential repository would be inhibited by several barriers, including the geochemical barriers of solubility and sorption. Sorption coefficients for radionuclides of interest were obtained using water and rock samples from the site (Assumptions 1–10 in Section 5). Sorption coefficients were obtained in batch-sorption experiments and saturated-column experiments. Experiments were performed at several pH levels to evaluate the impact of pH variations on the sorption coefficient. In general, oxidation/reduction conditions were oxidizing in all the experiments. A limited number of experiments were performed to evaluate the sorption of radionuclides during fracture flow. Similarly, a limited number of column experiments were carried out to evaluate whether or not batch-sorption coefficients could be used to model transport of reactive species in a dynamic (that is, flowing) system (Assumption 7 in Section 5). The potential effects of organics on actinide sorption were evaluated in batch-sorption experiments with model organic compounds in waters and rock samples from the site. Models were developed to explain the sorption coefficient data and to allow prediction of coefficient values under anticipated conditions. Batch experiments were also done to evaluate the sorption of radionuclides onto colloidal-sized materials. In this set of experiments, the issue of reversibility of the radionuclide sorption reactions was also addressed.

Effective diffusion coefficients for the radionuclides of interest were obtained in experiments with specially designed diffusion cells and beakers made of rock samples from the site. These experiments were performed with representative water and rock compositions from the site.

The applicability of this approach to the derivation of transport parameters was evaluated with two major field tests in which sorbing and nonsorbing tracers were injected into and recovered from hydrogeologic units representative of units between the proposed repository and the

accessible environment. The results of these tests were modeled with the codes to be used to model transport from the proposed repository at Yucca Mountain.

6.3 SOLUBILITY STUDIES

One of the objectives stated in CRWMS M&O (1999b) was an assessment of laboratory-derived radionuclide solubility limits to be used in performance assessment modeling of the site (CWRMS M&O 1999b). Solubility of radionuclide phases is the subject of a separate AMR (CRWMS M&O 2000a); none of these results are used in this AMR.

6.4 SORPTION STUDIES

6.4.1 Introduction

This section provides the sorption-coefficient data to be used in performance assessment calculations. This section also provides analysis of the sorption data for the elements of interest obtained in laboratory experiments by the YMP and from the literature. The laboratory data obtained include batch-sorption coefficients, crushed rock column and solid column experiments, fractured rock column experiments, and diffusion experiments.

6.4.2 Sorption Coefficients for Performance Assessment

The sorption-coefficient data to be used in performance assessment calculations are provided in the form of sorption-coefficient distributions. These sorption-coefficient distributions are contained in the Technical Product Output DTN: LA0003AM831341.001.

Sorption coefficients are required for the following chemical elements that represent the various radionuclides of interest:

- americium, thorium, zirconium, actinium, samarium, niobium, lead
- radium, strontium, cesium, lead, tin, plutonium
- neptunium, uranium, selenium, nickel, protactinium
- carbon, chlorine, technetium, iodine.

As will be shown later, this listing is generally in order of decreasing sorption potential.

The selection of the distributions provided in this section were based on a review of previous estimates (Wilson et al. 1994) and the qualified and corroborating data presented in this report. The results reflect the current best judgement of the author on the implications of these sources for estimating sorption-coefficient distributions to be used for the saturated zone. Many factors that determine sorption behavior were taken into account, such as: rock type, mineralogy, water chemistry, pH, reaction kinetics, competitive effects among sorbing constituents, and the presence or absence of microbial activity. The author also used his best judgement for

estimating distribution parameter values for the Unsaturated Zone, for which conditions differ from those in the Saturated Zone insofar as conditions are always oxidizing and porewaters generally have higher ionic strengths; hence more competitive ion effects, especially in zeolitic units. The distributions elicited for the Unsaturated Zone sorption parameter values are biased toward the tests that used p#1-water compositions, and those for the Saturated Zone parameter values. As in previous estimates (Wilson et al. 1994), two key assumptions were used to formulate the sorption-coefficient distributions. These assumptions were as follows (their technical basis is described in Section 5):

- Waters from Wells J-13 and p#1 bound the major ion chemistry of the groundwaters at Yucca Mountain (Assumption 3 in Section 5).

- The variations in rock type in Yucca Mountain can be reduced to three main classes: devitrified tuff, vitric tuff, and zeolitic tuff. Iron oxide was also added as a class to represent sorption on waste-package material (alluvium was added subsequent to the expert elicitation to represent sorption in the far field). It is assumed that hydrogeologic strata at the site can be classified as one of these representative rock types, that sorption coefficient distributions for a given rock type can be determined from a limited number of batch experiments, and that the sorption data are adequately representative of the rock types used in the transport calculations (Assumption 4 in Section 5; requires confirmation for alluvium).

Additional assumptions also underlie the selection of reasonable and technically defensible distribution parameters. These are described in Section 5 and include the following:

- It is assumed that sorption parameters determined in laboratory experiments using crushed tuff are applicable to transport through solid tuff matrix in the field (Assumption 2 in Section 5; requires confirmation for actinide elements).

- It is assumed that sorption parameters measured for a single radionuclide are applicable to the case where more than one radionuclide is present, that is, it is assumed that competitive effects are negligible (Assumption 5 in Section 5; requires confirmation for near-field conditions).

- It is assumed that the variability of the sorption parameter as a function of concentration can be adequately captured by lowering the minimum K_d value defined for the sorption distribution function so as to include the reduced K_d value expected under high concentration conditions (Assumption 6 in Section 5).

- It is assumed that in-situ flow rates are sufficiently slow that sorption equilibrium is achieved during solute transport (Assumption 7 in Section 5; requires confirmation for radionuclides with slow sorption reaction kinetic rates).

- It is assumed that sorption experiments conducted under saturated conditions yield results that are also applicable to unsaturated conditions (Assumption 8 in Section 5; requires confirmation).

- It is assumed that sorption parameters measured in laboratory experiments have not been significantly affected by microbial activity (Assumption 1 in Section 5; requires confirmation).

Table 2a shows the parameters for the sorption-coefficient distributions recommended for performance assessment for the unsaturated-zone units, and Table 2b shows the same parameters for saturated-zone units (DTN: LA0003AM831341.001). The parameters differ slightly for these two general types of environments because the higher ionic strength and higher redox potential of unsaturated-zone waters are expected to affect the sorption behavior of some elements relative to their behaviors in saturated-zone waters. The types of distributions considered include uniform, beta, and exponential beta distributions. The minimum and maximum values for each distribution are provided along with the expected value (E[x]) and the coefficient of variation (COV) for two of the types of distributions. The COV is defined as $\sigma[x]/E[x]$, where $\sigma[x]$ is the standard deviation of the distribution.

The information given in Tables 2a and b reflects the best judgment of the author regarding the shape of each distribution. These judgments erred on the side of conservatism by choosing minimum and maximum values that were smaller than the bounds dictated by the available data. This action was done in acknowledgement of the fact that the available database was incomplete. The experimental data on which the distributions are based are discussed in the following section as well as in the documentation associated with DTN: LA0003AM831341.001.

Americium, Thorium, Actinium, Samarium, Zirconium and Niobium
The sorption-coefficient distributions for these elements in Yucca Mountain tuffs and iron oxides given in Tables 2a and b were inferred from data presented by Thomas (1987, pp. 34–99, parameters *srd1* and *srd2*), Triay et al. (1991), and Meijer (1992, pp. 22–24) and from the review of the sorption characteristics of these elements in Triay et al. (1997, pp. 99–107).

Plutonium
The sorption-coefficient distributions for plutonium given in Tables 2a and b were inferred from data presented by Thomas (1987, pp. 34–99, parameters *srd1* and *srd2*) and Meijer (1992, pp. 22–24) and from data discussed in Section 6.4.4 (DTN: LA0010JC831341.006).

Uranium
The sorption-coefficient distributions for uranium given in Tables 2a and b were inferred from data presented by Thomas (1987, pp. 34–99, parameters *srd1* and *srd2*) and Meijer (1992, pp. 24, 26–29) and from data discussed in Section 6.4.5 (DTN: LA0010JC831341.005). Sorption-coefficient distributions for uranium on alluvium are based on data discussed in Section 6.4.5.1.4.4.

Neptunium
The sorption-coefficient distributions for neptunium on tuffs and iron oxide given in Tables 2a and b were inferred from data presented by Thomas (1987, pp. 34–99, parameters *srd1* and *srd2*), Meijer (1992, pp.24–29), and Triay, Robinson et al. (1993) and from data discussed in Section 6.4.5 (DTN: LA0010JC831341.007). Sorption-coefficient distributions for neptunium on alluvium are based on data discussed in Section 6.4.5 (DTN: LA0003JC831341.001).

Table 2a. Sorption-Coefficient Distributions for Unsaturated-Zone Units

Element	Rock type	Min K_d (mL g^{-1})	Max K_d (mL g^{-1})	E[*x*]	COV*	Distribution type
Americium (also Actinium, Niobium, Samarium, Thorium, Zirconium)	Devitrified	100	2000	—	—	Uniform
	Vitric	100	1000	400	0.20	Beta
	Zeolitic	100	1000	—	—	Uniform
	Iron oxide	1000	5000	—	—	Uniform
Plutonium	Devitrified	5	70	—	—	Uniform
	Vitric	30	200	100	0.25	Beta
	Zeolitic	30	200	100	0.25	Beta
	Iron oxide	1000	5000	—	—	Uniform
Uranium	Devitrified	0	2.0	0.5	0.3	Beta
	Vitric	0	1.0	0.5	0.3	Beta
	Zeolitic	0	10.0	4.0	1.0	Beta (exp)
	Iron oxide	100	1000	—	—	Uniform
Neptunium	Devitrified	0	1.0	0.3	0.3	Beta
	Vitric	0	1.0	0.3	1.0	Beta (exp)
	Zeolitic	0	3.0	0.5	0.25	Beta
	Iron oxide	500	1000	—	—	Uniform
Radium	Devitrified	70	300	—	—	Uniform
	Vitric	50	100	—	—	Uniform
	Zeolitic	800	2000	—	—	Uniform
	Iron oxide	0	500	30	1.0	Beta (exp)
Cesium	Devitrified	10	700	—	—	Uniform
	Vitric	10	100	—	—	Uniform
	Zeolitic	300	3000	—	—	Uniform
	Iron oxide	0	300	30	1.0	Beta (exp)
Strontium	Devitrified	5	30	—	—	Uniform
	Vitric	0	20	—	—	Uniform
	Zeolitic	200	2000	—	—	Uniform
	Iron oxide	0	20	10	0.25	Beta
Nickel	Devitrified	0	200	50	0.33	Beta
	Vitric	0	50	30	0.33	Beta
	Zeolitic	0	200	50	0.33	Beta
	Iron oxide	0	500	—	—	Uniform
Lead	Devitrified	100	500	—	—	Uniform
	Vitric	100	500	—	—	Uniform
	Zeolitic	100	500	—	—	Uniform
	Iron oxide	100	1000	—	—	Uniform
Tin	Devitrified	20	200	—	—	Uniform
	Vitric	20	200	—	—	Uniform
	Zeolitic	100	300	—	—	Uniform
	Iron oxide	0	5000	—	—	Uniform
Protactinium	Devitrified	0	100	—	—	Uniform
	Vitric	0	100	—	—	Uniform
	Zeolitic	0	100	—	—	Uniform
	Iron oxide	500	1000	—	—	Uniform
Selenium	Devitrified	0	1	0.1	1.0	Beta (exp)
	Vitric	0	1	0.1	1.0	Beta (exp)
	Zeolitic	0	1	0.2	1.0	Beta (exp)
	Iron oxide	0	200	30	1.0	Beta (exp)
Carbon	Iron oxide	10	100	—	—	Uniform
Chlorine, Technetium, Iodine	All rock types	0	0	—	—	—

DTN: LA0003AM831341.001

NOTES: *Coefficient of variation: COV = $\sigma[x]/E[x]$; in the table, where E[*x*] is the expected value of the distribution and $\sigma[x]$ is the standard of deviation of the distribution.
"—" means this parameter is not applicable.

Table 2b. Sorption-Coefficient Distributions for Saturated-Zone Units

Element	Rock type	Min K_d (mL g^{-1})	Max K_d (mL g^{-1})	E[*x*]	COV*	Distribution type
Americium (also Actinium, Niobium, Samarium, Thorium, Zirconium)	Devitrified	100	2000	—	—	Uniform
	Vitric	100	1000	400	0.20	Beta
	Zeolitic	100	1000	—	—	Uniform
	Iron oxide	1000	5000	—	—	Uniform
Plutonium	Devitrified	5	100	50	0.15	Beta
	Vitric	50	300	100	0.15	Beta
	Zeolitic	50	400	100	0.15	Beta
	Iron oxide	1000	5000	—	—	Uniform
Uranium	Devitrified	0	5.0	N/A	N/A	Uniform
	Vitric	0	4.0	N/A	N/A	Uniform
	Zeolitic	5	20.0	7.0	0.3	Beta
	Iron oxide	100	1000	N/A	N/A	Uniform
	Alluvium	0	8.0	N/A	N/A	Uniform
Neptunium	Devitrified	0	2.0	0.5	0.3	Beta
	Vitric	0	2.0	0.5	1.0	Beta (exp)
	Zeolitic	0	5.0	1.0	0.25	Beta
	Iron oxide	500	1000	—	—	Uniform
	Alluvium	0	100	18	1.0	Beta
Radium	Devitrified	100	500	—	—	Uniform
	Vitric	100	500	—	—	Uniform
	Zeolitic	1000	5000	—	—	Uniform
	Iron oxide	0	1500	30	1.0	Beta (exp)
Cesium	Devitrified	20	1000	—	—	Uniform
	Vitric	10	100	—	—	Uniform
	Zeolitic	500	5000	—	—	Uniform
	Iron oxide	0	500	30	1.0	Beta (exp)
Strontium	Devitrified	10	200	—	—	Uniform
	Vitric	20	50	—	—	Uniform
	Zeolitic	2000	5000	—	—	Log uniform
	Iron oxide	0	30	10	0.25	Beta
Nickel	Devitrified	0	200	—	—	Uniform
	Vitric	0	50	—	—	Uniform
	Zeolitic	0	200	—	—	Uniform
	Iron oxide	0	1000	—	—	Uniform
Lead	Devitrified	100	500	—	—	Uniform
	Vitric	100	500	—	—	Uniform
	Zeolitic	100	500	—	—	Uniform
	Iron oxide	100	1000	—	—	Uniform
Tin	Devitrified	20	200	—	—	Uniform
	Vitric	20	200	—	—	Uniform
	Zeolitic	100	300	—	—	Uniform
	Iron oxide	0	5000	—	—	Uniform
Protactinium	Devitrified	0	100	—	—	Uniform
	Vitric	0	100	—	—	Uniform
	Zeolitic	0	100	—	—	Uniform
	Iron oxide	500	1000	—	—	Uniform
Selenium	Devitrified	0	1.0	0.1	1.0	Beta (exp)
	Vitric	0	1.0	0.1	1.0	Beta (exp)
	Zeolitic	0	1.0	0.2	1.0	Beta (exp)
	Iron oxide	0	500	30	1.0	Beta (exp)
Carbon	Iron oxide	10	100	—	—	Uniform
Chlorine, Technetium, Iodine	All tuffs	0	0	—	—	—
Technetium	Alluvium	0.27	0.62	—	—	Uniform
Iodine	Alluvium	0.32	0.63	—	—	Uniform

DTN: LA0003AM831341.001

NOTES: *Coefficient of variation: COV = $\sigma[x]/E[x]$; in the table, where E[*x*] is the expected value of the distribution and $\sigma[x]$ is the standard of deviation of the distribution.
"—" means this parameter is not applicable.

Radium
The sorption-coefficient distributions for radium given in Tables 2a and b were inferred from data presented by Thomas (1987, pp. 34–99, parameters *srd1* and *srd2*), Meijer (1992, pp. 24–25), Triay et al. (1991), and Section 6.4.4.1.4.9. .

Cesium
Cesium sorption-coefficient distributions given in Tables 2a and b were inferred from data presented by Thomas (1987, pp. 34–99, parameters *srd1* and *srd2*), Meijer (1992, pp. 23–25), and Triay et al. (1991) and DTN: LA0010JC831341.002.

Strontium
Strontium sorption-coefficient distributions given in Tables 2a and b were inferred from data presented by Thomas (1987, pp. 34–99, parameters *srd1* and *srd2*), Triay et al. (1991) and DTN: LA0010831341.003.

Nickel
Nickel sorption-coefficient distributions given in Tables 2a and b were inferred from data presented by Meijer (1992, p. 25). For iron oxides, the nickel sorption-coefficient distribution was inferred from the data presented by Siegel et al. (1992; 1993, p. 355). The distributions for vitric tuff and iron oxide were also inferred from data presented in Triay et al. (1997, pp. 122–123).

Lead
The sorption-coefficient distributions for lead given in Tables 2a and b were inferred from data presented by Triay et al. (1997, pp. 122–123.

Tin
The sorption-coefficient distributions given in Tables 2a and b were inferred from the work by Andersson (1988); the uniform distributions chosen were the result of uncertainty about the sorption of tin.

Protactinium
The element protactinium was given the same distribution parameters as the element neptunium. The protactinium sorption-coefficient distributions presented in Tables 2a and b were inferred from data for protactinium presented by Allard (1982, pp. 32–33) and Rundberg et al. (1985, p. 63).

Selenium
Selenium sorption-coefficient distributions given in Tables 2a and b were inferred from data presented by Thomas (1987, pp. 34–99, parameters *srd1* and *srd2*) and data discussed in Section 6.4.5 (DTN: LA0010JC831341.004).

Carbon
Carbon is a special case because transport is expected to occur primarily in the gaseous phase as carbon dioxide. The major retardation mechanism is exchange of carbon-14 with the carbon in the carbon dioxide dissolved in the groundwater. Carbon sorption-coefficient distributions given in Tables 2a and b were inferred from data presented by Russell et al. (1975).

Iodine, Technetium, and Chlorine
Iodine, chlorine, and technetium do not appear to sorb onto tuffs under oxidizing conditions and, therefore, are assigned to have sorption coefficients of zero. Sorption-coefficient distributions for technetium and iodine in alluvium are based on data discussed in Section 6.4.5 (DTN: LA0003JC831341.002 and LA0003JC831341.003).

6.4.3 Hydrochemistry and Eh-pH Characteristics of the Saturated Zone

The hydrochemistry of the saturated zone at Yucca Mountain controls the solubility and speciation of radionuclides in the groundwater and, hence, their transport characteristics. For the purposes of this report, the main concern is not the details of the hydrochemical variations but the total variation in water chemistry to be expected in the Yucca Mountain flow system. That is, what is required are bounding values for hydrochemical parameters in the saturated zone at Yucca Mountain. As discussed in Meijer (1992), the total variation in water chemistry in the Yucca Mountain flow system can be reasonably bounded by the compositions of waters from Wells J-13 and p#1 (Table 3) with some provisos (Assumption 3 in Section 5). The provisos involve the parameters pH and Eh. That is, the waters from Wells J-13 and p#1 have pH and Eh values that do not bound the range of these two parameters in waters in the saturated zone at Yucca Mountain. For pH, the range is approximately 6.5 to 9.5 (DTN: GS930908312323.003, GS950808312322.001, GS990808312322.001, MO0007MAJIONPH.011, MO0007MAJIONPH.013, MO0007MAJIONPH.005, MO0007MAJIONPH.003). The pH values for J-13 and p#1 waters (6.9 and 6.7) are at the lower end of this range. For Eh, the range is approximately –100 to +400 mV (Standard Hydrogen Electrode, SHE) (DTN: LAAM831311AQ98.005, LAAM831311AQ98.007, LAAM831311AQ98.008, LAAM831311AQ98.010, LA9907AM831234.003, LA0004AM831234.001, LA9907AM831234.009, LA9907AM831234.010, LA9907AM831234.011, LA0004AM831234.002). The Eh values for J-13 and p#1 waters are both at the upper end of this range.

Table 3. Groundwater Compositions of Wells J-13 and p#1

Constituent	Concentration (mg L^{-1})	
	J-13 water	p#1 water
Sodium	45	171
Potassium	5.3	13.4
Magnesium	1.8	31.9
Calcium	11.5	87.8
Silicon	30	30
Fluoride	2.1	3.5
Chloride	6.4	37
Sulfate	18.1	129
Bicarbonate	143	698
pH	6.9	6.7

DTN: LAIT831361AQ95.003 (SEP Table S98491.002)

6.4.4 Sorption Experiments

Sorption coefficients are generally obtained from batch-sorption experiments. Such experiments are simple in design, fast, and inexpensive compared to other sources of sorption-coefficient data. However, batch experiments have some drawbacks in that they are not sensitive to the possibility that, for a given radionuclide, some species may exist in the solution (e.g., in a different oxidation state) that sorb less than other species of the same nuclide in that solution and that are not in equilibrium with those species. If the poorly sorbing species constitutes only a small fraction of the total species in solution, a large sorption coefficient could be obtained in a batch experiment. However, the less sorptive species in solution would be transported through the rock much more readily than would be predicted by the value of the batch-sorption coefficient. To test for such a possibility, column experiments are carried out. In the column experiments, the existence of a poorly sorbing species in solution would be evident in the breakthrough curve. That is, this species would elute from the column before the major species were eluted from the column. The results of a limited number of both crushed-rock and solid-rock column experiments are discussed in this section. The potential influence of organic constituents in groundwater on the sorption behavior of neptunium and plutonium is evaluated in batch experiments.

Because variations in groundwater chemistry have an impact on the sorption behavior of the radionuclides of interest, a strategy was required to account for the potential impact of these variations on sorption coefficients. The strategy developed assumes that the major ion compositions of waters from Wells J-13 and p#1 are bounding for purposes of quantification of the sorption behavior of the radionuclides of interest (Assumption 3 in Section 5). However, the pH and Eh variations of groundwaters in the Yucca Mountain flow system are not fully addressed by this choice in bounding water compositions. The pH of J-13 and p#1 waters in contact with atmospheric carbon dioxide levels is generally in the range of 8.2 to 8.5. To address the lower pH values observed among saturated-zone waters in the Yucca Mountain flow system, the pH of aliquots of J-13 and p#1 waters were adjusted to values near 7.0 by imposing an overpressure of carbon dioxide in a glove box. The Eh of the waters used in the experiments was

assumed to be oxidizing because the experiments were carried out in contact with atmospheric oxygen levels.

6.4.4.1 Batch-Sorption Experiments

Batch-sorption coefficients for radionuclides of interest were obtained using waters and rock samples from the site. Because of the large numbers of experiments required to address the sorption behavior of every radionuclide and every rock/water system of interest, some process for focusing the experimental program was required. The process developed has been called the "minimum K_d approach" (Meijer 1992, p. 9). The essence of this concept is that a "minimum K_d" exists for each radionuclide according to which the radionuclide will not reach the accessible environment through a groundwater pathway over the regulatory period of interest allowing for an adequate margin of error. Radionuclides that can be shown to possess this minimum K_d value in rock/water systems similar to those at Yucca Mountain, as based on literature data and any experimental data available for Yucca Mountain rock and water samples, would not require as much detailed investigation as radionuclides that do not. Those radionuclides with essentially no sorption potential were eliminated from further consideration. This approach allowed the experimental program to be focused on those radionuclides that would have the maximum potential for impacts on doses at the accessible environment over the regulatory time frame of interest.

6.4.4.1.1 The Distribution Coefficient

The batch-sorption distribution coefficient, K_d, was calculated using

$$K_d = \frac{F}{C} = \frac{\text{moles of radionuclide per g of solid phase}}{\text{moles of radionuclide per mL of solution}} \quad . \qquad \text{(Eq. 1)}$$

K_d thus has units of mL g^{-1}.

The K_d approach used here is by mass balance, that is, loss of solute from solution is assumed to have sorbed onto the solid. Some researchers measure solute concentrations in both the solution and on the solid. Also, because of mass measurements, results are sometimes given in units of g g^{-1} instead of mL g^{-1}, which are the same in dilute aqueous solutions. Only mL g^{-1} will be used here.

Determination of very small or very large batch-sorption distribution coefficients results in large uncertainties in the K_d values calculated. When very little sorption occurs, calculations can yield negative K_d values; the error is the result of subtracting two large numbers (the initial radionuclide concentration in solution and the radionuclide concentration after sorption) to obtain a small number (the amount of radionuclide left in the solid phase). Therefore, very small K_d values are not very precise. On the other hand, when a great deal of sorption occurs, there can be large uncertainties associated with the measurement of the small amount of radioactivity left in solution after sorption. This fact also results in large uncertainties in the calculated K_d. Because of these uncertainties, most K_d values are only reported to one significant figure.

6.4.4.1.2 Linear Versus Nonlinear Sorption

The sorption distribution coefficient, K_d, for the species being sorbed, is the ratio of its concentration in the solid phase, F, to its concentration in the solution phase, C, which implies a linear relationship between the concentrations:

$$F = K_d C \quad . \qquad \text{(Eq. 2)}$$

Nonlinear adsorption isotherms have been reviewed by de Marsily (1986, p. 258). A useful nonlinear relationship, Freundlich's isotherm, is given by the equation

$$F = K_c C^{1/n}, \qquad \text{(Eq. 3)}$$

where K_c and n are positive constants (with $n \geq 1$).

Another nonlinear relationship is Langmuir's isotherm, given by (de Marsily 1986, p. 258)

$$F = \frac{K_1 C}{1 + K_2 C}, \qquad \text{(Eq. 4)}$$

where K_1 and K_2 are positive constants. Part of the research discussed in this report was an attempt to assess the validity of using the linear distribution coefficients as opposed to other isotherm functional forms to describe retardation by sorption in transport calculations. However, in recommending sorption distribution coefficients for use in transport calculations, it was assumed in this AMR that the variability of the sorption parameter as a function of concentration can be adequately captured by lowering the minimum K_d value defined for the sorption distribution function so as to include the reduced K_d expected under high concentration conditions (Assumption 6 in Section 5).

6.4.4.1.3 Experimental Procedures

All batch-sorption experiments on Yucca Mountain samples reported here were performed at room temperature. The standard procedure first involved pretreating the solid phase with the groundwater being studied in the ratio of 1 g of solid to 20 mL of solution. The pretreated solid phase was then separated from the groundwater by centrifugation and exposed to 20 mL of a radionuclide solution (in the groundwater being studied) for approximately 3 weeks. After sorption, the phases were separated by centrifugation. The compositions of the groundwaters used were documented in the laboratory notebooks referenced by the DTNs for the experiments; these groundwaters were either natural or synthetic solutions of groundwaters from Wells J-13 or p#1 (see Assumptions 3 and 9 in Section 5). The nomenclature used for the tuff rock samples typically listed the borehole identifier followed by the sample depth in feet, for example, sample G1-2901 is tuff collected (as drillcore) from a depth of 2901 feet in borehole G-1.

The amount of radionuclide in solution initially and then after sorption was either determined with a liquid-scintillation counter (for neptunium and plutonium) or with inductively coupled

plasma mass spectrometry (for uranium). The amount of radionuclide in the solid phase was determined by difference. Container tubes without solid phases in them were used as controls to monitor radionuclide precipitation and sorption onto the container walls during the sorption experiment. The difference in the concentration of the radionuclide in the initial solution and that in the control-tube solution generally was only a few percent. In particular, results for the plutonium solution showed a small amount of sorption onto the container walls. Even in this case, the difference in concentration between the initial plutonium solution and the plutonium solution in the control tube never exceeded 7 percent for the experiments reported. Nevertheless, in the case of plutonium, the amount of radionuclide sorbed onto the solid phase was calculated by taking the difference of the final plutonium solution concentration both with the initial solution concentration and with the solution concentration in the control tube. The latter approach is conservative because plutonium may sorb to container walls only in the absence of the geologic material.

Batch-sorption experiments were performed under atmospheric conditions or inside glove boxes with a carbon-dioxide overpressure. The pH of the J-13 and p#1 waters under atmospheric conditions was approximately 8.5 and 9, respectively, and inside the glove boxes was 7 (the CO_2 overpressure was adjusted to bring the pH of both waters down to 7). A limited number of batch experiments were carried out with different initial radionuclide concentrations in solution as described below. The results of these experiments were used to gauge whether the sorption isotherm for the rock/water system of interest was linear or not (Assumption 6 in Section 5).

To investigate the kinetics of sorption reactions (i.e., the degree to which the reactions were instantaneous), batch experiments were carried out over different times (e.g., one day, one week, 2 weeks, 3 weeks) (Assumption 7 in Section 5). Three weeks was generally enough time for the sorption reactions to reach a steady state. The issue of the reversibility of a given sorption process was investigated by performing desorption experiments on the solid samples remaining after a sorption experiment. In this case, the water initially added to the experiment was free of the radionuclide of interest.

6.4.4.1.4 Data from Batch-Sorption Tests

Data from batch-sorption tests were obtained from several sources. Most of the data reported here were obtained by the YMP. Corroborative data and data for some of the less important radionuclides were obtained from literature sources.

6.4.4.1.4.1 Plutonium

Data from Sorption Experiments Reported in the Literature—The data discussed in this section are provided to show trends for the sorption of plutonium. Allard (1982, pp. 60–61) reported results on experiments involving plutonium sorption on quartz, apatite, attapulgite, montmorillonite, and various minerals rich in ferrous iron in a dilute groundwater containing plutonium at 1.8×10^{-11} M. For all the minerals, the sorption coefficients were greater than 10^3 mL g^{-1} over a pH range from 4 to 9. Apatite, attapulgite, biotite, and montmorillonite showed sorption coefficients greater than 10^4 mL g^{-1} over this pH range. Torstenfelt et al. (1988, pp. 115–116) presented data for plutonium sorption on feldspars, clays, and granite in contact with

J-13 water. The sorption coefficients reported by them are generally between 100 to 200 mL g^{-1} in neutral to alkaline solutions. These authors emphasized the importance of proper experimental technique in the determination of sorption-coefficient values for plutonium and noted the potential for colloid formation in these types of experiments. Data indicating high affinity of plutonium for ferric oxyhydroxide, manganese oxide, and carbonate mineral surfaces were presented by Means et al. (1978), Keeney-Kennicutt and Morse (1985, Figs. 2, 4–6), and Sanchez et al. (1985). Means et al. noted that manganese oxides sorb plutonium more strongly than ferric oxyhydroxides in natural environments (presumably as a result of redox reactions on the manganese-oxide surface).

Data from Laboratory Sorption Experiments with Yucca Mountain Rock and Water Samples Obtained prior to 1993—Measurements of plutonium sorption coefficients involving Yucca Mountain rock samples and J-13 groundwater were summarized by Thomas (1987, p. 21 and Appendix). The values measured for the plutonium sorption coefficient range from 20 to greater than 4,500 mL g^{-1} with most values lying between 100 to 2,000 mL g^{-1} within a pH range of 8.2 to 8.8. The coefficients determined during the desorption experiments were occasionally in the range of the sorption-coefficient values, but more typically, they were 10 to 20 times larger, reflecting the irreversibility of the sorption reactions. Zeolitic samples typically had lower sorption-coefficient values than vitric or devitrified samples. It appears that rocks that have essentially no reduction capacity remaining (that is, samples lacking ferrous iron or sulfide) show the lowest sorption coefficients for plutonium. Samples with calcite or clay showed the largest sorption coefficients (> 4,500 mL g^{-1} for samples with 30 percent calcite). There are clays in the vitric tuff that increase Pu sorption. Pu is not strongly sorbed by zeolites in general. Therefore, the relative amounts of clays and zeolites should be known for reasonable prediction of sorption, not just the average fines content.

Based on the eight experiments for which data are available (Meijer 1992), there was up to a factor of 12 variation in sorption coefficients as a function of groundwater composition. Water from Well p#1 was associated with the largest values (240 to 540 mL g^{-1}, sorption-desorption) with waters from Wells H-3 and J-13 showing the lowest values (20 to 230 mL g^{-1}). The higher values obtained with p#1 water may reflect calcite precipitation. There did not appear to be a dependence of the sorption coefficient on pH over the range from 7 to 9, although the available data are limited on this issue. Finally, there was less than a factor of four dependence of the sorption coefficient on radionuclide concentration over the range from 10^{-9} to 10^{-12} M.

Data from Laboratory Sorption Experiments with Yucca Mountain Rock and Water Samples Obtained after 1993—Plutonium sorption coefficients have been measured on a variety of solid samples in contact with Yucca Mountain groundwaters J-13 and p#1 under atmospheric conditions (i.e., oxidizing conditions and pH = 8.2 to 8.6). The data obtained are summarized in Table 4. As shown in the table, plutonium sorption coefficients are greater than 100 mL g^{-1} for vitric and zeolitic tuffs under these conditions. For devitrified tuffs, sorption coefficients are less than 100 mL g^{-1} in both water compositions.

Table 4. Plutonium Sorption Distribution Coefficients
(under atmospheric conditions)

Solid phase	K_d range in J-13 water (mL g^{-1})	K_d range in synthetic p#1 water (mL g^{-1})
Vitric tuff	600–2,000	100–400
Zeolitic tuff	300–500	100–400
Devitrified tuff	40–100	20–70
Synthetic hematite	> 10,000	> 10,000
Montmorillonite	> 10,000	> 10,000
Clinoptilolite	600–3,000	2,000–5,000
Calcite	200–1,000	100–800
Gibbsite	0–10	10–90
Albite	3–10	< 10
Quartz	< 10	< 10

DTN: LA0010JC831341.006

The sorption of plutonium onto the three main types of tuff in J-13 water at a pH of 7.0 was also studied using a carbon-dioxide overpressure to maintain a pH of 7. These experiments were also conducted under oxidizing conditions (i.e., atmospheric oxygen concentrations). The affinity of tuffs for plutonium at pH = 7 is, in decreasing order, zeolitic > vitric > devitrified (Triay et al. 1997, Figure 37). Compared to the data summarized in Table 4, plutonium appears to sorb somewhat less at pH 7 than at pH values between 8.2 and 8.6 (i.e., atmospheric conditions), particularly on devitrified tuff (K_d < 10 mL g^{-1} at pH 7).

To evaluate which minerals in the tuffs were responsible for most of the plutonium sorption, sorption experiments with pure mineral separates were carried out. The minerals investigated included hematite, clinoptilolite, albite, and quartz. The results of the batch-sorption experiments for plutonium on these minerals are shown in Table 4. The relative affinities of these minerals for plutonium are, in decreasing order, hematite > montmorillonite > clinoptilolite > calcite >> gibbsite > albite ≥ quartz. These data suggest that montmorillonite and zeolite minerals are likely responsible for most of the plutonium sorption onto the bulk tuffs. The trace amounts of hematite found in the tuffs do not appear to have a significant impact based on sorption data for neptunium and uranium (Triay et al. 1997, pp. 126, 133, and 145). However, the presence of calcite in the tuffs can have a significant impact depending on the amounts present and on the surface area of the calcite present.

As stated above, sorption coefficients are not necessarily constant with increasing concentration of the sorbing element. That is, sorption isotherms can be linear or nonlinear. To evaluate the shape of the plutonium sorption isotherm with increasing plutonium concentration, experiments were conducted over a range of solution concentrations with various rock/water combinations. The data obtained indicate that the plutonium sorption isotherm is generally nonlinear on tuffs from Yucca Mountain (Triay et al. 1997, Figures 38–42 and 44). The cause of the nonlinearity is not known. The solution concentrations in these experiments range from 3×10^{-10} to 2×10^{-7} M. Because the upper limit of this range is close to the solubility of plutonium in Yucca Mountain

waters, the concentration of plutonium transported in the flow system will likely not exceed this value. Experiments conducted with concentrations at the low end of the range produce sorption coefficients that are higher than experiments conducted with solution concentrations at the high end of the range. Therefore, the use of sorption coefficients in performance assessment calculations obtained with the more concentrated solutions will result in conservative predictions of plutonium transport rates (Assumption 6 in Section 5).

The sorption of plutonium onto tuffs and minerals in J-13 and synthetic p#1 water under atmospheric conditions was studied as a function of time and initial plutonium solution concentration. The resulting data (Triay et al. 1997, Figure 38) indicate that it takes more than a couple weeks for the plutonium sorption reactions to reach steady state. Even after 32 days, a steady-state concentration in solution had not been achieved in these experiments. This slowness in reaching a steady state may be due to redox reactions at solid surfaces in the samples.

Nitsche et al. (1993, pp. 52, 58–62) report that, even when a plutonium solution in J-13 or p#1 water is prepared starting in the +4 (IV) oxidation state, the predominant final oxidation state is +5, or Pu(V). The solution used for plutonium sorption experiments was prepared from a well-characterized Pu(V) acidic stock in J-13 well water. Consequently, it has been assumed that, during the few weeks over which the sorption experiments have been conducted (e.g., 30 days), the plutonium remained predominantly in the +5 oxidation state although, given more time, it may not have remained in that state.

Comparison of the data for plutonium sorption coefficients with similar data for neptunium and uranium indicates that significant plutonium sorption occurred in tuffs and minerals that exhibit very small sorption coefficients for Np(V) and U(VI). This result is puzzling; if plutonium in J-13 well water is predominantly Pu(V) and Pu(VI) (Nitsche et al. 1993, pp. 58–62), it is expected that its sorption behavior would have been similar to that observed for Np(V) and U(VI). Several possible explanations for this apparent discrepancy are:

- The data of Nitsche et al. (1993, pp. 58–62) for the oxidation states are incorrect, and the predominant plutonium oxidation state in J-13 well water at a pH of 7 is Pu(IV), not Pu(V) and Pu(VI)

- The Pu(IV) species is what sorbs from J-13 water but a re-equilibration in the solution phase produces more Pu(IV) to maintain equilibrium (which implies that the kinetics in plutonium speciation are fast in solution, but slow on the solid)

- Pu(V) and Pu(VI) reduce to Pu(IV) at solid surfaces (as a result of changes in the solution redox potential in the presence of the solid phases).

In general, slow sorption kinetics should generally result in conservative predictions of transport rates of plutonium in Yucca Mountain from the batch-test sorption coefficients (Assumption 7 in Section 5). However, the great complexity of unsaturated flow, in which the residence time of solutions in the matrix versus fractures at any particular time can change dramatically, means that one has to be cautious in interpreting batch tests for unsaturated flow systems.

Conclusions Regarding Sorption Behavior of Plutonium in the Yucca Mountain Flow System—On the basis of the discussion in the previous subsections, it appears the most important factors controlling the sorption of plutonium from oxidizing groundwater onto Yucca Mountain tuffs are the abundances of montmorillonitic clays and zeolite minerals in the tuffs. Calcite, if present, may also result in high plutonium sorption coefficients. The affinity of Yucca Mountain tuffs for plutonium is highest in zeolitic tuffs, slightly lower in vitric tuffs, and lowest in devitrified tuffs. Groundwater compositional parameters that appear to have the most impact on plutonium sorption behavior are redox potential (i.e., Eh) and pH. Under less oxidizing redox potentials than those maintained in the batch experiments, plutonium sorption coefficients would be larger. Therefore, the sorption coefficients reported here will result in conservative predictions of plutonium transport rates. The change in sorption coefficients that may result from variations in groundwater pH are accounted for in the distributions reported in Tables 2a and b. Similarly, the impact of potential variations in plutonium concentration are incorporated in the distributions by assuming the high end of the range of potential plutonium concentrations in groundwater pertain to the Yucca Mountain flow system (Assumption 6 in Section 5). Although the kinetics of the plutonium sorption reactions appear to be relatively slow compared to elements with simpler solution chemistry (e.g., cesium), the sorption coefficients reported here should result in conservative predictions of plutonium transport rates.

6.4.4.1.4.2 Neptunium

Neptunium, protactinium, selenium, and uranium share a common characteristic in that they all tend to show small values for sorption coefficients in the rock-water systems expected at Yucca Mountain under oxidizing conditions. Under more reducing conditions, they would all have much lower solubilities and higher sorption affinities in Yucca Mountain groundwaters. In solutions representative of oxidized water compositions expected within the Yucca Mountain flow system, neptunium will be predominantly in a +5 oxidation state. In this oxidation state, neptunium is quite soluble when compared to lower oxidation states. If reducing conditions are encountered along the flow path between the proposed repository and the accessible environment, neptunium could be reduced to the +4 oxidation state.

Data from Sorption Experiments Reported in the Literature—The results of neptunium sorption experiments with pure mineral separates have been reported by Allard (1982, pp. 15–17, 51–59) and Meijer et al. (1989). On the basis of these results, it is evident that in oxidizing solutions, neptunium has a high affinity for ferric oxides and oxyhydroxides, apatite, and attapulgite (magnesium-rich clay). It has a somewhat lower affinity for carbonates (such as calcite), sulfates (anhydrite), and manganese minerals (cryptomelane). It has a low affinity for most silicate minerals. Neptunium also shows high affinities for minerals that contain ferrous iron (such as pyrite, olivine, augite, magnetite, hornblende, epidote, biotite, and chlorite). This affinity is likely due to the reduction of Np(V) to Np(IV) by Fe(II) on the surfaces of these minerals. Although ferrous iron-bearing minerals are, at best, minor species in Yucca Mountain tuffs (Bish and Chipera 1989, Appendices A and B), they could be of considerable significance to neptunium sorption where present in the flow system.

In addition to the nature of the available mineral surfaces, it is evident that pH is also a critical parameter in neptunium sorption. In general, neptunium sorption increases with increasing pH.

This effect is particularly evident in the experiments with iron oxyhydroxides (Hobart 1990, p. 403). However, similar behavior is evident in the sorption experiments with silicate minerals (Allard 1982, pp. 15–16). In the latter case, the sorption edge (as a function of pH) is located at a higher pH (8–9) than the edge associated with the ferric oxyhydroxides (a pH of 6–7). Neptunium does not appear to have a high affinity for ion-exchange reactions on clays and zeolites (Allard 1982; Triay, Robinson et al. 1993, Table 3a). This phenomenon may be due to the small charge-to-radius ratio and the large size of the neptunyl ion.

Data from Laboratory Sorption Experiments with Yucca Mountain Rock and Water Samples Obtained Prior to 1993—The results of neptunium sorption experiments involving Yucca Mountain rock and water samples have been reported by Daniels et al. (1982, pp. 78, 79, 90, 98, 108), Thomas (1987, Appendix; 1988, pp. 35–37), and Triay, Robinson et al. (1993, Table 3a). These experiments indicate that neptunium has a low affinity (for example, K_d values of 0 to 5 mL g^{-1}) for the surfaces in Yucca Mountain tuffs over most of the pH range and water compositions expected in the Yucca Mountain flow system. The sorption mechanisms are apparently not entirely reversible as coefficients obtained from desorption experiments are commonly larger than those obtained from sorption experiments even though the isotherms are linear in the concentration range covered by these experiments. There is some indication of increased sorption coefficients (5 to 40 mL g^{-1}) at the highest pH values (8.5 to 9.0). Torstenfelt et al. (1988, p. 115) suggest that this result reflects increased hydrolysis of the neptunyl ion, resulting in an increase in surface-adsorption reactions. However, in Yucca Mountain rock-water systems, it could also reflect increased potential for calcite precipitation at high pH.

In the pH range from 6.5 to 8.5, the small but consistent affinity of neptunium for the tuffs most likely reflects the existence of a limited number of favorable adsorption sites for neptunium. This number apparently does not involve ion-exchange sites because zeolitic rock samples also show low sorption coefficients. For example, Thomas (1988, Table V) describes a case in which a zeolitic tuff sample (G4-1608) with a cation-exchange capacity of approximately 1.5 meq g^{-1} (based on the average value reported for other zeolitic tuff samples listed in the table cited) appears to have essentially the same affinity for neptunium as a devitrified tuff sample (GU3-433) with an exchange capacity of approximately 0.02 meq g^{-1}. These sites are apparently not present in the same abundance on all tuff samples. That is, some zeolitic, vitric, and devitrified tuff samples have almost no affinity for neptunium over the pH range from 6.5 to 8.5, whereas other samples with similar proportions of major minerals show sorption coefficients in the range of 5 to 10 mL g^{-1} (Meijer 1992). This result suggests, but does not prove, that the favorable sites are associated with some minor primary or secondary phase that has variable abundance. Hematite and calcite are candidates for this phase based on pure mineral studies. Because ferric oxides are present at trace levels in most of the rock units within Yucca Mountain, they could be the source of the low but consistent values (0.5 to 2 mL g^{-1}) observed in experiments on devitrified and zeolitic tuffs. Alternatively, neptunium may be sorbed (through reduction to Np(IV)) by the small amounts of ferrous-iron-bearing minerals present in the rock samples used in the sorption experiments.

The increased sorption of neptunium on tuffaceous samples known to contain calcite suggests this mineral is of considerable potential significance to neptunium sorption on Yucca Mountain tuffs. If so, prediction of the adsorption behavior of neptunium will depend on knowledge of the

surface areas of calcite in the various hydrologic units or on the saturation state of calcite in groundwaters present in these units. Because even small amounts of calcite appear to significantly increase neptunium sorption coefficients, current mineral identification techniques may not be adequate for prediction of neptunium sorption behavior involving calcite. For vitric units lacking iron oxides and calcite, neptunium may not be sorbed at all.

Data from Laboratory Sorption Experiments with Yucca Mountain Rock and Water Samples Obtained after 1993 (data discussed in this section are reported in DTN: LA0010JC831341.007)—Sorption coefficients for Np(V) on individual samples of the three main types of tuff under atmospheric conditions (pH = 8.2–8.6; oxidizing) are shown in Figure 1. Note that the sorption coefficients for all samples are less than 5.0 mL g^{-1}. The values less than 1.0 are generally for vitric and devitrified samples. Those greater than 1.0 are for zeolitic samples.

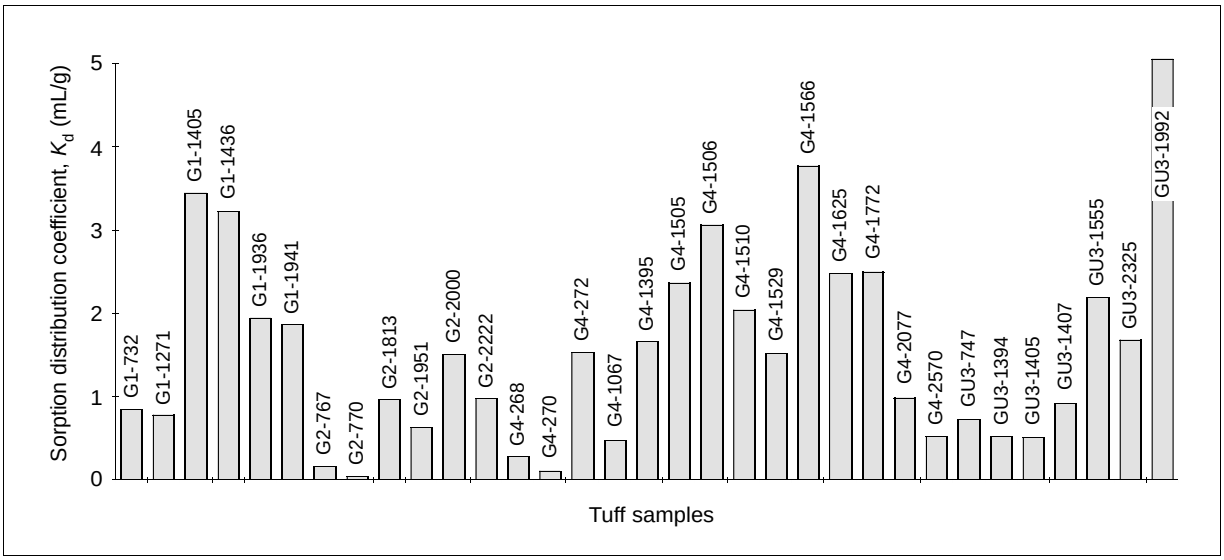

DTN: LA0010JC831341.007

Note: These values of the batch-sorption distribution coefficient, K_d, obtained in separate experiments, illustrate the limited sorption of neptunium onto a large range of Yucca Mountain tuffs in J-13 well water under atmospheric conditions. The initial neptunium concentration ranged from 6 to 8 x 10^{-7} M. The tuffs were wet-sieved to particle sizes that ranged from 75 to 500 µm. The pretreatment period was 2 to 14 days; the sorption period was 3 to 23 days. Samples are shown in order of borehole and depth. Figure from Triay et al. (1997, Fig. 66).

Figure 1. Neptunium Sorption in J-13 Well Water

Zeolitic tuffs show substantial variation in the neptunium sorption coefficient in different samples and under different pH conditions. Some zeolitic samples show very little affinity for neptunium, although more at a pH value of 8.5 than at 7.0 (Figure 2). Other zeolitic samples (e.g., G4-1510 and GU3-1992) show a higher affinity (that is, higher K_d), particularly at a pH value of 7.0. Why some zeolitic samples show substantially higher neptunium sorption coefficients is not entirely clear. The explanation likely revolves around the type of zeolite structure and the chemistry of the zeolite.

The impact of pH variations on neptunium sorption behavior was also investigated with experiments on devitrified and vitric tuff and albite and quartz in J-13 water (under oxidizing

conditions) at two pH values (7 and 8.5). It was found that in J-13 water neptunium sorbs only sparingly onto devitrified and vitric tuffs under both pH conditions.

Experiments with pure clinoptilolite indicate that sorption increases with decreasing pH for Np(V). Because the major constituent of tuff sample G4-1510 is clinoptilolite, predictions of the K_a (K_d divided by the solid-phase surface area per unit mass) were made for neptunium sorption onto this tuff by assuming that clinoptilolite is the only sorbing phase. Table 5 shows measured and predicted values of K_a for the clinoptilolite-rich tuff sample G4-1510 at two different pH values. Because sorption is correlated with surface area, similar calculations (Table 6) were made for a series of tuff samples containing various amounts of clinoptilolite for which the surface area had been measured. The values in these two tables indicate that reasonable predictions can be made based on Np sorption data for pure clinoptilolite (assuming clinoptilolite is the only sorptive mineral).

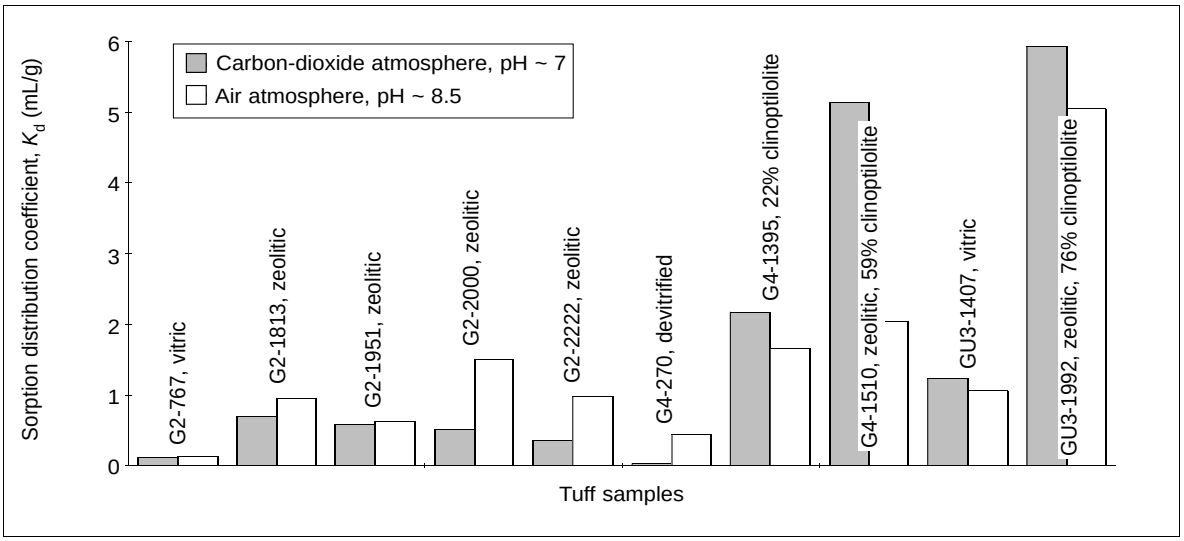

DTN: LA0010JC831341.007

Note: Experimental values of K_d for the sorption of neptunium onto tuffs in J-13 water at initial concentrations of 6 to 7 x 10^{-7} M are compared for atmospheric conditions (pH ~8.5) and a carbon-dioxide overpressure (pH ~7). Tuffs were wet-sieved (75 to 500 µm); the pretreatment period was 2 to 3 days; the sorption period was 3 to 5 days. Samples are shown in order of borehole and depth. Figure from Triay et al. (1997, Figure 62).

Figure 2. pH Dependence of Neptunium Sorption onto Tuffs at 10^{-7} M

Table 5. Prediction of Neptunium Sorption on Clinoptilolite-Rich G4-1510 Tuff in J-13 Water[a]

Initial concentration (M)	pH	Measured K_a (m)	Predicted K_a (m)
1 x 10^{-7} to 3 x 10^{-5}	7	1 x 10^{-7}	1 x 10^{-7}
	8.5	6 x 10^{-8}	1 x 10^{-7}

DTN: LA0004AM831341.002.

Note: [a]Assuming clinoptilolite is the only sorbing mineral in the tuff, present at 59 weight %.

Table 6. Neptunium Sorption onto Clinoptilolite-Rich Tuffs in J-13 Water[a]

Tuff sample	Measured K_a (m)	Predicted K_a (m)	Clinoptilolite %
G4-1505	8×10^{-8}	1×10^{-7}	74 ± 7
G4-1506	2×10^{-7}	1×10^{-7}	62 ± 7
G4-1510	6×10^{-8}	1×10^{-7}	59 ± 7
G4-1529	6×10^{-8}	1×10^{-7}	59 ± 8
G4-1625	7×10^{-8}	1×10^{-7}	61 ± 7
G4-1772	9×10^{-8}	1×10^{-7}	63 ± 5
G4-2077	1×10^{-8}	1×10^{-7}	51 ± 8

DTN: LA0004AM831341.002

NOTE: [a]Atmospheric conditions; initial neptunium concentrations ranged from 6 to 8 x 10^{-7} M; tuffs were wet-sieved to particle sizes ranging from 75 to 500 μm; the pretreatment period was 2 to 14 days; the sorption period was 3 to 23 days; and the pH was 8.5 ± 0.3.

The dependence of neptunium sorption on neptunium concentrations for zeolitic tuffs and pure zeolites was tested in two samples. The sorption of neptunium onto zeolitic tuffs and clinoptilolite appears to be linear in the concentration range from 1 x 10^{-7} to 3 x 10^{-5} M and can be fitted using a constant K_d. In a zeolite-rich tuff at pH = 7.0, the K_d = 3 mL g^{-1}; whereas, at pH = 8.5, the K_d = 1.5 mL g^{-1} (Figure 3). Similar results were obtained with a pure zeolite sample (Figure 4). The higher sorption of neptunium onto zeolites at a pH of 7 might be explained by the larger amount of NpO_2^+ relative to $NpO_2CO_3^-$ in J-13 well water at a pH value of 7 compared to that at a pH of 8.5 (Nitsche et al. 1993, Table VII; CRWMS M&O 2000a, Table 3).

The relatively small amount of sorption observed in the zeolitic tuffs, given the large cation-exchange capacity of zeolites, suggests that the mechanism for neptunium sorption onto clinoptilolite is a surface reaction involving only the cation sites accessible on the zeolite surface. One possible explanation for this behavior is that the shape and large size of the neptunyl cation prevents it from entering the pores in the zeolite structure, thereby gaining access to most of the exchange sites. This ion likely has a trans-dioxol configuration normal to a puckered equatorial ring containing six bound water molecules.

Because neptunium was thought to sorb with a surface mechanism even in zeolitic tuffs and because the batch experiments are conducted with crushed tuff samples (i.e., increased surface area), the sorption coefficient for neptunium was investigated as a function of sieving procedure for devitrified (G4-270) and zeolitic (G4-1506) tuffs and calcite in J-13 and p#1 well waters. The data obtained in these experiments indicate that dry-sieving probably produces artificially high K_d values because of the increased surface area contributed by the small particles. As previously determined by Rogers and Meijer (1993), the optimal batch-sorption procedure involves wet-sieving the tuff samples to a size of 75 to 500 μm.

The sorption of neptunium onto pure iron oxides (hematite) in J-13 water was also measured. The measured values of K_d for hematite range from 100 to 2000 mL g^{-1} (Triay, Cotter, Kraus et al. 1996, p. 15). Although the sorption onto the pure iron oxide hematite is very large, neptunium sorption onto devitrified tuffs, which appear to have traces of hematite (1 percent

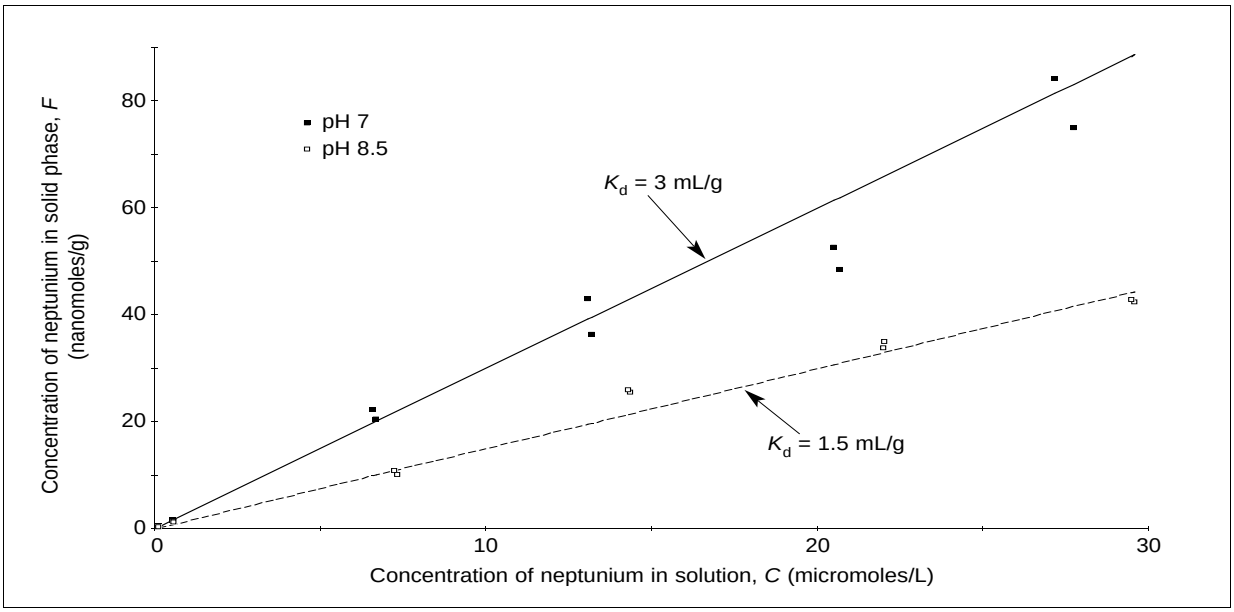

DTN: LA0010JC831341.007

NOTE: A plot is shown of the concentration, *F*, of neptunium in the solid phase of the clinoptilolite-rich tuff G4-1510 versus the concentration, *C*, of neptunium in the solution phase of J-13 well water and linear (K_d) fits to the data for two values of pH. From Triay et al. (1997, Figure 55).

Figure 3. Neptunium Sorption onto Clinoptilolite-Rich Tuff

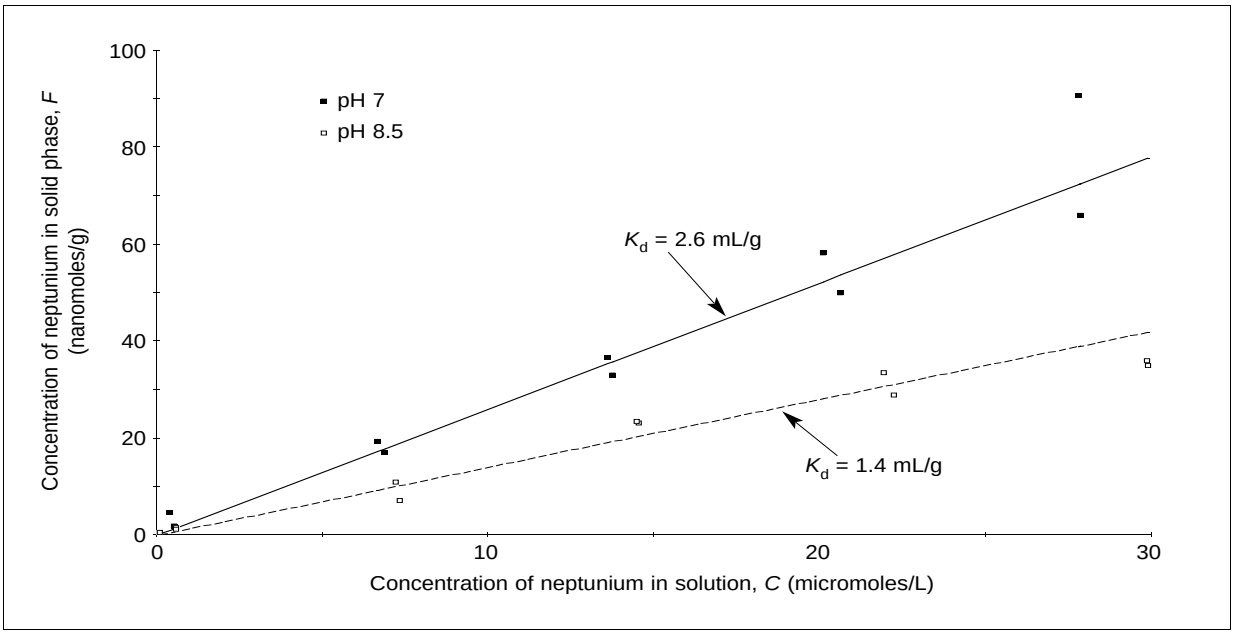

DTN: LA0010JC831341.007

NOTE: A plot is shown of the concentration, *F*, of neptunium in the solid phase of clinoptilolite versus the concentration, *C*, of neptunium in the solution phase of J-13 well water and linear (K_d) fits to the data for two values of pH. From Triay et al. (1997, Figure 56).

Figure 4. Neptunium Sorption onto Clinoptilolite

± 1), is close to zero (Triay, Cotter, Kraus et al. 1996, p. 10). This result could be due to differences in the surface chemistry of pure hematite compared to hematite in tuff. For example, it could be due to passivation of the hematite surfaces in the tuff by elements (such as the rare earths) that have a higher affinity for hematite than neptunium and thus occupy the sorption sites. Alternatively, there may be too little hematite present in the tuffs to provide an adequate number of sorption sites.

The kinetics of neptunium sorption onto tuffs and pure minerals were investigated, and it was found that the sorption of neptunium onto tuffs and clinoptilolite appears to be fast, with steady-state conditions reached in 5 to 7 days, with no significant changes thereafter, in experiments conducted for up to 30 days (Triay et al. 1997, Figure 59). Although the data are scant, they can be used as guidelines. This is not the case for pure minerals that tend to sorb by means of a co-precipitation mechanism (such as calcite) or by surface complexation (such as hematite) (Triay et al. 1997, Figure 60). The dissolution/precipitation reactions that may accompany the co-precipitation of neptunium with calcite appear to be slow compared with other sorption mechanisms.

Experiments with p#1 water indicate that neptunium sorption onto tuffs and zeolites is very limited (K_d < 1 mL g^{-1}) in this water regardless of conditions (pH and neptunium concentration) (Triay, Cotter, Huddleston, et al. 1996, pp. 27–49, 56). If clinoptilolite is the only mineral affecting neptunium sorption on tuffs and if ion exchange at the surface is the dominant sorption mechanism, then the lack of neptunium sorption onto clinoptilolite could be the formation of the neptunium carbonado complex ($NpO_2CO_3^-$) in p#1 water to the exclusion of the neptunyl cation. Another possibility is that in p#1 water there is strong competition for sorption sites due to the higher ionic strength of this water compared with J-13 water.

Figures 5 and 6 summarize the sorption of neptunium under atmospheric conditions for tuffs and minerals as a function of water type. Sorption onto zeolitic tuffs decreases considerably with increasing carbonate content and ionic strength of the water (compare sorption measured using carbonate-rich p#1 waters to those obtained using J-13 waters in Figure 5). Figure 6 shows that calcite and hematite have high affinities for neptunium, particularly in p#1 water. The calcite-rich tuff G2-723 (34 percent calcite), exhibits considerable sorptive capacity for neptunium. Assuming that the calcite in the tuff sample has the same surface area as the natural calcite used for the experiments (and that calcite is the only sorptive mineral in the tuff), one would predict from neptunium sorption on pure calcite a log K_d for tuff G2-723 of 1.5. This prediction agrees well with the measured K_d (Figure 6).

Conclusions Regarding Sorption Behavior of Neptunium with Respect to Variations in Groundwater Composition—The mechanisms by which neptunium appears to sorb onto mineral surfaces in the Yucca Mountain flow system appear to be ion exchange or surface complexation on zeolitic phases and co-precipitation and surface adsorption involving carbonate minerals. The ion-exchange/surface-complexation mechanism appears to be responsible for the 0.5 to 5.0 mL g^{-1} range in sorption-coefficient values consistently measured in zeolitic rock samples. The high end of this range may reflect other mechanisms, such as the presence of trace minerals with high affinities for neptunium.

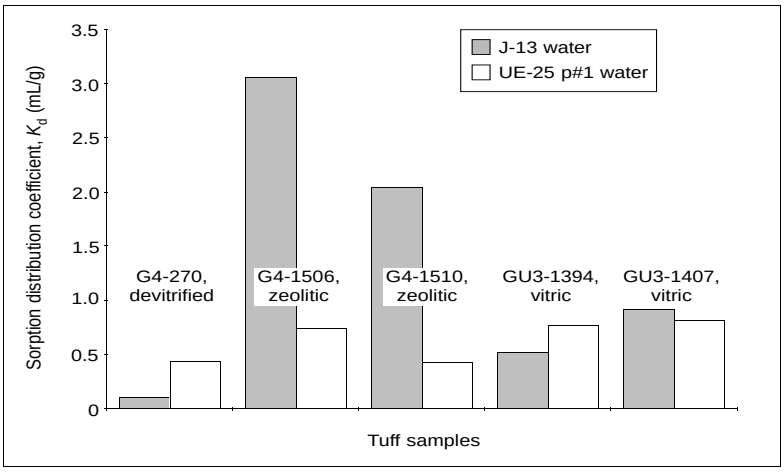

DTN: LA0010JC831341.007

NOTE: Values of K_d for sorption of neptunium onto several tuffs that allow comparison of sorption (under atmospheric conditions) for the two types of groundwaters. The initial neptunium concentration ranged from 6×10^{-7} to 8×10^{-7} M. The tuffs were wet-sieved to particle sizes ranging from 75 to 500 µm. The pretreatment period was 2 to 14 days, and the sorption period was 3 to 23 days. From Triay et al. (1997, Figure 68).

Figure 5. Dependence on Water for Sorption onto Tuffs

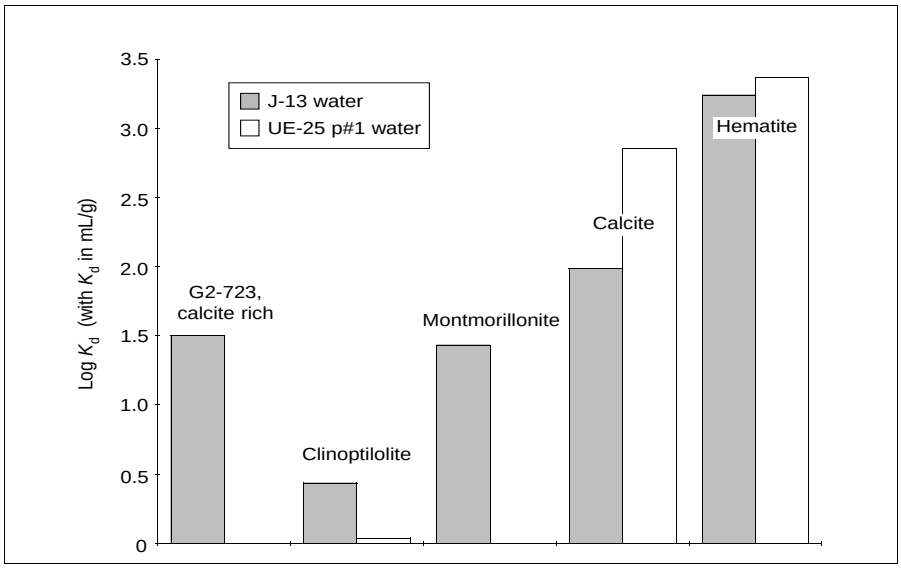

DTN: LA0010JC831341.007

NOTE: Values of K_d for neptunium onto several minerals and a calcite-rich tuff that allow comparison of sorption (under atmospheric conditions) for the two groundwaters. The initial neptunium concentration ranged from 6×10^{-7} to 8×10^{-7} M. The tuff and the calcite were wet-sieved to particle sizes ranging from 75 to 500 µm; the montmorillonite was dry-sieved; the clinoptilolite and hematite were not sieved; the sorption period was 17 to 22 days. From Triay et al. (1997, Figure 69).

Figure 6. Dependence on Water for Sorption onto Minerals

6.4.4.1.4.3 Americium, Actinium, and Samarium

The radionuclides of concern represented by these elements have the following characteristics in common: (1) In groundwater-rock systems of concern in this report, these elements are all present in the +3 oxidation state. (2) In aqueous solutions with compositions typical of groundwaters, the solubility of these elements tends to be controlled by sparingly soluble carbonates, phosphates, fluoride-carbonate complexes, and to a lesser extent, hydroxycarbonate compounds (Mariano 1989). The elements may also form solid solutions with carbonates, phosphates, fluorides, and oxides of the major cations in groundwaters. (3) The dominant solution species associated with these elements are generally complexes with carbonate, phosphate, and hydroxide ligands (Sillen and Martell 1964; Cotton and Wilkinson 1988, pp. 985-987; Runde et al. 1992, p. 93). (4) The solution species tend to have high affinities for adsorption onto oxide surfaces as discussed below. The radionuclides represented by these elements are all in the "strongly sorbing" group discussed by Meijer (1992).

Because the chemistry of all three of these elements is similar in aqueous solution and sorption reactions, they will be discussed as a group.

Behavior in Solutions Representative of Yucca Mountain Groundwaters—In solution, americium, actinium, and samarium occur as simple (trivalent) cations, carbonate complexes, phosphate complexes, and hydrolysis products (Wood 1990). Complexes with other inorganic ligands (for example, Cl^-, F^-, and SO_4^{2-}) will not be of importance in the water compositions expected in the Yucca Mountain flow system. Therefore, speciation models for the rare-earth elements and trivalent actinides should consider pH, carbonate-ion concentration, and possibly phosphate-ion concentration as key variables. According to Byrne and Kim (1993), phosphate complexes will not be significant unless the ratio of the total phosphate concentration to the total carbonate concentration is greater than 1.3×10^{-3}. This condition makes it unlikely that phosphate complexes will be important in Yucca Mountain groundwaters. Therefore, carbonate complexes are expected to dominate the solution species for these elements. The solubility-controlling solids in Yucca Mountain groundwaters will likely be carbonates, hydroxycarbonates (Kerrisk 1984), and possibly phosphates (see the following section).

According to Nitsche et al. (1993; 1995), the solubilities of americium compounds in solutions representative of water compositions expected within Yucca Mountain are approximately 1 to 2×10^{-9} M in J-13 water and 3 to 30×10^{-7} M in p#l water as a function of pH at 25ºC. At 60ºC, the solubilities of americium compounds were 1×10^{-8} to 2.5×10^{-6} M in J-13 water and 7×10^{-10} to 3×10^{-9} M in p#l water as a function of pH. The solubility-controlling solids were found to be hexagonal and orthorhombic forms of $AmOHCO_3$. The speciation of americium in these solutions could not be determined due to the low solubilities of americium in these water compositions relative to the detection limits of the available spectroscopic techniques. Preliminary modeling calculations with the speciation code EQ3 suggest that carbonate complexes dominate in both J-13 and p#l waters at 25º and 60ºC (Ogard and Kerrisk 1984).

Qualitative Evidence for Behavior in the Surficial Environment—Although the geological community generally regards the rare-earth elements as immobile during most water-rock

alteration processes (Taylor and McLennan 1988), detailed studies of weathering profiles suggest that these elements may be redistributed within these profiles during weathering. Duddy (1980) studied a weathering profile formed on a homogeneous sedimentary rock unit in southeastern Australia. This profile was formed in a cool temperate climate with 200 cm yr^{-1} precipitation. The profile contained bleached zones and ferruginous zones in which iron was reduced or oxidized, respectively. The rare-earth elements were up to 7 times enriched in the bleached portions of the profile. Based on the sorption data discussed in the following section, this result is somewhat puzzling as one might expect these elements to be coprecipitated or adsorbed to the secondary ferric oxides formed in the profile. In fact, the rare-earth elements appeared to be enriched in vermiculite, an expanding magnesium-ferrous iron trioctahedral clay that formed in the weathering profile as a result of the alteration of biotite. Up to 10 weight percent (wt %) of rare-earth elements was reported in vermiculites on the basis of electron-probe analyses. The elements originated from the dissolution of apatite ($Ca_5(PO_4)_3(F,Cl,OH)$) and other minerals present higher in the profile.

Banfield and Eggleton (1989) studied the rare-earth elements in an Australian weathering profile formed on granite. These authors also noted that these elements were mobile in the profile. However, they found that (primary) biotite crystals in the granite contained apatite inclusions rich in rare-earth elements or cavities resulting from the dissolution of apatite. The apatite crystals were apparently dissolved during weathering leaving behind fine-grained (< 10 μm) rare-earth-element phosphate phases including florencite, rhabdophane ($CePO_4 \cdot H_2O$), and an unidentified phosphate-free aluminum-rare-earth-element mineral, possibly a carbonate, hydroxycarbonate, or fluorocarbonate. Vermiculites were also present in this profile, but they were not analyzed for rare-earth-element contents.

These two studies clearly indicate that the rare-earth elements can be mobilized in the surficial environment. However, they also suggest that this mobilization is generally of a local nature resulting in the precipitation of new rare-earth-element phases or the incorporation of these elements in other secondary phases, such as clays. These studies did not address the question of whether adsorption of the rare-earth elements onto the surfaces of other mineral phases is a significant process in controlling the mobility of these elements in surficial environments. Loubet and Allegre (1977) noted that the light rare-earth elements were not mobilized in the reactor zones at Oklo, Gabon.

Data on the behavior of americium in the surficial environment is limited to anthropogenic examples. Americium was found to be very immobile in most of the studies located in the literature (for example, Means et al. 1978; Carpenter et al. 1987). The main uncertainty regarding the surficial behavior of americium appears to be the degree to which it is mobilized through colloidal transport (Penrose et al. 1990).

Data from Laboratory Sorption Experiments—Ion-exchange studies involving the sorption of lanthanide ions on montmorillonitic clays have been reported by Frysinger and Thomas (1960), Aagaard (1974), Bruque et al. (1980), and Bonnot-Courtois and Jaffiezic-Renault (1982). These studies conclude that essentially all of the exchange capacity of the clays is available to lanthanide ions and that the exchange reactions are rapid (that is, minutes). Frysinger and Thomas noted that the Cs^+-Y^{3+} binary exchange was not dependent on pH over the range from 3

to 7. At low cesium concentrations, such as are likely to occur in the potential repository horizon, the clay showed a slight preference for the lanthanide ions relative to cesium, and this preference increased with temperature (30–75ºC).

Koeppenkastrop and De Carlo (1992; 1993) have evaluated the sorption of the rare-earth elements by iron oxides, manganese oxides, and apatite from high-ionic-strength aqueous solutions (ultraviolet-irradiated natural seawater). One nanomole of each rare-earth-element radiotracer was equilibrated with approximately 10 mg of the solid phase in 1 kg of seawater. The pH of the system was maintained at 7.8 in all the experiments. The percentage of rare-earth element adsorbed on FeOOH and MnO_2 was measured in the presence and absence of carbonate. Carbonate appeared to affect the kinetics of the adsorption reactions but not the extent of adsorption at equilibrium. The sorption reactions equilibrated within tens of minutes. Under the conditions of the experiments, the rare-earth elements are shown to have very high affinities for the oxide and phosphate phases (K_d >> 1,000 mL g^{-1}). Koeppenkastrop and De Carlo (1993) further state that modeling of sorption data derived from experiments with natural particles indicates that desorption rate constants are much smaller than adsorption rate constants.

The high affinity of the rare-earth elements for iron- and manganese-oxide phases suggests that these phases would act as "getters" for these elements in surficial environments. Yet, the data reported by Duddy (1980) suggest that the rare-earth elements in the weathering profile he studied were preferentially incorporated in vermiculite in the "bleached" zones and not adsorbed onto ferric oxides in the ferruginous zones. This effect suggests that there were other constituents in the solution phase of the profile investigated by Duddy (1980) that had higher affinities for the oxide surfaces than the rare-earth elements and that they were present in sufficient quantity to saturate the available surface sites. A possible candidate would be the Al^{3+} ion (see Brown et al. 1955).

Stammose and Dolo (1990) reported on batch-sorption experiments with americium (10^{-8} M) on clay as a function of pH and ionic strength. The clay used in the experiments was a mixed-layer clay consisting of kaolinite and smectite. At ionic strengths of 0.01 and 0.1 M ($NaClO_4$), the americium sorption coefficient was greater than 10^3 mL g^{-1} over the entire pH range (3–10) addressed by the experiments. In the higher ionic-strength solutions (1 and 3 M), the sorption coefficients were low (10 mL g^{-1}) at a pH of 2 but increased to values in the range of 10^4 to 10^5 mL g^{-1} for pH values greater than 6.

Overall, the data presented by these authors suggest: (1) the ion-exchange sites on the clay have a very high selectivity for americium at trace concentrations; (2) sodium ions at sufficiently high concentrations can displace the americium from these sites; (3) americium is also adsorbed in surface-complexation reactions; (4) the surface-complexation reactions define a sorption edge that has minimum values at low pH and reaches a maximum at a pH of approximately 7; (5) americium is adsorbed as an inner-sphere complex, and its adsorption affinity in surface-complexation reactions is therefore not a function of ionic strength; and (6) at trace americium concentrations, carbonate complexation of americium may compete with surface-complexation reactions in the pH range from 8 to 10, leading to a slight decrease in adsorption in this range.

Allard and Beall (1979) have presented americium sorption-coefficient data for a range of mineral types including clays, feldspars, carbonates, phosphates, oxides, oxyhydroxides, and other less common minerals. The sorption coefficients were measured over a range of pH from 4 to 9 in a low ionic-strength (synthetic) groundwater similar in composition to an average Yucca Mountain groundwater. Initial americium solution concentrations were in the range from 1.8 to 5.0×10^{-9} M. Data presented for clay minerals indicate that ion exchange occurred on these minerals in the lower pH range (< 6). Surface recrystallization reactions are evident in the low pH data for apatite (also, see Jonasson et al. 1985) and fluorite. On the remaining silicates and nonsilicates, americium appears to sorb dominantly by surface-complexation reactions. In all cases, the sorption-coefficient values are in excess of 10^3 mL g^{-1} over the pH range likely to be encountered in the Yucca Mountain groundwaters (CRWMS M&O 2000a, Table 3).

In summary, trivalent actinium, americium, and samarium likely sorb by at least two distinct mechanisms. At pH values less than approximately 6, ion-exchange reactions on clays and other ion-exchanging minerals may dominate the adsorption behavior of these elements in low ionic-strength solutions. These reactions will show dependencies on ionic strength and ion selectivity. At pH values greater than 6, sorption appears to involve primarily inner-sphere surface-complexation reactions. Although these reactions are independent of ionic strength, they will likely be subject to competition with other sorbing species at sufficiently high sorption densities. In the pH range from 8 to 10, carbonate-complexation reactions in solution may compete with the surface-complexation reactions involving these elements. However, the surface-complexation reactions are expected to dominate over carbonate-complexation reactions in Yucca Mountain groundwaters.

Sorption Data Obtained on Yucca Mountain Samples—Sorption coefficients for cerium, europium, and americium have been determined for a variety of rock samples from Yucca Mountain and in several groundwater compositions from the site (Thomas 1987; Knight and Thomas 1987). The data are generally consistent with the conclusions stated in the previous section. However, several additional points should be emphasized. First, experiments with rock samples that contained calcite (for example, G1-2901 and G2-723) or groundwater that was saturated with calcite (such as p#l) showed very large sorption coefficients for these elements. This result suggests the radionuclides were either coprecipitated with carbonates (for example, calcite) or formed solid solutions on the surfaces of existing carbonates. Because groundwaters in the unsaturated zone at Yucca Mountain are likely near saturation with calcite, this observation suggests the trivalent lanthanides and actinides will not be mobile in the proposed repository horizon. Second, experiments on samples with more than a few percent clay (for example, G1-3658) also showed high sorption coefficients. For these rock types, the ionic strength of the groundwaters may play a role in determining the magnitude of the sorption coefficients for these elements. Third, experiments with groundwaters containing high carbonate concentrations (such as p#l) show large sorption coefficients for these elements, suggesting that carbonate complexation in solution does not lead to significant decreases in the sorption coefficients for these elements in Yucca Mountain groundwaters.

Conclusions Regarding Sorption Behavior with Respect to Expected Variations in Groundwaters—The impact of variations in groundwater compositional parameters within the ranges expected in Yucca Mountain on the sorption behavior of actinium, americium, and samarium

should be relatively minor. Over the expected pH range (6–9), the trivalent actinides and lanthanides appear to sorb primarily by inner-sphere surface-complexation mechanisms. These mechanisms are not sensitive to variations in ionic strength. Further, these elements appear to have high affinities for the mineral surfaces typically available in the Yucca Mountain rock units over the entire pH range expected. This result suggests that the trivalent actinide and lanthanide radionuclides will be strongly sorbed (K_d > 100 mL g^{-1}) over the entire range of expected groundwater compositions.

6.4.4.1.4.4 Uranium

Behavior in Solutions Representative of Yucca Mountain Groundwaters—Under the redox potentials expected in Yucca Mountain groundwaters, particularly in the unsaturated zone, uranium should be in the +6 oxidation state. In this oxidation state, uranium will be present in solution in a variety of complexes including $(UO_2)_2CO_3(OH)_3^-$, $UO_2(CO_3)_2^{2-}$, $UO_2(CO_3)_3^{4-}$, $UO_2(OH)_2$(aq), $UO_2(CO_3)$(aq), and other minor species. Phosphate, fluoride, or sulfate species will not be significant within the concentration ranges for these anions and the pH range expected in Yucca Mountain groundwaters (CRWMS M&O 2000a, Table 3).

Qualitative Evidence for Behavior in the Surficial Environment—Data on the behavior of uranium in the surficial environment are available from various sources. Several types of uranium ore deposits have been studied as natural analogs to repository settings. Other sources of data include studies of uranium mill-tailings piles, waste-stream outfalls, and other uranium ore deposits. Only the natural analog studies will be discussed in this subsection.

The deposits that have been studied as natural analogs include the deposits at Oklo, Gabon, the Alligator Rivers region in Australia, Cigar Lake in Canada, Poços de Caldas in Brazil, and Peña Blanca in Mexico. Each of these deposits has been studied in considerable detail to define the geochemical behavior of uranium and its daughter products in the environments in which the ore deposits are found. Although none of the environments are completely analogous to the Yucca Mountain site, the Peña Blanca deposit is at least situated in Tertiary volcanic tuffs similar to those present at Yucca Mountain.

A critical aspect of any analog for potential uranium migration at the Yucca Mountain site is that the uranium source must be subject to redox potentials similar to those expected at Yucca Mountain, particularly in the unsaturated zone. This fact eliminates from detailed consideration data from the Cigar Lake and probably the Oklo deposits (Goodwin et al. 1989; Cramer and Sargent 1994; Brookins 1983).

The Alligator Rivers deposits are exposed to oxidizing conditions in a surficial environment (Giblin and Snelling 1983). Uranium isotope-disequilibrium studies at this site indicate that uranium migration has occurred relatively recently (Snelling and Dickson 1979). However, evidence for recent transport does not by itself provide an estimate of the rate of transport and, more importantly, of the chemical controls on this rate. The latter type of information could be very useful to the YMP.

At the Koongarra deposit, uranium migration is significantly retarded by the precipitation of uranyl phosphate minerals (Snelling 1980). Although phosphate concentrations in local groundwaters are not high (0.01 to 0.1 mg L^{-1}), significant phosphate concentrations are found in the country rocks in minerals such as apatite. The phosphate in the rocks is apparently redistributed locally by groundwater, resulting in the precipitation of uranyl phosphate minerals within the zone of weathering (Snelling 1980). This retardation mechanism is not expected to be important at Yucca Mountain, given the low phosphate concentrations found in Yucca Mountain rock units (Broxton et al. 1986).

Uranium in the zone of weathering at Alligator Rivers also appears to be associated with and is probably retarded by ferric-iron compounds (Payne et al. 1990). Sorption experiments have been carried out involving uranium sorption on whole-rock samples and on pure mineral samples (Payne et al. 1990). The results of these experiments suggest that ferric hydroxides are strong sorbers of uranium in this system over a pH range of 5 to 9. This result is not particularly new as similar results on ferric oxyhydroxides have been reported by others (for example, Hsi and Langmuir 1985). A potentially important result from these studies would be the derivation of some defensible estimate of the rate of transport of uranium in this system using the experimentally derived chemical constraints on uranium adsorption behavior and a valid groundwater flow model. However, the complicated nature of the flow system of the site may preclude the development of defensible flow models.

The Peña Blanca uranium deposits in Mexico provide a potentially more appropriate analog site in relation to Yucca Mountain. The primary uranium deposits at this site are hydrothermal in origin and were emplaced in structural features associated with Tertiary silicic volcanic tuffs that overlie Mesozoic calcareous basement (George-Aniel et al. 1991). In addition to the hydrothermal deposits, which contain sulfide minerals as well as uranium oxides, supergene deposits have formed locally through the leaching of uranium from the volcanic rocks and subsequent precipitation as uranyl silicate minerals, including uranophane (Murphy 1992). The supergene deposits are hosted by kaolinitized and silicified rhyolite and do not appear to contain sulfide minerals. The absence of sulfide minerals is important because sulfides, such as pyrite, oxidize readily in the surficial environment to produce acidic conditions unlike those expected within Yucca Mountain. The supergene deposits are thought to have formed in the surficial environment (George-Aniel et al. 1991), and their study may offer useful insight into the potential for migration of uranium from the proposed repository within Yucca Mountain. No data on the present-day sorption behavior or rate of migration of uranium in these deposits has been reported to date. However, several geochemical studies are currently underway to provide such data (Murphy 1992).

A qualitative study by Rosholt et al. (1971) established that uranium was leached from devitrified tuff samples but not from hydrated glassy samples obtained from a given geologic unit. This and other data presented suggest devitrification makes the uranium in tuffs more mobile in the surficial environment. Zielinski et al. (1986) and Flexser and Wollenberg (1992) observed that uranium in Yucca Mountain devitrified tuffs was commonly associated with manganese oxides. This fact suggests that, although uranium may be mobile in the unsaturated devitrified tuffs in Yucca Mountain, it could be retarded to the extent that there are manganese oxides present along the flow path with sufficient capacity to sorb the potential flux of uranium

from the proposed repository horizon. Given the amount of uranium to be emplaced in the potential repository, it would seem the sorption capacity of the manganese oxides present in the mountain (Bish and Chipera 1989) would be rapidly saturated. Nonetheless, manganese oxides may significantly retard the movement of uranium in some of the fracture-flow scenarios.

Data from the Literature—Data have been presented on the adsorption of uranium as U(VI) onto a variety of pure mineral phases in simple electrolytes. Among the solid phases investigated are goethite (for example, Hsi and Langmuir 1985), hematite (Ho and Miller 1986), silica gel (Zielinski 1980), clays (Tsunashima et al. 1981), and zeolites (Ames et al. 1983). The results reported are sometimes difficult to reconcile. For example, Hsi and Langmuir (1985) report that hematite sorbs very little of the uranium in solutions with 5×10^{-5} M uranium and 10^{-3} M total carbonate, whereas Ho and Miller (1986) report that hematite sorbs up to 100 percent of the uranium in their experiments with similar uranium and bicarbonate solution concentrations. Both sets of experiments had similar hematite surface areas. The main difference was that the solution phase in the Hsi and Langmuir (1985) experiments also contained 0.1 M $NaNO_3$. However, $NaNO_3$ is generally considered to be a nonreactive electrolyte, and nitrate does not form complexes with uranium in the pH range addressed in these experiments. Why there is a difference in these results is unclear. One possibility is that the surface characteristics of the solid phases used were not the same in the two sets of experiments.

Silica gel appears to have a clear affinity for uranium as established by the results of laboratory experiments and by observations on the association of uranium with opals in nature (Zielinski 1980). According to Maya (1982), the uranium is adsorbed to silica gel as the uranyl ion, free of carbonate ligands. Zielinski has shown that sorption of uranium onto silica gel is sensitive to the total carbonate concentration of the solution phase when this concentration is above 0.01 M. Experiments carried out at elevated temperatures (65 to 80ºC) resulted in somewhat higher sorption coefficients. Data regarding competitive effects on silica gel between uranium and other constituents in groundwaters at near-neutral pH have not been found in the literature.

Sorption of uranium by clays has been investigated in some detail. Borovec (1981) has presented data that indicate montmorillonite has a high selectivity for uranyl ions relative to divalent ions of zinc, manganese, calcium, magnesium, cobalt, cadmium, and nickel at a pH value of 6 in chloride solutions. However, Tsunashima et al. (1981) found montmorillonite has a greater selectivity for calcium, magnesium, and barium ions than for uranyl ions in nitrate solutions over the pH range from 4.0 to 4.5. Montmorillonite was found to have a greater selectivity for the uranyl ion than for sodium and potassium ions in the same solutions. Ames et al. (1983) found that uranium was strongly sorbed to montmorillonite from 0.01 M NaCl solutions but weakly sorbed from 0.01 M $NaHCO_3$ solutions in the pH range from 8 to 9.

Because groundwaters in Yucca Mountain contain significant concentrations of bicarbonate, calcium, and magnesium ions, these data suggest overall that uranyl ions may not compete favorably for exchange sites on clay minerals in Yucca Mountain, although quantitative prediction of the extent of exchange would require more detailed analysis.

Data available on uranium sorption on zeolitic minerals are very limited. Ames et al. (1983) report that clinoptilolite has a low affinity for trace levels of uranium in the pH range from 8 to 9 in 0.01 M $NaHCO_3$. Doi et al. (1975) found that uranium at concentrations of 10^{-6} g per g of

solution was strongly sorbed onto clinoptilolite from perchlorate solutions in the pH range from 4 to 8.5.

Data on uranium sorption on alluvium from the general vicinity of Yucca Mountain were obtained in two studies. Wolfsberg (1978, pp. 3, 7, 14) measured sorption of U(VI) on three alluvium samples obtained from NTS drillholes in Frenchman Flat (hole U5e, also called RNM-1) and Yucca Flat (hole U3bv). Measured values of K_d using groundwater from the alluvial aquifer in Frenchman Flat (hole RNM-2S) ranged from 6 to 9 mL g^{-1}. Wolfsberg et al. (1983, pp. 4–7) measured sorption of U(VI) on alluvial material collected from a trench at the Beatty, Nevada, Disposal Facility and from borehole U3hr in Yucca Flat. Water used for these sorption experiments was collected from supply wells located near the locations from which the alluvial materials were obtained. Average K_d values for the integral samples ranged from 1 to 3 mL g^{-1}; slightly higher K_d values of 6 to 9 mL g^{-1} were obtained for the silt and clay fractions.

Data from Laboratory Sorption Experiments with Yucca Mountain Rock and Water Samples Obtained Prior to 1993—Data on uranium sorption coefficients for Yucca Mountain rock/water systems were reported by Thomas (1987) and discussed by Meijer (1990; 1992). The affinity of the devitrified and vitric tuffs for trace levels of uranium is generally small (K_d < 5 mL g^{-1}) over the pH range from 6 to 9 in J-13 water. For zeolitic tuffs, the K_d is near zero at a pH value of 9 but increases with decreasing pH to values of approximately 25 mL g^{-1} at a pH of 6 in J-13 water. This behavior suggests the uranyl cations can exchange with the major cations in zeolites.

Uranium batch-sorption experiments in p#1 water were only carried out in the pH range from 8.3 to 9.3 with the result that measured sorption coefficients were small (0 to 2.7 mL g^{-1}; Thomas 1988). A devitrified sample showed the largest sorption coefficient. In the pH range from 6 to 8, it is expected that the sorption coefficients for uranium in p#1 water will increase with decreasing pH (because of predominance by $UO_2CO_3^0$ at higher pH values), but they will likely be smaller than the coefficients obtained for the same rock samples in J-13 water over this pH range. In H-3 groundwater, sorption coefficients were also low for zeolitic and devitrified rock types over the pH range from 9.2 to 9.3, presumably reflecting the elevated carbonate content of this water. However, data for a vitric sample showed a value of 6.2 mL g^{-1} for the uranium sorption coefficient at a pH value of 9. This relatively high value has not been explained.

Data from Laboratory Sorption Experiments with Yucca Mountain Rock and Water Samples Obtained after 1993—The sorption of U(VI) onto samples of the three types of tuff in J-13 water (under oxidizing conditions) at the two pH values (7 and 8.5) was studied. However, to identify the sorbing minerals in the tuffs, sorption onto the pure minerals hematite, clinoptilolite, albite, and quartz was also studied. It was found that uranium in J-13 water does not sorb onto devitrified and vitric tuffs, albite, and quartz (Table 7).

Wet-sieved tuffs, albite, and quartz samples with particle sizes in the range from 75 to 500 μm were used. Initial uranium concentrations ranged from 8 x 10^{-8} to 1 x 10^{-4} M. The pretreatment period was 2 to 4 days, and the sorption period, 3 to 4 days. The negative values reported in Table 7 are the result of analytical error for the case of very little sorption (that is, a small number obtained as the difference of two large numbers). For the experimental conditions cited,

uranium sorption onto zeolitic tuffs and clinoptilolite is nonlinear and can be fitted with Freundlich and Langmuir isotherms (Figures 7 and 8).

Table 7. Uranium Sorption in J-13 Water under Oxidizing Conditions

Solid phase	pH	K_d (mL g^{-1})
G4-268, devitrified tuff	7	-1×10^{-1}
	8.5	7×10^{-1}
GU3-1405, vitric tuff	7	-4×10^{-1}
	8.5	5×10^{-1}
Quartz	7	3×10^{-1}
	8.5	4×10^{-2}
Albite	7	-5×10^{-2}
	8.5	-1×10^{-1}

DTN: LA0004AM831341.001

For the clinoptilolite-rich zeolitic tuff sample G4-1510, the scatter in the data makes it impossible to conclude whether there is a significant difference between the experiments performed under a carbon-dioxide overpressure and a pH of 7 or at atmospheric conditions and a pH of 8.5 (Figure 7). However, the experiments with pure clinoptilolite indicate that sorption increases with decreasing pH for U(VI) (Figure 8), as is the case for Np(V). Because the major constituent of tuff sample G4-1510 is clinoptilolite, predictions of the K_a (K_d divided by the solid-phase surface area; Triay, Cotter, Kraus et al. 1996) were made for uranium sorption onto this tuff by assuming that clinoptilolite is the only sorbing phase. Inspection of Table 8 indicates that predictions obtained with this assumption are within a factor of 3 of the measured values for both pH conditions.

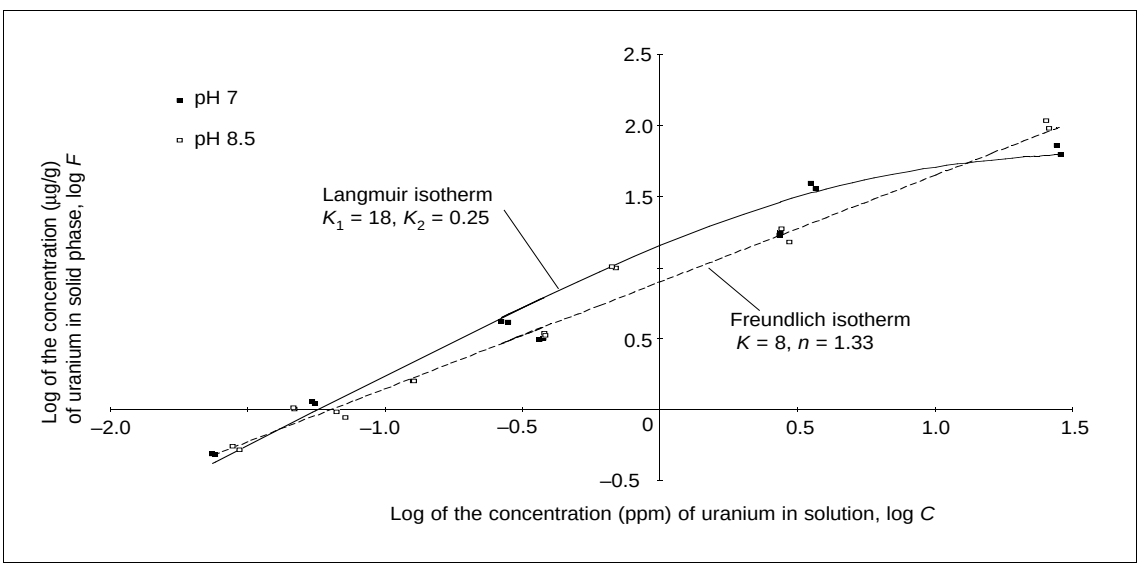

DTN: LA0010JC831341.005

NOTE: The graph is a log-log plot of the concentration of uranium in the solid phase, F, of the clinoptilolite-rich tuff G4-1510 versus the concentration of uranium in the solution phase, C, of J-13 well water. The tuff was wet-sieved to give particles that ranged in size from 75 to 500 m. The period of pretreatment was 2 to 4 days; the period of sorption was 3 to 4 days. The data for a pH of 7 have been fitted with a Langmuir isotherm; the data for a pH of 8.5 have been fitted with a Freundlich isotherm.

Figure 7. Uranium Sorption onto Clinoptilolite-Rich Tuff

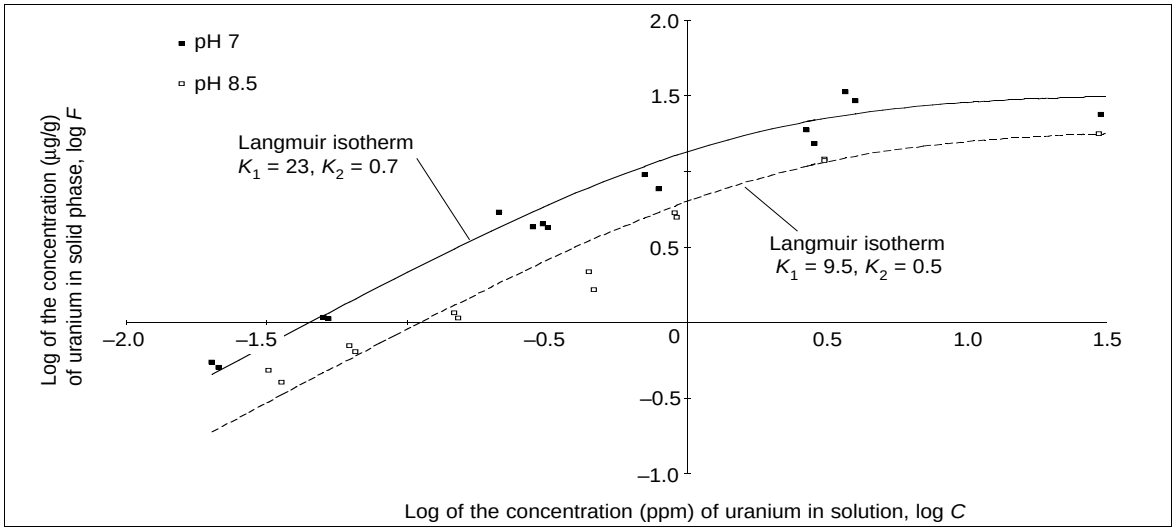

DTN: LA0010JC831341.005

NOTE: This is a log-log plot of the concentration of uranium in the solid phase, *F*, of clinoptilolite versus the concentration of uranium in the solution phase, *C*, of J-13 water. The mineral was unsieved. The period of pretreatment was 2 to 4 days; the period of sorption was 3 to 4 days. The data for each pH (7 and 8.5) have been fitted with a Langmuir isotherm.

Figure 8. Uranium Sorption onto Clinoptilolite

Table 8. Prediction of Uranium Sorption on Clinoptilolite-Rich G4-1510 Tuff in J-13 Water

Initial concentration (M)	pH	Measured K_a (m)	Predicted K_a (m)[a]
2×10^{-7} to 4×10^{-7}	7	4×10^{-7}	8×10^{-7}
	8.5	5×10^{-7}	2×10^{-7}

DTN: LA0004AM831341.001 (K_d) and LA0004AM831341.002 (surface area).

NOTE: [a]Assuming clinoptilolite is the only sorbing mineral in the tuff, present at 59 wt. %.

The sorption of uranium onto pure iron oxides (such as hematite) is very large (and large uncertainties in the K_d values result from measuring the small amounts of radionuclide left in solution after sorption). Although the measured sorption of uranium onto pure hematite is very large, sorption onto devitrified tuffs, which appear to have traces of hematite (1 percent ± 1), is essentially zero. As with neptunium, this result could be due to differences in the surface of pure hematite compared to hematite in tuff. Alternatively, it could be due to passivation of the hematite surfaces in the tuff by elements (such as the rare earths) that have a higher affinity for hematite than uranium and, thus, occupy the sorption sites.

Conclusions Regarding Sorption Behavior of Uranium with Respect to Expected Variations in Groundwaters—The dominant groundwater compositional controls on the sorption behavior of uranium on Yucca Mountain rock samples will likely be pH, carbonate content, and the concentrations of calcium and magnesium ions in solution. The pH and carbonate contents

influence the sorption largely as a result of the decrease in carbonate complexation of uranium with decreasing pH. These two parameters are therefore not entirely independent. However, different water compositions can have different carbonate contents at a given pH. The expectation is that waters with higher carbonate contents will be associated with lower sorption coefficients. This trend would apply to both ion-exchange and surface-complexation sorption mechanisms. However, decreasing pH will have different effects on uranium sorption behavior in zeolitic and clay-rich samples versus devitrified and vitric samples. In the former samples, the uranium sorption coefficient will likely increase with decreasing pH due to the increase in uranyl ion concentrations with decreasing pH. For a given rock-water system, the magnitude of this increase will depend on the concentrations of competing ions such as calcium and magnesium in the water. For high calcium and magnesium waters, the competition effects will be substantial. Because unsaturated-zone waters are relatively enriched in calcium and magnesium, uranium sorption coefficients in the unsaturated zone may be on the low end of the range reported to date (Thomas 1987; 1988) unless the low total carbonate concentrations in these waters balance the effect of the elevated calcium and magnesium concentrations.

6.4.4.1.4.5 Technetium

Technetium appears to show nonzero, although minimal, retardation in Yucca Mountain rock-water systems (Ogard and Vaniman 1985; Rundberg et al. 1985; Thomas 1988). However, the cause of this retardation has not been identified, and it may simply be an experimental artifact. If sufficiently reducing conditions could be shown to exist in portions of the flow system down-gradient of the proposed repository, retardation of technetium by the precipitation and sorption of Tc^{4+} species would provide a barrier for this element.

6.4.4.1.4.6 Protactinium

Behavior in Solutions Representative of Yucca Mountain Groundwaters—In aqueous systems, protactinium appears to exist dominantly in the +5 oxidation state, although the +4 state may occur in reducing environments (Brookins 1988). In both oxidation states, protactinium is strongly hydrolyzed and forms highly insoluble compounds (Cotton and Wilkinson 1988). This result implies that the +5 solution chemistry of protactinium is more akin to that of Nb(V) than to other actinides in +5 oxidation states, such as PuO_2^+ or NpO_2^+. If this interpretation is correct, the solution parameter of greatest importance to protactinium sorption behavior would be pH.

Sorption Data from the Literature—Batch-sorption experiments with protactinium have yielded some interesting results. In dilute to intermediate ionic-strength solutions, Allard (1982) report large values (10^4 mL g^{-1}) for the protactinium sorption coefficient on alumina and silica at pH values greater than about 7 but much lower values (90 to 500 mL g^{-1}) at pH values less than 7.

Data from Laboratory Sorption Experiments with Yucca Mountain Rock And Water Samples Obtained Prior to 1993—Rundberg et al. (1985) report protactinium sorption coefficients in the range from 3.7 to 8.2 mL g^{-1} for a zeolitic tuff in contact with J-13 water spiked with 10^{-11} to 10^{-14} M protactinium at pH values of 6.3 to 6.7. Combined with the data reported by Allard (1982), these data suggest that protactinium sorbs by a surface-complexation mechanism and that

there is a rather steep sorption edge for protactinium as a function of pH at a pH value of approximately 7.

Conclusions Regarding Sorption Behavior of Protactinium with Respect to Expected Variations in Groundwaters—Batch-sorption data for protactinium suggest that sorption coefficients for this element will be small (< 10 mL g^{-1}) at lower pH values. Because protactinium sorption experiments on rock samples from Yucca Mountain have only been carried out in the low pH range, no firm conclusions can be stated concerning sorption coefficients on Yucca Mountain tuffs at pH values from 7 to 9.

6.4.4.1.4.7 Selenium

Behavior in Solutions Representative of Yucca Mountain Groundwaters—Selenium will occur as anionic species in all water compositions expected at Yucca Mountain. Although the two oxidation states of +4 and +6 (Howard 1977) are found for selenium in surficial waters in contact with atmospheric oxygen, the +4 state predominates under the conditions expected for groundwaters at Yucca Mountain (Howard 1977; White et al. 1991). In that state, selenium is found as the SeO_3^{2-} and $HSeO_3^-$ selenite ions. In the +6 oxidation state, selenium occurs as the SeO_4^{2-} and $HSeO_4^-$ selenate ions.

Evidence for Behavior in the Surficial Environment—Selenium behavior in the surficial environment is very closely tied to the redox potential of different parts of the near-surface environment. Under reducing conditions, selenium is immobilized as $FeSe_2$ at low pH (< 5) and as native selenium at higher pH (Howard 1977). The stability range for native selenium extends nearly to surface redox conditions. When in contact with atmospheric oxygen levels, selenium is apparently stabilized as the selenite ion (SeO_3^{2-}). At higher redox potentials, selenium is oxidized to the selenate ion (SeO_4^{2-}), which appears to be more mobile in the surficial environment than the selenite ion (Howard 1977).

Sorption Data from the Literature—Because selenium occurs as anionic species in the surficial environment, its adsorption behavior is controlled primarily by surface-complexation reactions on oxide minerals including iron oxides and oxyhydroxides (Balistrieri and Chao 1987), manganese oxides and oxyhydroxides, clays (Bar-Yosef and Meek 1987), and other minerals with affinities for anionic species. These surface-complexation reactions are quite sensitive to pH. For example, adsorption on iron oxyhydroxides decreases for both selenite and selenate ions with increasing pH (Balistrieri and Chao 1987). Selenate ions appear to sorb dominantly in the outer layer of the electrical double layer present on oxide surfaces, whereas selenite tends to sorb in the inner layer (Hayes et al. 1987). Selenate ions are subject to ionic-strength effects as well as competitive effects with sulfate and other anions in solution, presumably because they sorb in the outer layer. Selenite ions are not subject to ionic-strength effects but may be subject to competition from other anions sorbing on inner-layer sites (Hingston et al. 1971).

Studies of selenite adsorption on soils in the pH range expected for Yucca Mountain groundwaters indicate relatively limited adsorption (< 30 percent) from 0.05 N chloride solutions containing 0.16 to 0.63 mg L^{-1} selenium (Neal et al. 1987). This limited sorption potential will likely be further decreased in natural waters containing high concentrations of competing anions.

Data from Laboratory Sorption Experiments with Yucca Mountain Rock And Water Samples Obtained Prior to 1993—Data for selenium sorption coefficients on Yucca Mountain rock samples in contact with J-13 water have been summarized by Thomas (1987). Most measured values are less than 5 mL g^{-1}, and they do not appear to correlate with rock type. A puzzling feature of the data is that, for a given rock sample, sorption coefficients are larger in the higher pH experiments (pH of 8.8) compared to the lower pH experiments (pH of 6.0). This result is contrary to the pH dependence predicted on the basis of double-layer theories. Neal et al. (1987) noted a similar effect for selenium sorption on soils for a solution phase enriched in calcium. They suggested the effect may be due to the formation of a calcium-rich surface precipitate or, alternatively, a change in surface charge due to the adsorption of divalent calcium cations. Benjamin (1983) made similar observations involving other divalent cations. These data suggest that in groundwaters relatively enriched in calcium, and perhaps other divalent cations, selenium adsorption may be somewhat enhanced in the alkaline pH range.

Conclusions Regarding Sorption Behavior of Selenium with Respect to Expected Variations in Groundwaters—Sorption coefficients for selenium on Yucca Mountain rock samples have only been measured in J-13 water. These experiments do not show the expected decrease in sorption coefficient with pH. Therefore, variations in pH over the range expected in Yucca Mountain groundwaters do not appear to be the most important groundwater compositional parameter in the sorption behavior of this element. Based on the data obtained in other studies, divalent cations may have a significant impact on the sorption behavior of this element in Yucca Mountain rock/water systems. Additional experiments with waters enriched in divalent cations (such as p#1 water) may be productive and may enlarge the range of selenium sorption-coefficient values appropriate for use in performance-assessment calculations.

6.4.4.1.4.8 Carbon, Chlorine, and Iodine

Because carbon, chlorine, and iodine are unlikely to have significant sorption affinity in the rock/water systems expected at Yucca Mountain, their sorption behavior will not be discussed in detail. For carbon, the most robust retardation mechanism will be isotopic exchange with stable carbon isotopes in groundwater and on carbonate mineral surfaces (Meijer 1993).

Chloride and iodide ions will have no significant retardation in Yucca Mountain rock/water systems and may even have slightly enhanced migration rates due to anion-exclusion effects (Ogard and Vaniman 1985). If conditions were to become sufficiently oxidizing to convert iodide to iodate, some retardation of iodine might occur in the flow system. Such conditions might occur locally, for example, due to radiolysis in the near field.

6.4.4.1.4.9 Cesium, Radium, and Strontium

Behavior in Solutions Representative of Yucca Mountain Groundwaters—These elements show relatively simple solution behavior in typical groundwaters. They are not subject to changes in oxidation state in the groundwater compositions expected in Yucca Mountain. Radium and cesium are invariably present as the simple Ra^{2+} and Cs^{+} cations in the expected groundwater compositions (Ogard and Kerrisk 1984). Strontium exists primarily as the Sr^{2+} ion in these waters but may also be present as the neutral aqueous species $SrSO_4$ at concentrations of a few

percent of the total strontium solution concentration (Ogard and Kerrisk 1984). The data of Langmuir and Riese (1985) indicate that $RaSO_4/Ra^{2+}$ will be greater or equal to 0.6 when the sulfate ion concentration is greater than 10^{-3} M. These numbers suggest that $RaSO_4$ will be a significant species ($RaCO_3$ and $SrCO_3$ may also be significant).

Sorption Data from the Literature—The literature on the behavior of cesium, radium, and strontium in the surficial environment is voluminous and will not be reviewed here. Their sorption behavior is fairly well understood and is largely controlled by ion-exchange reactions (Bolt and Bruggenwert 1976), although surface-complexation reactions involving these elements have also been discussed (for example, Balistrieri and Murray 1982). The dominant controls on the ion-exchange reactions are the cation-exchange capacities of the minerals in the system, the abundances of these ion-exchanging minerals, their selectivity coefficients for the various cations in the solution phase, and the concentrations of the competing cations in the solution phase. The selectivity of most clays and zeolites for cesium, radium, and strontium is greater than the selectivities for the major cations in solution. Further, pH does not have a significant effect on the sorption behavior of these elements over the pH range of interest. Because their sorption behavior is fairly well understood and because this behavior depends strongly on local conditions, data from sites other than Yucca Mountain will not be reviewed here.

Data from Laboratory Sorption Experiments with Yucca Mountain Rock And Water Samples Obtained Prior to 1993—Sorption coefficients for cesium, radium, and strontium were reviewed by Daniels et al. (1983), Thomas (1987), and Meijer (1990). For cesium at low concentrations (10^{-8} M), sorption coefficients are greater than 100 mL g^{-1} for all water-rock combinations tested except p#1 water in contact with vitric tuff (Knight and Thomas 1987). Cesium sorption coefficients for the devitrified-tuff/J-13-water system show a clear concentration dependence that has been modeled with a Fruendlich isotherm (Polzer and Fuentes 1988). The coefficients for this particular rock/water system are greater than 100 mL g^{-1} for cesium solution concentrations below 5 x 10^{-5} M. For p#1 water in contact with this rock type, the coefficient would be 100 mL g^{-1} at somewhat lower solution concentrations. In any case, in the higher ionic-strength waters (0.02 eq L^{-1}), including unsaturated-zone waters, the sorption coefficients for cesium on devitrified and vitric samples may be less than 100 mL g^{-1} if solution concentrations of cesium exceed 10^{-6} M. For zeolitic tuffs, cesium sorption coefficients are greater than 100 mL g^{-1} for all water compositions and cesium concentrations anticipated in the potential repository environment.

Radium appears to have a somewhat higher affinity for sorption onto Yucca Mountain tuffs than cesium. In addition, the solubility of $RaSO_4$ limits the concentrations in solution to trace levels (10^{-7}–10^{-8} M; Ogard and Kerrisk 1984). At concentrations below the solubility limit for $RaSO_4$, sorption coefficients for radium are greater than 100 mL g^{-1} in essentially all rock-water combinations tested, using barium as an analog for radium (Knight and Thomas 1987). This fact suggests that a minimum sorption coefficient of 100 mL g^{-1} can be used for radium in all rock/water systems. For zeolitic samples, minimum values of 1,000 mL g^{-1} can be used.

Strontium sorption behavior is more sensitive to mineral and water compositions than the other two elements discussed in this subsection. For devitrified and vitric tuffs, sorption coefficients for the higher ionic-strength waters (such as p#1) are in the range of 10 to 30 mL g^{-1} (Knight and

Thomas 1987). These sorption coefficients will decrease as the solution concentration of strontium is increased above approximately 10^{-5} M (Thomas 1987). However, this concentration is close to the solubility limit for $SrCO_3$ in these waters so that the 10 to 30 mL g^{-1} range is likely appropriate for use in performance-assessment calculations in the devitrified or vitric tuffs. For zeolitic tuffs, a minimum value of 1,000 mL g^{-1} would be appropriate (Knight and Thomas 1987).

Conclusions Regarding Sorption Behavior of Cesium, Radium, and Strontium with Respect to Expected Variations in Groundwaters—The existing sorption-coefficient database for cesium, radium, and strontium should be adequate for performance-assessment calculations. The main concern would be the concentration of cesium in the solution phase in contact with devitrified and vitric tuffs. If this concentration is over 10^{-5} M, the appropriate value for the sorption coefficient may be less than the minimum recommended value of 100 mL g^{-1}. The sorption coefficients for strontium in devitrified and vitric tuffs will be as low as 10 to 30 mL g^{-1} in higher ionic-strength waters. If additional experiments were to be carried out for this group of elements, they should focus on strontium in contact with devitrified and vitric tuffs in the higher ionic-strength waters.

6.4.4.1.4.10 Nickel and Lead

Behavior in Solutions Representative of Yucca Mountain Groundwaters—The aqueous solution behavior of nickel and lead is relatively simple. Within the range of groundwater compositions expected in the Yucca Mountain flow system, these elements are present in solution primarily as simple divalent cations. Several percent of the total nickel concentration will be present as the $NiSO_4$ (aq) complex. $NiCO_3$ may also be a significant aqueous species. Similarly, several percent of the total lead concentration will be present as the $PbCl^+$ complex.

Sorption Data from the Literature—The behavior of nickel and lead in the surficial environment has been studied in some detail (for example, Snodgrass 1980). These elements are generally quite particle-reactive. The dominant mechanisms that control their sorption behavior are ion exchange on clay minerals (Bowman and O'Connor 1982) and adsorption onto various oxides (Theis and Richter 1980). The selectivities of clay minerals for nickel and lead are large relative to the major cations (such as Mg^{2+}) in typical groundwaters (Decarreau 1985). Solution compositional parameters that can influence this adsorption behavior include pH, ionic strength, concentrations of competing ions, and concentrations of complexing agents (see review by Rai and Zachara 1984).

Data on sorption of transition metals on synthetic zeolites suggest that Pb^{2+} has a high affinity for ion exchange compared with Sr^{2+}, whereas Ni^{2+} has a lower affinity relative to Sr^{2+} (Barrer and Townsend 1976; Obeng et al. 1981; Blanchard et al. 1984). This result suggests the zeolitic zones within Yucca Mountain could be significant barriers to lead migration.

Data from Laboratory Sorption Experiments with Yucca Mountain Rock And Water Samples Obtained Prior to 1993—Data on the sorption behavior of nickel in Yucca Mountain rock-water systems were reported by Knight and Lawrence (1988). Sorption and desorption ratios were determined in several water compositions in the pH range from 8.3 to 9.0 with nickel

concentrations in solution of approximately 10^{-8} M. For devitrified and zeolitic samples, sorption coefficients were in the range of 200 to 400 mL g^{-1}. Sorption coefficients obtained in the desorption step were generally a factor of two larger than the sorption coefficients. In the only vitric sample analyzed, sorption coefficients ranged from approximately 30 to 70 mL g^{-1}. For the desorption step, the coefficients were in the range of 33 to 72 mL g^{-1} for this rock type. References to the adsorption behavior of lead on tuffaceous or even granitic rock samples were not found.

Conclusions Regarding Sorption Behavior of Nickel and Lead with Respect to Expected Variations in Groundwaters—Based on information in the literature, the sorption behavior of these elements will be determined largely by the free-ion activities in solution and the cation-exchange capacity of the host rock (for example, Bowman and O'Connor 1982; Rai and Zachara 1984). Solution pH and oxide-mineral abundances may be a factor in rocks in which nickel and lead sorb primarily by surface-complexation mechanisms. In any case, lead appears to sorb more strongly than nickel in most surficial environments, and both elements appear to sorb more strongly than strontium (Bowman and O'Connor 1982). The nickel sorption coefficients discussed in the previous subsection could reasonably be used as default values for lead in performance-assessment calculations. For nickel, a minimum sorption coefficient of 100 mL g^{-1} could be used in the devitrified and zeolitic zones. For the vitric zones, the performance-assessment calculations could be done using random sampling and a normal distribution ranging from 0 to 50 mL g^{-1}.

6.4.4.1.4.11 Thorium, Niobium, Tin, and Zirconium

The radionuclides of concern represented by these elements have several characteristics in common. First, in groundwater/rock systems of concern in this report, these elements have stable oxidation states. Niobium is present in a +5 oxidation state, whereas the others are typically in +4 oxidation states (Brookins 1988). Second, in aqueous solutions with compositions typical of Yucca Mountain groundwaters, these elements tend to occur as sparingly soluble oxides or silicates (Brookins 1988). They may also form solid solutions with other, more common, sparingly soluble oxides, such as titania (TiO_2). Third, the dominant solution species associated with these oxides are hydrolysis products (Baes and Mesmer 1986). Fourth, the hydrolyzed solution species tend to have high affinities for adsorption onto oxide surfaces as discussed further below. The radionuclides represented by these elements are in the "strongly sorbing" group discussed by Meijer (1992).

Niobium

Behavior in Solutions Representative of Yucca Mountain Groundwaters—According to Baes and Mesmer (1986), at a dissolved niobium concentration of 10^{-6} M, the dominant solution species in pure water are the neutral species $Nb(OH)_5$ and the anionic species $Nb(OH)_6^-$. The anionic species predominates at values of pH above 7, and the neutral species is stable below a pH of 7. At surficial temperatures and pressures, evidence for significant complexation of niobium by nonhydroxide ligands in natural aqueous solutions is lacking. As discussed below, carbonate complexation may occur at higher temperatures and pressures.

The concentrations of niobium in surficial aqueous solutions are extremely low, presumably due to the low solubility of the pentavalent oxide (Baes and Mesmer 1986) and to sorption onto mineral surfaces. In geologic systems, niobium may substitute as a trace element in the more abundant oxide phases such as micas, titanium oxides (for example, rutile), and clays (Goldschmidt 1954). This effect also leads to low solution concentrations.

Qualitative Evidence for Behavior in the Surficial Environment—The geologic literature contains numerous papers that qualitatively discuss the mobility, or more accurately, the immobility of niobium in rocks during alteration processes (for example, Cann 1970). In various studies of soils or altered, weathered, or metamorphosed rocks, geological, geochemical, and statistical evidence has been presented that supports the conclusion that niobium is essentially immobile in the surficial environment. Although some of these studies deal with rocks that have been altered under conditions of low fluid-to-rock ratios, the general lack of evidence for niobium mobility suggests that this element would also be immobile in systems with higher water/rock ratios, such as the Yucca Mountain flow system. For example, Brookins (1983) notes that 100 percent of the niobium produced by fission at the natural reactor at Oklo, Gabon, has been retained by the host pitchblende even though the reactor was active in water-bearing sandstones that were subjected to elevated temperatures during and after the critical (that is, nuclear) stage of the reactor.

Grimaldi and Berger (1961) studied the concentrations of niobium in twenty lateritic soils from West Africa and concluded that silica is depleted more rapidly from these soils than is niobium and niobium more rapidly than aluminum. Further, these workers note that there is a strong association of niobium with the clay-sized fraction and also with titanium. They propose that the association of niobium with the clay fraction may be due to the presence of niobium-rich authigenic rutile in the clays. The observation that niobium was mobilized more readily than aluminum in this environment does not necessarily imply niobium was transported out of the system as a dissolved solution species. The tendency of elements such as niobium, titanium, tin, and so forth to form very fine-grained precipitates is well known. Such colloidal-sized particles can be transported by soil solutions and surface waters.

Evidence for niobium mobility during greenschist metamorphism of mafic rocks has been presented by Murphy and Hynes (1986). These workers suggest that carbonate-rich metamorphic solutions can mobilize and transport niobium (as well as titanium, zirconium, phosphorus, and yttrium). Presumably, carbonate can form mobile complexes with niobium under conditions of elevated temperature and pressure. No references were found that address the ability of carbonate to complex niobium under low temperatures and near atmospheric pressures.

Conclusions Regarding Sorption Behavior of Niobium with Respect to Expected Variations in Groundwaters—On the basis of the geological evidence and because niobium forms primarily hydrolyzed species in groundwaters of the type associated with Yucca Mountain, niobium should be very insoluble in Yucca Mountain groundwaters and strongly sorbed onto mineral phases present in Yucca Mountain tuffs from the whole range of groundwater compositions expected at the site.

Thorium

Behavior in Solutions Representative of Yucca Mountain Groundwaters—Langmuir and Herman (1980) have compiled and critically reviewed thermodynamic data for thirty-two dissolved thorium species and nine thorium-bearing solid phases. In the groundwater compositions expected within Yucca Mountain, thorium will be fully hydrolyzed ($Th(OH)_4$), and thorium complexing with other inorganic ligands will be insignificant based on the data presented in Langmuir and Herman (1980). Thorium compounds are among the most insoluble in the group of elements considered in this report. Solubilities of the order of 10^{-50} M are common for thorium compounds (for example, thorianite (ThO_2) and thorite ($ThSiO_4$)). Nevertheless, concentrations well above this value have been found in various natural waters and appear to reflect complexation with organic ligands in organic-rich waters. Such waters are not expected at Yucca Mountain.

Qualitative Evidence for Behavior in the Surficial Environment—Thorium is one of the elements considered to be immobile in most surficial environments (Rose et al. 1979). Studies of the isotopic disequilibrium in the uranium and thorium decay series found in natural aquifers suggest that thorium isotopes are strongly retarded in these flow systems relative to other members of the decay series (Krishnaswami et al. 1982). Studies of the migration of thorium away from thorium ore bodies also indicate that it is "extraordinarily immobile" in these environments (Eisenbud et al. 1984). Brookins (1983) found that thorium was immobile in the Oklo reactor environment. Studies of thorium concentration gradients with depth in seawater also point to high sorption affinities for this element on oceanic particulate matter (Moore and Hunter 1985).

Data from Laboratory Sorption Experiments—Hunter et al. (1988) carried out thorium sorption experiments on MnO_2 and FeOOH in artificial sea-water and in a simple NaCl solution. The primary objective was to determine the effects of major ions (for example, Mg^{2+} and SO_4^{2-}) on the adsorption of thorium by goethite (FeOOH) and MnO_2 relative to sorption in a pure NaCl electrolyte system. The effects of magnesium and calcium ions on thorium adsorption were very small (probably within the margin of experimental error), but the presence of sulfate at seawater concentrations (0.028 M) increased the adsorption edge on FeOOH by one-half of a pH unit. Because the adsorption edge is in the range of pH values from 3 to 5 in all the experiments, this effect is not considered important for thorium sorption behavior at the Yucca Mountain site.

LaFlamme and Murray (1987) evaluated the effects of carbonate on the adsorption characteristics of thorium on goethite. They found that carbonate alkalinity could decrease thorium sorption onto goethite at alkalinity values greater than 100 meq L^{-1}. Because the alkalinity values expected in the Yucca Mountain flow system are orders of magnitude lower than this value, carbonate alkalinity is not expected to affect thorium adsorption behavior in this system.

According to Langmuir and Herman (1980), the adsorption of thorium from water onto clays, oxides, and organic material increases with pH and approaches 100 percent by a pH of about 6.5. As the thorium ion is largely hydrolyzed above a pH of about 3.2, it follows that hydroxy complexes of thorium are primarily involved in adsorption processes (in carbonate-poor systems). Using a mixed quartz-illite soil as a sorbent, Rancon (1973) measured a K_d value of 5 mL g^{-1} at a pH of 2, which increased to 5 x 10^5 mL g^{-1} at a pH of 6. With a quartz-illite-calcite-

organic-matter soil, Rancon found that the K_d decreased from 10^6 mL g^{-1} at a pH of 8 to 100 mL g^{-1} at a pH of 10. This change was attributed to the dissolution of soil humic acids and the formation of thorium-organic complexes at this high pH.

Lieser and Hill (1992) reported thorium sorption coefficients for rock/water systems associated with the Gorleben site in Germany. They found that thorium was strongly sorbed in such systems ($K_d = 10^3$ to 10^5 mL g^{-1}). However, they also found that colloidal transport may be of potential significance to the migration of thorium in the surficial environment.

Thorium sorption experiments on Yucca Mountain rock samples in J-13 groundwater were reported by Rundberg et al. (1985) and Thomas (1988). The sorption coefficients obtained in these experiments ranged from 140 to 23,800 mL g^{-1}. No correlations were noted between the values obtained for the sorption coefficient and rock type or pH (5.3–7.5). The large range in sorption coefficients obtained in these experiments may be explained by the presence of fine colloidal particles in the solution phase used to obtain the sorption coefficients (for example, Lieser and Hill 1992).

Conclusions Regarding Sorption Behavior of Thorium with Respect to Expected Variations in Groundwaters—The sorption coefficients for thorium are expected to be large (> 100 mL g^{-1}) in all hydrochemical environments associated with Yucca Mountain in the present day or in the future. This conclusion is based on the dominance of hydrolysis reactions in solution, the low solubility of thorium oxides and silicates, and the large values measured for thorium sorption coefficients in different water compositions, including seawater, combined with the general lack of evidence for mobility of thorium in the surficial environment.

Tin

Behavior in Solutions Representative of Yucca Mountain Groundwaters—The dominant tin solution species in surficial waters appears to be $Sn(OH)_4$. The concentrations of tin in natural groundwaters are extremely low due to the ion solubility of the tetravalent oxides (about 10^{-9} M in pure water; Baes and Mesmer 1986). Cassiterite (SnO_2) should be the solubility-limiting oxide in most groundwaters. Tin could also coprecipitate with other insoluble oxides or silicates such as niobium pentoxide, zirconium and thorium dioxide, and thorium silicate. In natural waters with high sulfide concentrations, tin sulfide minerals could control tin solubility. However, such water compositions are not expected in association with the proposed repository site at Yucca Mountain.

Qualitative Evidence for Behavior in the Surficial Environment—Tin is one of the elements considered to be immobile in most near-surface geologic environments (Rose et al. 1979). This assignment is based on various types of data, including observations on the mobility of tin in and around tin ore deposits. However, De Laeter et al. (1980) note that some tin has migrated out of the pitchblende at the natural reactor at Oklo, Gabon. The cause for this migration has not been established but may reflect the existence of reducing conditions during some phase of the history of the reactor.

Data from Laboratory Sorption Experiments Carried out Prior to 1993—Sorption experiments with tin have been carried out on several whole-rock samples from Yucca Mountain in contact

with J-13 water and p#l water and several other water compositions separately spiked with sodium sulfate, sodium bicarbonate, and calcium chloride (Knight and Thomas 1987). The measured sorption coefficients ranged from 77 to 35,800 mL g^{-1} at pH values in the range of 8.4 to 9.2. Coefficients obtained from desorption experiments were generally larger (300–52,500 mL g^{-1}) than those obtained from sorption experiments. The devitrified tuff samples produced the highest sorption and desorption-coefficient values (> 2900 mL g^{-1}), whereas the vitric and zeolitic tuff samples produced lower values. Sorption coefficients were generally highest in the p#l water and the calcium-chloride-spiked J-13 water. Apparently, high calcium concentrations in the solution phase result in high sorption-coefficient values for tin. Alternatively, high calcium concentrations cause the precipitation of some type of tin-bearing compound. As with thorium, the large range in sorption coefficients observed in the experiments may reflect the presence of colloidal-size particles in the solution phase used to obtain the coefficients.

Conclusions Regarding Sorption Behavior of Tin with Respect to Expected Variations in Groundwaters—The sorption coefficients for tin are expected to be large (> 100 mL g^{-1}) in all hydrochemical environments associated with Yucca Mountain in the present day or in the future. This conclusion is based on the dominance of hydrolysis reactions in solution, the low solubility of tin oxides, and the large values measured for tin sorption coefficients in different water compositions, combined with the general lack of evidence for mobility of tin in the surficial environment.

Zirconium

Behavior in Solutions Representative of Yucca Mountain Groundwaters—In near-neutral solutions, the dominant zirconium solution species appear to be hydrolysis products, such as $Zr(OH)_4$. The degree to which zirconium forms complexes with other inorganic ligands present in Yucca Mountain groundwaters is insignificant. The solubility of zirconium in dilute solutions is extremely small (Baes and Mesmer 1986, pp. 152–156; Cotton and Wilkinson 1988, pp. 780–782), although the identity of the solubility-controlling solid is uncertain. The solubility-controlling compounds for zirconium in most natural groundwaters are likely zircon ($ZrSiO_4$) or baddeleyite (ZrO_2). Zirconium solubilities in surficial environments may also reflect coprecipitation in other sparingly soluble oxides or silicates. The concentrations of zirconium in natural waters may be predominantly controlled by sorption reactions.

Qualitative Evidence for Behavior in the Surficial Environment—Zirconium is one of the elements considered to be immobile in most near-surface geologic environments (Rose et al. 1979). Studies of zirconium concentrations in altered and unaltered or less-altered rocks from the same original geologic unit (Cann 1970) form part of the basis for this conclusion. Other evidence includes the persistence of zircon ($ZrSiO_4$) in the weathering zone and the low concentrations of zirconium in waters associated with zirconium-rich rocks. Brookins (1983) noted that zirconium was retained within the reactor zones at Oklo, Gabon, although it may have been subject to very local-scale redistribution.

Sorption Data from the Literature—Data on the sorption behavior of zirconium in soil/rock/water systems have been reported by Rhodes (1957), Spitsyn et al. (1958), Prout (1959), and Serne and Relyea (1982). Rhodes (1957) has presented data on zirconium sorption coefficients for a soil-water system that show large values (> 1980 mL g^{-1}) up to a pH of 8.0

followed by a decrease to 90 mL g^{-1} at a pH of 9.6 and a return to high values at a pH of 12. He attributed the decreased sorption for values of pH from 8 to 12 to the stabilization of colloidal components in solution in this pH range. Spitsyn et al. (1958) observed little movement of zirconium through a sandy soil in a field test under both acidic and alkaline conditions. Serne and Relyea (1982) report large values for zirconium sorption coefficients in all media tested.

Conclusions Regarding Sorption Behavior of Zirconium with Respect to Expected Variations in Groundwaters—The dominance of zirconium hydrolysis reactions in solution suggests that pH will be the dominant groundwater compositional parameter controlling zirconium solubility and sorption behavior. The lack of evidence for zirconium transport in field tests under both acidic and alkaline conditions and the general lack of evidence for mobility of zirconium in the surficial environment combined with the large values of the sorption coefficient reported in the literature for zirconium suggest that in all hydrochemical environments associated with Yucca Mountain in the present-day or in the future this element's sorption coefficients will be large (> 100 mL g^{-1}).

6.4.4.2 Effects of Organics on Actinide Sorption

Naturally occurring organic compounds generated during the transformation of plant and animal debris over time and as a result of the synthetic activities of microorganisms are ubiquitous in surface and subsurface environments. For example, pore water from a well-developed soil environment usually contains dissolved organic carbon in quantities greater than 20 mg L^{-1} in top soils and in quantities of about 5 mg L^{-1} in subsoils. Dissolved organic carbon concentrations in groundwaters typically depend on the environment and are usually below 2 mg L^{-1} (Drever 1988). The decrease in concentrations of organic materials with increasing depth is attributed to chemical and biological degradation as well as to sorption on mineral surfaces. Sorption of organic materials onto mineral surfaces is considered the dominant contributing factor to the removal of organics from solution during percolation through the subsurface.

The interaction between organic materials and mineral surfaces in the natural environment is important to mineral surface geochemistry. Sorption of organic material onto mineral surfaces affects not only the solubility and charge of the organic materials in solution but also the properties of the mineral surfaces, such as their charge and hydrophobicity, thereby altering the reactivity of the mineral toward metal ions. A clear understanding of the effects of the organic materials that frequently coat mineral surfaces in natural environments will lead to improvements in the sorption models used to predict the mobility of radionuclides in natural aquatic environments (Choppin 1992).

Triay et al. (1997) presented laboratory results for the effect of organic materials on the sorption of plutonium and neptunium on selected mineral oxides and Yucca Mountain tuff. Triay et al. (1997) investigated Pu and Np sorption onto various Yucca Mountain tuffs, devitrified tuff (G4-270 and G4-275), vitric tuff (Gu3-1496) and zeolitic tuff (G4-1529), in natural J-13 and synthetic p#1 waters, in the presence of catechol, alanine, DOPA (dihydroxyphenylalanine), and NAFA (Nordic aquatic fulvic acid). Alanine is an amino acid that will complex with the hard acid form of metal ions in solution. Catechol is a phenolic compound that can chelate metal ions and undergo redox reactions with the metal. DOPA, a naturally occurring amino acid commonly found in plant seedlings, pods, and broad beans, was chosen because it contains well-defined

organic functional groups such as carboxylic acid, amine, and phenols. Triay et al. (1997) concluded the following:

- The sorption of organic material DOPA on oxide surfaces follows the order aluminum oxide > iron oxide. For a given sorbent, the higher the pH, the more DOPA is sorbed. Surface complexation is the most likely sorption mechanism.

- The sorption of plutonium generally follows the order hematite > ferrihydrite > goethite. The sorption of neptunium on iron oxide is higher than that on aluminum oxide. The sorption of neptunium on crushed tuff material was much lower than that on oxide surfaces.

- The sorption of plutonium and neptunium on iron oxides increases as the solution pH is raised, although the range in pH investigated was narrow (see Assumption 3 in Section 5). The sorption of plutonium is much higher than that of neptunium on hematite, goethite, and ferrihydrite. The applicability of these sorption data for modeling sorption onto waste packages is not known because the range of pH values for waters that might be in contact with a waste package is currently unbounded.

- The amount of neptunium sorption was not affected by any of the organic materials that were studied. The presence of the organic materials alanine, catechol, DOPA, and NAFA did not influence the sorption of neptunium on tuff or on iron and aluminum oxides. This lack of an observable effect is presumably a result of the weak complexation between neptunium and the model organics. Therefore, under the conditions that the experiments were conducted, the types of organics studied should have little effect on Np sorption.

- The sorption of plutonium was influenced by the presence of DOPA on goethite and ferrihydrite. Increasing the amount of DOPA resulted in higher sorption of plutonium on goethite and ferrihydrite. Alanine decreased the sorption of plutonium. However, in the system containing catechol, plutonium sorption was increased. The enhancement of plutonium sorption in the presence of catechol is probably due to the reduction of Pu(V) to Pu(IV) by the organic. The inhibition of plutonium sorption in the presence of alanine is probably caused by the lowering of the free plutonium-ion activity in solution by formation of an alanine-plutonium complex. No observable effect of organics on plutonium sorption was found in the hematite system under the conditions that the experiments were conducted, which is probably due to a relative high sorptivity of plutonium on the hematite surface.

6.4.5 Adsorption of Radionuclides by Alluvium

Alluvium is the generic name for clay silt, sand, gravel, or similar detrital material deposited by running water. Alluvium provides another natural barrier to migration of radionuclides along the flow path from Yucca Mountain. Because the alluvium through which a radionuclide may travel is relatively far from the repository, its retardation properties are important to PA with respect to the most mobile radionuclides, particularly ^{237}Np, ^{99}Tc, and ^{129}I. Consequently, the apparent distribution coefficient, K_d (mL g^{-1}), of these three radionuclides in alluvium has been determined for use in PA.

The water used in the experiments is groundwater from the alluvial aquifer, filtered through a 0.05-μm filter. Tracer solutions were prepared as a dilution using the filtered water from a stock solution, then passed through a 0.02-μm filter before use. The alluvial samples used in the experiments come from the three boreholes shown in Table 9. Also shown are the density values for the samples used in the sorption experiments that reflect the samples as they were prepared for the experiments. Standard batch adsorption experiments were performed on the 75- to 500-μm fraction.

Table 9. Depth Intervals (below the surface) and Bulk Densities of Alluvial Samples

Borehole NC-EWDP-02D (02D)		Borehole NC-EWDP-09Sx (09Sx)		Borehole NC-EWDP-03S (03S)	
Depth (ft)	Density (g cm^{-3})	Depth (ft)	Density (g cm^{-3})	Depth (ft)	Density (g cm^{-3})
395–400	1.3	145–150	1.3	60–65	1.3
400–405	1.2	150–155	1.3	65–70	1.2
405–410	1.3	155–160	1.3	70–75	1.3
410–415	1.3	160–165	1.2	75–80	1.2

DTN: LA0002JC831341.001

NOTE: Densities were measured in the laboratory and do not represent in-situ conditions.

6.4.5.1 Results and Discussion

Table 10 lists the QXRD results for the three samples used for the first adsorption kinetic experiments, which are the deepest samples tested from each borehole suite. The QXRD results show that the major mineral phase in these alluvial samples is feldspar, and that the amount of feldspar in the three samples is about the same. The amount of poorly sorbing minerals—tridymite, cristobalite, and quartz—is also about the same in these three samples. The important differences among these samples are the presence of smectite, clinoptilolite, calcite, and hematite.

6.4.5.1.1 Adsorption of ^{237}Np

Figure 9 presents the results of adsorption of ^{237}Np on the three alluvial samples. In general, the samples from Borehole 02D and Borehole 03S have relatively high retardation capacity. The K_d value for ^{237}Np on is 77 mL g^{-1} for the alluvium from Borehole 02D, 400–405 ft, and almost 45 mL g^{-1} for the samples from Borehole 03S, 60–65 ft. The highest ^{237}Np K_d value is for the

sample with the highest amount of the sorptive phases: calcite, smectite, clinoptilolite and hematite (Table 10). Calcite has a high affinity for ^{237}Np at this pH.

Table 10. Quantitative X-ray Diffraction (QXRD) Results of Three Alluvial Samples

Minerals	Mineral Percentage in Samples		
	NC-EWDP-02D 410–415 ft, 75–500 μm	NC-EWDP-03S 75–80 ft, 75–500 μm	NC-EWDP-09Sx 160–165 ft, 75–500 μm
Smectite	2 ± 1	1 ± 1	6 ± 2
Kaolinite	1 ± 1	1 ± 1	—
Clinoptilolite	4 ± 1	13 ± 1	3 ± 1
Tridymite	3 ± 1	—	1 ± 1
Cristobalite	16 ± 1	10 ± 1	18 ± 1
Quartz	18 ± 1	17 ± 1	14 ± 1
Feldspar	54 ± 8	53 ± 8	58 ± 8
Calcite	—	4 ± 1	—
Mica	Trace	1 ± 1	Trace
Hematite	1 ± 1	—	Trace
Hornblende	Trace	Trace	—
Unidentified Phases	Trace	—	—
Total	**99 ± 8**	**100 ± 8**	**100 ± 8**

DTN: LA0002JC831341.002

NOTE: — means mineral not detected

The deepest sample from each borehole was chosen to carry out the adsorption kinetic experiments. The results, depicted in Figure 10, suggest that adsorption of ^{237}Np on alluvium is fast.

6.4.5.1.2 Adsorption of ^{99}Tc

The results of adsorption of ^{99}Tc are presented for the three alluvial samples in Figure 11. Although the degree of retardation of ^{99}Tc on alluvium is low, it is non-zero and even this small degree of retardation could be significant for long-term performance.

Figure 12 indicates that adsorption of ^{99}Tc slowly increases in the first 10 days, then increases rapidly with time. Other mechanisms besides simple adsorption may be operating, such as redox reactions. Although no sulfides or other reduced minerals were indicated by the QXRD analyses, only trace amounts need be present to greatly affect the reactivity of the surfaces. The accuracy of QXRD is poor below a few percent and, also, if the phases are poorly crystalline.

6.4.5.1.3 Adsorption of ^{129}I

Experiments to determine the overall K_d values for ^{129}I are not yet complete, but the kinetic experiments have yielded some preliminary K_d values. Similar to ^{99}Tc, retardation of ^{129}I on alluvium is small but positive, as indicated in Figure 13. The K_d value from the sample from Borehole 03S, however, was still increasing at the time that this report was written.

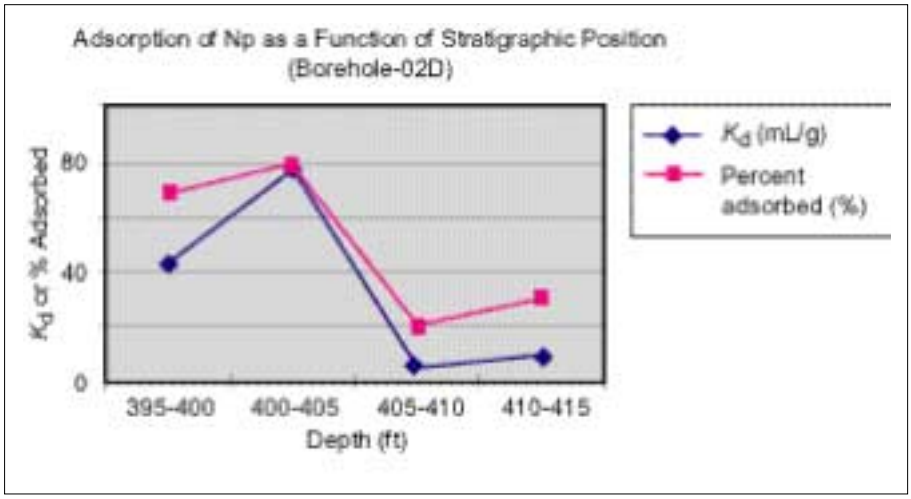

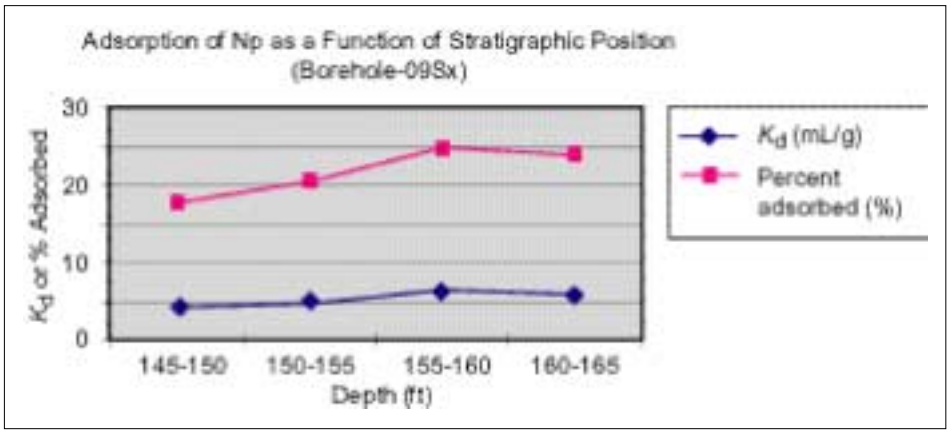

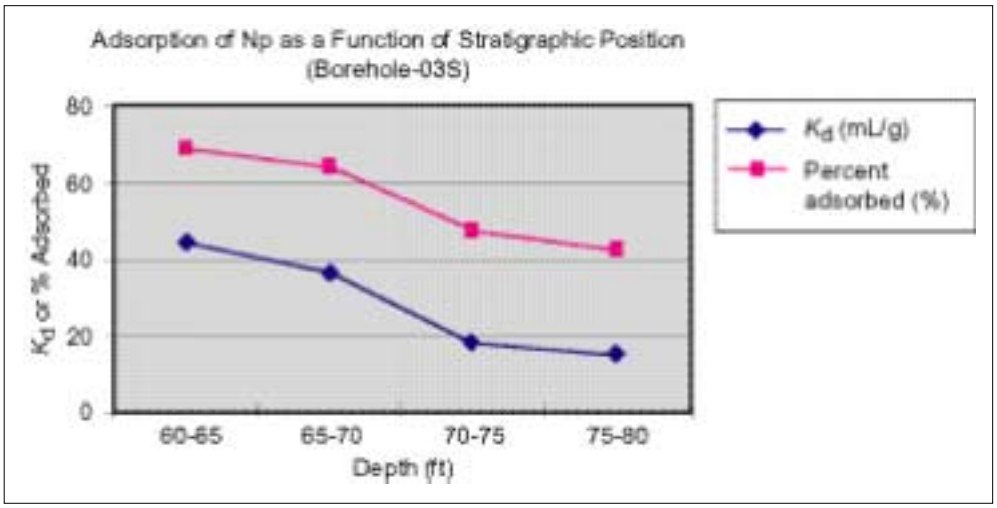

DTN: LA0003JC831341.001

NOTE: Borehole-02D signifies Borehole NC-EWDP-02D, Borehole-09Sx signifies Borehole NC-EWDP-09Sx, and Borehole-03S signifies Borehole NC-EWDP-03S.

Figure 9. Adsorption of ^{237}Np on Three Alluvial Samples

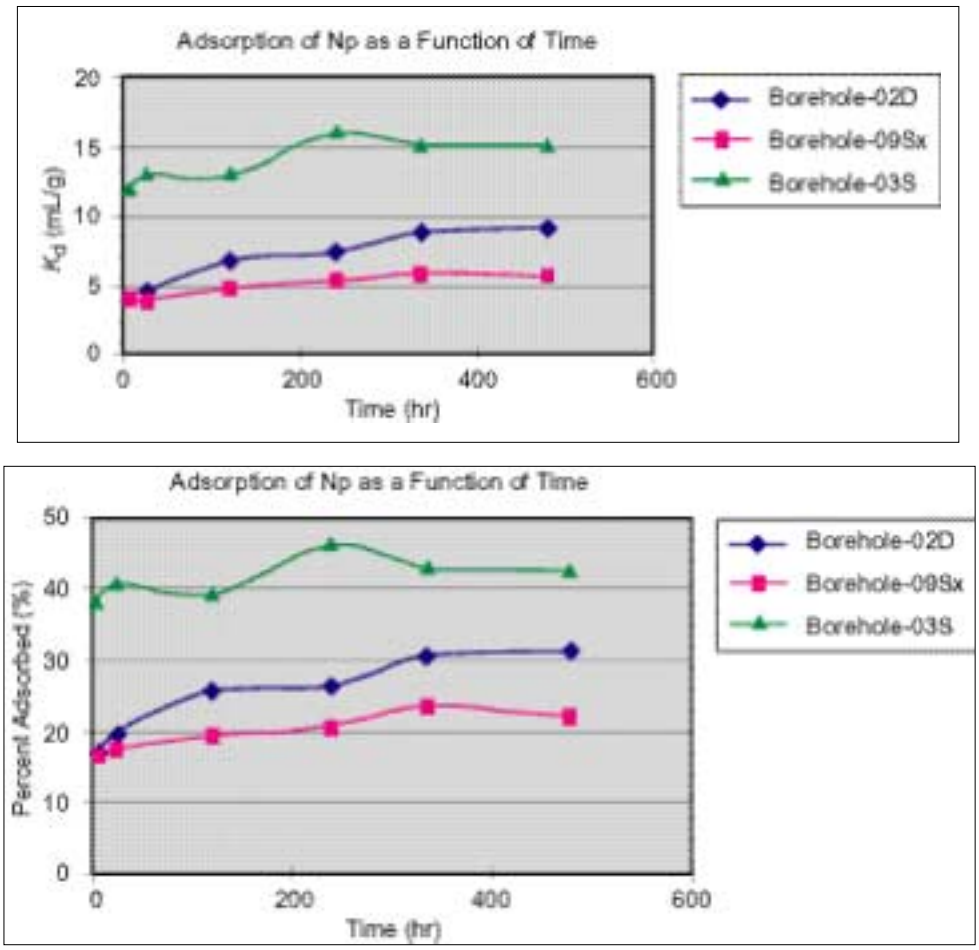

DTN: LA0003JC831341.001

NOTE: The top panel shows the change in sorption coefficient (K_d) with time; the bottom panel, the percent adsorbed. Borehole-02D signifies Borehole NC-EWDP-02D, Borehole-09Sx signifies Borehole NC-EWDP-09Sx, and Borehole-03S signifies Borehole NC-EWDP-03S.

Figure 10. Kinetics of ^{237}Np Adsorption on Three Alluvial Samples

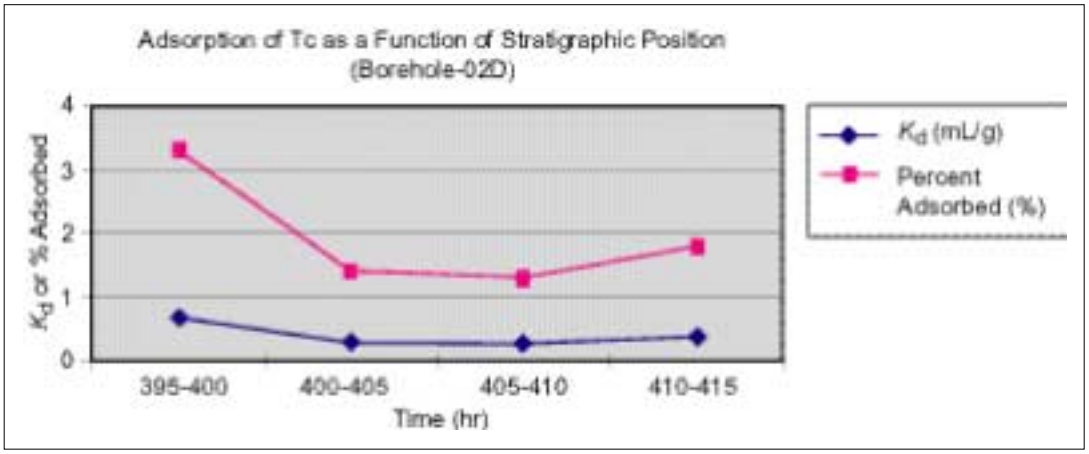

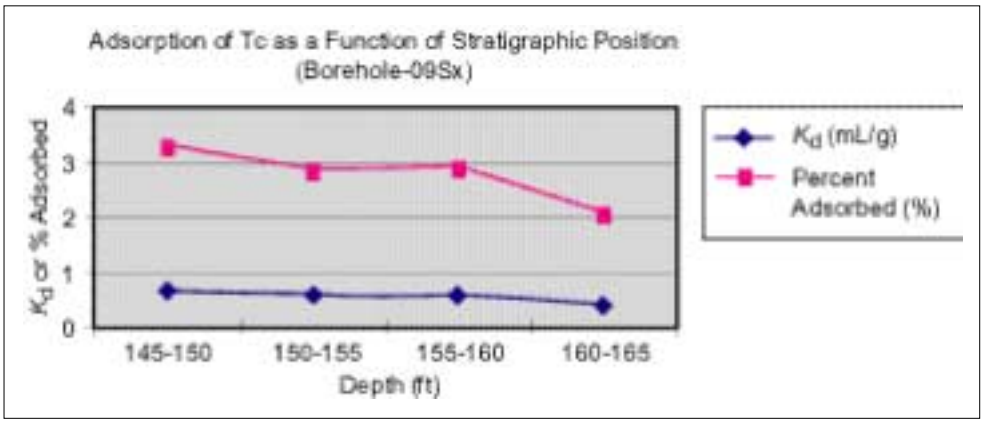

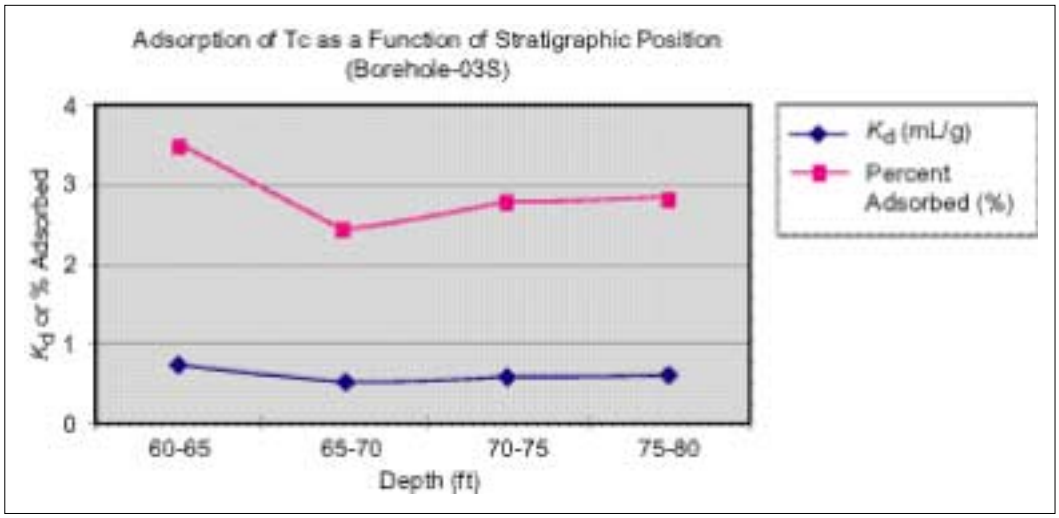

DTN: LA0003JC831341.002

NOTE: Borehole-02D signifies Borehole NC-EWDP-02D, Borehole-09Sx signifies Borehole NC-EWDP-09Sx, and Borehole-03S signifies Borehole NC-EWDP-03S.

Figure 11. Adsorption of ^{99}Tc on Three Alluvial Samples

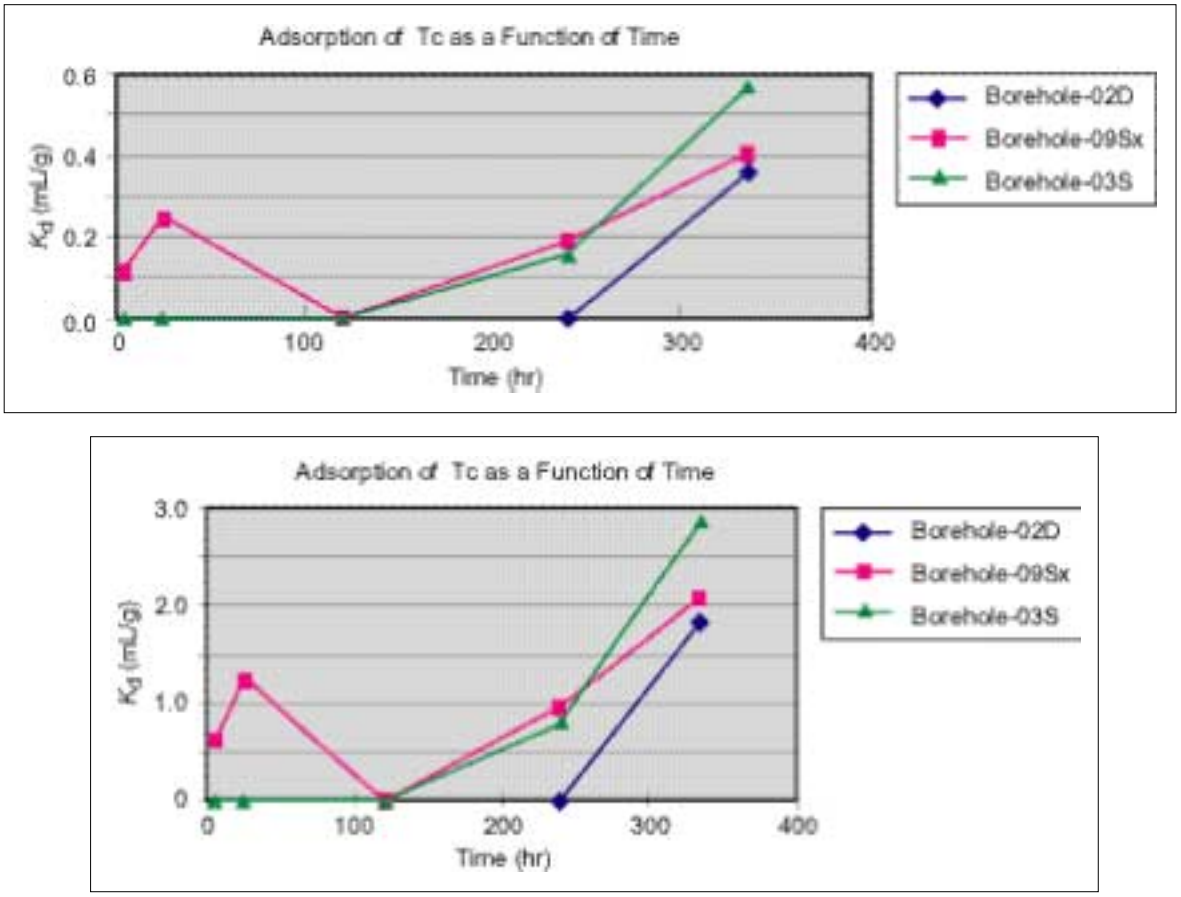

DTN: LA0003JC831341.002

NOTE: The top panel shows the change in sorption coefficient (K_d) with time; the bottom panel, the percent adsorbed. Borehole-02D signifies Borehole NC-EWDP-02D, Borehole-09Sx signifies Borehole NC-EWDP-09Sx, and Borehole-03S signifies Borehole NC-EWDP-03S.

Figure 12. Kinetics of ^{99}Tc Adsorption on Three Alluvial Samples

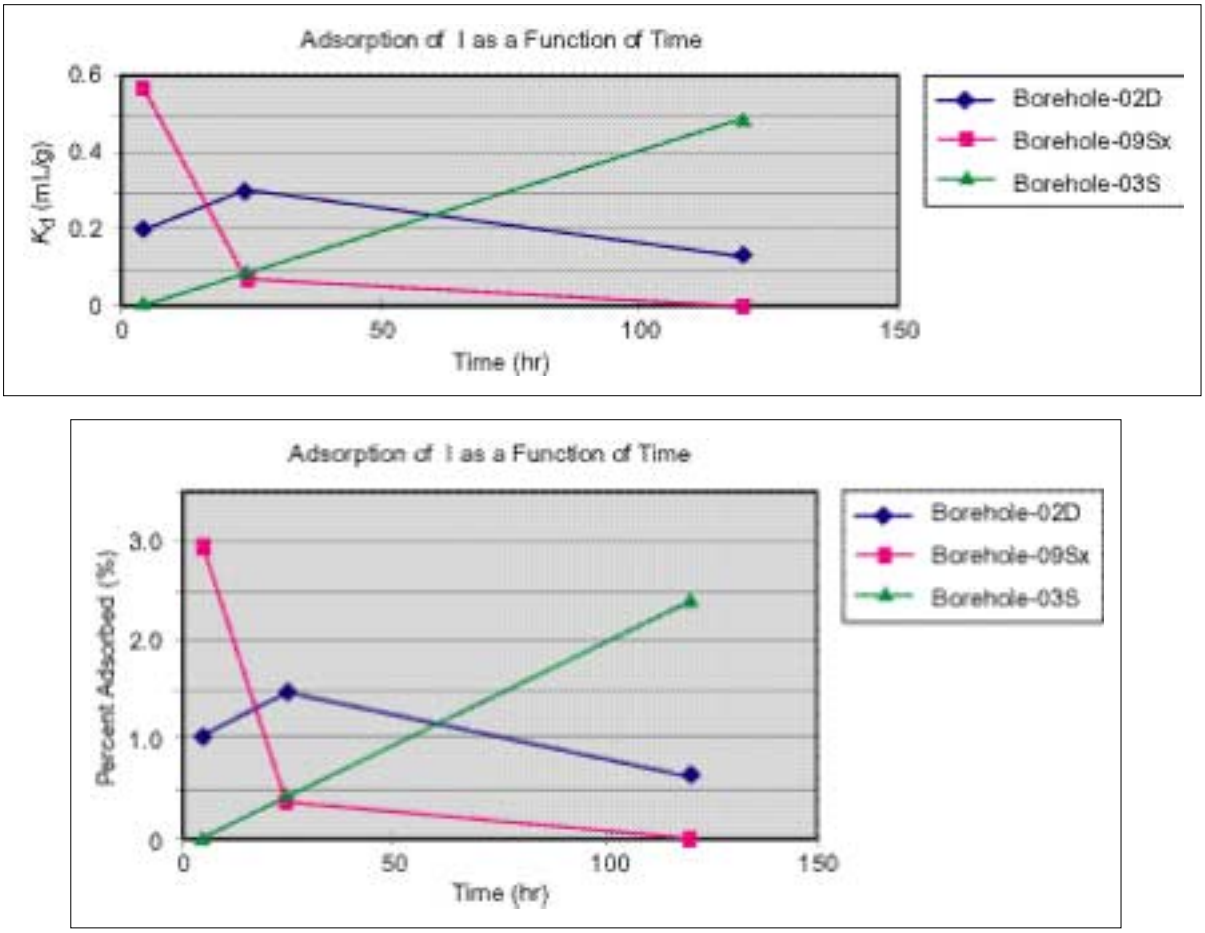

DTN: LA0003JC831341.003

NOTE: The top panel shows the change in sorption coefficient (K_d) with time; the bottom panel, the percent adsorbed. Borehole-02D signifies Borehole NC-EWDP-02D, Borehole-09Sx signifies Borehole NC-EWDP-09Sx, and Borehole-03S signifies Borehole NC-EWDP-03S.

Figure 13. Kinetics of ^{129}I Adsorption on Three Alluvial Samples

6.4.5.2 Conclusions about Sorption onto Alluvium

Although the available data cannot be used to make any strong conclusions, the alluvium does appear to be more sorptive than previously expected. Values of K_d for ^{237}Np ranged from about 5 to 77 mL g^{-1}; values of K_d for ^{99}Tc ranged from about 0.35 to 0.8 mL g^{-1}; and preliminary K_d values for ^{129}I ranged from about 0.41 to 0.75 mL g^{-1}. Sorption was much faster for ^{237}Np than for ^{99}Tc or ^{129}I. The differences in sorptive properties among samples probably results from differences in the amounts of the sorptive phases—smectite, clinoptilolite, calcite, and hematite—and perhaps from the presence of organic carbon and trace amounts of sulfides, which may explain the slow sorption response for ^{99}Tc and ^{129}I. Biological activity, or simple sorption onto organic material, could also be important and account for the slow sorption response for ^{99}Tc and ^{129}I.

6.4.6 Effects of Temperature Perturbations on Adsorption of Radionuclides

Little work has been done on the effects of repository perturbations on the transport of radionuclides. Some of the obvious effects involve increased temperatures as the repository heats up. These effects will be important for the drift and near-field environments. Increased temperature will affect the solubilities of existing phases, the precipitation of new phases, the generation and stability of colloids, and the overall aqueous geochemistry of the drift and near-field environments. This section discusses the effect of temperature on radionuclide adsorption (K_d values).

Temperature will affect adsorption by shifting equilibria among solution species, by changing the zero point of charge of the substrate surfaces, and by changing the ratio of adsorbed to solution-phase species. The magnitude of these effects can be modeled with standard thermodynamic relationships if solution and adsorption enthalpy data are available (Machesky 1990, pp. 283–288). Relationships such as the van't Hoff equation and Boltzmann functions have temperature in them and can be used to predict the effects of temperature (Machesky 1990, p. 283). This calculation should be done for all radionuclides of concern for Yucca Mountain. There is general agreement that increasing temperature increases the sorption of cations and decreases the sorption of anions (Machesky 1990, p. 287; Beckman et al. 1988, p. 13). The few data that exist support this assertion. Machesky (1990, p. 290) used the van't Hoff equation to predict a doubling of K_d values with every increase of 20°C.

Beckman et al. (1988, Figure 2) presented data that show barium adsorption onto tuff was increased by an order of magnitude going from 25°C to 70°C and described similar effects for cerium, europium, cesium and strontium. They also concluded that temperature effects are overwhelmingly more important than effects of concentration or particle size.

The effect of temperature on sorption coefficients was also reviewed by Meijer (1990, p. 17). Again, measured sorption coefficients onto tuffs were higher at elevated temperatures for all elements studied: americium, barium, cerium, cesium, europium, plutonium, strontium, and uranium. Consequently, the conclusion can be drawn that sorption coefficients measured at ambient temperatures should be applicable and generally conservative when applied to describing aqueous transport from a hot repository. This conclusion must be tempered by the possibility that high temperatures, sustained for long time periods due to potential high thermal loads, could result in changes in the near-field mineralogy and water chemistry at Yucca Mountain that are not predictable by short-term laboratory and field experiments.

As a preliminary evaluation, the effect of temperature in a perturbed repository will increase adsorption of cationic species and decrease adsorption of anionic species. Because anions do not adsorb very well at ambient temperatures, a conservative estimate is their K_d values at higher temperatures will be zero. However, the K_d values of cationic species at higher temperatures will increase significantly over those listed in Table 2a by as much as 10 times at repository temperatures above 70°C; more precise numbers should be estimated by modeling efforts.

6.5 DYNAMIC TRANSPORT STUDIES

Batch-sorption experiments are most commonly used to obtain sorption coefficients because such experiments are fast, easy, and inexpensive compared to other ways of obtaining sorption coefficients. However, batch-sorption experiments are appropriate for use in transport calculations only if the sorption reaction for a given radionuclide meets certain conditions. These conditions are the following (de Marsily 1986, Chapter 10).

- Microscopic equilibrium is attained between solution species and the adsorbate (sorption reaction is reversible) (Assumption 7 in Section 5).

- Only one soluble chemical species is present (or if more than one is present, they interchange rapidly relative to the time scale of the experiment) (Assumption 5 in Section 5).

- The radionuclides are sorbed and not precipitated (Assumption 10 in Section 5).

- The dependence of sorption on concentration is described by a linear isotherm (Assumption 6 in Section 5).

Although batch-sorption experiments can be used to test for the first and last conditions, they do not provide information on the second and third conditions. To test whether or not the latter conditions are met for a given radionuclide in the Yucca Mountain flow system, additional experiments must be carried out. The easiest way to test for these conditions is to perform column tests in which a solution bearing the radionuclide of interest is added to the top of a column of crushed rock and eluted from the bottom of the column. The rate at which the radionuclide is eluted from the column (the elution curve) provides information on the degree to which the conditions are met. Column studies are also the easiest way to investigate the sorption behavior of radionuclides during flow in unsaturated media. In this case, solid-rock columns are used. Finally, column studies allow the investigation of radionuclide transport along fractures in dense rock.

This section discusses the results of crushed-rock, solid-rock, and fractured-rock column experiments.

6.5.1 Crushed-Rock Columns

6.5.1.1 Approach

Column elution curves can be characterized by two parameters: the time of arrival of the radionuclide eluted through the column and the broadness (dispersion) of the curve. The arrival time depends, among other factors, on the retardation factor, R_f, which, for soluble radionuclides, depends, in turn, on the sorption distribution coefficient, K_d, together with the water content and bulk density of the solid phase. Significant deviations (those larger than expected based on sampling variability) in arrival times from those predicted on the basis of the batch-sorption distribution coefficients indicate one of the following problems:

- The presence of more than one chemical species that are not readily exchanged and that have different selectivities for tuff minerals

- The presence of the radionuclide as a colloid

- Extremely slow sorption kinetics

- Hydrologic parameters (preferential flow paths)

- Experimental artifacts.

The broadness, or apparent dispersion, of the curve depends on:

- The kinetics and reversibility of sorption

- The linearity of the isotherm that describes the dependence of sorption on radionuclide concentration.

The most comprehensive explanation of the fate of reactive and nonreactive solutes and suspended particles in porous and fractured media has been presented by de Marsily (1986, Chapter 10). The transport of radionuclides in porous media is governed by advection, diffusion, and kinematic dispersion. Advection is the mechanism in which dissolved species are carried along by the movement of fluid. Diffusion causes species to be transferred from zones of high concentration to zones of low concentration. Kinematic dispersion is a mixing phenomenon linked to the heterogeneity of the microscopic velocities inside the porous medium. The migration of a solute in a saturated porous medium is described by the following transport equation

$$\nabla \cdot (\mathbf{D} \nabla C - C\mathbf{U}) = \varepsilon \frac{\partial Q}{\partial t} + Q \quad , \qquad \text{(Eq. 5)}$$

where **D** is the dispersion tensor, C is the concentration of solute in the solution phase, **U** is the filtration velocity (Darcy's velocity), ε is the porosity, t is time, and Q is a "net source or sink term" that accounts for such things as reactivity or adsorption.

For the case of a sorbing, nonreactive solute, the equation becomes

$$\nabla \cdot (\mathbf{D} \nabla C - C\mathbf{U}) = \varepsilon \frac{\partial Q}{\partial t} + \rho_b \frac{\partial F}{\partial t} \quad , \qquad \text{(Eq. 6)}$$

where ρ_b is the dry bulk density of the medium and F is the mass of solute sorbed per unit mass of solid.

Dispersion has three components: the longitudinal dispersion coefficient in the direction of the flow, D_L, and the transverse dispersion coefficient, D_T, in the two directions at right angles to the velocity of the flow. These components are given by

$$D_L = \varepsilon d + \alpha_L |U| \text{ and} \qquad \text{(Eq. 7)}$$
$$D_T = \varepsilon d + \alpha_T |U| \ ,$$

where d is the effective diffusion coefficient in the medium and α is dispersivity.

The characteristics of the sorption determine the actual relationship between F and C. For the case in which sorption is linear, reversible, and instantaneous, the ratio between F and C is simply equal to the sorption distribution coefficient:

$$\frac{F}{C} = K_d \qquad \text{(Eq. 8)}$$

Substitution of Equation 8 into Equation 6 yields

$$\nabla \cdot (\mathbf{D} \nabla C - C\mathbf{U}) = \varepsilon \left[1 + \frac{\rho_b}{\varepsilon} K_d \right] \frac{\partial C}{\partial t} \qquad \text{(Eq. 9)}$$

The expression in brackets in Equation 9 corresponds to the retardation factor, R_f, given by

$$R_f = 1 + \frac{\rho_b}{\varepsilon} K_d \qquad \text{(Eq. 10)}$$

where ρ_b is the dry bulk density (including pores) and ε is the porosity (Hiester and Vermeulen 1952, Eq. 74). Thus, there is a way to compare sorption coefficients obtained under advective, diffusive, and dispersive conditions with sorption coefficients obtained from batch-sorption experiments. However, this approach is valid only if sorption is linear, reversible, and instantaneous.

6.5.1.2 Results and Discussion

Elution of neptunium, plutonium, and technetium were measured as a function of water velocity through zeolitic, devitrified, and vitric crushed tuff columns with J-13 well water and with synthetic p#1 water. Each experiment used the most thermodynamically stable species of the radionuclide of interest in oxidizing waters: Np(V), Pu(V), and pertechnetate (TcO_4^-). Porosities for these experiments were calculated as the free column volumes divided by the total column volumes. Empirical values of R_f were then calculated for the column experiments by dividing the free column volume into the volume of solution that had to be eluted to recover 50 percent of the injected radionuclide. This method does not assume linear equilibrium sorption and is just an empirical method for assigning a R_f value to column data. From these values of R_f, Equation 10 was used to calculate column sorption-distribution coefficients.

6.5.1.2.1 Neptunium Results

Elution curves for the Np(V) column have been previously published (Triay, Furlano et al. 1996, Appendix A). The sorption-distribution coefficients obtained for these column experiments are listed in Table 11. Inspection of Table 11 indicates good agreement between the values of K_d obtained by the two approaches (batch and column experiments), which means that the arrival time of ^{237}Np, as defined by $C/C_0 = 0.5$, can be predicted from a value for K_d. On the other hand,

the broad, dispersive shapes of the elution curves (Triay, Furlano et al. 1996, Appendix A) indicate that sorption of neptunium onto zeolitic and vitric tuffs is either nonlinear, nonreversible, or noninstantaneous. Previous work has found that sorption of neptunium onto clinoptilolite-rich tuffs is rapid (Triay, Cotter, Huddleston et al. 1996, Figure 7) and can be fit with a linear isotherm (Triay, Cotter, Kraus et al. 1996, Figure 4). Consequently, the degree of reversibility of neptunium sorption onto zeolitic and vitric tuffs may be the most likely reason for the broadening observed in the tuff-column elution curves.

Table 11. Comparison of Neptunium K_d Values from Batch and Column Measurements

Column number	Tuff type	Water type	Batch K_d (mL g^{-1})[a]	Column K_d (mL g^{-1})[a]
1	zeolitic	J-13	1.7 ± 0.4 (G4-1510)	1.7 (G4-1508)
2	zeolitic	J-13	1.7 ± 0.4 (G4-1510)	1.2 (G4-1508)
3	zeolitic	J-13	2.1 ± 0.4 (G4-1505)	2.8 (G4-1505)
4	zeolitic	Syn. p#1	0.2 ± 0.3 (G4-1506)	0.4 (G4-1505)
5	zeolitic	Syn. p#1	0.2 ± 0.3 (G4-1506)	0.2 (G4-1505)
6	zeolitic	Syn. p#1	0.2 ± 0.3 (G4-1506)	0.2 (G4-1505)
7	devitrified	J-13	–0.04 ± 0.2 (G4-268)	0.07 (G4-268)
8	devitrified	J-13	–0.04 ± 0.2 (G4-268)	0.01 (G4-268)
9	devitrified	J-13	–0.04 ± 0.2 (G4-268)	0.02 (G4-268)
10	devitrified	J-13	–0.04 ± 0.2 (G4-268)	0.01 (G4-268)
11	devitrified	Syn. p#1	0.2 ± 0.3 (G4-270)	0.06 (G4-272)
12	devitrified	Syn. p#1	0.2 ± 0.3 (G4-270)	0.03 (G4-268)
13	devitrified	Syn. p#1	0.2 ± 0.3 (G4-270)	0.03 (G4-268)
14	vitric	J-13	0.1 ± 0.5 (GU3-1407)	0.2 (GU3-1407)
15	vitric	J-13	0.1 ± 0.5 (GU3-1407)	0.1 (GU3-1407)
16	vitric	J-13	0.03 ± 0.2 (GU3-1405)	0.1 (GU3-1405)
17	vitric	Syn. p#1	0.2 ± 0.4 (GU3-1407)	0.1 (GU3-1405)
18	vitric	Syn. p#1	0.2 ± 0.4 (GU3-1407)	0.1 (GU3-1405)
19	vitric	Syn. p#1	0.2 ± 0.4 (GU3-1407)	0.1 (GU3-1405)

DTN: LA000000000106.001 (column Kd, SEP Table S99009.001), LA0010JC831341.007. Water compositions are described in the laboratory notebooks referenced by documentation associated with these DTNs.

NOTE: [a]Sample identifiers given in parentheses represent borehole code and drillcore depth in feet.

The elution curves also reveal that, regardless of the water being studied, the elution of ^{237}Np does not precede the elution of tritium for any of the tuffs. This observation is extremely important because if charge-exclusion effects were to cause the neptunyl-carbonato complex (an anion) to elute faster than neutral tritiated water molecules, significant neptunium releases could occur at Yucca Mountain. Another important observation that can be drawn from these experiments is that a batch K_d value can be used to obtain conservative estimates for neptunium transport through Yucca Mountain tuffs, assuming matrix flow.

6.5.1.2.2 Plutonium and Technetium Results

This section discusses the results from experiments in which Pu(V) was eluted through crushed-rock columns using J-13 well water and synthetic p#1 water. The elution curves for experiments in which vitric and zeolitic rock samples were used with J-13 water are shown in Figures 14 and 15. As shown in these figures, a small fraction of the Pu(V) breaks through early with the nonreactive tritium tracer. In the experiment with zeolitic tuff (Figure 15), an additional fraction breaks through between 10 and 20 column volumes followed by a slowly increasing amount of breakthrough. The early breakthrough observed in these experiments indicates there is a form of plutonium that is essentially unretarded under the experimental conditions. However, the data also indicate that the dominant fraction of plutonium in the experiments is retarded even after 50 column volumes have passed through the columns. The early breakthrough of Pu(V) is inconsistent with the batch retardation coefficients measured for similar rock samples in similar water compositions as discussed in Section 6.4.4.1.4.1 (Table 4). This inconsistency likely reflects slow kinetics for the plutonium sorption reaction in these rock/water systems. One possible explanation for such slow reaction kinetics is that the sorption reaction is coupled to a reduction reaction in which Pu(V) and Pu(VI) are reduced to Pu(IV) when in contact with the crushed-rock samples.

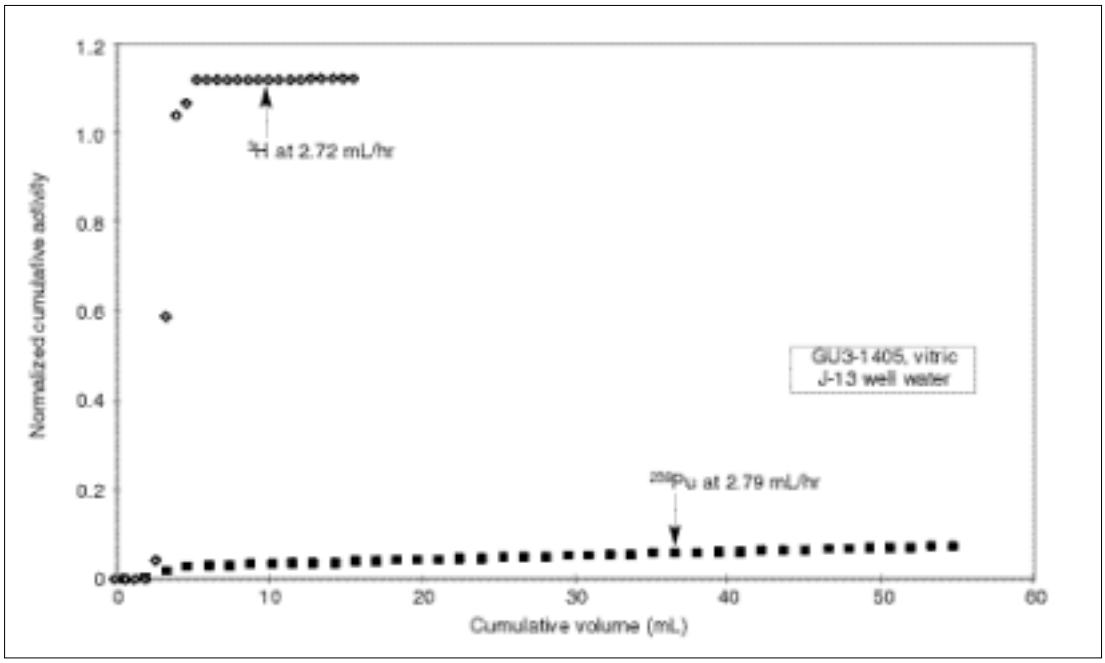

DTN: LAIT831361AQ95.001 (SEP Tables S98490.001 and .002)

NOTE: This plot shows the elution curves for tritium and plutonium-239 through vitric tuff sample GU3-1405 with J-13 well water.

Figure 14. Plutonium through Vitric Tuff

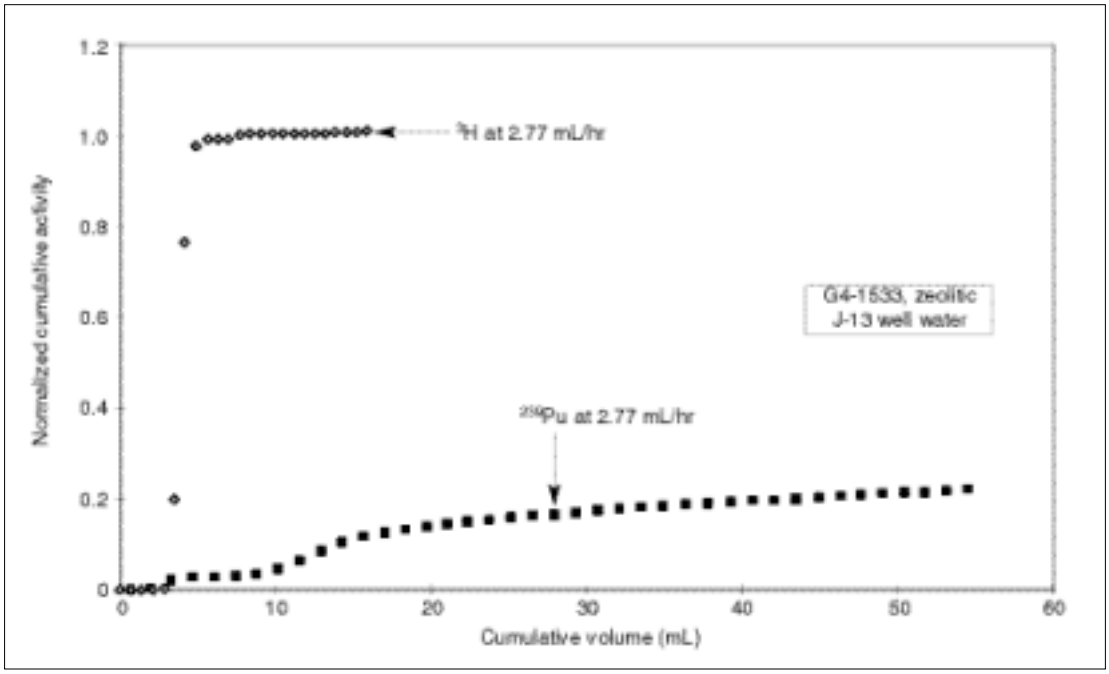

DTN: LAIT831361AQ95.001 (SEP Tables S98940.001 and .002)

NOTE: This plot shows the elution curves for tritium and plutonium-239 through zeolitic tuff sample G4-1533 with J-13 well water.

Figure 15. Plutonium through Zeolitic Tuff

The results of column experiments with devitrified tuff are presented in Figures 16 and 17. With this rock composition, the early breakthrough fraction, under flow conditions similar to those pertaining to the vitric and zeolitic column experiments discussed above, is approximately 60% in J-13 water and 20% in p#1 water. However, this fraction decreased substantially as the flow rate through the column was decreased. For the experiment with p#1 water, the early breakthrough fraction is absent when the flow rate is decreased to 0.4 mL g^{-1}. In J-13 water, a small (<10%) early breakthrough fraction is present even at a flow rate of 0.4 mL g^{-1}. These results reinforce the concept that plutonium sorption reactions on these types of tuffs are slow. An important question is, at what threshold velocity is the early breakthrough fraction eliminated for the various rock/water combinations encountered in the Yucca Mountain flow system? This question cannot be answered with the available data. Therefore, no definitive statements can be made regarding the applicability of batch-sorption coefficient data for plutonium to modeling of plutonium transport in the Yucca Mountain flow system.

The elution of pertechnetate (TcO_4^-) was also studied in columns of crushed devitrified, vitric, and zeolitic tuffs in J-13 and synthetic p#1 waters as a function of flow velocity. Inspection of the elution curves (Figures 18 to 20) indicate that anion-exclusion effects for pertechnetate in crushed tuff are essentially negligible except in the case of technetium transport through zeolitic tuff in J-13 well water (Figure 20). In this case, the anion-exclusion effect is small but measurable.

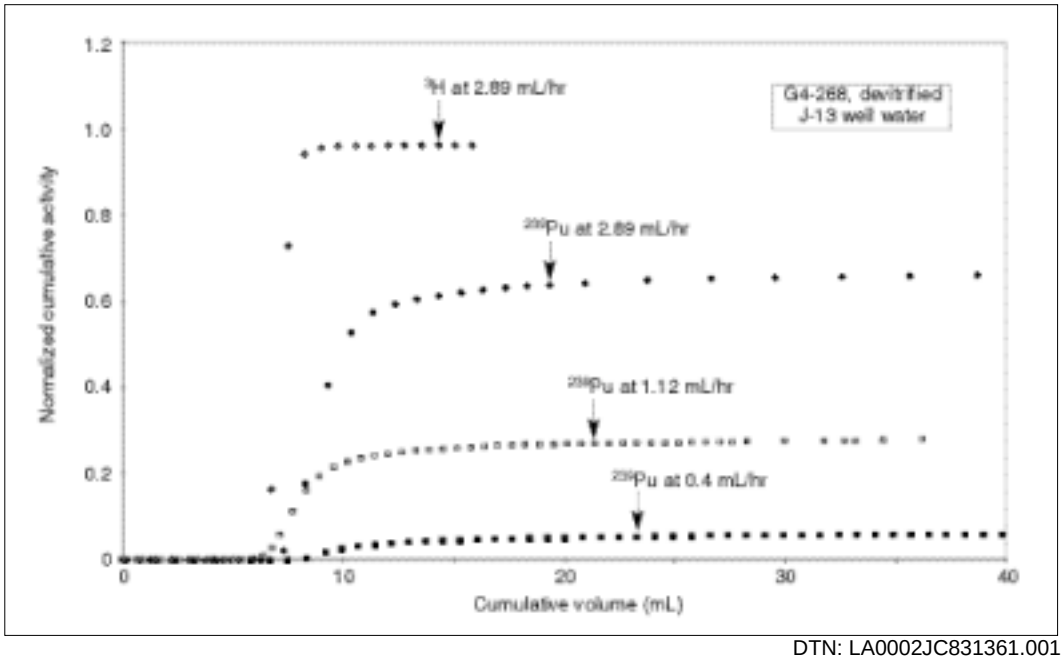

DTN: LA0002JC831361.001

NOTE: This plot shows elution curves for tritium and plutonium-239 at different flow rates with J-13 water through devitrified tuff sample G4-268.

Figure 16. Plutonium in Devitrified Tuff at Various Flow Rates (J-13 Water)

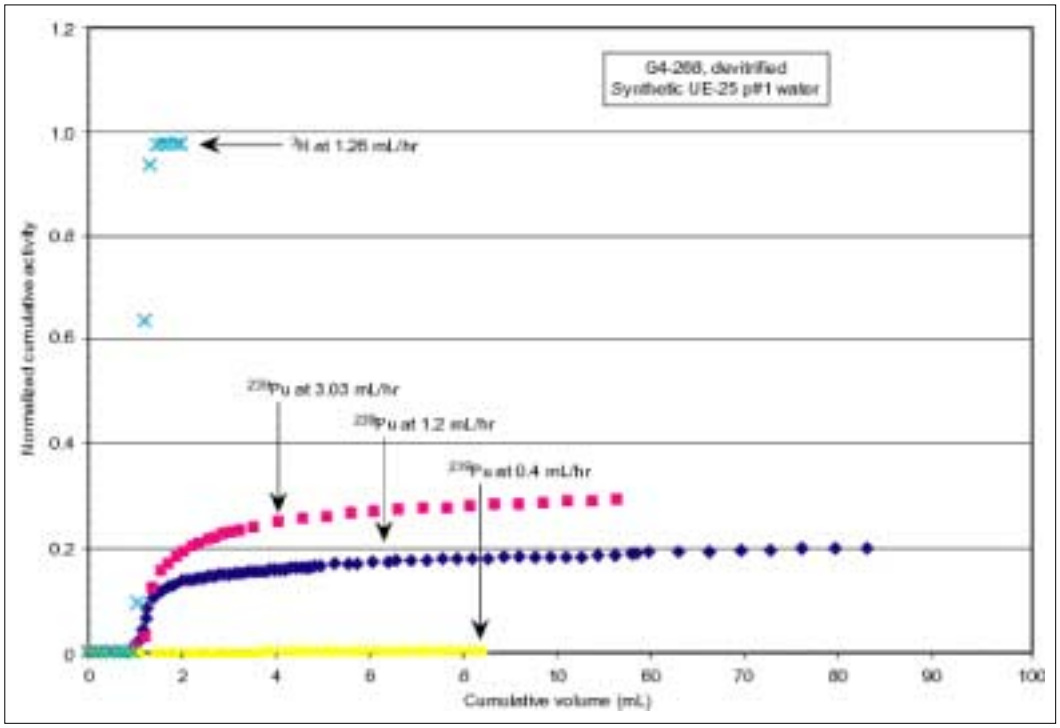

DTN: LA0002JC831361.002

NOTE: This plot shows elution curves for tritium and plutonium-239 at different flow rates in synthetic p#1 water and tuff sample G4-268.

Figure 17. Plutonium in Devitrified Tuff at Various Flow Rates (p#1)

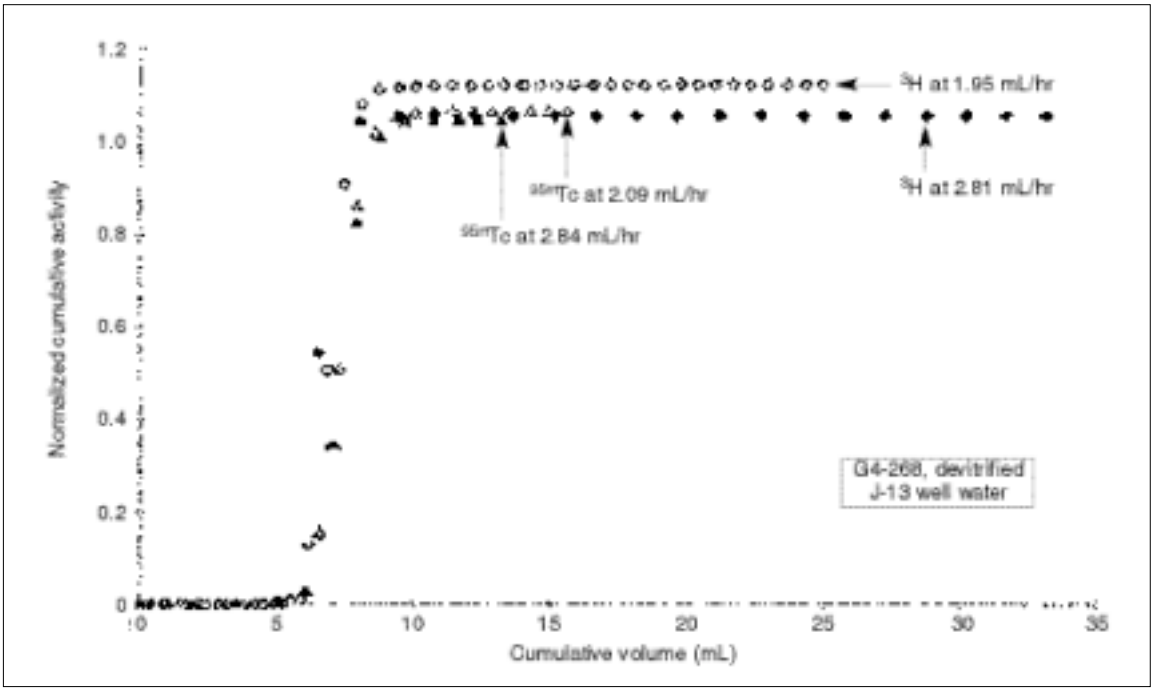

DTN: LA0002JC831361.003

NOTE: This plot shows the elution curves for tritium and technetium-95m at different flow rates with J-13 well water through devitrified tuff sample G4-268.

Figure 18. Technetium in Devitrified Tuff

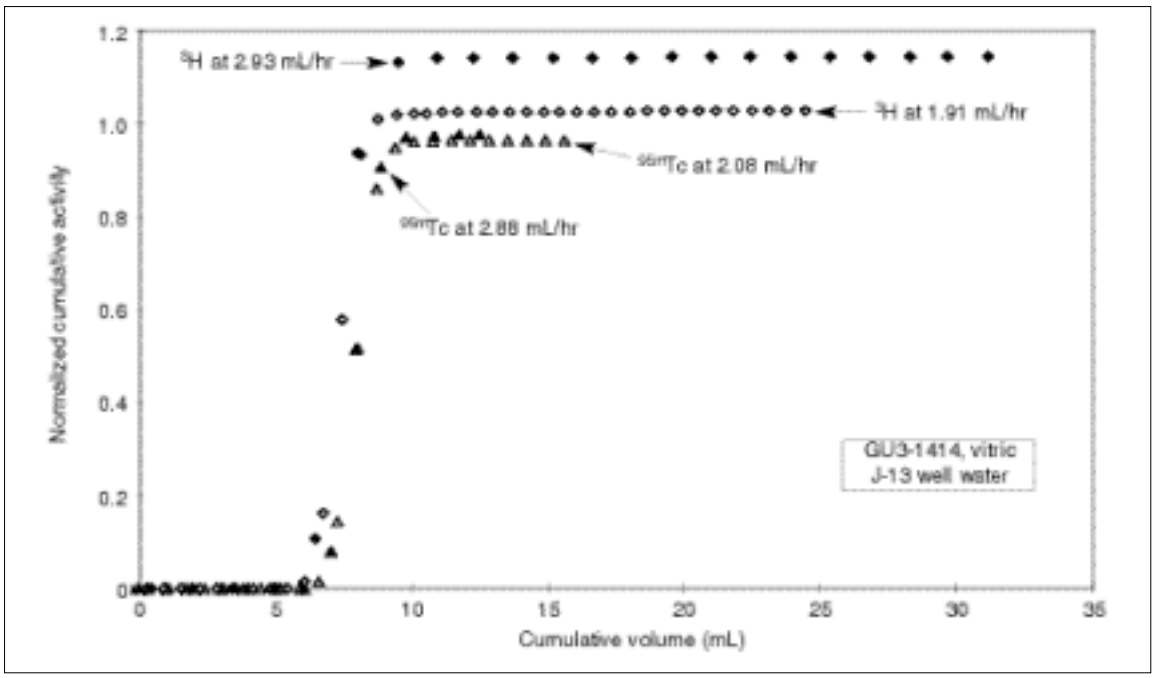

DTN: LA0002JC831361.004

NOTE: This plot shows the elution curves for tritium and technetium-95m at different flow rates with J-13 well water through vitric tuff sample GU3-1414.

Figure 19. Technetium in Vitric Tuff

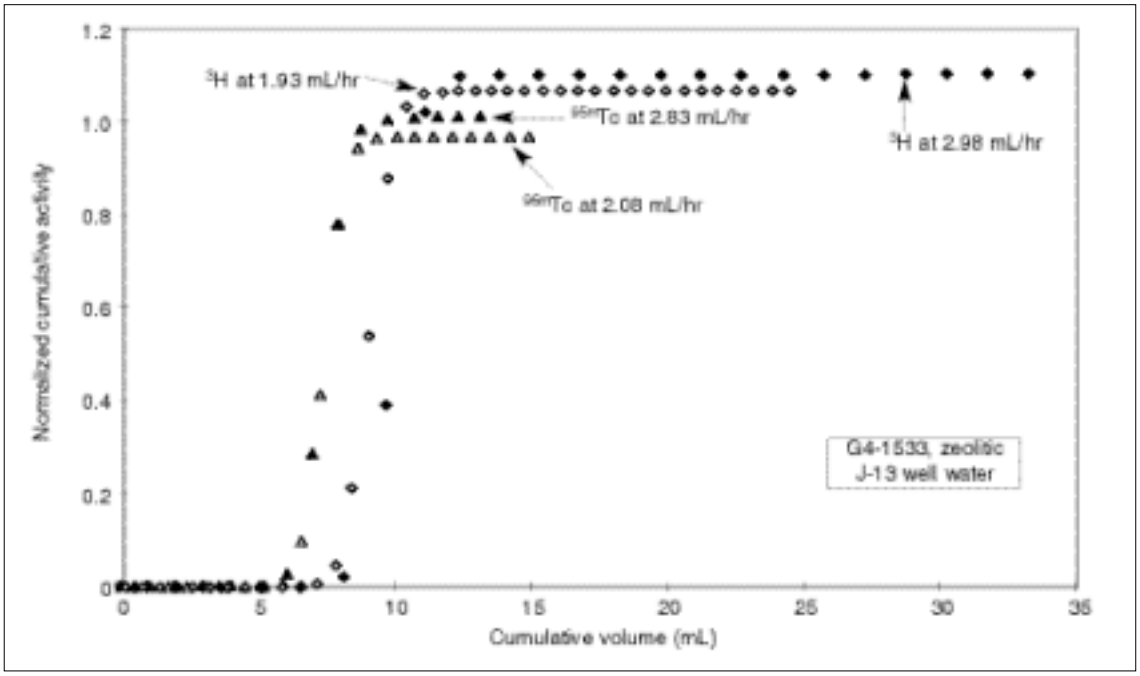

DTN: LA0002JC831361.005

NOTE: This plot shows the elution curves for tritium and technetium-95m at different flow rates with J-13 well water through zeolitic tuff sample G4-1533.

Figure 20. Technetium in Zeolitic Tuff

6.5.2 Solid-Rock Columns

Direct measurements of transport parameters in actual subsurface materials under subsurface conditions can provide defensible modeling of contaminant transport in host rocks and engineered barriers surrounding nuclear and hazardous waste repositories. The hydraulic conductivity, K, and the retardation factor, R_f, along with the associated distribution coefficient, K_d, are poorly known transport parameters for real systems but are key input parameters to existing and developing contaminant release models. Unsaturated R_f and K were experimentally determined for core samples of Yucca Mountain vitric-member tuff and zeolitic nonwelded tuff (from G Tunnel at Rainier Mesa about 45 km northeast of Yucca Mountain) with respect to J-13 well water with a selenium concentration (as selenite) of 1.31 mg L^{-1} (ppm) at 23ºC. The intent was to demonstrate that a method in which flow is induced with an ultracentrifuge could rapidly and directly measure R_f and K in whole-rock tuff cores and then to compare these directly measured unsaturated R_f values with those calculated from K_d values obtained through traditional batch tests on the same materials.

6.5.2.1 Methodology

6.5.2.1.1 Retardation

Retardation factors can be determined in flow experiments where R_f for a particular species is the ratio of the solution velocity to the species velocity. The retardation factor, a dimensionless parameter, for that species is given by (Bouwer 1991, p. 41):

$$R_f = \frac{V_{gw}}{V_{sp}} = 1 + \rho_d \frac{K_d}{\varepsilon} \quad , \qquad \text{(Eq. 11)}$$

where V_{gw} is the velocity of carrier fluid (cm^{-1}), V_{sp} is the velocity of the species (cm^{-1}), ρ_d is the dry bulk density ($g\ cm^{-3}$), ε is the porosity (dimensionless), and K_d is defined as the moles of the species per g of solid divided by the moles of the species per mL of solution ($mL\ g^{-1}$). If none of a particular species is lost to the solid phase, then $K_d = 0$ and $R_f = 1$ for that species. In column experiments, a breakthrough curve is obtained for the particular species and R_f is determined as the pore volume at which the concentration of the species in the solution that has passed through the column is 50 percent of the initial concentration ($C/C_0 = 0.5$). It is now generally assumed that, for unsaturated systems, $\varepsilon = \theta$, where θ is the volumetric water content (Bouwer 1991, p. 41). The study described in this section experimentally addresses this concern under unsaturated conditions in whole rock and evaluates the use of data from batch experiments in determining R_f in whole rock.

Solutions were prepared using J-13 well water with a selenite concentration of 1.31 mg L^{-1} (ppm). Selenium concentrations were measured with an inductively coupled, argon-plasma, atomic-emission spectrometer, with a selenium detection limit of about 0.1 mg L^{-1}. The speciation of selenium in solution was determined by ion chromatography. All selenium in the starting and effluent solutions was found to exist as selenite.

6.5.2.1.2 Hydraulic Conductivity

One way to drive fluid through rock is to use centripetal acceleration as the driving force. A new technology, the Unsaturated Flow Apparatus (UFA), was used to produce hydraulic steady-state; to control temperature, degree of saturation, and flow rates in all retardation experiments; and to measure the hydraulic conductivity. A specific advantage of this approach is that centripetal acceleration is a whole-body force similar to gravity. This force acts simultaneously over the entire system and independently of other driving forces, such as gravity or matrix suction. It has been shown that capillary bundle theory holds in the UFA method (Conca and Wright 1992, pp. 5, 19).

The UFA instrument consists of an ultracentrifuge with a constant, ultralow flow-rate pump that provides fluid to the sample surface through a rotating seal assembly and microdispersal system. Accelerations up to 20,000 g are attainable at temperatures from 220º to 150ºC and flow rates as low as 0.001 mL hr^{-1}. The effluent is collected in a transparent, volumetrically calibrated container at the bottom of the sample assembly. The effluent collection chamber can be observed during centrifugation using a strobe light.

The current instrument has two different rotor sizes that hold up to 50 and 100 cm^3 of sample, respectively. Three different rotating-seal assemblies facilitate various applications and contaminant compatibilities: a face seal, a mechanical seal, and a paramagnetic seal. The large sample option with the paramagnetic seal is a configuration that is optimal for adsorption and retardation studies.

Numerous studies have compared use of the UFA approach with traditional methods of measuring hydraulic conductivities in unsaturated soils and clays, and the agreement is excellent (Conca and Wright 1992, p. 20; Nimmo et al. 1987, pp. 128–134). Good agreement is expected because the choice of driving force does not matter provided the system is Darcian (see next paragraph) and the sample is not adversely affected by a moderately high driving force (≤ 1000 g for all samples run in these experiments); both of these provisions hold for most geologic systems. Additionally, all techniques for estimating hydraulic conductivity, $K(\theta)$, are extremely sensitive to the choice of the rock or soil residual water content, θ_r, and to the saturated hydraulic conductivity, K_s; minor variations in θ_r or K_s produce order-of-magnitude changes in $K(\theta)$ (Stephens and Rehfeldt 1985, p. 12).

The UFA technology is effective because it allows the operator to set the variables in Darcy's Law, which can then be used to determine hydraulic conductivity. Under a centripetal acceleration in which water is driven by both the potential gradient, $d\psi/dr$, and the centrifugal force per unit volume, $\rho\omega^2 r$, Darcy's Law is

$$q = -K(\psi)\left[\frac{d\psi}{dr} - \rho\omega^2 r\right] \quad , \qquad \text{(Eq. 12)}$$

where q is the flux density into the sample (cm s^{-1}); K, the hydraulic conductivity (cm s^{-1}), is a function of the matric suction, ψ, and, therefore, of water content, θ; r is the radius from the axis of rotation; ρ is the fluid density (g cm^{-3}); and ω is the rotation speed (radians per second). The gradient term, $d\psi/dr - \rho\omega^2 r$, is dimensionless. When multicomponent and multiphase systems are present in the UFA instrument, each component reaches its own steady state with respect to each phase, as occurs in the field. Appropriate values of rotation speed and flow rate into the sample are chosen to obtain desired values of flux density, water content, and hydraulic conductivity in the sample. Above speeds of about 300 rpm, depending upon the material and providing that sufficient flux density exists, $d\psi/dr << \rho\omega^2 r$. Under these conditions, Darcy's Law is given by $q = -K(\psi)\ [-\rho\omega^2 r]$. Rearranging the equation and expressing hydraulic conductivity as a function of water content, Darcy's Law becomes

$$K(\theta) = \frac{q}{\rho\omega^2 r} \quad . \qquad \text{(Eq. 13)}$$

As an example, a whole-rock core of Topopah Spring Member Tuff accelerated to 7,500 rpm with a flow rate into the core of 2 mL hr^{-1} achieved hydraulic steady-state in 30 hr with a hydraulic conductivity of 8.3 x 10^{-9} cm s^{-1} at a volumetric water content of 7.0 percent. Previous studies have verified the linear dependence of K on flux and the second-order dependence on rotation speed (Nimmo et al. 1987, pp. 124–126), and several comparisons between the UFA method and other techniques have shown excellent agreement (Conca and Wright 1992, p. 20). Because the UFA method can directly and rapidly control the hydraulic conductivity, fluid content, temperature, and flow rates, other transport properties can then be measured as a function of fluid content by associated methods either inside or outside the UFA instrument during the overall run.

Fundamental physics issues involving flow in an acceleration field have been raised and successfully addressed by previous research and in numerous forums (Conca and Wright 1992, pp. 16, 18; Nimmo et al. 1987, pp. 124–128; Nimmo and Akstin 1988, p. 303; Nimmo and Mello 1991, p. 1268). These studies have shown, first, that compaction from acceleration is negligible for subsurface soils at or near their field densities. Bulk density in all samples remains constant because a whole-body acceleration does not produce high point pressures. A notable exception is surface soils, which can have unusually low bulk densities; special arrangements must be made to preserve their densities. Whole rock cores are completely unaffected.

The studies have also shown that three-dimensional deviations of the driving force with position in the sample are less than a factor of 2, but moisture distribution is uniform to within 1 percent in homogeneous systems because water content depends only upon ψ, and unit gradient conditions are achieved in the UFA instrument in which $d\psi/dr = 0$. Hydraulic steady-state is not as sensitive to changes in rotation speed as to flux density. In heterogeneous samples or multicomponent systems such as rock, each component reaches its own hydraulic steady state and water content, as occurs for such materials under natural conditions in the field. This last effect cannot be reproduced with pressure-driven techniques but only under a whole-body force field, such as with gravity columns or centrifugal methods. The ratio of flux to rotation speed is always kept high enough to maintain the condition of $d\psi/dr = 0$.

6.5.2.2 Results and Discussion for Vitric and Zeolitic Tuff

6.5.2.2.1 Column Breakthrough Test Results

For these experiments, the rotation speed was set at 2,000 rpm with a flow rate into each sample of 0.2 mL hr^{-1}. The experiment was run for 9 days with an initial selenium concentration of 1.31 mg L^{-1}. Figure 21 shows the breakthrough curves for selenite (C/C_o is given for selenium as selenite) in the Yucca Mountain vitric member at 62.6% saturation and in the zeolitic nonwelded tuff at 52.8% saturation. Pore volume is given as water-filled, or effective pore volume, the same as the volumetric water content, θ, and is dimensionless. The experiment was stopped before full breakthrough in the zeolitic nonwelded tuff, but the $C/C_o = 0.5$ point was reached. The retardation factor for each tuff sample is 2.5. The K_d for each tuff sample can be calculated by rearranging Equation 11 into $K_d = (R_f - 1)$(water content)/(bulk density). The water content is the total porosity multiplied by the degree of saturation. For the Yucca Mountain vitric-member tuff $K_d = (2.5 - 1)(0.626)(0.23)/1.54 = 0.14$ mL g^{-1}, and for the zeolitic nonwelded tuff, $K_d = (2.5 - 1)(0.528)(0.4)/1.21 = 0.26$ mL g^{-1}.

During these experiments, the unsaturated hydraulic conductivity, K, for each sample at these water contents was 2.5×10^{-8} cm s^{-1} for the Yucca Mountain vitric-member tuff and 1.2×10^{-8} cm s^{-1} for the zeolitic nonwelded tuff. Figure 22 gives the characteristic curves, $K(\theta)$, for these tuffs determined in separate experiments, as well as measurements for other tuffs and materials for comparison.

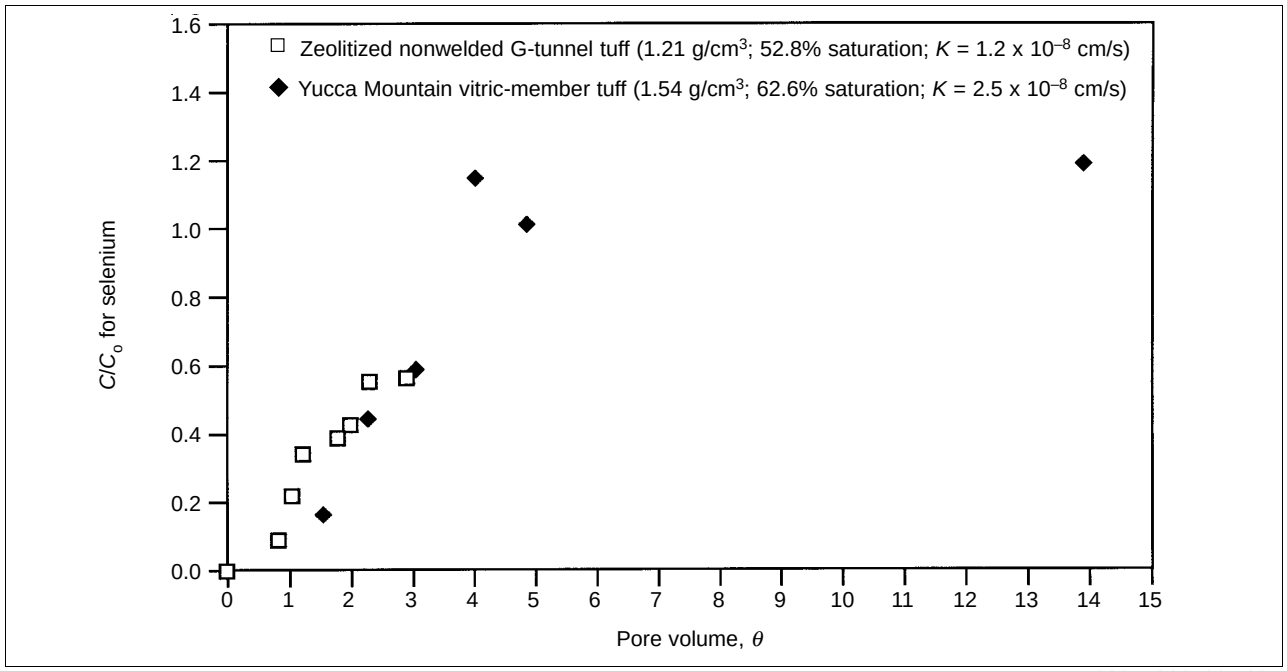

DTN: LA0004JC831361.001

NOTE: The UFA column data plotted here for a Yucca Mountain tuff retardation experiment show the breakthrough curves for selenium. The initial concentration, C_0, of selenium (as selenite) was 1.31 mg L^{-1} in J-13 well water.

Figure 21. Selenium Breakthrough Curves

6.5.2.2.2 Batch-Sorption Test Results

Batch-sorption tests were conducted using the same J-13 well water with the slightly lower selenium concentration, as selenite, of 1.1 mg L^{-1} and the same zeolitic nonwelded tuff as in the UFA column breakthrough test. The batch-adsorption tests consist of crushing and wet-sieving the tuff, pretreating the tuff with J-13 water, placing the selenium solution in contact with the tuff, separating the phases by centrifugation, and determining the amount of selenium in each phase by difference using inductively coupled plasma mass spectrometry. Control samples were used to determine the sorption of selenium onto the walls of the sorption containers. The control procedure consisted of following the described batch-sorption procedure with a sample containing the selenium solution, except with no tuff added. The results of the control experiments indicate no loss of selenium due to precipitation or sorption onto the walls of the container during the batch-sorption experiment. The sorption distribution coefficients obtained are given in Table 12. The Eh of all solutions, measured after the sorption experiments, varied from 140 to 150 mV.

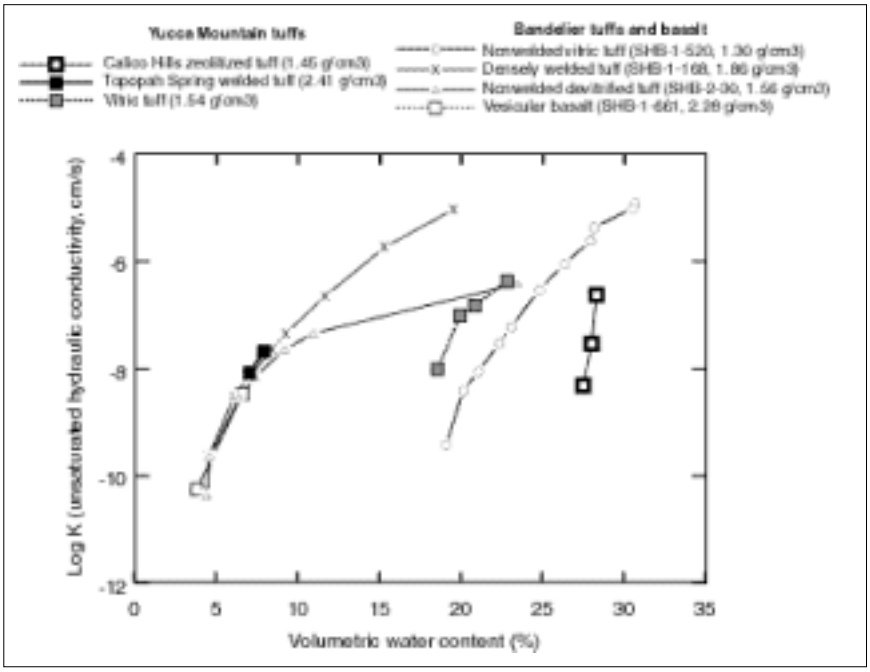

DTN: LA0004JC831224.001

NOTE: These UFA column data for various Yucca Mountain and Bandelier tuffs and other soil samples show the unsaturated hydraulic conductivity, K, as a function of volumetric water content, θ. The name and the density of each tuff is given in the legend.

Figure 22. Unsaturated Hydraulic Conductivity

Table 12. Selenium Batch Adsorption on Nonwelded Zeolitic Tuff [a]

Pretreatment period (days)	Sorption period (days)	K_d (mL g^{-1})
6.9	0.04	–0.2
6.9	0.04	0.3
6.8	13.9	0.0
6.8	13.9	0.2

DTN: LA0002JC831341.003

NOTE: [a] Experimental conditions: J-13 water; 20° C; 75–500μm tuff particle sizes; 1.1 mg L^{-1} initial selenium concentration; solution pH after sorption of 8.4; and samples from the same location as the tuff used in the column experiments.

The data presented in Table 12 and Figure 21 indicate agreement between the column and the batch-sorption experiments. At a selenium concentration of ~1 mg L^{-1}, no sorption of the selenium by the tuff is observed for the zeolitic tuff used in batch experiments (average K_d = 0.08 ± 0.22 mL g^{-1} from Table 12), and minimal sorption is observed for the zeolitic tuff used in the unsaturated column experiments (K_d of 0.26 mL g^{-1} from Section 6.5.2.2.1). The method used for the batch-sorption experiments to determine K_d values (by difference) involves subtracting the selenium concentration in solution after equilibration with the solid phase from the initial selenium concentration in solution. This method yields large scatter in the data when the batch-sorption distribution coefficient is small because two large numbers are subtracted to get a small

number. Inspection of Table 12 also suggests that the kinetics of selenium sorption onto tuff are fast.

6.5.2.2.3 Conclusions

This study demonstrated the feasibility of using the UFA technology to measure retardation factors and hydraulic conductivities rapidly and directly in whole-rock cores of tuff under the unsaturated conditions that exist in the field. In UFA column breakthrough tests, the retardation factor for the selenite species was only 2.5 in both Yucca Mountain vitric member tuff at 62.6 percent saturation and zeolitic nonwelded tuff at 52.8 percent saturation for a selenium concentration in J-13 water of 1.31 mg L^{-1}, corresponding to K_d values of 0.14 mL g^{-1} and 0.26 mL g^{-1}, respectively. In batch tests on the same material with an initial selenium concentration of 1.1 mg L^{-1}, the average K_d was 0.08 ± 0.2 mL g^{-1}, which gives retardation factors that are slightly lower than those from the UFA column breakthrough experiments. This finding suggests that using batch-sorption coefficients to predict radionuclide transport through unsaturated tuff will yield conservative results. The unsaturated hydraulic conductivities during the experiments were 2.5 x 10^{-8} cm s^{-1} for the Yucca Mountain vitric-member tuff and 1.2 x 10^{-8} cm s^{-1} for the zeolitic nonwelded tuff.

6.5.3 Radionuclide Transport Through Fractures

6.5.3.1 Overview

Among other reasons, Yucca Mountain was chosen as a potential site for a high-level nuclear-waste repository because its geochemistry is believed to form both a physical and a chemical barrier to radionuclide migration. As a result of regional tectonics and volcanism, many faults and fractures were produced within the tuffaceous units of Yucca Mountain as well as the surrounding region. In addition, volcanic tuffs are commonly fractured as a result of cooling. The numerous fractures present at Yucca Mountain represent a potential breach in the natural barrier, providing a fast pathway for radionuclide migration.

Radionuclide transport estimates commonly assume that radionuclides can travel through fractures unimpeded. This assumption is too simplistic and leads to overconservative predictions of radionuclide releases to the accessible environment. The assumption ignores two main mechanisms by which retardation of radionuclides migrating through fractures can occur: (1) diffusion of the radionuclides from the fractures into the rock matrix, and (2) sorption of radionuclides onto the minerals coating the fractures.

Minerals coating the fracture walls are generally different from the host-rock mineralogy due to a variety of factors ranging from precipitation of hydrothermal waters or meteoric waters to alteration of the pre-existing minerals. A review of the literature (Carlos 1985, Table I; 1987, Table I; 1989, Table II; 1994, Table 1; Carlos et al. 1990, Table II; 1993, Table 1) has provided a list of the minerals lining the fractures found at Yucca Mountain (Table 13).

Table 13. Minerals Coating Fracture Walls in Yucca Mountain Tuffs

	Zeolites	
Heulandite ↔ Clinoptilolite	$Ca_4Al_8Si_{28}O_{72}\cdot 24H_2O$ ↔ $(Na, K)_6Al_6Si_{30}O_{72}\cdot 24H_2O$	
(range of compositions with arbitrary division of Si/Al < 4.4 for heulandite and Si/Al > 4.4 for clinoptilolite)		
Mordenite	$(Ca,Na_2,K_2)_4Al_8Si_{40}O_{96}\cdot 28H_2O$	
Analcime	$NaAlSi_2O_6\cdot H_2O$	
Chabazite	$CaAl_2Si_4O_{12}\cdot 6H_2O$	
Phillipsite	$(K_2,Na_2,Ca)Al_2Si_4O_{12}\cdot 4–5H_2O$	
Erionite	$(Ca,Na_2,K_2)_4Al_8Si_{28}O_{72}\cdot 27H_2O$	
Stellerite	$CaAl_2Si_7O_{18}\cdot 7H_2O$	
	Silica	
Quartz	SiO_2—low-temperature polymorph of silica	
Tridymite	SiO_2—high-temperature polymorph of silica	
Cristobalite	SiO_2—highest-temperature polymorph of silica	
Opal	$SiO_2\cdot nH_2O$	
Feldspars		
Plagioclase (albite)	Solid solutions of albite ($NaAlSi_3O_8$) and anorthite ($CaAl_2Si_2O_8$)	
K-feldspar (sanidine)	Solid solutions of orthoclase ($KAlSi_3O_8$) and albite ($NaAlSi_3O_8$)	
	Clays	
Smectite family:		
Dioctahedral (montmorillonite)	$(Na,K,Mg_{0.5},Ca_{0.5},\text{possibly others})_{0.33}Al_{1.67}Mg_{0.33}Si_4O_{10}(OH)_2\cdot nH_2O$	
Trioctahedral (saponite)	$(Ca_{0.5},Na)_{0.33}(Mg,Fe)_3(Si_{3.67}Al_{0.33})O_{10}(OH)_2\cdot 4H_2O$	
Sepiolite	$Mg_4(Si_2O_5)_3(OH)_2\cdot 6H_2O$	
Palygorskite	$(Mg,Al)_2Si_4O_{10}(OH)\cdot 4H_2O$	
Illite	$(H_3O,K)_y(Al_4Fe_4Mg_4Mg_6)(Si_{8-y}Al_y)O_{20}(OH)_4$	
	Manganese oxides/hydroxides	
Pyrolusite	MnO_2	(1x1 tunnel structure)
Cryptomelane family:	$A_{0-2}(Mn^{4+},Mn^{3+})_8(O,OH)_{16}$	(2x2 tunnel structure)
Cryptomelane	A = K	
Hollandite	A = Ba	
Coronadite	A = Pb	
Romanechite	$(Ba,H_2O)_2Mn_5O_{10}$	(2x3 tunnel structure)
Todorokite	$(Na,Ca,Ba,Sr)_{0.3-0.7}(Mn,Mg,Al)_6O_{12}\cdot 3.2–4.5H_2O$	(3x3 tunnel structure)
Aurorite	$(Mn^{2+},Ag,Ca)Mn_3O_7\cdot 3H_2O$	
Lithiophorite	$m\{Al_{0.5}Li_{0.5}MnO_2(OH)_2\}\ n\{Al_{0.667}(Mn^{4+},Co,Ni,Mn^{2+})O_2(OH)_2\}\ pH_2O$	
Rancieite	$(Ca,Mn^{2+})(Mn^{4+})_4O_9\cdot 3H_2O$	
	Iron oxides/hydroxides	
Hematite	Fe_2O_3	
Magnetite	$(Fe,Mg)Fe_2O_4$	
	Carbonates	
Calcite	$CaCO_3$	
	Halides	
Fluorite	CaF_2	

Source: Carlos (1985, Table I; 1987, Table I; 1989, Table II; 1994, Table 1); Carlos et al. (1990, Table II; 1993, Table 1)

The transport of radionuclides through fractures from Yucca Mountain was examined to assess the retardation that can be provided by radionuclide diffusion into the matrix and sorption onto the minerals coating the Yucca Mountain fractures.

6.5.3.2 Experimental Procedures

Groundwaters—The groundwaters used for the experiments presented in this section were waters from Well J-13 (filtered through a 0.05-μm filter) and two sodium bicarbonate buffers that simulated the water chemistry of the groundwaters from Wells J-13 and p#1. The synthetic J-13 water was prepared by dissolving 0.03 g of Na_2CO_3 and 1.92 g of $NaHCO_3$ in 10 L of deionized water; the synthetic p#1 water by dissolving 0.39 g of Na_2CO_3 and 8.90 g of $NaHCO_3$ in 10 L of deionized water. The reasons for having to use synthetic waters for the fracture-column experiments was the unavailability of water from Well p#1 and the prevention of microbial activity in the columns.

Fractured-Tuff Samples—Tuff samples with natural fractures from drill holes at Yucca Mountain were selected from the YMP Sample Management Facility in Mercury, Nevada. The tuff matrix of all samples consisted of devitrified tuff, and the minerals lining the fractures were stellerite, magnetite, hollandite, and romanechite. The sampling criteria were confined to cores with natural fractures, determined by the presence of secondary mineral coatings, and fractures with removable fracture walls that could be repositioned to their original orientation. Based on this criteria, it was concluded that of the fractured-tuff cores selected (USW G1-1941, UZ-16 919, USW G4-2981, and USW G4-2954) all consisted of natural fractures except sample G1-1941, the only core sample that did not have secondary minerals coating its fracture. The fracture in sample G1-1941 is apparently induced.

Radionuclide Solutions—The radionuclide solutions (tritium, pertechnetate, and neptunium) were prepared in the same manner as for the crushed-tuff column experiments (Section 6.5.1.2).

Fractured-Column Procedure—The experimental setup was the same as that for the crushed-tuff column experiments except the column was replaced with a fractured-tuff column. The column was submerged in a beaker containing either synthetic p#1 or synthetic J-13 water. The beakers were subjected to a vacuum for a minimum of 2 weeks until all evacuating gas bubbles ceased. After saturation, the columns were connected, via one of the outflow ports, to a syringe pump, and the second outflow port was connected to a pressure transducer. The tracer was injected through the bottom. A constant flow rate was established, and a radionuclide tracer was introduced into the system through an injection valve. The column elutions were collected as a function of time and analyzed, using standard radiometric techniques, for the percentage of radionuclide tracer recovered. The aperture of the fractures has not yet been determined, but Table 14 gives the other characteristics of the four columns.

Batch-Sorption Experiments—For comparison with the fractured-column experiments, batch-sorption tests of neptunium onto the fracture minerals stellerite, hollandite, romanechite, and magnetite were conducted. These tests were performed under atmospheric conditions using J-13 well water with a Np(V) concentration of 6.7×10^{-7} M. The batch-sorption tests consisted of::

- Crushing and wet-sieving the minerals to a size of 75 to 500 μm
- Pretreating the minerals with J-13 water
- Placing the neptunium solution in contact with the minerals for a period of three days (using a solid to solution ratio of 1 g to 20 mL)
- Separating the phases by centrifugation
- Determining the amount of neptunium in each phase by difference using liquid scintillation counting.

Table 14. Characteristics of Fractured Devitrified-Tuff Columns

Characteristic	Column #1	Column #2	Column #3	Column #4
Sample identifier	G1-1941	UZ-16 919	G4-2981	G4-2954
SMF barcode number	N/A	0029365	0029366	0029368
Major minerals in tuff matrix	Alkali feldspar and quartz	Alkali feldspar and Quartz	Alkali feldspar and opal CT	Alkali feldspar and opal CT
Minerals coating the fracture	None (apparent induced fracture)	Stellerite Magnetite	Hollandite Romanechite	Hollandite Romanechite
Water type	Synthetic J-13	Synthetic p#1	Synthetic J-13	Synthetic J-13
pH	8.6	8.8	8.6	8.6
Concentration of ^{237}Np (M)	1.4×10^{-5}	4.8×10^{-6}	1.4×10^{-5}	1.4×10^{-5}
Length (cm)	12.6	6.1	6.0	not determined
Diameter (cm)	6.1	5.2	5.2	not determined
Volumetric flow rate (mL hr^{-1})	0.5	0.5	0.5	0.5

DTN: LAIT831361AQ95.003 (SEP Table S98491.001)

NOTE: Sample identifier is a combination of the borehole identifier and depth in feet.

Control samples were used to determine the sorption of neptunium onto the walls of the sorption containers. The control samples consisted of following the described batch-sorption procedure with a sample containing the neptunium solution only with no solid added. The results of the control experiments indicate no loss of neptunium from precipitation or sorption onto the walls of the container during the batch-sorption experiment. The pH of the water in these experiments was approximately 8.5.

6.5.3.3 Results and Discussion

As discussed earlier, neptunium does not sorb onto devitrified tuff (Triay, Cotter, Kraus et al. 1996, p. 18), which constitutes the matrix of all the fractures studied. Retardation during fracture flow occurs by diffusion of the radionuclides into the tuff matrix or by sorption of the radionuclides onto the minerals coating the fractures. Table 15 lists the results of batch-sorption

experiments describing the sorption of neptunium onto natural minerals that exist along flow paths in the tuff.

Table 15. Batch-Sorption Results for ^{237}Np in J-13 Well Water

Major mineral in solid phase	K_d (mL g^{-1})	Solid-phase composition [a]
Stellerite	~ 0	not analyzed
Hollandite	700	100% Hollandite
Romanechite	600	not analyzed
Magnetite	7	85% Magnetite
		12% Hematite
		3% Goethite

DTN: LAIT831361AQ95.003 (SEP Table S98491.003)

NOTE: [a] Determined by x-ray-diffraction analysis.

Although the extrapolation from these experiments to Yucca Mountain tuffs containing the same minerals is not immediate, the data of Table 15 show some important trends. Neptunium has a high affinity for hollandite and romanechite, whereas sorption onto the stellerite is not significant. If ion exchange is the main mechanism for neptunium sorption onto stellerite, changing the water from J-13 to p#1 will only result in less sorption (due to the formation of a larger amount of the neptunyl carbonado complex and competitive effects as a result of the higher ionic strength in the p#1 water). The sorption of neptunium onto magnetite does not appear to be significant either. As shown in Table 15, the magnetite sample studied contains hematite, which could account for the entire observed sorption (Triay, Cotter, Kraus et al. 1996, Figure 17).

Because no secondary minerals coating the fractures were observed for the G1-1941 fractured sample (Table 14, column #1, and Figure 23), it can be concluded that the retardation of neptunium observed for that column is due to diffusion into the matrix.

The total neptunium recovery of 70 percent in the UZ-16 919 fractured sample (Table 14, column #2, and Figure 24) could be due to minimal sorption onto the stellerite and magnetite coating that fracture or due to diffusion into the matrix. It is important to note that in changing the water for this column from synthetic J-13 to synthetic p#1, the speciation of neptunium changes from a mixture of neptunyl and carbonado complex to almost 100 percent carbonado complex (which can be excluded from tuff pores due to size and charge).

Neptunium seems to be significantly retarded even during fracture-flow in the sample G4-2981 fractured sample (Figure 25) that is coated with hollandite and romanechite. The recovery of neptunium in this fracture is less than 10 percent, and its first appearance is delayed with respect to tritium and technetium.

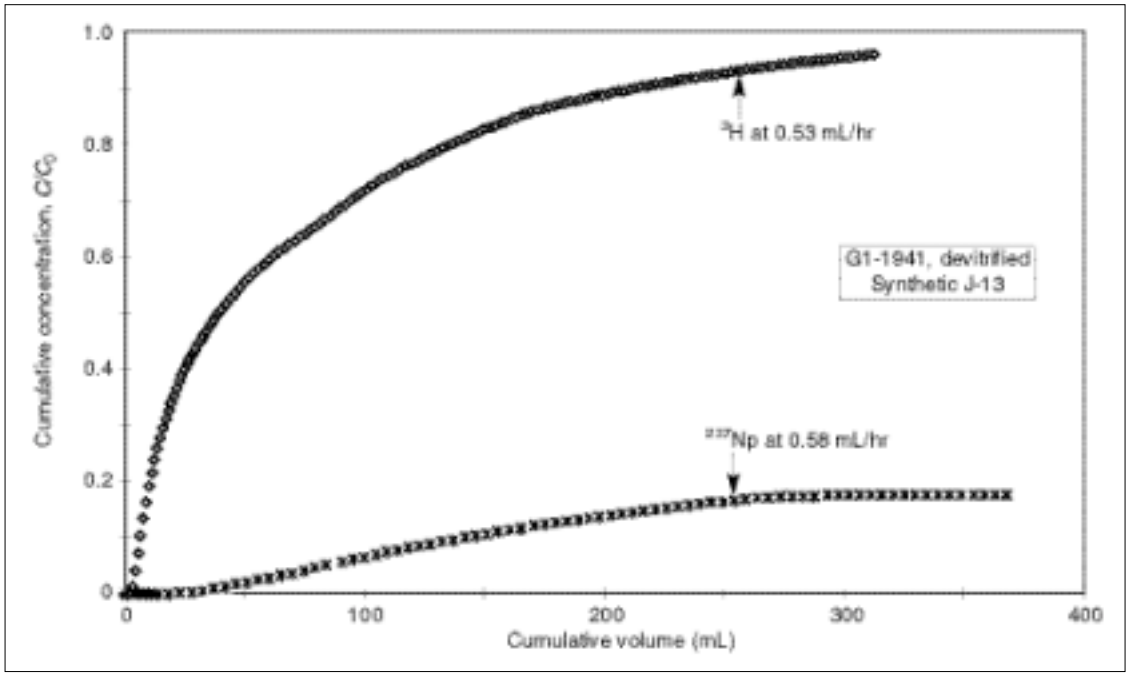

DTN: LA0001JC831361.001

NOTE: This plot shows the elution curves for tritium and neptunium-237 in synthetic J-13 water through a fractured column of devitrified tuff sample G1-1941.

Figure 23. Neptunium in Fractured Tuff G1-1941

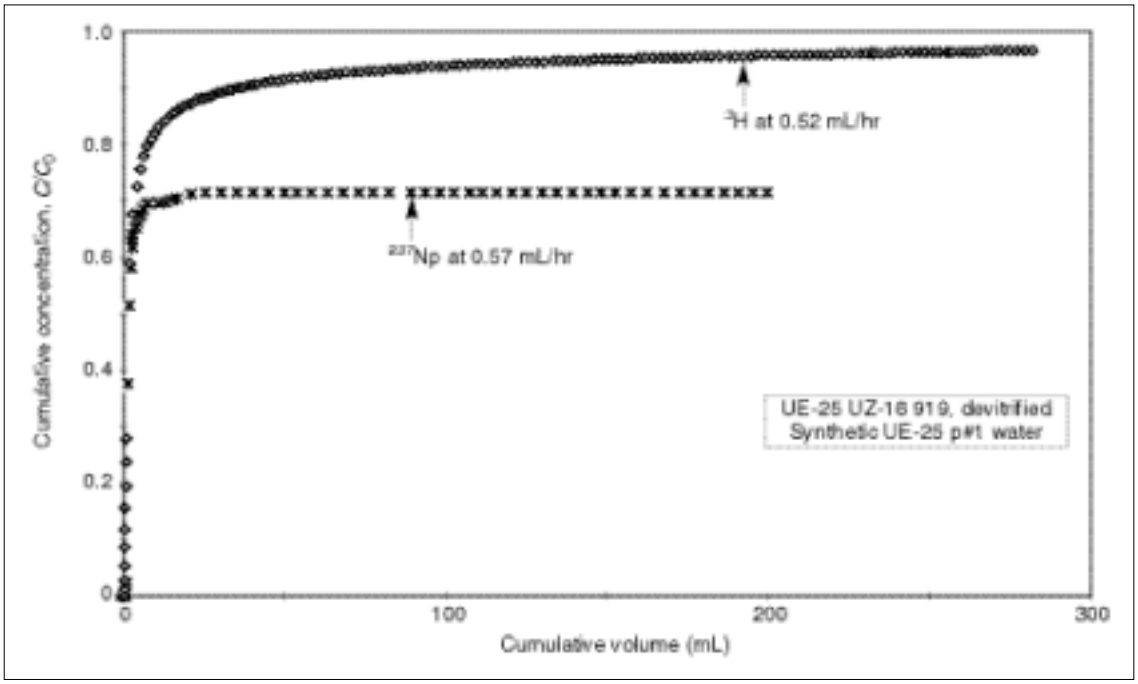

DTN: LA0001JC831361.001

NOTE: This plot shows the elution curves for tritium and neptunium-237 in synthetic p#1 water through a fractured column of devitrified tuff UZ-16 919.

Figure 24. Neptunium in Fractured Tuff UZ-16 919

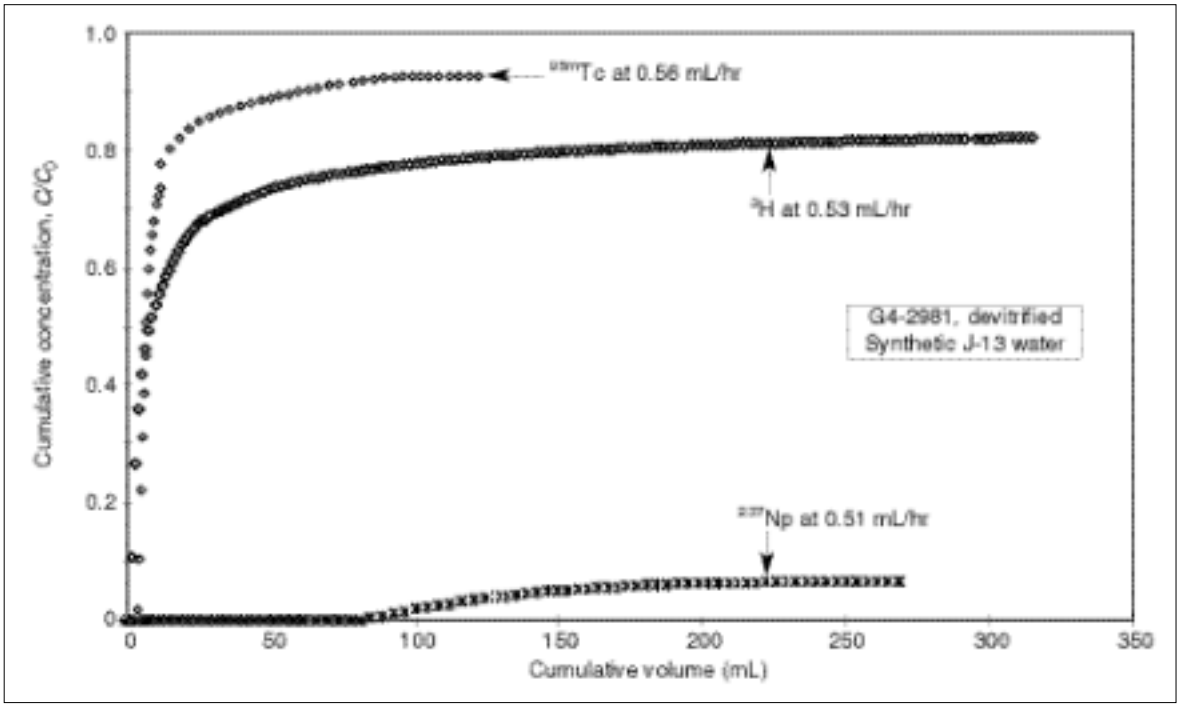

DTN: LA0001JC831361.001, LA0001JC831361.002

NOTE: Elution curves for ^{3}H, ^{237}Np, and ^{95m}Tc in synthetic J-13 water through a fractured column of tuff G4-2981.

Figure 25. Neptunium and Technetium in Fractured Tuff

Results illustrated in Figures 25 and 26 (columns #3 and #4 of Table 14) indicate that diffusion from the fracture into the matrix has taken place because recovery of tritium was only 80 percent compared to 90 percent for technetium. This trend agrees with diffusion data that were previously obtained for ^{3}H and ^{95m}Tc in devitrified tuff and water from well J-13. These data were fitted to the diffusion equation (Triay, Birdsell et al. 1993, Eq. 1) using the transport code TRACRN V1.0 (STN: 1010601.0-00), which yielded diffusion coefficients for saturated devitrified tuffs that were of the order of 10^{-6} cm^2 s^{-1} for tritiated water and 10^{-7} cm^2 s^{-1} for technetium. Anion exclusion, in which the large pertechnetate anion is excluded from tuff pores due to its size and charge, may be operative in this case. The alternative explanation, that ^{3}H is retarded relative to pertechnetate due to sorption, is ruled out; the K_d for ^{3}H is so infinitesimally small because the mass of ^{3}H in the water far exceeds that associated with clays or other minerals in the rock.

Continuing with the explanation by de Marsily (1986, Chapter 10) of the fate of reactive and nonreactive solutes in porous and fractured media, that was started in the earlier section on crushed-rock columns, the equation for a sorbing, nonreactive solute (Equation 6) can be expanded to account for a solute that also undergoes radioactive decay:

$$\nabla \cdot (\mathbf{D}\ \nabla C - C\mathbf{U}) = \varepsilon\left(\frac{\partial Q}{\partial t} + \lambda C\right) + \rho_b\left(\frac{\partial F}{\partial t} + \lambda F\right) \qquad \text{(Eq. 14)}$$

where λ is related to the half-life, $t_{1/2}$, of the decaying radionuclide by the relationship $\lambda = 0.693/t_{1/2}$.

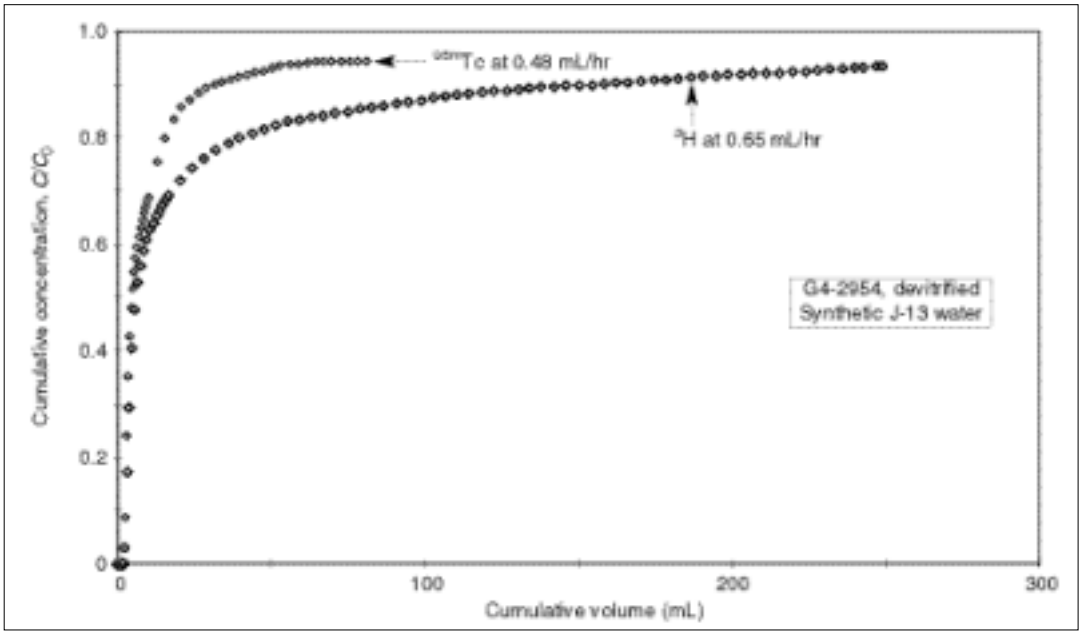

DTN: LA0001JC831361.001, LA0001JC831361.002

NOTE: This plot shows elution curves for ^{95m}Tc and ^{3}H in synthetic J-13 water through a fractured column of devitrified tuff sample G4-2954.

Figure 26. Technetium in Fractured Tuff

As was pointed out earlier, the mechanism of sorption determines the relationship between F and C. If the linear, reversible, and instantaneous relationship for sorption is substituted, that is $F = K_d C$, Equation 14 becomes

$$\nabla \cdot (\mathbf{D}\ \nabla C - C\mathbf{U}) = \varepsilon\left(1 + \frac{\rho_b}{\varepsilon} K_d\right)\left(\frac{\partial C}{\partial t} + \lambda C\right) \qquad \text{(Eq. 15)}$$

The expression inside the first set of parentheses in Equation 15 is the retardation factor, R_f, which, of course, is only valid if sorption is linear, reversible, and instantaneous.

For radionuclide elution through fractures, the porous medium and the fractured medium are treated separately, each with its own Darcy's velocity and porosity (de Marsily 1986, Chapter 10), then coupled by a convection and a dispersion-exchange term in the transport code. The radionuclide elution data through fractured media were reduced and analyzed using the transport code FEHM V2.00 (STN: 10031-2.00-00) and reported in Robinson et al. (1995, pp. 63–70). The report on ^{237}Np elution through fractured rock made it clear that the data are consistent with very large values of K_d, at least compared to the typical value of 2.5 for ^{237}Np on zeolitic tuff. The report also indicated that it is possible that minerals present in trace quantities in the bulk rock that appear to contribute insignificantly to sorption may be quite effective at retarding ^{237}Np transport when concentrated on fracture surfaces.

The most significant conclusion of the work presented here is that, contrary to previous assumptions about the role of fractures in radionuclide retardation, preliminary results from these experiments indicate that fracture flow does not necessarily result in a fast pathway for actinide

migration through fractures. As can be seen in the experiments described above, the migration of actinides through fractures could be significantly retarded by sorption onto minerals coating the fractures and by diffusion into the tuff matrix. This is corroborated by the Busted Butte and C-wells results in Sections 6.8 and 6.9.

6.6 DIFFUSION TRANSPORT STUDIES IN THE LABORATORY

Solute transport in fractured rock in a potential radionuclide waste repository has been discussed by Neretnieks (1990, p. 22) who concluded that most rocks (even dense rocks such as granites) have small fissures between the crystals that interconnect the pore system containing water. Small molecules of radioactive materials can diffuse in and out of this pore system. The inner surfaces in the rock matrix are much larger than the surfaces in the fractures on which the water flows. The volume of water in the microfissures is much larger than the volume in fractures. Therefore, over a long time scale, diffusion can play an important role in radionuclide retardation.

The objective of diffusion experiments was to provide diffusion information for nonsorbing neutral molecules and anions and sorbing radionuclides. Because the uptake of radionuclides by tuff is measured as a function of time, the experiments also yield information on kinetics of sorption.

6.6.1 Rock-Beaker Experiments

Rock-beaker experiments measure the diffusive loss of radionuclides into a rock from a solution placed in a cavity drilled into the rock. The radionuclides used in these experiments were ^{3}H, ^{95m}Tc, ^{237}Np, ^{241}Am, ^{85}Sr, ^{137}Cs, and ^{133}Ba. Batch-sorption results are used to correct for decreases in radionuclide concentrations in the solution due to sorption.

6.6.1.1 Experimental Procedure

The experimental technique involved fabricating rock beakers of tuff. The beaker sits inside a Plexiglas™ container surrounded by groundwater. A stopper is used to prevent evaporation. The cavity in the rock beaker has a radius of approximately 1.4 cm and a length of 2.5 cm. The beaker itself has a length of approximately 5 cm and a radius of 3.1 cm. A solution (prepared with groundwater from Well J-13) containing the radionuclide of interest was placed in the rock cavity and then aliquots of the solution from the beaker for the remaining radionuclide concentration were analyzed as a function of time. Also performed were batch-sorption experiments with J-13 water and the tuffs under study.

6.6.1.2 Data Analysis

The results of the rock-beaker experiments were corroboratively modeled using TRACRN V1.0 (STN: 10106-1.0-00), which is a 3-D geochemical/geophysical-model transport code. TRACRN is documented in Travis and Birdsell (1989). Using the criterion for validation of visual judgment of goodness of fit to the analytical solution, TRACRN was validated against an analytic solution by Kelkar and Travis (1999). The numerical and analytical solutions agree within 0.5%. In rock-beaker experiments the geometry is known; therefore, the mesh is

validated by inspection, and transport is by diffusion only in saturated rock. Consequently, the results are independent of the hydrogeologic properties of the rock. Because the geometry of the rock beaker is complex, an analytical solution is not available for this system. The concentration profiles of the diffusing tracer are fitted to the transport equation (de Marsily 1986, Chapter 10):

$$\nabla \cdot (\varepsilon d \nabla C) = \varepsilon \frac{\partial C}{\partial t} + Q \quad , \qquad \text{(Eq. 16)}$$

where ε is the total porosity of the tuff, d is the diffusion coefficient through the tuff, C is the concentration of the diffusing tracer in solution, and the source term, Q, is zero for a nonreactive tracer but for a sorbing solute

$$Q = \rho_b \frac{\partial F}{\partial t} \quad , \qquad \text{(Eq. 17)}$$

where F is the amount of tracer sorbed per unit mass of solid and ρ_b is the bulk tuff density ($\rho_b = (1 - \varepsilon)\rho_s$, where ρ_s is the density of the solid particles).

As discussed in previous sections, the mechanism of sorption determines the relationship between F and C. When sorption is linear, reversible, and instantaneous, the relationship between F and C is given by the sorption distribution coefficient

$$K_d = \frac{F}{C} \quad . \qquad \text{(Eq. 18)}$$

Substitution of this equation and Equation 17 into Equation 16 yields

$$\nabla \cdot (\varepsilon d \nabla C) = \varepsilon R_f \frac{\partial C}{\partial t} \quad , \qquad \text{(Eq. 19)}$$

where, once again, the retardation factor, R_f, is given by

$$R_f = 1 + \frac{\rho_b}{\varepsilon} K_d \quad , \qquad \text{(Eq. 20)}$$

Equation 20 provides a means of comparing results for sorption coefficients obtained under diffusive conditions with sorption coefficients obtained from batch-sorption experiments and is valid only if sorption is linear, reversible, and instantaneous (the Langmuir and the Freundlich isotherms are examples of nonlinear relationships between F and C).

Consequently, the diffusion coefficient can be determined by fitting concentration profiles for the nonsorbing tracers, and sorption parameters, such as K_d, can be determined by fitting concentration profiles for the sorbing tracers.

6.6.1.3 Results and Discussion

Figure 27 shows an example of a set of diffusion data for a rock beaker experiment in which the feldspar-rich tuff sample G4-737 and solutions of tracers in J-13 water were used. The concentration of tracer, C, remaining in the solution inside the cavity of the rock-beaker divided by the initial concentration, C_o, is plotted as a function of elapsed time.

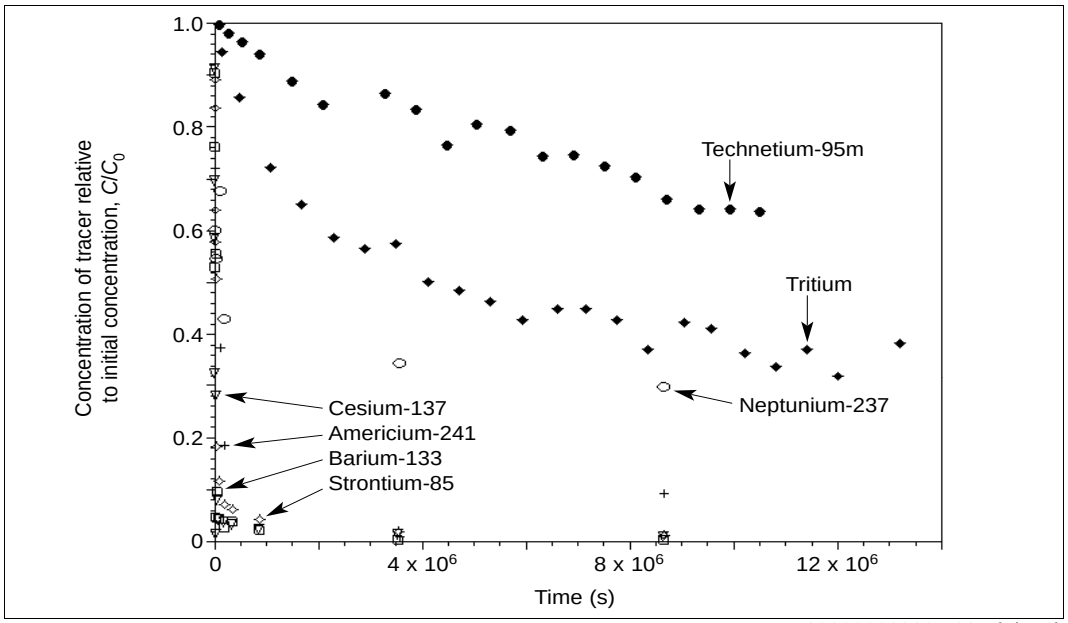

DTN: LA000000000034.001 (Fig. 2)

NOTE: These data for diffusion of tracers in J-13 water and in rock beakers made of tuff sample G4-737 show the concentration, C, of tracer (relative to the initial concentration, C_0) remaining in the beaker as a function of elapsed time.

Figure 27. Diffusion Data

The solid lines in Figure 28 are a fit of these same data to the diffusion equation (Equation 16) using the TRACRN V1.0 transport code for the two nonsorbing radionuclides, tritium and technetium-95m. The diffusion coefficients obtained in this manner for these radionuclides for all the tuff samples studied (Table 16) agree well with previous results (Rundberg et al. 1987, Table VI). These two tracers diffuse essentially as tritiated water and the pertechnetate anion, TcO_4^-. Large anions are excluded from tuff pores because of their size and charge, which can account for the lower diffusivity of TcO_4^-.

If sorption is linear, reversible, and instantaneous, then F/C is equal to a sorption coefficient, K_d. To test this assumption, values of K_d in batch-sorption experiments using the tuffs under study (Table 17) were determined. An expected diffusion curve was calculated using, for each tuff, the diffusion coefficient measured for tritiated water and the batch-sorption coefficient measured for each sorbing radionuclide. Figure 29 shows these calculated diffusion curves for devitrified tuff sample G4-737. Comparison of the calculated curves with the actual measured data (see the example in Figure 30) shows that the concentration of the sorbing radionuclides remaining in the rock beaker drops faster than predicted on the basis of a linear K_d. This result indicates that the diffusion of the sorbing radionuclides could not be fitted by assuming reversible, instantaneous, and linear sorption. These results also indicate that transport calculations using a batch-sorption K_d value and the diffusion coefficient measured for tritiated water will result in conservative predictions for the transport of sorbing radionuclides. Note that Cs appears to diffuse much faster than the tritium in tritiated water (Figure 30) because of the combined effects of diffusion and sorption of Cs, giving a conservative prediction (less apparent diffusion than observed) when using HTO diffusion and batch K_ds for Cs.

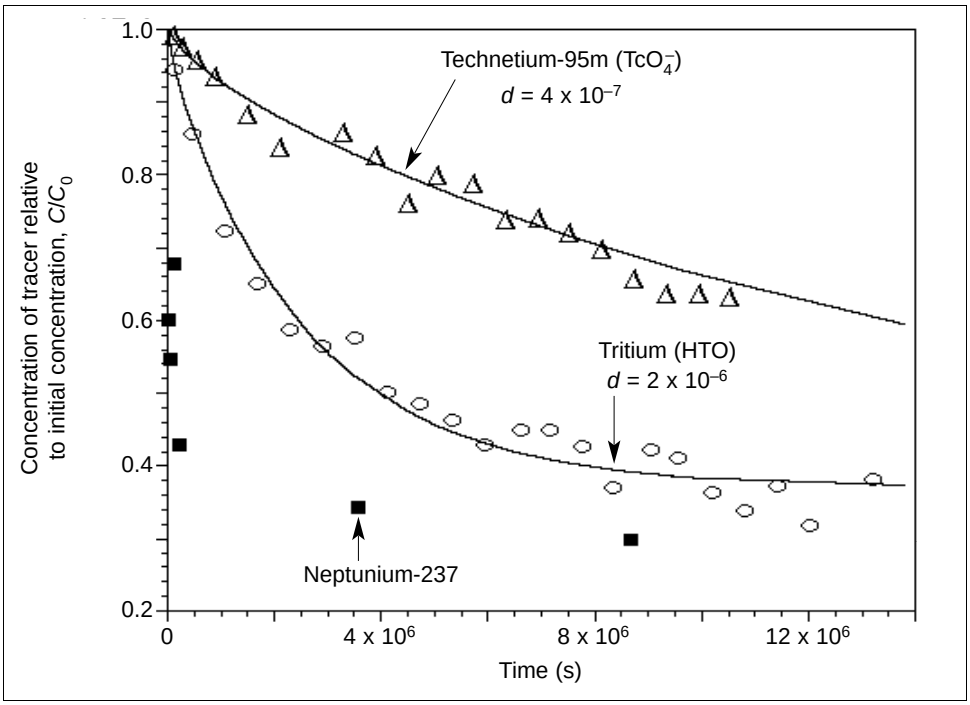

DTN: LA000000000034.001 (Fig. 3)

NOTE: The solid curves are fits to the diffusion data by the TRACRN V1.0 code for the nonsorbing tracers tritium and technetium in the rock-beaker experiments with tuff sample G4-737.

Figure 28. Diffusion Data Curve Fits

Table 16. Rock-Beaker Diffusion Results for Nonsorbing Radioisotopes and Devitrified Tuffs

Tuff sample	**Major minerals**	**Porosity**	**Diffusion coefficient, d (cm^2 s^{-1})**	
			HTO	**TcO_4^-**
G4-737	Alkali feldspar 68% Cristobalite 28%	0.07	2.2 x 10^{-6}	3.9 x 10^{-7}
GU3-304 #1	Alkali feldspar 75% Cristobalite 25%	0.06	1.5 x 10^{-6}	3.0 x 10^{-7}
GU3-304 #2			1.6 x 10^{-6}	3.0 x 10^{-7}
GU3-433	Alkali feldspar 76% Cristobalite 15%	0.10	3.5 x 10^{-6}	Not determined
GU3-1119	Alkali feldspar 70% Quartz 19%	0.10	2.0 x 10^{-6}	4.9 x 10^{-7}
Topopah outcrop	Alkali feldspar 59% Cristobalite 23% Quartz 12%	0.07	1.0 x 10^{-6}	1.0 x 10^{-7}

DTN: LA000000000034.002

Table 17. Batch-Sorption Coefficients for Devitrified Tuffs

Tuff sample	Major minerals	Sorption coefficient, K_d (mL g^{-1})				
		Np	Am	Cs	Sr	Ba
G4-737	Alkali feldspar 68% Cristobalite 28%	8	134	532	52	28
GU3-304	Alkali feldspar 75% Cristobalite 25%	8	no data	342	18	19
GU3-433	Alkali feldspar 76% Cristobalite 15%	9	154	1264	20	61
GU3-1119	Alkali feldspar 70% Quartz 19%	8	136	494	42	27
Topopah outcrop	Alkali feldspar 59% Cristobalite 23% Quartz 12%	9	no data	465	20	25

DTN: LA000000000034.001 (Table 2)

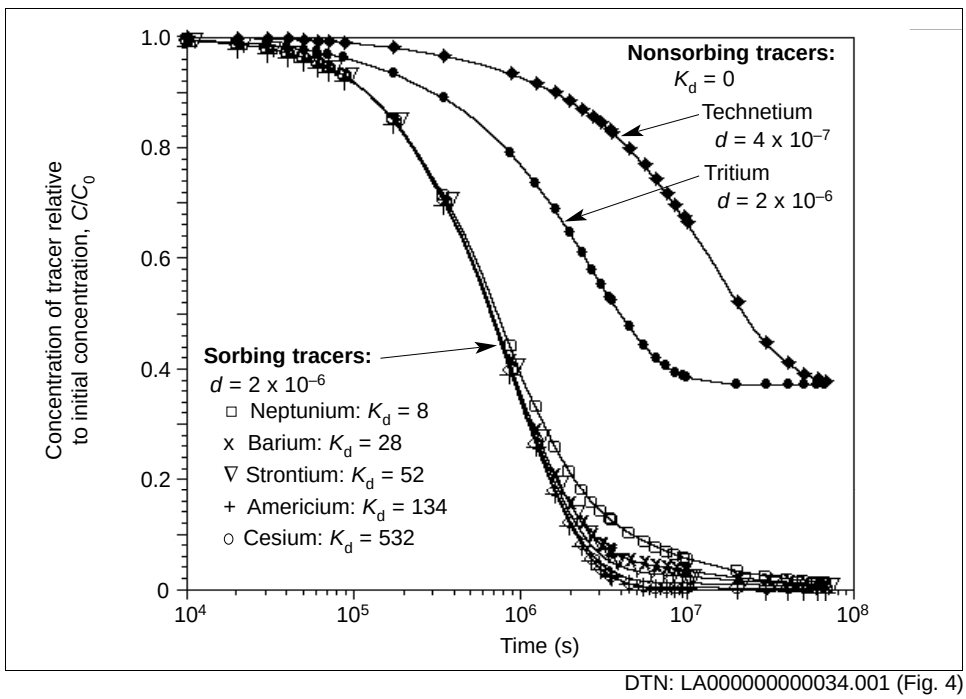

DTN: LA000000000034.001 (Fig. 4)

NOTE: These curves were calculated for tuff sample G4-737 using the diffusion coefficient, *d*, measured for tritiated water and the batch-sorption coefficients, K_d, measured for the sorbing radionuclides (Table 17). Diffusion curves for tritium and technetium are also shown.

Figure 29. Calculated Diffusion Curves

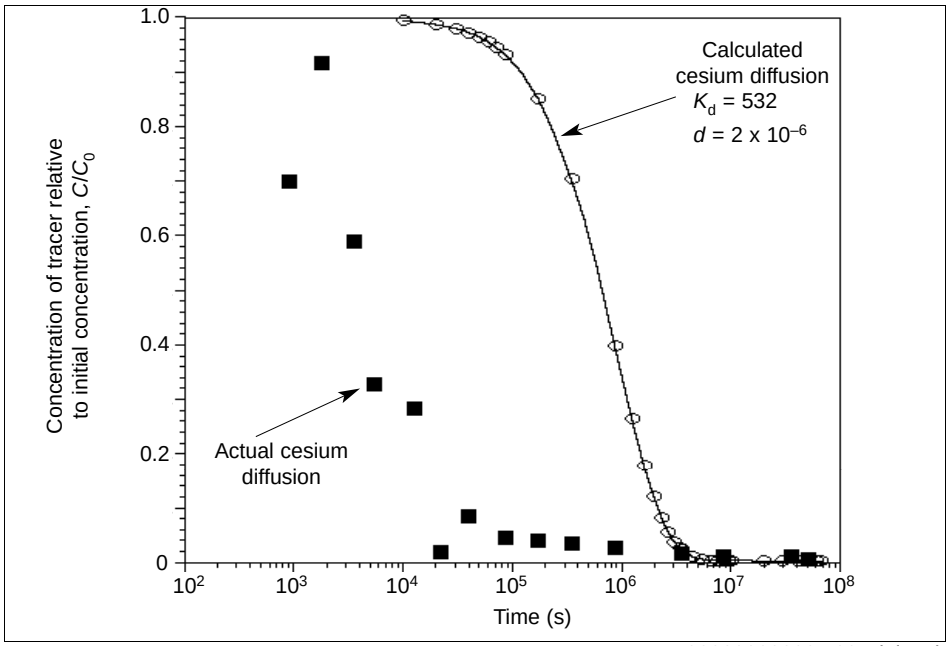

DTN: LA000000000034.001 (Fig. 5)

NOTE: The solid curve is the diffusion curve calculated for cesium using a K_d value and the diffusion coefficient for tritium (Figure 29); the squares are the actual diffusion data for cesium with tuff sample G4-737 (Figure 27).

Figure 30. Comparison of Calculated and Actual Diffusion Data

The results obtained from rock-beaker experiments agree with previous results (Rundberg 1987, Tables VI, VII). Experiments were performed on the uptake of sorbing radionuclides by tuff and it was found that rate constants for uptake of the sorbing cations from solution onto tuff were consistent with a diffusion-limited model in which diffusion occurs in two stages. In the first stage, the cations diffuse into rock through water-filled pores; in the second stage, they diffuse into narrower intracrystalline channels. This diffusion model yielded sorption coefficients for cesium, strontium, and barium, and these values agree well with the sorption coefficients determined by batch techniques (Rundberg 1987, Table VII).

6.6.2 Diffusion-Cell Experiments

Another experimental technique for deriving the diffusion coefficient is through the use of a diffusion cell, in which two chambers containing groundwater are separated by a slab of tuff. Radioactive tracers are added to one chamber, and the other (untraced) chamber is periodically sampled for the presence of radioactivity. The only driving force in this experimental setup is the chemical concentration gradient; thus, the solute flux is purely diffusive. The apparent time of arrival depends on the porosity, the heterogeneity of the pore structure, the retardation factor for a given radionuclide, and the sensitivity of radionuclide measurements. The rate of concentration increase in the untraced chamber depends on the ionic diffusivity, the tuff porosity, and the tuff tortuosity/constrictivity factor. Thus, by measuring the movement of sorbing and nonsorbing tracers through tuff slabs as a function of time, the rock-dependent diffusion parameters can be measured.

This technique was applied to the determination of diffusion coefficients for ^{3}H, ^{95m}Tc, natural U(VI), $^{237}Np(V)$, and $^{239}Pu(V)$ in devitrified and zeolitic tuff.

6.6.2.1 Experimental Procedures and Data Analysis

The dimensions of the diffusion cells used are given in Table 18.

Table 18. Dimensions of Diffusion Cells

Diameter of tuff slab	6 cm
Length of tuff slab	1 cm
Volume of traced chamber	750 cm^3
Volume of untraced chamber	80 cm^3

Source: Weaver et al. (1996), Attachment I, p. 1—Reference only

The two major rock types used for the diffusion-cell experiments were zeolitic tuff (sample 1362) and devitrified tuff (sample G4-287). The zeolitic tuff has a porosity of 0.4 and a bulk density of 1.5 g mL^{-1}. The devitrified tuff has a porosity of 0.2 and a bulk density of 2.3 g mL^{-1}. The major component of the zeolitic tuff is clinoptilolite; the major component of the devitrified tuff is alkali feldspar.

The solutions used for these experiments were prepared by taking an aliquot of a ^{3}H, ^{95m}Tc, natural U(VI), $^{237}Np(V)$, or $^{239}Pu(V)$ acidic stock and diluting it in the water being studied. The actinide concentration of the solutions used for the diffusion experiments was very close to the solubility limit of the actinides in the groundwaters. At 25ºC and for nominal pH values between 6 and 8.5, the experimentally determined solubilities of plutonium range from 2 x 10^{-7} M (J-13 water at a pH of 7) to 1 x 10^{-6} M (p#1 water at a pH of 8.5) and of neptunium range from 7 x 10^{-6} M (p#1 water at a pH of 8.5) to 5 x 10^{-3} M (J-13 water at a pH of 6) (Nitsche et al. 1993, Figures 1 and 15; Nitsche et al. 1995, Figures 1 and 9).

The experimental setup for the diffusion cells can be described by a 1-D diffusion model. Thus, Equation 19 (on rock-beaker experiments) can be rewritten as (Bradbury et al. 1986):

$$D_e \frac{\partial^2 C}{\partial x^2} = \alpha \frac{\partial C}{\partial t} \quad , \qquad \text{(Eq. 21)}$$

where x is the axis along the direction of tracer diffusion, D_e is the effective diffusivity (= εd), and α is the rock-capacity factor (= εR_f). This equation yields an analytic solution to diffusion through a slab.

Bradbury et al. (1986) solved Equation 21 for a porous rock. For the experimental setup, the boundary conditions can be taken to be:

- At $x = 0$, a constant source concentration, C_o, is maintained

- At $x = L$, where L is the tuff-slab thickness, the concentration measured at the initially untraced cell, C_t, is much smaller than the source concentration ($C_t << C_o$).

For these conditions, the total quantity, Q_t, diffused through a tuff slab of area A after a time t is given by the equation

$$\frac{Q_t}{ALC_o} = \frac{D_e t}{L^2} - \frac{\alpha}{6} - \frac{2\alpha}{\pi^2}\sum_{n=1}^{\infty}\frac{(-1)^n}{n^2}e^{-\left(\frac{D_e n^2 \pi^2 t}{L^2 \alpha}\right)} \quad . \qquad \text{(Eq. 22)}$$

As $t \rightarrow \infty$, the asymptotic solution becomes

$$Q_t = \frac{AC_o D_e}{L}t - \frac{AC_o L\alpha}{6} \quad . \qquad \text{(Eq. 23)}$$

Consequently, a plot of Q_t versus t yields the effective diffusivity, D_e, from the slope and the rock-capacity factor, α, from the intercept on the time axis of the extrapolated linear region. For a nonsorbing species, $K_d = 0$, $R_f = 1$, and $\alpha = \varepsilon$; for a sorbing species, K_d may be calculated from the value of α.

The diffusion coefficient, d, can be calculated from the effective diffusivity ($D_e = \varepsilon d$). The difference between the diffusion coefficient, d_s, for a tracer diffusing in the solution phase and the diffusion coefficient, d, for a tracer passing through tuff pores is given by (Neretnieks 1990, p. 23)

$$d = \frac{\delta}{\tau^2} d_s \ , \qquad \text{(Eq. 24)}$$

where δ is the constrictivity and τ is the tortuosity of the tuff pore structure.

6.6.2.2 Results and Discussion

The diffusion of ^{3}H, ^{95m}Tc, natural U(VI), ^{237}Np(V), and ^{239}Pu(V) through devitrified and zeolitic tuffs was studied using water from Well J-13 and synthetic p#1 water. The radionuclides ^{3}H, natural U(VI), and ^{239}Pu(V) were studied together in four diffusion cells (devitrified and vitric tuff cells, each with both types of water). Likewise, the radionuclides ^{95m}Tc and ^{237}Np(V) were studied together in another four diffusion cells. Typical results for these experiments are shown in Figures 31 to 33.

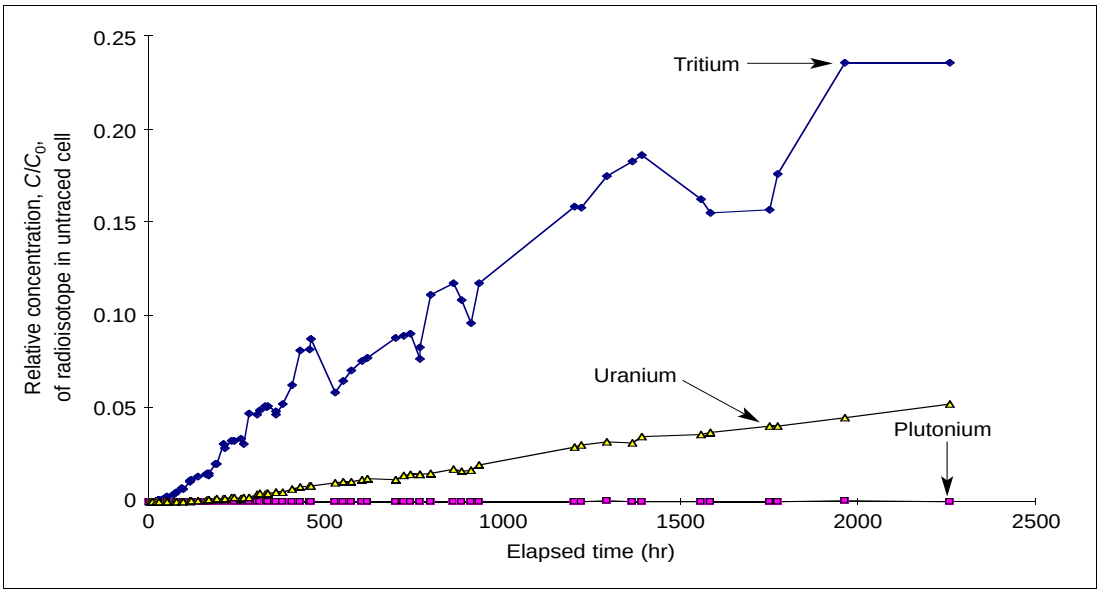

DTN: LAIT831362AQ95.001 (SEP Table S99010.001)

NOTE: The data show the concentration in synthetic p#1 water of ^{3}H, $^{239}Pu(V)$, and natural U(VI) (relative to the concentration in the traced cell, C/C_0) diffusing through devitrified tuff sample G4-287 into the untraced cell as a function of time.

Figure 31. Tritium, Plutonium, and Uranium Diffusion through Devitrified Tuff

The results indicate that the diffusion of nonsorbing radionuclides into saturated tuff (illustrated by the diffusion of tritiated water in Figures 31 to 33) is slower in devitrified tuffs than in zeolitic tuffs, probably because of the greater porosity of the zeolitic tuffs. Large anions such as pertechnetate (which are excluded from the tuff pores by size and charge) diffuse slower through the pores than tritium regardless of the groundwater or tuff type (as also observed in the rock-beaker experiments, Figure 29). The migration of plutonium through tuff under diffusive conditions is dominated by sorption (as shown by Figures 31 to 33). The migration of Np(V) and U(VI) through tuff depends on tuff type and water chemistry. In cases for which the reported sorption of neptunium is essentially zero, such as for devitrified tuff samples (Triay, Cotter, Kraus et al. 1996, pp. 14, 18; Triay, Cotter, Huddleston et al. 1996, pp. 32–36), the diffusion of neptunium through the tuff is slower than the diffusion of tritium but comparable to the diffusion of a nonsorbing, large anion, such as pertechnetate (Figure 32).

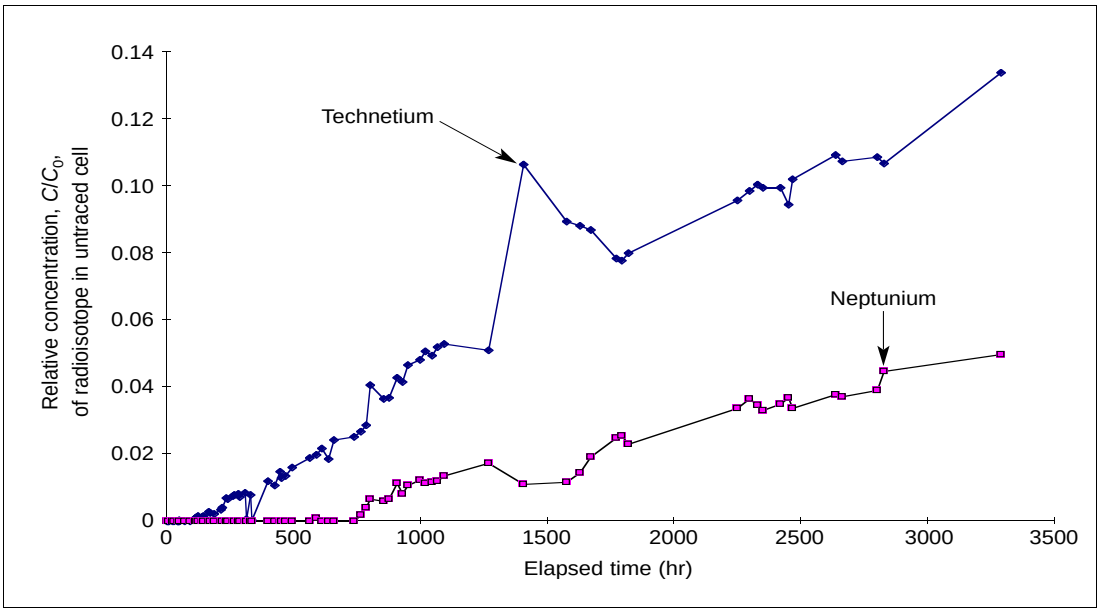

DTN: LAIT831362AQ95.001 (SEP Table S99010.002)

NOTE: The data show the concentration in synthetic p#1 water of ^{95m}Tc and ^{237}Np (relative to the concentration in the traced cell, C/C_0) diffusing through devitrified tuff sample G4-287 into the untraced cell as a function of time.

Figure 32. Technetium and Neptunium Diffusion through Devitrified Tuff

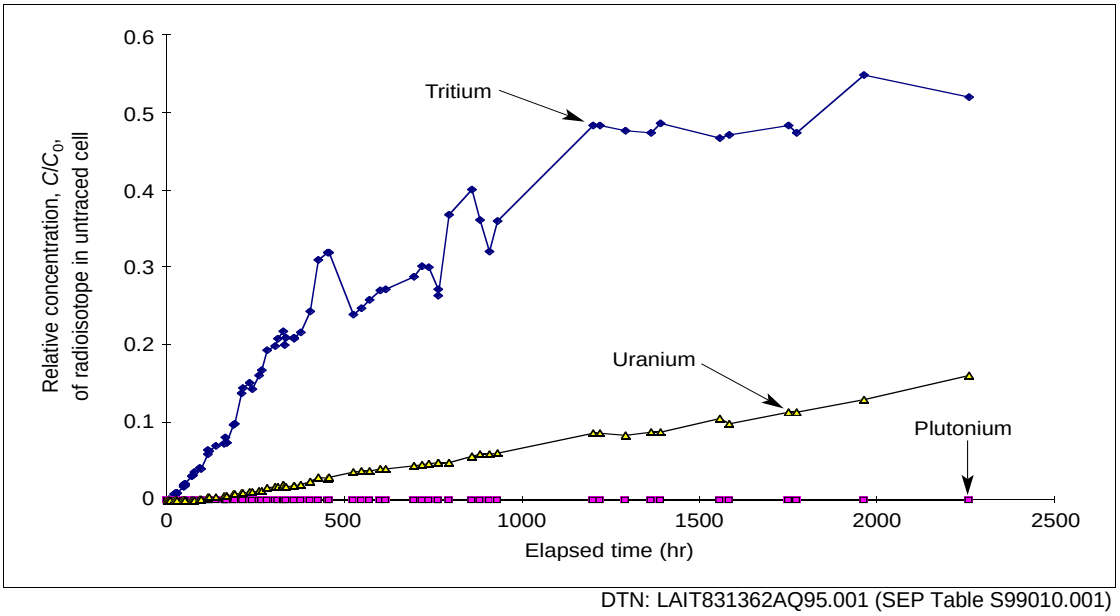

DTN: LAIT831362AQ95.001 (SEP Table S99010.001)

NOTE: The data show the concentration in synthetic p#1 water of ^{3}H, ^{239}Pu(V), and natural U(VI) (relative to the concentration in the traced cell, C/C_0) diffusing through zeolitic tuff sample #1362 into the untraced cell as a function of time.

Figure 33. Tritium, Plutonium, and Uranium Diffusion through Zeolitic Tuff

6.6.3 Distribution Parameters for Matrix Diffusion Coefficients

The following distribution parameters for matrix diffusion coefficients (DTN: LA0003JC831362.001) were developed based on a qualitative analysis of the data from reviews of the literature and results described above in section 6.6.1.3, Table 16 and Figures 29 and 30. For anions, the average matrix diffusion coefficient is 3.2×10^{-11} m^2 s^{-1} (3.2×10^{-7} cm^2 s^{-1}) with a standard deviation of 1×10^{-11} m^2 s^{-1}, a minimum value of zero and a maximum value of 10^{-9} m^2 s^{-1} (10^{-5} cm^2 s^{-1}) with a Beta distribution. For cations, the average matrix diffusion coefficient is 1.6×10^{-10} m^2 s^{-1} (1.6×10^{-6} cm^2 s^{-1}) with a standard deviation of 0.5×10^{-10} m^2 s^{-1}, a minimum value of zero and a maximum value of 10^{-9} m^2 s^{-1} (10^{-5} cm^2 s^{-1}) with a Beta distribution.

6.7 COLLOID-FACILITATED RADIONUCLIDE TRANSPORT

The potential role of colloids in the transport of radionuclides through the subsurface at Yucca Mountain was reviewed by Triay et al. (1997, Chapter V, Section D). These authors pointed out that radioactive-waste-derived colloids include the following three types:

- Degradation colloids generated directly from the waste form by disaggregation or spalling of actinide solid phases

- Precipitation colloids generated from solutions supersaturated with respect to actinide solid phases, including real actinide colloids produced by the agglomeration of hydrolyzed actinide ions, traditionally referred to as radiocolloids

- Pseudocolloids generated by the attachment of radionuclides (in soluble or colloidal form) to other colloids, such as naturally occurring groundwater colloids consisting of inorganic or organic constituents or microorganisms.

Triay et al. (1997, Chapter V, Section D) concluded that existing data in the literature suggest that colloidal species can enhance radionuclide transport in the unsaturated and saturated zones but that existing information was inadequate to assess the significance of this transport mechanism for Yucca Mountain. The present section summarizes the available data that are relevant to Yucca Mountain, including colloid types and concentrations, percent sorbed onto various substrates, and attachment/detachment rates for radionuclides interacting with various substrates.

6.7.1 Review of Geochemical Controls on Colloid Stability

Colloid concentrations in groundwater are a function of the colloid phase stability in the hydrochemical system. Key factors that affect colloid stability are pH, redox potential, salt (Na, Ca) concentrations, the presence of dissolved organics, and the extent to which the system exists at steady state with respect to chemistry and flow (Degueldre, Grauer et al. 1996; Degueldre, Pfeiffer et al. 1996; O'Melia and Tiller 1993). For an aquifer in a steady-state situation, decreases of the concentration of alkali elements (Na, K) below 10^{-2} M and of alkali-earth elements (Ca, Mg) below 10^{-4} M contribute to an increase in the colloid stability and concentration (Degueldre, Grauer et al. 1996; Degueldre, Pfeiffer et al. 1996). Mixing of waters

of different compositions and large concentrations of organic carbon also contribute to an increase in colloid stability and concentration. The presence of transient situations, such as changes of temperature, flow rate, or chemistry (pH, salt, or redox potential) in the aquifer induces larger colloid concentrations. Conversely, high ionic strength waters, low organic carbon concentrations, and stable conditions reduce the potential for colloid stability.

6.7.2 Colloid Concentrations at Yucca Mountain

Colloid concentration measurements for groundwaters collected in the vicinity of the Yucca Mountain site showed that the concentration of colloids in the 50 nm to 200 nm size range ranged between 1 x 10^6 (J-13) and 2 x 10^9 particles mL^{-1} (UE-25 WT#17) (DTN: LA0002SK831352.001, LA0002SK831352.002, LA9910SK831341.005), which is high enough to cause concern about colloid-facilitated radionuclide migration in any groundwater at Yucca Mountain.

6.7.3 Review of Sorption Behavior of Radionuclides on Colloids

The degree of reversibility of radionuclide sorption onto colloids has dramatic implications for colloid-facilitated radionuclide migration. Previous results have shown that the transport rate of a given radionuclide is not significantly affected if its sorption onto colloids is fully reversible (Noell et al. 1998). If the sorption reaction is irreversible, then the retardation properties of the radionuclide are determined in part by the stability of the colloid.

Studies of sorption rates of Pu and Am onto colloids of iron oxide, clays, and silica in groundwater show that colloidal Pu(IV), as well as soluble Pu(V), is rapidly sorbed by colloids of hematite, goethite, montmorillonite, and silica in both natural and synthetic J-13 and p#1 groundwaters (DTN: LAIT831341AQ97.002, SEP Table S97458.002). For example, after a 10-minute contact period, hematite sorbed about 57 percent to 66 percent of Pu(IV) colloids and 44 percent to 82 percent of soluble Pu(V), whereas goethite sorbed 29 percent to 34 percent of Pu(IV) colloid and 19 percent to 63 percent of Pu(V) (DTN: LAIT831341AQ97.002, SEP Table S97458.003). In contrast, desorption rates for Pu(IV) and Pu(V) are slow and insignificant on a laboratory timescale. After 30 days of desorption, Pu(V) was not desorbed from hematite, and less than 0.01 percent of Pu(V) desorbed from goethite (DTN: LA0003NL831352.002). Less than 0.01 percent of Pu(IV) colloids was desorbed from hematite, and less than 0.1 percent of Pu(IV) was desorbed from goethite.

Adsorption of ^{243}Am by hematite colloids was faster and higher than by montmorillonite and silica colloids (DTN: LA0005NL831352.001). Maximum sorption of ^{243}Am occurred at 1 hour for hematite, 48 hours for silica, and 96 hours for montmorillonite. After these time periods, partial desorption of ^{243}Am from colloids occurred. With the maximum sorption, K_d values for ^{243}Am were on the order of 10^4 mL g^{-1} for silica and 10^5 mL g^{-1} for hematite and montmorillonite.

These findings suggest that these types of inorganic colloids may facilitate transport of ^{239}Pu and, possibly, ^{243}Am along potential flowpaths. Uncertainties in the data summarized in this section do not significantly affect these generalizations because the degree to which colloid-facilitated

radionuclide transport is affected by hydrochemical conditions, colloid stability, and reversibility of sorption, has not been quantified and the available data can only be used to indicate expected trends. Measured desorption rates were so low as to not be quantifiable over the experimental period. However, even a low but finite desorption rate over thousands of years could decrease colloid-facilitated radionuclide transport to insignificant levels even though the colloids themselves may be transported. The development of a colloid transport model to test this conclusion is documented in CRWMS M&O 2000b.

6.8 BUSTED BUTTE UNSATURATED ZONE TRANSPORT TEST

FEHM V2.00 (STN: 10031-2.00-00) and STO-UNSAT V1.0 (STN: 10292-1.0LV-00) are used for the numerical analyses in Section 6.8 of this AMR. The model describes a meso-scale (approximately 12m x 12m x 12m) experiment in the Calico Hills and Topopah Spring units at Busted Butte. The FEHM models are deterministic two- or three-dimensional models of two of the phases of the Unsaturated Zone Transport Test (UZTT) (Phase 1A and Phase 2). Phase 1B has not been modeled for this report. The STO-UNSAT model is a two-dimensional stochastic flow representation of the UZTT Phase 1A. The simulations here represent the best knowledge at the time for the stratigraphy and hydrogeologic parameters at the site. The model description is detailed in Sections 6.8.6 and 6.8.7.

Visual inspection of model outputs presented in Sections 6.8.6 and 6.8.7 (and comparison with the transport behavior expected for sorbing and nonsorbing tracers) confirms that the models used in Section 6 of this AMR are appropriate for their intended use. This inspection also confirms that the input data, including material properties and K_d values, are appropriate for their intended use.

6.8.1 Overview

6.8.1.1 Unsaturated Zone Transport Test Location

The Busted Butte test facility is located in Area 25 of the Nevada Test Site (NTS) approximately 160 km northwest of Las Vegas, Nevada, and 8 km southeast of the potential Yucca Mountain repository area. The site was chosen based on the presence of a readily accessible exposure of the Topopah Spring Tuff and the Calico Hills Formation and the similarity of these units to those beneath the potential repository horizon. The test facility consists of an underground excavation along a geologic contact between the Topopah Spring Tuff (Tpt) and the Calico Hills Formation (Tac). This facility also provides access to the contact between the Topopah Spring welded (TSw) hydrogeologic unit and the Calico Hills nonwelded (CHn) hydrogeologic unit (which is comprised of the nonwelded portion of the basal vitrophyre (Tptpv1) of the Topopah Spring Tuff and the Calico Hills Formation). Details of the test configuration are given in Section 6.8.2.

6.8.1.2 Unsaturated Zone Transport Test Concept

The test block was located at Busted Butte where the exposure of Calico Hills rocks represents a distal extension of the formation located immediately beneath the potential repository horizon. Because of its location, the UZTT experimental blocks are in the vitric Calico Hills. This location means that the site is not an analog site but, to the best of our knowledge, represents both the vitric Calico Hills Formation and the Topopah Spring Tuff units as they exist beneath the potential repository horizon west of the Ghost Dance fault.

The UZTT is comprised of three integrated efforts: the field test, a parallel laboratory-scale testing program, and validation and assessment of models used for PA. The field test involves design of the test, analysis of the geology, identification of tracer breakthrough using geochemical analyses, in-situ imaging of liquid and tracer migration through geophysical techniques, and ultimately, destructive testing to identify tracer migration.

The UZTT was designed for two test phases. The first phase, including test Phases 1A and 1B, was designed as a scoping study to assist in design and analysis of Phase 2. The second phase is the mesoscale study, which incorporates a larger region than Phase 1 with a broader, more complex scope of tracer injection, monitoring, and collection.

In addition to field testing, parallel laboratory analytical and testing programs in geochemistry, tracer evaluation, hydrology, and mineralogy are designed to help interpret the field results. The geochemistry program includes measurement of in-situ pore-water chemistry and development of a synthetic injection matrix. The tracer evaluation program includes batch-sorption studies on Busted Butte samples using Phase-1 and Phase-2 conservative and reactive analog and radioactive tracers. The lab program also includes modeling of the geochemical behavior of those tracers in the ambient water chemistry. The hydrology program involves the measurement of the matric potentials and conductivities as a function of saturation for core samples from Busted Butte. The porosity of each sample is also characterized. The mineralogy/petrology (Min/Pet) activities involve the mineralogic characterization of the Busted Butte samples from cores taken from Phases 1 and 2. When possible, splits from the core samples are used in all three characterization programs.

Because the principal objective of the test is to evaluate the validity of the flow and transport site-scale process models used in PA abstractions, a flow and transport modeling program has also been implemented. This effort will allow us to update the site-scale flow and transport model by simulating and predicting experimental field results and by addressing the effects of scaling from laboratory to field scales. Initial predictions of the field tests are included in Sections 6.8.6 and 6.8.7.

6.8.1.3 Unsaturated Zone Transport Test Project Objectives

The principal objectives of the test are to address uncertainties associated with flow and transport in the UZ site-process models for Yucca Mountain. These include but are not restricted to the following.

- The effect of heterogeneities on flow and transport in unsaturated and partially saturated conditions in the Calico Hills Formation. In particular, the test aims to address issues relevant to fracture/matrix interactions and permeability contrast boundaries.

- The migration behavior of colloids in fractured and unfractured Calico Hills rocks.

- The validation through field testing of laboratory sorption experiments in unsaturated Calico Hills rocks.

- The evaluation of the 3-D site-scale flow and transport process model (i.e., equivalent-continuum/dual-permeability/discrete-fracture-fault representations of flow and transport) used in the PA abstractions for LA.

- The effect of scaling from lab scale to field scale and site scale.

The discussion in Section 6.8 presents relevant data and background on all aspects of the UZTT, which is a complex medium-scale coupled field/laboratory/analyses test. Section 6.8.2 presents an overview of the design of the test. Section 6.8.3 covers geology and geologic/ hydrogeological properties of the units existing in the UZTT test blocks, and Section 6.8.4 presents the geophysical effort. Geochemistry is discussed in Section 6.8.5. Section 6.8.6 gives details of the Phase-1 computational modeling, and 6.8.7 covers computational modeling of Phase 2. Model validation is discussed in Section 6.8.8. In Section 6.8.9 the UZ transport testing results at Busted Butte are discussed in view of their importance to PA needs to build confidence in and reduce the uncertainty of site-scale flow and transport models and their abstractions for performance.

6.8.2. Test Design

The UZTT is comprised of the main drift tunnel, which is 75 m in length, and a test alcove, which is 19 m in length. The configuration of the UZTT site is shown in Figure 34.

6.8.2.1 Site Description

Design, construction, and scientific teams were all involved in insuring that the test block itself remained undisturbed by construction activities. Minimal disturbance of the in-situ test block in the initial stages of unsaturated tracer transport testing was the foremost objective. Shotcrete and sodium silicate glass applications to the tunnel walls were coordinated so as to optimize safety concerns and testing requirements. Details of the design and construction criteria can be found elsewhere (Sub Terra, Inc. 1998, pp. 9–21, 33–44).

The site characterization of the potential test block involved the mapping of the main drift wall, core sampling for min/pet, and recovery of samples from outcrops. These samples were used for the initial laboratory characterization studies of hydrologic properties and mineralogy. The geological context and lithological descriptions of core samples from the test site were used to provide further information on the geometry of the beds at the site to guide the construction of the tunnel.

Samples were collected from the dry drilling of the boreholes from the main drift and the test adit to provide core samples for geologic, hydrologic, and geochemical laboratory investigations and scoping calculations. The boreholes were then surveyed and instrumented for the injection tests. Laboratory measurements of hydrologic, mineralogic, and tracer sorption and matrix diffusion properties of the core samples collected once the tunnel was excavated are now providing important information for predictive modeling studies.

6.8.2.2 Experimental Design: Test Phases

6.8.2.2.1 Test Phase 1

Phase 1 represents a simple test program that serves both as a precursor or scoping phase to Phase 2 and as a short-term experiment aimed at providing initial transport data for early fiscal year 1999 model updates. Phase 1 involves six single-point injection boreholes and two inverted-membrane collection boreholes. All Phase-1 boreholes are 2 m in length and 10 cm in diameter. A mixture of conservative tracers (bromide, fluorescein, pyridone, and fluorinated

benzoic acids (FBAs)), a reactive tracer (lithium), and fluorescent polystyrene microspheres are being used to track flow, reactive transport, and colloid migration, respectively.

Phase 1A, located in the nonwelded Calico Hills (CHn) hydrogeologic unit spanning both the geologic Calico Hills Formation (Tac) and the nonwelded subzone of the lowermost Topopah Spring Tuff (Tptpv1), is a noninstrumented or "blind" test consisting of four single-point injection boreholes. Continuous injection started on April 2, 1998. Injection rates varied from 1 mL hr^{-1} (boreholes 2 and 4) to 10 mL hr^{-1} (boreholes 1 and 3). The field test was completed through excavation by "mini-mineback" and auger sampling in March/April, 1999. Test predictions are included in this report. Initial model predictions associated with Phase 1A (presented in Section 6.8.6) were done "blind" and are meant to test our ability to predict the flow and transport results given present YMP databases and modeling capabilities.

Phase 1B involved both injection and collection membranes. Injection started on May 12, 1998, in the lower section of the Topopah Spring Tuff (Tptpv2), and ended November 18, 1998. Phase 1B involved two injection rates, 1 mL hr^{-1} in borehole 7 and 10 mL hr^{-1} in borehole 5. Because of the paucity of data on fracture/matrix interactions in these lithologies, this test serves as a "calibration" test for fracture/matrix interactions to be used in Phase-2 conceptual models. Geochemical analysis results of Phase 1B are presented and discussed in Section 6.8.5.

6.8.2.2.2 Test Phase 2

Phase-2 testing involves a large 7-m high, 10-m wide, and 10-m deep block comprising all the lithologies of Phase 1 (Figure 34). Unlike the single-point injection geometries in Phase 1, the injection systems in Phase 2 are designed to activate large surfaces of the block. Due to the short time frame available for testing, both upper and lower injection planes are used for testing in Phase 2. The injection points for this phase are distributed in two horizontal, parallel planes arranged to test the properties of the lower Topopah Spring Tuff (Tptpv2) and the hydrologic Calico Hills (Tptpv1 and Tac). There are 4 upper injection holes and 4 lower injection holes. Note that six upper injection holes were originally drilled, but two were accidentally grouted in and so were not used in the test. Phase-2 mixed-tracer solutions include those used in Phase 1 plus three additional fluorinated benzoic acids (FBAs), a mixture of new reactive tracers (Ni^{2+}, Co^{2+}, Mn^{2+}, Sm^{3+}, Ce^{3+}, and Rhodamine WT), and starting in August 1999, an additional conservative tracer (I^-).

Phase 2 is subdivided into three subphases (2A, 2B, and 2C) according to location and the injection rates used. Phase 2A consists of a single borehole in the upper injection plane instrumented with 10 injection points and 10 moisture sensors, one at each injection point. The injection rate is 1 mL hr^{-1} per injection point, which corresponds to an overall infiltration rate of 30 mm yr^{-1} (Bussod 1998). This borehole is restricted to the Tptpv2 lithology, which consists of fractured, moderately welded tuff from the basal vitrophyre. Phase-2A injection began on July 23, 1998, and is ongoing. A completion date is not fixed but is anticipated around October, 2000. Results from the ongoing test will be reported as available in further report revisions.

Phase 2B consists of four injection boreholes in the lower injection plane, each instrumented with 10 injection points and 10 moisture sensors, one at each injection point. The injection rate is 10 mL hr^{-1} per injection point, which corresponds to an overall infiltration rate of 380 mm yr^{-1}

(Bussod 1998). This injection plane is restricted to the Calico Hills Formation (Tac) and is meant to activate the lower section of the test block simultaneously with the upper section (Phases 2A and 2C). Phase-2B injection began on July 30, 1998, and is ongoing.

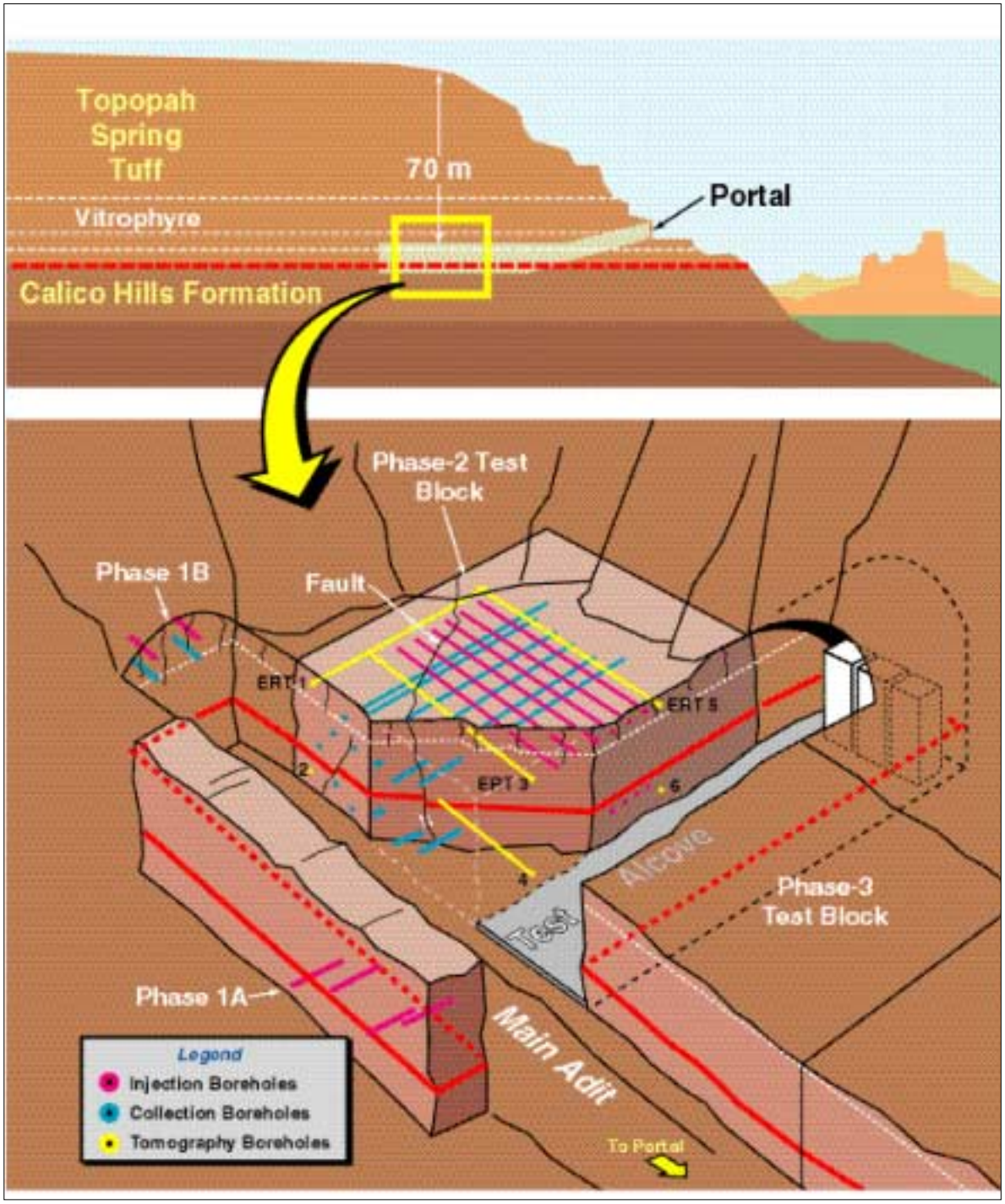

N/A – For illustration purposes only

NOTE: This schematic of the Busted Butte UZTT shows the relative locations of the different experiment phases and borehole locations.

Figure 34. Busted Butte Unsaturated Zone Transport Test

Phase 2C consists of three upper injection boreholes, each instrumented with 9 injection points and 12 moisture sensors, one at each injection point and two additional sensors located toward the borehole collar to detect tracer movement towards the front of the borehole. The injection rate is 50 mL hr^{-1} per injection point, which corresponds to an overall infiltration rate of 1550 mm yr^{-1} (Bussod 1998). As in Phase 2A, this injection system is restricted to a horizontal plane in the Tptpv2 lithology. Phase-2C injection was initiated on August 5, 1998, and is ongoing.

A geochemistry-based discussion of the current status of Phase 2 is included in Section 6.8.5.

Natural infiltration rates at Yucca Mountain vary between 0.01 and 250 mm yr^{-1} with an average of 5 mm yr^{-1} (Flint et al. 1996). Phase 2A falls within the range of natural present-day infiltration rates at Yucca Mountain, whereas Phase 2B lies at the high end of predicted values for a pluvial climate scenario. Phase-2C infiltration rates are artificially higher than expected natural infiltration rates for the region but provide for the best testing conditions given the short duration of the experiment. Further, these high injection rates may provide insight into system behavior during unnaturally high flow potentially caused by repository heating. Model simulations indicate that even at these high injection rates, the system is expected to remain unsaturated.

The upper injection plane consists of fractured Topopah Spring Tuff Tptpv2. As in Phase 1B, this unit represents the base of the TSw basal vitrophyre and is characterized by subvertical fractured surfaces representing columnar joints. Thirty-seven injection points distributed along 4 injection holes (Phase 2A and 2C) approximately 8 m deep each are used for tracer injection along a horizontal surface. The natural fracture pattern present in this unit serves as the conduit for tracer migration into the non-welded Calico Hills. The lower horizontal injection plane is located in the Calico Hills Formation (Tac). There are 40 injection points distributed in 4 horizontal and parallel boreholes. This test (Phase 2B) is meant to activate the lower part of the block in the event that the top injection system does not activate the entire block in the short duration of the testing program (2 years maximum).

Whereas all injection boreholes are located in the Test Alcove, the 12 collection boreholes associated with Phase 2 are located in the Main Adit. These boreholes are 8.5 to10.0 m in length, and each contains 15 to 20 collection pads evenly distributed on inverted membranes. Because of the complexity of the flow fields expected in this block, two techniques [i.e., electrical resistance tomography (ERT) and ground-penetrating radar tomography (GPR-T)] are used to image the 2- and 3-D saturation state of the block in monthly to bimonthly intervals.

6.8.2.3 Borehole Injection And Sampling Systems

Injection and sampling of the liquid tracers was accomplished by two pneumatically inflated borehole sealing and measurement systems (Figure 35). To allow visual inspection of the injection points under both standard and ultraviolet (UV) illumination, a transparent packer system was developed for the tracer-injection systems (Figure 36). Moisture sensing and sampling were accomplished using pneumatically emplaced inverting membranes. To accomplish moisture sampling in the collection boreholes, inverting membranes were fabricated

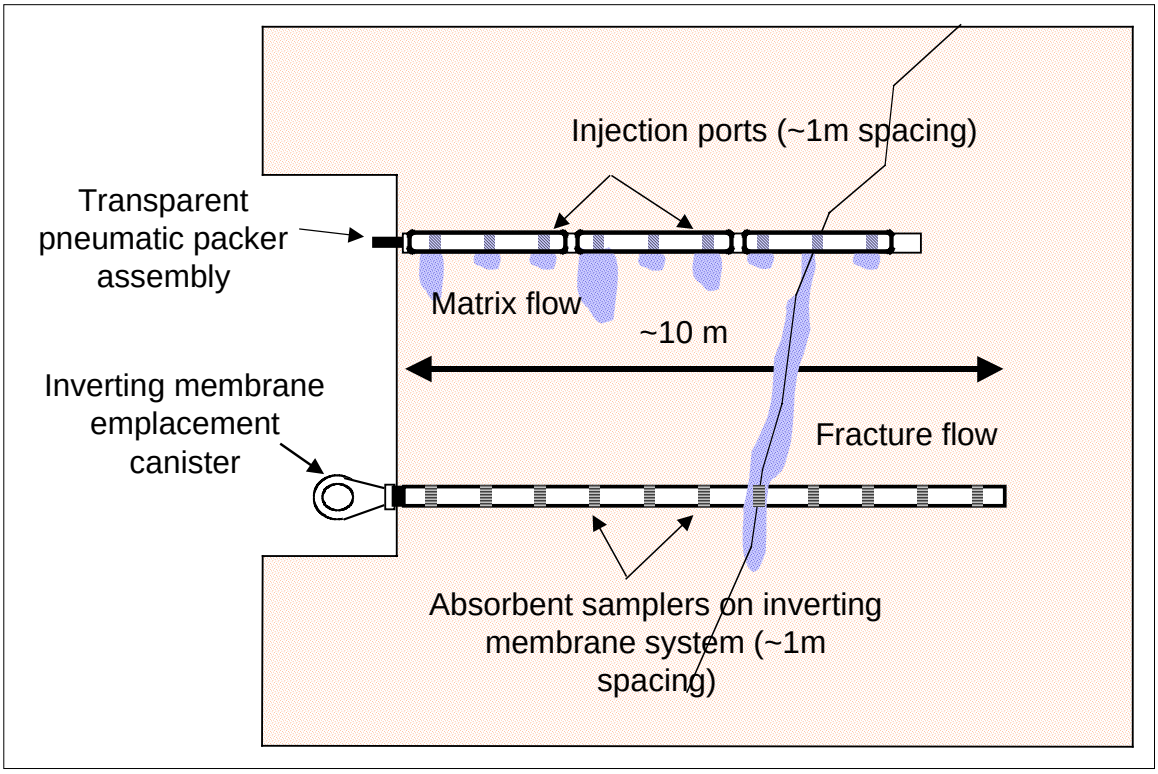

N/A – For illustration purposes only

NOTE: This figure shows a vertical cross-section of the test configuration.

Figure 35. Injection and Collection System Configuration

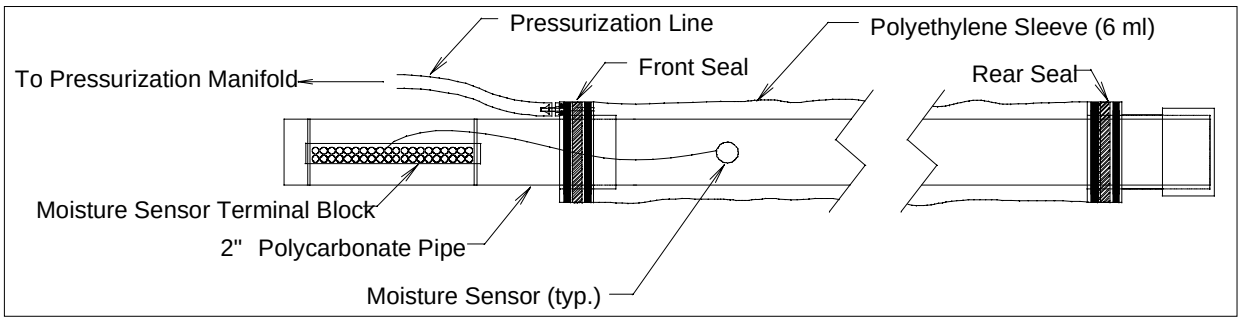

N/A – For illustration purposes only

Figure 36. Injection-System Transparent Packer

with mesh pockets to retain absorbent sample pads. The inverting membranes are removed from the boreholes regularly (as frequently as weekly) for sample-pad removal and replacement, whereas the injection packers remain in the holes for the duration of the test program. Each system is maintained at slight overpressure (1.7 to 3.5 kPa) to maintain contact between the sampling/injection pads and the tuff and, also, to prevent circulation of air within the borehole.

6.8.2.3.1 Moisture Sensors

Simple resistive moisture sensors were installed to diagnose the relative moisture state of the injection pads and the arrival of liquid tracer at the sampling-pad membranes. These sensors consisted of two wires separated a fixed distance apart and embedded in an absorbent-pad assembly. Their signal level was sensed by the Campbell Scientific dataloggers, using an alternating polarity resistance measurement technique to avoid charge polarization. The sensors operate by measuring resistance across the exposed leads of the wires. Moisture absorbed by the fabric reduces the resistance between the two exposed wires. The wetter the fabric, the lower the resistance. Although the sensor output is not quantitative, the values successfully indicated the general state of the sensing location: dry pads before installation tended to be in the 300- to 500-kohm range, pads equilibrated with the tuff moisture showed 80- to 100-kohm resistance, and pads sensing the arrival of the more conductive tracer mixture were distinctly lower in resistance at 10 to 30 kohms. These moisture indications were meant to guide the inverting-membrane sampling operations (indicating tracer arrival) and diagnose the injection-pad moisture state, indicating loss of injection or over injection.

6.8.2.3.2 Phase-1 and Phase-2 Data Collection

Campbell Scientific dataloggers are being used to collect measurement data from sensors and instrumentation. These data can be used to either help understand or validate the collected experimental chemical data or aid in ongoing decisions in conducting the Busted Butte saturated-flow tracer experiments. Environmental and experimental control data are measured and collected with two dataloggers. The data are stored in the dataloggers at user-defined intervals. A computer outside the tunnel portal connects to the dataloggers periodically via a short-haul modem and downloads the data. The data can then be transferred to a remote computer using a phone link and modem.

Phase 1
For the Phase-1A Busted Butte test, the dataloggers measured the pressure in the injection/sampling manifold, 12 to 14 moisture sensors, the datalogger panel temperature and battery voltage, the number of times the syringe pumps cycled in a given period of time, and the relative humidity, air temperature, and atmospheric pressure in the experimental area. For the Phase-1B test, the same data were collected only for a total of 32 moisture sensors and with the addition of an anemometer in the tunnel.

Phase 2
For the Phase-2 experiment, over 200 different sensors were measured. The data that are (or can be) collected include:

- Environmental information, such as ambient pressure, temperature, and relative humidity and wind speed in the vent system.

- Experimental control information, such as injection pressure, the number of times pumps are activated, and relative saturation at injection points, at the face of boreholes or along sampling membranes.

6.8.2.4 Conservative and Reactive Tracers and Microspheres

To predict the performance of the Calico Hills barrier to radioactive waste migration at Yucca Mountain under different percolation flux scenarios, a series of process models in flow and transport have been developed by the project based on theory and on field and laboratory studies. For viability assessment, site suitability, and licensing, the effectiveness and reliability of the geologic barriers will be determined using modeling predictions of radionuclide migration to the accessible environment. Measurements on a small scale can be conducted in the laboratory, but validating the extrapolation of these data in the presence of larger-scale heterogeneities requires field-tracer tests. However, the behavior of actual radionuclides of concern has been extensively studied in the laboratory; regulatory and environmental concerns prevent the use of these materials in the field. For the Busted Butte field tests, analog conservative and reactive tracers are used as surrogates for radionuclides. To validate the use of these tracers and the site-scale use of the K_d approach to modeling sorption and the processes of matrix diffusion and colloid migration, laboratory batch studies of radionuclide and tracer sorption onto Busted Butte core samples have been completed. The tracers were chosen so that conservative, reactive, and colloid-like behaviors could be monitored in a single continuous injection scenario. The tracers were mixed together to normalize the hydrologic conditions of the injection. The tracer matrix was synthetic pore water, which is based on the measured composition of Busted Butte pore waters (Section 6.8.5). The recipe for the synthetic water is provided in Section 6.8.2.4.3.

6.8.2.4.1 Phase-1 Tracers

Phase-1 tracers were chosen based on the list of tracers permitted for use in the C-wells tests. Analog conservative and reactive tracers and colloids are mixed together so as to normalize the hydrologic conditions they experience and provide for higher accuracy of the results. The tracers used in the Busted Butte experiments of Phase 1 include the following:

- Lithium bromide
- Fluorescent polystyrene latex microspheres
- Sodium fluorescein
- “Pyridone” (3-carbomoyl-2(1H)-pyridone)
- 2,6-difluorobenzoic acid (2,6-DFBA)
- Pentafluorobenzoic acid (PFBA).

The reactive tracer used is lithium ($K_d \leq 1.0$), and the colloid analogs are fluorescent polystyrene latex microspheres of two sizes: 0.3 and 1 μm diameter. The 2,6-DFBA and PFBA are conservative tracers used to tag the various injection boreholes according to injection rates (i.e., 1 and 10 mL hr^{-1} rates). Sodium fluorescein and pyridone are UV fluorescent and are used as conservative tracer markers that can be detected in the field at a concentration level of approximately 10 ppm using UV illumination. Borehole numbers are shown in Figure 37 for Phase 1A and Figure 38 for Phase 1B and Phase 2.

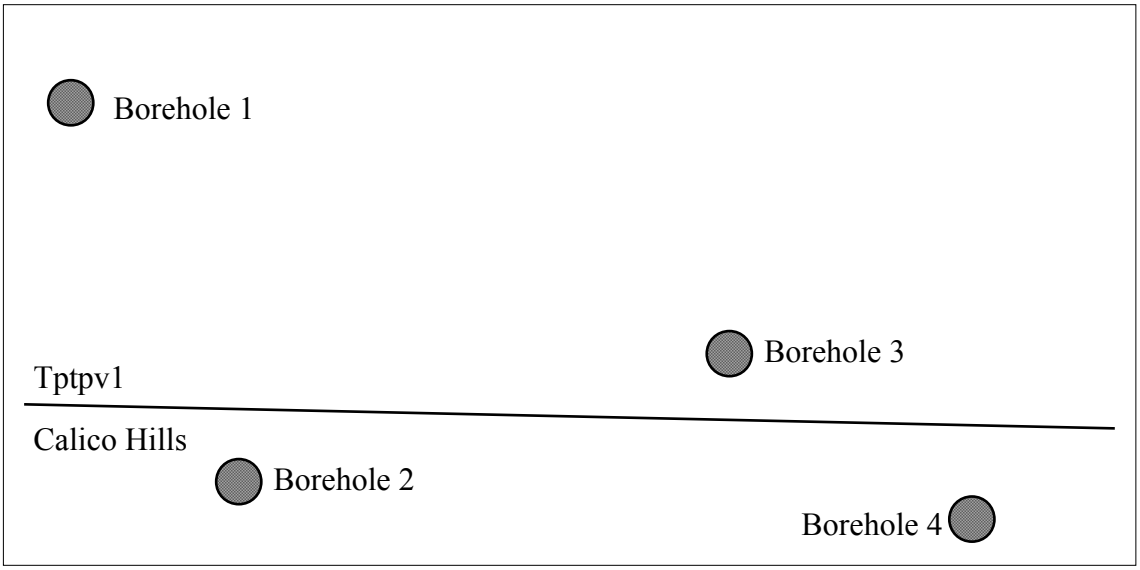

N/A – For illustration purposes only

Figure 37. Phase-1A Borehole Numbers and Relative Locations

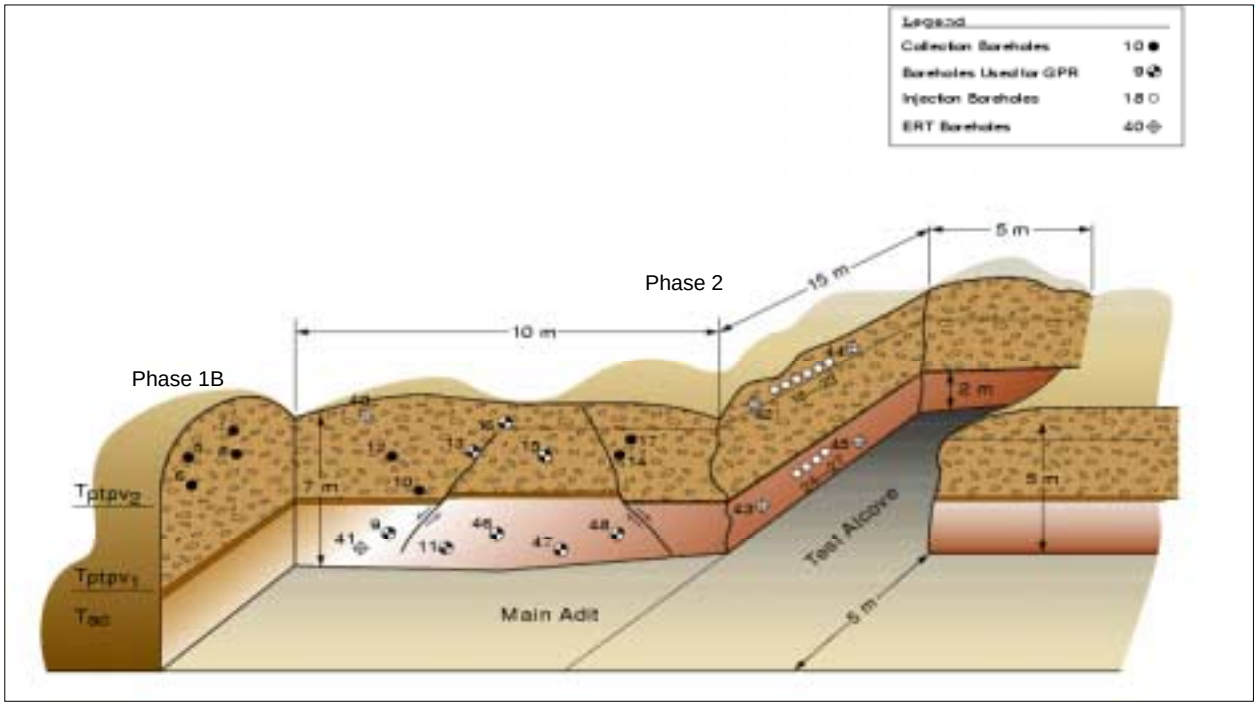

N/A – For illustration purposes only

Figure 38. Phase-1B and Phase-2 Borehole Numbers and Relative Locations

Phase 1A—10 mL hr^{-1} Injection Rate; Boreholes 1 and 3:

- 500 mg kg^{-1} lithium bromide
- 500 mg kg^{-1} sodium fluorescein
- 100 mg kg^{-1} 2,6-DFBA
- 1 mL kg^{-1} fluorescent polystyrene microspheres.

Phase 1A—1 mL hr^{-1} Injection Rate; Boreholes 2 and 4:

- 500 mg kg^{-1} lithium bromide
- 500 mg kg^{-1} sodium fluorescein
- 100 mg kg^{-1} PFBA
- 1 mL kg^{-1} fluorescent polystyrene microspheres.

Phase 1B—10 mL hr^{-1} Injection Rate; Borehole 5:

- 500 mg kg^{-1} lithium bromide
- 500 mg kg^{-1} sodium fluorescein
- 100 mg kg^{-1} 2,6-DFBA
- 100 mg kg^{-1} pyridone
- 1 mL kg^{-1} fluorescent polystyrene microspheres.

Phase 1B—1 mL hr^{-1} Injection Rate; Borehole 7:

- 500 mg kg^{-1} lithium bromide
- 500 mg kg^{-1} sodium fluorescein
- 100 mg kg^{-1} PFBA
- 100 mg kg^{-1} pyridone
- 1 mL kg^{-1} fluorescent polystyrene microspheres.

6.8.2.4.2 Phase-2 Tracers

Phase-2 tracers include those used in Phase 1 but with three additional FBAs (2,4-DFBA, 2,4,5-triFBA, 2,3,4,5-tetraFBA), iodide, a fluorescent reactive tracer (Rhodamine WT), and additional reactive ions that serve as analogs for neptunium, plutonium, and americium. (See Figure 38 for Phase-2 borehole locations.)

- Neptunium Analogs (NpO_2^+, Np(V)):
  - Nickel (Ni^{2+})
  - Cobalt (Co^{2+})
  - Manganese (Mn^{2+})

- Plutonium Analog (Pu^{3+}):
  - Samarium (Sm^{3+})

- Plutonium Analogs (colloidal form):
  - Polystyrene microspheres

- Americium Analog (Am^{3+}):

- Cerium (Ce^{3+}).

Phase-2 tracer recipes are as follows.

Phase 2A—1 mL hr^{-1} Injection Rate; Borehole 23:

- 1000 mg kg^{-1} lithium bromide
- 10 mg kg^{-1} sodium fluorescein
- 100 mg kg^{-1} 2,4,5-TriFBA
- 10 mg kg^{-1} pyridone
- 1 mL kg^{-1} microspheres,

and starting October 7, 1998:

- 10 mg L^{-1} rhodamine WT
- 10 mg kg^{-1} $NiCl_2 \cdot 6H_2O$ (2.47 mg/kg of Ni^{2+})
- 10 mg kg^{-1} $MnCl_2 \cdot 4H_2O$ (2.78 mg/kg of Mn^{2+})
- 10 mg kg^{-1} $CoCl_2 \cdot 6H_2O$ (2.48 mg/kg of Co^{2+})
- 5 mg kg^{-1} $SmCl_3 \cdot 6H_2O$ (2.06 mg/kg of Sm^{3+})
- 5 mg kg^{-1} $CeCl_3 \cdot 7H_2O$ (1.88 mg/kg of Ce^{3+}).

On September 30, 1999, the Phase-2A recipe was changed with the elimination of the microspheres and the addition of 500 mg kg^{-1} potassium iodide.

Phase 2B—10 mL hr^{-1} Injection Rate; Boreholes 24, 25, 26, 27:

- 1000 mg kg^{-1} lithium bromide
- 10 mg kg^{-1} sodium fluorescein
- 100 mg kg^{-1} 2,6-DFBA (Borehole #26,Borehole #27)
- 100 mg kg^{-1} 2,3,4,5-TetraFBA (Borehole #24, Borehole #25)
- 10 mg kg^{-1} pyridone
- 10 mg kg^{-1} rhodamine WT
- 1 mL kg^{-1} microspheres

and starting September 2, 1998:

- 10 mg kg^{-1} $NiCl_2 \cdot 6H_2O$ (2.47 mg/kg of Ni^{2+})
- 10 mg kg^{-1} $MnCl_2 \cdot 4H_2O$ (2.78 mg/kg of Mn^{2+})
- 10 mg kg^{-1} $CoCl_2 \cdot 6H_2O$ (2.48 mg/kg of Co^{2+})
- 5 mg kg^{-1} $SmCl_3 \cdot 6H_2O$ (2.06 mg/kg of Sm^{3+})
- 5 mg kg^{-1} $CeCl_3 \cdot 7H_2O$ (1.88 mg/kg of Ce^{3+}).

On August 18, 1999, the Phase-2B recipe was changed with the elimination of the microspheres and the addition of 500 mg kg^{-1} potassium iodide.

Phase 2C—50 mL hr^{-1} Injection Rate; Boreholes 18, 20, 21:

- 1000 mg kg^{-1} lithium bromide
- 10 mg kg^{-1} sodium fluorescein
- 100 mg kg^{-1} 2,6-DFBA (Borehole #18)
- 100 mg kg^{-1} PFBA (Borehole #20)
- 100 mg kg^{-1} 2,4-DFBA (Borehole #21)
- 10 mg kg^{-1} pyridone

- 10 mg kg^{-1} rhodamine WT
- 1 mL kg^{-1} microspheres

and starting September 2, 1998:

- 10 mg kg^{-1} $NiCl_2 \cdot 6H_2O$ (2.47 mg/kg of Ni^{2+})
- 10 mg kg^{-1} $MnCl_2 \cdot 4H_2O$ (2.78 mg/kg of Mn^{2+})
- 10 mg kg^{-1} $CoCl_2 \cdot 6H_2O$ (2.48 mg/kg of Co^{2+})
- 5 mg kg^{-1} $SmCl_3 \cdot 6H_2O$ (2.06 mg/kg of Sm^{3+})
- 5 mg kg^{-1} $CeCl_3 \cdot 7H_2O$ (1.88 mg/kg of Ce^{3+}).

On August 18, 1999, the Phase-2C recipe was changed with the elimination of the microspheres and the addition of 500 mg kg^{-1} potassium iodide.

6.8.2.4.3 Synthetic Pore-Water Recipe

To minimize the reactivity of the tracer solution with the country rock, a synthetic pore water, based on measured in-situ composition (Section 6.8.5.2), is used as a matrix for the tracers in solution.

Phase-1 Synthetic Pore Water:

- 76.8 mg kg^{-1} $SiO_2 \cdot nH_2O$ (amorphous silica),
- 36.8 mg kg^{-1} $CaCl_2 \cdot 2H_2O$ (calcium chloride dihydrate)
- 44.8 mg kg^{-1} $Ca(NO_3)_2 \cdot 4H_2O$ (calcium nitrate tetrahydrate)
- 3.8 mg kg^{-1} NaF (sodium fluoride)
- 10.7 mg kg^{-1} Na_2SO_4 (sodium sulfate)
- 51.2 mg kg^{-1} $NaHCO_3$ (sodium bicarbonate)
- 9.0 mg kg^{-1} $KHCO_3$ (potassium bicarbonate)
- 36.9 mg kg^{-1} $MgSO_4 \cdot 7H_2O$ (magnesium sulfate heptahydrate)
- 7.8 mg kg^{-1} $Ca(OH)_2$ (calcium hydroxide).

Phase-2 Synthetic Pore Water:

Phase 2 is identical to Phase 1 with the exception that, due to the large quantities required, the source of water is J-13 water that has been deionized (DI) using resin cartridges. This results in a DI water with approximately 30 ppm Si, so that no additional silica is added.

6.8.2.5 Use of Numerical Simulations for Test Design

6.8.2.5.1 Sample Collection Analyses Simulating Performance of a Sampling Pad

Increasing attention has been paid in recent years to the collection of comprehensive large-scale field data. Considerable effort has been expended during the last few decades for various modifications in solution sampler design and improved collection techniques, leading to a better performance and ease of operation in various sampling conditions. To date, a variety of modified sampler types are available depending on their shapes, materials, functions, and operations. Unfortunately, little attention has been paid to how such instruments and the related operations might influence their surroundings and alter the background flow field and the resulting solute transport.

The objective of this study was to test the performance of the pad sampling system used in Busted Butte field test site using numerical experiments. The simulation results were subsequently analyzed to evaluate any significant effect the sampler pads may have on the interpretation of transport phenomena and the underlying process hypothesis.

Numerical Experiments

Numerical simulations were designed to closely approximate the experimental setup of the sampler system at the Busted Butte field test site. For the purpose of testing the general performance of this new methodology, soil hydraulic properties representing Calico Hills tuff (Tac) (DTN: GS990308312242.007, GS990708312242.008) and a loamy sand (Carsel and Parrish 1988) were chosen for this study. The simulations were conducted using the FEHM V2.00 (STN: 10031-2.00-00) code assuming two-dimensional air-water flow under isothermal conditions.

Model Description

The performance of the pad sampling system was tested by applying a narrow pulse of solute after a sufficient period of constant, uniform irrigation so as to establish a reasonably steady water flow field within the simulation domain. The subsequent leaching of solute is observed frequently at selected nodes representing a sampling pad during the numerical experiments. In general, a pad is replaced periodically after the water potential within the pad reaches equilibrium with its ambient flow condition. The time required to reach this equilibrium depends highly upon the hydraulic properties of the pad and the soil.

The simulations were conducted in a homogeneous two-dimensional vertical cross-section of 2 m by 2 m with a 0.1-m-diameter access borehole located at the center of the domain. A 3.175-mm thick pad of 0.05-m diameter was located on the inner upper center of the borehole. The hydraulic properties of the pad and the two selected soils are given in Table 19. The lateral boundaries were assumed to be a no-flux condition for both water flow and solute transport. A prescribed water potential was assumed on the surface boundary. The corresponding water input rate was calculated internally by FEHM (V2.00, STN: 10031-2.00-00) and used subsequently for solute flux calculations. The pulse of solute input lasted for one day. The lower boundary was assumed to be a gravity-drained or natural drainage flux condition for water flow. At the bottom boundary, solute leaves the system freely with water at a water flux rate equal to the unsaturated hydraulic conductivity of a given water potential.

Table 19. Hydraulic Parameter Sets used to Define the Material Properties for the Simulations

Material [Source]	Permeability (m^2)	Residual saturation	α (m^{-1})	*n*	Porosity
Calico Hills (Tac) [DTN: GS990308312242.007, GS990708312242.008]	5×10^{-12}	0.0001	3.5	1.19	0.50
Loamy Sand [Carsel and Parrish (1988)]	4.65×10^{-12}	0.139	12.4	2.28	0.41
Pad [SEA (1992)]	2.19×10^{-11}	0.05	17.0	1.12	0.85

DTN: LA9909WS831372.019 (except loamy sand)

The pad sampling system contains three major components that can adversely affect the flow field and the resulting solute transport. These three components are: the borehole, the pad, and the effect due to periodic replacement of the pad. A borehole within the unsaturated flow domain acts like an obstacle to water flow (Philip et al. 1989, pp. 16–28). The collection pad disturbs the flow field due to the difference of its hydraulic properties from the neighboring porous material even under equilibrium condition with the ambient flow field. Finally, the periodic replacement of a new pad causes a highly transient flow condition at least in the vicinity of the sampling location. To best evaluate and analyze the influence of the experimental setup on the overall behavior of the physical system, each component is tested separately during steady water flow conditions.

Modeling Results

Water Flow

Simulations were run for both the Tac and the loamy sand. The background water saturation for steady-state flow for Tac was assumed to be 0.35, whereas for the loamy sand, it was 0.5. When a borehole is constructed within an unsaturated domain, water tends to build up on the upstream side of the borehole and creates different shapes of so-called roof-drip lobes, depending largely upon the soil hydraulic properties (Philip et al. 1989, pp. 16–28). The addition of a pad slightly changes the pattern of the water potential (or saturation) distributions. Figure 39 shows the saturation distributions for the Tac when a borehole and a pad are added to the system. Notice that the contour levels used for plotting the results of a borehole and a borehole plus a pad are the same for easy identification of the influences between different tests. Differences in flow patterns are not distinguishable for the loamy sand soil for the cases with and without a pad.

The dynamic responses of both systems to a pad plotted at three selected observation nodes are shown in Figure 40. The results show the water extraction rate and the equilibrium time needed when a new pad is added to a steady-state system. The background saturation during steady-state flow was 0.35 for the Tac and 0.5 for the loamy sand. Two observation nodes were located within the pad. The rock node in Figure 40 indicates an observation immediately upstream of the pad within the porous media domain. The results revealed that for Tac, it took approximately 10 days to reach equilibrium, whereas for loamy sand, the equilibrium time was less than half a day.

Solute Transport

Figure 41 shows the solute resident concentrations plotted as a function of time for various simulation scenarios for the Tac. Solute concentration is in moles of solute per kg of liquid water. The solute transport was delayed when a borehole and a pad were added to the physical system. On the other hand, the periodic replacement of a pad causes an early arrival for the travel times as illustrated for a step input of solute. The pad was assumed to be replaced every week during the simulations. As can be observed on the upper panel of Figure 42, the concentrations dropped periodically to a value of zero corresponding to the replacement operations. The periodic change of concentrations on a nearby porous rock node, as depicted on the lower panel of Figure 42, also shows a reduction of concentration when the soil water solution was absorbed into the pad.

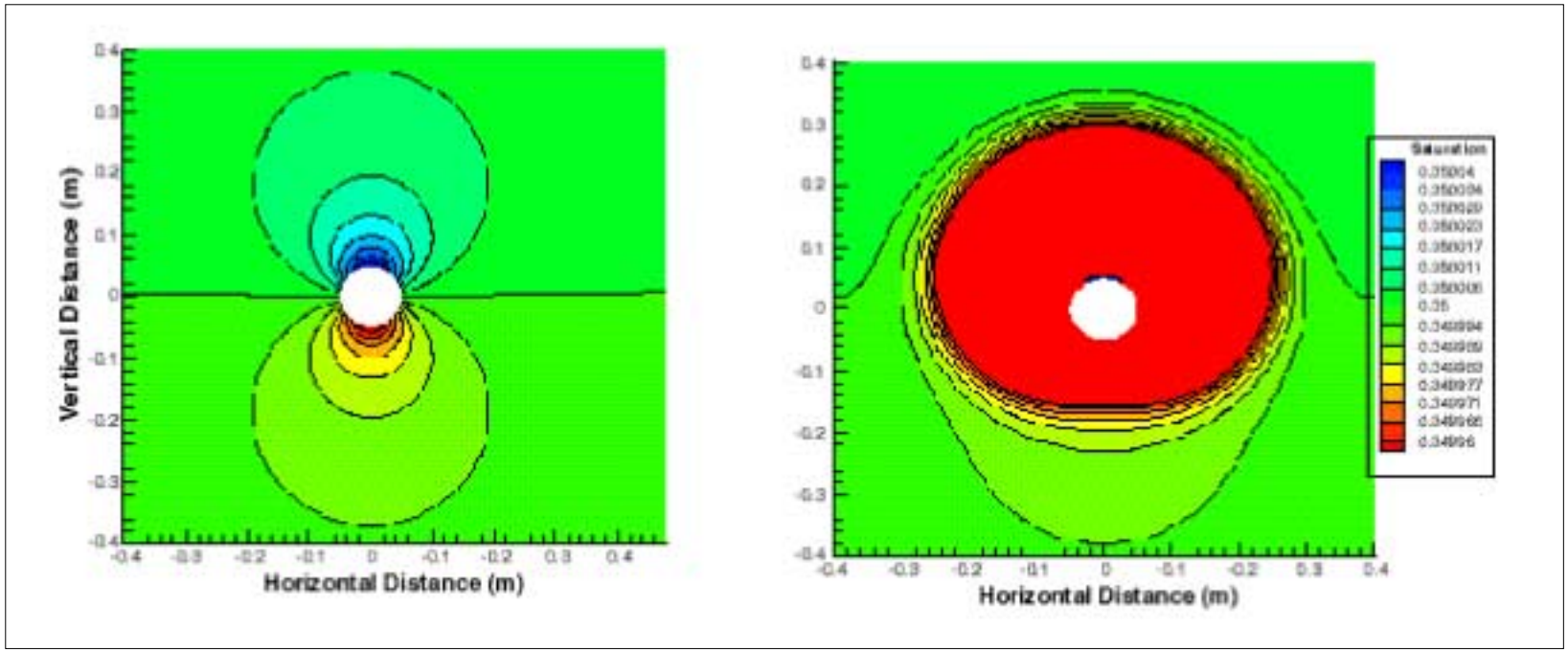

DTN: N/A—simulation results for illustrative purposes only

NOTE: The left frame shows the influence of a borehole and the right frame shows the same condition with the addition of a pad.

Figure 39. Distributions of Saturation under Steady-State Water Flow Conditions Within the Tac

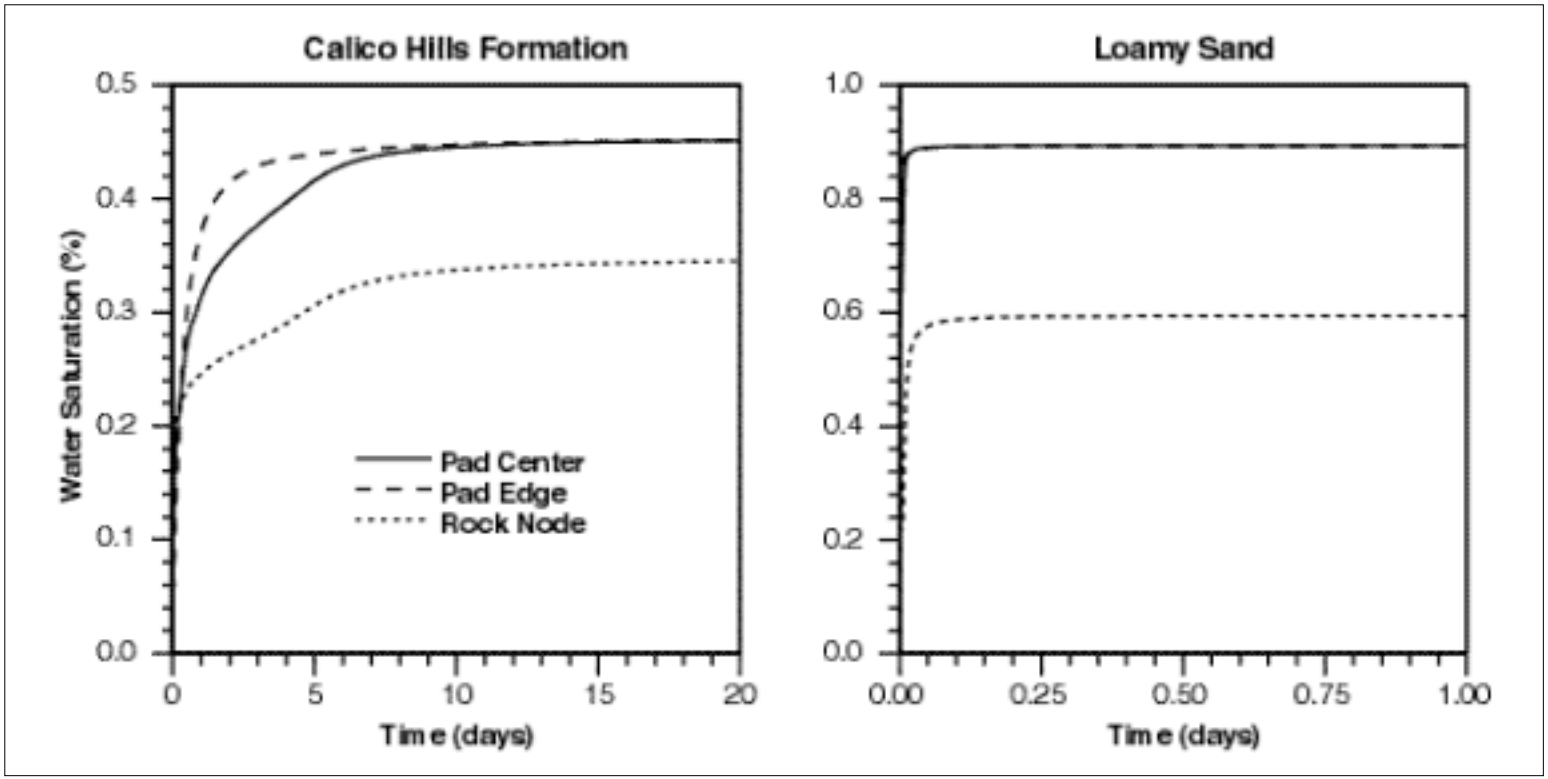

DTN: N/A—simulation results for illustrative purposes only

Figure 40. Water Saturation as a Function of Time for a New Pad Attached to the System

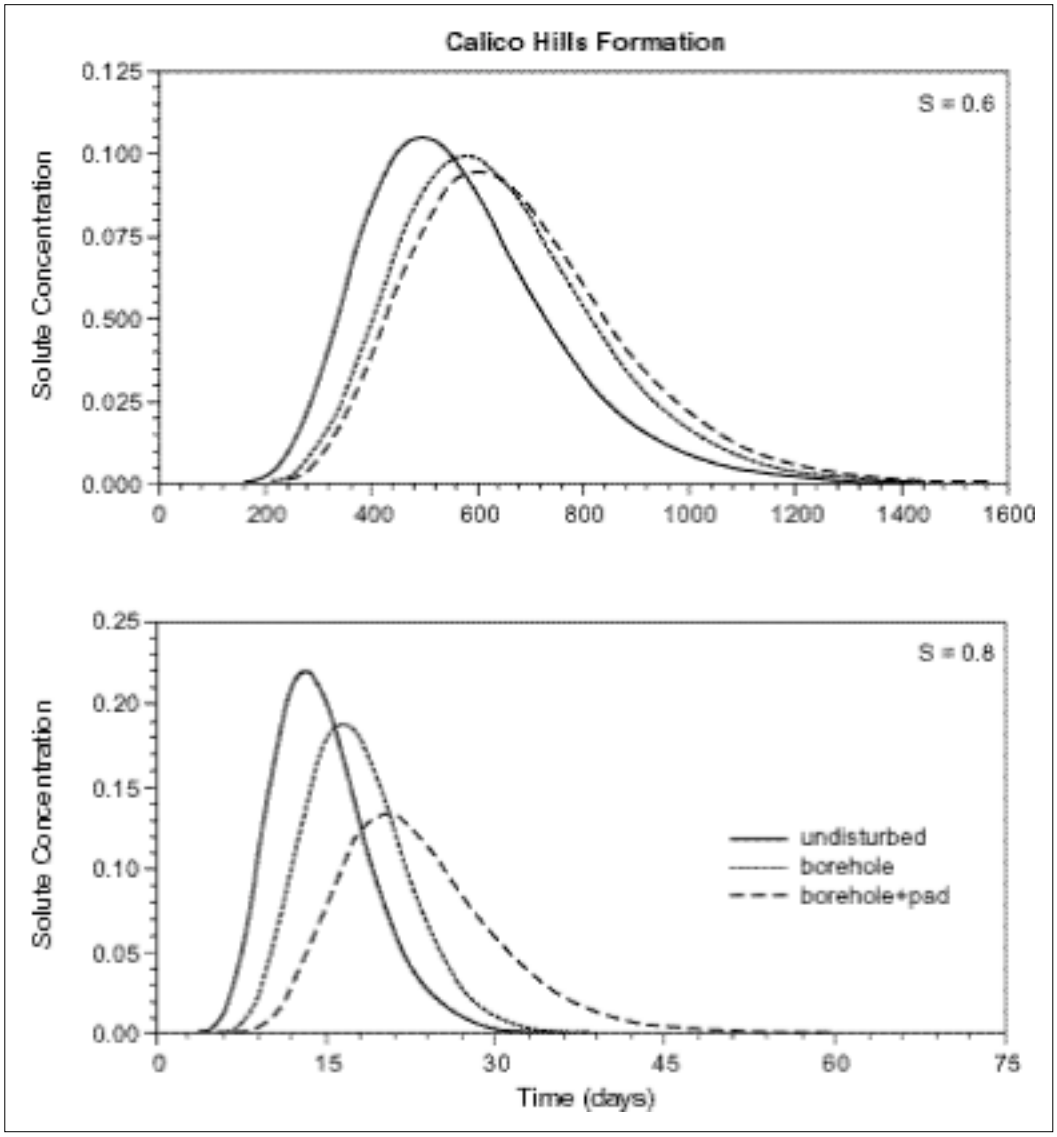

DTN: N/A—simulation results for illustrative purposes only

NOTE: The solute resident concentrations above were observed at a point corresponding to a position at the center of the pad during steady-state water flow conditions in Tac. Concentration is in moles of solute per kg of liquid water. The parameter S is water saturation.

Figure 41. Solute Resident Concentrations in Tac

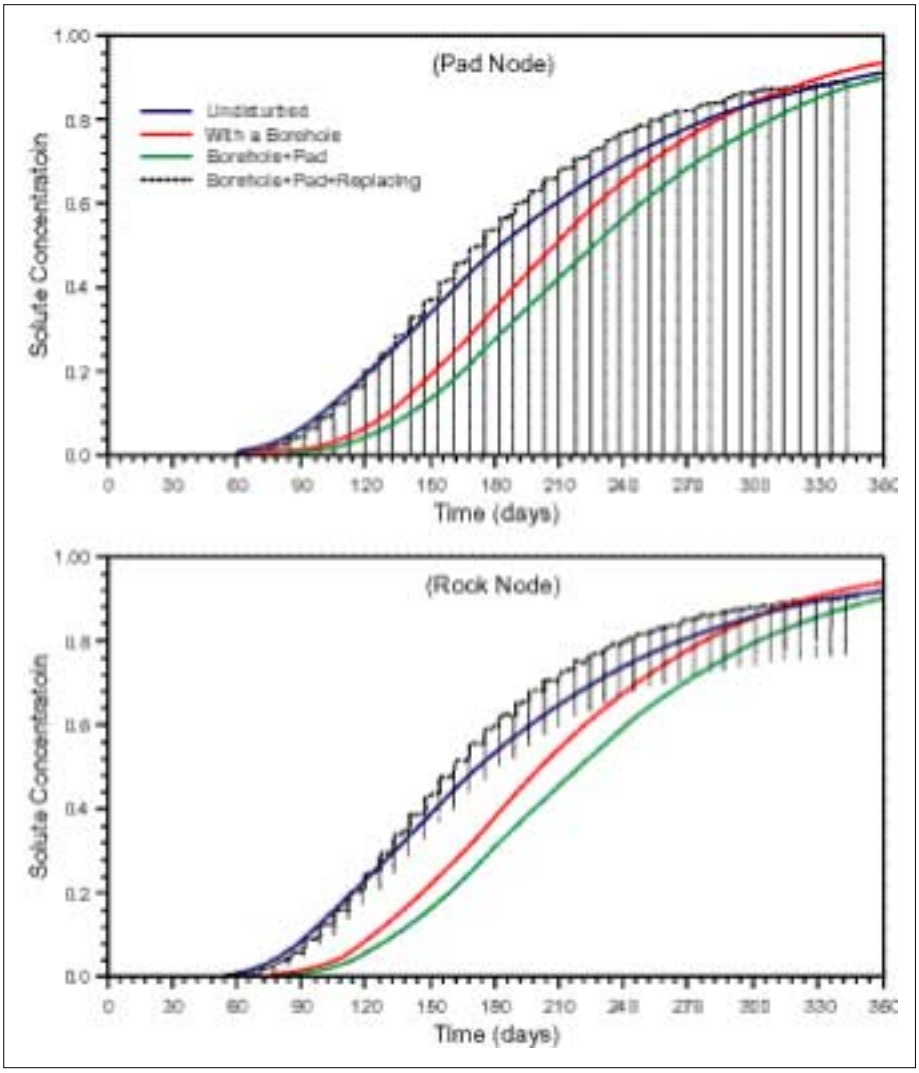

DTN: N/A—simulation results for illustrative purposes only

NOTE: A point injection of 10 mL hr^{-1} with a step input of solute located 30 cm above a collection pad was assumed. Concentration is in moles of solute per kg of liquid water.

Figure 42. Performance of a Collection Pad in Tac

The dimensionless mean and variance of travel times were plotted as a function of steady-state fluid saturation in Figure 43 for Tac. The normalized dimensionless quantities give a relative quantification of each separate effect that influences system behavior. For instance, the influence of a pad can be evaluated on a relative basis when one normalizes the effect caused by a borehole plus pad with the corresponding quantities for a borehole without pad. Notice again that the resident concentrations observed as a function of time at a given location do not have an obvious physical implication in terms of parameter estimation and moment analysis as discussed above. The results revealed that the disturbance of both a borehole and a pad to the solute transport is highly dependent upon the fluid saturation of the system. In a natural situation when the flow field is inherently transient, the saturation-dependent condition must be integrated into the system for the evaluation of the possible influence on solute transport.

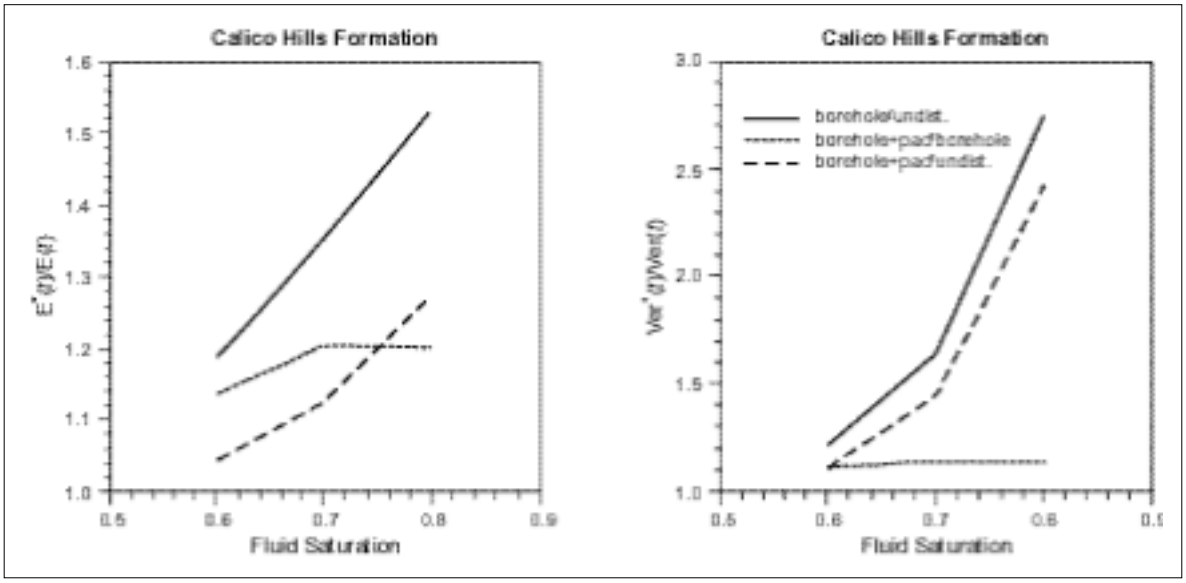

DTN: N/A—simulation results for illustrative purposes only

NOTE: The plots show influence of a borehole and a pad on (left) the dimensionless mean $E^*(t)/E(t)$ and (right) the dimensionless variance $\mathrm{Var}^*(t)/\mathrm{Var}(t)$ of solute travel times plotted as a function of fluid saturation for the Tac.

Figure 43. Influence of Borehole and Pad on Solute Travel Times for Tac

Future Efforts

The last step of converting this effort to an application tool is to derive relationships between measured data and undisturbed true system behavior using available information. After that, this methodology can be applied to the Phase-1A and Phase-1B tests using hydraulic properties data (DTN: GS990308312242.007; GS990708312242.008) as part of model-calibration and validation practices. The calibrated model can then be applied to the Phase-2 test evaluation and will help PA represent anthropogenically altered sites more accurately.

6.8.2.5.2 Performance Measures

Determining the validity of current concepts for unsaturated-zone flow and transport, and simultaneously demonstrating and documenting the improvement of the model as new data are incorporated, requires making predictions throughout the different stages of the testing program. The cyclic process of prediction, measurement, and model refinement adopted in this work will result in increased confidence in the site-scale unsaturated-zone flow and transport model. The predictive simulations will serve to document our ability to forecast the experimental results using current YMP databases and models.

Numerical simulations are, therefore, intimately involved in the prediction and analysis of the test phases as well as the scaling of parameters for the site-scale models. In support of the numerical models, hydrologic, geologic, mineralogic, and geochemical parameters from the test block are being measured. Furthermore, the physical state of the block (e.g., saturation and pore-

water chemistry) and the boundary conditions are being measured for incorporation in the numerical models. Due to the time constraints of the field test, these measurements are being collected in conjunction with the test instrumentation rather than prior to it. However, the impacts of this procedure on formal predictions are minimal due to the phased development of the testing program. That is, parameters and boundary conditions necessary for the large block simulations are being measured during the single-borehole testing phase.

Scoping calculations, test design, and Phase-1 predictions were done using a high-resolution unstructured grid. These predictions are described in Section 6.8.6. For Phase 2, the mapped tunnel walls are being incorporated into a 3-D computational grid with 500,000+ nodes for the test block using LAGRIT software (V1.0, STN: 10212-1.0-00). A series of numerical simulations have been carried out in support of the design of the unsaturated-zone transport tests at Busted Butte. These calculations are presented in Section 6.8.7.

Because of the paucity of data for the properties of the Calico Hills rocks, the predictions are likely to produce results having a high range of uncertainty. However, this exercise serves to document the full impact of the test at Busted Butte on both YMP databases and models. As more data become available, these predictions will be updated and modified. The UZTT provides field and laboratory experimental data and modeling analyses that increase the amount of data and understanding of the Calico Hills unit.

6.8.3 Geology, Mineralogy, and Hydrologic Properties

The unsaturated-zone flow and transport test at Busted Butte was sited in the same stratigraphic units as those underlying the potential repository at Yucca Mountain. As mentioned in Section 6.8.1.2, this was done to achieve optimal applicability of the test results at least to the portion of the repository west of the Ghost Dance fault. This section describes the current early state of the characterization effort documenting the degree of lithologic, mineralogic, and hydrologic correspondence between Busted Butte and western Yucca Mountain.

One objective of the Busted Butte test, as stated in Section 6.8.1.3, is to investigate the effects of heterogeneities on flow and transport in unsaturated rocks. Permeability changes are associated with boundaries between rocks of different textures and constituents and with different mineralogic alteration (Loeven 1993, pp. 15–20). Initial observations of the Phase-1A tracer test suggest that this is true for the rock units of the Busted Butte test facility (Section 6.8.5.3.1.1). The mineralogic composition of rocks in the test block is a potentially relevant factor in the analysis of reactive-tracer movement and the prediction of radionuclide transport. The effects of faults and fractures on flow and transport are also a topic of study; no results are available for this analysis. The rock-characterization results presented here represent a preliminary stage of the complete lithologic analysis.

6.8.3.1 Geology of the Busted Butte Test Facility

Busted Butte is a small (2.5 km by 1 km) north-trending mountain block primarily made up of thick ignimbrite deposits of the Paintbrush Group. This fault-block uplift is bound by northeast- and north-trending normal faults, and it is split by a north-trending down-to-the-west normal fault that gives Busted Butte its distinctive appearance. Tuff units generally have dips less than 10° except where affected by drag near large faults. Small windows of older volcanic units below the Paintbrush Tuff, including the Calico Hills Formation, Wahmonie Formation, and Prow Pass Tuff, are exposed through colluvial deposits on the north and southeast sides of Busted Butte.

The test facility is located within a small horst on the southeast side of Busted Butte. The horst is 300 to 350 m wide. Geologic units exposed in the vicinity of the test facility include, in ascending stratigraphic order, the Wahmonie Formation, the Calico Hills Formation, and the Topopah Spring Tuff (Figure 44). The test facility is constructed in the Topopah Spring Tuff and the Calico Hills Formation. The Wahmonie Formation, which is not present below the potential repository, is similarly absent from the UZTT test block itself (see Section 6.8.3.2).

A brief description of geologic units in the underground test facility is given below (Bussod et al. 1997, pp. 30–32). Nomenclature and symbols for subunits of the Topopah Spring Tuff follow the usage of Buesch et al. (1996, pp. 5–8)

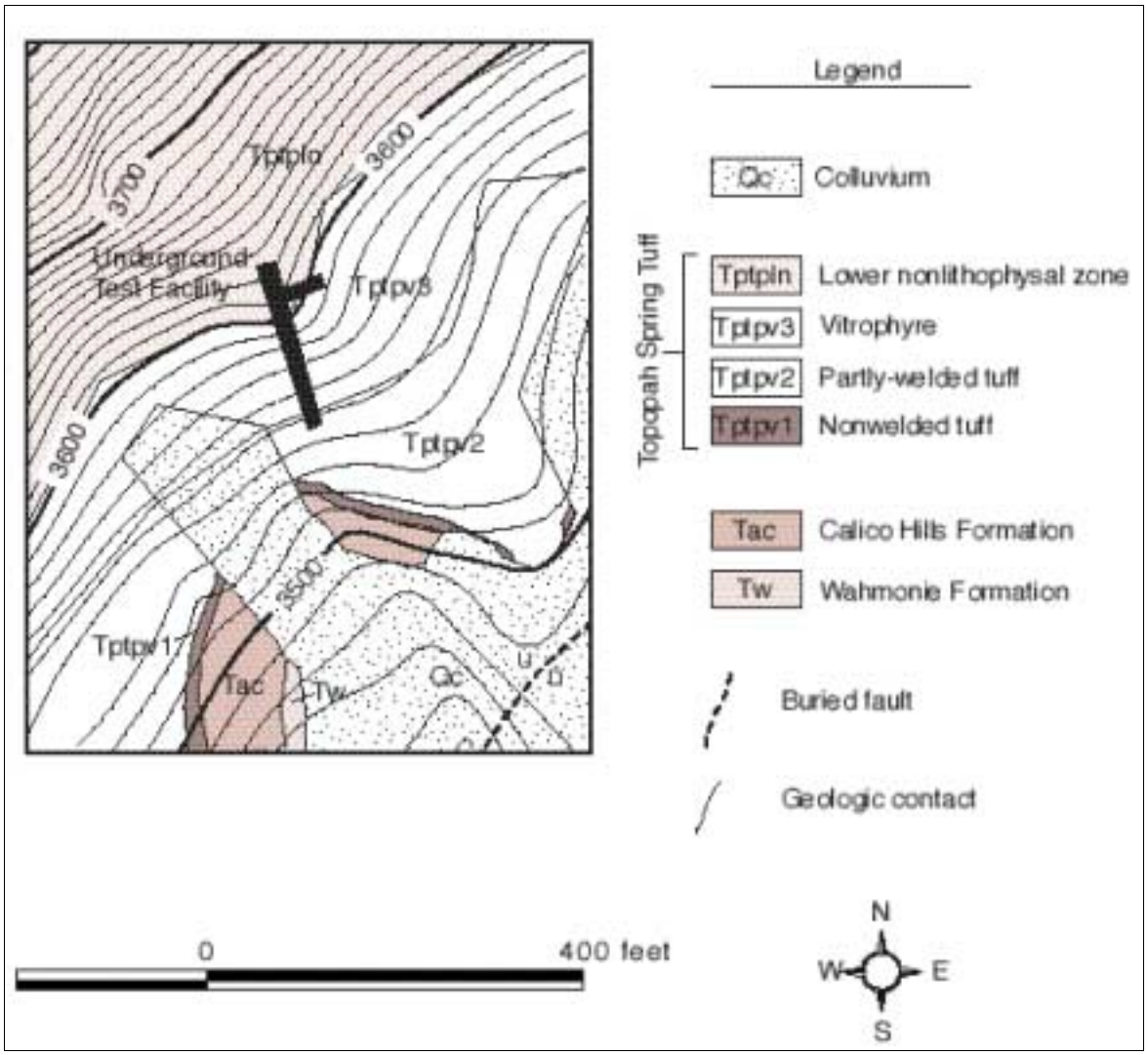

N/A - For illustration purposes only

NOTE: The plot is a geologic map of the area around the underground test facility in the southeastern part of Busted Butte. The contour interval is 10 feet. The tunnel entrance is at the southern end of the facility.

Figure 44. Busted Butte Geologic Map

6.8.3.1.1 Calico Hills Formation

Up to several meters of nonwelded Calico Hills Formation are exposed in the test area of the facility in the lower walls of both the Main Adit and the Test Alcove. The exposed Calico Hills Tuff consists of alternating beds of poorly cemented salmon-pink massive tuff and variably cemented, white ash beds.

The salmon-pink tuffs contain round to slightly elongated white vitric pumices that are generally less than a centimeter in diameter. The matrix is a mixture of fine ash, phenocrysts, and locally abundant fragments of black glass. The salmon-pink tuffs gradually become more deeply colored

upsection, suggesting that the upper parts of these units are more oxidized and may represent weakly developed paleosols. The clay content of these tuffs is low (see Table 22).

There are two variably cemented ash beds intercalated with the salmon-pink tuffs in the Main Adit and Test Alcove. These ash beds are about 130 cm apart on the right rib of the Main Adit. The ash beds are 15 to 20 cm thick and typically form resistant ledges in outcrops outside of the test facility and resistant layers inside the facility.

6.8.3.1.2 Topopah Spring Tuff

Tptpv1—The lowermost 1 to 1.5 m of the Topopah Spring Tuff is nonwelded ash-flow unit Tptpv1. The base of Tptpv1 is locally marked by a 3- to 4-cm coarsely bedded ashfall deposit. This deposit consists of 0.5- to 3-cm pumice fragments and 0.25-cm black perlitic lava clasts. This thin deposit pinches out laterally and is similar to thin discontinuous beds of ashfall deposits at the base of the Topopah Spring Tuff in outcrops outside of the test facility. A 4.5-cm-thick, crudely laminated shardy tuff overlies the ashfall deposit. The shardy tuff is also discontinous laterally.

Above the thin bedded deposits, Tptpv1 consists of light-gray nonwelded ignimbrites. The ignimbrite flow units contain medium-gray pumice clasts in a pink-gray matrix. Near the top of Tptpv1, the pumice clasts are tan. Glassy lava fragments and red-brown lithics are common. Pumice clasts increase in size and abundance upsection in individual ignimbrite flow units. The two lowermost ignimbrite flow units are separated by one or more bedded tuffs 0.2 to 8 cm thick. The lithology of the bedded tuffs is variable, consisting of laminated shardy tuff in some places and clast-supported pumiceous deposits in others. Because of relief differences on the surface on which these bedded tuffs were deposited, they fall within Tptpv1 in the Test Alcove and within Tptpv2 toward the back of the Main Adit.

In the Test Alcove, the upper part of Tptpv1 contains a distinctive zone of clay alteration typically about 70 cm thick. The clay occurs both as rinds around pumice clasts and as complete replacement of the pumice clasts. The clays are typically reddish brown but also include small round bodies of white clay within the reddish-brown clays (giving it a mottled appearance). In some replaced pumice clasts, white clay overlies layers of reddish-brown clay. Clay alteration also occurs in the tuff matrix and along subhorizontal fractures. One such fracture contains four different layers of clay up to 1.5 cm thick. The lower boundary of clay alteration is undulatory and has up to 0.5 m of relief.

Tptpv2—Tptpv2 is the highest stratigraphic unit exposed in the back of the Main Adit and in the Test Alcove area. It is characterized by tan, partly welded ignimbrite that has well-developed columnar joints. The matrix of the ignimbrite has a distinctive salt and pepper appearance due to the presence of black glass shards in a tan ashy matrix. Pumice clasts are typically 1 to 6 cm in their long dimension and exhibit flattening ratios from 6:1 to 8:1. Welding increases upsection through Tptpv2.

6.8.3.2 Mineralogy of the Busted Butte Locality

Samples from outcrops were collected at the Busted Butte site for mineralogic and petrologic analysis. Some of these samples were also used for determinations for hydrologic properties. Other samples were collected from the test block walls throughout the year for the study, and descriptions of the lithologies present in the test area were gathered.

The tables below summarize the mineralogic data for outcrop samples at the Busted Butted test locality. Tables 20 and 21 are for the Tpt samples. Table 20 provides stratigraphic descriptions for the samples in Table 21. The calcite and gypsum reported in the Tpt samples represent pedogenic calcrete contamination in the surface samples.

Table 20. Descriptions of Outcrop Samples Collected from Busted Butte

Sample	Lithology
SPC #517962	densely welded perlitic vitrophyre (upper Tptpv3)
SPC #517963	densely to moderately welded vitric tuff (mid Tptpv2)
SPC #517964	moderately welded to nonwelded vitric tuff (mid Tptpv1)
LANL #2814	densely welded perlitic vitrophyre (lower Tptpv3)
LANL #2815	densely to moderately welded vitric tuff (upper Tptpv2)
LANL #2816	densely to moderately welded vitric tuff (mid Tptpv2)
LANL #2817	densely to moderately welded vitric tuff (lower Tptpv2)
LANL #2818	moderately welded to nonwelded vitric tuff (upper Tptpv1)
LANL #2819	moderately welded to nonwelded vitric tuff (lower Tptpv1)
LANL #2820	vitric pumice swarm at base of the Topopah Spring Tuff (basal Tptpv1)

DTN: LA9909WS831372.005

The samples from the Tptpv2 and Tptpv1 intervals show that the poorly welded to nonwelded vitric portions of the lower Topopah Spring Tuff at this site are largely unaltered, without zeolites but with modest smectite occurrences. The Tptpv3 interval, although not part of the transport test section, is also largely unaltered.

The mineralogy of the Calico Hills Formation and the Wahmonie Formation is available from two locations at Busted Butte (Tables 22 and 23). The three lowest samples from auger hole AUG-1 in the floor of the Busted Butte Alcove were analyzed (Table 23) for comparison with the mineralogy of the vitric Calico Hills Formation near the crest of Yucca Mountain (see Section 6.8.3.2.1). Alteration in the alcove samples shown on Table 23 is generally similar, with smectite > clinoptilolite in all three samples. The low biotite and feldspar contents of the AUG-1 samples are characteristic of the Calico Hills Tuff, indicating that Wahmonie deposits are at least 396 cm below the present alcove floor and are not expected to have measurable influence on the test results. Table 22 presents corroborating mineralogic data for the Calico Hills Formation and the Wahmonie Formation from surface samples at the Busted Butte site. These samples are arranged in Table 22 by relative depth and generally corroborate the results for the vitric interval sampled in AUG-1. The samples also indicate that the lowermost part of the Calico Hills Formation (Tac) contains appreciable amounts of

Table 21. Quantitative X-ray Diffraction Results for Samples from Lower Tpt Section (weight %)

Sample	Smec-tite	Opal-CT/ Cristob.	Quartz	Feld-spar	Glass/ Amorph	Hema-tite	Mica/ Illite	Cal-cite	Gyp-sum	Kaoli-nite	Total
Tptpv3											
SPC #517962	1 ± 1	2 ± 1	tr	4 ± 1	93 ± 2	—	tr	tr	—	—	100 ± 2
LANL #2814p1	1 ± 1	4 ± 1	tr	3 ± 1	92 ± 2	—	tr	—	—	—	100 ± 2
Tptpv2											
LANL #2815p1	—	4 ± 1	1 ± 1	5 ± 1	90 ± 2	—	—	tr	—	—	100 ± 2
SPC #517963	1 ± 1	—	tr	3 ± 1	95 ± 2	tr	tr	1 ± 1	tr	—	100 ± 2
LANL #2816p1	2 ± 1	4 ± 1	tr	4 ± 1	90 ± 2	—	tr	—	—	—	100 ± 2
LANL #2817p1	3 ± 1	3 ± 1	tr	3 ± 1	91 ± 2	—	tr	—	—	—	100 ± 2
Tptpv1											
SPC #517964	tr	—	tr	2 ± 1	95 ± 1	—	tr	3 ± 1	—	—	100 ± 1
LANL #2818p1	tr	2 ± 1	tr	2 ± 1	96 ± 1	—	tr	tr	—	—	100 ± 1
LANL #2819p1	3 ± 1	1 ± 1	tr	3 ± 1	91 ± 2	—	tr	tr	—	2 ± 1	100 ± 2
LANL #2820p1	2 ± 1	1 ± 1	4 ± 1	8 ± 1	84 ± 2	1 ± 1	tr	tr	—	—	100 ± 2

DTN: LA9909WS831372.005

NOTE: — = not detected. tr = Trace abundance of < 0.5 wt %. Errors are conservative 2-sigma values. The "p1" appended to LANL samples is a designator for the X-ray diffraction split of the sample.

Table 22. Mineral Abundances (weight %) in Calico Hills Formation (Tac) and Wahmonie Formation Surface Samples from Busted Butte

Sample	Smec-tite	Clinop-tilolite	Crist./ OpalCT	Quartz	Feld-spar	Glass	Hema-tite	Bio-tite	Total
vitric Tac									
DEB 3/90-10	1(1)	—	—	2(1)	11(1)	86(2)	—	tr	100(2)
DEB 3/90-9	6(2)	—	—	4(1)	15(2)	74(3)	—	tr	100(3)
DTV-97-2	2(1)	—	1(1)	1(1)	2(1)	94(2)	—	tr	100(2)
DEB 3/90-8a	—	—	1(1)	1(1)	1(1)	97(2)	—	tr	100(2)
DEB 3/90-8b	1(1)	—	1(1)	4(1)	7(1)	86(2)	—	tr	100(2)
DEB 3/90-7	3(1)	1(1)	1(1)	7(1)	12(1)	76(2)	tr	tr	100(2)
zeolitic Tac									
DTV-97-3	—	9(1)	1(1)	7(1)	16(2)	64(3)	1(1)	2(1)	100(3)
DEB 3/90-6	1(1)	12(1)	1(1)	7(1)	16(2)	62(3)	—	1(1)	100(3)
Wahmonie									
DEB 3/90-5	5(2)	—	—	1(1)	26(3)	54(5)	1(1)	9(3)	100(5)
DEB 3/90-4	4(1)	—	—	2(1)	24(3)	46(6)	2(1)	17(5)	100(6)

DTN: LA9909WS831372.006

NOTE: — = not detected. tr = trace abundance. Numbers in parentheses are 2-sigma standard errors.

Table 23. Mineral Abundances (weight %) in Calico Hills Formation (Tac) Samples from Auger Hole AUG-1 in the Floor of the Busted Butte Test Alcove

Sample	Depth (cm)	Smec-tite	Clinop-tilolite	Crist./ OpalCT	Quartz	Feld-spar	Glass	Hema-tite	Bio-tite	Total
vitric Tac										
AUG-1-P	375–383	3(1)	1(1)	1(1)	8(1)	12(2)	74(3)	tr	1(1)	100(3)
AUG-1-Q	383–389	6(2)	1(1)	1(1)	8(1)	18(3)	65(4)	tr	1(1)	100(4)
AUG-1-R	389–396	3(1)	1(1)	1(1)	7(1)	11(2)	76(3)	tr	1(1)	100(3)

DTN: LA9909WS831372.010

NOTE: tr = trace abundance. Numbers in parentheses are 2-sigma standard errors.

clinoptilolite. The upper part of the Calico Hills Formation at this site, however, is characterized more by smectite than by zeolite alteration. Access to both types of alteration is, therefore, possible at this site.

6.8.3.2.1 Mineralogic Comparison with Yucca Mountain: Boreholes H-5 and SD-6

The excavated section at Busted Butte is in the lower Topopah Spring Tuff and the upper Calico Hills Formation (Tac). The vitric nature of this section and the relatively low abundances of smectite and clinoptilolite alteration are similar to that in drill holes near the crest of Yucca Mountain, such as USW H-5 (Table 24) and USW SD-6 (Table 25). The increase in zeolitization at the base of the Calico Hills Formation, particularly in the bedded tuff (Tacbt) unit, is comparable to the localized zeolitization in the lower part of the Calico Hills Formation at Busted Butte (Tables 22 and 23). The data indicate a distribution of alteration similar to that at Busted Butte. In considering the SD-6 and H-5 data, however, it is important to bear in mind that both drill holes had only partial core or cuttings recovery, potentially skewing the mineralogic information. A much more accurate picture of these poorly indurated vitric units is obtained by excavation, as was accomplished at Busted Butte.

6.8.3.3 Hydrologic Properties

Samples of the Calico Hills Formation and Topopah Spring Tuff exposed in Busted Butte outcrops were used to determine the hydrologic properties of the formations in the test block. These results are reported in DTNs: GS990308312242.007 and GS990708312242.008.

Table 24. Quantitative X-ray Diffraction Results (weight %) for USW H-5 Core and Drill Cuttings

Sample	Depth (m)	Smec-tite	Clinop-tilolite	Mor-denite	Tridy-mite	Cristo-balite	Opal-CT	Quartz	Feld-spar	Glass	Mica	Hema-tite	Calcite	Horn-blende	Total
Tptpv2	***505.7–509.6***														
Tptpv1	***509.6–517.9***														
Tpbt1	***517.9–519.7***														
Tac	***519.7–573.0***														
1710/1720	522.7	3 ± 2	—	—	—	5 ± 3	—	5 ± 3	20 ± 10	70 ± 10	—	—	—	—	103 ± 15
1750 (DC)	533.4	—	tr?	—	—	5 ± 5	—	2 ± 3	5 ± 5	85 ± 5	—	—	—	—	97 ± 9
1762 (SW)	537.1	—	—	—	—	1 ± 1	—	1 ± 1	5 ± 5	95 ± 5	—	—	—	—	102 ± 7
1760/1770	538.0	—	6 ± 1	—	—	—	4 ± 1	3 ± 1	6 ± 1	81 ± 2	—	—	—	—	100 ± 2
1800 (SW)	548.6	—	—	—	—	2 ± 3	—	2 ± 3	10 ± 5	85 ± 5	1 ± 1	—	—	—	100 ± 8
1820/1830	556.3	tr	4 ± 1	—	—	—	2 ± 1	4 ± 1	10 ± 1	80 ± 2	—	—	—	—	100 ± 2
1852 (SW)	564.5	—	—	—	—	—	—	2 ± 3	7 ± 3	90 ± 5	1 ± 1	—	—	—	100 ± 7
1875 (SW)	571.5	—	tr?	—	—	—	tr?	2 ± 3	5 ± 5	92 ± 3	—	—	—	—	99 ± 7
Tacbt	***573.0–592.0***														
1890/1900	577.6	1 ± 1	11 ± 1	—	—	—	3 ± 1	4 ± 1	6 ± 1	75 ± 2	—	—	—	—	100 ± 2
1900/1910	580.6	tr	10 ± 1	—	—	—	1 ± 1	3 ± 1	8 ± 1	78 ± 2	tr	—	—	—	100 ± 2
1910/1920	583.7	tr	18 ± 1	—	—	—	5 ± 1	5 ± 1	7 ± 1	65 ± 2	tr	—	—	—	100 ± 2
1917 (SW)	584.3	—	25 ± 5	—	—	—	10 ± 5	30 ± 5	35 ± 10	—	tr	—	—	—	100 ± 13
1920/1930	586.7	3 ± 1	52 ± 3	—	—	—	7 ± 2	14 ± 1	16 ± 3	6 ± 5	2 ± 1	—	—	—	100 ± 5
1930 (DC)	588.3	2 ± 3	50 ± 10	—	—	—	—	15 ± 5	30 ± 5	—	1 ± 1	—	—	—	98 ± 13

DTN: LA9909WS831372.007

NOTE: — = not detected. tr = trace abundance. DC = drill-bit cutting sample. SW = sidewall core sample.

Table 25. Quantitative X-ray Diffraction Results (weight %) for Samples from Drill Hole USW SD-6

Sample	Depth (m)	LANL number [a]	Smec-tite	Clinop-tilolite	Tridy-mite	Cristo-balite	Opal-CT	Quartz	Feld-spar	Glass	Hema-tite	Mica	Horn-blende	Cal-cite	Total
Tptpv2	***455.7–461.5***														
1496.5/1496.7	456.2	2984p1	—	—	—	—	17 ± 4	1 ± 1	11 ± 2	71 ± 4	—	tr	—	—	100 ± 5
1500.1/1500.2	457.3	2985p1	2 ± 1	—	—	—	17 ± 4	1 ± 1	12 ± 2	68 ± 4	—	tr	—	—	100 ± 5
1503.3/1503.4	458.2	2986p1	2 ± 1	—	—	—	20 ± 6	2 ± 1	16 ± 2	60 ± 6	tr	tr	—	—	100 ± 6
1506.2/1506.3	459.1	2987p1	3 ± 1	—	—	—	18 ± 5	1 ± 1	13 ± 2	65 ± 5	tr	tr	—	—	100 ± 6
1509.2/1509.3	460.0	2988p1	3 ± 1	—	—	—	15 ± 4	1 ± 1	11 ± 2	70 ± 4	tr	—	—	—	100 ± 5
1512.1/1512.2	460.9	2989p1	4 ± 1	—	—	—	14 ± 4	1 ± 1	12 ± 2	69 ± 4	—	tr	—	—	100 ± 5
Tptpv1	***461.5–471.7***														
1516.9/1517.0	462.4	2990p1	4 ± 1	—	—	—	9 ± 2	1 ± 1	10 ± 1	76 ± 2	tr	tr	—	—	100 ± 3
1521.5/1521.6	463.8	2991p1	5 ± 2	—	—	—	4 ± 1	1 ± 1	5 ± 1	85 ± 2	—	tr	—	—	100 ± 3
1524.9/1525.0	464.8	2992p1	5 ± 2	—	3 ± 1	2 ± 1	—	2 ± 1	11 ± 2	77 ± 3	tr	tr	—	—	100 ± 3
1527.8/1527.9	465.7	2993p1	3 ± 1	—	2 ± 1	4 ± 1	—	5 ± 1	21 ± 3	65 ± 3	tr	tr	—	—	100 ± 4
1546.5/1546.6	471.4	2994p1	1 ± 1	—	—	1 ± 1	—	5 ± 1	10 ± 1	83 ± 2	tr	tr	—	—	100 ± 2
Tpbt1	***471.7–473.8***														
Tac	***473.8–526.5***														
1560.8/1560.9	475.8	2995p1 [b]	tr	4 ± 1	6 ± 1	10 ± 1	—	27 ± 2	53 ± 8	—	tr	tr	—	—	100 ± 8
1563.3/1563.4	476.5	2996p2 [b]	—	6 ± 1	5 ± 1	13 ± 1	—	25 ± 2	53 ± 8	—	tr	tr	—	—	102 ± 8
1563.3/1563.4	476.5	2996p1	4 ± 1	4 ± 1	—	2 ± 1	—	2 ± 1	7 ± 1	81 ± 2	—	tr	—	—	100 ± 2
1566.7/1566.8	477.6	2997p1	—	2 ± 1	1 ± 1	2 ± 1	—	4 ± 1	10 ± 1	81 ± 2	tr	tr	—	—	100 ± 2
1570.3/1570.5	478.7	2998p1	—	1 ± 1	1 ± 1	3 ± 1	—	8 ± 1	16 ± 2	71 ± 2	tr	tr	—	—	100 ± 3

DTN: LASC831321AQ98.003

NOTES: — = not detected tr = Trace abundance
[a]The "p1" or "p2" appended to LANL numbers of samples denote specific X-ray diffraction splits.
[b]The analyses 2995p1 and 2996p2 are from large (> 5 cm) lithic clasts that occur at these depths.

6.8.4 Tomographic Studies: Geophysical Techniques at the Busted Butte Unsaturated Zone Test Facility—Overview

Real-time geophysical monitoring techniques may be used to provide real-time data on the advance of fluid fronts and tracer fronts through the block and enable us to optimize our collection-pad sampling schedule to collect data. Combining two techniques enables the collection of detailed, high-resolution, 3-D, calibrated, real-time monitoring of moisture and tracer movement through the unsaturated fractured medium. Specifically, electrical resistance tomography (ERT) provides 3-D global coverage and ground-penetrating radar tomography (GPR-T) provides high spatial resolution. The techniques are listed below, along with their characteristics and the advantages they bring to the test program at Busted Butte.

Electrical Resistance Tomography (ERT):

- 3-D snapshot of moisture content and tracer front
- Covers entire test block
- Half-meter spatial resolution
- Measurements on demand (probably weekly or monthly).

Ground Penetrating Radar Tomography (GPR-T):

- 2-D slices of moisture content
- Selected locations through available boreholes
- 1- to 10-cm spatial resolution
- Measurements at opportunistic intervals (tied to collection-borehole sampling frequency)
- Can determine matrix permeabilities.

Ongoing geophysical monitoring is presently helping us guide the timing of collection-pad retrieval for detailed tracer analysis. Independent physical measurement techniques (collection pads and block mineback) will ultimately provide field-scale evaluation of geophysical techniques, increasing their applicability and acceptability for other YMP activities. None of these techniques interfere physically with the test or with the testing schedule.

6.8.4.1 Ground-Penetrating Radar Tomography

6.8.4.1.1 Experimental Objective and Status

The objective of the ground penetrating radar (GPR) data acquisition is to monitor the tracer injection of the Busted Butte UZTT both spatially and temporally and to investigate the nature of fluid migration through the Calico Hills member of the Yucca Mountain lithologic sequence. The data collected, analyzed, and submitted to the Technical Data Management System (TDMS) thus far include the pre-injection baseline radar velocity measurements as well as the subsequent velocity measurements made after the start of tracer injection (seven data collection visits through September 1999). Additional measurements shall continue to be made on a regular schedule approximately every three to four months. All analyzed data are periodically compared to the other available geophysical data as well as to the tracer breakthrough data in order to better constrain the interpretation of fluid/tracer migration within the block.

6.8.4.1.2 Background and Experimental Approach

The borehole radar method is one in which modified surface radar antennae are emplaced into a rock formation and high-frequency electromagnetic signals are transmitted through the formation to a receiving antenna. The electrical properties of the subsurface material greatly influence the transmitted electromagnetic signal. In particular, the dielectric permittivity of the rock has a strong influence on the propagation of the signal and whether it travels at a high or low velocity. Moisture content has such an effect. The high dielectric permittivity (κ) of water ($\kappa \sim 80$) or wet rock ($\kappa \sim 20$–30) in contrast to drier rock ($\kappa \sim 3$–6) typically results in greatly reduced signal velocities. Changing chemical compositions (i.e., tracers) may also alter the bulk dielectric permittivity of the rock and, hence, the velocity of propagation of the radar wave. Because such changes in signal character are what are to be measured over the course of the Busted Butte UZTT, any increase (or decrease) in background moisture content or chemical composition resulting from the tracer injection (or rock dry-out) should result in changes in the received radar wave velocity.

The transmitted signals may be represented as multiple ray paths crossing through a zone of interest within the block. If sufficient ray paths are recorded, a tomographic image may be obtained through computer processing. The information extracted from such data consists of the transit time, which depends on the wave velocity. This information, in the form of a processed radar velocity tomogram, offers a high-resolution approach to monitoring the changes occurring in the rock over the duration of the tracer-injection experiment.

6.8.4.1.3 Equipment Description, Component Specifications, Operating Principles, and Survey Methodology

A description of the equipment used, the component specifications, the operating principles, and the GPR-T survey methodology can be found in the Technical Implementing Procedure governing all GPR-T data acquisition done in support of the Yucca Mountain site characterization effort (YMP-LBNL-TIP/GP 5.0, Rev. 0, Mod. 0).

6.8.4.1.4 Results of Busted Butte Unsaturated Zone Transport Test Radar Data Acquisition

The radar data were acquired in eight of the Phase-2 collection boreholes orthogonal to the direction of the Phase-2 injection boreholes. Additionally, two of the Phase-2 injection boreholes were used to acquire data only one time, after the boreholes were apparently affected by grout infiltration resulting from nearby electrical resistance tomography (ERT) borehole grouting. The 10 boreholes include the following: 9, 11, 13, 15, 16, 46, 47, and 48 (Phase-2 collection); 19 and 22 (Phase-2 injection). The configuration and layout of the boreholes used are illustrated in Figure 38.

The radar data are acquired in the two-dimensional planes defined by two boreholes, more commonly referred to as well pairs. The well pairs acquired in support of the Busted Butte UZTT are the following: 15-13, 48-46, 47-11, 46-9, 46-16, and 22-19 (one time only for the last pair listed). The decision to acquire data in these particular well pairs was made based on their

relative proximity to the injection boreholes. Data from both the upper horizontal well pair 15-13 and the vertical well pair 46-16 are acquired to monitor tracer injection associated with the upper injection boreholes 18, 20, 21, and 23. Data from the lower horizontal well pairs 46-9, 47-11, and 48-46 are acquired to monitor tracer injection associated with the lower injection boreholes 24, 25, 26, and 27. The vertical well pair 46-16 may also be used to image any tracer injection associated with the lower injection boreholes and the progress of the tracer beneath the horizontal well pair 15-13.

Thus far the data collected have been processed for travel times with the result being radar velocity tomograms (DTN: LB00032412213U.001). Differencing or subtraction of the velocity tomograms over time has also been completed for each of the well pairs. Such differencing or subtraction allows for the highlighting of the tracer or moisture front as it changes spatially and temporally. In essence, the background formation remains static in those areas not affected by the changing tracer or moisture front. By subtracting one velocity tomogram from another, we are able to discount those areas remaining static while emphasizing those areas where change is occurring.

Two of the well pairs differ slightly in the acquisition method used between the baseline and the post-injection surveys. These well pairs are 46-16 and 46-9. Data for well pair 46-16 was collected at a higher frequency (200 MHz) during the post-injection survey to better match the data collected in all of the other well pairs. Higher frequencies generally result in data of higher resolution (approximately 10.0 cm for 200 MHz), so the highest-frequency antennae should be used if at all possible. Data were not originally acquired in well pair 46-9 because it was believed that well pair 48-46 provided sufficient coverage in the area of the lower injection boreholes. A decision was subsequently made after tracer injection began to gather more spatial information below the lower injection boreholes and, hence, well pair 46-9 was added to the GPR acquisition list. Also, it should be noted that the pre-injection baseline data for several of the well pairs differs significantly from data acquired just one month after tracer injection began. The differences are likely the result of changes in the overall block assemblies (e.g. grouting of the ERT boreholes, addition of the injection apparatus, etc.) rather than the immediate consequence of the tracer injection. In order to enhance the subsequent differencing tomography, the “baseline” set of velocity tomograms chosen are those collected in August-September 1998 approximately one month after tracer injection began. Comparison with tracer breakthrough data on the collection pads indicates that tracer had not yet significantly entered those regions imaged by the GPR tomograms. Therefore, it was determined that the August–September 1998 data would provide an adequate starting point from which to evaluate the changes in the block over time.

Each of the well pairs have witnessed some degree of velocity change over the course of the experiment. For the purposes of this AMR, however, only three of the well pairs will be discussed in detail: 46-16, 46-9 and 15-13. This is done in an effort to be concise as the results for each well pair are essentially similar. Again, all of the data from each of the well pairs have been submitted to the TDMS and are available for review.

Well Pair 46-16

This well pair represents the only vertical slice through the block (approximately 9.5 m in length and 3.5 m in height). It images tracer and moisture contributions from both the upper and the lower injection boreholes. When evaluating changes in velocity over time, one would expect such changes to occur in the regions directly surrounding the injection boreholes with decreased velocities representing areas of increased moisture content. This is exactly what is seen in the differenced tomograms. Figures 45 to 47 represent several time steps throughout the course of the experiment (dates of data acquisition are noted above each tomogram). As can be seen, decreases in the velocity relative to the baseline (August–September 1998) data are immediately obvious surrounding the high and low injection boreholes (these locations are marked on the tomogram as small white dots). Furthermore, the zones of decreased velocity can be seen to expand away from the injection boreholes over time both in a vertical as well as a horizontal direction. Such vertical and horizontal spreading is to be expected as a result of matrix or capillary-driven flow and was, in fact, confirmed in the Phase-1A excavation. Precluding a similar excavation of the rock included by this well pair, the GPR data would seem to indicate a similar mechanism of flow for the Phase-2 block.

Also of note is the seemingly large extent of decreased velocity. It should be restated that low velocities are indicative of zones of higher dielectric permittivity; zones of higher dielectric permittivity are indicative of zones of elevated moisture content. That being the case, those zones of decreased velocity may represent regions of elevated moisture content and not simply the presence of tracer. This subtlety is born out when comparing the tracer breakthrough data with the tomography results. The zones of increased moisture content (i.e., decreased velocity) do not directly overlay the tracer breakthrough within boreholes 46 or 16. In fact, the locations of tracer breakthrough are contained within the zones of decreased velocity. This result implies that as the fluid front containing the tracer spreads away from the injection boreholes, some of the tracer may be retarded in relation to the spread of the moisture front. In effect, the tracer may be moving more slowly through the block than its associated fluid or water component. Conversely, the fluid front leaving the injection boreholes may be simply displacing existing pore fluids and mobilizing them within the block. The radar velocities are insensitive to this effect and are thus incapable of distinguishing between existing pore waters, introduced pore waters or tracers. Again, comparing the tomography results with those recorded in the tracer breakthrough logs, it appears that some form of fluid breakthrough is occurring in the collection boreholes which is not comprised of tracer. This is evidently what is being imaged by the differenced radar tomograms and it is not an inconsequential finding.

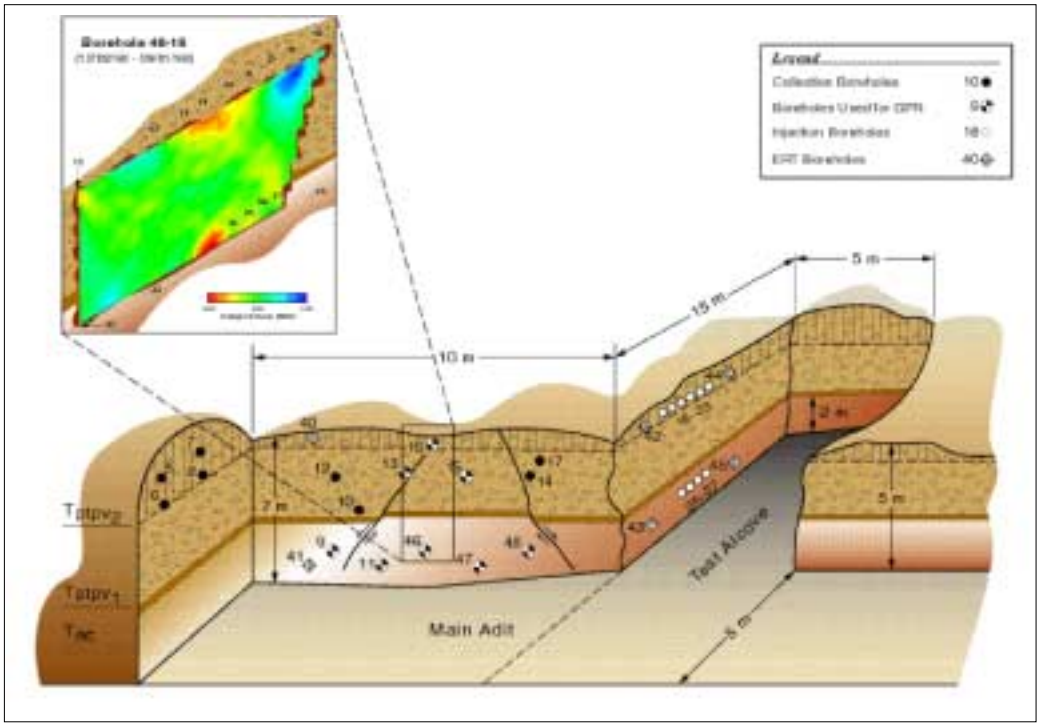

DTN: LB00032412213U.001; MO0004GSC00167.000 (for location)

Figure 45. Tomography (GPR-T) Results for Well Pair 46-16, December 1998

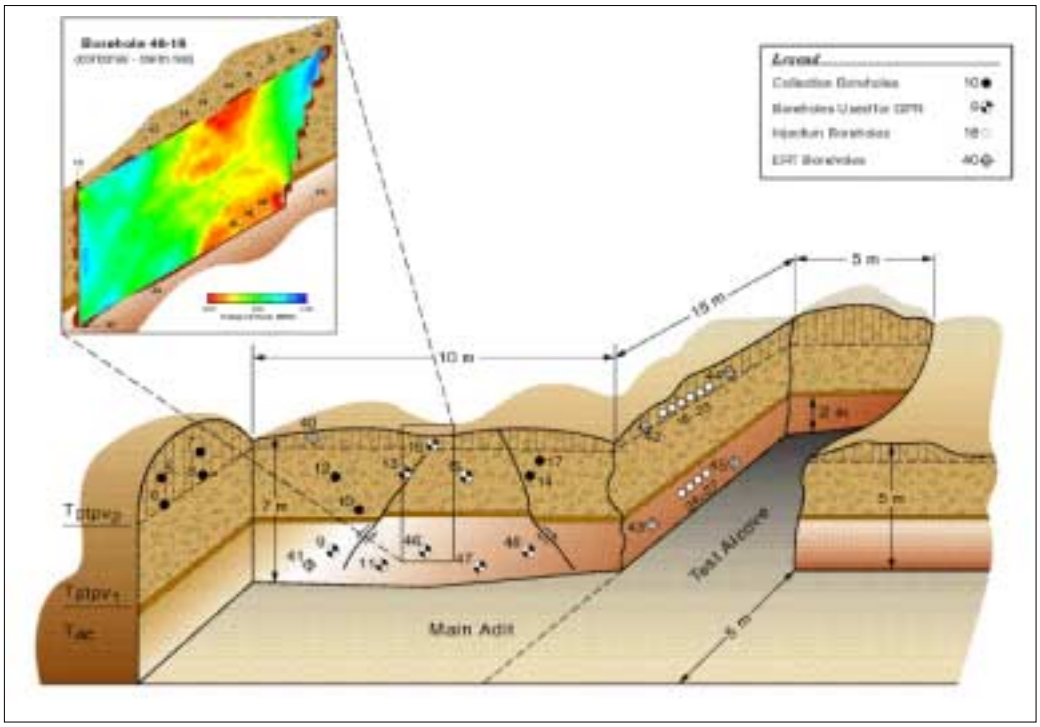

DTN: LB00032412213U.001; MO0004GSC00167.000 (for location)

Figure 46. Tomography (GPR-T) Results for Well Pair 46-16, March 1999

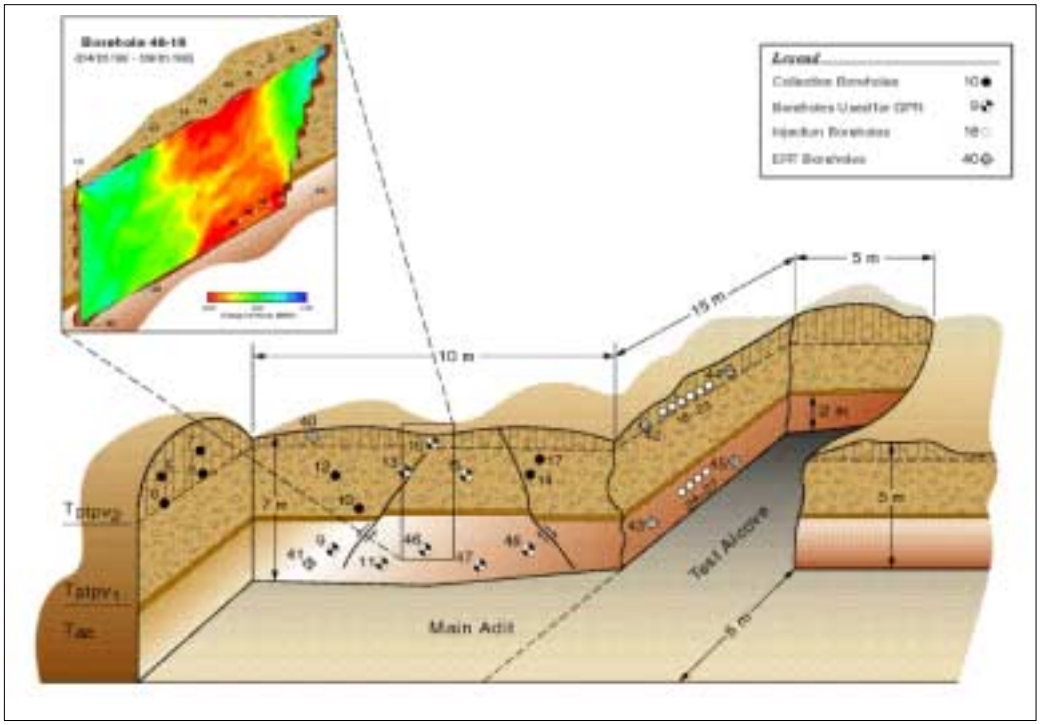

DTN: LB00032412213U.001; MO0004GSC00167.000 (for location)

Figure 47. Tomography (GPR-T) Results for Well Pair 46-16, April 1999.

Well Pair 46-9

This well pair represents a horizontal slice (approximately 8.0 m in length and 2.6 m in width) through the block and images the tracer/moisture front associated with the lower injection boreholes. Figures 48 and 49 represent two time steps throughout the course of the experiment (dates of data acquisition are noted above each tomogram). As can be seen, decreases in the velocity relative to the baseline (August-September 1998) data are immediately obvious surrounding the low injection boreholes (these locations are marked on the tomogram as orthogonal tubes). Furthermore, the zones of decreased velocity can be seen to expand away from the injection boreholes over time in a horizontal direction. Because a horizontal well pair cannot capture the vertical flow of moisture away from the boreholes, only the extent of the horizontal flow can be imaged. What is observed is that the decrease in velocity (i.e., the increase in moisture content), moves rapidly away from the injection boreholes early on in the experiment and then remains relatively constant aside from some localized changes. This would seem to imply that much of the moisture front moves away from the injection apparatus to its greatest possible horizontal extent at which time it can no longer spread in such a direction. Presumably, the majority of fluid flow from this time on continues in a direction other than horizontal.

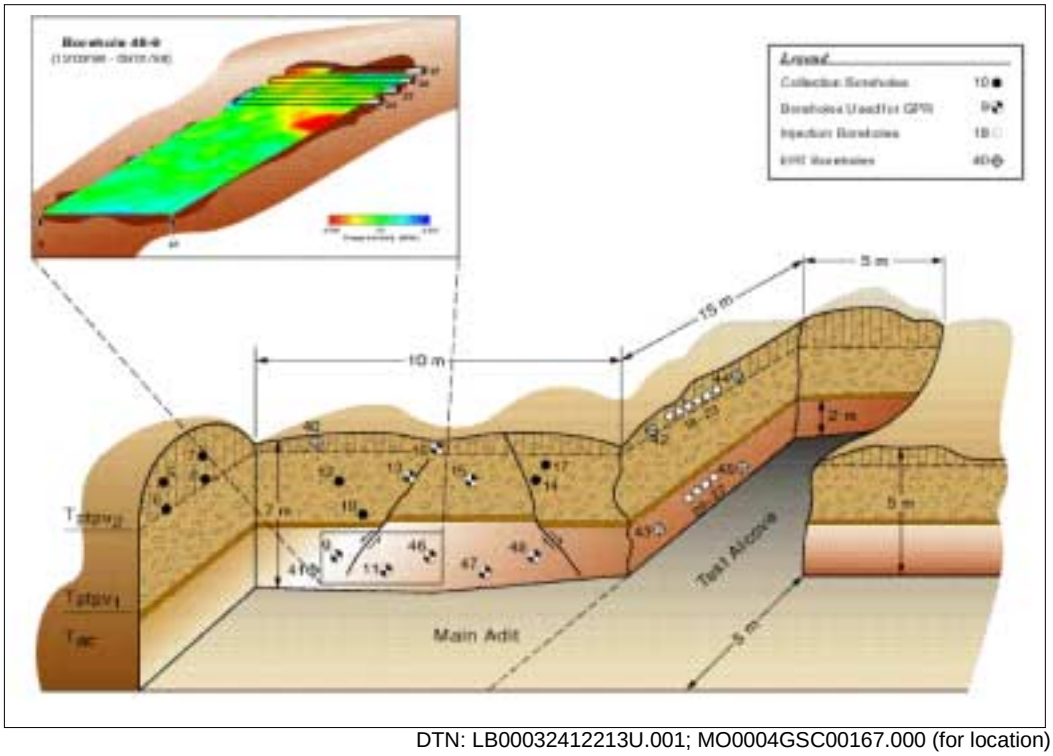

DTN: LB00032412213U.001; MO0004GSC00167.000 (for location)

Figure 48. Tomography (GPR-T) Results for Well Pair 46-9, December 1998.

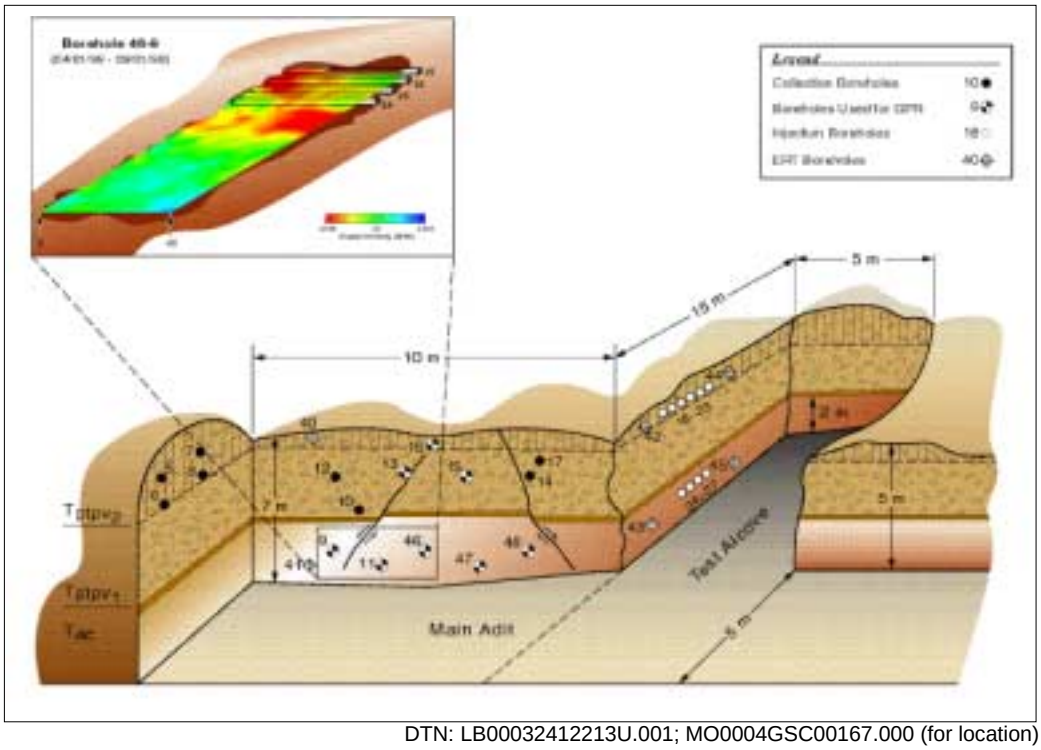

DTN: LB00032412213U.001; MO0004GSC00167.000 (for location)

Figure 49. Tomography (GPR-T) Results for Well Pair 46-9, April 1999.

The results implied by the radar tomograms are in concurrence with the tracer breakthrough logs for boreholes 46 and 9. Again, those zones of decreased velocity overlay those locations in the boreholes where tracer has been seen to break through. The additional contribution of the moisture front relative to the tracer (as described above for well pair 46-16) does not appear to be as significant for this horizontal well pair. It is not yet clear whether this is because the region imaged is smaller or spatially closer to the injection boreholes.

Well Pair 15-13

This well pair represents a horizontal slice (approximately 9.5 m in length and 2.0 m in width) through the block and images the tracer/moisture front associated with the upper injection boreholes. Figure 50 represents one time step throughout the course of the experiment (dates of data acquisition are noted above each tomogram). As can be seen, decreases in the velocity relative to the baseline (August-September 1998) data are immediately obvious surrounding the upper injection boreholes (these locations are marked on the tomogram as orthogonal tubes). Furthermore, the zones of decreased velocity can be seen to expand away from the injection boreholes over time in a horizontal direction. What is observed is that the decrease in velocity (i.e., the increase in moisture content), moves steadily away from the injection boreholes throughout the course of the experiment. This varies a bit from the analogous well pair 46-9. Rather than reaching a maximum extent, the moisture front appears to be continually expanding away from the boreholes. This is probably the result of the well pair's increased distance beneath the injection boreholes and the much larger volume of fluid being introduced by the upper injection boreholes.

The results implied by the radar tomograms are in concurrence with the tracer breakthrough logs for boreholes 15 and 13. Again, those zones of decreased velocity overlay those locations in the boreholes where tracer has been seen to break through. The additional input of the moisture front relative to the tracer (as described above for well pair 46-16) does not appear to be as significant for this well pair. As for well pair 46-9, it is not yet clear whether this is because the region imaged is smaller or spatially closer to the injection boreholes. Also, the much larger volume of tracer injected into the region of this well pair may account for the lack of a discrepancy (i.e. there is simply more tracer in the area of the collection boreholes). Additionally, the neutron probe data collected in these two boreholes implies a very similar pattern of elevated moisture content. Those zones that appear to be wetting as well as those that remain dry agree nicely with the same regions on the tomograms. The ERT data in this region appear to indicate an area of changing resistivity with time. It remains to be seen if this anomalous zone of resistivity correlates with the zone of decreased velocity imaged by the radar tomograms. Further analysis is planned to resolve this issue.

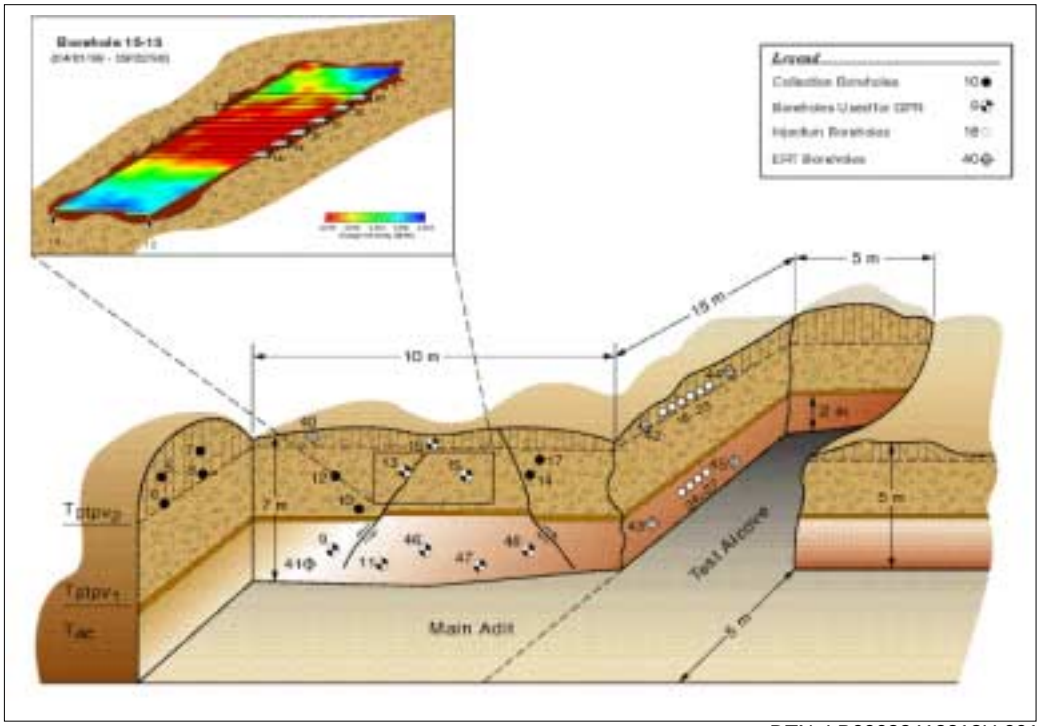

DTN: LB00032412213U.001

Figure 50. Tomography (GPR-T) Results for Well Pair 15-13, April 1999

6.8.4.1.5 Conclusions

The radar data collected thus far in support of the Busted Butte UZTT suggest that the method is an appropriate one for investigating subsurface velocity anomalies that may be related to tracer injection and moisture migration. Such anomalies are the result of changes in the dielectric permittivity of the rock mass. As noted above, such changes are most likely the result of some combination of the injected tracer and its associated fluid component. The regions of low velocity (i.e. elevated moisture content) appear to be in very close agreement with the other complementary evidence, including the tracer breakthrough logs and the neutron logging results. At this time, it appears very likely that the differenced radar tomograms are defining the total extent of elevated moisture content within those zones defined by the radar well pairs. By defining the extent of this front, the radar tomography should provide an excellent control mechanism for any planned excavation of the Phase-2 block or any hydrologic flow modeling done to date.

6.8.4.2 Electrical-Resistance Tomography

6.8.4.2.1 Experimental Objective

The objective of this work is to provide 3-D electrical-resistance tomography (ERT) images of the movement of a tracer through the test block at the UZTT at Busted Butte. ERT was chosen as an appropriate technology based on its success at many other locations, including the Drift Scale Test at Yucca Mountain. This report describes the results obtained during four separate data collections starting in July and ending in early September 1998.

6.8.4.2.2 Description of the Electrical-Resistance Tomography Method

Electrical-resistance tomography (ERT) is a new geophysical imaging technique that can be used to map subsurface liquids as flow occurs during natural or man-induced processes and to map geologic structure. Man-induced processes, such as tank leaks and clean-up processes such as steam injection, can create changes in a rock's electrical properties that are readily measured. ERT is a technique for reconstruction of subsurface electrical resistivity. The result of such a reconstruction is a 2- or 3-D map of the electrical resistivity distribution underground made from a series of voltage and current measurements from buried electrodes. The ERT approach we follow here relies on detection and mapping of the changes in electrical resistivity associated with the movement of a tracer through the test block at the UZTT site.

ERT surveys are performed using a number of electrodes in boreholes and/or at the rock surface to image the resistivity distribution between two boreholes. Using an automatic data-collection and switching system, we collect a few hundred electrical-resistance measurements. The data are then processed to produce electrical-resistivity tomographs using state-of-the-art data-inversion algorithms. We use these measurements to calculate tomographs that show the spatial distribution of the subsurface resistivities.

6.8.4.2.3 Description of 2-D Algorithms

Finite-element Iterative Algorithm

This algorithm involves solving both the forward and inverse problems. The forward and inverse algorithms used in this work are described in detail by LaBrecque et al. (1996, pp. 538–548) and summarized below. The solution to the forward problem uses the finite-element method (FEM) to compute the potential electrical response of a 2-D earth to a 3-D source. To avoid the difficulty of numerically solving a 3-D problem, Poisson's equation is formulated in the wave-number domain using the Fourier transformation in the strike (y) direction. The governing equation is:

$$\frac{\partial}{\partial x}\left(\sigma\frac{\partial V}{\partial x}\right)+\frac{\partial}{\partial z}\left(\sigma\frac{\partial V}{\partial z}\right)-\lambda^2\sigma V=-I\delta(x)\delta(z), \qquad \text{(Eq. 25)}$$

where V is the potential in the Fourier transform domain, σ is the conductivity, λ is the Fourier-transform variable, I is the source current, and $\delta(x)$ is the delta function.

Using the FEM, we can calculate the potentials for a discrete number of transform variables at the nodes of a mesh of quadrilateral elements. We can then transform the potentials back into the Cartesian domain. The boundary conditions are assumed to be Neumann (zero potential gradient, no vertical current flow) at the ground-air interface and Dirichlet (potential set to zero) along the other three boundaries.

The inverse algorithm iteratively finds the maximum value of the stabilization parameter α to minimize the objective function for the stabilization parameter:

$$Y(\mathbf{P})=\chi^2(\mathbf{P})+\alpha W(\mathbf{P}) \qquad \text{(Eq. 26)}$$

where **P** is the vector of unknown parameters, $W(\mathbf{P})$ is the roughness operator, and χ^2 is the chi-squared statistic. Minimizing this function yields a value of $\chi^2(\mathbf{P})$ equal to an a-priori value, $\chi^2_{\text{a-priori}}$, which in our work, is assumed to equal the number of data points. The inverted parameters are the natural logarithms of the conductivities of pixels, where each pixel contains the elements of a rectangular region of a FEM mesh. The chi-squared statistic is given by:

$$\chi^2 = \left[\mathbf{D} - \mathbf{F}(\mathbf{P})\right]^{\mathrm{T}} \mathrm{W}^{-1} \left[\mathbf{D} - \mathbf{F}(\mathbf{P})\right] \qquad \text{(Eq. 27)}$$

where **D** is the vector of known data values, $\mathbf{F}(\mathbf{P})$ is the forward solution, T signifies transpose, and **W** is the data covariance matrix.

The roughness operator stabilizes and removes ambiguity in the resistivity inversion by minimizing the model roughness, which is referred to as "smoothest inversion." The roughness operator $W(\mathbf{P})$ is given by:

$$W(\mathbf{P}) = \mathbf{P}^{\mathrm{T}} \mathbf{R}(\mathbf{P}) \ , \qquad \text{(Eq. 28)}$$

where, here, **R** is the roughness matrix.

At the *ith* iteration, our algorithm begins by approximating the forward solution by a first-order Taylor's series of the form:

$$\mathbf{F}(\mathbf{P}) = \mathbf{F}(\mathbf{P}_i) + \mathbf{A}(\mathbf{P} - \mathbf{P}_i), \qquad \text{(Eq. 29)}$$

where **F(P)** is the forward solution, **A** is the sensitivity matrix, and $\mathbf{P}_i$ is the vector of estimated parameters at the *i*th iteration.

Using a root-finding algorithm, we estimate α for this linearized system. We then use a modified Marquardt method iteration to find the parameters that minimize the objective function (Equation 26) for the estimated value of α. Iteration is repeated until the changes in α and χ^2 from one iteration to the next are suitably small.

Single-pass Image Reconstruction

The computational demands and potential convergence failure of a formal inverse solution such as that above has prompted the development of a number of image-reconstruction algorithms that are purely qualitative. We use an algorithm that computes a "gray scale" associated with each element j =1, 2, ... m according to a simple matrix-vector product:

$$\mathrm{P}j = \sum_{i=1}^{n} S_{i,j} \ln(\mathrm{T}'_i / \mathrm{T}_i) \qquad j = 1, 2, \ldots. m \qquad \text{(Eq. 30)}$$

where n is the number of independent measurements, T_i and T'_i are the *i*th-measured boundary transfer resistances before and after a change in resistivity within the region, and $S_{i,j}$ is a sensitivity coefficient for element j and independent measurement i derived in the same manner as the smoothness algorithm in the previous section.

The sensitivity matrix is computed on a finite-element mesh with uniform resistivity. Because no inverse matrices are required, the algorithm is computationally efficient and very fast as only one matrix vector product is required for each image.

6.8.4.2.4 Description of the 3-D Imaging Algorithm

Our 3-D inversion algorithm requires a forward solution, which can numerically solve the potential equation:

$$\frac{\partial}{\partial x}\left(\sigma\frac{\partial}{\partial x}V\right)+\frac{\partial}{\partial y}\left(\sigma\frac{\partial}{\partial y}V\right)+\frac{\partial}{\partial z}\left(\sigma\frac{\partial}{\partial z}V\right)=I(x,y,z)\,, \qquad \text{(Eq. 31)}$$

where V is the scalar electrical potential and $I(x,y,z)$ is the distribution of electrical current sources and sinks. We convert the differential equation (Equation 25) into a system of linear equations. This system of equations is then solved iteratively using the diagonally weighted preconditioned-conjugate-gradient method. The boundary conditions are assumed to be Neumann (zero potential gradient, no vertical current flow) at the ground-air interface and Dirichlet (potential set to zero) along the other five boundaries.

Three-dimensional inversion is by nature strongly underdetermined, and so, inverse solutions that consider only the fitting of the forward model to field data are nonunique. Therefore, we implemented a regularized solution that jointly minimizes the misfit of the forward model to the field data and stabilizes the inverted value of the parameters. To find the optimal value of the parameter vector **P**, our algorithm finds the maximum value of α, the stabilization parameter, for which minimizing:

$$Y(\mathbf{P}) = \chi^2(\mathbf{P}) + \alpha\ \mathbf{P}^{\mathsf{T}}\underline{\mathbf{R}}\mathbf{P} \qquad \text{(Eq. 32)}$$

gives

$$\chi^2(\mathbf{P}) = \chi^2_{\text{a-priori}} \qquad \text{(Eq. 33)}$$

In Equation 32, we have chosen to use, $\underline{\mathbf{R}}$, the solution roughness, as the stabilizing functional. This parameter is approximated by:

$$\underline{\mathbf{R}} = \underline{\mathbf{x}}^{\mathsf{T}}\underline{\mathbf{x}} + \underline{\mathbf{y}}^{\mathsf{T}}\underline{\mathbf{y}} + \underline{\mathbf{z}}^{\mathsf{T}}\underline{\mathbf{z}}\ , \qquad \text{(Eq. 34)}$$

where $\underline{\mathbf{x}}$, $\underline{\mathbf{y}}$, and $\underline{\mathbf{z}}$ are the first-order difference operators in the x, y, and z directions. Also in Equation 33, $\chi^2_{\text{a-priori}}$ is equal to the number of data points, and χ^2 is given by:

$$\chi^2 = (\mathbf{D} - \mathbf{F(P)})^{\mathsf{T}}\underline{\mathbf{W}}(\mathbf{D} - \mathbf{F(P)})\ , \qquad \text{(Eq. 35)}$$

where **D** is the vector of known data values, **F(P)** is the forward solution and $\underline{\mathbf{W}}$ is a data weight matrix. The diagonal elements of $\underline{\mathbf{W}}$ are the reciprocals of the data variances and the nondiagonal elements are zero. This assumes noncorrelated data errors.

The parameters, **P,** are the natural logarithms of the conductivity of the FEM elements. In the foreground (the part of the FEM mesh between the boreholes and near the boreholes), each parameter corresponds to a single finite element. In the background (the region away from the boreholes), we lump several finite elements together into a single parameter.

The nonlinear inversion is carried out iteratively as:

$$\mathbf{P}_{k+1} = \mathbf{P}_k + \Delta\mathbf{P}_k \ , \qquad \text{(Eq. 36)}$$

where $\mathbf{P}_k$ is the vector of parameters from the previous iteration and $\Delta\mathbf{P}_k$ is the parameter change vector. The $\Delta\mathbf{P}_k$ vector is found by solving the linear problem:

$$\Delta\mathbf{P}_k = \left(\underline{\mathbf{A}}_k^{\mathsf{T}}\,\mathbf{W}\,\underline{\mathbf{A}}_k + \alpha\underline{\mathbf{R}}\right)^{-1}\left(\underline{\mathbf{W}}\,\Delta\mathbf{D}_k - \alpha\mathbf{R}\,\mathbf{P}_k\right) , \qquad \text{(Eq. 37)}$$

where $\underline{\mathbf{A}}_k$ is the sensitivity matrix and $\Delta\mathbf{D}_k = \mathbf{F(P)} - \mathbf{D}$. The elements of the sensitivity matrix, $a_{i,j}$, are:

$$a_{i,j} = \frac{\partial F_i(\mathbf{P}_k)}{\partial p_j} \ , \qquad \text{(Eq. 38)}$$

where p_j is the jth element of $\mathbf{P}_k$ and $F_i(\mathbf{P}_k)$ is the forward solution for the ith data point. Solving Equation 37 exactly is not practical because the system is very large (50,000 by 50,000), full, and ill-conditioned. Instead, we use the conjugate-gradient method described by Mackie and Madden (1993, pp. 215–219) to give a stable, approximate solution to this linear system. The details will not be repeated here, but note that the solution does not require the calculation of the full sensitivity matrix, only the calculation of the sensitivity matrix and its transpose multiplied by a vector.

Our routine differs from that of Mackie and Madden in three ways. First, we use a method similar to that described by Rodi (1976, pp. 483–506) to calculate $\underline{\mathbf{A}}^{\mathsf{T}}\mathbf{u}$ and $\underline{\mathbf{A}}\mathbf{v}$ where **u** and **v** are vectors. Since we calculate a forward model for every electrode, this method does not require any additional forward solutions during the conjugate gradient iterations. Second, we use more conjugate gradient iterations than Mackie and Madden (1993). For the magnetotelluric inverse problem, Mackie and Madden found that the nonlinear inversion routine converged well with three conjugate gradient iterations. We usually require between 10 and 40 conjugate gradient iterations to achieve adequate convergence. Third, we use smoothness instead of comparison with an a-priori model to stabilize the inverse solution.

We found that choosing the correct value of α is critical for both achieving rapid convergence of the nonlinear inversion and for finding a good final parameter estimate. With our method, a new value of α is estimated at the end of each nonlinear iteration. The estimate uses the assumption that the relation between χ^2 and α can be approximated by the rational function:

$$\chi^2 \cong \frac{b\,\alpha}{\alpha + a} \ . \qquad \text{(Eq. 39)}$$

The constant a is estimated from the values of α and χ^2 of the previous iteration. If the misfit is χ^2_k and the desired misfit is χ^2_{target}, then the new estimate of α, α_{k+1}, is:

$$\alpha_{k+1} = \frac{\dfrac{b}{\chi_k^2} - 1}{\dfrac{b}{\chi_{\text{target}}^2} - 1}\,\alpha_k \,. \qquad \text{(Eq. 40)}$$

The value of χ^2_{target} is chosen as the larger of $\chi^2_{\text{a-priori}}$ and $0.5\chi^2_k$.

Although the approach is simplistic, it usually converges to the correct value of χ^2 in 10 to 20 iterations.

6.8.4.2.5 Electrical-Resistance Tomography Data-Collection and Processing Codes

Computer codes are used for both data collection and processing/presentation. Figure 51 contains a block diagram flow chart summarizing these codes and a description of how they are used.

6.8.4.2.6 Electrical-Resistance Tomography Data-Collection System

As shown in the block diagram of Figure 52, the data-collection system is composed of three main parts: a transmitter, a receiver, and a laptop computer to control the system and archive the data. The action of the system can be described briefly, as follows. The computer sets the switches in the MX-30 multiplexer according to a predefined schedule so as to connect the transmitter to a particular electrode pair and the receiver channels in the GDP-32 receiver to other sets of electrode pairs. The GDP-32 tells the ZT-30 to apply current to the transmitter pair and measures the resulting potentials at the other pairs. The data are then sent back to the computer and stored. A new transmitter pair is selected according to the schedule, and the process begins again until all the combinations in the schedule have been used.

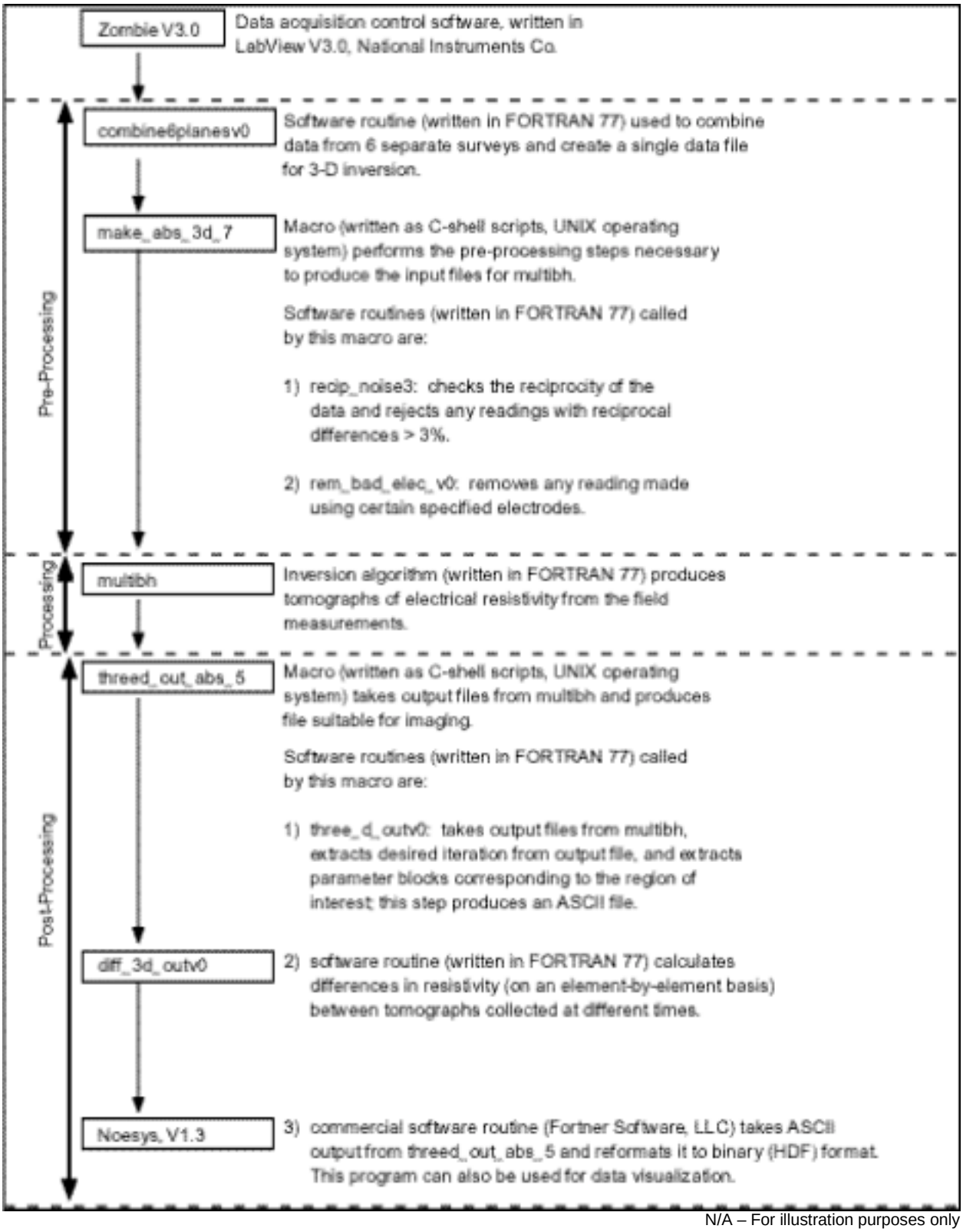

N/A – For illustration purposes only

Figure 51. Flow Chart of Computer Codes Used for Electrical-Resistance Tomography Data Collection and Processing at Busted Butte

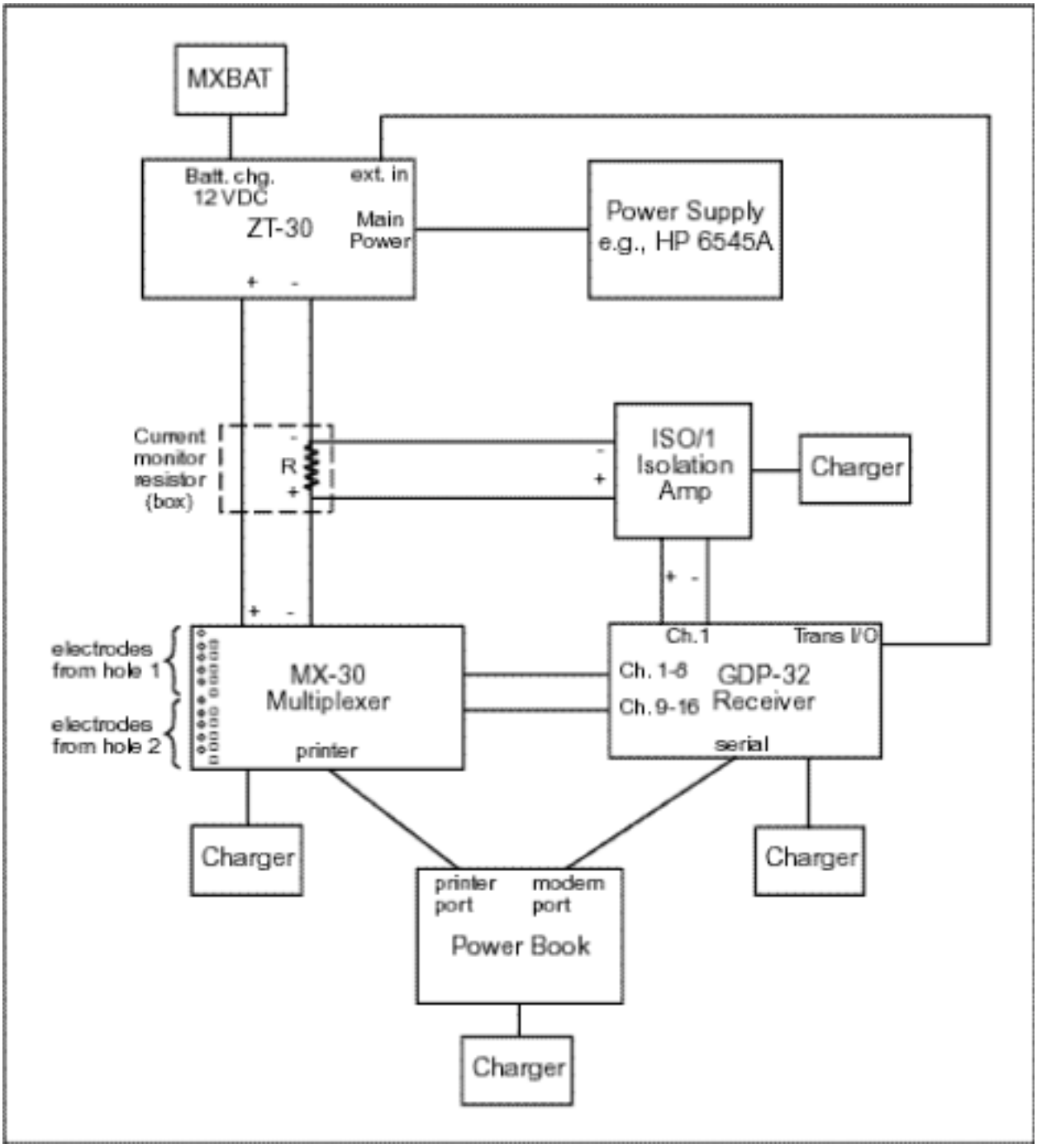

N/A – For illustration purposes only

NOTE: This block diagram illustrates the ERT data-collection system used at Busted Butte.

Figure 52. Electrical-Resistance Tomography Data-Collection System

6.8.4.2.7 Results of Data Collections—July to Early September

ERT data were collected four times: July 2, July 14, August 19, and September 9, 1998. The intent was to make comparisons between the baseline condition on July 2 and data collected at later times. Comparisons between July 2 and August 19 and between July 2 and September 9 are presented because the data from July 14 were of questionable quality. These data have been submitted to the YMP Technical Data Management System (DTN: LL990612704244.098).

Sixty ERT electrodes were installed in the test block as shown in Figure 53. The electrodes were placed in six drilled holes, ERT-1 though ERT-6, and two surface arrays (upper and lower). Holes ERT-3, 4, 5, and 6 and the surface arrays were drilled perpendicular to and from the instrumentation alcove. Holes ERT-1 and 2 were drilled from the main drift. The electrodes were grouped into boreholes 1 through 4 as shown in Figure 54. As is evident, each borehole is L-shaped and contains 15 electrodes. For example, borehole 1 is composed of the 8 electrodes in hole ERT-3 along with the 7 electrodes in the upper-surface array.

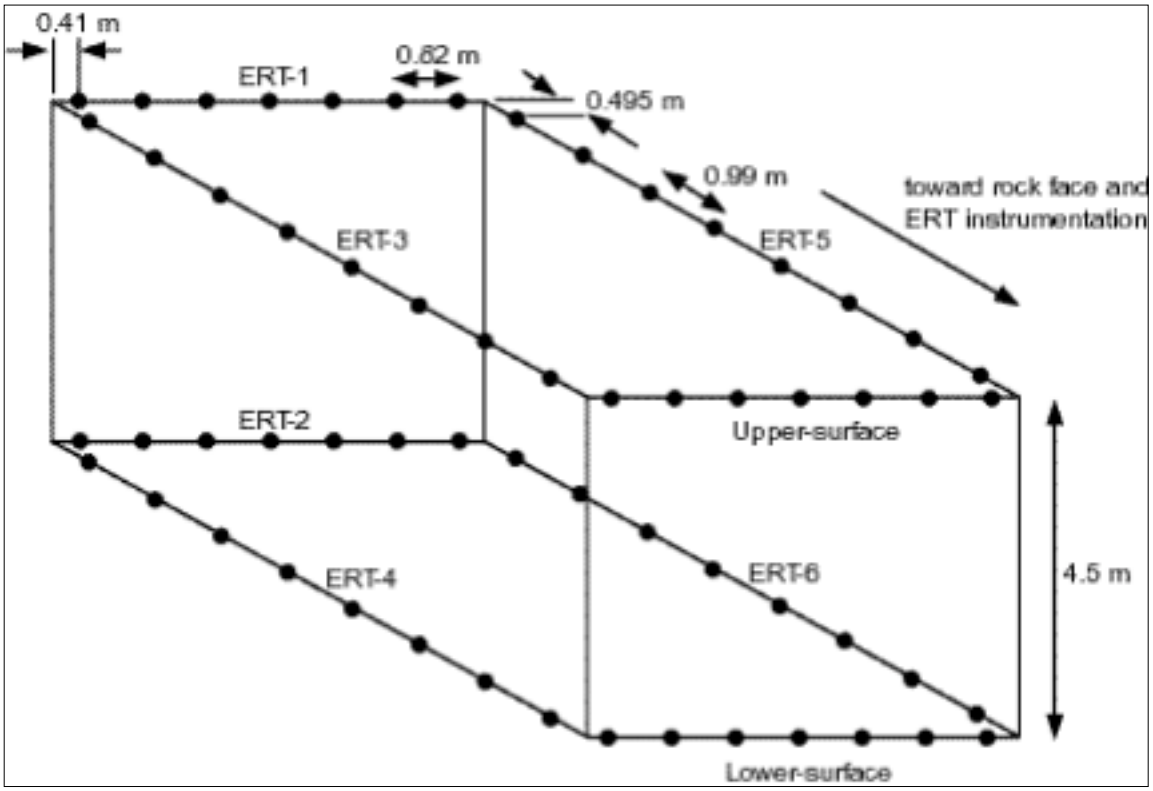

N/A - For illustration purposes only

NOTE: This diagram gives the layout of drilled holes, ERT electrode locations, and spacing in the UZTT test block at Busted Butte.

Figure 53. Electrical-Resistance Tomography Layout

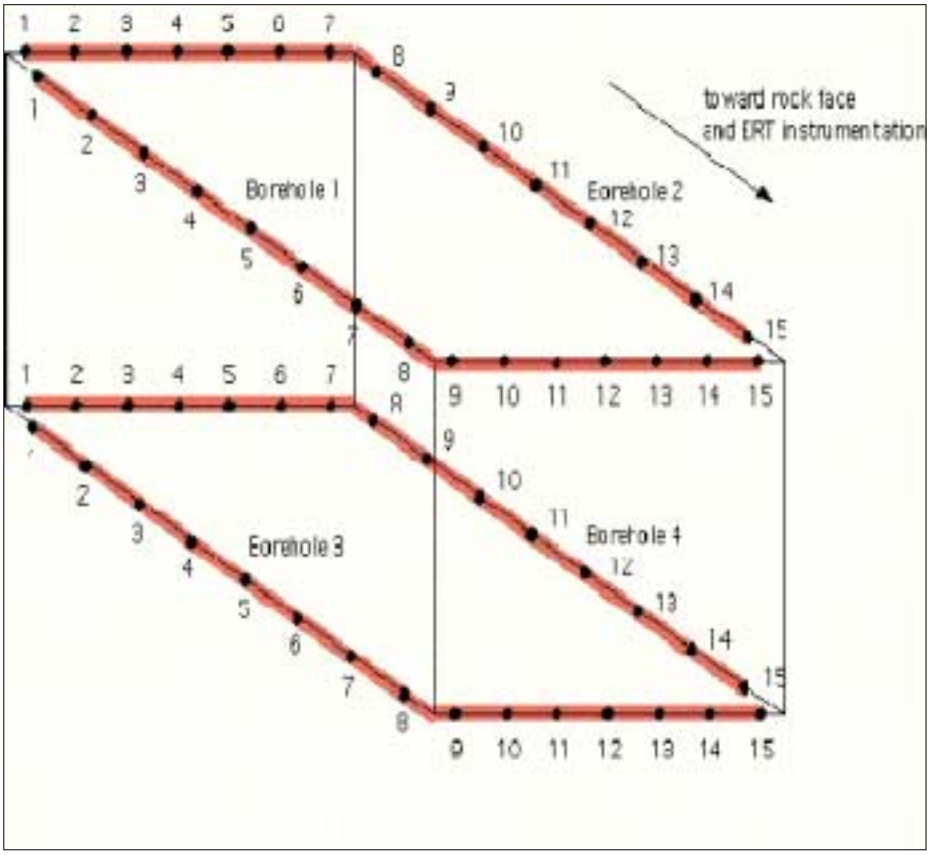

N/A – For illustration purposes only

NOTE: This diagram gives the layout of the ERT boreholes and electrode assignments in the UZTT test block at Busted Butte.

Figure 54. Electrical-Resistance Tomography Electrode Assignments

The ERT data are collected between borehole pairs. Thus, the data are collected between boreholes 1 and 2 (upper horizontal plane), 3 and 4 (lower horizontal plane), 1 and 3 (left vertical plane), 2 and 4 (right vertical plane), 1 and 4 (diagonal), and finally 2 and 3 (diagonal) for a total of six data sets. The total number of data values collected is 2430. These 2430 values provide the 3-D sampling of the test block resistivity, and the 3-D inversion algorithm operates on these data to produce a reconstruction of the 3-D resistivity distribution, a 3-D ERT image, of the block.

One could look at absolute ERT images or comparison images. It is most useful to look at comparison images when changes are taking place over time. The results presented here consider difference images that compare the resistivity of the block on August 19 and September 9 to July 2. Because the water injected during Phase 2 of the UZTT experiment was approximately eight times more conductive than the pore water, resistivity decreases in the images are of interest.

6.8.4.2.8 Absolute Electrical-Resistance Tomography Images of the Block

Figure 55 shows an absolute image of the baseline condition of July 2 (top) and the difference between August 19 and July 2 (bottom). The baseline image shows a layered structure consistent with the lithology in the rear half of the block. That is, a high-resistivity layer over most of the middle of the block, Tptpv1, with a lower-resistivity region, Tptpv2, at the top, and a low-resistivity region, Tac, at the bottom. The image also shows an anomalously low resistivity region in the front half of the block, particularly near the bottom.

6.8.4.2.9 Difference Electrical-Resistance Tomography Images of the Block

The difference image of Figure 55 shows regions of resistivity decrease near injection holes 18, 20, and 21, as one would expect from the injection of conductive water. It is apparent that a pronounced resistivity decrease exists in the slice 2.66 m from the front of the block, which could be associated with water moving downward in the block. The region of the block between 1.33 and 4.0 m, which contains this slice, also appears to be a low-resistivity region in the absolute image.

The September 9 to July 2 difference (Figure 56) also shows regions of resistivity decrease near injection holes 18, 20, and 21. The effect is even stronger in the 5.33-m slice. Moreover, the effect of water moving down into the block seems to be more pronounced in the 4.0-m slice compared to August 19.

6.8.4.2.10 Conclusions

The ERT baseline images show a resistivity structure that is consistent with the known lithology in the rear part of the block. There appears to be a low-resistivity region in the front half of the block, particularly near the bottom. This is not well understood and should be confirmed, if possible, by other means.

The difference images from August 19 and September 9 show clear and consistent resistivity decreases in the region near holes 18, 20, and 21 that can be associated with the injection of conductive water. This effect appears to be stronger on September 9 in the 5.33-m slice. The images show very little effect in the region around the other injection holes, 23 and 24 through 27, where far less water was injected.

In addition, the difference images from August 19 and September 9 show resistivity decreases that could be interpreted as water moving down into the block between the 1.33-m and 4.0-m slices. This is the same region that has an anomalously low resistivity in the baseline image.

These results should be considered preliminary and subject to change based on new information, such as borehole radar data and, perhaps, neutron data.

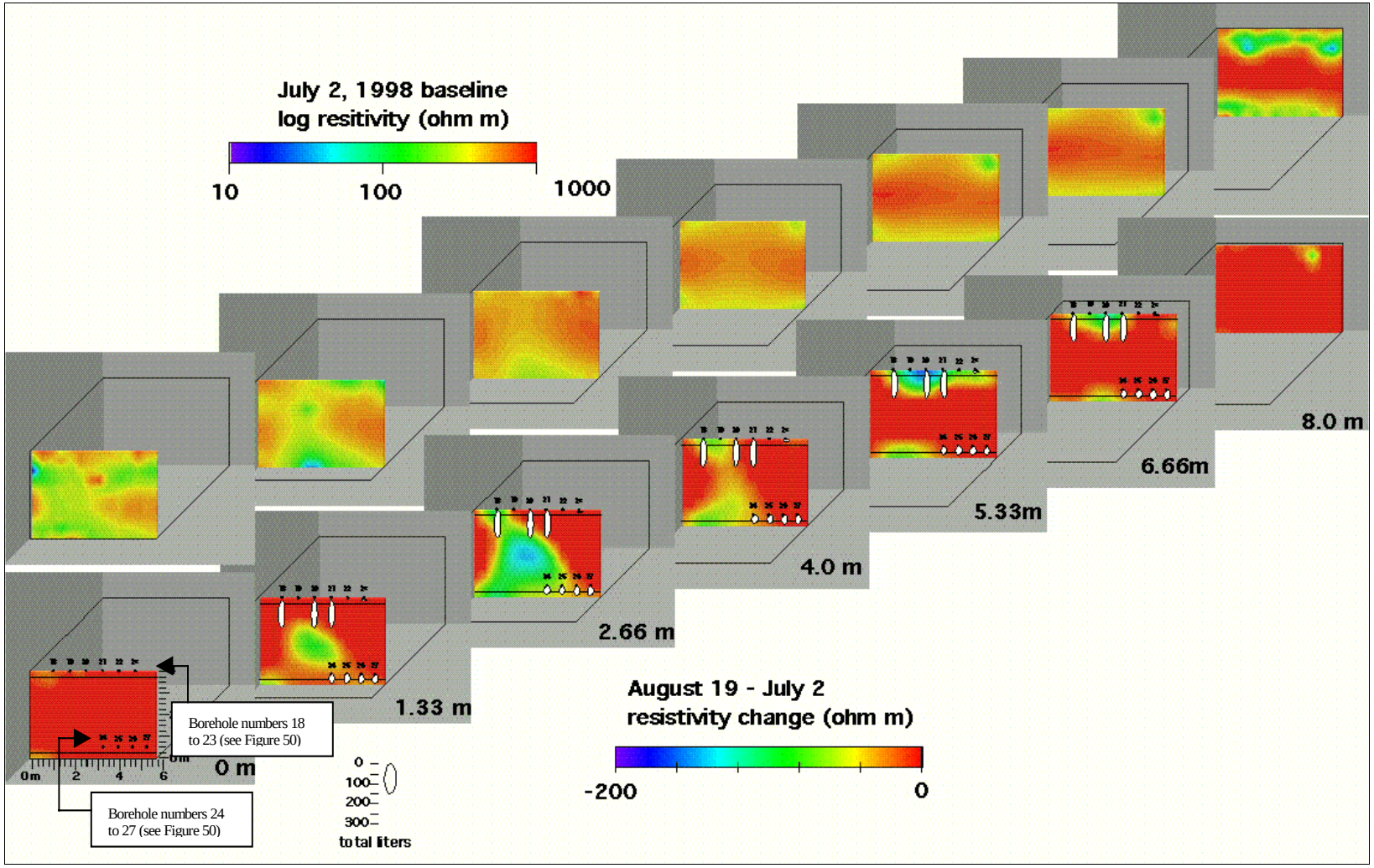

DTN: LL990612704244.098

NOTE: The diagram shows vertical slices through block at 0, 1.33 2.66, 4.0, 5.33,6.66, and 8.0 m. The top series is an absolute image (baseline, July 2), and the bottom series is the August 19–July 2 difference images.

Figure 55. Electrical-Resistance Tomography Images of Test Block Viewed from Test Alcove: Baseline and August Differences

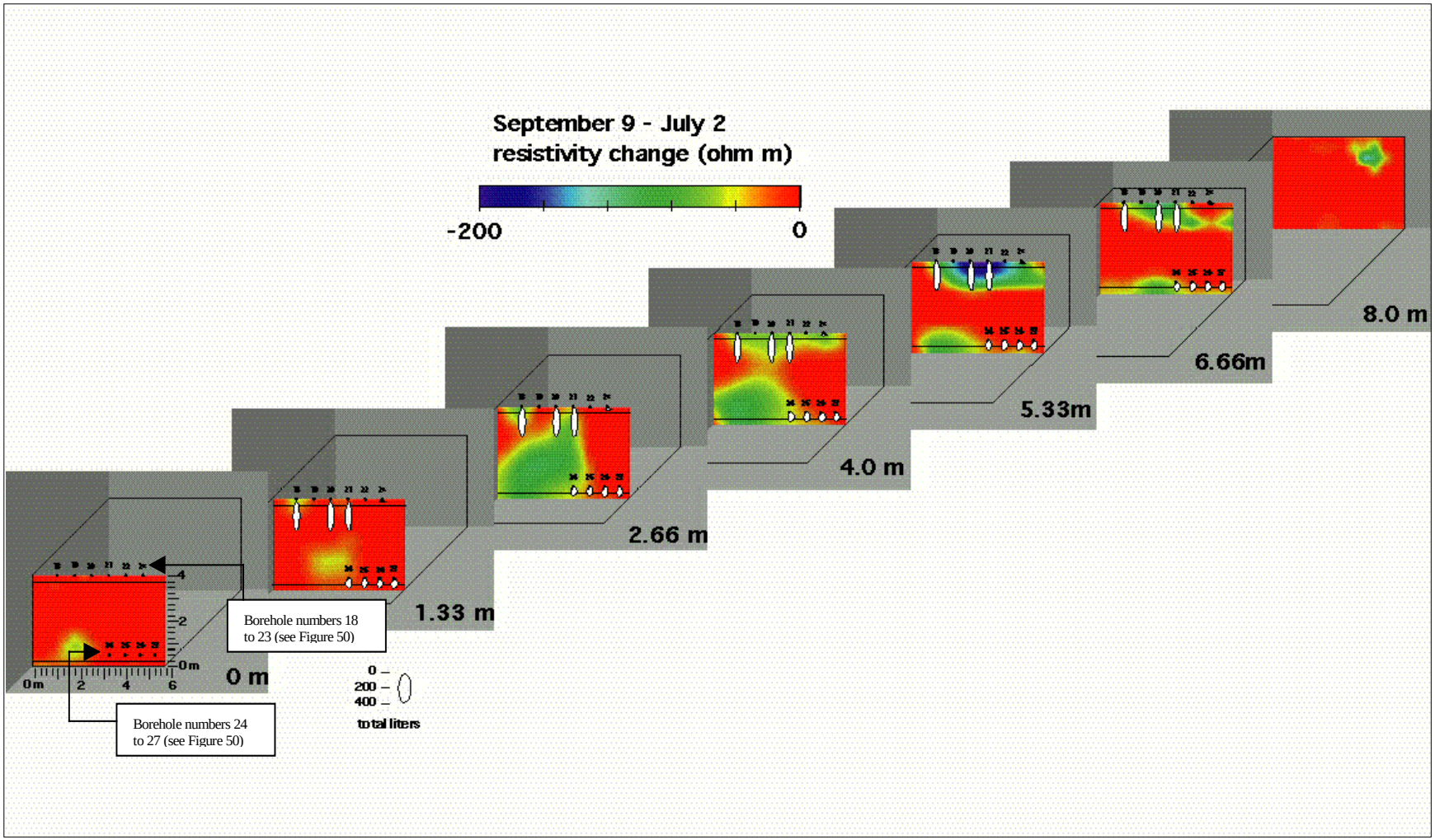

DTN: LL990612704244.098

NOTE: The diagram shows vertical slices through the block at 0, 1.33, 2.66, 4.0, 5.33, 6.66, and 8.0 m that represent September 9–July 2 difference images.

Figure 56. Electrical-Resistance Tomography Images of Test Block Viewed from Test Alcove: September Differences

6.8.5 Geochemistry and Tracer Migration - Laboratory and Field Tests

This section discusses all aspects of chemical and geochemical measurements that have been conducted in association with the Busted Butte project. These include laboratory measurements of sorption of both radionuclides and tracers onto Busted Butte rock samples, measurements of in-situ pore-water chemistry used in formulating the field tracer mixture, and measurements of field-scale tracer transport.

6.8.5.1 Laboratory Sorption Studies

As discussed in Section 6.8.2.4, analog conservative and reactive tracers are used as surrogates for radionuclides. To validate the use of these tracers and the site-scale use of the minimum-K_d approach for sorption and the processes of matrix diffusion and colloid migration, a series of laboratory batch-sorption studies have been conducted. Preliminary tracer sorption studies used in tracer selection are complete, detailed radionuclide sorption studies are complete, and detailed tracer sorption studies are in progress. Each type of study will be discussed in turn.

6.8.5.1.1 Preliminary Studies

A large number of possible tracers were proposed in the Busted Butte work plan. Final determination of tracer selection and concentration was dependent on both rock and pore-water characteristics. Rock and pore-water samples became available in early 1998, and a set of fast-turnaround batch studies and geochemical modeling efforts were initiated.

Preliminary batch-sorption studies were conducted using proposed reactive tracers and two rock samples from the Main Adit at Busted Butte. Tracers tested included lithium, manganese, cobalt, nickel, molybdate, and perrhenate (this list differs from the final list of tracers used in the field and described in section 6.8.2.4.1 and 6.8.2.4.2); rocks were samples of the Calico Hills (Tac) and Topopah Spring (Tptpv2) from Phase-1 boreholes 4 and 7. The results of the preliminary sorption studies for lithium, manganese, cobalt, and nickel are presented in Table 26. The results indicate that the Tac sample sorbed the metals more strongly than the Tptpv2 sample and that, on both samples, the metals showed a consistent sequence of sorption: Li << Mn << Ni < Co. Based on these results, all four of these metals show significant sorption and may be useful reactive tracers in the field. Neither of the proposed pertechnetate analogues (molybdate and perrhenate) displayed any significant sorption and were, therefore, eliminated from further consideration in our testing.

Table 26. Preliminary Measured Sorption Coefficients

Rock sample	Measured K_d (mL g^{-1})			
	Li	Mn	Co	Ni
Tac (Phase 1, borehole 4)	≤ 1	16	38	34
Tptpv2 (Phase 1, borehole 7)	≤ 1	6	14	13

DTN: LA9909WS831372.011

6.8.5.1.2 Detailed Studies

6.8.5.1.2.1 Sample Description

Three core samples were selected for detailed sorption and mineralogic characterization. These samples are described in Table 27. These rock samples were uniformly ground, sieved, and homogenized, and subsamples were used for radionuclide sorption, tracer sorption, and quantitative x-ray diffraction studies (QXRD).

Table 27. Sorption Mineralogy Samples

Sample Source	Sample Name	Short Name	Geologic Unit
Phase 1A, borehole 3	UZTT-BB-PH1-3	PH1-3	Tptpv1
Phase 1A, borehole 4	UZTT-BB-PH1-4	PH1-4	Tac
Phase 1B, borehole 7	UZTT-BB-PH1-7	PH1-7	Tptpv2

NOTE: Borehole locations and lithology are from Figures 37 and 38.

6.8.5.1.2.2 Radionuclide Sorption

The sorption of Np, Pu, and Am to the three Busted Butte rock samples was measured at five different concentration levels; each measurement was conducted in duplicate. The radionuclide sorption studies were completed in fiscal year 1999, and the results are summarized in Table 28.

Table 28. Summary of Radionuclide Sorption Results

Sample	Approximate Average K_d (mL g^{-1})		
	Np	Am	Pu
PH1-3	0.3	380	19
PH1-4	1.4	470	2500
PH1-7	1.1	460	1100

DTN: LA0004WS831372.002

6.8.5.1.2.3 Tracer Sorption

Laboratory batch measurements of the sorption of the field tracers onto the same three rock samples were begun in fiscal year 1999. The laboratory procedures and the chemical analysis of the sorption supernatant are underway.

6.8.5.1.2.4 Quantitative X-ray Diffraction

QXRD analysis have been obtained for subsamples of the same three rock samples (DTN: LA9910WS831372.009).

6.8.5.2 In-Situ Pore-Water Chemistry

Field-scale transport behavior is primarily a function of the ambient flow field and the interactions between the geologic host and the material being transported. Secondary influences include details of the pore-water chemistry, including pH, Eh, ionic strength, and chemical composition. Changes in any of these variables may affect solute sorption behavior and colloid stability and may lead to dissolution or precipitation of minerals resulting in permeability changes. These considerations lead to a fundamental conflict in field-tracer studies. Alteration of the in-situ water chemistry should be limited to minimize the artificial perturbations introduced by chemistry variations. Introduction of any artificial tracer will inherently alter water chemistry. (One exception might be the use of miniscule amounts of isotopic tracers—not a practical alternative at this phase of the Busted Butte studies.)

The plan at Busted Butte was to introduce artificial tracers in a matrix designed to mimic natural pore-water chemistry as closely as practical, acknowledging that some alterations were inevitable. Accordingly, pore-water samples from rock cores collected in the Adit were analyzed, a recipe for "synthetic" Busted Butte water that closely resembled the in-situ chemistry was developed, and this synthetic water was used as our injection matrix. Results of the chemical analyses are presented here, and details of the synthetic water recipe are presented in Section 6.8.2.4.3.

A set of rock samples were collected in the Test Alcove on January 30, 1998. These samples were collected from the Tac horizon by hand augering and immediately sealed. A series of samples were collected in sequence, starting with sample 3A at the Adit wall, extending to Sample 3U, 1.93 m away from the tunnel into the wall.

Pore water was extracted from a subset of these samples by ultracentrifugation. Gravimetric moisture contents of the rock samples were determined by weight difference upon drying, and the chemical composition of the extracted pore water was determined using standard ion chromatography (IC) and inductively coupled-plasma/atomic-emission spectrometry (ICP/AES). Full results are presented in Table 29. Note that the IC analyses involve a bicarbonate buffer and, thus, no direct measurement of bicarbonate is possible. The bicarbonate concentrations listed in Table 29 are estimated by charge balance.

The results in Table 29 show that the pore water is a mixed-ion water (Ca-Na-HCO_3-SO_4) with an average total dissolved solids (TDS) of approximately 200 mg L^{-1}. Compared to more typical groundwater compositions, the pore water shows high nitrate (probably due to soil biological activity) and high silica (due to relatively rapid equilibration with amorphous silica in the tuff). Sample 3B, from near the Adit wall, differs somewhat from the other samples, perhaps due to the influence of construction water and atmospheric CO_2 levels. The compositions of the other three pore-water samples were averaged (as shown in the table), and these average values were used to develop the synthetic pore-water recipe presented in Section 6.8.2.4.3.

Also listed in Table 29 are pH values measured on extracted pore water. Despite obvious opportunities for pH alteration due to CO_2 exchange during sample collection, extraction, and analysis, these pH values were the best available at the time of Phase-1 planning. Thus, Phase-1

tracer mixtures were pH-adjusted to a value of 8.4 ± 0.1. During Phase-2 installation, attempts were made to measure pH in situ by inserting pH paper into boreholes for a few days. Results were mixed but seemed to indicate lower in-situ pH values than those measured in the laboratory (consistent with degassing of excess soil CO_2 before lab analysis). Accordingly, Phase-2 tracer mixtures were pH adjusted to a value of 7.0 ± 0.1.

Table 29. Chemical Composition of Busted Butte Pore Water with J-13 Groundwater for Comparison

Constituent	Concentrations (mg L^{-1})					
	Sample 3B	**Sample 3N**	**Sample 3Q**	**Sample 3U**	**Average 3N – 3U**	**J-13 water**
Br	0.06	0.07	0.06	0.06	0.06	—
Ca	17.73	24.35	21.16	19.81	21.77	12.5
Ce	< 0.5	< 0.5	< 0.5	< 0.5	< 0.6	—
Cl	16.13	19.06	17.71	16.74	17.84	6.5
Co	< 1.0	< 1.0	< 1.0	< 1.0	< 1.1	—
F	2.36	1.82	1.85	1.41	1.69	0.53
Fe	< 0.1	< 0.1	< 0.1	< 0.1	< 0.2	< 0.05
HCO_3 (est.)	*33.0*	*52.7*	*45.6*	*40.6*	*46.3*	*137.2*
K	4.14	3.35	3.37	3.44	3.39	4.5
Li	0.11	0.11	0.10	< 0.1	0.10	< 0.1
Mg	3.20	4.13	3.64	3.19	3.66	2.1
Mn	< 0.5	< 0.5	< 0.5	< 0.5	< 0.6	< 0.01
Mo	< 1.0	< 1.0	< 1.0	< 1.0	< 1.1	—
Na	17.67	21.36	19.63	17.89	19.63	44.6
Ni	< 1.0	< 1.0	< 1.0	1.34	1.34	—
NO_3	22.76	26.48	22.62	20.99	23.36	1.3
PO_4	< 0.1	< 0.1	< 0.1	< 0.1	< 0.2	—
Re	< 1.0	< 1.0	< 1.0	< 1.0	< 1.1	—
Si	29.69	31.85	34.10	31.00	32.32	29.6
Sm	< 0.5	< 0.5	< 0.5	< 0.5	< 0.6	—
SO_4	31.29	33.63	31.36	30.08	31.69	18.6
Sr	0.37	0.49	0.42	0.38	0.43	—
TDS	178.5	219.4	201.6	186.9	203.6	257.4
pH	8.20	8.48	8.45	8.28	8.40	7.3–8.4
Gravimetric moisture content:	0.123	0.134	0.158	0.109	0.133	n/a

DTN: LA9909WS831372.015, LA9909WS831372.016, LA9909WS831372.017, LA9909WS831372.018

6.8.5.3 Field-Scale Tracer Transport

6.8.5.3.1 Phase 1A

6.8.5.3.1.1 Description

Phase 1A consisted of four 2-m injection boreholes (boreholes 1–4). The Phase-1A tracer mixture was described in Section 6.8.2.4.1. The tracer mixture was injected at 10 mL hr^{-1} in boreholes 1 and 3, and at 1 mL hr^{-1} in boreholes 2 and 4. Phase-1A injection ran continuously from April 2, 1998, until January 12, 1999. Mineback of the Phase-1A test block began on January 15, 1999, and ended on March 3, 1999. During mineback, as successive layers of the Adit wall were removed, digital photographs under visible and UV illumination were taken, rock samples were collected by augering, and the exposed face was accurately surveyed.

6.8.5.3.1.2 Results

The visualization of the tracer plume using UV illumination of the fluorescein tracer was very successful, and the digital imagery resulting from this effort serves as the primary result of Phase 1A. Detailed comparison of the digital plume imagery and numerical modeling results is underway and will be completed this year.

A small number of augered rock samples have been analyzed for bromide and moisture content (DTN: LA9910WS831372.008). Values from these analyses will be used for re-calibrating the Phase 1A model (Section 6.8.6 discusses the blind modeling results).

6.8.5.3.2 Phase 1B

6.8.5.3.2.1 Description

Phase 1B consisted of two 2-m injection boreholes (5 and 7) and two 2-m collection boreholes (6 and 8). The Phase-1B tracer mixture was described in Section 6.8.2.4.1. The tracer mixture was injected at 10 mL hr^{-1} in borehole 5 and at 1 mL hr^{-1} in borehole 7. Phase-1B injection began on May 12, 1998. Borehole 7 injection was terminated on November 9, 1998, and borehole 5 injection was terminated on November 18, 1998. Throughout the experiment, rock pore-water samples were collected at regular intervals using collection pads installed in boreholes 6 and 8. A total of 558 pad samples were collected and shipped to the laboratory for analysis.

At the conclusion of the experiment, overcoring of the Phase-1B boreholes was conducted as follows: moisture pad collection was conducted on collection hole 8 directly below injection hole 7 until injection shut down of hole 7 on November 9, 1998. Tracer injection and moisture pad collection was continued in holes 5 and 6 while two 10-inch-diameter overcores were drilled approximately tangential to one another with their centerlines in a vertical plane and contained in the area between the top of injection borehole 7 and the bottom of collection borehole 8. When injection hole 5 was shut down, three 10-inch-diameter overcores were drilled approximately tangential to one another with their centerlines in a vertical plane and contained in the area between the top of injection borehole 5 and 10 inches below the bottom of collection borehole 6.

As soon as each of the injection holes was turned off, the injection and collection holes were surveyed as well as video and neutron logged.

6.8.5.3.2.2 Results

There were 176 selected pads extracted for tracers, and the extracts were analyzed by IC, ICP/MS, HPLC, spectrofluorimetry, and epifluorescent microscopy. The extraction/analysis procedure is shown schematically in Figure 57. Also, 883 individual analyses were conducted, and full results were submitted (DTNs: LA9909WS831372.001 and LA9909WS831372.002). Breakthrough of all 5 solute tracers was detected in borehole 6, directly below the 10 mL hr^{-1} injection site in borehole 5. No breakthrough was detected in borehole 8 below the 1 mL hr^{-1} injection site in borehole 7. No clear evidence of microsphere breakthrough was detected in either borehole, but this may be due to analytical difficulties, discussed below in Section 6.8.5.3.5. The borehole-6 breakthrough results are summarized in Figure 58 (a through e), which shows tracer concentration in pad moisture (C) normalized by the theoretical input tracer concentration (C_0) listed in Table 30.

Table 30. Tracer C_0 Values for Phase 1B Injection

Tracer	C_0 (mg/kg)
Lithium	40
Bromide	460
2,6-DFBA (Borehole #5 only)	100
Pyridone	100
Sodium fluorescein	500

Note: Initial chemical concentration calculated from information presented in Section 6.8.2.4.1.

All five tracers shown in Figure 58 give clear evidence of breakthrough by the end of the experiment. All of the figures show peak concentrations at a (horizontal) depth of approximately 130 cm, directly below the injection port in borehole 5; but maximum recovery varies greatly. Bromide and 2,6-DFBA, both anionic supposedly nonreactive tracers, show similar and reasonable breakthrough patterns, with initial breakthrough detected in mid-late June 1998, after approximately 1 month of injection. Both bromide and 2,6-DFBA reached 50% injection concentrations in mid-July, after 2 months of injection. The fluorescein breakthrough pattern is more erratic. In particular, the peak concentration measured is over twice the injected concentration, which is clearly not reasonable. These anomalies probably reflect analytical difficulties associated with the extremely high concentration of fluorescein injected. The high concentration succeeded in improving field visualization of the plumes during mineback and overcore, even though it hurt the laboratory quantification. This analytical problem will be less severe for Phase 2, in which injected fluorescein concentrations are just 1/50 of that used in Phase 1. The later breakthrough and lower detected concentrations of pyridone may also reflect analytical difficulties; if real, they may indicate either sorption or degradation of this supposedly conservative tracer. Ongoing laboratory sorption and degradation studies will provide more information. Finally, although detected lithium concentrations are quite low, their contrast with background levels and their consistent location both in time and space indicate that true lithium

breakthrough was observed in the field. The low and late breakthrough indicate that lithium was sorbed quite significantly. Ongoing numerical analyses will provide quantitative field retardation estimates, which can be compared with lab sorption estimates.

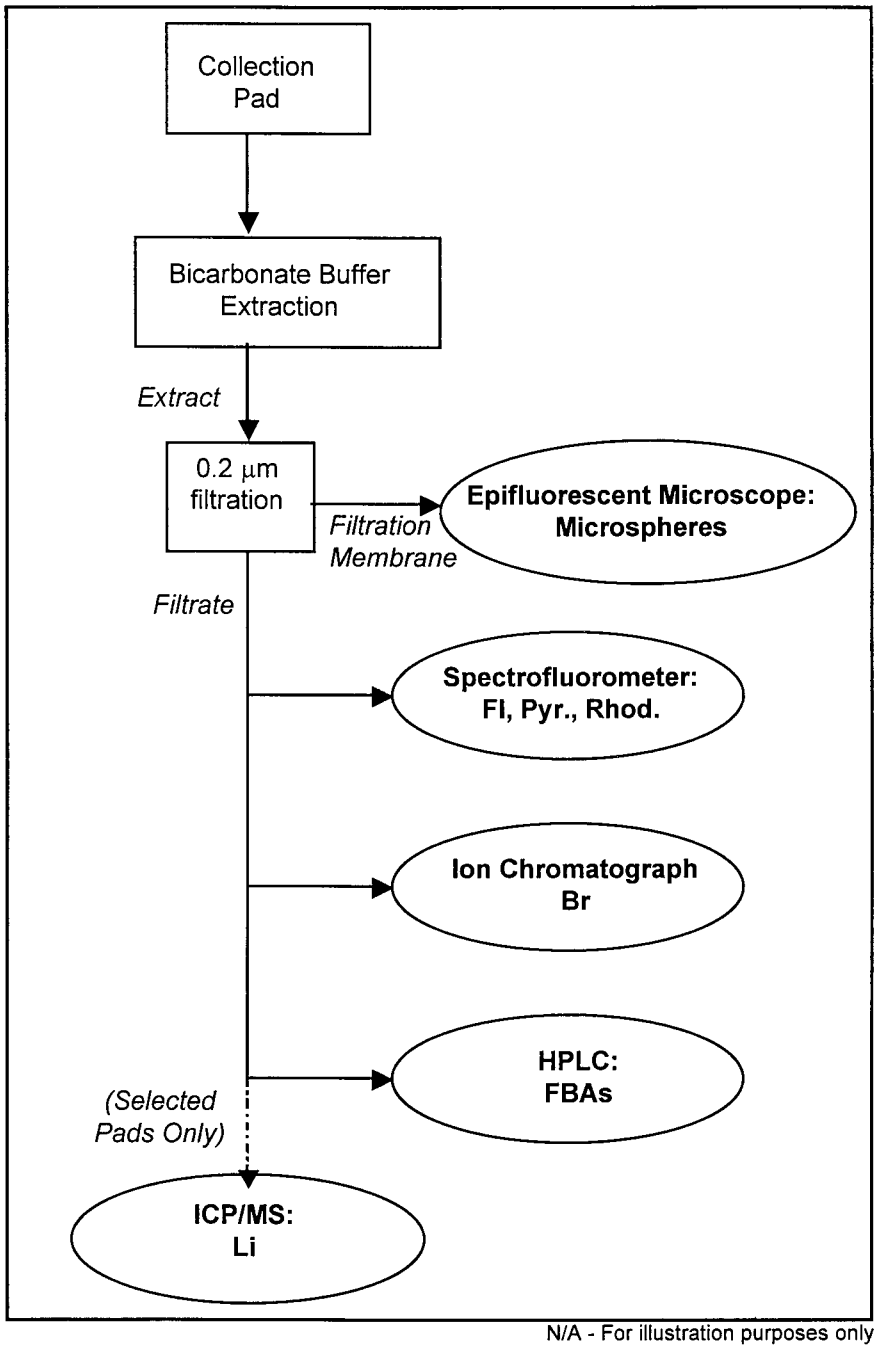

N/A - For illustration purposes only

Figure 57. Phase-1B Pad Extraction/Analysis Scheme

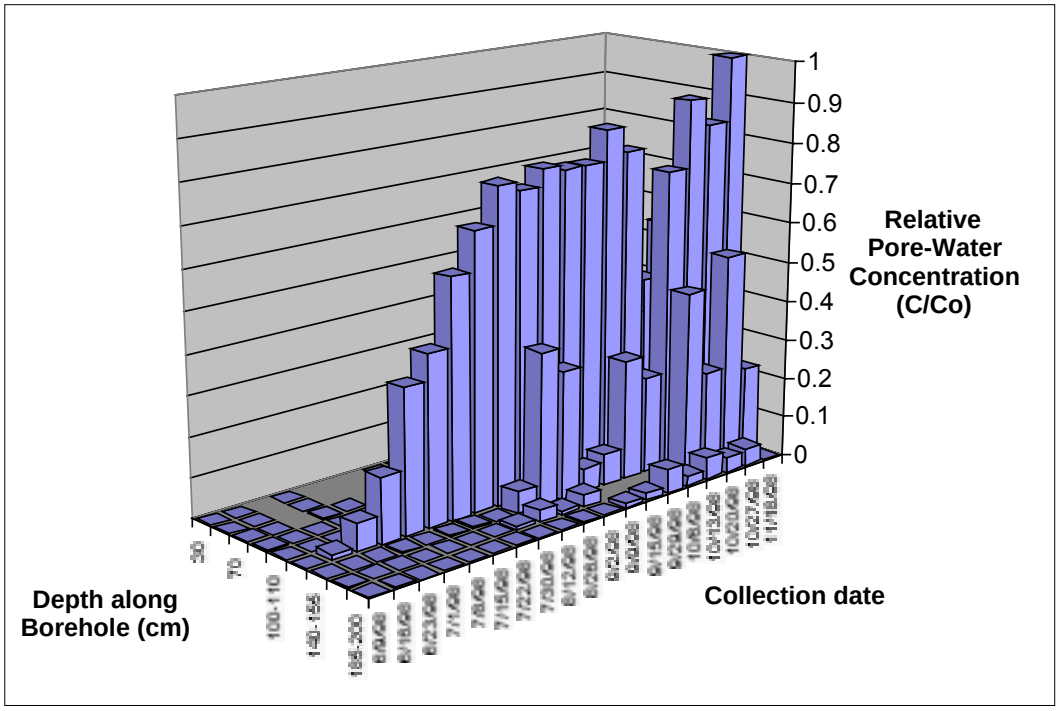

DTN: LA9909WS831372.001; LA9909WS831372.002

Figure 58a. Bromide Concentrations in Borehole 6 for Phase 1B

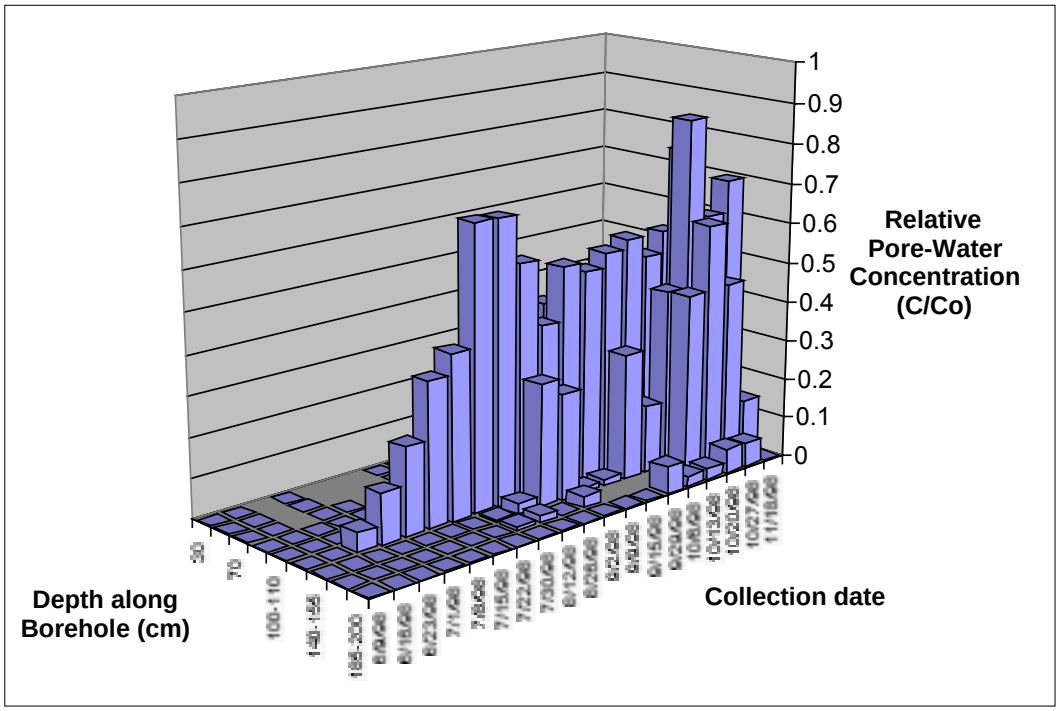

DTN: LA9909WS831372.001; LA9909WS831372.002

Figure 58b. 2,6-DFBA Concentrations in Borehole 6 for Phase 1B

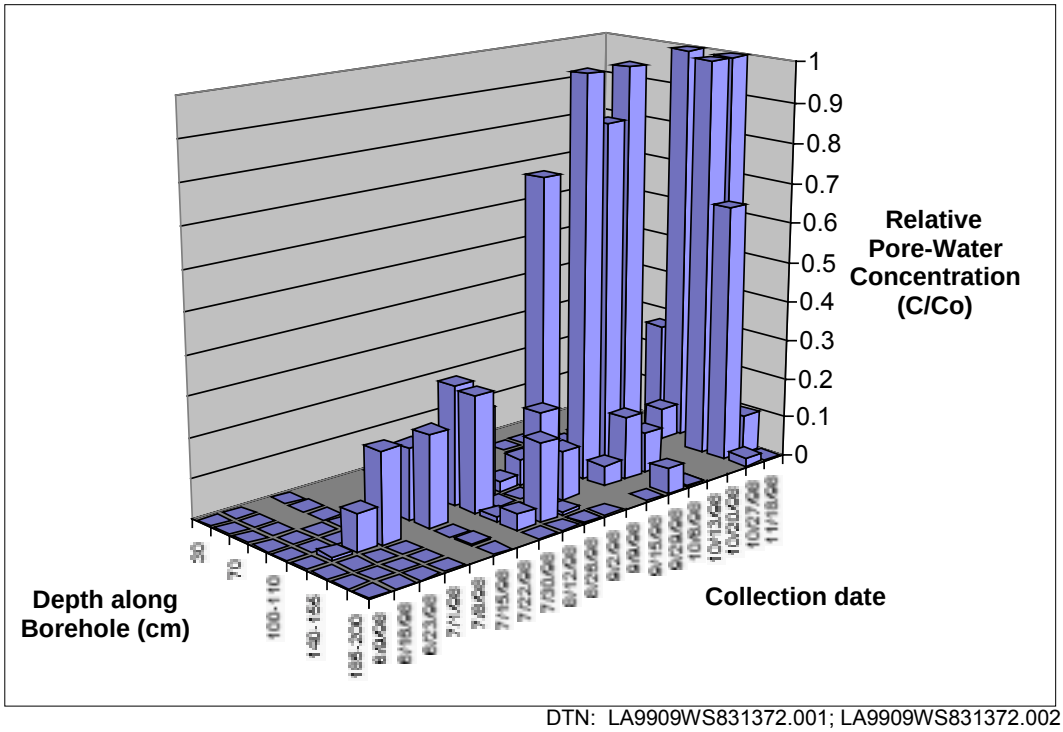

DTN: LA9909WS831372.001; LA9909WS831372.002

Figure 58c. Fluorescein Concentrations in Borehole 6 for Phase 1B

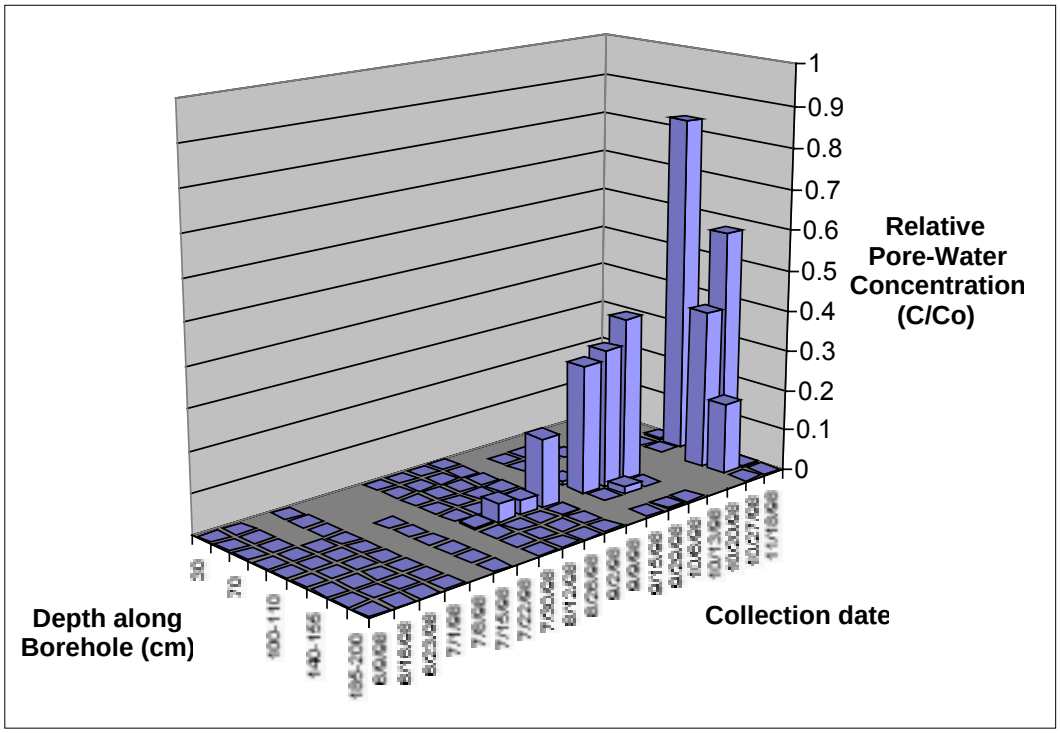

DTN: LA9909WS831372.001; LA9909WS831372.002

Figure 58d. Pyridone Concentrations in Borehole 6 for Phase 1B

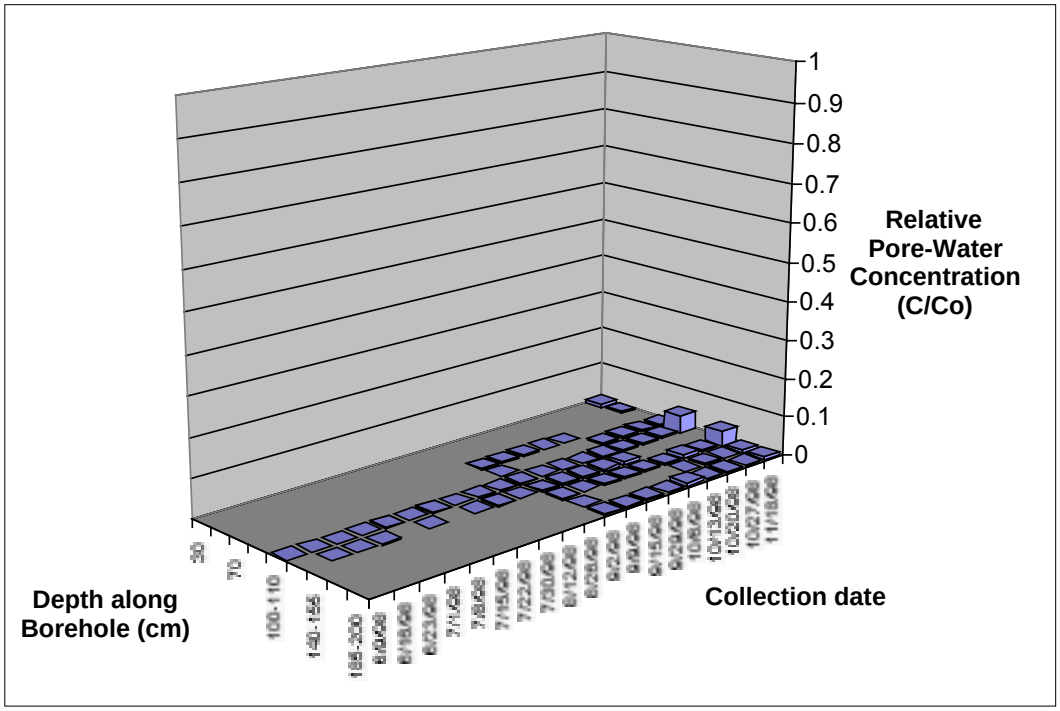

DTN: LA9909WS831372.001; LA9909WS831372.002

Figure 58e. Lithium Concentrations in Borehole 6 for Phase 1B

6.8.5.3.3 Phase 2

6.8.5.3.3.1 Description

Phase 2 involves eight injection boreholes and 12 collection boreholes drilled into the Phase-2 test block from the Test Alcove. The injection boreholes are subdivided into three subphases. Phase 2A consists of a single horizontal borehole (23) in the Tptpv2 horizon. The borehole has 10 injection points, each injecting tracer at 1 mL hr^{-1}. Phase-2A injection began on July 23, 1998, and is ongoing. Phase 2B consists of four parallel horizontal injection boreholes (24, 25, 26, and 27) in the Tac horizon. Each borehole is fitted with 10 injection points flowing at 10 mL hr^{-1}. Phase-2B injection began on July 30, 1998, and is ongoing. Phase 2C consists of three parallel horizontal injection boreholes (18, 20, and 21) coplanar with the Phase-2A borehole in the Tptpv2 horizon. Each borehole is equipped with 9 injection points flowing at 50 mL hr^{-1}. Phase-2C injection was initiated on August 5, 1998, and is ongoing. Details on the tracer mixtures for each borehole are presented in Section 6.8.2.4.2.

The 12 collection boreholes were drilled into the Phase-2 test block from the Main Adit and are, thus, perpendicular to the injection boreholes. Ten of the collection boreholes are horizontal, whereas the two deepest boreholes (11 and 47) are dipping downward beneath the block. The collection boreholes are arranged to allow interception of the tracer plumes after varying travel distances. Figure 59 is a schematic layout of the collection boreholes.

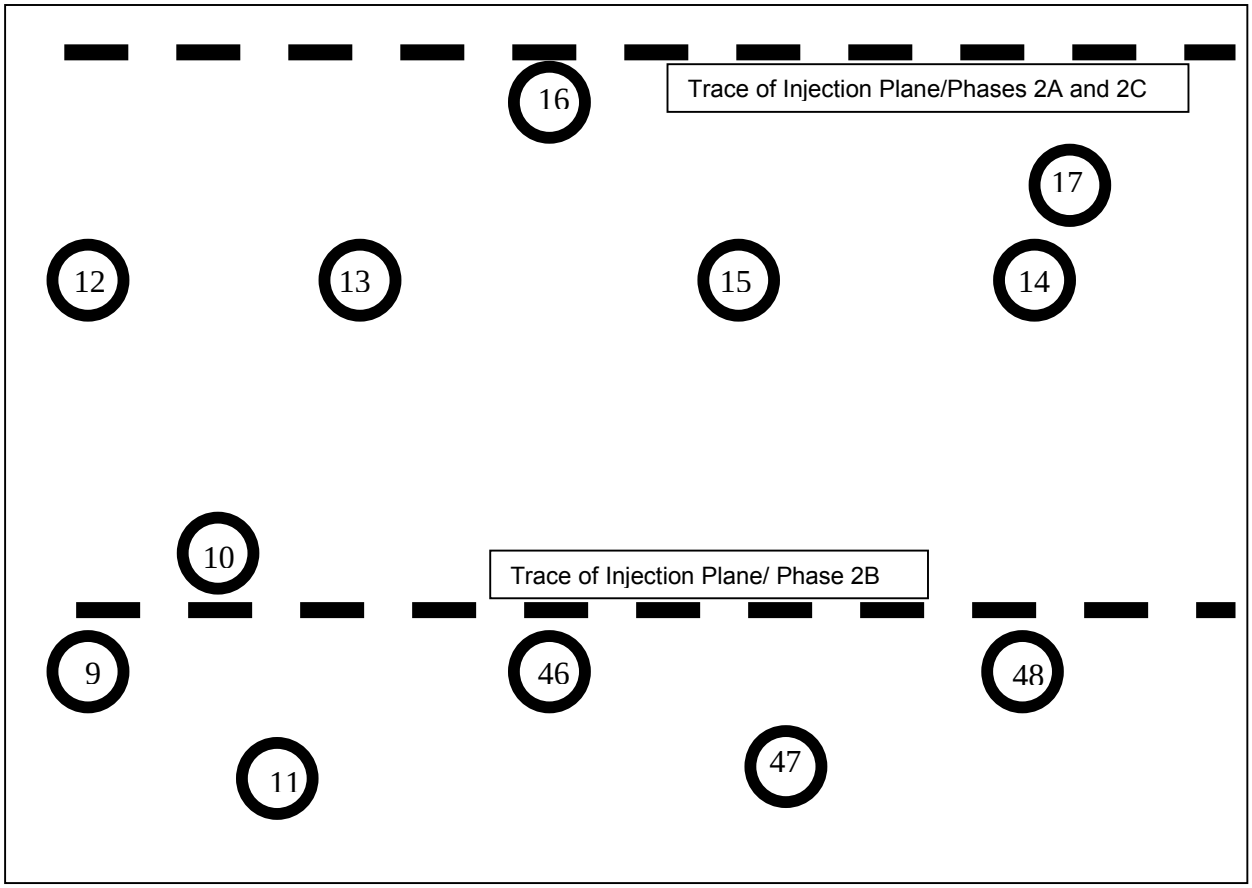

N/A – For illustration purposes only

Figure 59. Schematic Layout of Phase-2 Collection Boreholes (not to scale)

6.8.5.3.3.2 Status

Between the initiation of Phase-2 activities and September 21, 1999, a total of 9,188 sampling pads have been collected. Of these, over 2,200 have been extracted for the Phase-2 extraction/ analysis scheme, shown in Figure 60. Over 10,000 individual analyses have been conducted by the various instrument laboratories shown in Figure 59, and more are being received on a day-to-day basis. The results will help guide decisions on the future course of the field test and will be reported in future revisions of YMP documents.

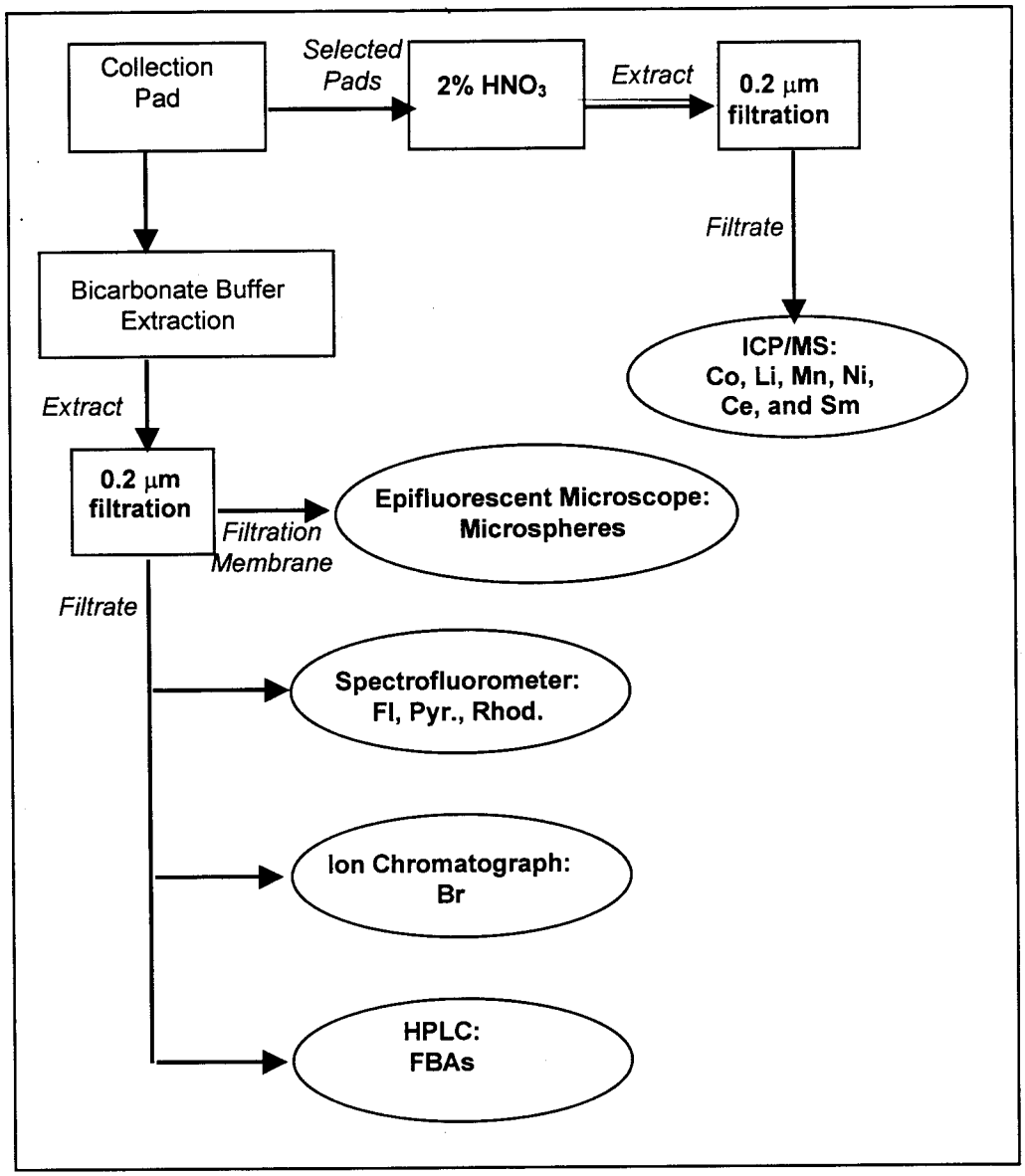

N/A – For illustration purposes only

Figure 60. Phase-2 Pad Extraction/Analysis Scheme

6.8.5.4 Special Topic—Microsphere Measurements

Fluorescent polystyrene microspheres were injected in both Phase-1 and Phase-2 tracer solutions. Two sizes of microspheres have been used at Busted Butte: 0.3-μm-diameter nile red spheres, and 1.0-μm-diameter blue spheres (these are nominal diameters; actual measurements are detailed in DTN: LA9909WS831372.014). Stock microsphere suspensions were prepared by taking aliquots of commercially produced microsphere latex (colloidal suspension) and diluting them with deionized water to give approximately 10^9 to 10^{10} nile red particles per mL and 10^8 to 10^9 blue particles per mL (the higher concentration of particles was used for Phase 1; the lower concentration for Phase 2).

Stock microsphere suspensions are then added in sufficient amounts to tracer solutions to further reduce the number of microspheres to ~10^6-nile-red particles mL^{-1} for Phase 2 and 10^7-nile-red particles per mL for Phase 1. Concentrations of blue particles for Phase 1 and Phase 2 were ~10^6 and ~10^5 particles per mL, respectively.

Initial microscopic examination of a few collection pads from both Phase 1 and Phase 2 produced no evidence for microsphere transport; however, subsequent verification studies cast serious doubt on the ability of our simple extraction method to extract microspheres from the pads efficiently and reproducibly. Progress on resolution of this issue will be reported in future YMP documents.

6.8.5.5 Special Topic—Tracer Degradation

One concern that has been raised is the possible biodegradation of some of the tracers on the collection pads during transportation and storage. This concern only applies to the organic tracers (dyes and FBAs); the metals, inorganic anions (bromide and iodide), and polystyrene microspheres are not subject to degradation. Among the organic tracers, FBAs are unlikely to degrade rapidly due to their strong fluorine-carbon bonds; the dyes' primary purpose is field-screening, so degradation, if it occurs, is not particularly damaging to the overall goals of the test. Nevertheless, to address this concern, a long-term tracer biodegradation study was initiated in 1999 and will be concluded in 2000, at which time data and discussion of the potential impacts of tracer degradation will be reported.

6.8.5.6 Forward Efforts

Current plans (as of February 2000) call for continued operation of the Phase-2 field study through at least September 2000. Collection pads from the collection boreholes shown in Figure 59 will continue on a regular basis and the pads will be analyzed for both nonreactive and reactive tracers. Three new collection boreholes will be drilled in the February/March 2000 timeframe; selected rock samples collected during drilling will be analyzed for tracers, collection pad membranes will be installed in the holes, and these new collection boreholes will be added to the ongoing pad collection schedule.

6.8.6 Phase-1A Predictions

6.8.6.1 Deterministic Model

This section reports predictions of the behavior of Phase 1A of the UZTT. The numerical experiments presented here were set up to determine the ability of numerical models to predict actual field response of flow and transport in porous media. These predictions were done previous to any actual experiment data being available. The simulations are intended to provide insight into the quality and extent of the information needed to accurately represent a physical system and to identify physical processes that are not currently adequately represented in numerical models.

Here, parameters from the available Yucca Mountain hydrologic database, as well as initial laboratory values on samples taken from the Busted Butte site are used. At the time of this document, additional data from Phase 1A were just becoming available but not early enough to be incorporated into the modeling work for Rev 00 of this AMR.

The computer code FEHM V2.00 (STN: 10031-2.00-00) is used in the development of the predictions presented here. FEHM is a multidimensional, multiphase, unsaturated and saturated, transient, finite-element code and is used by YMP for radionuclide migration predictions.

6.8.6.1.1 Model Configuration and Parameter Set

In these simulations of Phase 1A, the focus is on the injection of a conservative tracer into the vitric Calico Hills Formation via a single injection point in a borehole. The simulations of the Phase-1A field experiment were run in a model system that approximates the field configuration as closely as possible. The model system was a single borehole with a diameter of 0.10 m embedded in a matrix of tuff in the Tac unit. The domain size for the simulations is 6 m by 6 m by 1.5 m. The borehole extends the full 1.5-m length of the z direction, and gravity acts in the $-x$ direction. The system configuration is shown in Figure 61. Both 2-D and 3-D simulations of the system were run. The 2-D system was a vertical plane, an x-y slice through the injection point at 0.75 m.

The model accurately captured the configuration of the injection pad, as well. The tracer solution is injected through a polypropylene pad located 0.75 m down the length of the borehole. The injection pad resided inside the borehole, centered at $x = 0.0$, $y = 0.05$, $z = 0.75$ (Figure 61). The pad was 0.05-m by 0.05-m polypropylene material, with material parameters shown at the bottom of Table 30. Injection occurred at a single point in the center of the pad, consistent with the actual physical injection system. For Phase 1A, the pad and injection point are located on the side of the borehole, 90º off vertical, as shown in Figure 61.

Simulations were done before having detailed geologic and hydrologic property distributions in three dimensions for the UZTT. The simulation domain used a homogeneous, isotropic, unfractured description of the porous media. However, 3-D effects are likely to become important in representing the test. Therefore, the model is fully three dimensional from the outset to make it possible to capture any of these effects.

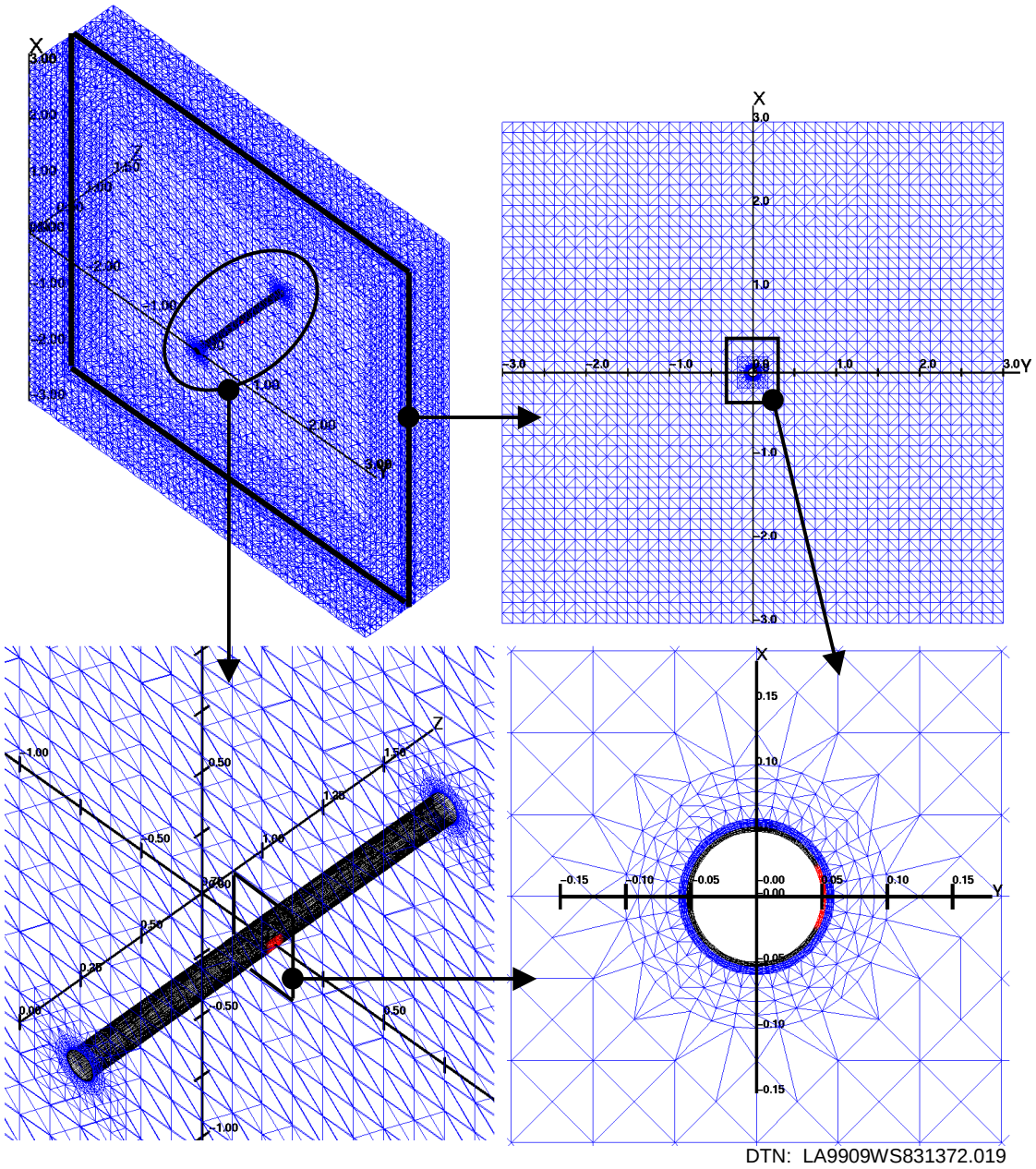

NOTE: LAGRIT-generated computational grid for single-borehole simulations. The grid has 82,000 nodes. The domain is 6 m x 6 m x 1.5 m and includes the porous rock matrix (blue) and the injection pad (red).

Figure 61. Computational Grid for UZTT Single-Borehole Simulations

An 82,000-node, 3-D, unstructured grid represents the single borehole configuration. This grid was generated using the LAGRIT V1.0 (STN: 10212-1.0-00) computer code. It contains the full representation of the injection borehole, the 25-cm^2 injection pad, and 54 m^3 of the surrounding rock mass (Figure 61).

The boundary conditions for the simulation were no flow for the lateral sides ($y = \pm 3$ m) and the front face of the borehole ($z = 0$ m). The exposed face of the rock in the field ($z = 0$ m) has been sealed to minimize evaporative losses resulting from the experimental tunnel. The top and bottom faces ($x = \pm 3$ m) of the model, as well as the back side ($z = 1.5$ m), were held at a fixed capillary pressure. Capillary pressures were chosen to match measured in-situ saturation and capillary-pressure conditions. The use of capillary-pressure boundary conditions provide the most accurate means of capturing the real saturation distribution of the system. Although for a homogeneous rock matrix, capillary pressure can readily be converted to a constant saturation boundary, in a heterogeneous system, the saturation may vary drastically around the boundary, though the capillary pressure is relatively constant. In the vadose zone, the capillary pressure provides a much better representation of the steady-state condition of the system, and measured in-situ saturations can be much better captured by a model.

In the simulations, the influence of a number of model parameters were assessed that can, at best, be only approximately known. These parameters include rock permeability, relative permeability, porosity, and in-situ conditions (saturation). For these simulations, the constitutive relationships (relative permeability versus saturation and capillary pressure versus saturation) are characterized using the van Genuchten curve fit (van Genuchten 1980, pp. 892–898). The van Genuchten method fits the data points of permeability versus saturation measured in the laboratory to a two-parameter function. The two parameters are typically denoted as α and n. The α parameter represents the air entry pressure and is given here in units of m^{-1}. The n parameter controls the slope of the capillary-pressure saturation curve, and is nondimensional.

Tables 31 and 32, respectively, list the different parameter combinations that were run in 2-D and 3-D representations of Phase 1A. The "base case" represents our current best knowledge of the properties and conditions of the system. Using available data from Flint (1998, Figure 3, p. 22-23; Figure 9, p. 30; Figure 10, p. 31; Table 7, p. 44; and Table 8, p. 45) and DTN: LB970601233129.001, a range for each parameter was simulated. Calculations were initiated in January 1998. Since these calculations are only scoping calculations and since a range of values was being used, the exactness of the data is not critical to the results presented here. Note that this situation also applies to data used for Phase-1A Monte Carlo simulations, Section 6.8.6.3, and Phase-2 modeling, Section 6.8.7.

The response of the system to various rates of injection of the tracer fluid was also assessed. Injection rates simulated were 1, 10, and 50 mL hr^{-1}. These injection rates were chosen to span the range of rates being applied in the various UZTT phases.

Table 31. Hydrologic Parameters Used for the 2-D Simulations

Parameter List for 2-D Simulations						
Simulation variable	**Porosity**	**Permeability (m^2)**	**α (m^{-1})**	***n***	**Saturation, *S* (in situ)**	**Inj. rate (mL hr^{-1})**
1. Base Case	0.30	1.3×10^{-12}	0.82	1.31	0.30	10
2. Matrix perm.=0.1x base case perm.	0.30	1.3×10^{-12}	0.82	1.31	0.30	10
3.Matrix perm.=10x base case perm.	0.30	1.3×10^{-12}	0.82	1.31	0.30	10
4. Porosity = 0.20	0.20	1.3×10^{-12}	0.82	1.31	0.30	10
5. Porosity = 0.40	0.40	1.3×10^{-12}	0.82	1.31	0.30	10
6. α low, *n* low	0.30	1.3×10^{-12}	0.60	1.20	0.30	10
7. α high, *n* low	0.30	1.3×10^{-12}	1.20	1.20	0.30	10
8. α low, *n* high	0.30	1.3×10^{-12}	0.60	1.80	0.30	10
9. α high, *n* high	0.30	1.3×10^{-12}	1.20	1.80	0.30	10
10. *In situ S* = 0.2	0.30	1.3×10^{-12}	0.82	1.31	0.20	10
11. *In situ S* = 0.4	0.30	1.3×10^{-12}	0.82	1.31	0.40	10
12. *In situ S* = 0.5	0.30	1.3×10^{-12}	0.82	1.31	0.50	10
13. *In situ S* = 0.6	0.30	1.3×10^{-12}	0.82	1.31	0.60	10
14. *In situ S* = 0.7	0.30	1.3×10^{-12}	0.82	1.31	0.70	10
15. *In situ S* = 0.8	0.30	1.3×10^{-12}	0.82	1.31	0.80	10
16. *In situ S* = 0.9	0.30	1.3×10^{-12}	0.82	1.31	0.90	10
17. *In situ S* = 0.2, Inj = 1	0.30	1.3×10^{-12}	0.82	1.31	0.20	1
18. *In situ S* = 0.3, Inj = 1	0.30	1.3×10^{-12}	0.82	1.31	0.30	1
19. *In situ S* = 0.4, Inj = 1	0.30	1.3×10^{-12}	0.82	1.31	0.40	1
20. *In situ S* = 0.5, Inj = 1	0.30	1.3×10^{-12}	0.82	1.31	0.50	1
21. *In situ S* = 0.6, Inj = 1	0.30	1.3×10^{-12}	0.82	1.31	0.60	1
22. *In situ S* = 0.7, Inj = 1	0.30	1.3×10^{-12}	0.82	1.31	0.70	1
23. *In situ S* = 0.8, Inj = 1	0.30	1.3×10^{-12}	0.82	1.31	0.80	1
24. *In situ S* = 0.9, Inj = 1	0.30	1.3×10^{-12}	0.82	1.31	0.90	1
25. *In situ S* = 0.3, Inj = 50	0.30	1.3×10^{-12}	0.82	1.31	0.30	50
26. *In situ S* = 0.9, Inj = 50	0.30	1.3×10^{-12}	0.82	1.31	0.90	50
Polypropylene pad	0.85	2.2×10^{-11}	17.0	1.12	N/A	N/A

DTN: LA9909WS831372.019

NOTE: [a]The simulation-variable column shows the parameter being varied (tested) in the simulation. Permeability is the intrinsic value (value under saturated conditions). The variables α and *n* are the van Genuchten function parameters taken from laboratory measurements; Inj. stands for injection rate in mL hr^{-1}.

Table 32. Hydrologic Parameters Used for the 3-D Simulations

Parameter List for 3-D Simulations						
Simulation variable	**Porosity**	**Permeability (m^2)**	**α (m^{-1})**	***n***	**Saturation, *S* (in situ)**	**Inj. rate (mL hr^{-1})**
1. Base Case	0.35	1.3×10^{-12}	0.82	1.31	0.35	10
2. Matrix perm.=0.1x base case perm	0.35	1.3×10^{-12}	0.82	1.31	0.35	10
3. Porosity = 0.20	0.20	1.3×10^{-12}	0.82	1.31	0.35	10
4. α high, *n* low	0.35	1.3×10^{-12}	1.20	1.20	0.35	10
5. α high, *n* high	0.35	1.3×10^{-12}	1.20	1.80	0.35	10
6. *In situ S* = 0.2	0.35	1.3×10^{-12}	0.82	1.31	0.20	10
7. *In situ S* = 0.6	0.35	1.3×10^{-12}	0.82	1.31	0.60	10
8. *In situ S* = 0.9	0.35	1.3×10^{-12}	0.82	1.31	0.90	10
9. *In situ S* = 0.2, Inj = 1	0.35	1.3×10^{-12}	0.82	1.31	0.20	1
10. *In situ S* = 0.35, Inj = 1	0.35	1.3×10^{-12}	0.82	1.31	0.35	1
11. *In situ S* = 0.6, Inj = 1	0.35	1.3×10^{-12}	0.82	1.31	0.60	1
12. *In situ S* = 0.9, Inj = 1	0.35	1.3×10^{-12}	0.82	1.31	0.90	1
13. *In situ S* = 0.2, Inj = 50	0.35	1.3×10^{-12}	0.82	1.31	0.20	50
14. *In situ S* = 0.35, Inj = 50	0.35	1.3×10^{-12}	0.82	1.31	0.35	50

DTN: LA9909WS831372.019

NOTE: The simulation-variable column shows the parameter being varied (tested) in the simulation. Permeability is the intrinsic value (value under saturated conditions). The variables α and *n* are the van Genuchten function parameters taken from laboratory measurements; Inj. stands for injection rate in mL hr^{-1}.

6.8.6.1.2 Modeling Results

All simulated concentrations presented in Section 6.8.6 are normalized (C/C_0) concentrations and, as such, are dimensionless.

6.8.6.1.2.1 Overview of Simulations

The large 3-D system size required relatively long simulation times. In an effort to minimize computer time and use the time most effectively, 2-D simulations were run first. These simulations were used as scoping calculations to identify important simulations to run in three dimensions. As shown in the numerical results, the 2-D simulations showed shorter travel distances for the tracer than did the same simulation in 3-D. The differences in tracer movement between 2-D and 3-D simulations at the same effective injection rate are primarily due to the effective volume of injection. The 2-D system is implicitly 1 m in depth, resulting in a lower effective point-injection rate. Therefore, all quantitative predictions are made using values from the 3-D simulations; however, the 2-D simulations can be used to identify the relative response of one set of conditions versus another. The results indicate that trends in the 2-D simulations mirror those in the 3-D simulations.

A series of 2-D simulations (Table 31) were run to identify the relative importance of different parameters and injection scenarios. Figure 62, a graph of concentration versus distance from the borehole center, indicates that this system is relatively insensitive to many of the parameters but is quite sensitive to some. Three-dimensional simulations were then chosen from the parameter sets to which the system was most sensitive; the parameter combinations are listed in Table 32.

The most influential parameter, based on Figure 62, is the value of the van Genuchten power *n*. Figure 62 shows the two simulations with a high *n* value dramatically increase concentration at a given distance over the other simulations. The values of both van Genuchten parameters, α and *n*, for the base case were taken from laboratory measurements made on cores from the Busted Butte site. Available data for the Tac unit were also collected from other sources (GS000408312231.003, GS951108312231.009, GS960808312231.003, GS960808312231.005, GS950408312231.004, GS990408312231.001, GS940508312231.006, GS960808312231.001, GS950608312231.008, LB970601233129.001) to try to capture the uncertainty in these parameters. From these data, high and low reported values of α and *n* were selected, testing the range of responses for the combinations of those values. The value of *n* strongly controls the relative influence of capillary forces and gravity forces. Increasing *n* decreases the capillary forces, resulting in more gravity-driven flow.

Another parameter that clearly influenced the tracer transport was the porosity. Although flow is only slightly affected by even relatively large changes in porosity, transport is more strongly affected. Porosity affects transport because the bulk velocity of the fluid is divided by the porosity to get the pore velocity. Two-dimensional and 3-D simulations were run with porosity increased and decreased by 10% to 15%. The higher porosity did not substantially change the transport, but the lower porosity made an observable difference.

A third factor affecting tracer transport was the injection rate. Prior to starting Phase 1A, simulations were run using different injection rates to help select a rate for Phase 1A that would allow the tracer to move sufficiently far to produce readily measurable distributions but not so far that the tracer could not be fully recovered. Testing multiple injection rates was also intended to help select injection rates for Phase 2. An injection rate of 10 mL hr^{-1} was chosen for Phase 1A. Therefore, the discussion below focuses on simulation results using 10 mL hr^{-1}. Results with other injection rates are presented later, for completeness. These other injection scenarios are also useful for making predictions for Phase 2.

Simulation results are presented as both spatial and time-history concentration profiles. For Phase 1A, however, the concentration distribution between 180 days and 365 days after injection is of most interest. Temporal snapshots are presented for 180 days, as this is the time corresponding to the original mineback and auger schedule for Phase 1A. The mineback was actually delayed until 284 days.

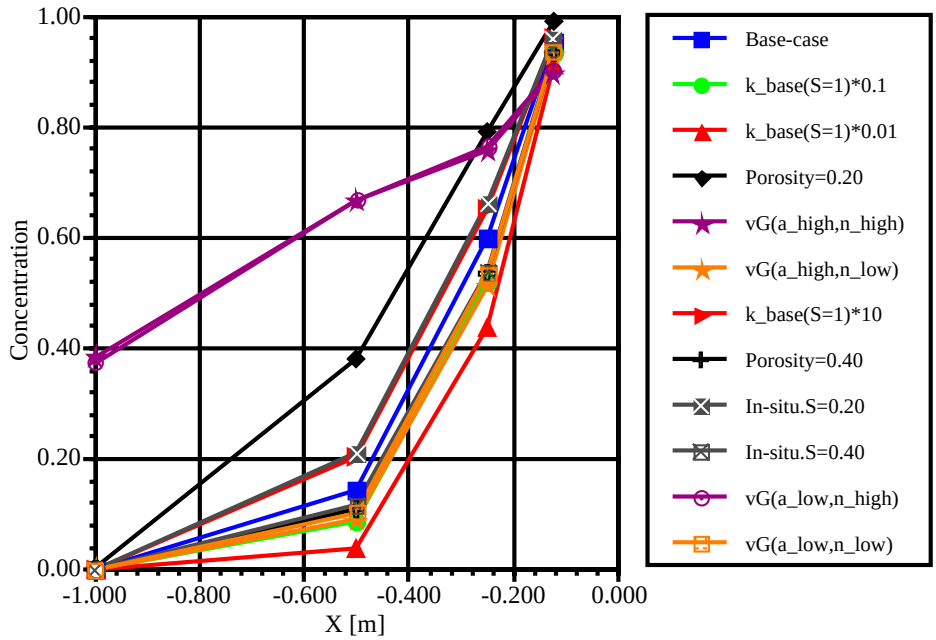

DTN: LA9909WS831372.019

NOTE: Normalized concentration as a function of vertical distance from the injection point for different 2-D sensitivity runs. Parameter values for each case shown in the legend are listed in Table 31.

Figure 62. 2-D Sensitivity Runs

6.8.6.1.2.2 Discussion of Simulations: Base Case

Tables 33 and 34 present the results from the 3-D base-case simulation, against which all other runs were compared. Using the experimental injection rate of 10 mL hr^{-1}, after 180 days, the model predicts tracer transport distances as shown in the Table 32. (In all the simulations discussed in this section, the tracer was injected at a concentration of "1," and cited concentration values are relative to this initial value.)

Measurements from core samples suggested in-situ saturations in the range of 20 to 40%. In the simulations, an initial capillary pressure of 5.6 MPa corresponds to a saturation of 20%, 0.55 MPa corresponds to 35%, and 0.07 MPa corresponds to 60%. Comparing locally measured values and values reported for the Tac unit, the in-situ saturation of approximately 35% most closely represented "reality."

Table 33. Predicted Transport Distances for a Given Concentration

Normalized concentration (C/C_0)	Distance traveled
0.01	0.85 m
0.1	0.67 m
0.25	0.56 m
0.50	0.45 m

DTN: LA9909WS831372.019

The predicted distribution of the tracer is generally uniform in all directions, that is, a spherical distribution (see Figure 62). Changes in saturation from the background (in-situ) level are generally small. Table 34 shows the saturation at different distances from the injection point at 180 days for the base-case simulation. Note that the initial background saturation for this simulation is 35%, based on measured moisture contents of 14.0 ± 2.5% and a porosity of approximately 0.5.

Table 34. Simulation Results at 180 Days

Distance from injection point (m)	Saturation at 180 days
0.125	0.402
0.25	0.381
0.50	0.366
1.00	0.357

DTN: LA9909WS831372.019

The saturation of the system changed only slightly over the 180-day period for the base case. After 180 days, at a distance of 0.125 m below the injection point, the saturation had increased by only 5%, whereas at a distance of 1 m it had increased by only a fraction of a percent (0.7%). The tracer distributes relatively evenly in all directions, centered at the injection point. Some asymmetry is introduced, however, by the presence of the borehole and by injecting 90 degrees off vertical. Water and tracer must move around the borehole to flow in the negative horizontal direction where there is no impedance in the positive horizontal direction. Thus, flow and transport are somewhat asymmetric.

The relatively even distribution of tracer and the lack of increase in saturation near the borehole indicate that this system is dominated by capillary forces over gravitational forces. Gravitationally dominated flows have a much more asymmetric character. These simulations show that a 10-mL hr^{-1} injection rate should not introduce enough water to change the overall flow and transport processes that occur in the undisturbed system.

At 180 days, for the 2-D run, the approximate radius of the tracer at a normalized concentration of 0.01 is 0.75 m and at a concentration of 0.5 is 0.30 m. Normalized concentrations of 0.01 and 0.5 for the 3-D simulation occur, respectively, at 0.85 m and 0.45 m. Figure 63 plots the concentration as a function of distance from the borehole center at 180 days for the 2-D and 3-D systems. In the 3-D simulation, at a distance of 0.125 m, the normalized concentration is almost 1 (0.96), whereas at 1 m the concentration has fallen to 2×10^{-4}.

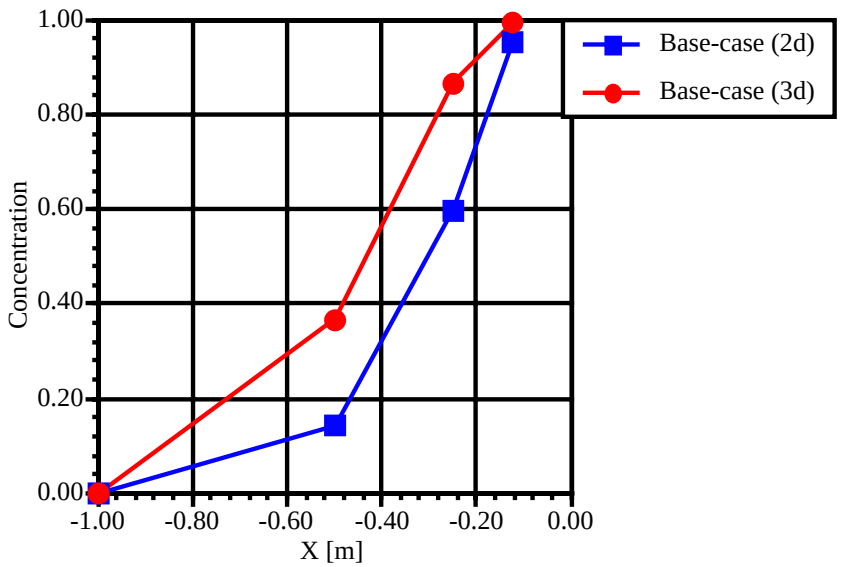

DTN: LA9909WS831372.019

NOTE: The graph shows tracer concentration as a function of vertical distance from the injection point. Although the shapes of the curves are similar, the 2-D system lags the 3-D system by a concentration of approximately 0.20. Parameter values used in these simulations are listed in row 1 of Tables 31 and 32.

Figure 63. Tracer Concentration versus Distance for 2-D and 3-D Simulations

Figure 64 plots the time history of concentration at a vertical distance of 0.125 m, 0.25 m, 0.5 m, and 1m below the center of the borehole for the 3-D simulation. Figure 64 shows that, at 180 days and a distance of 0.125 m, the tracer concentration has almost reached a value of 1.0, whereas at 0.5 m, the concentration is still increasing rapidly.

6.8.6.1.2.3 Discussion of Simulations: Sensitivity Analyses

Knowledge of the actual hydrologic and material properties will always contain some uncertainty. Furthermore, these properties vary somewhat within the hydrogeologic units, as reflected in variations in measured values from different cores. Using stochastic methods, these uncertainties can be incorporated directly into the calculations. Such predictions will be presented in later sections. Within this deterministic modeling approach, an attempt has been made to account for and understand the influence of such uncertainty by assessing the sensitivity of the simulation to various system parameters (Table 32). Figures 65 to 68 compare the results of these simulations. Figure 65 shows the effect of water injection on matrix saturation with time for the different sensitivity runs. Figure 66 plots concentration against distance from the borehole for the 3-D simulations 1 through 6 in Table 32. Figure 67 shows the same information plotted as concentration versus time with each graph plotting a different distance from the borehole. Figure 68 compares the 3-D concentration-versus-time values against those for 2-D.

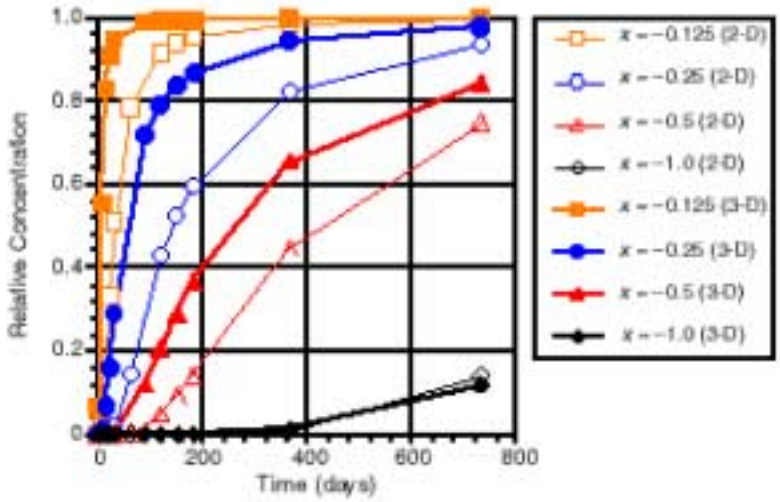

DTN: LA9909WS831372.019

NOTE: The graph shows plots of normalized tracer concentration as a function of time for different vertical distances (x in meters) from the injection point. Curves for both 2-D and 3-D simulations (2d and 3d in legend, respectively) are shown.

Figure 64. Time Profiles of Tracer Concentrations

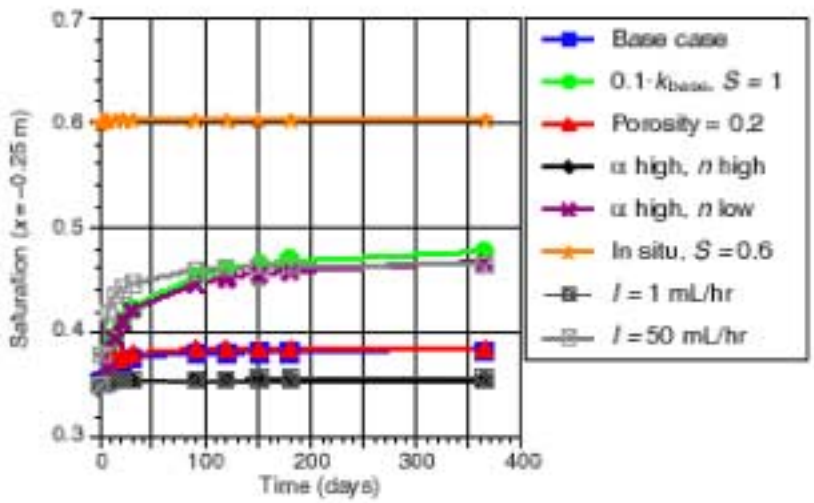

DTN: LA9909WS831372.019

NOTE: The graph shows changes in saturation through time at a distance of 0.25 m from the injection point. Note that in most cases there is little change in saturation over a year. Parameter values for the cases shown in the legend are listed in Table 32 (rows 1, 2, 3, 5, 4, 7, 10, and 14, respectively).

Figure 65. Effect of Water Injection on Matrix Saturation

Figure 65 shows that saturation for the Phase-1A model system is not greatly affected by any of the simulation scenarios. Further, the saturation is not particularly sensitive to many of the parameters. The biggest changes are observed for conditions that increase the relative influence of gravity forces over the otherwise prevailing capillary forces. Both a higher α and the much

higher injection rate produce relatively rapid and readily apparent increases in saturation. Otherwise little change in saturation is observed.

At 180 days, Figure 66 demonstrates that, based on simulated measurements at a distance of 0.25 m from the borehole, it is not likely that actual field measurements at such a distance would be useful for evaluating how well the system characteristics have been captured by the model for a 10 mL hr^{-1} injection rate. At 0.25 m, there is negligible difference in concentrations among the different simulations. At a distance of 0.5 m, however, variations in system characteristics result in a 60% range of concentrations. Figure 66 shows that a system with an order-of-magnitude lower intrinsic permeability *k* is indistinguishable from one with a value of van Genuchten power *n* that is at the low end of reported values. Both of these cases are very similar to the base case as well. This fact indicates that transport in this system is not particularly sensitive to the values of *k* or α; errors in these values are not expected to demonstrably influence the accuracy of predictions in this system.

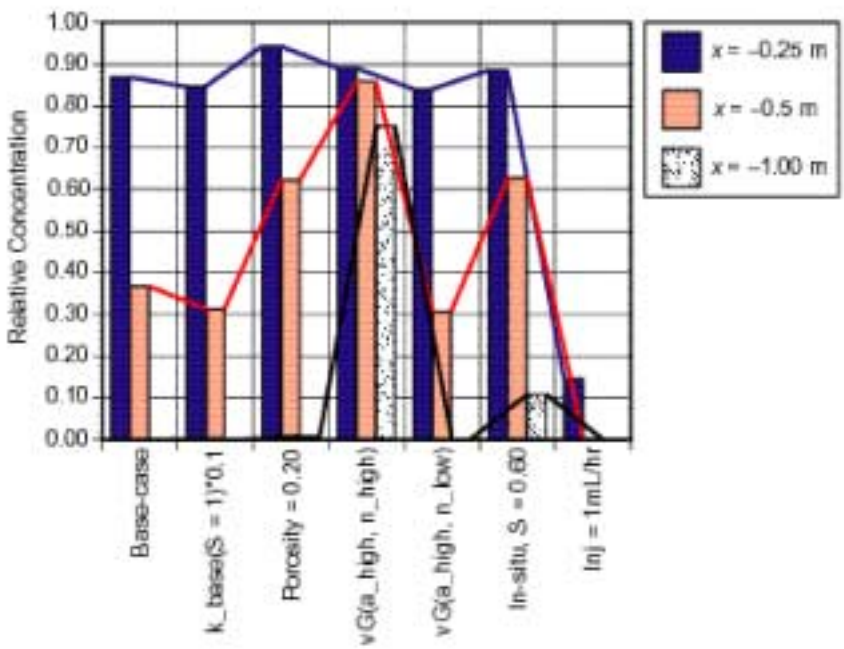

DTN: LA9909WS831372.019

NOTE: The graph shows differences in normalized concentration for different sensitivity runs at three distances (*x* in meters) from the injection point. The sensitivity to the system parameters is not captured at the smallest distances but is apparent at a distance of 0.5 m. Parameter values for the cases shown along the horizontal axis are listed in Table 32 (rows 1, 2, 3, 5, 4, 7, and 10, respectively).

Figure 66. Tracer Concentration for Different Sensitivity Runs

If the reported porosity is in error by as much as 15% (0.20 instead of 0.35), tracer concentration at 0.5 m and 180 days is expected to be 0.58, which is a difference of 25% from the base value. By 365 days, as seen in Figure 67, the difference in concentration has decreased somewhat but is still a substantial 10%. At shorter distances from the injection point, the low-porosity system is very close to the fastest transport system—one with high van Genuchten *n*—and leads the base prediction by 10% concentration.

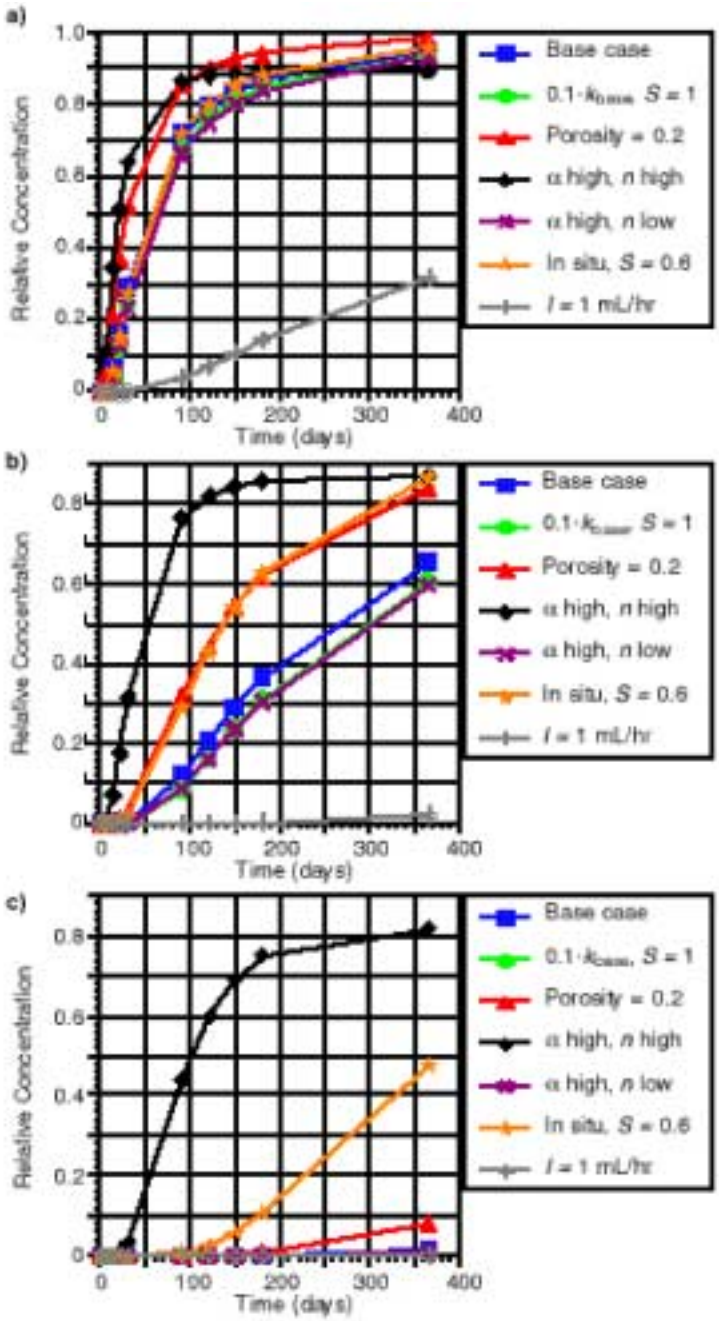

DTN: LA9909WS831372.019

NOTE: These plots show concentration changes as a function of time for a distances from the injection point of (a) 0.25 m, (b) 0.5 m, and (c) 1.0 m. Note that at a 1-m distance, there is, in most cases, little change in concentration after injecting tracer for 1 year. Parameter values for the cases shown in the legend are listed in Table 32 (rows 1, 2, 3, 5, 4, 7, and 10, respectively).

Figure 67. Concentration versus Time at Various Distances from Injection

Flow in the simulation that starts with an in-situ saturation of 60%, instead of the estimated 35%, is dominated by gravity rather than capillarity. For this simulation, tracer is carried much farther down than in any of the lateral directions. At 180 days and a vertical distance of 0.5 m below the borehole, the concentration is 0.57 versus 0.11 laterally. The transport rate is substantially faster than the base case, as demonstrated by much higher concentrations at greater distances (Figure 66). At a distance of 0.5 m below the borehole, decreased porosity and increased saturation runs are virtually indistinguishable but differ significantly in 3-D distribution. The lower-porosity transport is capillary-driven, producing a relatively uniform tracer cloud, whereas the high-saturation system produces a highly elongated tracer profile. Note that saturation as high as 60% is not indicated by the reported capillary pressures measured in this system. The measured pressures indicate an in-situ saturation in the vicinity of 25 to 35%.

The simulation results were most sensitive to the value of the van Genuchten parameter n. Reported values for this parameter ranged from 1.2 to 1.8, with the value from Busted Butte samples being 1.31. At a value of $n = 1.8$, transport was strongly gravity-dominated. The resulting concentration profiles were long vertically and thin laterally. This effect was much stronger than that observed for the high-saturation simulation. Concentration at a vertical distance of 0.5 m was 0.88 versus 0.04 at the same lateral distance. At a distance of 0.5 m, tracer concentration was 60% higher than the base case and 30% higher than the high-saturation case. Furthermore, by 180 days, this system had just about reached its steady-state distribution, whereas even at 365 days (Figure 67), the other systems were continuing to change. If the actual value of n at Busted Butte is significantly different from the value used here, it should be recognizable by the distinct, long and thin, tracer distribution and by the high vertical concentrations.

The 2-D simulations (Figure 62) indicated that the value of α appears to have little influence on the system as compared to n. As a result, 3-D simulations were only done for the two different variations in van Genuchten parameters presented.

6.8.6.1.2.4 Discussion of Simulations: 2-D versus 3-D

The 2-D and 3-D simulations followed very much the same trends in tracer distribution and concentrations in space and time. Figure 68 shows concentration as a function of time, measured at a distance of 0.5 m vertically below the borehole center for both 2-D and 3-D simulations. The numerical difference in concentration between equivalent 2-D and 3-D systems remained relatively constant, approximately 10 to 15% after 90 simulation days. Concentration values between the 2-D runs and the 3-D runs were much closer at early times and began to converge at later times, as all concentrations approached unity.

6.8.6.1.3 Implications for Unsaturated Zone Transport Test Phase-2 Design and Analysis

Using different tracers at various injection rates and injection separation distances can provide an opportunity to differentiate controlling processes and material features. These simulations provide us with a tool to select injection rates for the Phase-2 experiment, as well as to help understand how the injection rates used influence what is observed at different monitoring locations. For example, after 180 days at an injection rate of 10 mL hr^{-1}, normalized

concentrations had increased to greater than 0.20 within a radius of 0.4 m from the injection point but fell off rapidly beyond that and were below 1% beyond 0.9 m. Thus, a 2-m spacing between boreholes and injection points within boreholes would probably produce a system in which each injection location was distinct from every other.

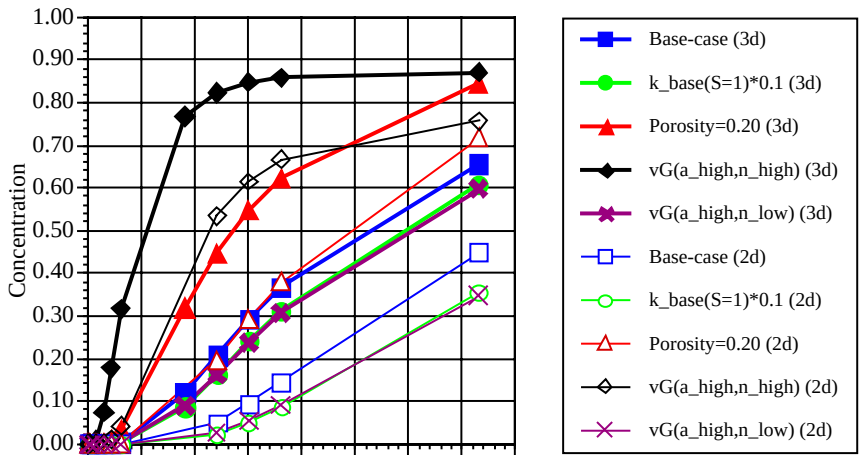

DTN: LA9909WS831372.019

NOTE: These plots of normalized concentration versus time show that differences between 2-D and 3-D values are fairly consistent between different runs. The concentration is measured at a distance of 0.5 m vertically below the borehole center. Parameter values for the cases shown in the legend are listed in Table 32 for 3-D cases and in Table 31 for 2-D cases.

Figure 68. Differences in 2-D and 3-D Predicted Concentrations

Faster injection rates, such as 50 mL hr^{-1}, can be expected to strongly modify natural flow patterns, producing gravity-dominated flow. At this injection rate, concentrations 0.5 m from the injection point are predicted to rise to 0.80 in only 3 months. Thus, boreholes or injection points spaced 1 m apart are expected to start influencing each other very early in the experiment.

On the other hand, an injection rate of 1 mL hr^{-1} is seen to hardly influence the system at all. Even after 1 yr, normalized concentrations do not rise even to 0.05 at the 0.5-m distance. At such a low injection rate, it would take an extremely long time to characterize the behavior of the system or identify important physical and chemical processes that are occurring. Further, at such slow rates of movement, it is very difficult to distinguish differences in tracer movement that might arise due to geochemical effects.

6.8.6.2 Stochastic Model

6.8.6.2.1 Introduction

The purpose of this section is to document the use of stochastic predictions made for Phase 1A of the Busted Butte testing program. At this time, there is a paucity of physical-properties information on the lithologies of that site, and the spatial variability of rock properties cannot be accurately depicted. Although this lack of information results in uncertainties for any flow and

transport prediction, this section attempts to use stochastic predictions for the site using current YMP databases. The input uncertainties from these databases are directly incorporated into flow predictions through a recently developed stochastic model. The predictions represent the first two moments (expected value and standard deviation) of flow quantities, and these two moments are used to construct confidence intervals for the flow quantities.

It is expected that the field-test results will fall within the predicted confidence intervals with a 68% probability. However, because the statistical and other input parameters are taken or estimated from the YMP databases, these parameters may or may not represent the rock properties at the test site, thereby introducing another level of uncertainty in the analyses. Some sensitivity analyses were performed on these parameters and found that the flow predictions are sensitive to the background saturation, the mean and variance of pore-size-distribution parameter α, the mean and variance of the logarithm of the saturated hydraulic conductivity, and the injection rate. This indicates that the refinement of these parameters is important.

6.8.6.2.2 Stochastic Modeling

Although geologic media exhibit a high degree of spatial variability, rock properties, including fundamental parameters such as permeability and porosity, are usually observed only at a few locations due to the high cost associated with subsurface measurements. This combination of significant spatial heterogeneity with a relatively small number of observations leads to uncertainty about the values of material properties and, thus, to uncertainties in predicting flow and solute transport in such media. It has been recognized that the theory of stochastic processes provides a natural method for evaluating flow and transport uncertainties. In the last two decades, many stochastic theories have been developed to study the effects of spatial variability on flow and transport in both saturated (e.g., Gelhar and Axness 1983, pp. 161–180; Dagan 1984, pp. 151–177; Neuman et al. 1987, pp. 453–466; Graham and McLaughlin 1989, pp. 2331–2355; Zhang and Neuman 1995, pp. 39–51) and unsaturated zones (e.g., Yeh et al. 1985, pp. 457–464; Mantoglou and Gelhar 1987, pp. 37–46; Russo 1995, pp. 1647–1658; Harter and Yeh 1996, pp. 1585–1595; Zhang and Winter 1998, pp. 1091–1100). In the unsaturated zone, the problem is complicated by the fact that the flow equations are nonlinear because unsaturated hydraulic conductivity depends on pressure head.

In many of these previous theories, there are a number of simplifying assumptions such as gravity-dominated flow (for steady-state cases) and slow-varying gradient (for transient flow). These assumptions restrict the applicability of existing theories to modeling the UZTT results. For example, the assumption of gravity-dominated flow excludes the presence of domain boundaries and the existence of a water table. In addition, a slow-varying gradient does not permit local injection or fast-varying recharge. Recently, a stochastic model for transient unsaturated flow in bounded domains free of the above mentioned assumptions (STO-UNSAT, V1.0, STN: 10292-1.0LV-00) was developed. The model results are the first two moments of the flow quantities, which may be used to construct confidence intervals for these quantities. The confidence intervals are a measure of the uncertainty caused by incomplete knowledge of material heterogeneities.

6.8.6.2.3 Phase-1A Modeling

For Phase-1A simulations, the input uncertainties from YMP databases are directly incorporated into flow predictions using STO-UNSAT, V1.0 (STN: 10292-1.0LV-00). This model requires that the first two statistical moments for rock properties, such as saturated hydraulic conductivity and pore-size-distribution parameter α, be specified. Because the variabilities of porosity and residual water content are likely to be small compared to that of hydraulic conductivity, both of them are assumed to be known with certainty. To model unsaturated flow, the constitutive relationships between capillary pressure and unsaturated hydraulic conductivity and between capillary pressure and saturation must also be specified. Although the parameters characterizing these relationships are reported in the YMP databases (Schenker et al. 1995; Flint 1998), these are based on the van Genuchten model (van Genuchten 1980, pp. 892–808). Conversely, STO-UNSAT, V1.0 assumes the constitutive relationships to obey the Gardner-Russo model (Gardner 1958, pp. 228–232; Russo 1988, pp. 453–459). In this study, the Gardner-Russo parameter α is estimated from the reported van Genuchten parameters by matching the main features of the retention curves for these two models. The first row of Table 35 summarizes the relevant parameters that are taken or estimated from the YMP databases (Schenker et al. 1995). No information is found with respect to the correlation lengths of the logarithm of the hydraulic conductivity and pore size distribution. The value of 20 cm is assumed for both of these correlation lengths.

Baseline Case

In the baseline case, the size domain is 200 cm by 200 cm with material properties specified in Table 35. The steady-state simulations are run with the following boundary conditions: specified flux at the top, a constant head of –488 cm at the bottom, and no-flow boundaries at the sides. The specified flux is consistent with the constant head at the bottom such that at steady-state (t = 0), the flow is gravity-dominated with a constant mean pressure head (h = –488 cm) and a constant saturation (S = 30%) through the whole domain. Specifically, the initial mean saturation is assumed to be 30% and then the initial mean head is computed to be –488 cm using the gravity-dominated condition and the specified characteristic curves. However, the head standard deviation is not uniform in such a bounded domain. The head standard deviation is zero at the bottom boundary, increases with distance from there, and reaches its maximum at the top. Figure 69 shows the confidence intervals for the pressure head h and the saturation S along horizontal (y) and vertical (z) lines passing through the injection point. The profiles are obtained by adding one standard deviation to the result and subtracting it from the mean quantity. This result corresponds to the 68% confidence intervals for the flow quantities. By comparing the vertical profiles for pressure head and saturation (Figure 69), it is seen that unlike the head standard deviation, the saturation standard deviation is not zero at the bottom boundary of constant head. This result happens because the uncertainty in saturation comes from the uncertainty in the soil parameter α, even though the head is specified with certainty there.

An injection of rate Q = 1 mL hr^{-1} starts at time t = 0, and lasts for 150 days. The actual injection at the field test site is a point in 3-D, whereas the model is in 2-D. In the model, the injection is approximated by a line source of length L_3 perpendicular to the 2-D domain. Therefore, the injection rate is Q/L_3 in 2-D. In this baseline case, L_3 = 50 cm. It should be realized that the 2-D representation is an approximation and the accuracy of this approximation

depends strongly on the choice of L_3, which is, in turn, a strong function of injection rate. The 2-D predictions should have the same general trend as the 3-D predictions.

Table 35. Case Description

Case	Description
1	$\langle f \rangle = -6.258$, $\sigma^2_f = 2.459$, $\lambda_f = 20$ cm, $\langle \alpha \rangle = 0.01$ cm^{-1}, $\sigma^2_\alpha = 9 \times 10^{-6}$ (cm^{-1})^2, $\lambda_\alpha = 20$ cm, $\phi = 0.5$, $L_1 = L_2 = 200$ cm, $L_3 = 50$ cm, $Q = 1$ mL hr^{-1}, $S_o = 30\%$
2	Same as in Case 1, except $\lambda_f = \lambda_\alpha = 30$ cm
3	Same as in Case 1, except $L_1 = L_2 = 400$ cm
4	Same as in Case 1, except $S_o = 20\%$
5	Same as in Case 1, except $S_o = 40\%$
6	Same as in Case 1, except $S_o = 60\%$
7	Same as in Case 1, except $\phi = 0.3$
8	Same as in Case 1, except $\langle f \rangle = -4.258$ and $L_1 = L_2 = 400$ cm
9	Same as in Case 1, except $\langle \alpha \rangle = 0.02$ cm^{-1}
10	Same as in Case 1, except $\sigma^2_\alpha = 0$
11	Same as in Case 1, except $Q = 10$ mL hr^{-1}
12	Same as in Case 8, except $Q = 50$ mL hr^{-1}, $L_3 = 100$ cm
13	Same as in Case 1, except $\langle f \rangle = -4.258$ and $L_1 = L_2 = 400$ cm, and $Q = 10$ mL hr^{-1}
14	Same as in Case 13, except $Q = 50$ mL hr^{-1} and $L_3 = 100$ cm

Data Source: Schenker et al. 1995; DTN: LA9909WS831372.020

NOTE: $f = \ln K_s$ is the log-transformed saturated hydraulic conductivity (for Case 1, the mean $\langle f \rangle$ and variance σ^2_f are obtained with $\langle K_s \rangle = 6.552 \times 10^{-3}$ cm hr^{-1} and $\sigma_{Ks} = 2.143 \times 10^{-2}$ cm hr^{-1}), α is a parameter related to pore-size distribution, λ_f and λ_α are the respective correlation lengths of f and α, ϕ is porosity, L_1 and L_2 are the vertical and horizontal dimensions of the domain, L_3 is the length of the third dimension used to calculate the injection rate for 2-D simulation, S_o is the background saturation, and Q is the actual injection rate.

Figure 70 shows the vertical and horizontal profiles of pressure head and saturation at 150 days. It is seen that the impact of injection is the increase of pressure head and saturation in the vicinity of injection. The effects seem to be even in all directions near the injection. This result is caused by the fact that the injection rate is overwhelmingly large compared to the background unsaturated hydraulic conductivity. The approximate radius of noticeable pressure head and saturation changes is 40 cm.

Other flow quantities (e.g., flux and velocity) and their associated uncertainties can be given similarly. In principle, the concentration field and its associated uncertainty may be predicted based on this information. However, at this stage, there is no existing model for solute transport in a nonstationary, unsaturated flow field. Our ongoing related research may provide us with a model during Phase-2 prediction.

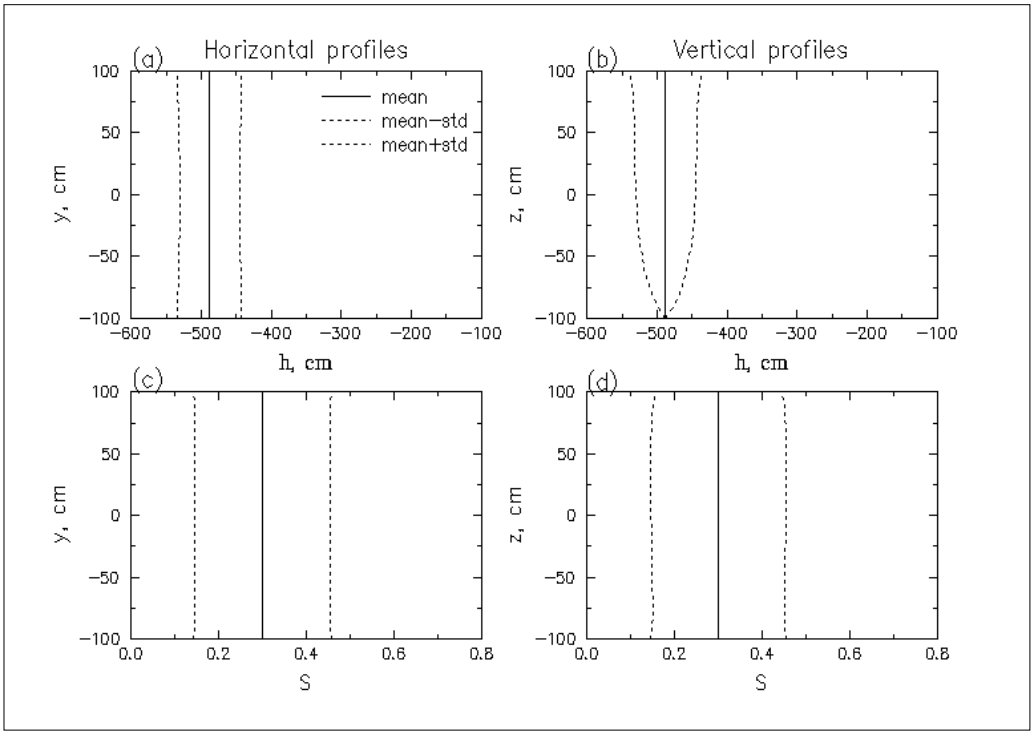

DTN: LA9909WS831372.020

NOTE: Horizontal and vertical profiles of pressure head *h* and saturation *S* under steady-state conditions.

Figure 69. Steady-State Profiles

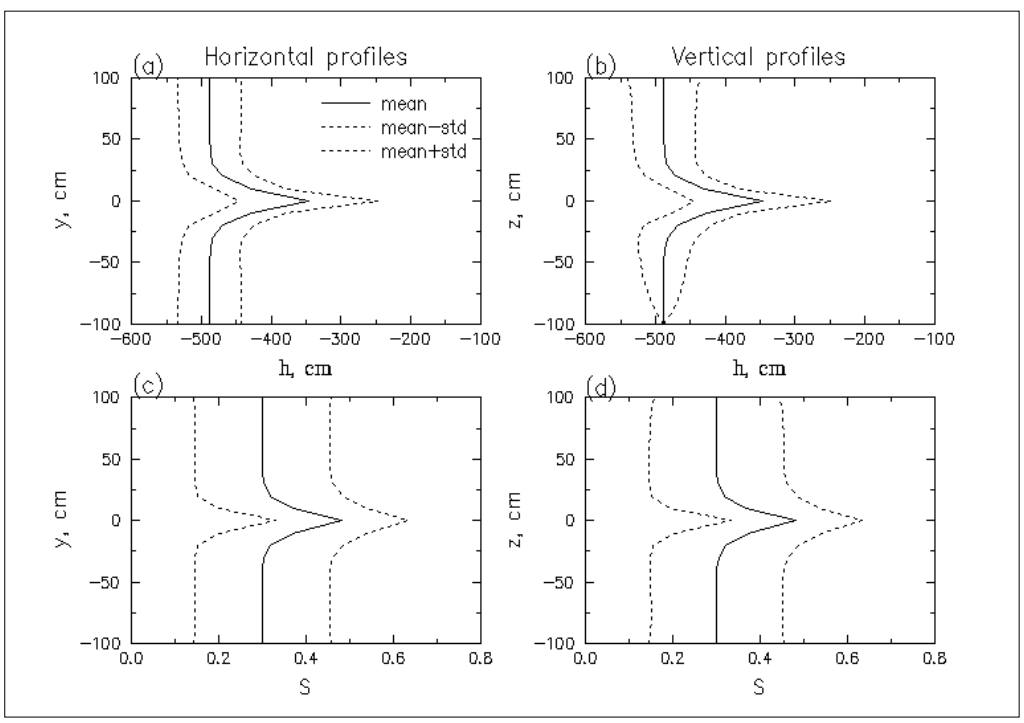

DTN: LA9909WS831372.020

Figure 70. Case 1. Horizontal and Vertical Profiles of Pressure Head *h* and Saturation *S* at 150 Days after Injection Started

Sensitivity Cases

Because the number of actual measurements at the site is too few to perform any statistical analysis, the statistical parameters are either taken or estimated from the relevant YMP databases. There is another level of uncertainty associated with inaccurate statistical and other parameters. Sensitivity studies, presented below, are performed using the stochastic model.

As mentioned before, there is no information regarding the correlation lengths of the log of the saturated hydraulic conductivity and the rock pore-size distribution parameter α. Case 2 investigates the effect of the correlation lengths by changing it from 20 cm to 30 cm. Figure 71 shows the corresponding profiles of pressure head and saturation. Comparison of Figures 70 and 71 reveals that the prediction is insensitive to the correlation lengths.

In the base case, the domain size is taken to be L_1 = 200 cm by L_2 = 200 cm. However, the real domain is much larger than this. The size of the domain is expected to affect the standard deviations of flow quantities to some extent. In Case 3, L_1 = 400 cm and L_2 = 400 cm. It is seen from Figure 72 that, in areas away from the boundaries, the confidence intervals are quite insensitive to the domain size.

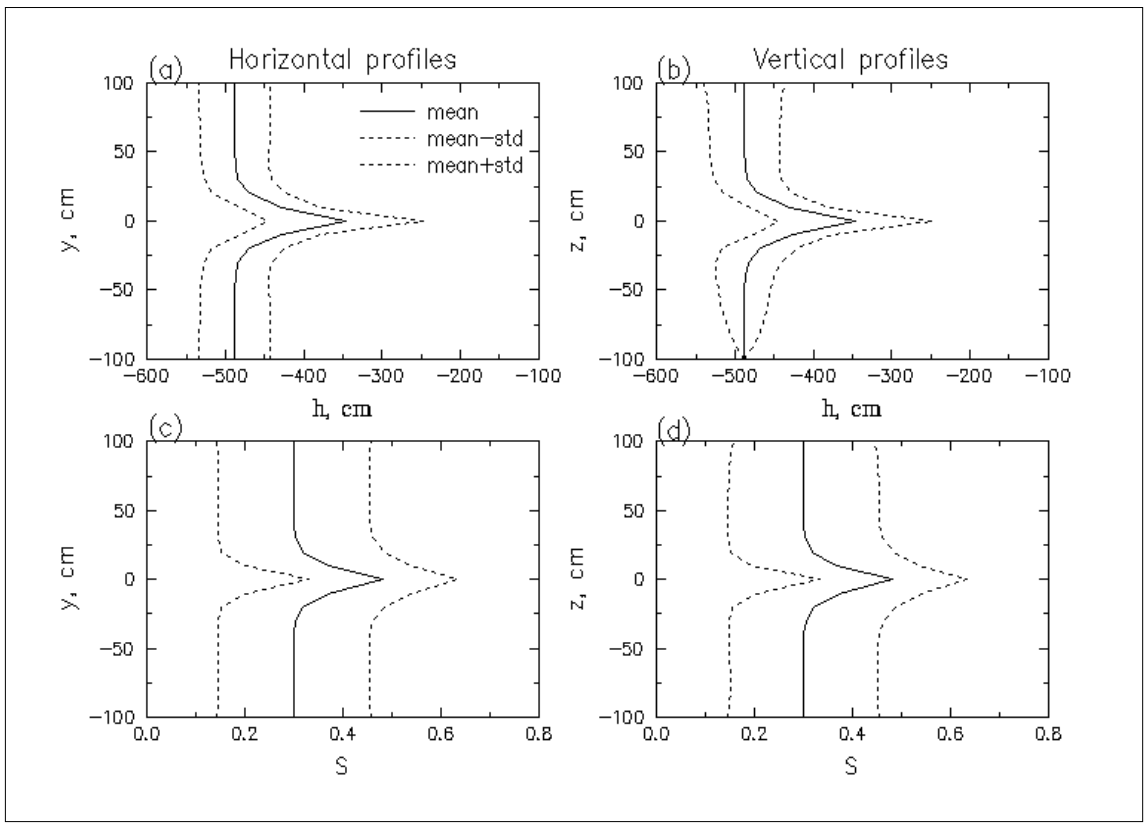

DTN: LA9909WS831372.020

Figure 71. Case 2. The Same as Case 1 in Figure 70 but with $\lambda_f = \lambda_\alpha$ = 30 cm

Cases 4 through 6 from Table 35 investigate the effect of background saturation by changing the specified flux at the top and the constant head at the bottom. Figures 73 to 74 show the cases for

S_o = 20%, 40%, and 60%, respectively. It is seen that the peak pressure head and saturation at the injection location decrease with the increase of the background saturation, but the impact radius increases with it. The width of confidence intervals for pressure head decreases with the increase of background saturation, whereas that for saturation profiles is quite insensitive to the background saturation.

In Case 7, the porosity is varied from ϕ = 0.5 to 0.3 (Figure 76). Comparison of Figure 76 and Figure 77 reveals that a lower porosity results in a slight increase in both the peak saturation and the radius of influence. However, the effect of porosity on solute transport is expected to be greater.

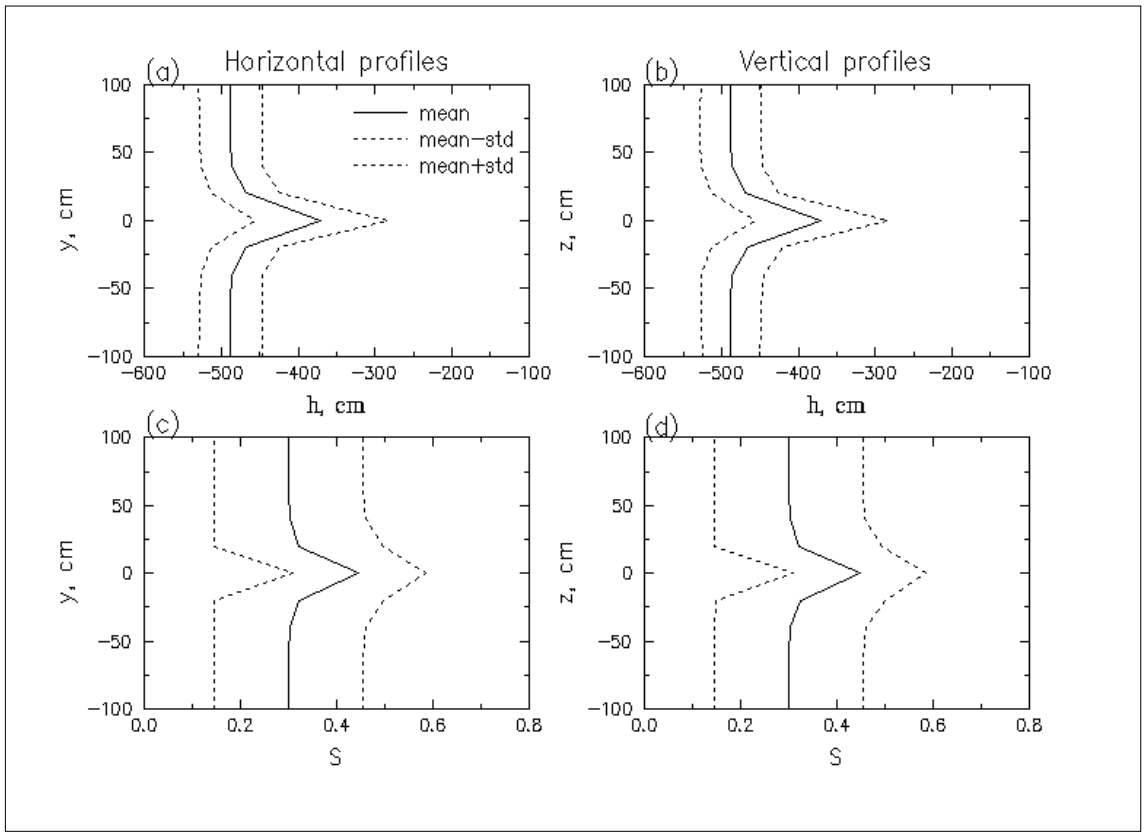

DTN: LA9909WS831372.020

Figure 72. Case 3. The Same as Case 1 in Figure 70 but with $L_1 = L_2$ = 400 cm

In Case 8, the mean of the log of the saturated hydraulic conductivity K is increased from $\langle f \rangle$ = –6.258 to –4.258 (where $f = \ln K$). As one should expect, a larger hydraulic conductivity renders a lower peak saturation and a larger radius of influence (Figure 77). In this case, the size of the domain was changed to 400 cm by 400 cm to accommodate the increase of saturation at large distance. In Case 9, the mean of α is varied from 0.01 to 0.02 cm^{-1} while the variance of α is kept the same. It is seen that the mean head has increased significantly with a larger α for a given saturation (Figure 78). The confidence intervals are qualitatively similar to those in Figure 70, but the intervals are tighter in Figure 79. This difference occurs because the variability in α is actually reduced by keeping the same variance but with an increased mean value. As expected, the prediction—in particular, the width of confidence intervals—is sensitive to the

variabilities in saturated hydraulic conductivity and pore size distribution α. Case 10 shows the case in which the variability of α is zero. It is seen from Figure 79 that the width of the confidence intervals is significantly reduced in the absence of variability in α. In this case, the uncertainties in the prediction are entirely caused by the variability in saturated hydraulic conductivity K_s. In the baseline case, the coefficient of variation $CV_\alpha = \sigma_\alpha/\langle\alpha\rangle = 0.3$, while $CV_{Ks} = 3.27$. That is to say, the variability in saturated hydraulic conductivity K_s is much larger than that in pore size distribution α. Therefore, it may be concluded that the results are much more sensitive to the variability in α than to that in K_s.

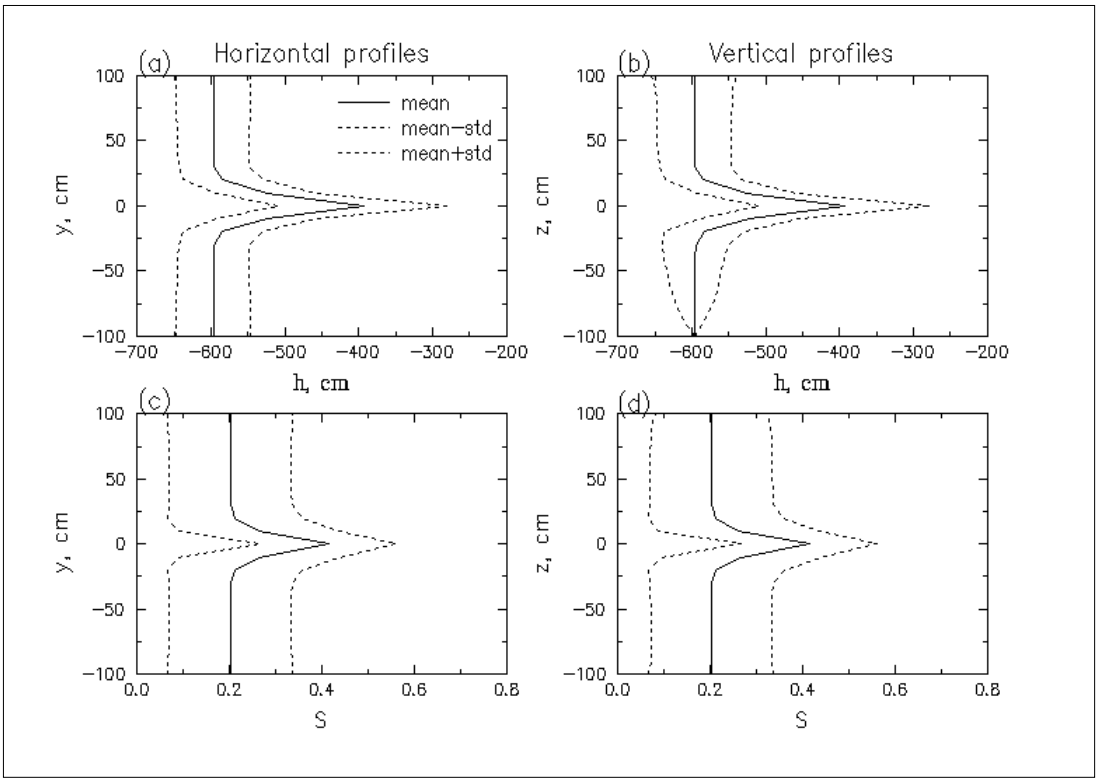

DTN: LA9909WS831372.020

Figure 73. Case 4. The Same as Case 1 in Figure 70 but with S_o = 20%

As one should expect, the behaviors of pressure head and saturation profiles are very sensitive to the injection rate. In Case 11, the injection rate is Q = 10 mL hr^{-1} (Figure 80). The peak saturation is much higher than that in Case 1 (Figure 70) and the radius of influence is also larger. This difference is even clearer from Case 12 (Figure 81), for which Q = 50 mL hr^{-1}.

In the last two cases, the mean saturated hydraulic conductivity $\langle K_s \rangle$ is taken to be 4.68 cm hr^{-1}. This value is based on some site-specific measurements and is three orders of magnitude larger than the value found in the YMP databases mentioned earlier. As for sensitivity runs, this value is taken as the mean and $CV_{Ks} = \sigma_{Ks}/\langle K_s\rangle = 3.27$, as in the baseline case. Equivalently, $\langle f\rangle$ = 0.314 and $\sigma^2_f = 2.459$. In Case 13, Q = 10 mL/hr and L_3 = 50 cm (Figure 82); in Case 14, Q = 50 mL hr^{-1} and L_3 = 100 cm (Figure 83). As found in Case 8 (Figure 77), a larger hydraulic conductivity renders a lower peak saturation and a larger radius of influence. It is expected that the tracer travels significantly faster in these cases.

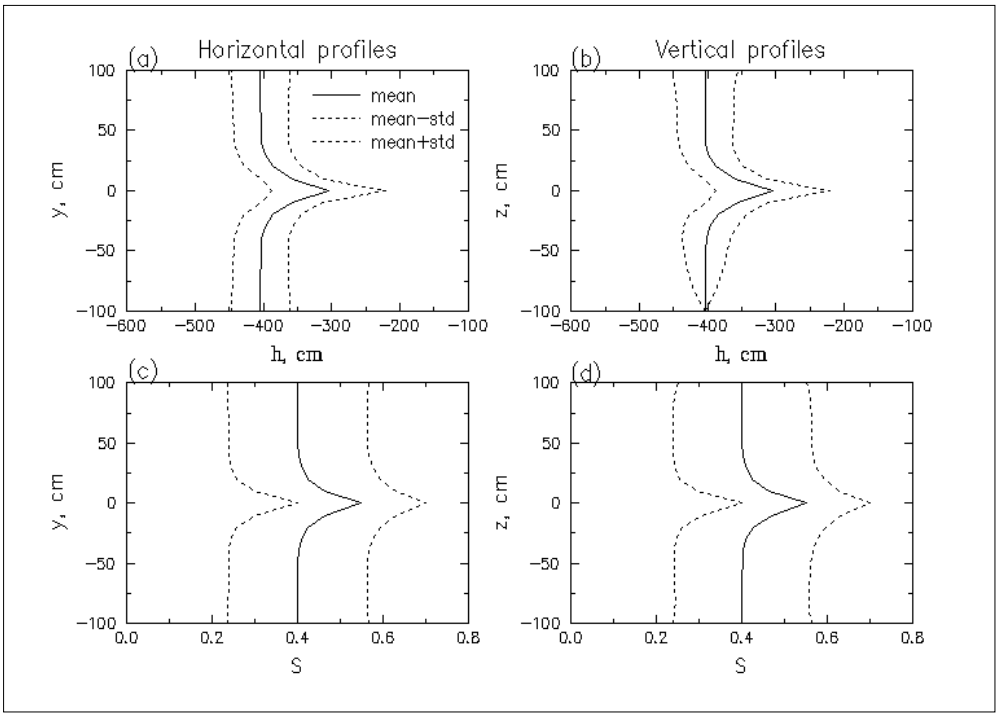

DTN: LA9909WS831372.020

Figure 74. Case 5. The Same as Case 1 in Figure 70 but with S_o = 40%

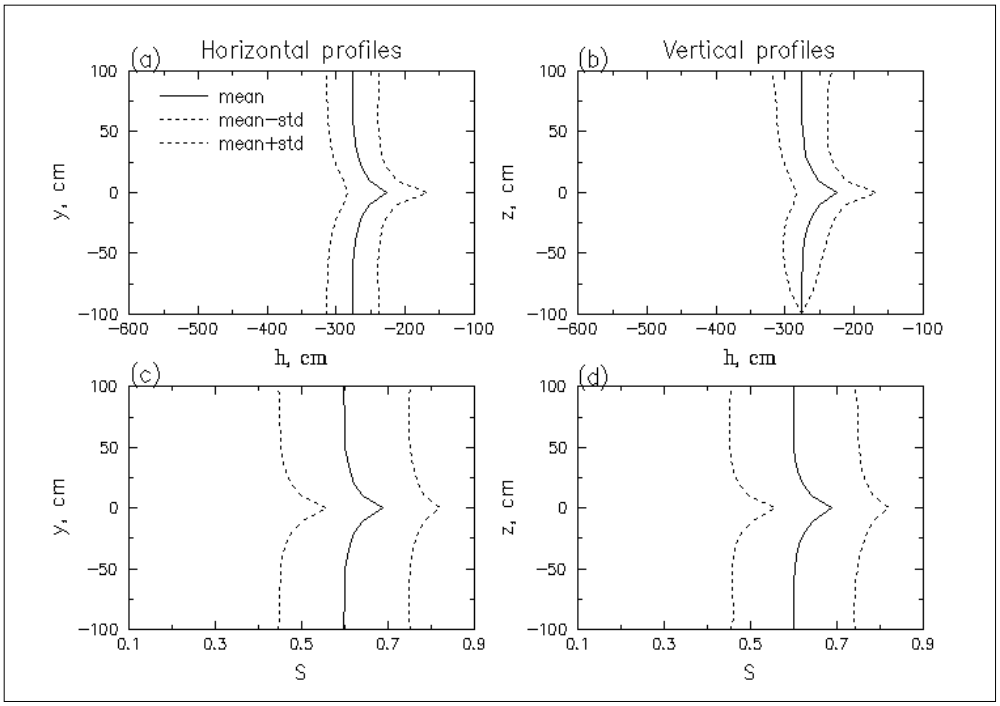

DTN: LA9909WS831372.020

Figure 75. Case 6. The Same as Case 1 in Figure 70 but with S_o = 60%

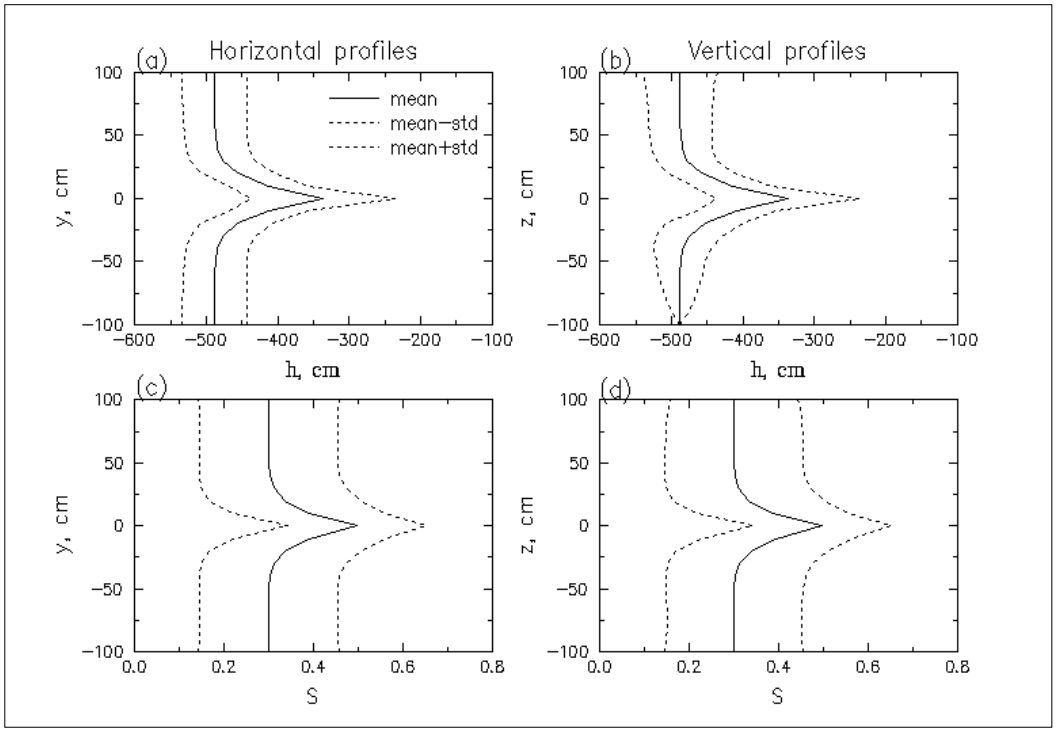

DTN: LA9909WS831372.020

Figure 76. Case 7. The Same as Case 1 in Figure 70 but with $\phi = 0.3$

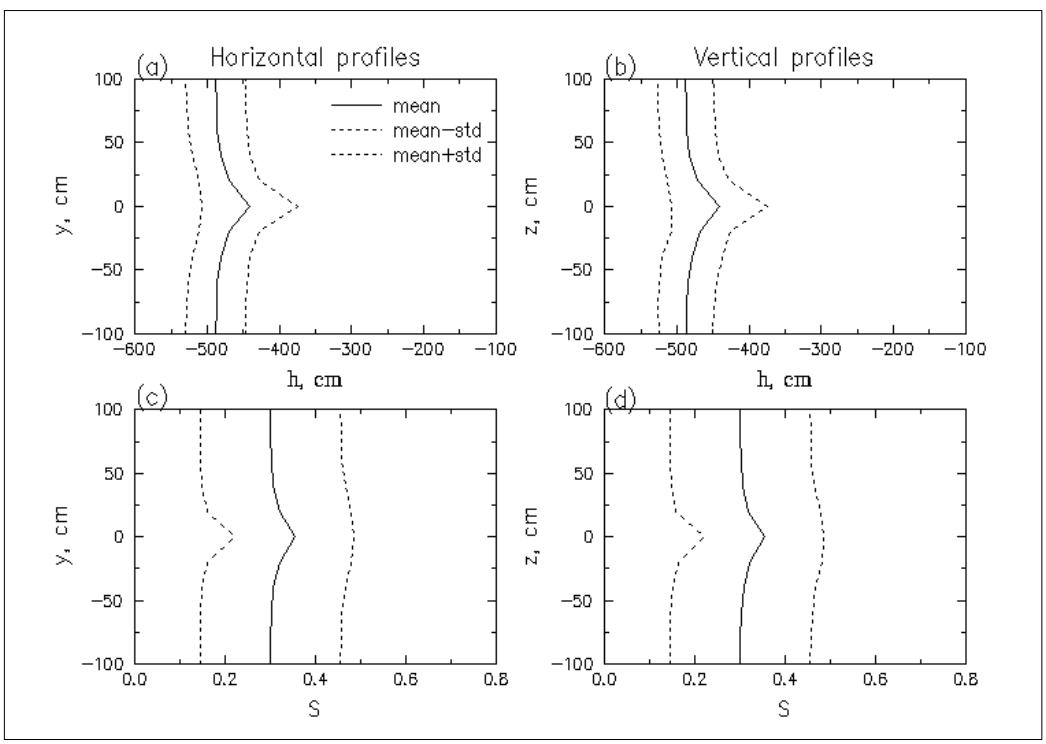

DTN: LA9909WS831372.020

Figure 77. Case 8. The Same as Case 1 in Figure 70 but with $\langle f \rangle = -4.258$ and $L_1 = L_2 = 400$ cm

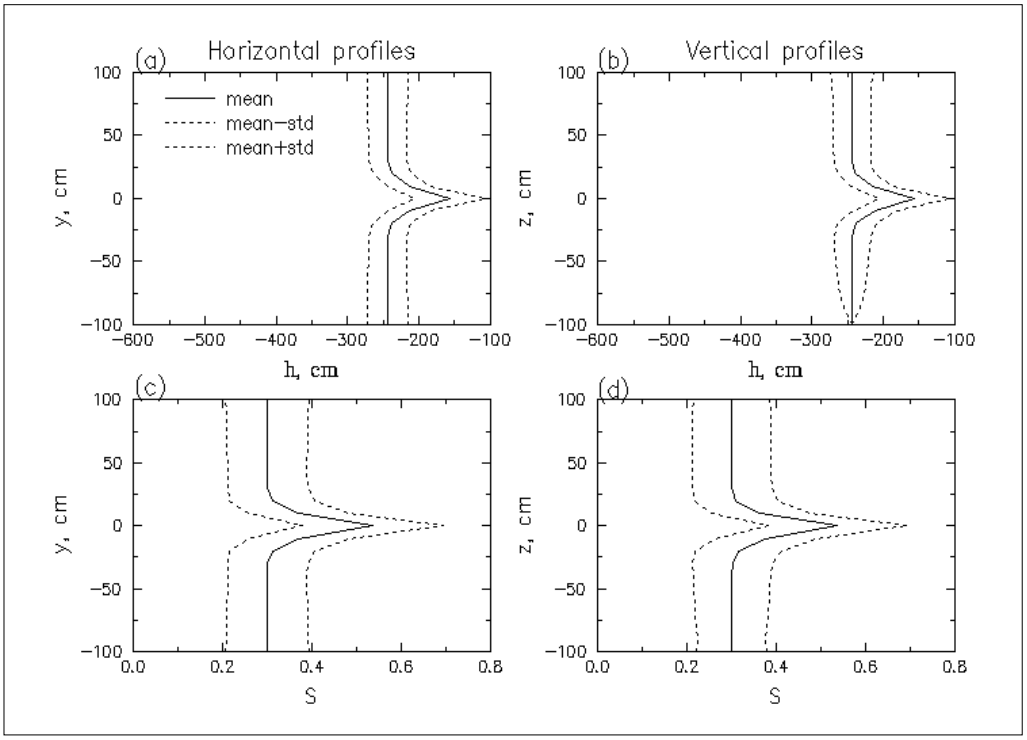

DTN: LA9909WS831372.020

Figure 78. Case 9. The Same as Case 1 in Figure 70 but with $\langle \alpha \rangle$ = 0.02 cm^{-1}

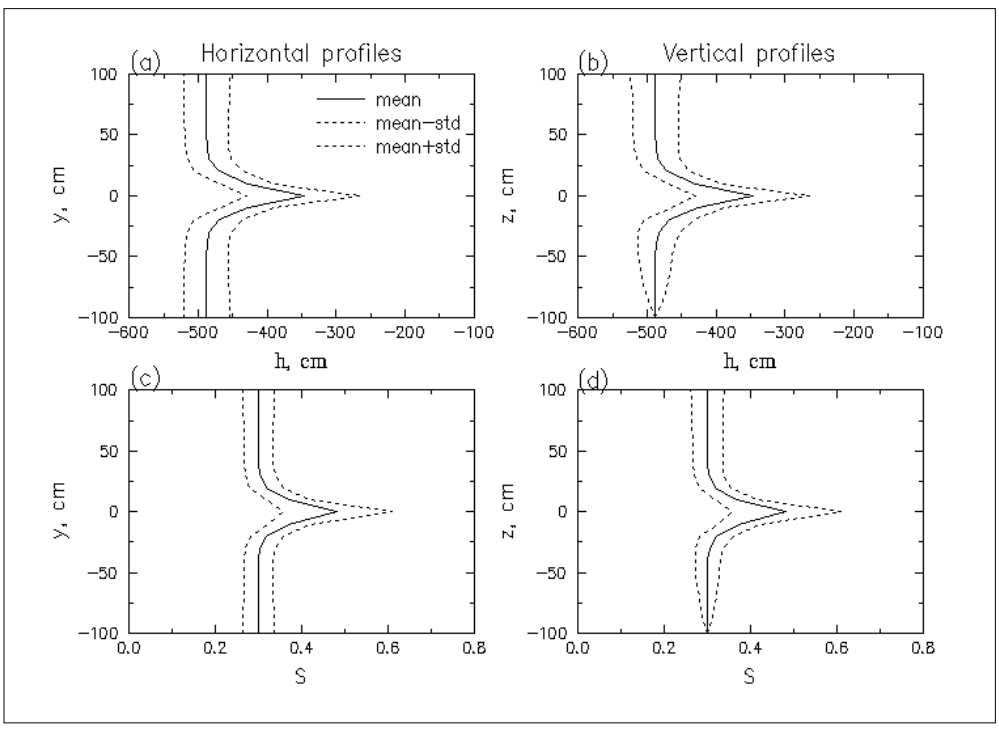

DTN: LA9909WS831372.020

Figure 79. Case 10. The Same as Case 1 in Figure 70 but with σ_α = 0

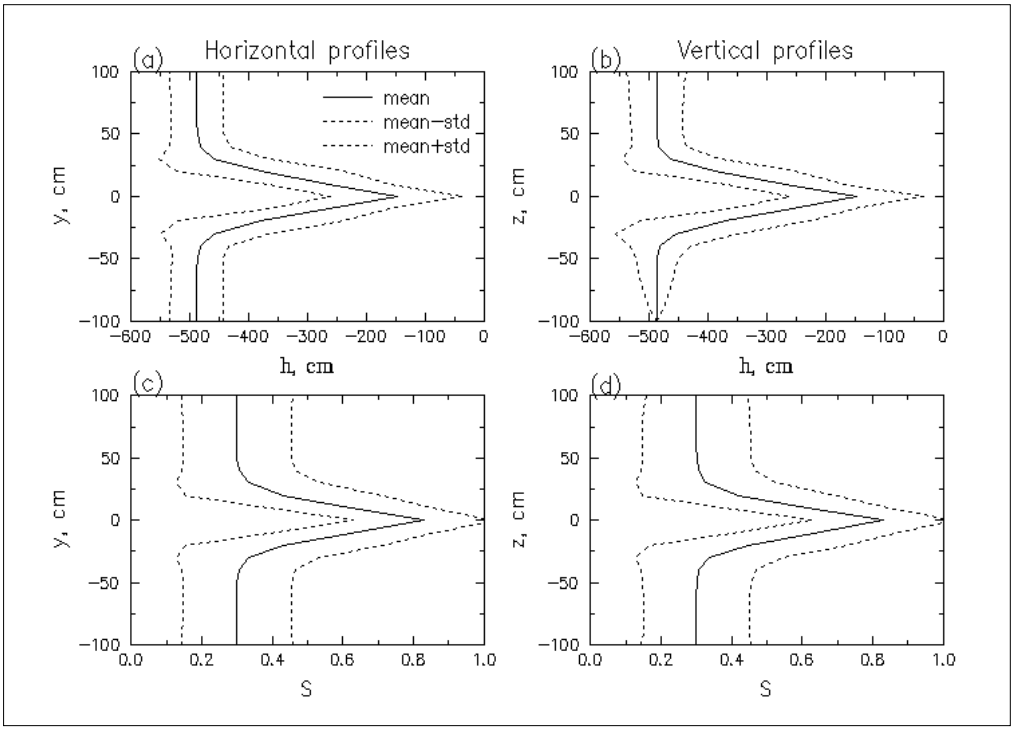

DTN: LA9909WS831372.020

Figure 80. Case 11. The Same as Case 1 in Figure 70 but with Q = 10 mL hr^{-1}

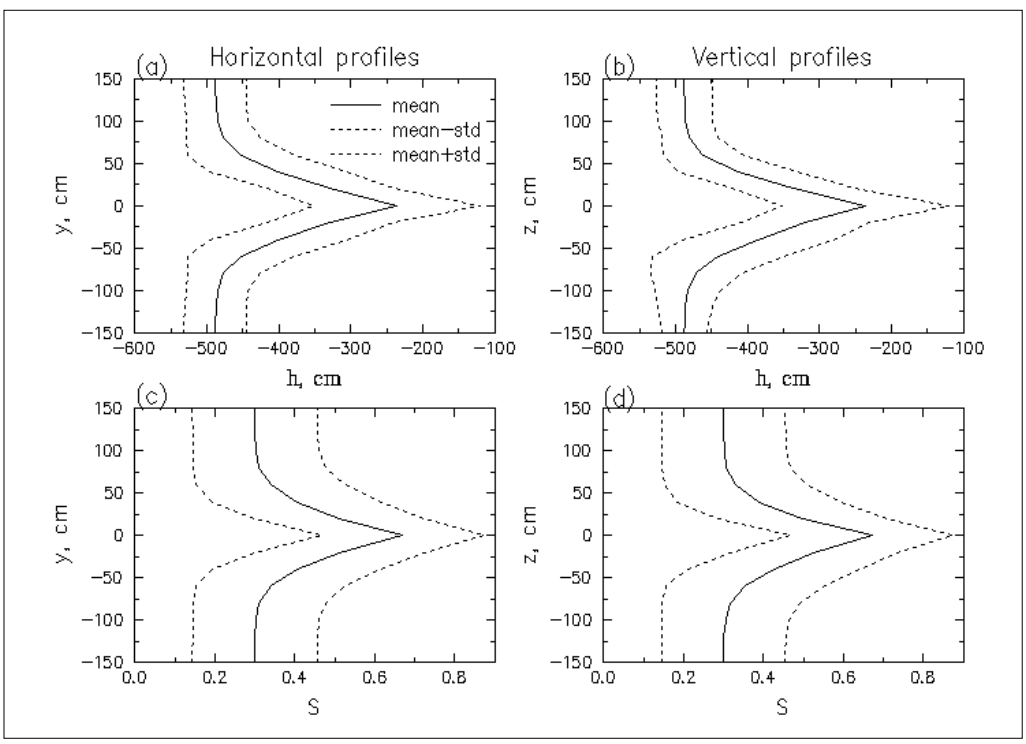

DTN: LA9909WS831372.020

Figure 81. Case 12. The Same as Case 8 in Figure 77 but with Q = 50 mL hr^{-1} and L_3 = 100 cm

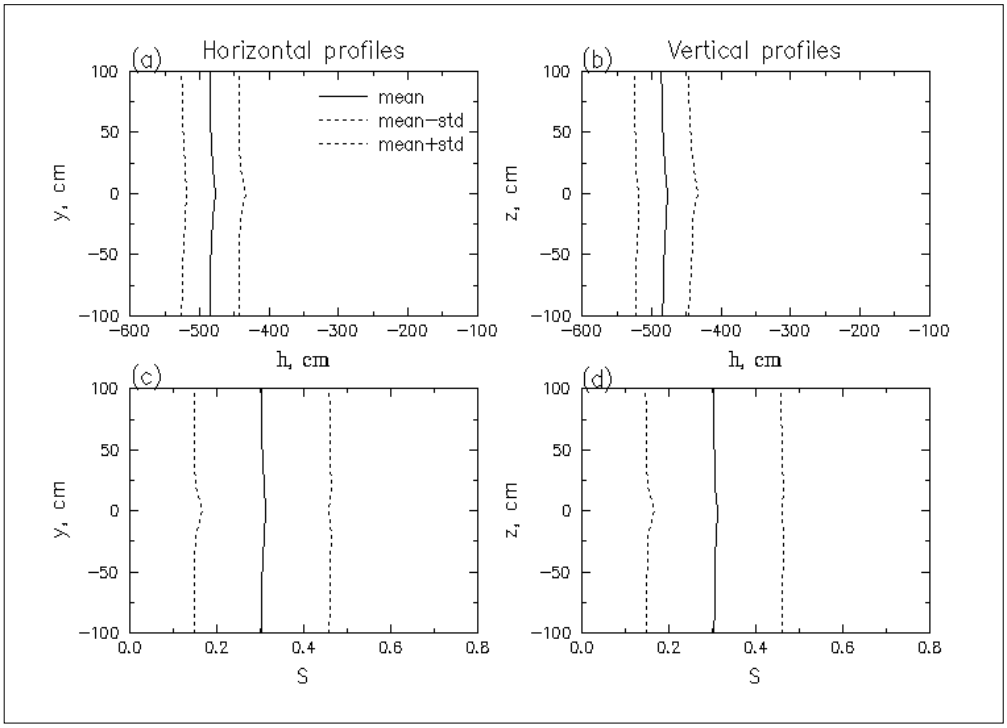

DTN: LA9909WS831372.020

Figure 82. Case 13. The Same as Case 1 in Figure 70 but with $\langle f \rangle = 0.314$, $L_1 = L_2 = 400$ cm, and $Q = 10$ mL hr^{-1}

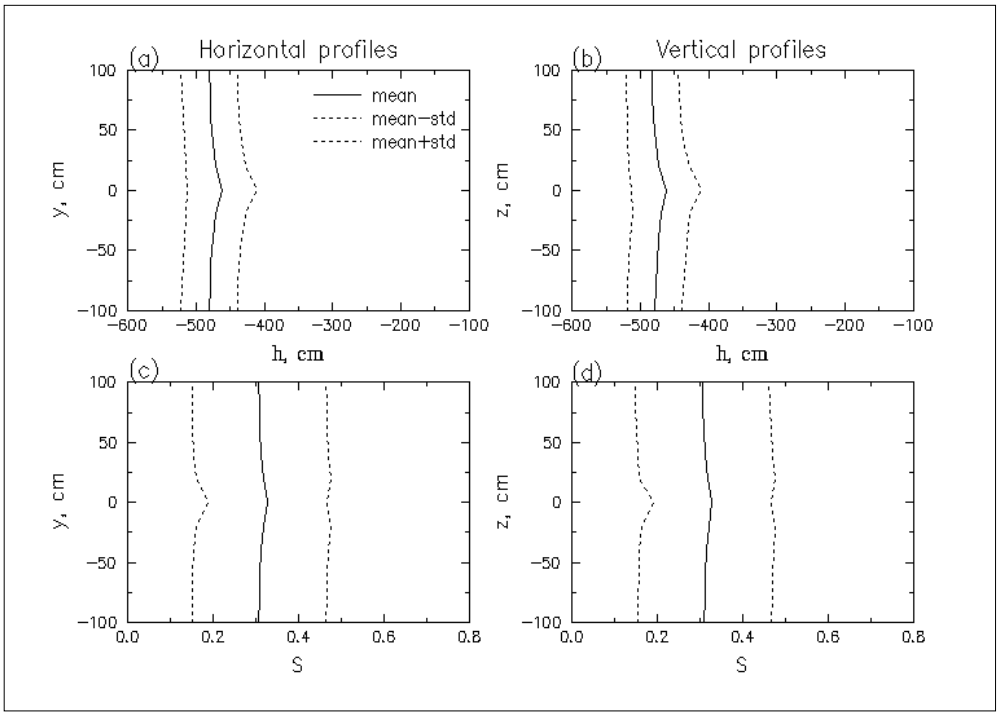

DTN: LA9909WS831372.020

Figure 83. Case 14. The Same as Case 13 in Figure 82 but with $Q = 50$ mL hr^{-1} and $L_3 = 100$ cm

6.8.6.2.4 Nonstationarity

The stochastic model of transient fluid flow in unsaturated, stationary (statistically homogeneous) media was modified to account for nonstationary features such as distinct layers in the rock properties. This extension was then implemented into the stochastic model and tested with some two-dimensional examples. In these examples, some special cases of medium nonstationarity are considered: trending in the statistical moments of the log of saturated hydraulic conductivity and pore size distribution parameter; zones of different rock properties existing in the domain; and different layers present in the domain. The effect of an embedded thin layer on fluid flow for the Phase-1A test was investigated with this modified stochastic model. It was found that this thin layer acts like a barrier to fluid flow and induces lateral fluid spreading. Only after accounting for this thin layer did the stochastic model produce fluid redistribution behaviors that are qualitatively similar to those observed by the mineback. A quantitative comparison will be made after the site-specific statistical parameters are obtained from the on-going geostatistical analysis of the rock property measurements at the site. In addition, it was found that the flow nonstationarity under unsaturated conditions significantly affects the behaviors of solute migration in such flow fields. The effect of the thin layer in the Phase-1A area on the migration of injected tracers can be assessed with site-specific statistical parameters.

6.8.6.3 Monte Carlo Flow and Transport Simulations

6.8.6.3.1 Introduction

To augment the results of the sensitivity analyses for the homogeneous-model calculations and the stochastic-model results, a series of Monte Carlo analyses were carried out in two dimensions. The goal of these simulations is to bracket the range of possible transport behaviors that could arise due to variability in the hydrologic parameters. To accomplish this goal, a refined 2-D grid was generated (Figure 84) for performing flow and transport calculations. As in the homogeneous simulations using FEHM (V2.00, STN: 10031-2.00-00), the top and bottom boundaries of the model are held at constant capillary pressure. A single realization of the model consists of two simulations: a background simulation (without fluid injection at the borehole) to establish a steady-state flow condition followed by a simulation in which fluid of unit concentration (arbitrary concentration units) is injected for 180 days, the planned duration of the Phase-1A experiments. To simulate a heterogeneous system, the model is populated with a distribution of permeability values with a given mean value and an assumed correlation length. Figure 85 shows a permeability distribution chosen at random from the Case-1 simulations (see Table 36 for a summary of the different cases treated in the Monte Carlo simulations; detailed discussion of the individual cases considered is described below). Contrasting permeability values within the region of rock in which fluid is injected is expected to affect the flow and transport behavior by providing preferential pathways for fluid migration through the rock.

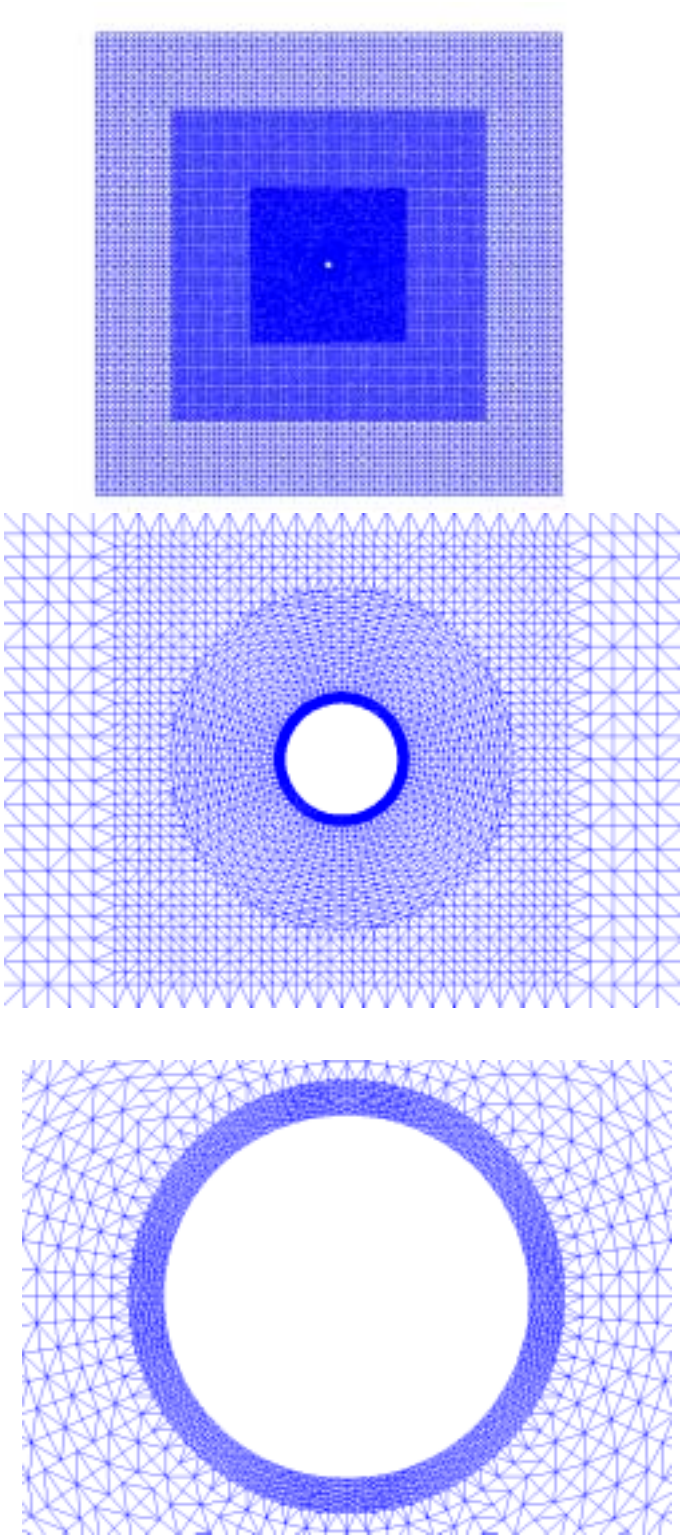

DTN: LA9909WS831372.021

NOTE: Top: full view (6 m x 6 m); Middle: intermediate close-up view (0.4 m x 0.5 m); Bottom: close-up of borehole.

Figure 84. Finite-Element Grid Used in the Monte Carlo Simulation

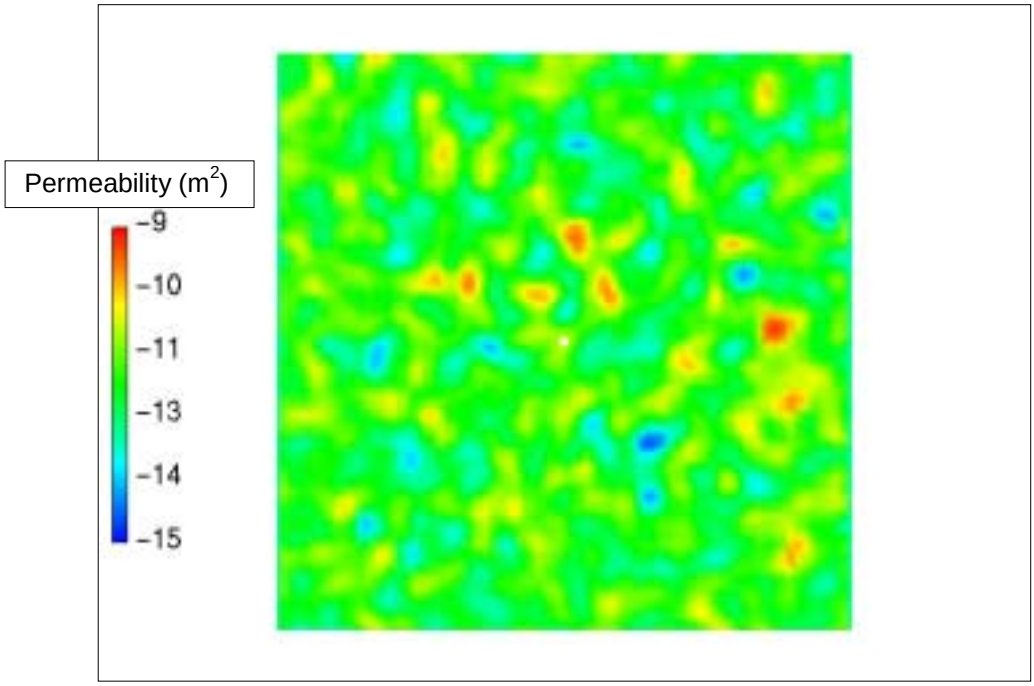

DTN: LA9909WS831372.021

NOTE: This plot shows the permeability distribution for the Monte Carlo realization selected for discussion.

Figure 85. Permeability Distribution

Table 36. Summary of Monte Carlo Cases*

Case number	Correlation of α and permeability	Correlation length of heterogeneities
1	None	0.2 m
2	Altman et al. (1996, Eq. on p. 34)	0.2 m
3	Altman et al. (1996, Eq. on p. 34)	0.1 m
4	Altman et al. (1996, Eq. on p. 34)	0.5 m

DTN: LA9909WS831372.021

NOTE: *All cases assume $\ln(k_s) = 1.54$, where k_s is in cm hr^{-1}.

6.8.6.3.2 Methodology

The Monte Carlo approach considers the results of all individual realizations to be equally likely outcomes of the behavior of the system. Therefore, once a metric is chosen for quantifying the behavior of the system, statistical properties of the behavior of the system can be established. In the present study, the movement of a conservative solute injected with the fluid is used. The maximum penetration distances in all four directions away from the injection point are recorded for several different concentrations to establish the direction of movement of tracer. Then, for all 50 realizations in a given case, the mean values for these distances are recorded along with the standard deviation. The mean values establish the general location of the concentration front,

whereas the standard deviation is a measure of the uncertainty in the predictions of concentration-front movement due to the heterogeneities of the rock mass.

6.8.6.3.3 Statistical Results

One advantage of the Monte Carlo approach is that an individual realization can be examined in detail to understand the behavior of the system, after which, the multiple realizations can be used to quantify the uncertainty. The behavior of the flow and transport system is now examined (Figure 86) for the permeability distribution shown in Figure 85. The background saturation distribution shows little or no variability. This result is in contrast to the variability in predicted fluid saturation for the cases in which permeability and van Genuchten α are correlated.

For that type of heterogeneous field, the fluid saturation is a strong function of α. The left-hand panels of Figure 86 show the movement of the saturation front into the rock mass for various times during the injection phase, and the right-hand panels are the concentrations of the conservative tracer for those same times. For this rock at this injection rate, there appears to be a relatively uniform migration of fluid and tracer away from the injection point in all directions, even upward. Under these conditions, the capillary-pressure driving forces are strong enough to pull water against the force of gravity. The presence of the borehole produces a "shadow effect" in which fluid must migrate around the borehole to reach the rock on the opposite side of the injection pad. Regarding the influence of heterogeneities, there is some tendency for fluid to be drawn preferentially into portions of the rock with higher capillary suction. The resulting saturation and concentration fronts exhibit an irregular pattern that tracks the heterogeneities. Nevertheless, the general patterns of movement of fluid and solute match fairly closely those of the homogeneous simulations.

Now the results of the statistical analyses of the Monte Carlo simulations are examined. Table 37 shows the mean and standard-deviation values for the four cases summarized in Table 36. The y coordinate in the table represents the vertical direction, with negative values below the borehole injection point. The x coordinate is laterally away from the borehole, with positive values located on the side at which the injection pad is located. First consider the results of Case 1, in which the permeability field is assumed to vary but the van Genuchten α value is constant. The mean values for the minimum and maximum y values illustrate the degree to which the transport occurs uniformly in upward and downward directions. The Case-1 results show that capillary forces tend to pull water (and tracer) uniformly upward and downward with little or no tendency for downward migration due to gravity. The $C = 0.01$ isoconcentration value is meant to represent the migration of the front edge of the concentration plume; it travels approximately 40 to 45 cm in the upward, downward, and outward (positive x) directions, on average. The injection point is located at approximately $x = 5$ cm and $y = 0$. The travel distance for the $C = 0.5$ isoconcentration value is more indicative of bulk plume movement, rather than the leading edge. This front travels approximately 30 cm in the three directions. The $x_{\min}$ values suggest a slight asymmetry in plume migration. This asymmetry is caused by the "shadow effect" due to the presence of the borehole, as described above.

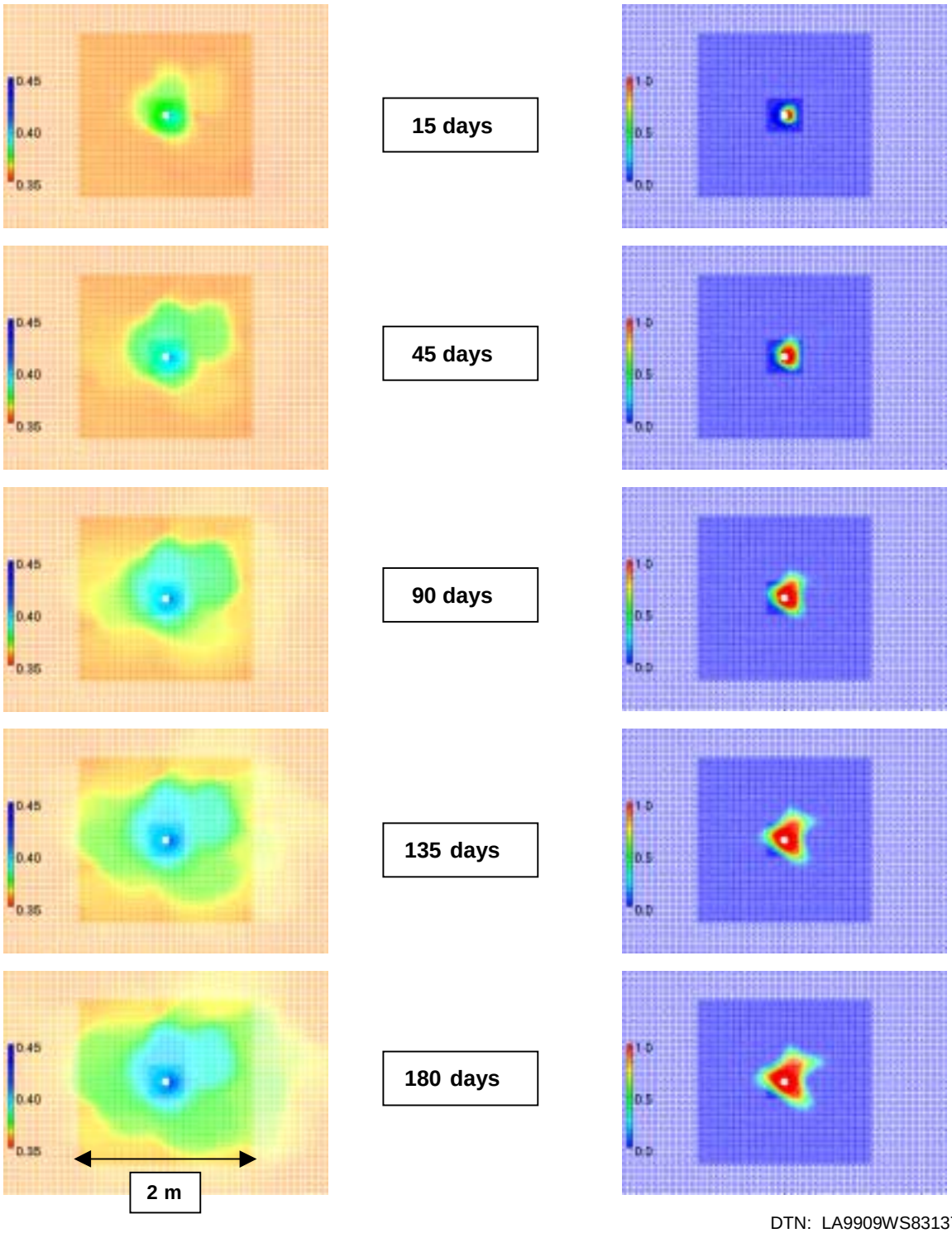

DTN: LA9909WS831372.021

NOTE: These plots show fluid saturations (left panels) and tracer concentrations (right panels) at various times during a Monte Carlo simulation. Note the restricted range of saturation values used.

Figure 86. Fluid Saturations and Tracer Concentrations

Table 37. Statistical Results of Monte Carlo Simulations

	***C* = 0.01**				***C* = 0.1**				***C* = 0.5**			
	x_{min}	x_{max}	y_{min}	y_{max}	x_{min}	x_{max}	y_{min}	y_{max}	x_{min}	x_{max}	y_{min}	y_{max}
Case 1												
Mean	–0.35	0.53	–0.45	0.42	–0.28	0.46	–0.37	0.35	–0.20	0.37	–0.29	0.27
Std. dev.	0.11	0.12	0.082	0.093	0.098	0.11	0.077	0.085	0.08	0.098	0.070	0.068
Case 2												
Mean	–0.30	0.47	–0.42	0.41	–0.23	0.41	–0.35	0.35	–0.16	0.33	–0.27	0.27
Std. dev.	0.019	0.014	0.015	0.012	0.016	0.013	0.013	0.013	0.010	0.012	0.011	0.013
Case 3												
Mean	–0.29	0.48	–0.41	0.41	–0.22	0.41	–0.35	0.35	–0.15	0.33	–0.27	0.27
Std. dev.	0.014	0.012	0.011	0.011	0.011	0.012	0.011	0.011	0.007	0.013	0.011	0.010
Case 4												
Mean	–0.28	0.49	–0.41	0.42	–0.22	0.42	–0.35	0.35	–0.15	0.34	–0.27	0.27
Std. dev.	0.027	0.024	0.022	0.024	0.022	0.020	0.019	0.018	0.015	0.017	0.018	0.017

DTN: LA9909WS831372.021

NOTE: Results based on 50 realizations for each case listed in Table 36.

The borehole causes the plume to have more difficulty migrating in the negative *x* direction. The standard deviation values reflect the uncertainty in the predicted migration of the plume caused by the heterogeneous permeability distribution. For Case 1, the uncertainty in the $C = 0.01$ isoconcentration value is about 8 to 12 cm (depending on direction), whereas for the $C = 0.5$ value, the uncertainty ranges from about 7 to 10 cm. Therefore, for Case 1, the heterogeneous permeability field (with no variability in α) adds considerable uncertainty to the predictions.

A comparison of Cases 1 and 2 illustrates the influence of imposing a correlation of permeability and α on the uncertainty of the predictions. The mean values for the spreading of the plume in all directions are very similar for the two cases, but the uncertainty due to heterogeneity is much smaller when α is assumed to be correlated with permeability (Case 2). The correlation imposes a larger α for lower permeability, resulting in a larger capillary suction for regions of the rock with lower permeability. This result counteracts the tendency for fluid to travel preferentially through higher permeability rock, as in Case 1. Therefore, the spreading of tracer in Case 2 is more uniform, and the standard deviation values are consequently smaller.

Finally, the influence of correlation length on plume spreading can be examined by comparing Cases 2, 3, and 4, which assumed correlation lengths of 0.2 m, 0.1 m, and 0.5 m, respectively. The mean behavior of the plumes is very insensitive to the correlation length. Regarding the uncertainty in plume prediction (as measured by the standard deviation), there is a trend toward larger uncertainty as the correlation length increases, as expected. Nevertheless, the uncertainty for these cases is much smaller than the correlation length itself. This result is caused by the assumed correlation of permeability and α for each of these cases, which, as just discussed, largely negates the distribution of permeability values. Therefore, the largest uncertainty in these simulations appears to be the nature of the correlation (or lack thereof) of different hydrologic

properties. Permeability and the van Genuchten α parameter were correlated in these simulations. Altman et al. (1996, p. 34) also propose correlations between permeability and porosity for Yucca Mountain tuffs. Therefore, the most important data that could be collected to further constrain these predictions are hydrologic property measurements on a much larger set of samples from the test block. A full suite of property measurements (porosity, permeability, and unsaturated hydrologic parameters) on samples collected from known locations in the block would be useful to set correlations between parameters and assign correlation lengths for future simulations.

6.8.6.3.4 Interpretations of the Monte Carlo Phase-1A Study

The modeling analyses for Phase 1A indicate that strong capillary forces in the rock matrix of the Tac unit are likely to modulate fracture flow from overlying units, thereby dampening pulses of infiltrating water and providing a large degree of contact between radionuclides and the rock matrix. Several modeling approaches, from deterministic to Monte Carlo to stochastic models, were used to simulate the Phase-1A experiments. All yielded similar qualitative results. From these results, the tentative conclusion is that the deterministic modeling approach taken at the site scale may be adequate. As the data from the UZTT become available, parameterizations used in these calculations will be updated.

A particularly interesting observation from the Phase-1B experiment is that, even when injection occurs immediately adjacent to a fracture, water appears to be imbibed quickly into the surrounding matrix. The transport times observed immediately below the injection point were on the order of 30 days, whereas pure fracture flow would have resulted in travel times of minutes to hours at this flow rate. Site-scale models must be evaluated in light of this observation. Models that predict significant fracture flow at percolation rates low enough for the matrix to transmit the flow may be inconsistent with the Phase-1B experiment.

6.8.6.3.5 Forward Efforts

In Phase 1A, the fluorescein image information is being incorporated into the modeling effort. Also, a small number of moisture and bromide samples from the Phase-1A rock are being analyzed. The strengths and weaknesses of the three conceptual approaches presented in this section are being assessed based on their relative accuracy in predicting flow and concentration. Predictions will be compared with flow and transport experimental data.

Measurements of the tracer concentrations from collected samples are to be conducted after that date. After auger samples are collected and analyzed and mineback completed, the numerical predictions will be compared against the measured values, and the accuracy of the model configuration will be addressed.

6.8.7 Initial Phase-2 Model Predictions

6.8.7.1 Introduction

In this section, conservative and reactive tracer breakthrough times are predicted for each of the sampling boreholes for up to one year from the start of Phase-2 injection. This work constitutes the first "blind" prediction on the behavior of the Phase-2 block of the Busted Butte transport test prior to injection. These predictions were made and presented prior to starting Phase-2 injection. These predictions are intended to test the current modeling concepts and tools available to the integrated site-scale model and the validity of the abstractions of that model for performance assessment. The predictions use parameters from currently available Yucca Mountain hydrologic and geochemical databases. At this stage, no model calibration to the UZTT has been performed. As data become available from the various phases of the UZTT, they will be incorporated into refined versions of the model. The new information will be used to make improved predictions.

The computer code FEHM (V2.00, STN: 10031-2.00-00), which was used in the site-scale UZ flow and transport model and its abstractions for performance assessment, is also used in the development of the 3-D model presented in this report. Specifically, this code is used for radionuclide migration predictions using "calibrated" site-scale flow solutions. Although detailed geologic and hydrologic property distributions in three dimensions are not available at present for the UZTT, it is anticipated that during the course of the testing, these data will become available. Three-dimensional effects will probably become important as data specific to the test block become available for the Phase-2 block. The model is, therefore, being developed in three dimensions at the outset to capture these effects and to anticipate the 3-D property database that will be collected for the test block.

6.8.7.2 Model Description

The Phase-2 test block at Busted Butte encompasses, from top to bottom, the lower section of the Topopah Spring Tuff vitrophyre (Tptpv2) and the hydrologic Calico Hills unit (CHn, comprised of Tptpv1 and Tac). The first step in constructing a 3-D finite-element model of the Phase-2 test is to build a finite-element mesh using the coordinates of the injection and collection boreholes. The file used in this work contains the surveyed local coordinates of the boreholes and the layered stratigraphy at the site.

Figure 87 gives a representation of the Phase-2 block with the boreholes represented as colored lines. The simulation block is approximately 7-m high by 12-m deep by 12-m wide and contains 28 boreholes ranging from 7.5 m to 10.0 m in length. The 8 injection boreholes (shown in red) all originate in the left rib of the Test Alcove (located in front of the figure). These boreholes are subparallel, distributed along two horizontal planes, and are perpendicular to the 12 collection boreholes (dark blue) coming from the right rib of the Main Adit (to the left of the vertical *yz* plane). The other boreholes (light blue) are dedicated to ERT and GPR-T measurements.

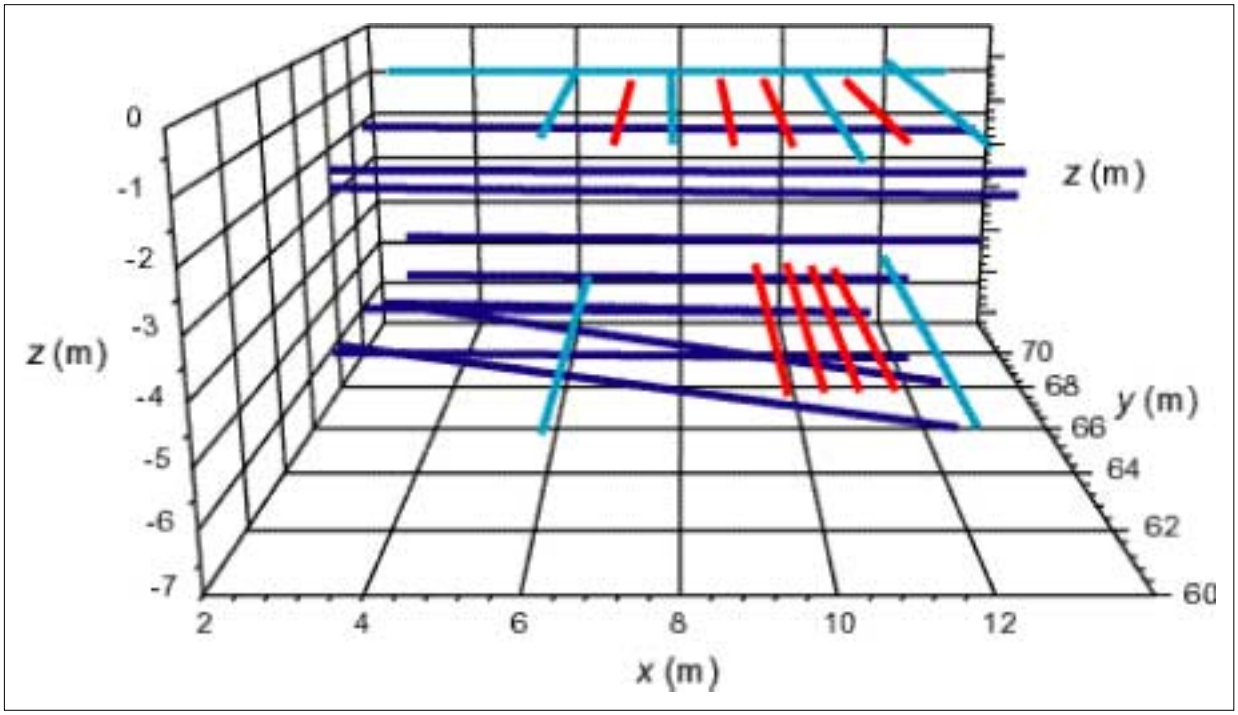

DTN: MO0004GSC00167.000 (for location); LA9909WS831372.022

NOTE: The red lines represent injection boreholes; the dark blue lines collection boreholes; and the light blue lines are devoted to tomography. In this view, the Test Alcove is located in front of the figure, and the Main Adit is to the left of the figure (beyond the x = 2 plane). Dimensions are in meters.

Figure 87. Three-Dimensional View of the Injection and Collection Boreholes

The model domain extends from +2 to +14 m in the x-direction, +60 to +72 m in the y-direction, and –8.2845 to +2.5015 m in the z-direction. These coordinates are consistent with the surveyed local coordinates and the stratigraphy of the block. Figure 88 shows a top view of the finite-element grid with the borehole locations.

In general, the mesh was refined at locations between the injection and collection boreholes to accurately capture the migration of the tracers and heterogeneities at scales smaller than the layer thickness. In the x-direction, a grid spacing of 0.25 m at locations close to the boreholes was chosen. In both the x- and y-directions, a coarse mesh spacing at the block boundaries was chosen because no transport is expected at these locations. In the y-direction, a mesh spacing of 0.125 m at locations close to boreholes was chosen. A slightly finer grid spacing was used in the y-direction than the x-direction to capture accurately the location of the injection points, which are spaced 0.61 m apart in the y-direction (10 injection points per injection borehole). In the z-direction, the stratigraphy is represented with 6 distinct layers: 5 layers to represent the Calico Hills hydrogeologic unit (Tac: 3 layers; Tptpv1: 2 layers), and 1 layer to represent Tptpv2. The discretization in the z-direction is dependent on the particular layer because some layers are thicker than others. The discretization ranged from 0.15 to 0.25 m. The entire model is

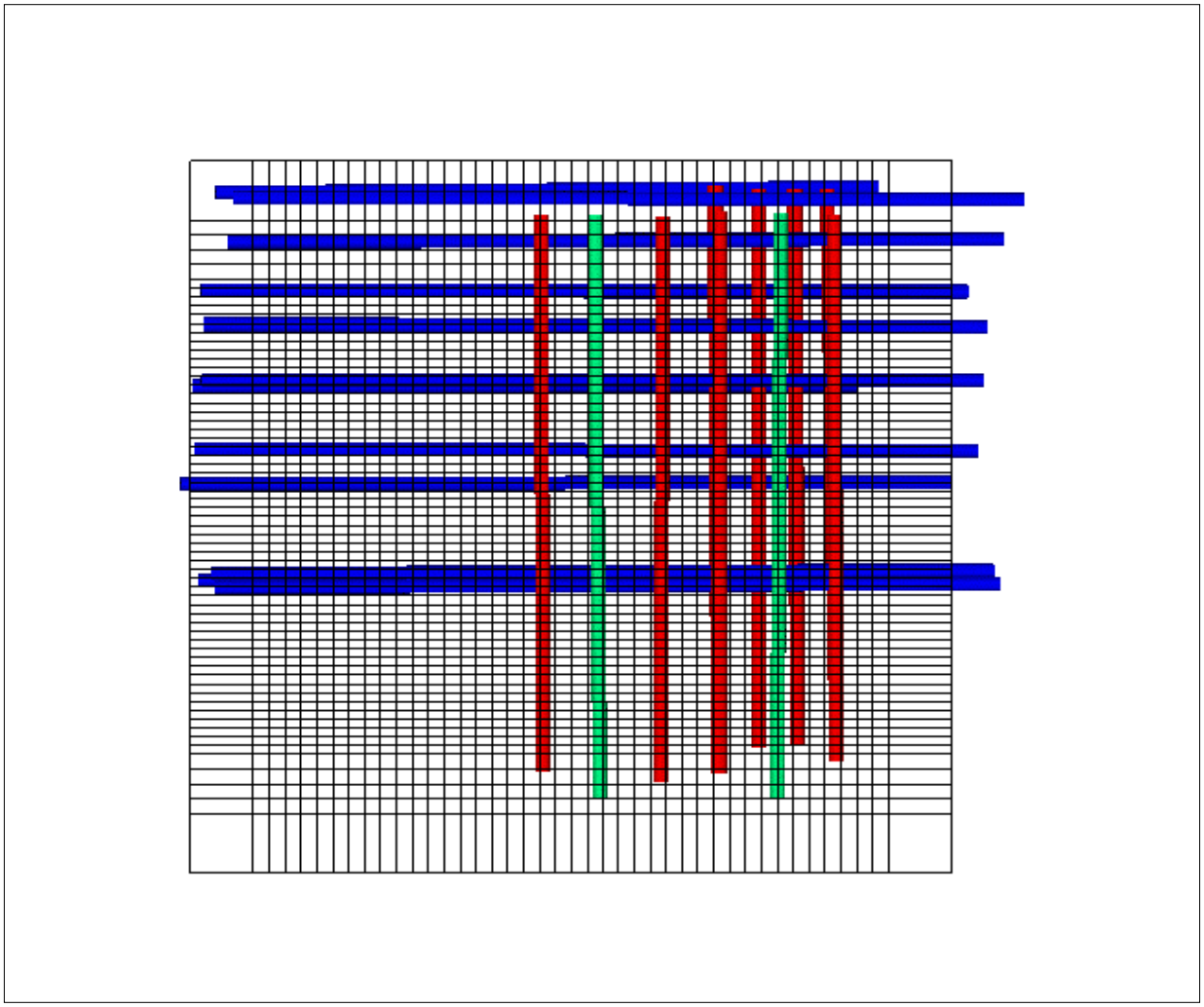

DTN: MO0004GSC00167.000 (for location); LA9909WS831372.022

NOTE: As in Figure 87, injection boreholes are depicted as red lines, collection boreholes as blue, and ERT boreholes as green. The horizontal axis represents the *x*-direction, increasing to the right. The vertical axis represents the *y*-direction, increasing bottom to top.

Figure 88. Top View of Finite-Element Grid and the Injection and Collection Boreholes

comprised of 128,570 nodes. Figures 89 and 90 show views of the grid from the Test Alcove and the Main Adit, respectively. Once the mesh was constructed, the next step was to assign properties to the model. Table 38 contains the property sets used in the different layers. These properties are based upon measurements collected from the same units in the Yucca Mountain area but not actually from Busted Butte.

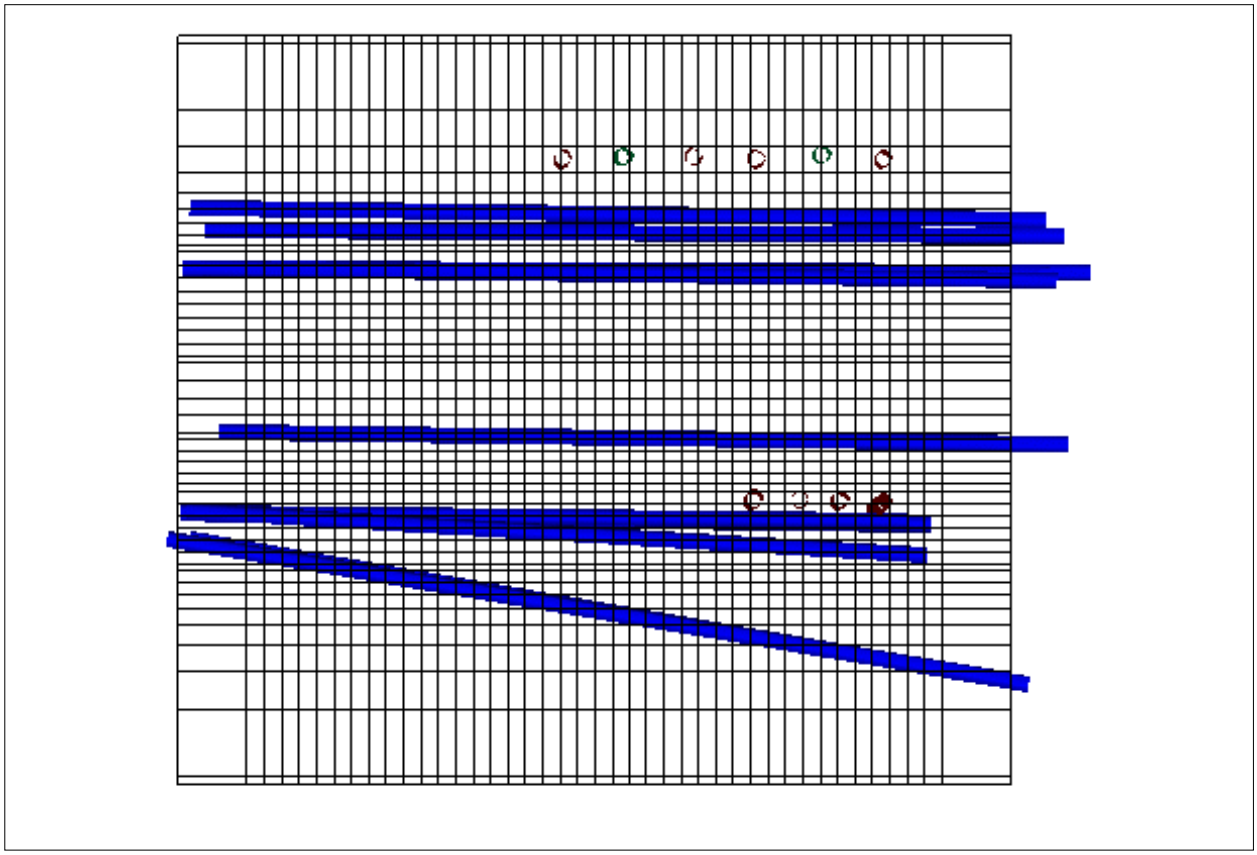

DTN: MO0004GSC00167.000 (for location); LA9909WS831372.022

NOTE: The blue colored lines represent collection boreholes. Because the injection boreholes originate in the Test Alcove, they are perpendicular to the plane of the figure and are depicted as circles. The horizontal axis represents the *x*-direction. The vertical axis represents the *y*-direction.

Figure 89. Finite-Element Grid as seen from the Test Alcove

Table 38. Property Sets for the Phase-2 Test

Busted Butte Layer	Matrix Material (Flint 1998)				Fracture Material					
	Layer	α_m (m^{-1})	n_m	K_m (m^2)	Layer	α_f (m^{-1})	n_f	K_f (m^2)	ϕ_f	θ
Tac1	CHv	3.5	1.19	5×10^{-12}	CH1v	11.52	3.0	2.43×10^{-9}	7.14×10^{-5}	0.5
Tac2	CHv	3.5	1.19	5×10^{-12}	CH1v	11.52	3.0	2.43×10^{-9}	7.14×10^{-5}	0.5
Tac3	CHv	3.5	1.19	5×10^{-12}	CH1v	11.52	3.0	2.43×10^{-9}	7.14×10^{-5}	0.5
Tptpv1	BT1	0.56	1.31	1×10^{-13}	CH1v	11.52	3.0	2.43×10^{-9}	7.14×10^{-5}	0.5
Tptpv1	BT1	0.56	1.31	1×10^{-13}	CH1v	11.52	3.0	2.43×10^{-9}	7.14×10^{-5}	0.5
Tptpv2	PV2	2.2	1.25	1×10^{-16}	TSW2	0.91	2.92	6.6×10^{-9}	1.29×10^{-4}	0.25

DTN: LA9909WS831372.022, LB970601233129.001

NOTE: Here, α and n are the van Genuchten parameters, K is permeability, ϕ is volume fraction, and θ is porosity. The subscript m signifies matrix material and the subscript f signifies fracture material.

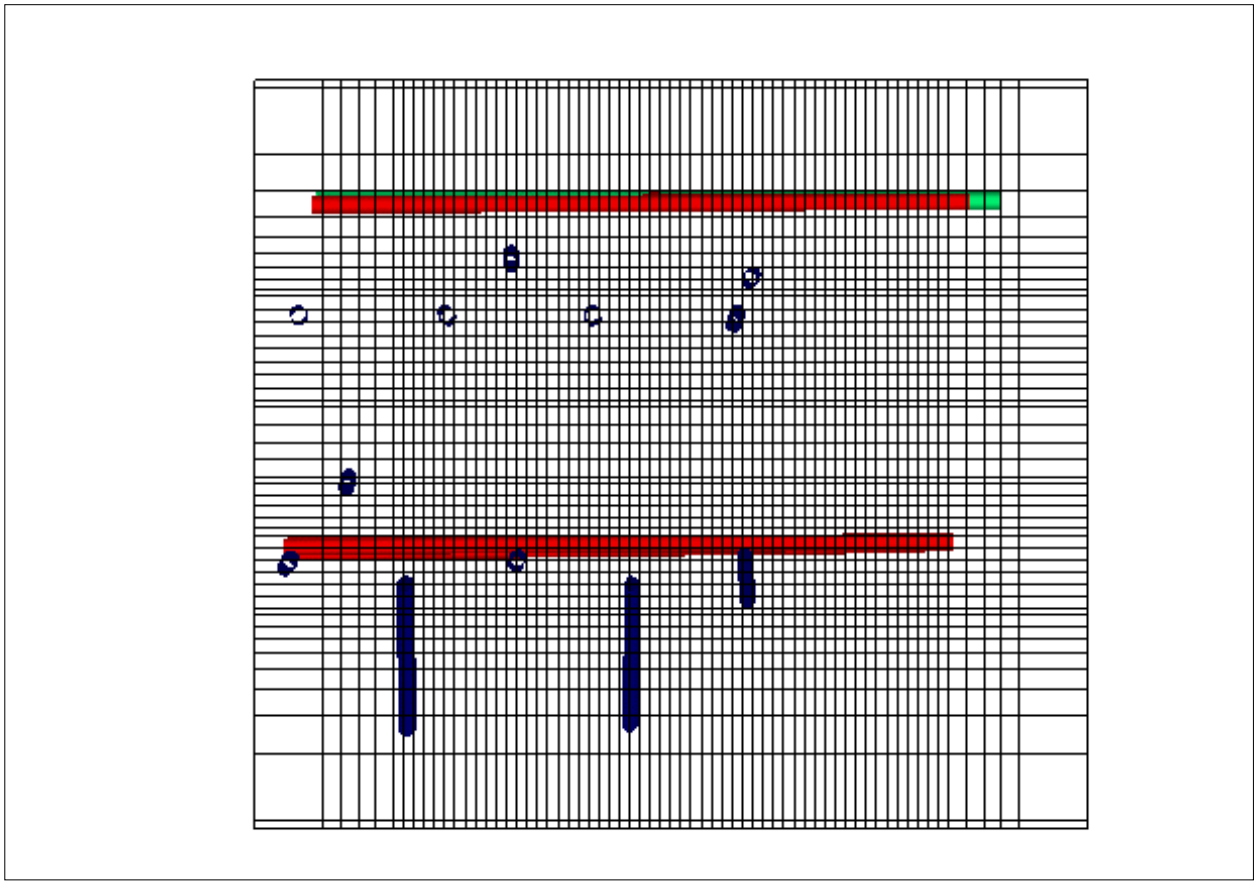

DTN: LA9909WS831372.022

NOTE: The horizontal red lines represent the location of injection boreholes, which are perpendicular to the collection boreholes (blue). The collection boreholes originate in the Main Adit, but several are plunging down and, thus, appear as blue lines rather than circles. The green line represents one of the tomography boreholes. The horizontal axis represents the *y*-direction, and the vertical axis represents the *z*-direction.

Figure 90. Finite-Element Grid as seen from the Main Adit

For this preliminary investigation, layers 1 through 3 were combined into a single Calico Hills unit (Tac), layers 4 to 5 were assigned Tptpv1 properties, and layer 6 was assigned Tptpv2 properties. As additional data become available, layers 1 through 3 and 4 through 5 will all be treated as distinct layers. Porosity values were obtained from a few samples from the Busted Butte site. Permeabilities and van Genuchten relative-permeability parameters for the matrix were obtained from Flint (1998). This study (Flint 1998) was chosen because it represents the existing YMP database for the unsaturated zone and contains sufficient samples to generate statistics on the variability of key parameters, such as matrix permeability and matrix van Genuchten parameters. Fracture van Genuchten parameters were taken from the "calibrated" flow model in DTN: LB970601233129.001. These data were obtained by fitting field data at the site scale. Although there is a great amount of uncertainty in fracture properties, this data set is considered to be a reasonable representation of YMP material properties applicable to Busted Butte.

For this "blind" investigation, and in view of the absence of data on fracture-matrix interactions in the Calico Hills, the equivalent-continuum model (ECM) was used to model Phase 2. The

ECM was also used in scoping calculations done during design of the test and is currently being used to understand both Phases 1A and 1B.

Tracer breakthrough has occurred in the 10 mL hr^{-1} injection system of Phase 1B (borehole 6). Specifically, tracer was detected at the pad 35 days after injection. This result means the time of breakthrough occurred between 28 and 35 days in relation to the collection-pad schedule. To compare model predictions with test breakthrough times as defined by the appearance of fluorescein tracer on a collection pad, the concentration of the tracer must be known. For example, if the time of breakthrough is defined to be when the normalized concentration reaches 0.5, then for Tptpv2, the ECM predicts a breakthrough at 47 days for a distance traveled by the tracer of 28 cm (Figure 91). At a normalized concentration of 0.3, the model predicts breakthrough at 31 days for the same distance, which is close to the observed breakthrough time for borehole 6.

For the first phase of predictive modeling and in the absence of appropriate data, the property sets listed in Table 38 were used with no attempt at calibration. The background flow conditions were obtained by setting a capillary pressure at the top and bottom boundaries and allowing the block to equilibrate to a steady-state saturation profile. A capillary pressure of 200 m of water was chosen, which is within the range of capillary-pressure measurements at Yucca Mountain (Altman et al. 1996, p. 34). The capillary pressure was set so that a saturation of about 0.35 to 0.45 was obtained in the block. Moisture measurements and preliminary porosity data from test-block lithologies indicate that these saturation values are reasonable. Once the background conditions are set, the next step is to begin pumping and injecting tracer.

Three different pumping rates were used for injection boreholes in the Phase 2 experiment: (a) 1 mL hr^{-1} (1 upper borehole), (b) 10 mL hr^{-1} (4 lower boreholes), and (c) 50 mL hr^{-1} (3 upper boreholes). The 1 mL hr^{-1} rate is equivalent to an infiltration rate of approximately 30 mm yr^{-1}, which is well within the range of infiltration rates at Yucca Mountain. The predictions made (given below) show that during a 1-yr test, the 1 mL-hr^{-1} pumping rate is not expected to transport any tracer to the sampling boreholes. Injection borehole 23 will be the only one that pumps at 1 mL hr^{-1}. The 10-mL-hr^{-1} injection rate is equivalent to an infiltration rate of approximately 380 mm yr^{-1}, which is slightly higher than the highest anticipated infiltration that could occur at Yucca Mountain. The lower injection boreholes 24, 25, 26, and 27 will operate at 10 mL hr^{-1}. Finally, 50 mL hr^{-1} is equivalent to an approximate infiltration rate of 1550 mm yr^{-1}. This infiltration rate is far higher than what is expected at Yucca Mountain even under wetter, future climate scenarios. The purpose of the 50 mL hr^{-1} rate is to obtain enough separation in travel times between the conservative and reactive tracers so as to be visible and distinct in the field test. Injection boreholes 18, 20, and 21 will pump continuously at 50 mL hr^{-1}.

6.8.7.3 Predictions

The predictions below are borehole specific and can, therefore, be used to compare directly to test-block results. Phase-2 borehole numbers and relative locations were presented in Figure 38 (Section 6.8.2.4.1). Table 39 shows the distance between the closest sampling point and the injection planes. Tables 40 through 48 predict the tracer breakthroughs at each of these locations.

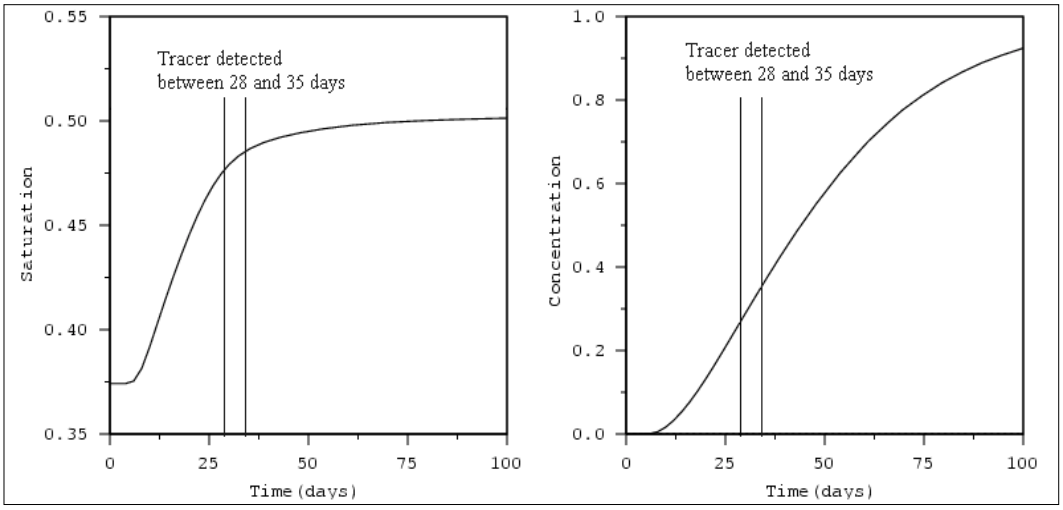

DTN: LA9909WS831372.022, file: *inject.trc*

NOTES: The plots show the conservative breakthrough of tracer 28 cm from the injection pad: (a) saturation breakthrough, (b) concentration breakthrough

Figure 91. Phase-1B Breakthrough Predictions Using Equivalent-Continuum Model and Tptpv2 Properties

Table 39. Closest Sampling Point to the Injection Planes Within Each Collection Borehole

Collection borehole	Distance from top injection plane (m)	Collection borehole	Distance from bottom injection plane (m)
16	0.61	46	0.175
17	0.80	48	0.175
14	1.17	9	0.175
15	1.17	10	0.59 (above plane)
13	1.17		
12	1.17		

DTN: LA9909WS831372.022

For all predictions, three criteria were used for tracer-breakthrough times: (a) a 5% concentration limit, (b) a 50% concentration limit, and (c) the concentration after 1 year from the time of injection (the time of submittal of results for TSPA-LA). Note that it was assumed that the concentration of tracer in the injection fluid is unity. Also, note that tracers are continuously injected for the duration of the test.

A diffusion coefficient of 1 x 10^{-11} m^2 s^{-1} was used for all tracers. Longitudinal and transverse dispersivities were zeroed out for this preliminary set of calculations. However, as with any finite-element model, some numerical dispersion is present. Due to the fine mesh spacing and small time steps taken in these simulations, numerical dispersion is not expected to play a significant role in these simulations. A bulk-rock density of 2,580 kg m^{-3} was used for all layers. This parameter only affects the reactive-tracer breakthrough times. As more data become available, all of these parameters will be adjusted. However, the values chosen are reasonable representations of Yucca Mountain properties, given the existing database.

Conservative Tracers

Travel times were first predicted for fluorescein, a conservative tracer. Uniform properties were assumed for porosity, permeability, and van Genuchten model parameters within each of the six layers of the test block. The effect of heterogeneous property distributions is discussed at the end of this subsection. Figure 92 depicts a concentration plume for fluorescein after 1 year.

Table 40. Fluorescein from Upper Injection Boreholes

Borehole number	5% Breakthrough concentration	50% Breakthrough concentration	Normalized concentration at 1 yr
16	27 days	68 days	1.0
17	48 days	118 days	1.0
14	118 days	238 days	0.87
15	103 days	218 days	0.90
13	103 days	218 days	0.90
12	212 days	> 1 yr	0.46
Remaining collection boreholes	> 1 yr	> 1 yr	0.0

DTN: LA9909WS831372.022, file: *cons.trc*

Table 41. Fluorescein from Lower Injection Boreholes

Borehole number	5% Breakthrough concentration	50% Breakthrough concentration	Normalized concentration at 1 yr
46	4 days	30 days	1.0
48	20 days	91 days	0.98
9	53 days	166 days	0.91
10	171 days	> 1 yr	0.37

DTN: LA9909WS831372.022, file: *cons.trc*

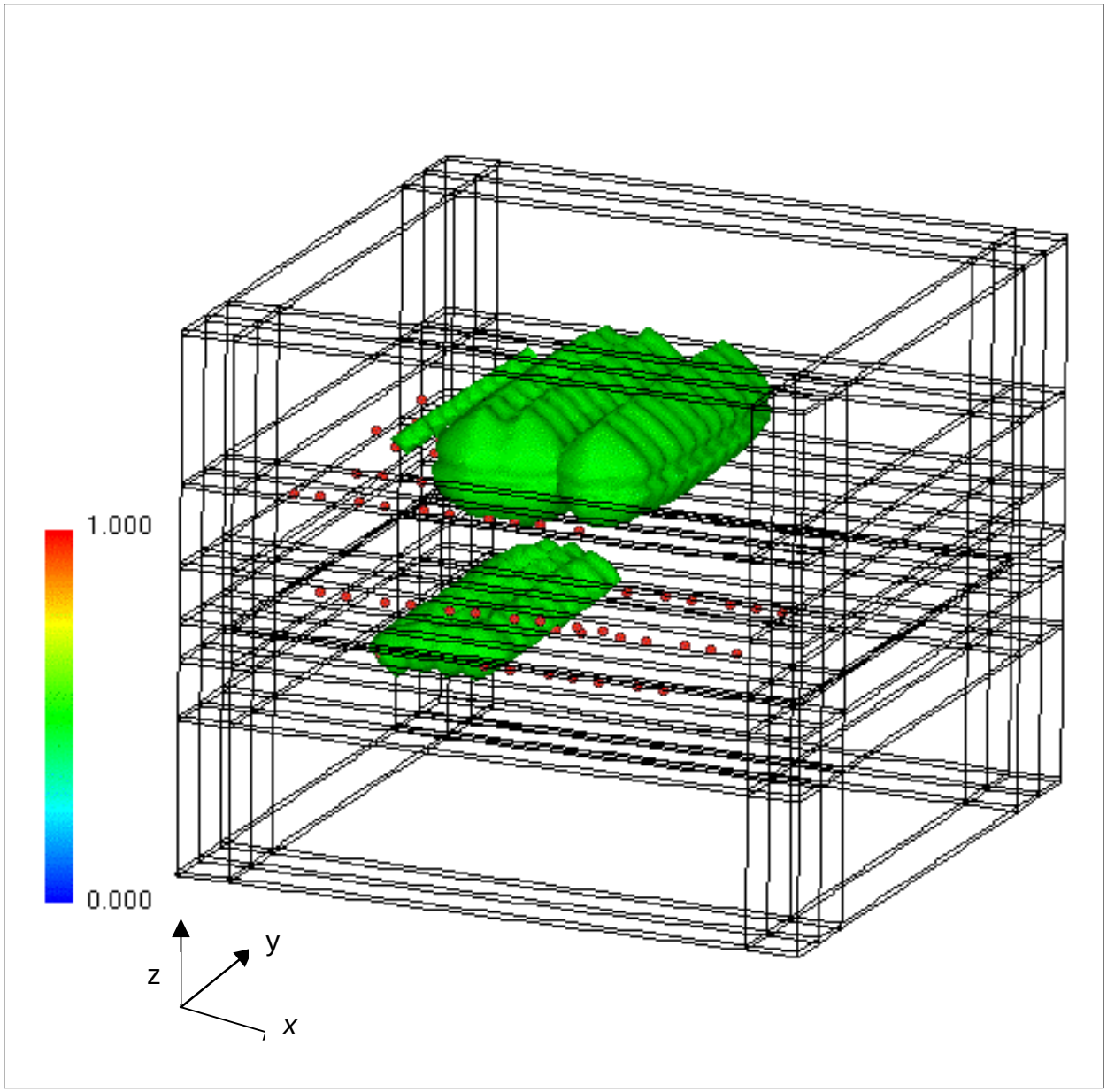

DTN: LA9909WS831372.022, file: *inject.10004_con_node*

NOTES: The figure depicts the concentration plume after 1 year of conservative-tracer injection. The green isosurface represents a normalized concentration of 0.5; the red dots represent the sampling points along the collection boreholes.

Figure 92. A Conservative Tracer Concentration Plume

Tables 40 and 41 show the predicted breakthrough times of tracer for the upper and lower collection sampling points, respectively. As expected, sampling locations closer to the injection planes exhibit tracer breakthrough times that are earlier than those from more distant locations. As discussed in the next section, for simulations involving heterogeneous property distributions, this result may be modified due to preferential flow paths. The results indicate that tracer breakthrough is expected at several sampling locations within the first year, and some are expected within the first month. Conservative tracer breakthroughs could occur at earlier times than predicted by the ECM model if the model assumptions are erroneous. Fracture flow through Tptpv2, for example, could result in faster travel times. Even so, an additional year of operation may be required to achieve transport distances on the order of the entire length of the block.

Nonconservative Tracers

Table 42 shows the distribution coefficients, K_d, for the reactive, nonconservative tracers determined by parallel laboratory studies and used in Phase 2 for the various units. The measurements are preliminary but provide a starting point for the modeling effort. Travel times for reactive tracers are extremely sensitive to these distribution coefficients, and errors in these parameters strongly bias the results. One major deficiency in the preliminary measurements is that these results do not include reversible sorption, and equilibrium may not have been achieved when obtaining the distribution coefficients.

Table 42. Retardation of Reactive Tracers

Tracer	Tptpv1, Tac K_d (mL g^{-1})	Tptpv2 K_d (mL g^{-1})
Lithium	1.0	0.0
Manganese	15.6	6.5
Nickel/cobalt	34.0	13.0

DTN: LA9909WS831372.022

The next set of tables shows the predicted breakthroughs for the three reactive tracers: lithium Tables 43 and 44), manganese (Tables 45 and 46), and nickel or cobalt (Tables 47 and 48).

The data indicate that lithium does not sorb in Tptpv2 but mildly sorbs in Tac and Tptpv1. Although lithium sorption in Tac is mild when compared to manganese and nickel or cobalt, the sorption has a large effect on travel times over the time scale of interest. The lithium only breaks through at locations that are extremely close to the injection boreholes (i.e., boreholes 16, 17, 46, 48 and 9).

Manganese is predicted to sorb much more strongly than lithium. For this reason, manganese is only expected to break through at boreholes 46 and 48 within a one-year time span. Cobalt or nickel sorbs even more strongly than manganese and is not expected to break through at any of the boreholes during the time of the test.

Table 43. Lithium from Upper Injection Boreholes

Borehole number	5% Breakthrough concentration	50% Breakthrough concentration	Normalized concentration at 1 yr
16	52 days	193 days	0.79
17	257 days	> 1 yr	0.12
14	> 1 yr	> 1 yr	0.0
15	> 1 yr	> 1 yr	0.02
13	> 1 yr	> 1 yr	0.0
12	> 1 yr	> 1 yr	0.0
Remaining collection boreholes	> 1 yr	> 1 yr	0.0

DTN: LA9909WS831372.022, file: *chem.trc*

Table 44. Lithium from Lower Injection Boreholes

Borehole number	5% Breakthrough concentration	50% Breakthrough concentration	Normalized concentration at 1 yr
46	28 days	267 days	0.62
48	63 days	327 days	0.55
9	242 days	> 1 yr	0.12
10	> 1 yr	> 1 yr	0.0

DTN: LA9909WS831372.022, file: *chem.trc*

There are many caveats that could strongly affect the predicted travel times of the reactive tracers. First, the model is extremely sensitive to the values of K_d, and the current K_d measurements are uncertain at this time. A simple K_d may not be sufficient to model sorption of these tracers due to chemical heterogeneities and nonlinear reactions. Finally, these immobile reactive tracers may sorb onto colloids, thereby enhancing their mobility.

Heterogeneous System

A major assumption of the above modeling results is that properties are homogeneous within a layer. In this section, the effects of the heterogeneity of properties within the layers are explored. In these simulations, permeability values are distributed within each layer. The means of the permeability values for each layer are assumed to be the same as the permeability values used in the homogeneous simulations. In each layer, a log-normal distribution of permeability with a ln (k) variance of 2.0 and a correlation length of 1 m in the x, y and z directions is assumed. In the Tac and Tptpv1 units, an equation has been proposed to represent the correlation between the van Genuchten parameter α_m and matrix permeability (Altman et al. 1996, unnumbered equation on p. 34). To explore the sensitivity of the model results to this type of correlation, this relation is used to distribute α_m throughout these units.

Table 45. Manganese from Upper Injection Boreholes

Borehole number	5% Breakthrough concentration	50% Breakthrough concentration	Normalized concentration at 1 yr
16	> 1 yr	> 1 yr	0.0
17	> 1 yr	> 1 yr	0.0
14	> 1 yr	> 1 yr	0.0
15	> 1 yr	> 1 yr	0.0
13	> 1 yr	> 1 yr	0.0
12	> 1 yr	> 1 yr	0.0
Remaining collection boreholes	> 1 yr	> 1 yr	0.0

DTN: LA9909WS831372.022, file: *chem.trc*

Table 46. Manganese from Lower Injection Boreholes

Borehole number	5% Breakthrough concentration	50% Breakthrough concentration	Normalized concentration at 1 yr
46	277 days	> 1 yr	0.06
48	328 days	> 1 yr	0.06
9	> 1 yr	> 1 yr	0.0
10	> 1 yr	> 1 yr	0.0

DTN: LA9909WS831372.022, file: *chem.trc*

Figure 93 shows the background saturation profile and the saturation profile after one year of continuous injection. The saturation profile shows that the 50 mL hr^{-1} boreholes have a strong effect on the saturation profile. This effect is for two reasons, including the obvious reason that 50 mL hr^{-1} is the high injection rate. The second reason is that the 50 mL hr^{-1} boreholes inject into the Tptpv2 layer, which has a much lower matrix permeability than the Calico Hills hydrogeologic unit (Tac and Tptpv1). The 10-mL hr^{-1} injections in the Tac unit do not have a large effect on the saturation profile. The simulations indicate that capillary action is an important process around the 10 mL hr^{-1} injections, which is mostly due to the high matrix permeabilities in this unit.

Table 47. Nickel or Cobalt from Upper Injection Boreholes

Borehole number	5% Breakthrough concentration	50% Breakthrough concentration	Normalized concentration at 1 yr
16	> 1 yr	> 1 yr	0.0
17	> 1 yr	> 1 yr	0.0
14	> 1 yr	> 1 yr	0.0
15	> 1 yr	> 1 yr	0.0
13	> 1 yr	> 1 yr	0.0
12	> 1 yr	> 1 yr	0.0
Remaining collection boreholes	> 1 yr	> 1 yr	0.0

DTN: LA9909WS831372.022, file: *chem.trc*

Table 48. Nickel or Cobalt from Lower Injection Boreholes

Borehole number	5% Breakthrough concentration	50% Breakthrough concentration	Normalized concentration at 1 yr
46	> 1 yr	> 1 yr	0.0
48	> 1 yr	> 1 yr	0.0
9	> 1 yr	> 1 yr	0.0
10	> 1 yr	> 1 yr	0.0

DTN: LA9909WS831372.022, file: *chem.trc*

Tables 49 and 50 show the breakthrough times for two realizations. As expected, heterogeneities do add some fluctuations in the trends observed previously; however, many of the trends still hold.

6.8.7.4 Summary and Interpretation

This section constitutes a preliminary "blind" prediction of the behavior of the Phase-2 block of the UZTT at Busted Butte. The prediction is intended to test the current modeling concepts and tools available to the integrated site-scale model and their abstractions for performance assessment. This prediction uses parameters from the available Yucca Mountain hydrologic and geochemical databases and is considered to be preliminary because calibrations have not been performed using information from Busted Butte.

Modeling results for fluorescein, a conservative tracer, indicate that tracer breakthrough is expected at several sampling locations within the first year of testing. For some sampling locations, tracer breakthrough is predicted for travel times of less than a month. Tracer breakthroughs could be even quicker than predicted if the ECM assumption does not hold.

Table 49. Fluorescein from Upper Injection Boreholes with Physical Heterogeneities

Borehole number	5% Breakthrough concentration		50% Breakthrough concentration		Normalized concentration at 1 yr	
	Real.* 1	Real. 2	Real. 1	Real. 2	Real. 1	Real. 2
16	28 days	36 days	70 days	106 days	1.0	0.96
17	70 days	60 days	238 days	161 days	0.7	0.91
14	173 days	170 days	> 1 yr	> 1 yr	0.35	0.38
15	126 days	126 days	278 days	267 days	0.72	0.76
13	118 days	142 days	247 days	347 days	0.80	0.54
12	222 days	247 days	> 1 yr	> 1 yr	0.42	0.29
Remaining collection boreholes	> 1 yr		> 1 yr	> 1 yr	0.0	0.0

DTN: LA9909WS831372.022, files: *real1.trc* and *real2.trc*

NOTE: *Real. = realization

Table 50. Fluorescein from Lower Injection Boreholes with Physical Heterogeneities

Borehole number	5% Breakthrough concentration		50% Breakthrough concentration		Normalized concentration at 1 yr	
	Real.* 1	Real. 2	Real. 1	Real. 2	Real. 1	Real. 2
46	4 days	4 days	37 days	32 days	1.0	1.0
48	24 days	22 days	106 days	96 days	0.97	0.98
9	52 days	47 days	156 days	> 1 yr	0.94	0.94
10	197 days	202 days	> 1 yr	> 1 yr	0.28	0.26

DTN: LA9909WS831372.022, files: *real1.trc* and *real2.trc*

NOTE: *Real. = realization

Fracture flow through the Topopah Spring (Tptpv2) could result in faster travel times. The fracture parameters for the van Genuchten model are not known to a high degree of accuracy. Another caveat in these modeling results is the effect of physical heterogeneities within each layer. Small-scale heterogeneities could result in preferential flow paths, which results in faster flow paths in some parts of the block and slower flow paths in other parts of the block. Monte Carlo simulations and more elegant stochastic techniques could be employed to capture the uncertainty in the travel times.

More uncertainty exists in the predicted travel times of the reactive tracers when compared with the conservative-tracer predictions. The strongly sorbing tracers manganese and cobalt (or nickel) are not expected to break through within the first year of testing. Even weakly sorbing

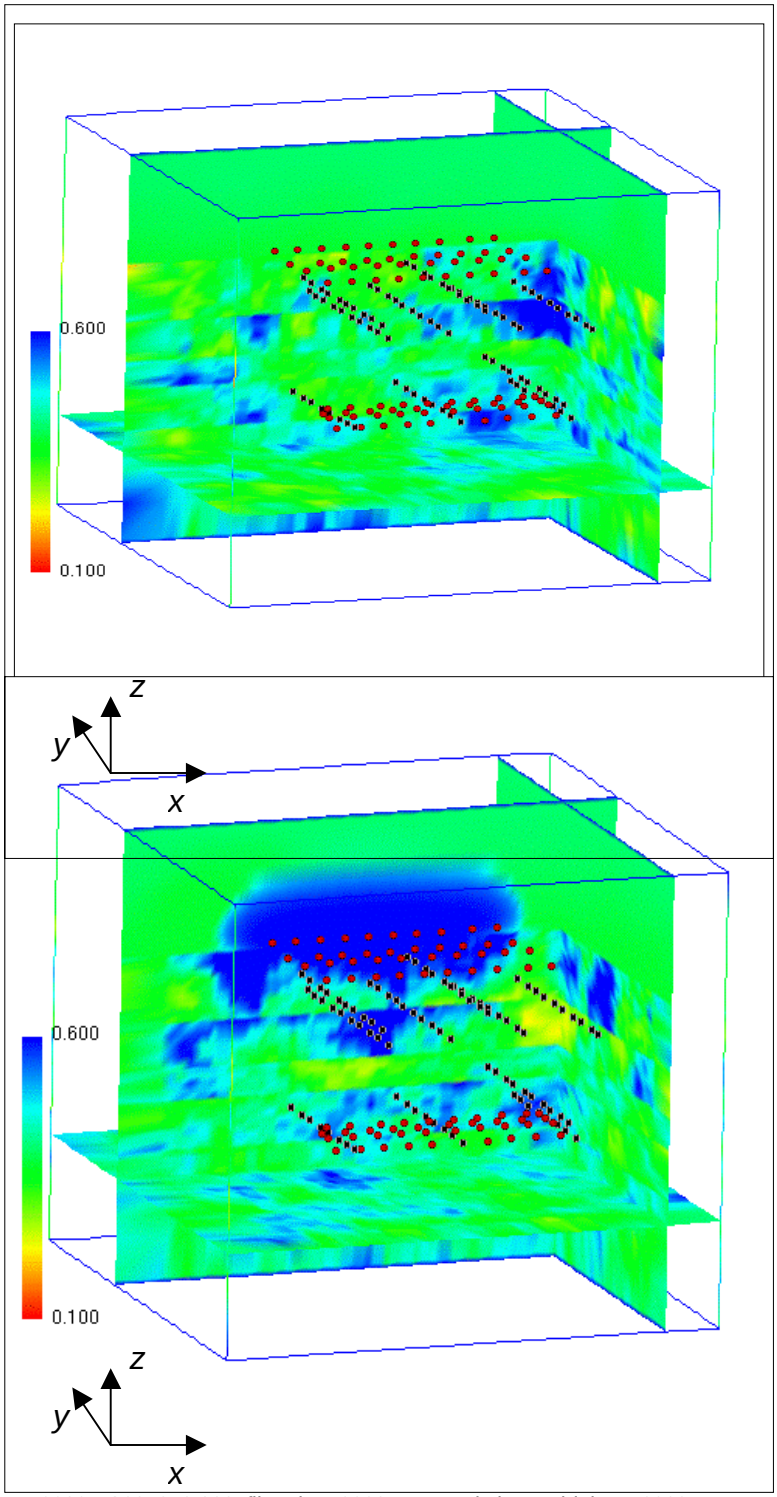

DTN: LA9909WS831372.022, files: *bg.10002_sca_node.inp* and *inject.10002_sca_node.inp*

NOTES: These saturation profiles are from 10 to 60% of the heterogeneous Realization 1: (a) background saturation, (b) saturation profile after 1 yr of injection. In the figure, injection points are red dots and collection points are blue dots.

Figure 93. Predicted Saturation Profiles for Phase 2

lithium only reaches a few collection boreholes. Therefore, an additional year of operation may be required to achieve transport distances that reach more sampling points. At this stage, it is important to note that the model is extremely sensitive to the values of K_d used, which are preliminary. In addition, a linear K_d model may not be sufficient to model sorption of these tracers due to chemical heterogeneities and nonlinear reactions. More rigorous reactive transport models could be used to check the linear K_d assumption. Finally, these immobile reactive tracers may sorb onto colloids, thereby enhancing their mobility.

6.8.8 Model Validation

Model validation is a process to demonstrate and document that a model is appropriate and adequate for its intended use. Models used in this AMR express a conceptual model of unsaturated flow as mathematical equations, which are solved by computer codes that execute numerical methods. Input to the problem includes rock properties and, in the case of FEHM V2.00 (STN: 10031-2.00-00), a mesh or grid that expresses the geometry. Validation includes developing confidence in the grid, the input values, and the code.

The conceptual model underlying the models used in this AMR is the standard model of unsaturated Darcy flow with constitutive relationships defined by either van Genuchten or Gardner-Russo equations (van Genuchten 1980; Gardner 1958; Russo 1988), which are generally accepted by the scientific community. For this work, all rock property values were measured on samples either from the Busted Butte site or from the same geologic units at Yucca Mountain (Table 1e). Mesh validation was done by plotting the location of features such as boreholes and geologic contacts and comparing them visually with the known geometry, such as shown in Figures 34, 45, and 87. The codes were validated by comparing outputs for simple problems against analytical solutions where such exist. Close correspondence between the analytical and numerical methods was judged visually by inspection of plotted output. Output was also inspected visually to ensure that the behavior of the system conformed to what is expected for this conceptual model.

The UZTT is an integration of field experiment, laboratory analysis, and conceptual and numerical simulation. The UZTT is designed to verify and validate the project's ability to capture transport, dispersion, fracture flow, and other features significant to the Yucca Mountain site in a computational model.

The UZTT applies a variety of computer codes for the computational analyses. The primary flow and transport modeling code being used is FEHM. Computational grids for FEHM were generated using LAGRIT V1.0 (STN: 10212-1.0-00). The software code STO-UNSAT V1.0 (STN: 10292-1.0LV-00) is used for stochastic flow modeling. STO-UNSAT numerically solves the moment differential equations that describe transient unsaturated flow in randomly heterogeneous porous media (Zhang 1999). Verification of this code included running solutions to steady state and then comparing with published one- and two-dimensional steady-state solutions (Zhang et al. 1998; Zhang and Winter 1998). All other computational tools used are standard commercial software as listed in Section 3.0 of this AMR.

Computational grids were generated using site data from the TDMS (Table 1e). Domain size, stratigraphy, and borehole configuration were taken from site survey data and measurements.

These configurations generated by LAGRIT were visually compared against the input data and judged to be accurate representations of these data. The correctness of the computational grids themselves was tested by running simple steady-state flow- and heat-conduction simulations with homogeneous material properties. Phase-1A deterministic and Monte Carlo simulations and Phase-2 simulations were run using FEHM V2.00, which is the primary code used to simulate the flow and transport of the field experiment. FEHM was chosen because it is the code that will be used to simulate flow and transport at the proposed repository for PA. FEHM has been used extensively within the YMP, and no modifications of FEHM were made for the UZTT modeling. In addition to extensive verification and validation of FEHM reported in Dash et al. (1997), these FEHM simulations were initially validated for simple homogeneous flow under uniform saturation. Plots of model results at a range of saturations showed the expected transition from capillary-dominated to gravity-dominated between 60% and 90% initial saturation. This agreement with expected behavior and the previously documented agreement with analytical solutions (Dash et al. 1997) indicates that the computational code was running correctly for this configuration (Soll 1997, pp. 18 to 26).

Material properties used in the model were either site-specific when available or otherwise were derived from field and laboratory measurements made at or near Yucca Mountain. The ultimate validation of the UZTT models will be with data collected from the UZTT itself. The model results presented in this AMR are predictions that will be compared against actual field results. Full validation of these models at this time is, thus, premature. The only data currently available to validate the Phase-2 FEHM model qualitatively are those depicting the first detection of fluorescein (Figure 91). The Phase-2 model reported here adequately met the criterion that the tracer concentration predicted in the time interval when breakthrough actually occurred must be between 25% and 75%.

STO-UNSAT, a stochastic differential equation code for modeling flow and transport, was used to develop a 2-D model for Phase-1A predictions. The STO-UNSAT model was validated by first running a simple homogeneous case (Zhang and Winter 1998, Figures 1 and 2) and comparing against the analytical results derived in Zhang et al. 1998 (Equations 63 and 46, respectively). Good agreement was also found between Phase-1A stochastic simulations using STO-UNSAT and Phase-1A deterministic predictions using the FEHM model. Further examples are contained in Zhang 1998 (pp. 12 to 21, 76).

Note that the UZTT is itself a model validation process. As additional data become available, they will be incorporated into the UZTT computational models to improve their representativeness. Validation of the UZTT models to date has shown that they adequately reproduce input data and provide similar results in comparison tests. Because of the limited comparisons of UZTT model predictions and test data that are available to date, a final conclusion regarding the validity of these models for simulating the test conditions and environments of the UZTT cannot be made at this stage of the testing and modeling program. However, the results obtained thus far, as described in this AMR, support the conclusion that these models are adequate for their intended use.

6.8.9 Summary: Implications for Performance Assessment

The UZ transport test is designed to provide information suitable for assessing the validity of flow and transport models used in the site characterization and performance assessment programs for Yucca Mountain. Observations of the available data collected to date for Phase 1 and Phase 2, and the modeling of these data, lead to several key conclusions of relevance to performance assessment. These conclusions are summarized below, categorizing them with respect to the particular field or modeling activity in this report.

1. *Laboratory measurements*: The collection of unsaturated hydrologic property data using the UFA provides data of particular relevance to flow and transport models because they are direct measurements under unsaturated conditions rather than indirect, model-derived parameters. The Monte Carlo analyses (Section 6.8.6) indicate that the nature of the correlations between parameters such as permeability and the van Genuchten α parameter have a strong impact on the predictability of the flow and transport system. Therefore, additional measurements of hydrologic and transport parameters under unsaturated conditions could be used to constrain models and develop correlations.

2. *Phase-1A and -1B model results*: In addition to the point just made, the modeling analyses for Phase 1A indicate that strong capillary forces in the rock matrix of the Tac unit are likely to modulate fracture flow from overlying units, thereby damping pulses of infiltrating water and providing a large degree of contact between radionuclides and the rock matrix. Several modeling approaches, from deterministic to Monte Carlo and stochastic models, were used to simulate the Phase-1A experiments (Sections 6.8.6 and 6.8.7). All yielded similar qualitative results. From this we conclude tentatively that the deterministic modeling approach taken at the site scale may be adequate. The parameterizations used in performing these calculations must be evaluated after data from the UZTT are available.

   A particularly interesting observation from the Phase-1B experiment is that, even when injection occurs immediately adjacent to a fracture, water appears to be imbibed quickly into the surrounding matrix. The transport times observed immediately below the injection point were on the order of 30 days, whereas pure fracture flow would have resulted in travel times of minutes to hours at this flow rate. Site-scale models must be evaluated in light of this observation. Models that predict significant fracture flow at percolation rates low enough for the matrix to transmit the flow may be inconsistent with the Phase-1B experiment.

3. *Phase-2 modeling*: Significant uncertainties uncovered by the modeling include the adequacy of continuum models in nonwelded units of high matrix permeability and the nature of the transition from fracture flow to matrix flow at contacts between hydrogeologic units. These are exactly the issues being studied within the UZTT.

Primary focus over the past year has been on flow and transport field data collection. Data collection/analysis for Phase 2 will be continuing through September 2000, with continuing compilation, analysis, and interpretation of the field data.

6.9 C-WELLS FIELD AND LABORATORY TRANSPORT TESTING

6.9.1 Introduction

To test conceptual SZ transport models for YMP, two major cross-hole, forced-gradient tracer tests were conducted at the C-wells (UE-25c#1, c#2, and c#3), which are located approximately 2 km southeast of the potential repository footprint (Figure 94), and completed in fractured volcanic tuffs. Groundwater flow at this location is thought to be toward the southeast, which puts the C-wells directly downgradient of the southern end of the potential repository. The tracer tests were conducted in two different saturated intervals that differed in horizontal hydraulic conductivity by about 2 orders of magnitude: the lower Bullfrog Tuff, with a conductivity of 27 to 52 m d^{-1} (Geldon et al. 1997, p. 34 in Hydraulic Tests section), and the lower Prow Pass Tuff, with a conductivity of 0.8 to 1.0 m d^{-1} (Reimus et al. 1999, p. A.7). Figure 95 depicts the hydrogeology of the C-wells and shows the packer locations in the tracer tests. Note from Figure 95 that the vast majority of the water produced at the C-wells comes from a small number of relatively discrete zones, most of which are located in the lower half of the Bullfrog Tuff. Both tracer tests were conducted between wells c#2 and c#3 (a linear distance of approximately 30 m), with c#3 being the production well in the Bullfrog Tuff test and c#2 the production well in the Prow Pass Tuff test.

The two tracer tests featured the simultaneous injection of several different tracers having different physical and chemical characteristics: (1) nonsorbing solutes with different diffusion coefficients (Br^- and pentafluorobenzoate), (2) a weakly-sorbing solute (Li^+), and (3) carboxylate-modified latex (CML) polystyrene microspheres, which served as colloidal tracers (Reimus et al. 1999, pp. 5.1-5.2 and C.1-C.2). Two additional tracer tests in the Bullfrog Tuff were conducted, each of which involved the injection of only a single nonsorbing solute (Reimus et al. 1999, Appendix C, Section C.2). These additional tests were conducted primarily to determine the optimal injection well for the test involving multiple tracers, and they will not be discussed further here except in the context of how they supported the interpretation of the multiple tracer test in the Bullfrog Tuff. The simultaneous injection of multiple tracers offers significant advantages over single tracer injections because it allows transport processes to be better distinguished and quantified by comparing the responses of the different tracers.

A series of laboratory studies were conducted in parallel with the field testing efforts to help support and constrain the interpretations of the field tests. These studies included (1) batch-sorption tests to characterize Li^+ sorption to C-wells tuffs, (2) diffusion-cell tests to determine matrix diffusion coefficients of tracers used in the field, and (3) dynamic-transport tests to study tracer transport in fractured and crushed tuffs under more controlled conditions than in the field. The batch-sorption tests and dynamic-transport tests have provided estimates of lithium sorption parameters for comparison with sorption parameters derived from the field tests. Such comparisons are important because they offer an indication of whether laboratory-derived radionuclide sorption parameters can be used defensibly in field-scale predictive calculations.

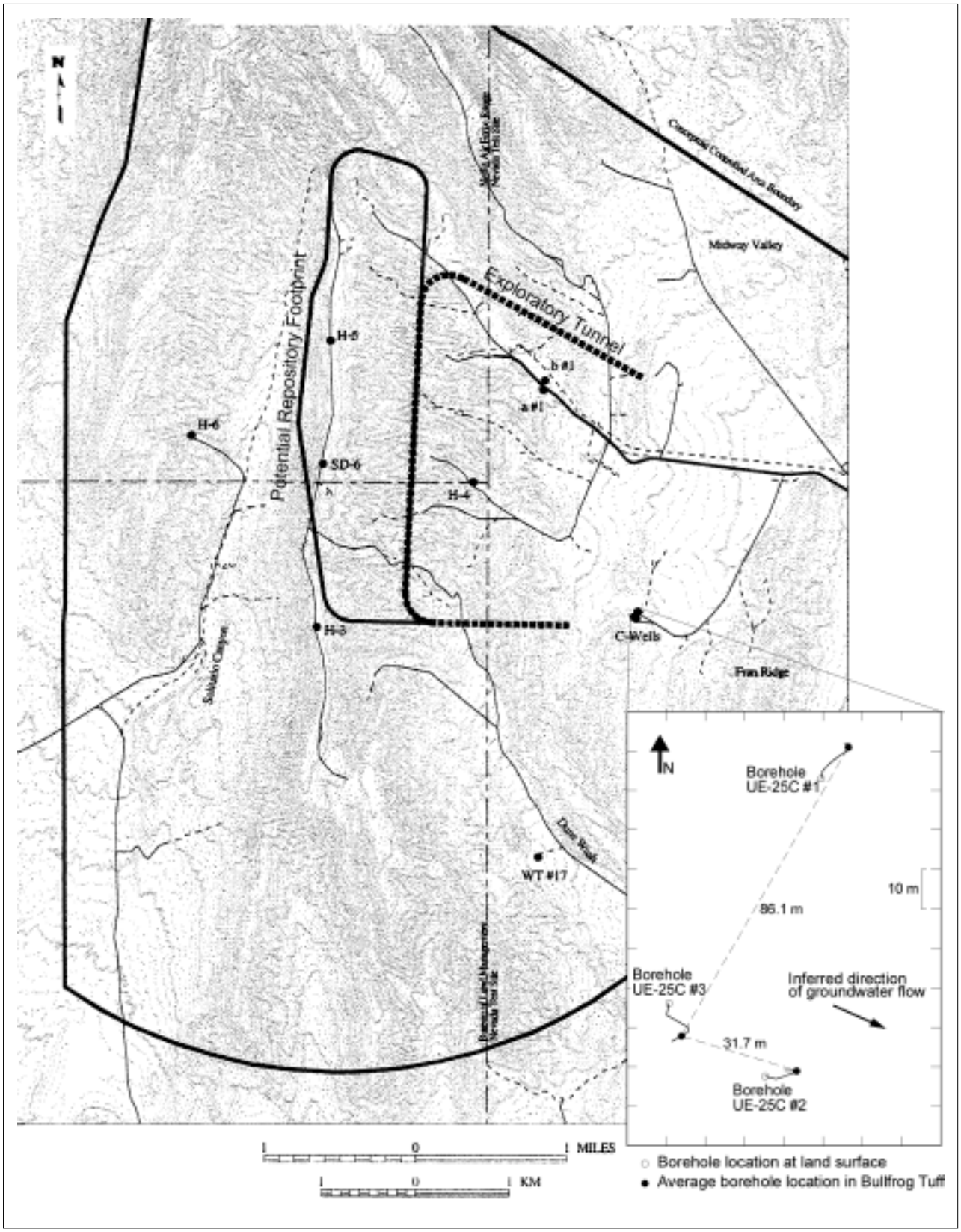

DTN: MO9906GPS98410.000 and GS981008312314.003 (borehole coordinates)

Figure 94. Location and Layout of the C-Wells Complex

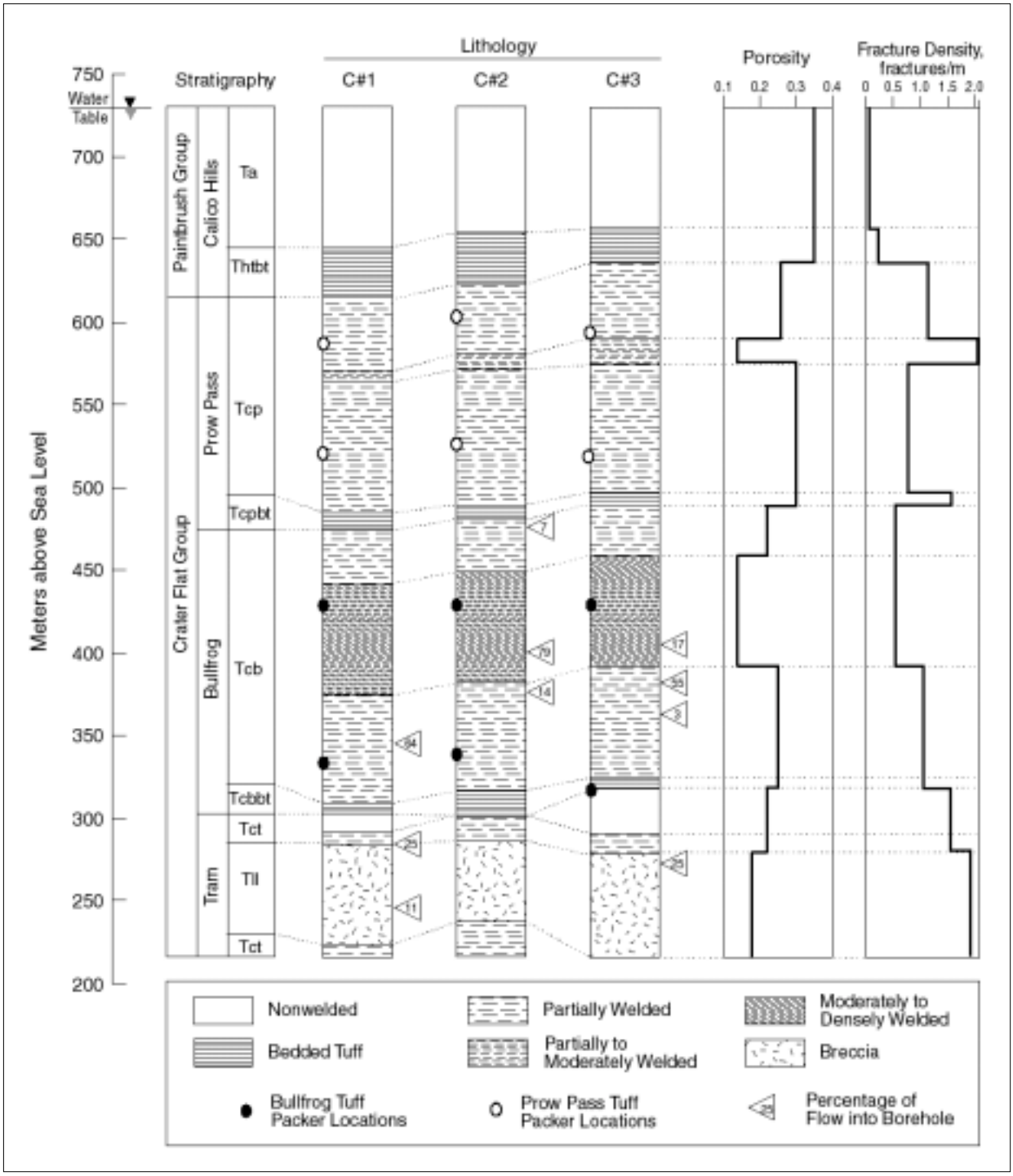

DTN: GS970708312314.007 (lower Bullfrog packer locations); GS990408312315.002 (Prow Pass); GS981008312314.002; all are reference only

NOTE: Packer locations indicate intervals in which hydraulic and tracer tests were conducted (the two tracer tests involving multiple tracers were conducted between c#2 and c#3). Packer locations for lower Bullfrog tests were derived from Geldon et al. (1997, Table 2). Porosity data are from Geldon (1993, Table 13), and fracture density data are from Geldon (1993, Tables 6 and 7); these data sets are shown only for reference purposes and have not been used in any of the analyses discussed in this report.

Figure 95. Stratigraphy, Lithology, Matrix Porosity, Fracture Density, and Inflow from Open-Hole Flow Surveys at the C-Wells

6.9.2 Summary of Field Test Results and Interpretations

Figure 96 shows the normalized tracer responses (concentrations divided by injection masses) in the multiple tracer test in the Bullfrog Tuff. Figure 97 shows the normalized tracer responses in the Prow Pass multiple tracer test. Note that the concentrations and times for the Bullfrog Tuff test in Figure 96 are shown on log-log axes. The test conditions and tracer injection masses in the two tests are described in detail in Reimus et al. (1999), Chapter 5 (Prow Pass Tuff) and Appendix C (Bullfrog Tuff). Both tests featured partial recirculation of the water produced from the pumped well: ~3.5% recirculation in the Bullfrog Tuff and ~30% recirculation in the Prow Pass Tuff.

The most striking feature of the tracer breakthrough curves in the Bullfrog Tuff test (Figure 96) is their bimodal (double-peaked) behavior. This behavior is attributed to a relatively small fraction (~13%) of the tracer solution exiting the injection borehole in short-residence-time pathways in the upper half of the injection interval, whereas the remaining tracer mass exited the borehole primarily in pathways of longer travel time deeper in the interval. The greater density of the tracer solution (injected just below the top packer) relative to the groundwater would have caused it to preferentially sink to the bottom of the relatively long (and unmixed) injection interval. Figure 98 shows that there was only one pentafluorobenzoate (PFBA) peak in a tracer test conducted earlier in the Bullfrog Tuff (same interval, same flow rates). The only difference between the two tests was that ~1,000 L of tracer solution was injected in the first test, and ~12,000 L was injected in the second test. The packed-off injection interval volume was ~4300 L, so in the first test, only about one-fourth of an interval volume was injected. Therefore, it is likely that only flow pathways in the lower part of the injection interval conducted tracers out of the borehole because of the tendency of the tracers to sink. In contrast, in the second test, approximately three interval volumes of tracer solution were injected, so the volume between the packers should have eventually filled with tracer solution, and tracers would have, thus, accessed flow pathways throughout the entire length of the interval. The flow survey information depicted in Figure 95 suggests that the zone of highest flow in the injection well (c#2) occurred in the upper half of the injection interval.

The PFBA and bromide responses in both the Bullfrog Tuff tracer test and the Prow Pass Tuff test show clear qualitative evidence of matrix diffusion. The peak-normalized PFBA concentrations are higher than the peak-normalized bromide concentrations in both tests, and the second bromide peak in the Bullfrog Tuff test is somewhat delayed relative to the PFBA with a tail that appears to cross over the PFBA at long times. These features are all consistent with greater matrix diffusion of the more diffusive tracer (bromide) relative to the less diffusive tracer (PFBA). Another qualitative indication of matrix diffusion in the Prow Pass Tuff test is the "jump(s)" in solute tracer concentrations after each of the three major flow interruptions during the tailing portion of the test, which indicate diffusion of tracers out of the matrix and into fractures during the interruptions. Thus, the two tests support the concept of dual-porosity behavior (where flow occurs primarily in fractures, but there is a large amount of stagnant water available for tracer/contaminant storage in the near-stagnant water of the rock matrix) in the saturated, fractured system at the C-wells.

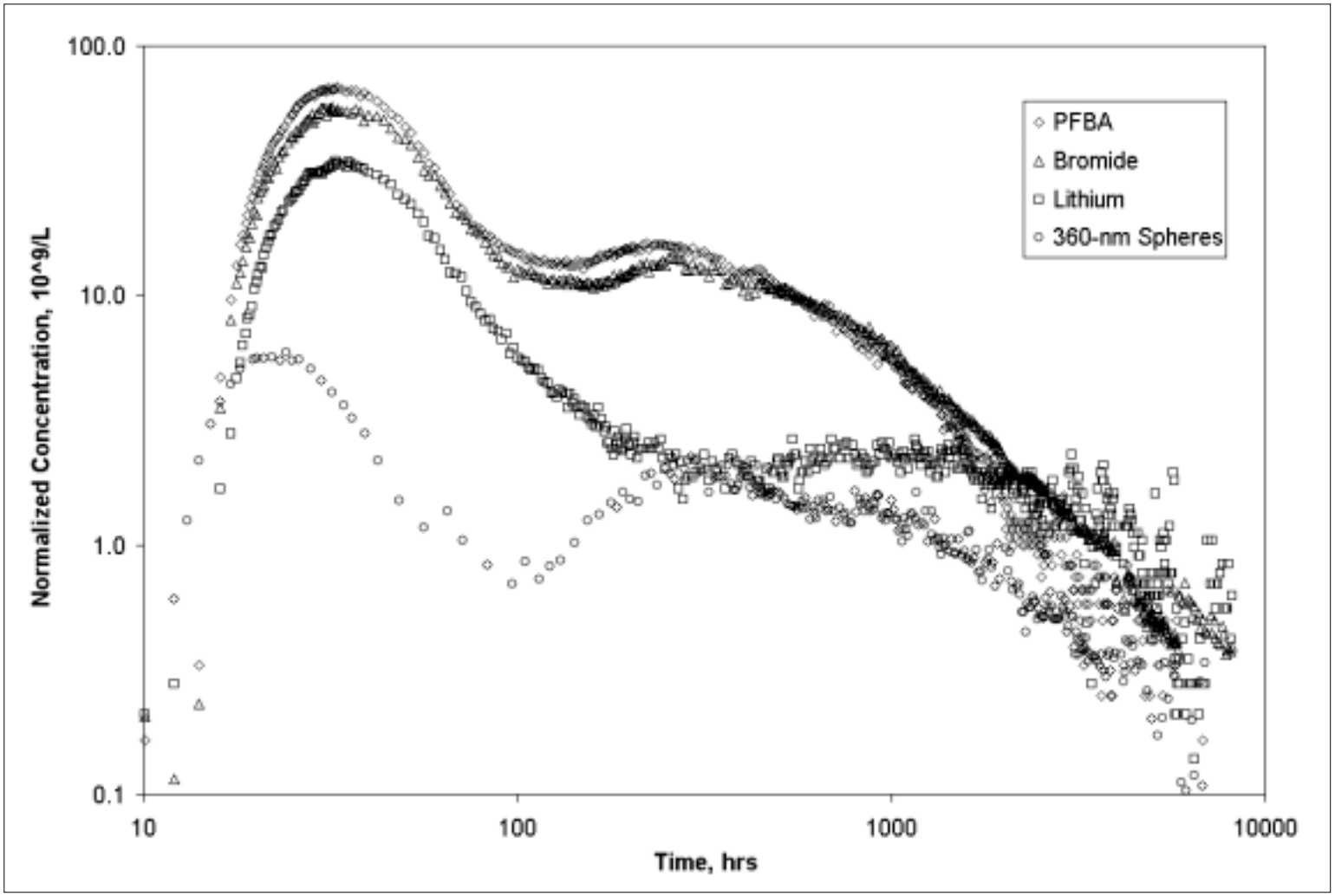

DTN: LA0002PR831231.001 (SEP Tables S00086.001 and S00086.004)

NOTE: Normalized tracer responses in the Bullfrog Tuff multiple tracer test (note both axes are log scale). Tracer recoveries were ~69% for PFBA, ~69% for bromide, ~39% for lithium, and ~15% for microspheres. Concentrations are normalized to mass injected.

Figure 96. Normalized Tracer Responses in the Bullfrog Tuff Multiple Tracer Test

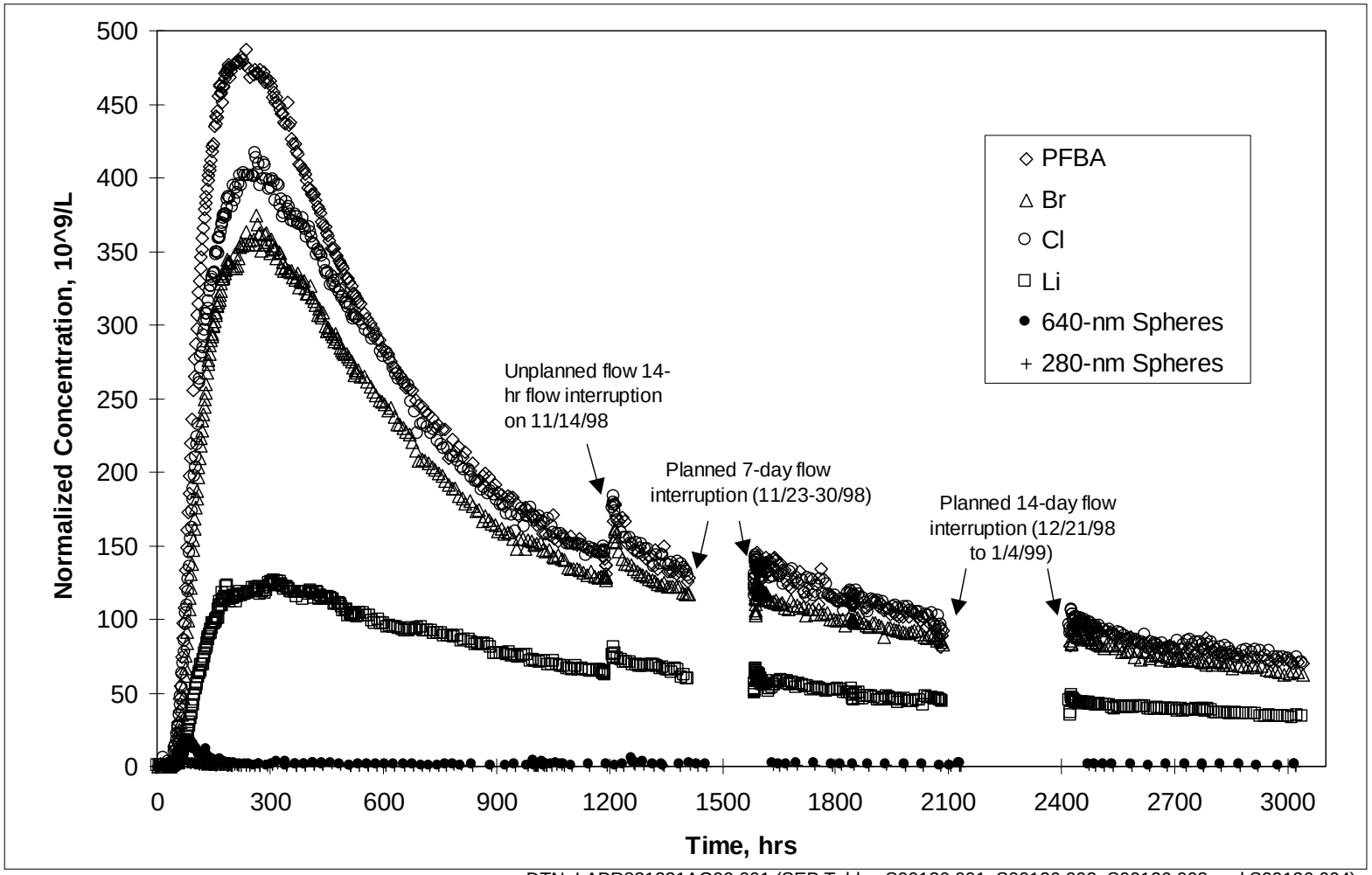

DTN: LAPR831231AQ99.001 (SEP Tables S99126.001, S99126.002, S99126.003 and S99126.004)

NOTE: Normalized tracer responses in the Prow Pass Tuff multiple tracer test. Microsphere responses are shown more clearly in Figure 99. Tracer recoveries were 52% for PFBA, 49% for Cl, 43% for Br, 19% for Li, 0.3% for 640-nm spheres, and 0.1% for 280-nm spheres.

Figure 97. Normalized Tracer Responses in the Prow Pass Tuff Multiple Tracer Test

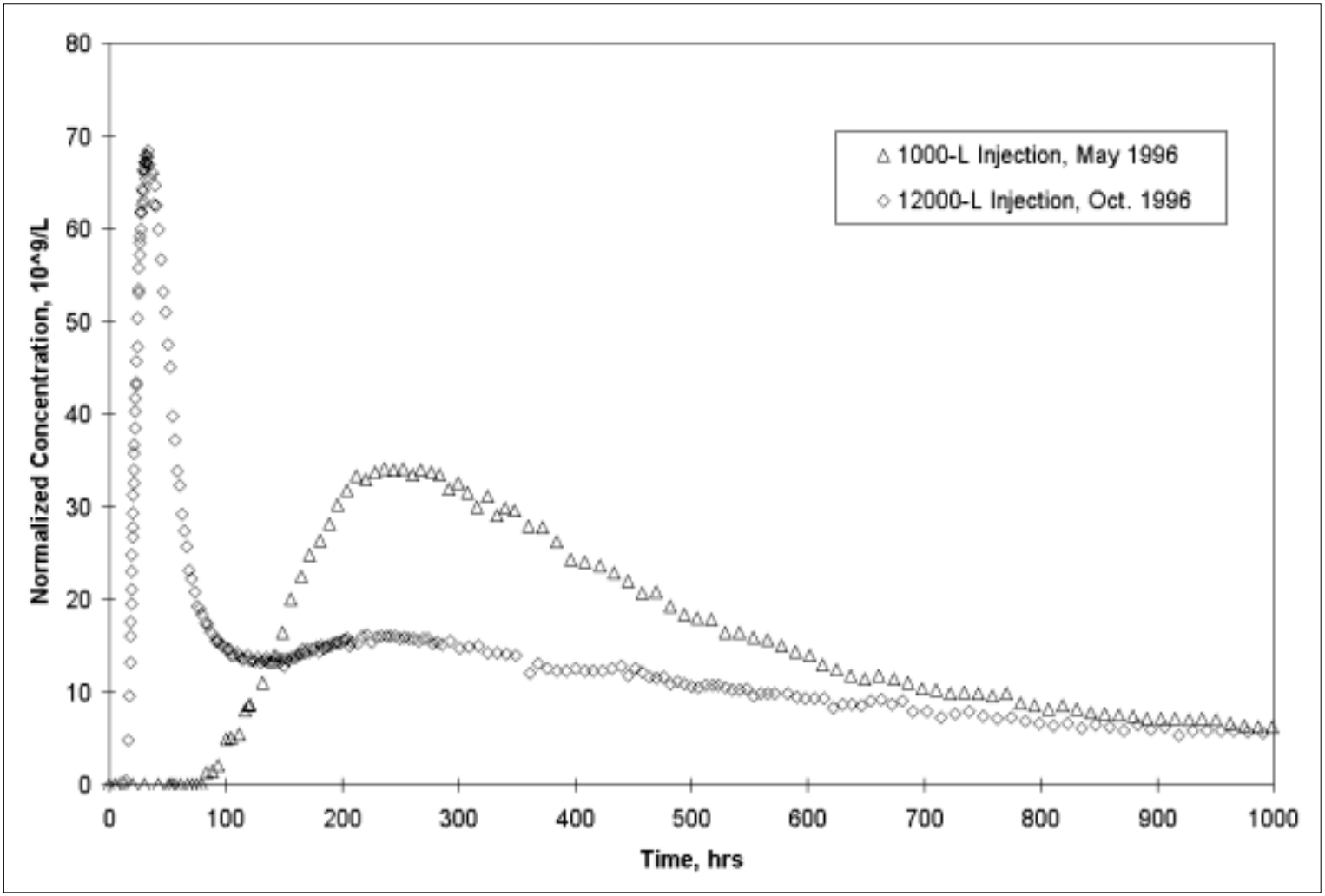

DTN: LA0002PR831231.001 (SEP Tables S00086.001 and S00086.003)

NOTE: The axes are both linear. These tests differed only in the amount of tracer solution injected.

Figure 98. Normalized PFBA Responses in Two Different Tracer Tests in the Bullfrog Tuff

The lithium responses in the two tests show obvious attenuation relative to the nonsorbing tracers, which is indicative of lithium sorption. The attenuation in the Prow Pass test and in the first peak of the Bullfrog Tuff test is almost exclusively a lowering of the peak concentration with little or no delay in arrival time. This behavior is consistent with lithium sorption in the matrix (after diffusion into the matrix). The attenuation in the second peak of the Bullfrog Tuff test involves a clear time delay along with a dramatic lowering of concentration. This behavior is consistent with sorption in both the fracture flow pathways and the matrix.

The CML microsphere responses in the two tests indicate that the microspheres were significantly attenuated relative to the solute tracers in both tests with the attenuation relative to solutes being greater in the Prow Pass Tuff test. The microsphere responses in the Prow Pass test are shown more clearly on a plot of log-normalized concentration versus time in Figure 99. The responses in both tests (including both sizes of spheres in the Prow Pass test) are characterized by truncated tails relative to the solutes but with measurable concentrations that persist throughout the tests. This behavior is consistent with filtration followed by some sort of nonlinear or stochastic resuspension of the microspheres.

The tracer responses in both tests were interpreted by simultaneously fitting the breakthrough curves using a semianalytical, dual-porosity transport model, RELAP, which is described in detail in Reimus et al. (1999, Appendix D). RELAP is part of the Reactive Transport Application (RTA) V1.1 (STN: 10032-1.1-00) software package. It solves Laplace domain "transfer functions" that describe tracer injection, well-bore mixing, recirculation, and tracer transport in a dual-porosity system. The equations used for transport in the flow system can take various forms depending on whether: (1) flow is assumed to be linear or radial, (2) the matrix is assumed to be finite or semi-infinite, or (3) sorption is assumed to be equilibrium or rate limited (Reimus et al. 1999, Appendix D).

The interpretation strategy in the Bullfrog Tuff test was to (1) fit the first tracer peaks, (2) subtract the fitted responses from the complete breakthrough curve(s), and (3) fit the resulting residual second peak(s) with a second set of transport parameters. In the Prow Pass test, a single set of transport parameters was sufficient to fit the single modal tracer responses. The sequence of fitting the different tracer responses in each test was as follows.

1. The Br^- and PFBA responses were fit simultaneously using RELAP. It was assumed that both tracers experienced the same mean residence time and the same longitudinal dispersivity (because they were injected simultaneously), but they had diffusion coefficients that differed by a factor of 3. Both tracers were assumed to be conservative (nonsorbing). (Assumptions 22, 23, and 24 in Section 5).

2. The lithium response was fit by assuming that the lithium experienced the same mean residence time and dispersivity as the bromide and PFBA, but it had a diffusion coefficient two-thirds that of bromide and twice that of PFBA. (Assumptions 22 and 24 in Section 5). The only parameters adjusted to obtain a fit to the lithium data were sorption parameters.

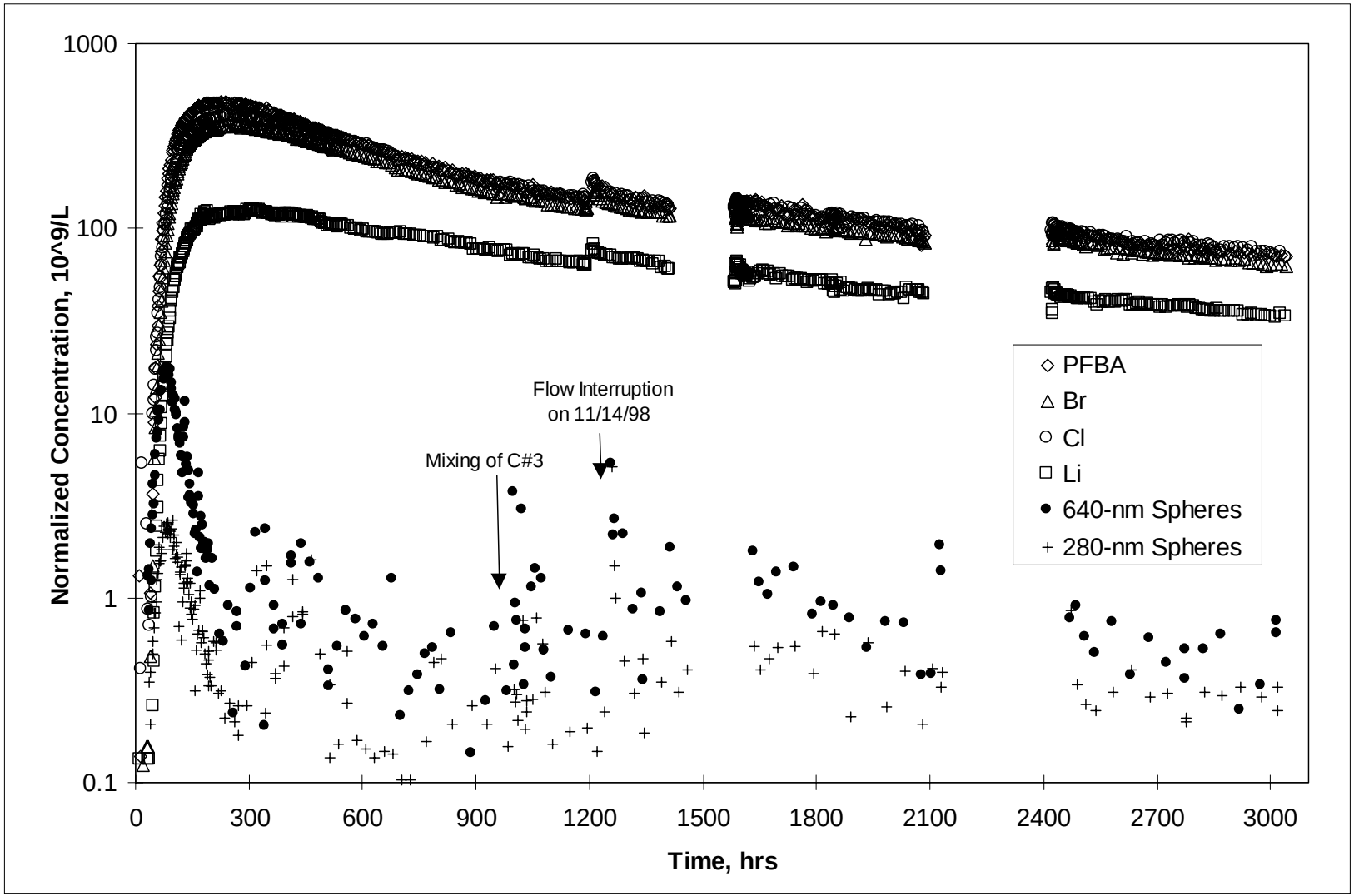

DTN: LAPR831231AQ99.001

NOTE: The time scale (*x* axis) is linear. The microspheres appeared to respond after pressure transients associated with mixing the injection well bore (c#3) and an unplanned flow interruption.

Figure 99. Log Normalized Tracer Responses in the Prow Pass Tuff Multiple Tracer Test

3. The microsphere responses were fitted assuming the same mean residence times and dispersion coefficients as the solute tracers but without any diffusion into the matrix (diffusion coefficient of zero) (Assumptions 22 and 25 in Section 5). The rate-limited sorption features of RELAP were used to adjust filtration and resuspension rate constants until a fit to the data was obtained.

4. To simulate the flow interruptions in the Prow Pass Tuff tracer test, a numerical code called RETRAN, also part of the RTA software package, was used. Unlike RELAP, RETRAN is capable of simulating nonlinear behavior and flow transients (Laplace transforms are limited to linear functions and steady-state flow behavior). RELAP fits were extended beyond the flow interruptions by using the transport parameters obtained from RELAP (up until the time of the flow interruptions) as inputs to RETRAN. RETRAN was also used to simulate nonlinear sorption behavior of lithium.

The model RETRAN solves the concentration of tracer only at the breakthrough point, using a semi-analytical method. No mesh is required. The breakthrough curve is obtained by numerical inversion of the solution in Laplace space. Complete model documentation is reported in Reimus and Dash (1999), including discussion on stability and accuracy of solutions. RETRAN was validated for this application by fitting the observed breakthrough curves and visually judging the goodness of fit as shown in Appendix C of Reimus et al. (1999). RETRAN was chosen for this application because no data other than breakthrough data are available to fit. Therefore, there is no advantage to using a model that predicts concentrations everywhere. The model fits to the tracer breakthrough curves are not shown here graphically; the reader is referred to Reimus et al. (1999, Chapter 5 and Appendix C) for graphical representations of the fits. All transport parameters obtained from the fits, with the exception of lithium sorption parameters, are listed in Tables 51 and 52 for the Bullfrog and Prow Pass Tuff tests, respectively. Note that there are separate estimates of mean residence times and dispersivities depending on whether "radial" or "linear" flow is assumed (the two possible extremes for flow to a pumped well in a confined aquifer). These values reflect the parameter uncertainty associated with not knowing the true nature of the flow field. Figure 100 shows the range of longitudinal dispersivities deduced from the C-wells tracer tests on a plot of dispersivity versus length scale taken from Neuman (1990, Figure 3). It is apparent that the C-wells longitudinal dispersivities (the darkened box) are in relatively good agreement with Neuman's published relationship of dispersivity versus length scale. Note that the lower end of the range of length scales associated with the darkened box corresponds to the interwell separation in the tracer tests and the upper end corresponds to the test interval thickness (used as an upper bound for the transport distance). The effective flow porosities listed in Tables 51 and 52 were calculated from the deduced mean tracer residence times using the following expression (Reimus et al. 1999, Section 5.6), which assumes radial convergent flow in a homogeneous, isotropic medium:

$$\eta = \frac{Q\,\tau}{\pi R^2 L} \qquad \text{(Eq. 41)}$$

where

η = flow porosity
Q = production rate (m^3/hr)
τ = mean tracer residence time (hr)
R = distance between boreholes (m)
L = formation thickness (m).

Table 51. Transport Parameters Deduced from Fits of the Bullfrog Tuff Tracer Responses [d]

Parameter	Pathway 1 [e]	Pathway 2
mass fraction in pathway	0.12	0.59
residence time, linear flow (hr)	37	995
longitudinal dispersivity, linear flow (m)	5.3	18.8
residence time, radial flow (hr)	31	640
longitudinal dispersivity, radial flow (m)	3.6	10.7
effective flow porosity, linear (radial) [a]	0.0029 (0.0025)	0.026 (0.017)
$\frac{\phi}{b}\sqrt{D_m}$ for bromide ($sec^{-1/2}$) [b]	0.00158	0.000458
microsphere filtration rate constant (hr^{-1}) [c]	0.2	0.04

DTN: LA9909PR831231.003

NOTES: [a] Based on flow log information (see Figure 95), it was assumed that 75% of the production flow contributed to the pathway 1 responses and 25% of the flow contributed to the pathway 2 responses. Equation 41 was used to estimate the flow porosity.
[b] This parameter is an effective matrix diffusion mass transfer coefficient (Reimus et al. 1999, Section 5.6). The value of the parameter for PFBA was assumed to be 0.577 times that for bromide.
[c] Multiple resuspension/detachment rate constants were assumed in each pathway to obtain a fit to the microsphere responses (see Reimus et al. 1999, Section C.5). Filtration coefficients (m^{-1}) can be calculated from the filtration rate constants (k_{filt}) using k_{filt}/V, where V = average linear velocity determined from mean fluid residence times.
[d] See Table 53 for lithium sorption parameters.
[e] Note that "Pathway 1" refers to pathways that resulted in the first tracer peak, and "Pathway 2" refers to pathways that resulted in the second peak.

Table 52. Transport Parameters Deduced from Fits of the Prow Pass Tuff Tracer Responses

Parameter	Value
mass fraction participating in test	0.75
residence time, linear flow (hr)	1230
longitudinal dispersivity, linear flow (m) [a]	23.1
residence time, radial flow (hr)	620
longitudinal dispersivity, radial flow (m) [a]	6.3
effective flow porosity, linear (radial)	0.0068 (0.0034)
$\frac{\phi}{b}\sqrt{D_m}$ for bromide ($sec^{-1/2}$) [b]	0.000968
640-nm sphere filtration rate constant (hr^{-1}) [c]	0.043
280-nm sphere filtration rate constant (hr^{-1}) [c]	0.07

DTN: LA9909PR831231.005

NOTES: [a] Longitudinal dispersivities calculated after subtracting out apparent dispersion due to the recirculating flow field (see Reimus et al. 1999, p. 5.14).
[b] See Table 51 for footnotes.
[c] See Table 53 for lithium sorption parameters.

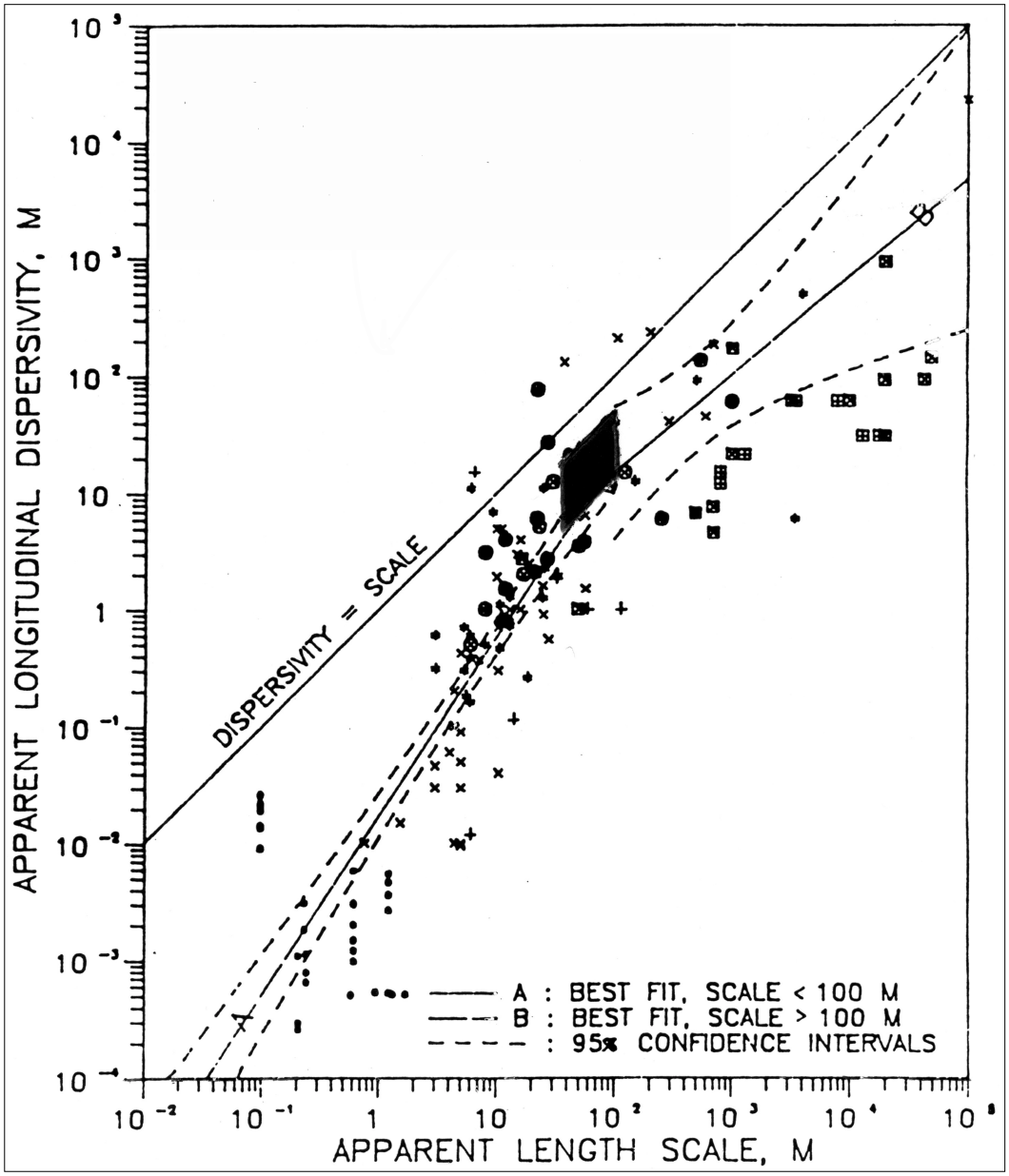

DTN: LA9909PR831231.003

NOTES: This figure shows the range of C-wells values derived from interpretations of the Prow Pass and Bullfrog reactive tracer tests (darkened box). Plot taken from Neuman (1990, Figure 3). Note that the right edge of the box corresponds to the interwell separation distance and the left edge of the box corresponds to the test interval thickness (taken to be the upper limit of transport distance).

Figure 100. Longitudinal Dispersivity versus Length Scale of C-Wells Values from Interpretations of the Prow Pass and Bullfrog Reactive Tracer Tests

The "mass tracer solution (which may have resulted in tracers "sinking" out of the zone of influence of the pump). Finite but slow flow through the matrix may also have resulted in some tracer being pushed out of the injection well into the matrix (rather than fractures) where it would have been effectively "lost" from the fracture flow system.

The parameter describing matrix diffusion in Tables 51 and 52 is actually a "lumped" parameter (Reimus et al. 1999 pp. C.7 and 5.15) which could be called the "mass transfer coefficient,"

$$\frac{\phi}{b}\sqrt{D_{\mathrm{m}}}$$

consisting of the matrix porosity, ϕ, the fracture half-aperture, b, and the matrix diffusion coefficient, D_{m}. These parameters cannot be easily separated because it is not possible to obtain independent estimates of their in-situ values. It should be noted that the simultaneous fits to the nonsorbing tracer responses were *not* significantly improved by assuming a finite matrix (versus an infinite matrix) or by assuming multiple pathways with different matrix diffusion mass transfer coefficients (versus a single mass transfer coefficient).

Lithium sorption parameters deduced from the field tracer tests are listed in Table 53. Laboratory-derived lithium sorption parameters (see below) are also listed in Table 53 to allow a comparison between field- and laboratory-derived sorption data. Table 53 indicates that lithium sorption in the field was always approximately equal to or greater than the sorption measured in the laboratory. It should be noted that although Table 53 lists only linear equilibrium sorption parameters (K_{d} values), the first lithium peak in the Bullfrog Tuff tracer test was actually a better fit assuming either rate-limited sorption or nonlinear sorption. A discussion of these and other alternative approaches to fitting the early lithium peak in the Bullfrog Tuff test is provided by Reimus et al. (1999, Section C.4.2). For the second lithium peak in the Bullfrog Tuff test and the only peak in the Prow Pass test, the assumption of linear equilibrium sorption provided very good fits to the data.

The microsphere fitting procedure in the Bullfrog Tuff test is described in detail in Reimus et al. (1999, Section C.5). Two sets of pathways were assumed, each having a unique linear filtration rate constant. However, to fit the long tailing behavior, it was necessary to assume that there were multiple resuspension rate constants for different mass fractions of the spheres within each pathway. To match the low recovery of the spheres, a relatively large fraction of mass in each pathway was assumed to be irreversibly filtered (a resuspension rate constant of zero). The filtration rate constants resulting in a good fit to the complete microsphere response are given in Table 51. In the Prow Pass Tuff test, the microsphere responses were fit assuming only linear forward filtration with no resuspension (Reimus et al. 1999, p. 5.10). The resulting filtration rate constants are provided in Table 52. The fits provided a good match to the data up until the tails of the breakthrough curves began to flatten out. The long flat tails could probably be explained by multiple resuspension rate constants, but this was not attempted.

Table 53. Comparison of Field- and Laboratory-Derived Sorption Parameters for Lithium Ion [a]

Parameter	Field K_d	Laboratory K_d [b]
Prow Pass matrix K_d assuming Central Prow Pass Tuff	0.66	0.13 (0.26 at infinite dilution)
Prow Pass matrix K_d assuming Lower Prow Pass Tuff	1.68	0.084 (0.44 at infinite dilution)
Bullfrog matrix K_d in Pathway 1 assuming Central Bullfrog Tuff [c]	0.24	0.19 (0.44 at infinite dilution)
Bullfrog matrix K_d in Pathway 1 assuming Lower Bullfrog Tuff [c]	0.97	0.32 (1.64 at infinite dilution)
Bullfrog matrix K_d in Pathway 2 assuming Central Bullfrog Tuff [c]	0.67	0.19 (0.44 at infinite dilution)
Bullfrog matrix K_d in Pathway 2 assuming Lower Bullfrog Tuff [c]	2.75	0.32 (1.64 at infinite dilution)

DTN: LA9909PR831231.003 (field K_d for Bullfrog); MO0012BRLI25C2.000 (laboratory K_d); LA9909PR831231.005 (field K_d for Prow Pass)

NOTES: [a] This comparison assumes linear sorption isotherms.
[b] Values at "infinite dilution" obtained from slopes of Langmuir isotherm fits to the data (asymptotic slope at very low concentrations). Other values obtained from a simple linear fit to the entire range of data.
[c] Pathway 1 refers to pathways that resulted in the first tracer peak in the Bullfrog reactive tracer test, and Pathway 2 refers to pathways that resulted in the second peak in this test. K_d values were calculated from the smallest matrix retardation factors obtained from alternative interpretations of the test (see Reimus et al. 1999, Section C.4.2, Table C-8).

Only one other C-wells tracer test involved the simultaneous injection of more than one tracer (the combined iodide and 2,4,5-trifluorobenzoate (TFBA) injection in the Prow Pass Tuff in June 1998). This test exhibited the same qualitative behavior as the multiple tracer tests described above, that is, the iodide was more attenuated than the TFBA due to greater matrix diffusion. The comparisons of tracer responses resulting from injections into well c#1 and into either well c#2 while pumping well c#3 provided some insights into flow heterogeneity/ anisotropy in the lower Bullfrog Tuff at the C-wells. Table 54 lists the ratios of peak response times or first arrival times for conservative tracers between c#1 and c#3 and between c#2 and c#3 for the two tests in which a comparison was possible. For a homogeneous, isotropic medium, the response times under radial flow conditions are expected to vary as R^2, which is the distance between injection and production well squared. The ratios of R^2 values corresponding to both cases are also listed in Table 54. Note that the ratios of tracer response times and R^2 values are in reasonably good agreement in both cases, suggesting that anisotropy in the lower Bullfrog Tuff at the C-holes may be relatively small despite the apparent orientation of the fracture network in the general direction of c#1 to c#2 (Geldon 1993, pp. 44-46).

Table 54. Ratios of Observed Tracer Arrival Times and Distances Squared for C-Wells Tracer Tests

Tests	Time c#1/Time c#2–c#3	R^2 c#1/R^2 c#2–c#3
Bullfrog, PFBA (c#2) and Iodide (c#1) [a]	6	7.4
Bullfrog, 2,6-DFBA (c#2) and Pyridone (c#1) [b]	10	7.4

DTN: GS970708312315.001, LA0002PR831231.001.

NOTES: [a] Both tests conducted with 2.5 to 3.5% recirculation into injection well. Peak tracer arrivals compared.
[b] Both tests conducted with no recirculation. First tracer arrivals compared.

6.9.3 Summary of Laboratory Test Results and Interpretations

6.9.3.1 Batch-Sorption Testing of Lithium Ion

Batch-sorption tests were conducted to determine equilibrium sorption isotherms of lithium ion to seven different C-wells tuff lithologies over a three order-of-magnitude range of lithium solution concentrations that effectively spanned the range of concentrations in field tests (~1 to 1000 mg L^{-1}). The resulting best-fitting Langmuir isotherms for each lithology are shown in Figure 102 (without the fitted data, which would excessively clutter the plot) (Reimus et al. 1999, Section 6.2, Figures 6-3 to 6-9). In most cases, a Langmuir isotherm offered a better fit to the data than either a linear or Freundlich isotherm because of the tendency of the isotherm to plateau at higher concentrations, suggesting a "saturation" of the surface with lithium. These tests and their results are described in more detail in Reimus et al. (1999, Section 6.2).

In conjunction with the batch-sorption tests, all tuffs tested were analyzed quantitatively for major mineral phases by x-ray diffraction (XRD) (DTN: MO0012MINLCHOL.000). Cation exchange capacity experiments were also conducted on each rock (DTN: MO0012CATECHOL.000). Not surprisingly, the tuffs that had the highest lithium sorption capacity (Bedded Prow Pass and Lower Bullfrog) also had the highest percentages of smectite clays and/or zeolites and the highest cation exchange capacities (Reimus et al. 1999, Table 6-4, Figure 6-2). The primary cations exchanging with the lithium in the cation exchange capacity tests were sodium and calcium.

6.9.3.2. Diffusion Cell Testing

Laboratory "diffusion cell" tests involved measuring the diffusion coefficients of the nonsorbing tracers used in field tests in intact blocks of saturated matrix material. The experimental apparatus and details of the test interpretations are presented in Reimus et al. (1999, Chapter 8). The diffusion coefficients of PFBA and bromide were measured in five different tuff lithologies, as listed in Table 55. Each of these lithologies could have been involved in the field tests. Table 55 also gives the measured matrix porosities and permeabilities of the tuffs. It is evident that the diffusion coefficients are positively correlated with both of these rock properties, although the correlation is better with permeability. The two diffusion cell tests conducted in the lower Prow Pass Tuff indicate very good experimental reproducibility using two different pieces of core from this lithological unit.

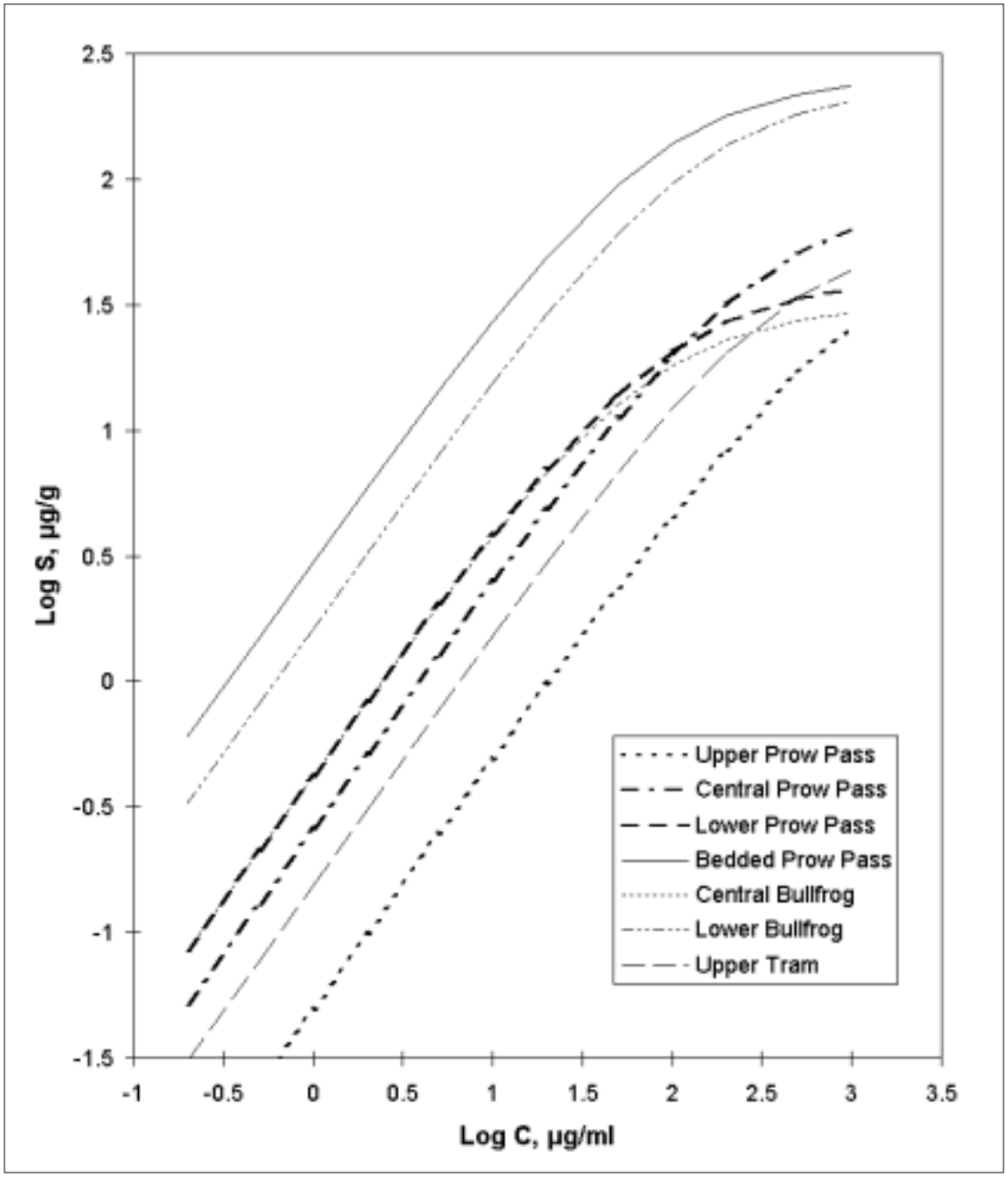

DTN: MO0012SORBCHOL.000, LA9909PR831231.005

NOTES: See Figure 95.
The units are ordered in the legend from shallowest to deepest. Lithium concentrations in the field tests ranged from less than 0.1 mg L^{-1} to 2600 mg L^{-1}.
These isotherms are based on log amount sorbed versus log solution concentration.

Figure 101. Fitted Langmuir Sorption Isotherms for Lithium Sorption onto C-Wells Tuffs from Different Units/Lithologies

The ratio of bromide to PFBA diffusion coefficients in the diffusion cell tests was consistently about 3:1, regardless of the absolute values of the diffusion coefficients. This ratio was used as a constraint when simultaneously fitting the responses of these tracers in the field tests.

Table 55. Laboratory-Measured Matrix Diffusion Coefficients of Bromide and PFBA in Various C-Wells Tuffs [a]

Tuff	Porosity	Permeability (mDarcy)	L (cm) [b]	Matrix diff. coeff. ($cm^2\ s^{-1} \times 10^6$)		
				Br	PFBA	Br/PFBA
Central Bullfrog	0.094	0.00107	1.16	0.45	0.13	3.46
Lower Bullfrog	0.298	0.0949	0.84	1.0	0.35	2.86
Upper Prow Pass	0.272	4.72	0.91	6.0	1.9	3.16
Central Prow Pass	0.138	0.000786	1.23	0.4	0.13	3.08
Lower Prow Pass-1 [c]	0.288	0.455	2.27	3.0	1.1	2.73
Lower Prow Pass-2 [c]	0.288	0.455	1.82	3.0	1.0	3.0

DTN: LA9909PR831231.003, MO0012PERMCHOL.000, MO0012POROCHOL.000, LA9909PR831231.005

NOTES: [a] The porosities and permeabilities of the tuffs are also listed in this table.
[b] L = thickness of tuff "wafer" used in diffusion cell experiment.
[c] Duplicate experiments were conducted in the lower Prow Pass Tuff.

6.9.3.3 Flowing Transport Experiments in Crushed and Fractured Tuffs

Two types of flowing transport experiments were conducted to support the field testing efforts: (1) crushed-tuff column experiments, and (2) fractured-core column experiments. In the former, lithium bromide solutions were eluted through columns of the same crushed Central Bullfrog Tuff at different concentrations and different flow rates. These tests showed that lithium sorption under flowing conditions was in very good agreement with batch-sorption measurements and demonstrated that lithium sorption kinetics were rapid enough that lithium sorption in the field should be well approximated by assuming local equilibrium between the solution and solid phases. More details of the crushed-tuff column experiments and their results are given in Reimus et al. (1999, Section 7.1). The tests were interpreted using the RELAP and RETRAN components of the RTA (STN: 10032-1.1-00) software package.

The fractured-core experiments offered more realistic laboratory simulations of the field tracer tests. These tests were conducted in induced (unnatural) fractures in both the Upper and Central Prow Pass Tuff lithologies (16–17 cm long). Experimental methods are described in Reimus et al. (1999, Section 7.2). Two different sets of tests were conducted in each fracture: (1) multiple tests at different flow rates using only iodide as a tracer and (2) tests involving the simultaneous injection of lithium, bromide, and PFBA (analogous to the field experiments). The first set of tests consistently exhibited higher peak concentrations of iodide at higher flow rates, consistent with matrix diffusion (more iodide would be expected to diffuse into the matrix as residence times increase). Simultaneous RELAP fits of these data sets allowed estimates of matrix diffusion parameters in the columns. The second set of tests exhibited behavior that was very consistent with the field observations, that is, peak normalized PFBA concentrations that were greater than peak Br concentrations and lithium concentrations that were lower yet but not significantly attenuated in time (Reimus et al. 1999, pp. 7.8 to 7.9, Figures 7-8 to 7-9, 7-11). All

of these features are consistent with dual-porosity transport behavior in the columns. These tests were interpreted using the same techniques (RTA) as the field tests involving multiple tracers. For brevity, the test results and interpretations are not presented here (see Reimus et al. 1999, Section 7.2). In general, apparent matrix-diffusion-mass-transfer coefficients were greater in the laboratory than in the field, and lithium sorption parameters in the laboratory were smaller than in the field.

6.9.4 Conclusions from C-Wells Field and Laboratory Testing

The C-wells field and laboratory tests have resulted in the following conclusions relevant to performance assessments of the potential Yucca Mountain repository.

- The responses of nonsorbing tracers in all field and laboratory tracer tests in fractured rocks have been consistent with matrix diffusion behavior. This result supports the use of a dual-porosity conceptual model to describe radionuclide transport through the saturated, fractured volcanic rocks near Yucca Mountain.

- Sorption of lithium ion in the field was greater than or equal to its measured sorption in the laboratory (see Table 53 for a comparison of lab- and field-derived sorption parameters). Although lithium does not behave identically to any radionuclide, this result suggests that the use of laboratory-derived radionuclide sorption parameters in field-scale transport predictions is defensible and may even be conservative.

- The effective flow porosities deduced from the field tests were less than 1% for all tracer responses except for the second tracer peak(s) in the Bullfrog Tuff test, for which the deduced flow porosity was several percent (even after apportioning 75% of the production flow to the first tracer peak). However, if the second peak was really the result of only 10% of the production flow, then the effective flow porosity would be only ~1%, and if it were only 5% of the production flow, then the flow porosity would be less than 1%. Such small percentages of production flow resulting in the second tracer response(s) are entirely possible in a heterogeneous fracture flow system such as that at the C-wells.

- The longitudinal dispersivities deduced from the field-scale experiments are consistent with published relationships of dispersivity versus length scale (see, for example, Figure 100).

- Matrix-diffusion-mass-transfer coefficients in the field experiments were less than in the laboratory experiments, and they generally decreased as tracer residence times increased. There are several possible explanations for this behavior including (1) larger average fracture apertures as length (and time) scales increase, (2) an increasingly greater influence of true matrix diffusion, as opposed to diffusion into stagnant free water as test durations increase, and/or (3) a greater tendency to encounter diffusion barriers in longer duration tests for which characteristic diffusion distances are greater. It should be noted that all tracer responses could be adequately fitted assuming a single matrix-diffusion-mass-transfer rate for each tracer peak.

7. CONCLUSIONS

Sorption is a function of water chemistry and the type of tuff at Yucca Mountain. It is assumed for the performance-assessment recommendations that the waters from wells J-13 and p#1 bound the major-ion chemistry of the groundwaters at Yucca Mountain, and that the number of sorption-coefficient distributions elicited to four per radionuclide: iron oxides, devitrified tuff, vitric tuff, and zeolitic tuff. The basis for this grouping is the fact that sorption of radionuclides is the result of a chemical reaction between the radionuclide in the groundwater and the minerals in the tuff. The mineralogy of the different strata of the same rock group is very similar, and the sorption coefficients can be grouped in terms of these rock types. Iron oxides were added to the list of "rock" types to reflect the containers to be used in the repository and the possibility that the corrosion by-products of a massive multipurpose container could become a substrate for sorption. Measured sorption coefficients onto tuffs were higher at elevated temperatures for all elements studied: americium, barium, cerium, cesium, europium, plutonium, strontium, and uranium. Therefore, sorption coefficients measured at ambient temperatures should be applicable and generally conservative when applied to describing aqueous transport from a hot repository. Table 2a gives recommended parameters for the sorption-coefficient probability models for performance assessment for unsaturated-zone units, and Table 2b shows the same parameters for the saturated zone.

The alluvium exhibited significant sorptive properties with respect to Np, Tc, and I. Distribution coefficients (K_ds) varied as a function of depth and borehole. K_d values for Np ranged from about 5 to 77 mL g^{-1}; K_d values for Tc ranged from about 0.35 to 0.8 mL g^{-1}; and preliminary K_d values for ^{129}I ranged from about 0.41 to 0.75 mL g^{-1}. Sorption was much faster for Np than for Tc or ^{129}I. The differences in sorptive properties among samples probably result from differences in the amount of the sorptive phase—smectite, clinoptilolite, calcite, and hematite—and perhaps from the presence of organic carbon and trace amounts of sulfides, which may explain the slow sorption response for Tc and ^{129}I. Biological activity, or simply sorption onto organics, could also be important and account for the slow sorption responses for Tc and ^{129}I. During these tests, significant amounts of colloids were also found, but their transport properties could not be investigated. These values are incorporated into Table 2a and b.

Conclusions drawn from available data regarding radionuclide transport through fractured-rock columns show that, contrary to previous views about the role of fractures in radionuclide retardation, fracture flow does not necessarily result in a fast pathway for actinide migration through fractures. The migration of actinides through fractures can be significantly retarded by sorption onto minerals coating the fractures and by diffusion into the tuff matrix, a result consistent with the results of the Busted Butte tests.

The results obtained from rock-beaker experiments agree with previous results and found that rate constants for uptake onto tuff of the sorbing cations from solution were consistent with a diffusion-limited model in which diffusion occurs in two stages. In the first stage, the cations diffuse into rock through water-filled pores; in the second stage, they diffuse into narrower intracrystalline channels. This diffusion model yielded sorption coefficients for cesium, strontium, and barium that agree well with the sorption coefficients determined by batch techniques.

The UZTT at Busted Butte was designed to provide information suitable for assessing the validity of flow and transport models used in the site characterization and performance assessment programs for Yucca Mountain. Critical evaluation and iterative improvement of the flow and transport conceptual and numerical models await the collection of further data, which is currently in progress. The first step in this process was reported in this AMR, namely the predictions of flow and transport behavior for both the Phase-1 and Phase-2 experiments and the preliminary results of those experiments. As discussed in Sections 6.8.6 and 6.8.7, the models are doing a reasonable job of capturing the flow phenomenon at this site. The major prediction is that fracture flow is not dominant at this site.

Although flow and transport field data collected to date are limited, observations of the available data collected so far, and the modeling of these data, lead to several key conclusions of relevance to performance assessment. These conclusions are summarized below, categorized with respect to the particular field or modeling activity in this report.

- *Laboratory measurements:* The collection of unsaturated hydrologic property data using the Unsaturated Flow Apparatus (UFA) provides data of particular relevance to flow and transport models because they are direct measurements under unsaturated conditions rather than indirect, model-derived parameters. The Monte Carlo analyses (Section 6.8.6) indicate that the nature of the correlations between parameters such as permeability and the van Genuchten α parameter have a strong impact on the predictability of the flow and transport system. This impact could be better defined by conducting a full suite of measurements of hydrologic and transport parameters on rock samples to constrain models and develop correlations.

- *Phase-1A and -1B model results for UZTT:* The modeling analyses for Phase 1A indicate that strong capillary forces in the rock matrix of the Tac unit are likely to modulate fracture flow from overlying units, thereby damping pulses of infiltrating water and providing a large degree of contact between radionuclides and the rock matrix. Several modeling approaches, from deterministic to Monte Carlo and stochastic models, were used to simulate the Phase-1A experiments (Sections 6.8.6 and 6.8.7). All yielded similar qualitative results. From this we conclude tentatively that the deterministic modeling approach taken at the site scale may be adequate. The parameterizations used in performing these calculations will be confirmed as data from the UZTT are available.

  A particularly interesting observation from the Phase-1B experiment is that, even when injection occurs immediately adjacent to a fracture, water appears to be imbibed quickly into the surrounding matrix. The transport times observed immediately below the injection point were on the order of 30 days, whereas pure fracture flow would have resulted in travel times of minutes to hours at this flow rate. Site-scale models must be evaluated in light of this observation. Models that predict significant fracture flow at percolation rates low enough for the matrix to transmit the flow are inconsistent with the Phase-1B experimental data results. This behavior was demonstrated in the Phase 1B experiments that occurred in the lower section of the TS (tptpv2), but the same general behavior should occur in the Calico Hills unit because the matrix capillarity is even stronger than the TS unit, and the in situ saturation is low.

- *Phase-2 modeling:* Because there were not field-test results at the time of preparation of this AMR, it is difficult to draw conclusions relevant to the evaluation of models. Significant uncertainties uncovered by the modeling include the adequacy of continuum models in nonwelded units of high matrix permeability, and the nature of the transition from fracture flow to matrix flow at contacts between hydrogeologic units. These are the issues being studied within the UZTT. Therefore, preliminary answers to these important questions are anticipated after test data have been collected and analyzed.

The UZTT has demonstrated that in the vitric Calico Hills unit, fluid movement is dominated by capillary forces and, thus, is predominantly matrix flow with little influence of fractures. Even with an overlying fractured unit (Topopah Spring welded tuff), the Calico Hills Formation below it strongly damps any fracture-dominated influence. These results suggest that commonly held views regarding the Calico Hills as a fast path for contaminants may be overstated. However, the UZTT is still in progress, and additional data regarding the influence of sorption and movement of radionuclides, as well as non-reactive contaminants, are still being collected for evaluation.

Some conclusions from the C-wells field and laboratory tests are relevant to performance assessment of the potential repository. The responses of nonsorbing tracers in all field and laboratory tracer tests in fractured rocks have been consistent with matrix diffusion behavior. This result supports the use of a dual-porosity conceptual model to describe radionuclide transport through saturated, fractured volcanic rock near Yucca Mountain. Results also suggest that the use of laboratory-derived radionuclide sorption parameters in field-scale transport predictions is defensible and conservative. The effective flow porosities deduced from the field tests were less than 1% for all tracer responses except for the second tracer peak in the Bullfrog Tuff test, for which the deduced flow porosity was several percent. Such small percentages of production are entirely possible in a heterogeneous fracture flow system such as that at the C-wells. The longitudinal dispersivities deduced from the field-scale experiments are consistent with published relationships of dispersivity versus length scale. Matrix diffusion mass transfer coefficients in the field experiments were less than in the laboratory experiments, and they generally decreased as tracer residence times increased. There are several possible explanations for this behavior, including (1) larger average fracture apertures as length (and time) scales increase, (2) an increasingly greater influence of true matrix diffusion, as opposed to diffusion into stagnant free water, as test durations increase, and/or (3) a greater tendency to encounter diffusion barriers in longer duration tests in which characteristic diffusion distances are greater. It should be noted that all tracer responses could be adequately fitted assuming a single matrix diffusion mass transfer rate for each tracer peak.

7.1 RECOMMENDATIONS

Sorption

The sorption data suggest that there are definite upper and lower bounds for the K_d values recommended to PA. Unfortunately, the ranges can be large, and large uncertainties in K_d values between 0 and 5 can result in very large uncertainties in predicted travel times. Further experiments under a wide variety of conditions relevant to the repository situation could reduce uncertainty in K_d values.

Because sorption is sensitive to the mineralogy, it is critical to either have an adequate understanding of the mineralogy and distributions along the flow pathway to the accessible environment or to accommodate this uncertainty in the PA evaluations. As an example, sorption of Np by hematite is thousands of times greater than sorption by the vitric tuff, and fracture coatings of hematite will influence transport well beyond what is indicated by its mass fraction in the system.

Sorption of Tc and I by the alluvium may be an important mechanism to be considered in PA evaluations. The preliminary data show non-zero K_d values of these radioisotopes in the 75-to-500-μm fraction of the alluvium (the standard size range for YMP sorption experiments). However, although this size range is appropriate for crushed whole-rock tuff samples, it omits the most sorptive components of the alluvium. Therefore, the alluvium may have higher K_d values than those measured to date.

Colloid-facilitated transport

The degree to which colloid-facilitated radionuclide migration will be a problem at Yucca Mountain depends very strongly on water chemistry, the specific radionuclide, type and size of the colloid, and ambient conditions, including degree of saturation. Unfortunately, the few colloid transport studies that have been documented have been conducted on systems and under conditions not relevant to the YMP. The data collected for this AMR are also of limited usefulness because they lack accompanying physical colloid transport data, such as colloid transport through fractured rock columns or invert/backfill materials in the laboratory or through tuff units in the field. In addition, a few well-designed studies on YMP-specific problems could resolve most of the colloid issues with respect to the repository environment.

1. The chemistry and type of colloids present in groundwaters should be determined.

2. Column experiments should be performed to determine the transport properties of colloids in Yucca Mountain materials.

3. The stability of colloids under various repository conditions should be determined.

4. The radionuclide and colloid attachment/detachment properties should be determined for all colloids anticipated in the repository environment.

5. The flux and water chemistry through the drift should be determined or more accurately bounded.

Busted Butte UZTT and C-Wells

The Busted Butte UZTT shows that there is no significant fracture flow through unsaturated nonwelded units and that the travel speed through these units are presently overestimated by orders of magnitude. This observation, together with the likely retardation properties of the alluvium units for Tc, I, and Np, and the corroboration of a dual-porosity conceptual model to describe radionuclide transport through the saturated, fractured volcanic rocks near Yucca Mountain determined from the C-wells field and laboratory tests, provides the greatest technical support for a successful LA, and it is recommended that their completion be a major focus of efforts leading to the LA.

7.2 IMPACTS

K_d values and diffusion coefficients enter into the Principal Factor of Dilution of Radionuclide Concentrations in the Geologic Setting and perhaps some of the Other Factors For the Post-Closure Safety Case. Consequently, PA calculations using these data will better illustrate the sensitivity of radionuclide release rates to the data, and an exact impact will be determinable; similarly, for Busted Butte and C-wells results.

If TBV data are not verified, the impact would be to invalidate the conclusions and recommendations, and this could significantly impact PA evaluations.

This document may be affected by technical product input information that requires confirmation. Any changes to the document that may occur as a result of completing the confirmation activities will be reflected in a subsequent revision. The status of the input information quality may be confirmed by review of the DIRS database.

7.3 OUTPUT DATA

Data developed by this analysis are included in the following.

- Sorption parameter values for both the unsaturated and the saturated zones can be found in DTN: LA0003AM831341.001.

- The matrix diffusion coefficients recommended for use in PA can be found in DTN: LA0003JC831362.001.

- Output data for the Busted Butte simulations are found in DTN: LA9909WS831372.019, LA9909WS831372.020, LA9909WS831372.021, and LA9909WS831372.022.

INTENTIONALLY LEFT BLANK

8. INPUTS AND REFERENCES

8.1 DOCUMENTS CITED

Aagaard, P. 1974. "Rare Earth Elements Adsorption on Clay Minerals." *Bulletin du Groupe Francais des Argiles, 26*, (2), 193–199. Paris, France: Centre National de la Recherche Scientifique. Copyright Requested Library Tracking Number: 236921.

Allard, B. 1982. *Sorption of Actinides in Granitic Rock*. KBSTR 82-21. Goteborg, Sweden: Chalmers University of Technology. TIC: 205892.

Allard, B. and Beall, G.W. 1979. "Sorption of Americium on Geologic Media." *Journal of Environmental Health, A14*, (6), 507–518. New York, New York: Marcel Dekker. TIC: 224102.

Altman, S.J.; Arnold, B.W.; Barnard, R.W.; Barr, G.E.; Ho, C.K.; McKenna, S.A.; and Eaton, R.R. 1996. *Flow Calculations for Yucca Mountain Groundwater Travel Time (GWTT-95)*. SAND96-0819. Albuquerque, New Mexico: Sandia National Laboratories. ACC: MOL.19961209.0152.

Ames, L.L., Jr.; McGarrah, J.E.; and Walker, B.A. 1983. "Sorption of Trace Constituents from Aqueous Solutions onto Secondary Minerals: 1. Uranium." *Clays and Clay Minerals, 31*, (5), 321–334. Long Island City, New York: Pergamon Press. TIC: 238914.

Andersson, K. 1988. *SKI Project-90: Chemical Data*. SKI Technical Report 91:21. Stockholm, Sweden: Swedish Nuclear Power Inspectorate. TIC: 242643.

Baes, C.F., Jr. and Mesmer, R.E. 1986. *The Hydrolysis of Cations*. Malabar, Florida: Krieger Publishing Company. TIC: 223481.

Balistrieri, L.S. and Chao, T.T. 1987. "Selenium Adsorption by Goethite." *Soil Science Society of America Journal, 51*, (5), 1145–1151. Madison, Wisconsin: Soil Science Society of America. TIC: 223172.

Balistrieri, L.S. and Murray, J.W. 1982. "The Adsorption of Cu, Pb, Zn, and Cd on Goethite from Major Ion Seawater." *Geochimica et Cosmochimica Acta, 46*, 1253–1265. New York, New York: Pergamon Press. TIC: 238913.

Banfield, J.F. and Eggleton, R.A. 1989. "Apatite Replacement and Rare Earth Mobilization, Fractionation, and Fixation during Weathering. *Clays Minerals Society, 37*, (2), 113–127. Long Island, New York: Pergamon Press. TIC: 236948.

Bar-Yosef, B. and Meek, D. 1987. "Selenium Sorption by Kaolinite and Montmorillonite." *Soil Science, 144*, (1), 11–19. Philadelphia, Pennsylvania: Lippincott, Williams & Wilkins. TIC: 237321.

Barrer, R.M. and Townsend, R.P. 1976. "Transition Metal Ion Exchange in Zeolites: Part 1.– Thermodynamics of Exchange of Hydrated Mn^{2+}, Co^{2+}, Ni^{2+}, Cu^{2+}, and Zn^{2+} Ions in Ammonium Mordenite." *Journal of the Chemical Society, Faraday Transactions I, 72*, 661–673. London, England: Royal Society of Chemistry. TIC: 239144.

Beckman, R.; Thomas, K.; and Crowe, B. 1988. *Preliminary Report on the Statistical Evaluation of Sorption Data: Sorption as a Function of Mineralogy, Temperature, Time, and Particle Size*. LA-11246-MS. Los Alamos, New Mexico: Los Alamos National Laboratory. ACC: NNA.19890918.0500.

Benjamin, M.M. 1983. "Adsorption and Surface Precipitation of Metals on Amorphous Iron Oxyhydroxide." *Environmental Science and Technology, 17*, 686–692. Easton, Pennsylvania: American Chemical Society. TIC: 239143.

Bird, R.B.; Stewart, W.E.; and Lightfoot, E.N. 1960. *Transport Phenomena*. New York, New York: John Wiley and Sons. TIC: 208957.

Bish, D.L. and Chipera, S.J. 1989. *Revised Mineralogic Summary of Yucca Mountain, Nevada*. LA-11497-MS. Los Alamos, New Mexico: Los Alamos National Laboratory. ACC: NNA.19891019.0029.

Blanchard, G.; Maunaye, M.; and Martin, G. 1984. "Removal of Heavy Metals from Waters by Means of Natural Zeolites." *Water Research, 18*, (12), 1501–1507. Oxford, Great Britain: Pergamon Press. TIC: 239004.

Bolt, G.H. and Bruggenwert, M.G.M., eds. 1978. *Soil Chemistry: A. Basic Elements.* Developments in Soil Science 5A. 2nd Revised Edition. New York, New York: Elsevier Scientific Publishing Company. TIC: 243742.

Bonnot-Courtois, C. and Jaffezic-Renault, N. 1982. "Etude des Echanges Entre Terres Rares et Cations Interfoliares de Deux Argiles." *Clays Minerals, 17*, 409–420. London, England: Mineralogical Society. TIC: 237359.

Borovec, Z. 1981. "The Adsorption of Uranyl Species by Fine Clay." *Chemical Geology, 32*, 45–58. Amsterdam, The Netherlands: Elsevier Science Publishing Company. TIC: 237323.

Bouwer, H. 1991. "Simple Derivation of the Retardation Equation and Application to Preferential Flow and Macrodispersion." *Ground Water, 29*, (1), 41–46. Dublin, Ohio: Water Well Publishing Company. TIC: 224079.

Bowman, R.S. and O'Connor, G.A. 1982. "Control of Nickel and Strontium Sorption by Free Metal Ion Activity." *Soil Science Society of America Journal, 46*, 933–936. Madison, Wisconsin: Soil Science Society of America. TIC: 236910.

Bradbury, M.H.; Green, A.; Lever, D.; and Stephen, I.G. 1986. *Diffusion and Permeability-Based Sorption Measurements in Sandstone, Anhydrite, and Upper Magnesian Limestone Samples*. AERE-R 11995. Oxfordshire, United Kingdom: Harwell Laboratory. TIC: 237243.

Brookins, D.G. 1983. "Migration and Retention of Elements at the Oklo Natural Reactor." *Environmental Geology, 4*, 201–208. New York, New York: Springer-Verlag. TIC: 239003.

Brookins, D.G. 1988. *Eh-pH Diagrams for Geochemistry*. New York, New York: Springer-Verlag. TIC: 237943.

Brown, R.E.; Parker, H.M.; and Smith, J.M. 1955. "Disposal of Liquid Wastes to the Ground." *Proceeding of the International Conference on the Peaceful Uses of Atomic Energy, August 8–20, 1955, Geneva, Switzerland, 9*, 669–675. New York, New York: United Nations Publications. TIC: 236932.

Broxton, D.E.; Warren, R.G.; Hagan, R.C.; and Luedemann, G. 1986. *Chemistry of Diagenetically Altered Tuffs at a Potential Nuclear Waste Repository, Yucca Mountain, Nye County, Nevada*. LA-10802-MS. Los Alamos, New Mexico: Los Alamos National Laboratory. ACC: 19980527.0202.

Bruque, S.; Mozas, T.; and Rodriguez, A. et al. 1980. "Factors Influencing Retention of Lanthanide Ions by Montmorillonite." *Clays Minerals, 15*, 413–420. London, England: Mineralogical Society. TIC: 237358.

Buesch, D.C.; Spengler, R.W.; Moyer, T.C.; and Geslin, J.K. 1996. *Proposed Stratigraphic Nomenclature and Macroscopic Identification of Lithostratigraphic Units of the Paintbrush Group Exposed at Yucca Mountain, Nevada*. Open File Report 94-469. Denver, Colorado: U. S. Geological Survey. ACC: MOL.19970205.0061.

Bussod, G.Y. 1998. Busted Butte On-Site Log Book #1/UZ Transport Field Test (LA-EES-5-NBK-98-010). SN-LANL-SCI-040-V1. ACC: MOL.20000321.0288.

Bussod, G.Y.; Robinson, B.A.; Vaniman, D.T.; Broxton, D.E.; and Viswanathan, H.S. 1997. *UZ Field Transport Test Plan*. SP341SM4. Los Alamos, New Mexico: Los Alamos National Laboratory. ACC: MOL.19980806.0715.

Byrne, R.H. and Kim, K.-H. 1993. "Rare-Earth Precipitation and Coprecipitation Behavior: The Limiting Role of PO_4^{3-} on Dissolved Rare-Earth Concentrations in Seawater." *Geochimica et Cosmochimica Acta, 57*, 519–526. New York, New York: Pergamon Press. TIC: 239120.

Cann, J.R. 1970. "Rb, Sr, Y, Zr, and Nb in Some Ocean Floor Basaltic Rocks." *Earth and Planetary Science Letters, 10*, 7–11. Amsterdam, The Netherlands: North Holland. TIC: 236899.

Carlos, B.A. 1985. *Minerals in Fractures of the Unsaturated Zone from Drill Core USW G-4, Yucca Mountain, Nye County, Nevada*. LA-10415-MS. Los Alamos, New Mexico: Los Alamos National Laboratory. ACC: NNA.19920506.0037.

Carlos, B.A. 1987. *Minerals in Fractures of the Saturated Zone from Drill Core USW G-4, Yucca Mountain, Nye County, Nevada*. LA-10927-MS. Los Alamos, New Mexico: Los Alamos National Laboratory. ACC: NNA.19900222.0149.

Carlos, B.A. 1989. *Fracture-Coating Minerals in the Topopah Spring Member and Upper Tuff of Calico Hills from Drill Hole J-13*. LA-11504-MS. Los Alamos, New Mexico: Los Alamos National Laboratory. TIC: 202383.

Carlos, B.A. 1994. *Field Guide to Fracture-Lining Minerals at Yucca Mountain, Nevada*. LA-12803-MS. Los Alamos, New Mexico: Los Alamos National Laboratory. ACC: MOL.19950717.0113.

Carlos, B.A.; Bish, D.L.; and Chipera, S.J. 1990. *Manganese-Oxide Minerals in Fractures of the Crater Flat Tuff in Drill Core USW G-4, Yucca Mountain, Nevada*. LA-11787-MS. Los Alamos, New Mexico: Los Alamos National Laboratory. ACC: NNA.19900206.0163.

Carlos, B.A.; Chipera, S.J.; Bish, D.L.; and Craven, S.J. 1993. "Fracture-Lining Manganese Oxide Minerals in Silicic Tuff, Yucca Mountain, Nevada, USA." *Chemical Geology, 107*, 47–69. Amsterdam, the Netherlands: Elsevier Science Publishers B.V. TIC: 208629.

Carpenter, R.; Beasley, T.M.; Zahnle, D.; and Somayajulu, B.L.K. 1987. "Cycling of Fallout (Pu, ^{241}Am, ^{137}Cs) and Natural (U, Th, ^{210}Pb) Radionuclides in Washington Continental Slope Sediments." *Geochimica et Cosmochimica Acta, 51*, 1897–1921. New York, New York: Pergamon Press. TIC: 239140.

Carsel, R.F. and Parrish, R.S. 1988. "Developing Joint Probability Distributions of Soil Water Retention Characteristics." *Water Resources Research, 24*, (5), 755–769. Washington, D.C.: American Geophysical Union. TIC: 247697.

Choppin, G.R. 1992. "The Role of Natural Organics in Radionuclide Migration in Natural Aquifer Systems." *Radiochimica Acta, 58/59*, 113–120. New York, New York: Academic Press. TIC: 222387.

Conca, J.L. and Wright, J. 1992. "Diffusion and Flow in Unsaturated Gravel, Soil, and Whole Rock." *Applied Hydrogeology, 1*, 5–24. Hanover, Germany: Verlag Heinz Heise GmbH. TIC: 224081.

Cotton, F.A. and Wilkinson, G. 1988. *Advanced Inorganic Chemistry*, Fifth Edition. New York, New York: John Wiley and Sons. TIC: 236867.

Cramer, J.J. and Sargent, F.P. 1994. "The Cigar Lake Analog Study: An International R&D Project." *High Level Radioactive Waste Management, Proceedings of the Fifth Annual*

International Conference, Las Vegas, Nevada, May 22–26, 1994, 4, 2237–2242. LaGrange Park, Illinois: American Nuclear Society. TIC: 210984.

CRWMS M&O (Civilian Radioactive Waste Management System Management and Operating Contractor) 1999a. *Work Package Planning Summary for Saturated Zone Flow and Transport PMR, 8191213SU1, Revision 00*. WPP-NBS-MD-000009. Las Vegas, Nevada: CRWMS M&O. ACC: MOL.19991008.0221.

CRWMS M&O 1999b. *UZ/SZ Transport Properties Data*. Development Plan TDP-NBS-HS-000041, Revision 00. Las Vegas, Nevada: CRWMS M&O. ACC: MOL.19990819.0270.

CRWMS M&O 1999c. *Work Package Planning Summary for Unsaturated Zone Transport Test, FY00 WP #1401213UM6 and 891213UU6, Revision 00A*. WPP-NBS-MD-000013. Las Vegas, Nevada: CRWMS M&O. ACC: MOL.19991021.0079.

CRWMS M&O 1999d. *M&O Site Investigations–(Q)*. Activity Evaluation, September 28, 1999. Las Vegas, Nevada: CRWMS M&O. ACC: MOL.19990928.0224.

CRWMS M&O 2000a. *Pure Phase Solubility Limits—LANL*. ANL-EBS-MD-000017, Rev 00. Las Vegas, Nevada: CRWMS M&O. ACC: MOL.20000504.0311.

CRWMS M&O 2000b. *Unsaturated Zone Colloid Transport Model*. ANL-NBS-HS-000028, Rev 00. Las Vegas, Nevada: CRWMS M&O. Submit to RPC. URN-0031.

CRWMS M&O 2000c. *Technical Work Plan for Unsaturated Zone (UZ) Flow and Transport Process Model Report*. TWP-NBS-HS-000001, Rev 00, ICN 2. Las Vegas, Nevada: CRWMS M&O. Submit to RPC, URN-0747.

Dagan, G. 1984. "Solute Transport in Heterogeneous Porous Formations." *Journal of Fluid Mechanics, 145*, 151–177. Cambridge, United Kingdom: Cambridge University Press. TIC: 247700.

Daniels, W.R.; Erdal, B.R.; and Vaniman, D.T., eds. 1983. *Research and Development Related to the Nevada Nuclear Waste Storage Investigations, July 1–September 30, 1982*. LA-9577-PR. Los Alamos, New Mexico: Los Alamos National Laboratory. ACC: NNA.19870406.0180.

Daniels, W.R.; Wolfsberg, K.; Rundberg, R.S.; Ogard, A.E.; Kerrisk, J.F.; Duffy, C.J.; Newton, T.W.; Thompson, J.L.; Bayhurst, B.P.; Bish, D.L.; Blacic, J.D.; Crowe, B.M.; Erdal, B.R.; Griffith, J.F.; Knight, S.D.; Lawrence, F.O.; Rundberg, V.L.; Skyes, M.L.; Thompson, G.M.; Travis, B.J.; Treher, E.N.; Vidale, R.J.; Walter, G.R.; Aguilar, R.D.; Cisneros, M.R.; Maestas, S.; Mitchell, A.J.; Oliver, P.Q.; Raybold, N.A.; and Wanek, P.L. 1982. *Summary Report on the Geochemistry of Yucca Mountain and Environs*. LA-9328-MS. Los Alamos, New Mexico: Los Alamos National Laboratory. ACC: NNA.19870406.0243.

Dash, Z.V.; Robinson, B.A.; and Zyvoloski, G.A. 1997. *Software Requirements, Design, and Verification and Validation for the FEHM Application—A Finite-Element Heat- and Mass-Transfer Code*. LA-13305-MS. Los Alamos, New Mexico: Los Alamos National Laboratory. TIC: 235234.

De Laeter, J.R.; Rosman, J.K.R.; and Smith, C.L. 1980. "The Oklo Natural Reactor: Cumulative Fission Yields and Retentivity of the Symmetric Mass Region Fission Products." *Earth and Planetary Science Letters, 50*, 238–246. Amsterdam, The Netherlands: Elsevier Scientific Publishing Company. TIC: 237501.

de Marsily, G. 1986. *Quantitative Hydrogeology: Groundwater Hydrology for Engineers.* San Diego, California: Academic Press. TIC: 208450.

Decarreau, A. 1985. "Partitioning of Divalent Transition Elements between Octahedral Sheets of Trioctahedral Smectites and Water." *Geochimica et Cosmochimica Acta, 49*, 1537–1544. New York, New York: Pergamon Press. TIC: 237522.

Degueldre, C.; Grauer, R.; Laube, A.; Oess, A.; and Silby, H. 1996. "Colloid Properties in Granitic Groundwater Systems: II. Stability and Transport Study." *Applied Geochemistry, 11*, 697–710. Oxford, England: Elsevier Science. TIC: 236569.

Degueldre, C.; Pfeiffer, H.-R.; Alexander, W.; Wernli, B.; and Bruetsch, R. 1996. "Colloid Properties in Granitic Groundwater Systems: I. Sampling and Characterization." *Applied Geochemistry, 11*, 677–694. Oxford, England: Elsevier Science. TIC: 236886.

DOE (U.S. Department of Energy). 2000. *Quality Assurance and Requirements Description*. DOE/RW-0333P, Rev. 10. Washington, DC.: DOE OCRWM. ACC: MOL.20000427.0422.

Doi, K.; Hirono, S.; and Sakamaki, Y. 1975. "Uranium Mineralization by Groundwater in Sedimentary Rocks, Japan." *Economic Geology, 70*, 628–646. El Paso, Texas: Economic Geology Publishing Company. TIC: 236987.

Drever, J.I. 1988. *The Geochemistry of Natural Waters*. 2nd Edition. Englewood Cliffs, New Jersey: Prentice Hall. TIC: 242836.

Duddy, I.R. 1980. "Redistribution and Fractionation of Rare-Earth and Other Elements in a Weathering Profile." *Chemical Geology*, (30), 363–381. Amsterdam, The Netherlands: Elsevier Scientific Publishing. TIC: 237498.

Dyer, J.R. 1999. "Revised Interim Guidance Pending Issuance of New U.S. Nuclear Regulatory Commission (NRC) Regulations (Revision 01, July 22, 1999), for Yucca Mountain, Nevada." Letter from J.R. Dyer (DOE/YMSCO) to D.R. Wilkins (CRWMS M&O), September 3, 1999, OL&RC:SB-1714, with enclosure, "Interim Guidance Pending Issuance of New U.S. Nuclear Regulatory Commission (NRC) Regulations for Yucca Mountain (Revision 01)." ACC: MOL.19990910.0079.

Eisenbud, M.; Krauskopf, K.; Franca, E.P.; Lei, W.; Ballad, R.; and Linsalata, P. 1984. "Natural Analogues for the Transuranic Actinide Elements: An Investigation in Minas Gerais, Brazil." *Environmental Geology and Water Science, 6*, (1), 1–9. New York, New York: Springer-Verlag. TIC: 219069.

Flexser, S. and Wollenberg, H.A. 1992. "Radioelements and their Occurrence with Secondary Minerals in Heated and Unheated Tuff at the Nevada Test Site." *High Level Radioactive Waste Management, Proceedings of the Third International Conference, Las Vegas, Nevada, April 12–16, 1992*, 1593–1598. LaGrange Park, Illinois: American Nuclear Society. TIC: 239302.

Flint, A.L.; Hevesi, J.A.; and Flint, L.E. 1996. *Conceptual and Numerical Model of Infiltration for the Yucca Mountain Area, Nevada.* Milestone 3GUI623M. Denver, Colorado: U.S. Geological Survey. ACC: MOL.19970409.0087.

Flint, L.E. 1998. *Characterization of Hydrogeologic Units Using Matrix Properties, Yucca Mountain, Nevada*. Water-Resources Investigations Report 97-4243. Denver, Colorado: U.S. Geological Survey. ACC: MOL.19980429.0512.

Frysinger, G.R. and Thomas, H.C. 1960. "Adsorption Studies on Clay Minerals: VII. Yttrium-Cesium and Cerium(III)-Cesium on Montmorillonite." *Journal of Physical Chemistry*, (64), 224–228. Easton, Pennsylvania: American Chemical Society. TIC: 237120.

Gardner, W.R. 1958. "Some Steady-State Solutions of Unsaturated Moisture Flow Equations with Application to Evaporation from a Water Table." *Soil Science, 85*, 228–232. Baltimore, Maryland: Williams and Wilkins. TIC: 240150.

Geldon, A.L. 1993. *Preliminary Hydrogeologic Assessment of Boreholes UE-25 c#1, UE-25 c#2, and UE-25 c#3, Yucca Mountain, Nye County, Nevada*. Water Resources Investigations Report 92-4016. Denver, Colorado: U.S. Geological Survey. ACC: MOL.19960808.0136.

Geldon, A.L.; Umari, A.M.A.; Fahy, M.F.; Earle, J.D.; Gemmell, J.M.; and Darnell, J. 1997. *Results of Hydraulic and Conservative Tracer Tests in Miocene Tuffaceous Rocks at the C-Hole Complex, 1995 to 1997, Yucca Mountain, Nye County, NV*. Milestone SP23PM3. Denver, Colorado: U. S. Geological Survey. ACC: MOL.19980122.0412.

Gelhar, L.W. and Axness, C.L. 1983. "Three-Dimensional Stochastic Analysis of Macrodispersion in Aquifers." *Water Resources Research, 19*, (1), 161–180. Washington, D.C.: American Geophysical Union. TIC: 222815.

George-Aniel, B.; Leroy, J.L.; and Poty, B. 1991. "Volcanogenic Uranium Mineralizations in the Sierra Peña Blanca District, Chihuahua, Mexico: Three Genetic Models." *Economic Geology, 86*, (2), 233–248. El Paso, Texas: Economic Geology Publishing Company. TIC: 237050.

Giblin, A.M. and Snelling, A.A. 1983. "Application of Hydrogeochemistry to Uranium Exploration in the Pine Creek Geosyncline, Northern Territory, Australia." *Journal of*

Geochemical Exploration, 19, 33–55. Amsterdam, The Netherlands: Elsevier Science Publishers B.V. TIC: 237423.

Goldschmidt, V.M. 1954. *Geochemistry*. London, United Kingdom: Oxford University Press. TIC: 243052.

Goodwin, B.W.; Cramer, J.J.; and McConnell, D.B. 1989. "The Cigar Lake Uranium Deposit: An Analogue for Nuclear Fuel Waste Disposal." Appendix B of *Natural Analogues in Performance Assessments for the Disposal of Long Lived Radioactive Wastes*. Technical Reports Series 304. Vienna, Austria: International Atomic Energy Agency. TIC: 7851.

Graham, W. and McLaughlin, D. 1989. "Stochastic Analysis of Nonstationary Subsurface Solute Transport: 2. Conditional Moments." *Water Resources Research, 25,* (11), 2331–2355. Washington, D.C.: American Geophysical Union. TIC: 239451.

Grimaldi, F.S. and Berger, I.A. 1961. "Niobium Content of Soils from West Africa." *Geochimica et Cosmochimica Acta, 25,* 71–80. Washington, D.C.: American Geophysical Union. TIC: 237436.

Harter, T. and Yeh, T.-C.J. 1996. "Stochastic Analysis of Solute Transport in Heterogeneous, Variably Saturated Soils." *Water Resources Research, 32,* (6), 1585–1595. Washington, D.C.: American Geophysical Union. TIC: 247170.

Hayes, K.F.; Roe, A.L.; Brown, G.E., Jr.; Hodgson, K.O.; Leckie, J.O.; and Parks, G.A. 1987. "In-Situ X-Ray Absorption Study of Surface Complexes: Selenium Oxyanions on α-FeOOH." *Science, 238,* 783–786. Washington, D.C.: American Association for the Advancement of Science. TIC: 237033.

Hiester, N.K. and Vermeulen, T. 1952. "Saturation Performance of Ion-Exchange and Adsorption Columns." *Chemical Engineering Progress, 48,* (10), 505–516. New York, New York: American Institute of Chemical Engineers. TIC: 224052.

Hingston, F.J.; Posner, A.M.; and Quirk, J.P. 1971. "Competitive Adsorption of Negatively Charged Ligands on Oxide Surfaces." *Surface Chemistry of Oxides, Discussions of the Faraday Society, 52,* 334–351. London, England: Royal Society of Chemistry. TIC: 237679.

Ho, C.H. and Miller, N.H. 1986. "Adsorption of Uranyl Species from Bicarbonate Solution onto Hematite Particles." *Journal of Colloid and Interface Science, 110,* (1) 165–171. New York, New York: Academic Press. TIC: 226326.

Hobart, D.E. 1990. "Actinides in the Environment." Chapter XIII of *Fifty Years with Transuranium Elements, Proceedings of the Robert A. Welch Foundation Conference on Chemical Research, XXXIV, Houston, Texas, October 22-23, 1990.* Houston, Texas: Robert A. Welch Foundation. TIC: 237030.

Howard, J. H., III. 1977. "Geochemistry of Selenium: Formation of Ferroselenite and Selenium Behavior in the Vicinity of Oxidizing Sulfide and Uranium Deposits." *Geochimica et Cosmochimica Acta, 41*, 1665–1678. New York, New York: Pergamon Press. TIC: 239142.

Hsi, C-K.D. and Langmuir, D. 1985. "Adsorption of Uranyl onto Ferric Oxyhydroxides: Application of the Surface Complexation Site-Binding Model." *Geochimica et Cosmochimica Acta, 49*, 1931–1941. New York, New York: Pergamon Press. TIC: 224090.

Hunter, K.A.; Hawke, D.J.; and Choo, L.K. 1988. "Equilibrium Adsorption of Thorium by Metal Oxides in Marine Electrolytes." *Geochimica et Cosmochimica Acta, 52*, 627–636. New York, New York: Pergamon Press. TIC: 237440.

Jonasson, R.G.; Bancroft, G.M.; and Nesbitt, H.W. 1985. "Solubilities of Some Hydrous REE Phosphates with Implications for Diagenesis and Seawater Concentrations." *Geochimica et Cosmochimica Acta, 49*, 2133–2139. New York, New York: Pergamon Press. TIC: 236998.

Keeney-Kennicutt, W.L. and Morse, J.W. 1985. "The Redox Chemistry of $Pu(V)O_2^+$ Interaction with Common Mineral Surfaces in Dilute Solutions and Seawater." *Geochimica et Cosmochimica Acta, 49*, 2577–2588. New York, New York: Pergamon Press. TIC: 237000.

Kelkar, S. and Travis, B. 1999. *Independent Test Case for TRACRN, Version 1.0*. Los Alamos, New Mexico: Los Alamos National Laboratory. ACC: MOL.19991221.0361.

Kerrisk, J.F. 1984. *Americium Thermodynamic Data for the EQ3/6 Database*. LA-10040-MS. Los Alamos, New Mexico: Los Alamos National Laboratory. TIC: 202354.

Knight, S.D. and Lawrence, F.O. 1988. *Sorption of Nickel and Neptunium in Tuff Using Groundwaters of Various Compositions*. Milestone R505. Los Alamos, New Mexico: Los Alamos National Laboratory. ACC: NN1.19881028.0004.

Knight, S.D. and Thomas, K.W. 1987. *Sorption of Radionuclides Using Different Groundwater Compositions*. Milestone M316. Los Alamos, New Mexico: Los Alamos National Laboratory. ACC: MOL.19980625.0236; NNA.19870902.0098.

Koeppenkastrop, D. and De Carlo, E.H. 1992. "Sorption of Rare-Earth Elements from Seawater onto Synthetic Mineral Particles: An Experimental Approach." *Chemical Geology, 95*, 251–263. Amsterdam, The Netherlands: Elsevier Science Publisher B.V. TIC: 237044.

Koeppenkastrop, D. and De Carlo, E.H. 1993. "Uptake of Rare-Earth Elements from Solution by Metal Oxides." *Environmental Science and Technology, 27*, (9), 1796–1802. Easton, Pennsylvania: American Chemical Society. TIC: 237057.

Krier, D.; Longmire, P.; Gilkeson, R.; and Turin, H.J. 1997. *Geologic, Geohydrologic, and Geochemical Data Summary of Material Disposal Area G, Technical Area 54, Los Alamos National Laboratory*. LAUR-95-2696. Los Alamos, New Mexico: Los Alamos National Laboratory. TIC: 247472.

Krishnaswami, S.; Graustein, W.C.; Turekian, K.K., and Dowd, J.F. 1982. "Radium, Thorium, and Radioactive Lead Isotopes in Groundwaters: Application to the In Situ Determination of Adsorption-Desorption Rate Constants and Retardation Factors." *Water Resources Research, 18*, (6), 1633–1675. Washington, D.C.: American Geophysical Union. TIC: 224108.

La Flamme, B.D. and Murray, J.W. 1987. "Solid/Solution Interaction: The Effect of Carbonate Alkalinity on Adsorbed Thorium." *Geochimica et Cosmochimica Acta, 51*, 243–250. New York, New York: Pergamon Press. TIC: 237034.

LaBrecque, D.J.; Miletto, M.; Daily, W.; Ramirez, A.; and Owen, E. 1996. "The Effects of Noise on Occam's Inversion of Resistivity Tomography Data." *Geophysics, 61*, (2), 538–548. Tulsa, Oklahoma: Society of Exploration Geophysicists. TIC: 247174.

Langmuir, D. and Herman, J.S. 1980. "The Mobility of Thorium in Natural Waters at Low Temperatures." *Geochimica et Cosmochimica Acta, 44*, 1753–1766. New York, New York: Pergamon Press. TIC: 237029.

Langmuir, D. and Riese, A.C. 1985. "The Thermodynamic Properties of Radium." *Geochimica et Cosmochimica Acta, 49*, 1593–1601. New York, New York: Pergamon Press. TIC: 241035.

Lieser, K.H. and Hill, R. 1992. "Chemistry of Thorium in the Hydrosphere and in the Geosphere." *Radiochimica Acta, 56*, 141–151. Munchen, Germany: R. Oldenbourg Verlag. TIC: 237124.

Loeven, C. 1993. *A Summary and Discussion of Hydrologic Data from the Calico Hills Nonwelded Hydrologic Unit at Yucca Mountain, Nevada*. LA-12376-MS. Los Alamos, New Mexico: Los Alamos National Laboratory. ACC: NNA.19921116.0001.

Loubet, M. and Allegre, C.J. 1977. "Behavior of the Rare-Earth Elements in the Oklo Natural Reactor." *Geochimica et Cosmochimica Acta, 41*, 1539–1548. New York, New York: Pergamon Press. TIC: 237069.

Machesky, M.L. 1990. "Influence of Temperature on Ion Adsorption by Hydrous Metal Oxides." *Chemical Modeling of Aqueous Systems II, Los Angeles, California, September 25–30, 1988.* Melchior, D.C., and Bassett, R.L., eds., *ACS Symposium Series 416*, 282–292. Washington, D.C.: American Chemical Society. TIC: 241139.

Mackie, R.L. and Madden, T.R. 1993. "Three-Dimensional Magnetotelluric Inversion Using Conjugate Gradients." *Geophysical Journal International, 115*, (1) 215–229. Oxford, England: Blackwell Scientific. TIC: 247175.

Mantoglou, A. and Gelhar, L.W. 1987. "Stochastic Modeling of Large-Scale Transient Unsaturated Flow Systems." *Water Resources Research, 23*, (1), 37–46. Washington, D.C.: American Geophysical Union. TIC: 223510.

Mariano, A.N. 1989. "Economic Geology of Rare-Earth Elements." *Geochemistry and Mineralogy of Rare Earth Elements*, Lipin, B.R. and McKay, G.A., eds. *Reviews in Mineralogy, 21*, 309–337. Washington, D.C.: Mineralogical Society of America. On Order Library Tracking Number-1684.

Maya, L. 1982. "Sorbed Uranium(VI) Species on Hydrous Titania, Zirconia, and Silica Gel." *Radiochimica Acta, 31*, 147–151. München, Germany: R. Oldenbourg Verlag. TIC: 236887.

Means, J.L.; Crerar, D.A.; and Borcsik, M.P. 1978. "Adsorption of Co and Selected Actinides by Mn and Fe Oxides in Soils and Sediments." *Geochimica et Cosmochimica Acta, 42*, 1763–1773. New York, New York: Pergamon Press. TIC: 218336.

Meijer, A. 1990. *Yucca Mountain Project Far-Field Sorption Studies and Data Needs*. LA-11671-MS. Los Alamos, New Mexico: Los Alamos National Laboratory. ACC: NNA.19920131.0363.

Meijer, A. 1992. "A Strategy for the Derivation and Use of Sorption Coefficients in Performance Assessment Calculations for the Yucca Mountain Site." *Proceedings of the DOE/Yucca Mountain Site Characterization Project Radionuclide Adsorption Workshop at Los Alamos National Laboratory, September 11–12, 1990*. Canepa, J.A., ed. LA-12325-C. Los Alamos, New Mexico: Los Alamos National Laboratory. ACC: NNA.19920421.0117.

Meijer, A. 1993. "Far-Field Transport of Carbon Dioxide: Retardation Mechanisms and Possible Validation Experiments." *Proceedings of the Topical Meeting on Site Characterization and Model Validation, Focus '93, September 26–29, 1993, Las Vegas, Nevada*, 110–114. La Grange Park, Illinois: American Nuclear Society. TIC: 102245.

Meijer, A.; Triay, I.; Knight, S.; and Cisneros, M. 1989. "Sorption of Radionuclides on Yucca Mountain Tuffs." *Proceedings, Nuclear Waste in the Unsaturated Zone, Focus '89, September 17–21, 1989, Las Vegas, Nevada*, 113–117. La Grange Park, Illinois: American Nuclear Society. TIC: 222552.

Montazer, P. and Wilson, W.E. 1984. *Conceptual Hydrologic Model of Flow in the Unsaturated Zone, Yucca Mountain, Nevada*. Water-Resource Investigations Report 84-4345. Lakewood, Colorado: U.S. Geological Survey. ACC: NNA.19890327.0051.

Moore, R.M. and Hunter, K.A. 1985. "Thorium Adsorption in the Ocean: Reversibility and Distribution Amongst Particle Size." *Geochimica et Cosmochimica Acta, 49*, 2253–2257. New York, New York: Pergamon Press. TIC: 237520.

Murphy, J.B. and Hynes, A.J. 1986. "Contrasting Secondary Mobility of Ti, P, Zr, Nb, and Y in Two Metabasaltic Suites in the Appalachians." *Canadian Journal of Earth Sciences, 23*, (8), 1138–1144. Ottawa, Canada: National Research Council. TIC: 237341.

Murphy, W.M. 1992. "Natural Analog Studies for Geologic Disposal of Nuclear Waste." *Technology Today*, 16–21. San Antonio, Texas: Southwest Research Institute. TIC: 238853.

Neal, R.H.; Sposito, G.; Holtzclaw, K.M.; and Traina, S.J. 1987. "Selenite Adsorption on Alluvial Soils: I. Soil Composition and pH Effects." *Soil Science Society of America Journal, 51*, 1161–1165. Madison, Wisconsin: Soil Science Society of America. TIC: 237059.

Neretnieks, I. 1990. *Solute Transport in Fractured Rock—Applications to Radionuclide Waste Repositories*. SKB Technical Report 90-38. Stockholm, Sweden: Swedish Nuclear Fuel and Waste Management Company. TIC: 208618.

Neuman, S. P. 1990. "Universal Scaling of Hydraulic Conductivities and Dispersivities in Geologic Media." *Water Resources Research, 26,* (8), 1749–1758. Washington, D.C.: American Geophysical Union. TIC: 237977.

Neuman, S.P.; Winter, C.L.; and Newman, C.M. 1987. "Stochastic Theory of Field-Scale Fickian Dispersion in Anisotropic Porous Media." *Water Resources Research, 23,* (3), 453–466. Washington, D.C.: American Geophysical Union. TIC: 225294.

Newman, J. 1973. *Electrochemical Systems*. Englewood Cliffs, New Jersey: Prentice-Hall. TIC: 210201.

Nimmo, J.R. and Akstin, K.C. 1988. "Hydraulic Conductivity of a Sandy Soil at Low Water Content after Compaction by Various Methods." *Soil Science Society of America Journal, 52,* (2), 303–310. Madison, Wisconsin: Soil Science Society of America. TIC: 224083.

Nimmo, J.R. and Mello, K.A. 1991. "Centrifugal Techniques for Measuring Saturated Hydraulic Conductivity." *Water Resources Research, 27,* (6), 1263–1269. Washington, D.C.: American Geophysical Union. TIC: 224084.

Nimmo, J.R.; Rubin, J.; and Hammermeister, D. P. 1987. "Unsaturated Flow in a Centrifugal Field: Measurement of Hydraulic Conductivity and Testing of Darcy's Law." *Water Resources Research, 23,* (1), 124–134. Washington, D.C.: American Geophysical Union. TIC: 216671.

Nitsche, H.; Gatti, R.C.; Standifer, E.M.; Lee, S.C.; Müller, A.; Prussin, T.; Deinhammer, R.S.; Maurer, H.; Becraft, K.; Leung, S.; and Carpenter, S.A. 1993. *Measured Solubilities and Speciations of Neptunium, Plutonium, and Americium in a Typical Groundwater (J-13) from the Yucca Mountain Region*. LA-12562-MS. Los Alamos, New Mexico: Los Alamos National Laboratory. ACC: MOL.19950621.0265.

Nitsche, H.; Roberts, K.; Prussin, T.; Muller, A.; Becraft, K.; Keeny, D.; Carpenter, S.A.; and Gatti, R.C. 1995. *Measured Solubilities and Speciations from Oversaturation Experiments of Neptunium, Plutonium, and Americium in UE-25 p#1 Well Water from the Yucca Mountain Region*. LA-12563-MS. Los Alamos, New Mexico: Los Alamos National Laboratory. ACC: MOL.19951006.0171.

Noell, A.L.; Thompson, J.L.; Corapcioglu, M.Y.; and Triay, I.R. 1998. "The Role of Silica Colloids on Facilitated Cesium Transport Through Glass Bead Columns and Modeling."

Journal of Contaminant Hydrology, 31 (1-2), 23–56. Amsterdam, the Netherlands: Elsevier Science B.V. TIC: 245510.

O'Melia, C. and Tiller, C. 1993. "Physicochemical Aggregation and Deposition in Aquatic Environment." Chapter 8 of *Environmental Particles*. Buffle, J. and van Leeuwen, H.P., eds. Volume 2. New York, New York: Lewis Publishers. TIC: 238504.

Obeng, L.A.; Carrondo, M.J.T.; Perry, R.; and Lester, J.N. 1981. "The Influence of Zeolite Type A on Metal Concentrations in Water and Waste Water." *Journal of the American Oil Chemists' Society, 58*, (1), 81–85. Champaign, Illinois: American Oil Chemists' Society. TIC: 237902.

Ogard, A.E. and Kerrisk, J.F. 1984. *Groundwater Chemistry Along Flow Paths Between a Proposed Repository Site and the Accessible Environment*. LA-10188-MS. Los Alamos, New Mexico: Los Alamos National Laboratory. ACC: HQS.19880517.2031.

Ogard, A.E. and Vaniman, D.T., editors. 1985. *Research and Development Related to the Nevada Nuclear Waste Storage Investigations: July 1–September 30, 1984*. LA-10299-PR. Los Alamos, New Mexico: Los Alamos National Laboratory. ACC: NNA.19920922.0014.

Ortiz, T.S.; Williams, R.L.; Nimick, F.B.; Whittet, B.C.; and South, D.L. 1985. *A Three-Dimensional Model of Reference Thermal/Mechanical and Hydrological Stratigraphy at Yucca Mountain, Southern Nevada*. SAND84-1076. Albuquerque, New Mexico: Sandia National Laboratories. ACC: MOL.19980602.0331.

Payne, T.E.; Davis, J.A.; and Waite, T.D. 1990. "Modeling of Uranium Sorption to Substrates from the Weathered Zone in the Vicinity of the Koongarra Ore Body." *Alligators Rivers Analogue Project, First Annual Report 1988–89*. Duerden, P., ed. Menai, New South Wales, Australia: Australian Nuclear Science and Technology Organization. TIC: 244780.

Penrose, W.R.; Polzer, W.L.; Essington, E.H.; Nelson, D.M.; and Orlandini, K.A. 1990. "Mobility of Plutonium and Americium Through a Shallow Aquifer in a Semiarid Region." *Environmental Science and Technology, 24*, 228–234. Washington, D.C.: American Chemical Society. TIC: 224113.

Philip, J.R.; Knight, J.H.; and Waechter, R.T. 1989. "Unsaturated Seepage and Subterranean Holes: Conspectus, and Exclusion Problem for Circular Cylindrical Cavities." *Water Resources Research, 25*, (1), 16–28. Washington, D.C.: American Geophysical Union. TIC: 239117.

Polzer, W.L. and Fuentes, H R. 1988. "The Use of a Heterogeneity-Based Isotherm to Interpret the Transport of Reactive Radionuclides in Volcanic Tuff Media." *Radiochimica Acta, 44/45*, 361–365. München, Germany: R. Oldenbourg Verlag. TIC: 240183.

Prout, W.E. 1959. "Adsorption of Radioactive Waste by Savannah River Plant Soil." *Soil Science, 86*, 13–17. Baltimore, Maryland: Williams and Wilkins. TIC: 237056.

Rai, D. and Zachara, J.M. 1984. *A Critical Review*. Volume 1 of *Chemical Attenuation Rates, Coefficients, and Constants in Leachate Migration*. EPRI EA-3356. Palo Alto, California: Electric Power Research Institute. TIC: 237846.

Rancon, D. 1973. "Comportement Dans Les Milieux Souterrians De L'Uranium et Du Thorium Rejetes Par L'Industrie Nucleaire." *Environmental Behavior of Radionuclides Released in the Nuclear Industry, Proceedings of a Symposium Organized by the International Atomic Energy Agency, the OECD Nuclear Energy Agency, and the World Health Organization, Held in Aix-en-Provence, 14–18 May 1973*. IAEA-SM-172/55, 333–346. Vienna, Austria: International Atomic Energy Agency. TIC: 237674.

Reimus, P.W. and Dash, Z.V. 1999. *Models and Methods for the Reactive Transport Application, STN: 10032-MMS-1.1-00*. Los Alamos, New Mexico: Los Alamos National Laboratory. ACC: MOL.19990810.0051.

Reimus, P.W.; Adams, A.; Haga, M.J.; Humphrey, A.; Callahan, T.; Anghel, I.; and Counce, D. 1999. *Results and Interpretation of Hydraulic and Tracer Testing in the Prow Pass Tuff at the C-Holes*. Milestone SP32E7M4. Los Alamos, New Mexico: Los Alamos National Laboratory. TIC: 246377.

Rhodes, D.W. 1957. "Adsorption of Plutonium by Soil." *Soil Science, 84*, 465–469. Baltimore, Maryland: Williams and Wilkins. TIC: 237905.

Robinson, B.A.; Wolfsberg, A.V.; Zyvoloski, G.A.; and Gable, C.W. 1995. *An Unsaturated Zone Flow and Transport Model of Yucca Mountain*. Milestone 3468. Draft. Los Alamos, New Mexico: Los Alamos National Laboratory. ACC: MOL.19960415.0218

Rodi, W.L. 1976. "A Technique for Improving the Accuracy of Finite Element Solutions for Magnetotelluric Data." *Geophysics Journal of the Royal Astronomical Society, 44*, (2), 483–506. Oxford, England: Blackwell Science. TIC: 247178.

Rogers, P.S.Z. and Meijer, A. 1993. "Dependence of Radionuclide Sorption on Sample Grinding Surface Area and Water Composition." *High-Level Radioactive Waste Management, Proceedings of the Fourth Annual International Conference, Las Vegas, Nevada, April 26-30, 1993, 2*, 1509–1516. LaGrange Park, Illinois: American Nuclear Society. TIC: 208542.

Rose, A.W.; Hawkes, H.E.; and Webb, J.S. 1979. *Geochemistry in Mineral Exploration*, 2nd Edition. New York, New York: Academic Press. TIC: 247731.

Rosholt, J.N.; Prijana; and Noble, D.C. 1971. "Mobility of Uranium and Thorium in Glassy and Crystallized Silicic Volcanic Rocks." *Economic Geology, 66*, 1061–1069. El Paso, Texas: Economic Geology Publishing Company. TIC: 219186.

Rundberg, R.S. 1987. *Assessment Report on the Kinetics of Radionuclide Adsorption on Yucca Mountain Tuff*. LA-11026-MS. Los Alamos, New Mexico: Los Alamos National Laboratory. ACC: NNA.19930405.0075.

Rundberg, R.S.; Ogard, A.E.; and Vaniman, D.T. 1985. *Research and Development Related to the Nevada Nuclear Waste Storage Investigations, April 1–June 30, 1984*. LA-10297-PR. Los Alamos, New Mexico: Los Alamos National Laboratory. ACC: NNA.19920922.0018.

Rundberg, R.S.; Partom, I.; Ott, M.A.; Mitchell, A.J.; and Birdsell, K. 1987. *Diffusion of Nonsorbing Tracers in Yucca Mountain Tuff*. Milestone R524. Los Alamos, New Mexico: Los Alamos National Laboratory. ACC: NNA.19930405.0074.

Runde, W.; Meinrath, G.; and Kim, J.I. 1992. "A Study of Solid-Liquid Phase Equilibria of Trivalent Lanthanide and Actinide Ions in Carbonate Systems." *Radiochimica Acta, 58/59*, 93–100. München, Germany: R. Oldenbourg Verlag. TIC: 237409.

Russell, J.D.; Paterson, E.; Fraser, A.R.; and Farmer, V.C. 1975. "Adsorption of Carbon Dioxide on Goethite (α-FeOOH) Surfaces, and its Implications for Anion Adsorption." *Journal of the Chemical Society of London, Faraday Transactions I, 71*, 1623–1630. London, England: Royal Society of Chemistry. TIC: 224557.

Russo, D. 1988. "Determining Soil Hydraulic Properties by Parameter Estimation: On the Selection of a Model for the Hydraulic Properties." *Water Resources Research, 24*, (3), 453–459. Washington, D.C.: American Geophysical Union. TIC: 247182.

Russo, D. 1995. "Stochastic Analysis of the Velocity Covariance and the Displacement Covariance Tensors in Partially Saturated Heterogeneous Anisotropic Porous Formations." *Water Resources Research, 31*, (7), 1647–1658. Washington, D.C.: American Geophysical Union. TIC: 247180.

Sanchez, A.L.; Murray, J.W.; and Sibley, T.H. 1985. "The Adsorption of Plutonium IV and V on Goethite." *Geochimica et Cosmochimica Acta, 49*, (11), 2297–2307. New York, New York: Pergamon Press. TIC: 224091.

Schenker, A.R.; Guerin, D.C.; Robey, T.H.; Rautman, C.A.; and Barnard, R.W. 1995. *Stochastic Hydrogeologic Units and Hydrogeologic Properties Development for Total-System Performance Assessments*. SAND94-0244. Albuquerque, New Mexico: Sandia National Laboratories. ACC: MOL.19960318.0528.

SEA (Science and Engineering Associates). 1992. *The Use of Absorbent Materials to Collect In Situ Vadose Zone Liquids*. Topical Report No. SEATR-92-01. Santa Fe, New Mexico: Science and Engineering Associates, Inc. TIC: 247944.

Serne, R.J. and Relyea, J.F. 1982. *The Status of Radionuclide Sorption-Desorption Studies Performed by the WRIT Program*. PNL-3997. Richland, Washington: Pacific Northwest Laboratory. ACC: NNA.19900416.0121.

Siegel, M.D.; Hopkins, P.L.; Glass, R.J.; and Ward, D.B. 1992. "Design of an Intermediate-Scale Experiment to Validate Unsaturated-Zone Transport Models." *High Level Radioactive Waste Management: Proceedings of the Third International Conference, Las Vegas, Nevada,*

April 12–16, 1992, 2, 1972–1984. La Grange Park, Illinois: American Nuclear Society. TIC: 4447

Siegel, M.D.; Ward, D.B.; Cheng, W.C.; Bryant, C.; Chocas, C.S.; and Reynolds, C.G. 1993. "Preliminary Characterization of Materials for a Reactive Transport Model Validation Experiment." *High Level Radioactive Waste Management, Proceeding of the Fourth Annual International Conference, Las Vegas, Nevada, April 26–30, 1993, 1,* 348–358. La Grange Park, Illinois: American Nuclear Society. TIC: 208542.

Sillen, L.G. and Martell, A.E. 1964. *Stability Constants of Metal-ion Complexes.* Second edition. Special Publication No. 17. London, England: The Chemical Society. TIC: 247801.

Snelling, A.A. 1980. "Uraninite and its Alteration Products: Koongarra Uranium Deposit." *Proceedings of International Uranium Symposium on the Pine Creek Geosyncline, 1980.* Ferguson, J., and Goleby, A. B., eds. 487–498. Vienna, Austria: International Atomic Energy Agency. TIC: 236806.

Snelling, A.A. and Dickson, B.L. 1979. "Uranium-Daughter Disequilibrium in the Koongarra Uranium Deposit, Australia." *Mineralium Deposita, 14,* 109–118. New York, New York: Springer-Verlag. TIC: 237067.

Snodgrass, W.J. 1980. "Distribution and Behavior of Nickel in the Aquatic Environment." Chapter 9 of *Nickel in the Environment*. 203–274. New York, New York: John Wiley and Sons. TIC: 237686.

Soll, W.E. 1997. *Busted Butte Modeling, UZ Transport Modeling Notebook #1* (LA-EES-5-NBK-98-018). SN-LANL-SCI-048-V1. ACC: MOL.19991221.0369.

Spitsyn, V.I.; Balukova, V.D.; Naumova, A.F.; Gromov, V.V.; Spiridonov, F.M.; Vetrov, E.M.; and Grafov, G.I. 1958. "A Study of the Migration of Radioelements in Soils." *Proceedings of the International Conference on the Peaceful Uses of Atomic Energy, Geneva, September 1–13, 1958: Waste Treatment and Environmental Aspects of Atomic Energy, 18,* 439–448. Geneva, Switzerland: United Nations. TIC: 247777.

Stammose, D. and Dolo, J-M. 1990. "Sorption of Americium at Trace Levels on a Clay Mineral." *Radiochimica Acta, 51,* 189–193. München, Germany: R. Oldenbourg Verlag. TIC: 237004.

Stephens, D.B. and Rehfeldt, K.R. 1985. "Evaluation of Closed-Form Analytical Models to Calculate Conductivity in a Fine Sand." *Soil Science Society of America Journal, 49,* 12–19. Madison, Wisconsin: Soil Science Society of America. TIC: 224082.

SubTerra. 1998. *Final Report, TRW Environmental Safety Systems, Inc., Busted Butte Test Facility.* Project: 97-35. Preston, Washington: Sub Terra. TIC: 247628.

Taylor, S.R. and McLennan, S.M. 1988. "The Significance of the Rare Earths in Geochemistry and Cosmochemistry." Chapter 79 of *Handbook on the Physics and Chemistry of Rare Earths, Volume 11—Two-Hundred-Year Impact of Rare Earths on Science*. Gschneidner, K.A., Jr., and Eyring, L., eds. 485–580. New York, New York: North Holland Physics. TIC: 247238

Theis, T.L. and Richter, R.O. 1980. "Adsorption Reactions of Nickel Species at Oxide Surfaces." Chapter 4 of *Advances in Chemistry Series*. Washington, D.C.: American Chemical Society. TIC: 236944.

Thomas, K.W. 1987. *Summary of Sorption Measurements Performed with Yucca Mountain, Nevada, Tuff Samples and Water from Well J-13*. LA-10960-MS. Los Alamos, New Mexico: Los Alamos National Laboratory. ACC: NNA.19900604.0045.

Thomas, K.W. 1988. *Research and Development Related to the Nevada Nuclear Waste Storage Investigations, October 1–December 31, 1984*. LA-11443-PR. Los Alamos, New Mexico: Los Alamos National Laboratory. ACC: NNA.19920131.0372.

Torstenfelt, B.; Rundberg, R.S.; and Mitchell, A.J. 1988. "Actinide Sorption on Granites and Minerals as a Function of pH and Colloids/Pseudocolloids." *Radiochimica Acta, 44/45*, 111–117. München, Germany: R. Oldenbourg Verlag. TIC: 237496.

Travis, B.J. and Birdsell, K. *TRACRN 1.0: A Model of Flow and Transport in Porous Media for the Yucca Mountain Project, Model Description and User's Manual*. YMP Milestone Report T421. Los Alamos, New Mexico: Los Alamos National Laboratory. ACC: NNA.19891017.0060.

Triay, I.R.; Birdsell, K.H.; Mitchell, A.J.; and Ott, M.A. 1993. "Diffusion of Sorbing and Nonsorbing Radionuclides in Tuff." *High Level Radioactive Waste Management, Proceedings of the Fourth Annual International Conference, Las Vegas, Nevada, April 26–30, 1993, 2*, 1527–1532. La Grange Park, Illinois: American Nuclear Society. TIC: 208542.

Triay, I.R.; Cotter, C.R.; Huddleston, M.H.; Leonard, D.E.; Weaver, S.C.; Chipera, S.J.; Bish, D.L.; Meijer, A.; and Canepa, J.A. 1996. *Batch Sorption Results for Neptunium Transport through Yucca Mountain Tuffs*. LA-12961-MS. Los Alamos, New Mexico: Los Alamos National Laboratory. ACC: MOL.19980924.0050.

Triay, I.R.; Cotter, C.R.; Kraus, S.M.; Huddleston, M.H.; Chipera, S.J.; and Bish, D.L. 1996. *Radionuclide Sorption in Yucca Mountain Tuffs with J-13 Well Water: Neptunium, Uranium, and Plutonium*. LA-12956-MS. Los Alamos, New Mexico: Los Alamos National Laboratory. TIC: 226117.

Triay, I.R.; Furlano, A.C; Weaver, S.C.; Chipera, S.J.; and Bish, D.L. 1996. *Comparison of Neptunium Sorption Results Using Batch and Column Techniques*. LA-12958-MS. Los Alamos, New Mexico: Los Alamos National Laboratory. ACC: MOL.19980924.0049.

Triay, I.R.; Meijer, A.; Cisneros, M.R.; Miller, G.G.; Mitchell, A.J.; Ott, M.A.; Hobart, D.E.; Palmer, P.D.; Perrin, R.E.; and Aguilar, R.D. 1991. "Sorption of Americium in Tuff and Pure Minerals Using Synthetic and Natural Groundwaters." *Radiochimica Acta, 52/53*, 141–145. München, Germany: R. Oldenbourg Verlag. TIC: 222704.

Triay, I.R.; Meijer, A.; Conca, J.L.; Kung, K.S.; Rundberg, R.S.; Strietelmeier, B.A.; Tait, C.D.; Clark, D.L.; Neu, M.P.; and Hobart, D.E. 1997. *Summary and Synthesis Report on Radionuclide Retardation for the Yucca Mountain Site Characterization Project.* LA-13262-MS. Los Alamos, New Mexico: Los Alamos National Laboratory. ACC: MOL.19971210.0177.

Triay, I.R.; Robinson, B.A.; Lopez, R.M.; Mitchell, A.J.; and Overly, C.M. 1993. "Neptunium Retardation with Tuffs and Groundwaters from Yucca Mountain." *High Level Radioactive Waste Management, Proceedings of the Fourth Annual International Conference, Las Vegas, Nevada, April 26-30, 1993, 2*, 1504–1508. LaGrange Park, Illinois: American Nuclear Society. TIC: 208542.

Tsunashima, A.; Brindley, G.W.; and Bastovanov, M. 1981. "Adsorption of Uranium from Solutions by Montmorillonite: Compositions and Properties of Uranyl Montmorillonites." *Clays and Clay Minerals, 29*, (1), 10–16. Boulder, Colorado: Clay Minerals Society. TIC: 236914.

van Genuchten, M.T. 1980. "A Closed-Form Equation for Predicting the Hydraulic Conductivity of Unsaturated Soils." *Soil Science Society of America Journal, 44*, (5), 892–898. Madison, Wisconsin: Soil Science Society of America. TIC: 217327.

Weaver, S.C.; Triay, I.R.; and Clevenger, M.C. 1996. *Saturated Diffusion Cell Experiment*. LANL-CST-DP-66, R3. Los Alamos, New Mexico: Los Alamos National Laboratory. ACC: MOL.19971021.0345.

Wemheuer, R.F. 1999. "First Issue of FY00 NEPO QAP-2-0 Activity Evaluations." Interoffice correspondence from R.F. Wemheuer (CRWMS M&O) to R.A. Morgan, October 1, 1999, LV.NEPO.RTPS.TAG.10/99-155, with enclosures. ACC: MOL.19991028.0162.

White, A.F.; Benson, S.M.; Yee, A.W.; Wollenberg, H.A., Jr.; and Flexser, S. 1991. "Groundwater Contamination at the Kesterson Reservoir, California: 2. Geochemical Parameters Influencing Selenium Mobility." *Water Resources Research, 27*, (6), 1085–1098. Washington, D.C.: American Geophysical Union. TIC: 237455.

Wilson, M.L.; Gauthier, J.G.; Barnard, R.W.; Barr, G.E.; Dockery, H.A.; Dunn, E.; Eaton, R.R.; Guerin, D.C.; Lu, N; Martinez, M.J.; Nilson, R.; Rautman, C.A.; Robey, T.H.; Ross, B.; Ryder, E.E.; Schenker, A.R.; Shannon, S.A.; Skinner, L.H.; Halsey, W.G.; Gansemer, J.D.; Lewis, L.C.; Lamont, A.D.; Triay, I.R.; Meijer, A.; and Morris, D.E. 1994. *Total-System Performance Assessment for Yucca Mountain—SNL Second Iteration (TSPA-1993).* SAND93-2675. Executive Summary and two volumes. Albuquerque, New Mexico: Sandia National Laboratories. ACC: NNA.19940112.0123.

Wolfsberg, K. 1978. *Sorption-Desorption Studies of Nevada Test Site Alluvium and Leaching Studies of Nuclear Test Debris*. LA-7216-MS. Los Alamos, New Mexico: Los Alamos Scientific Laboratory. TIC: 201575.

Wolfsberg, K.; Bayhurst, B.P.; Levy, S.S.; Lawrence, F.O.; Knight, S.D.; Mitchell, A.J.; Ogard, A.E.; and Wanek, P.L. 1983. *Research and Development Related to Sorption of Radionuclides on Soils*. LA-UR-83-800. Los Alamos, New Mexico: Los Alamos Scientific Laboratory. TIC: 228735.

Wood, S.A. 1990. "The Aqueous Geochemistry of the Rare-Earth Elements and Yttrium: 1. Review of Available Low-Temperature Data for Inorganic Complexes and the Inorganic REE Speciation of Natural Waters." *Chemical Geology, 82*, 159–186. Amsterdam, The Netherlands: Elsevier Science Publishers B.V. TIC: 237051.

Yeh, T.-C.; Gelhar, L.W.; and Gutjahr, A.L. 1985. "Stochastic Analysis of Unsaturated Flow in Heterogeneous Soils: 2. Statistically Anisotropic Media with Variable α." *Water Resources Research, 21*, (4), 457–464. Washington, D.C.: American Geophysical Union. TIC: 239649.

YMP-LBNL-TIP/GP 5.0, Rev 0, Mod 0. *Ground Penetrating Radar Data Acquisition*. Berkeley, California: Lawrence Berkeley National Laboratory. ACC: MOL.19990205.0129.

Zhang, D. 1998. *Stochastic Model Notebook #1* (LA-EES-5-NBK-98-017). SN-LANL-SCI-047-V1. ACC: MOL.19991214.0179.

Zhang, D. 1999. "Nonstationary Stochastic Analysis of Transient Unsaturated Flow in Randomly Heterogeneous Media." *Water Resources Research, 35* (4), 1127–1141. Washington, D.C.: American Geophysical Union. TIC: 247193.

Zhang, D. and Neuman, S.P. 1995. "Eulerian-Lagrangian Analysis of Transport Conditioned on Hydraulic Data: 1. Analytical-Numerical Approach." *Water Resources Research, 31* (1), 39–51. Washington, D.C.: American Geophysical Union. TIC: 247195.

Zhang, D. and Winter, C.L. 1998. "Nonstationary Stochastic Analysis of Steady State Flow through Variably Saturated, Heterogeneous Media." *Water Resources Research, 34* (5), 1091–1100. Washington, D.C.: American Geophysical Union. TIC: 247192.

Zhang, D.; Wallstrom, T.C.; and Winter, C.L. 1998. "Stochastic Analysis of Steady-State Unsaturated Flow in Heterogeneous Media: Comparison of the Brooks-Corey and Gardner-Russo Models." *Water Resources Research, 34* (6), 1437–1449. Washington, D.C.: American Geophysical Union. TIC: 247194.

Zielinski, R.A. 1980. "Uranium in Secondary Silica: A Possible Exploration Guide." *Economic Geology, 75*, 592–602. El Paso, Texas: Economic Geology Publishing Company. TIC: 237418.

Zielinski, R.A.; Bush, R.W.; Spengler, R.W.; and Szabo, B.J. 1986. "Rock-Water Interaction in Ash Flow Tuffs (Yucca Mountain, Nevada, U.S.A.) – The Record from Uranium Studies."

Uranium, 2, 361–386. Amsterdam, The Netherlands: Elsevier Science Publishers B.V. TIC: 222472.

Zyvoloski, G.A.; Robinson, B.A.; Dash, Z.V.; and Trease, L.L. 1995. *Models and Methods Summary for the FEHM Application.* LA-UR-94-3787, Revision 1. Los Alamos, New Mexico: Los Alamos National Laboratory. TIC: 222337.

8.2 CODES, STANDARDS, REGULATIONS, AND PROCEDURES

AP-2.13Q, Rev. 0, ICN 4. *Technical Product Development Planning.* Washington, D.C.: U.S. Department of Energy, Office of Civilian Radioactive Waste Management. ACC: MOL.20000620.0067.

AP-2.21Q, Rev. 0, ICN 0. *Quality Determinations and Planning for Scientific, Engineering, and Regulatory Compliance Activities*. Washington, D.C.: U.S. Department of Energy, Office of Civilian Radioactive Waste Management. ACC: MOL.20000802.0003.

AP-3.10Q, Rev. 2, ICN 3. *Analysis and Models*. Washington, D.C.: U.S. Department of Energy, Office of Civilian Radioactive Waste Management. ACC: MOL.20000918.0282.

AP-3.15Q, Rev. 2. *Managing Technical Product Inputs*. Washington, D.C.: U.S. Department of Energy, Office of Civilian Radioactive Waste Management. ACC: MOL.20001109.0051.

AP-SIII.2Q, Rev. 0, ICN 3. *Qualification of Unqualified Data and the Documentation of Rationale Accepted Data*. Washington, D.C.: U.S. Department of Energy, Office of Civilian Radioactive Waste Management. ACC: MOL.20001002.0152.

AP-SI.1Q, Rev. 2, ICN 4, ECN 1. *Software Management*. Washington, D.C.: U.S. Department of Energy, Office of Civilian Radioactive Waste Management. ACC: MOL.20001019.0023.

AP-SV.1Q, Rev. 0, ICN 2. *Control of Electronic Management of Data*. Washington, D.C.: U.S. Department of Energy, Office of Civilian Radioactive Waste Management. ACC: MOL.20000831.0065.

LANL-CST-DP-66, R3, Appendix 1. 1996. *Saturated Diffusion Cell Experiment*. Los Alamos, New Mexico: Los Alamos National Laboratory. ACC: MOL.19971021.0345.

LANL-YMP-QP-S5.01, Rev 0. 2000. *Electronic Data Management*. Los Alamos, New Mexico: Los Alamos National Laboratory. ACC: MOL.20000621.0094.

QAP-2-0, Rev. 5. *Conduct of Activities*. Las Vegas, Nevada: CRWMS M&O. ACC: MOL.19980826.0209.

QAP-2-3, Rev. 10. *Classification of Permanent Items*. Las Vegas, Nevada: CRWMS M&O. ACC: MOL.19990316.0006.

8.3 SOFTWARE

DeltaGraph, V4.0.1, Macintosh.

LBNL 1999. *Software Code: CART V1.0*. 10046-1.0-00. SUN, UNIX. URN-0384.

LLNL 2000. *Software Code: ZOMBIE V3.0*. 10298-3.0-00. URN-0385.

Los Alamos National Laboratory 1999. *Software Code: FEHM V2.00*. V2.00. SUN Ultra Sparc. 10031-2.00-00.

LANL (Los Alamos National Laboratory) 1999. *Software Code: RTA V1.1*. V1.1. SUN. 10032-1.1-00.

LANL (Los Alamos National Laboratory) 1999. *Software Code: TRACRN V1.0*. V1.0. SUN Ultra 2. 10106-1.0-00.

LANL 2000. *Software Code: LAGRIT V1.0*. 10212-1.0-00. URN-0351.

LANL 2000. *Software Code: STO-UNSAT V1.0*. 10292-1.0LV-00. URN-0387.

Microsoft Excel, V5, Macintosh.

Microsoft Excel 97 SR-1.

8.4 SOURCE DATA, LISTED BY DATA TRACKING NUMBER

GS000408312231.003. Relative Humidity Calculated Porosity Measurements on Samples from Borehole USW SD-9 Used for Saturated Hydraulic Conductivity. Submittal date: 04/10/2000.

GS930908312323.003. Hydrochemical Data from Field Tests and Lab Analyses of Water Samples Collected at Field Stations USW VH-1, JF3, UE-29 UZN#91, Virgin Spring, Nevares Spring, UE-25 J#12, UE-25 J#13, UE-22 Army#1, and USW UZ-14. Submittal date: 09/30/1993.

GS940508312231.006. Core Analysis of Bulk Density, Porosity, Particle Density, and In Situ Saturation for Borehole UE-25 UZ#16. Submittal date: 05/04/1994.

GS950408312231.004. Physical Properties and Water Potentials of Core from Borehole USW SD-9. Submittal date: 03/01/1995.

GS950608312231.008. Moisture Retention Data from Boreholes USW UZ-N27 and UE-25 UZ#16. Submittal date: 06/06/1995.

GS950808312322.001. Field, Chemical, and Isotopic Data Describing Water Samples Collected in Death Valley National Monument and at Various Boreholes and around Yucca Mountain, Nevada, between 1992 and 1995. Submittal date: 08/16/1995.

GS951108312231.009. Physical Properties, Water Content, and Water Potential for Borehole USW SD-7. Submittal date: 09/26/1995.

GS960808312231.001. Water Permeability and Relative Humidity Calculated Porosity for Boreholes UE-25 UZ#16 and USW UZ-N27. Submittal date: 08/28/1996.

GS960808312231.003. Moisture Retention Data for Samples from Boreholes USW SD-7, USW SD-9, USW SD-12, and UE-25 UZ#16. Submittal date: 08/30/1996.

GS960808312231.005. Water Permeability and Relative Humidity Calculated Porosity for Samples from Boreholes USW SD-7, USW SD-9, USW SD-12, and USW UZ-14. Submittal date: 08/30/1996.

GS970708312314.007. Results of Hydraulic Conservative Tracer Tests in Miocene Tuffaceous Rocks at the C-Hole Complex, 1995-1997, Yucca Mountain, Nevada. (Submitted Input Request Tracking Number 00067.R). Submittal date: 07/31/1997.

GS970708312315.001. Concentrations of 2,6 DFBA and Pyridone from Tracer Tests Conducted at the C-well complex, 1/8/97–7/11/97. Submittal date: 07/18/97.

GS981008312314.002. Pump Test Data Collected at the C-wells Complex, 1/8/97–3/31/97. (Submitted Input Request Tracking Number 00067.R) Submittal date: 10/28/1998.

GS981008312314.003. Pumping Test Data Collected at the C-wells Complex, 5/7/96–12/31/96. Submittal date: 10/28/1998.

GS990308312242.007. Laboratory and Centrifuge Measurements of Physical and Hydraulic Properties of Core Samples from Busted Butte Boreholes UZTT-BB-INJ-1, UZTT-BB-INJ-3, UZTT-BB-INJ-4, UZTT-BB-INJ-6, UZTT-BB-COL-5, AND UZTT-BB-COL-8. Submittal date: 03/22/1999.

GS990408312231.001. Saturated Hydraulic Conductivity of Core from SD-9, 2/27–3/27/95. Submittal date: 04/27/1999.

GS990408312315.002. Transducer, Barometric Pressure, and Discharge Data Collected from 4/18/98 through 11/24/98 in Support of the Ongoing Hydraulic and Tracer Tests Being Conducted at the UE-25 C-Well Complex, Nevada. Submittal date: 04/06/1999.

GS990708312242.008. Physical and Hydraulic Properties of Core Samples from Busted Butte Boreholes. Submittal date: 07/01/1999.

GS990808312322.001. Field and Isotopic Data from Ground Water Samples from Wells in the Amargosa Valley and NTS. Submittal date: 08/23/1999.

LA000000000034.001. Diffusion of Sorbing and Non-Sorbing Radionuclides. Submittal date: 01/22/1993.

LA000000000034.002. Diffusion of Sorbing and Non-Sorbing Radionuclides. Submittal date: 06/22/1993.

LA000000000106.001. Report on the Study of Kinetic Effects Using Crushed Tuff Columns: Neptunium in Sodium Bicarbonate Waters. Submittal date: 11/01/1994.

LA0001JC831361.001. Radionuclide Transport through Saturated Fractures. Submittal date: 01/14/2000.

LA0001JC831361.002. Radionuclide Transport through Saturated Fractures. Submittal date: 01/14/2000.

LA0002JC831341.001. Depth Intervals and Bulk Densities of Alluviums. Submittal date: 03/08/2000.

LA0002JC831341.002. Quantitative X-ray Diffraction (QXRD) Results of Three Alluviums. Submittal date: 03/08/2000.

LA0002JC831341.003. Selenium Batch Adsorption on Nonwelded Zeolitic Tuff. Submittal date: 03/08/2000.

LA0002JC831361.001. Column Studies Using G4-268 Devitrified Tuff with J-13 Well Water and Radionuclides (H-3 and Pu-239). Submittal date: 03/16/2000.

LA0002JC831361.002. Column Studies Using G4-268 Devitrified Tuff with Synthetic UE-25 p#1 Water and Radionuclides (H-3 and Pu-239). Submittal date: 03/16/2000.

LA0002JC831361.003. Column Studies Using G4-268 Devitrified Tuff with J-13 Well Water and Radionuclides (H-3 and Tc-95m). Submittal date: 03/16/2000.

LA0002JC831361.004. Column Studies Using GU3-1414 Vitric Tuff with J-13 Well Water and Radionuclides (H-3 and Tc-95m). Submittal date: 03/16/2000.

LA0002JC831361.005. Column Studies Using G4-1533 Zeolitic Tuff with J-13 Well Water and Radionuclides (H-3 and Tc-95m). Submittal date: 03/16/2000.

LA0002PR831231.001. Bullfrog Reactive Tracer Test Data. Submittal date: 02/04/2000.

LA0002SK831352.001. Total Colloidal Particles Concentration and Size Distribution in Groundwaters from the Nye County Early Warning Drilling Program. Submittal date: 02/24/2000.

LA0002SK831352.002. Total Colloidal Particles Concentration and Size Distribution in Groundwaters around Yucca Mountain. Submittal date: 02/25/2000.

LA0003JC831341.001. Adsorption of Np-237 in Three Types of Alluvium as a Function of Time and Stratigraphic Position. Submittal date: 03/09/2000.

LA0003JC831341.002. Adsorption of Tc-99 in Three Types of Alluvium as a Function of Time and Stratigraphic Position. Submittal date: 03/09/2000.

LA0003JC831341.003. Adsorption of I-129 in Three Types of Alluvium as a Function of Time and Stratigraphic Position. Submittal date: 03/09/2000.

LA0003NL831352.002. The K_d Values of ^{239}Pu on Colloids of Hematite, Ca-Montmorillonite, and Silica in Natural and Synthetic Groundwater. Submittal date: 03/29/2000.

LA0004AM831234.001. Flow-through Cell Measurements for NC-EWDP-01S, 22-Feb-99 and 23-Feb-99. Submittal date: 04/17/2000

LA0004AM831234.002. Downhole Probe Measurements for NC-EWDP-03S, 23-Feb-99. Submittal date: 04/17/2000.

LA0004AM831341.001. Uranium Sorption Coefficients for Minerals and Tuff under Oxidizing Conditions in J-13 Water. Submittal date: 05/01/2000.

LA0004AM831341.002. Np Sorption onto Clinoptilolite-rich Tuff in J-13 Water under Atmospheric Conditions with Ka, Kd, and SA. Submittal date: 05/03/2000.

LA0004JC831224.001. Preliminary Unsaturated Hydraulic Conductivities of Tuffs from Yucca Mountain Boreholes, Tunnel Bed 5 (G-Tunnel) and Bandelier Tuff (Los Alamos). Submittal date: 05/01/2000.

LA0004JC831361.001. Preliminary Retardation Data for Selenium Transport through Unsaturated Tuffs. Submittal date: 04/19/2000.

LA0004WS831372.002. Sorption of Np, Pu, and Am on Rock Samples From Busted Butte, NV. Submittal date: 04/19/2000.

LA0005NL831352.001. The K_d Values of ^{243}Am on Colloids of Hematite, Montmorillonite, and Silica in Natural and Synthetic Groundwater. Submittal date: 05/03/2000.

LA0010JC831341.002. Radionuclide Retardation Measurements of Sorption Distribution Coefficients for Cesium. Submittal date: 10/19/2000.

LA0010JC831341.003. Radionuclide Retardation Measurements of Sorption Distribution Coefficients for Strontium. Submittal date: 10/19/2000.

LA0010JC831341.004. Radionuclide Retardation Measurements of Sorption Distribution Coefficients for Selenium. Submittal date: 10/19/2000.

LA0010JC831341.005. Radionuclide Retardation Measurements of Sorption Distribution Coefficients for Uranium. Submittal date: 10/19/2000.

LA0010JC831341.006. Radionuclide Retardation Measurements of Sorption Distribution Coefficients for Plutonium. Submittal date: 10/19/2000.

LA0010JC831341.007. Radionuclide Retardation Measurements of Sorption Distribution Coefficients for Neptunium. Submittal date: 10/19/2000.

LA9907AM831234.003. Downhole Eh and pH Measurements for NC-EWDP-01S, 11-Jan-99. Submittal date: 01/27/2000.

LA9907AM831234.009. Flow-through Cell Measurements for NC-EWDP-01S, NC-EWDP-03S, NC-EWDP-09SX, 5/17/99, 5/18/99, 5/20/99. Submittal date: 01/27/2000.

LA9907AM831234.010. Flow-through Cell Measurements for SD6-ST1, 02-Jun-99 and 08-Jun-99. Submittal date: 01/27/2000.

LA9907AM831234.011. Flow-through Cell Measurements for AD-2, 10-Jun-99. Submittal date: 01/27/2000.

LA9909PR831231.003. Interpretations of Bullfrog Reactive Tracer Test Data—Modeling Data. Submittal date: 09/02/1999.

LA9909PR831231.005. Interpretations of Tracer Data–Modeling Data. Submittal date: 09/02/1999.

LA9909WS831372.001. Busted Butte UZ Transport Test: Phase I Collection Pad Extract Concentrations. Submittal date: 09/29/1999.

LA9909WS831372.002. Busted Butte UZ Transport Test: Phase I Collection Pad Tracer Loading and Tracer Concentrations. Submittal date: 09/30/1999.

LA9909WS831372.005. QXRD Results for Samples from Lower Tpt Section. Submittal date: 10/04/1999.

LA9909WS831372.006. Mineral Abundances (weight %) in Calico Hills Formation. Submittal date: 10/01/1999.

LA9909WS831372.007. Quantitative XRD Results for USW H-5 Core and Drill Cuttings. Submittal date: 10/04/1999.

LA9909WS831372.010. Mineral Abundances (weight %) in Calico Hills Formation. Submittal date: 10/01/1999.

LA9909WS831372.011. Preliminary Measured Sorption Coefficients. Submittal date: 10/13/1999.

LA9909WS831372.014. Microsphere Suspension Preparation for the Busted Butte UZ Transport Test. Submittal date: 09/30/1999.

LA9909WS831372.015. ICPAES Porewater Analysis for Rock Samples from Busted Butte, NV. Submittal date: 10/01/1999.

LA9909WS831372.016. Ion Chromatography Porewater Analysis for Rock Samples from Busted Butte, NV. Submittal date: 09/30/1999.

LA9909WS831372.017. pH of Porewater of Rock Samples from Busted Butte, NV. Submittal date: 09/30/1999.

LA9909WS831372.018. Gravimetric Moisture Content of Rock Samples from Busted Butte, NV. Submittal date: 09/30/1999.

LA9910SK831341.005. Total Colloidal Particles Concentration and Size Distribution in NTS-ER-20-5-1, NTS-ER-20-5-3, and J-13 Groundwater. Submittal date: 12/07/1999.

LA9910WS831372.008. Busted Butte UZ Transport Test: Gravimetric Moisture Content and Bromide Concentration in Selected Phase 1A Rock Samples. Submittal date: 11/03/1999.

LA9910WS831372.009. QXRD Data for UZTT Busted Butte Samples. Submittal date: 11/03/1999.

LAAM831311AQ98.005. Geochemical Field Measurements for UE-25 WT#17, 27-Jan-98. Submittal date: 09/14/1998.

LAAM831311AQ98.007. Flow-through Cell and Static Measurements at UE-25 WT#3, 22-Jun-98. Submittal date: 09/14/1998.

LAAM831311AQ98.008. Analysis of Bailed Sample for UE-25 WT#17, 04-Jun-98. Submittal date: 09/14/1998.

LAAM831311AQ98.010. Static Measurements for US-25 WT#17, 01-Jul-98. Submittal date: 09/14/1998.

LAIT831341AQ97.002. Reversibility of Radionuclide Sorption. Submittal date: 06/09/1997.

LAIT831361AQ95.001. Crushed Rock Column Data to Obtain Sorption Coefficients for Pu(IV), Np, Tc-95m, Using J-13 and UE-25 p#1 Waters, Yucca Mountain, Nevada. Submittal date: 09/29/1995.

LAIT831361AQ95.003. Transport Data of H-3, Np, and Tc-95m Collected to Calculate Retardation Coefficients Using J-13 and UE-25 p#1 Waters. Submittal date: 08/20/1997.

LAIT831362AQ95.001. Solid Rock Diffusion Data Collected to Determine Rate of Movement for Np, U, and HTO through an Unsaturated Tuff. Submittal date: 09/29/1995.

LAPR831231AQ99.001. Prow Pass Reactive Tracer Test Field Data. Submittal date: 02/10/1999.

LASC831321AQ98.003. Results of Real Time Analysis for Erionite in Drill Hole USW SD-6, Yucca Mountain, Nevada. Submittal date: 06/11/1998.

LB00032412213U.001. Busted Butte Ground Penetrating Radar Data Collected June 1998 through February 2000 at the Unsaturated Zone Transport Test (UZTT): GPR Velocity Data. Submittal date: 03/24/2000.

LB970601233129.001. The Site-Scale Unsaturated Zone Model of Yucca Mountain, Nevada for the Viability Assessment. Submittal date: 06/09/1997.

LL990612704244.098. ERT Data for Busted Butte. Submittal date: 06/21/1999.

MO0004GSC00167.000. As-built Coordinate of Boreholes in the Test Alcove and Running Drift, Busted Butte Test Facility. Submittal date: 04/20/2000.

MO0007MAJIONPH.003. Major Ion Content of Groundwater from Yucca Mountain Project Borehole USW G-2, Extracted from ANL-NBS-HS-000021, Geochemical and Isotopic Constraints on Groundwater Flow Directions, Mixing, and Recharge at Yucca Mountain, Nevada. Submittal date: 07/27/2000. Submit to RPC, URN-0507.

MO0007MAJIONPH.005. Major Ion Content of Groundwater from Boreholes UZ-14, WT-17 and WT #3, Extracted from ANL-NBS-HS-000021, Geochemical and Isotopic Constraints on Groundwater Flow Directions, Mixing and Recharge at Yucca Mountain, Nevada. Submittal date: 07/27/2000. Submit to RPC, URN-0509.

MO0007MAJIONPH.011. Major Ion Content of Groundwater from Selected Yucca Mountain Project Boreholes Extracted from ANL-NBS-HS-000021, Geochemical and Isotopic Constraints on Groundwater Flow Directions, Mixing and Recharge at Yucca Mountain, Nevada. Submittal date: 07/27/2000. Submit to RPC, URN-0520.

MO0007MAJIONPH.013. Major Ion Content of Groundwater from Selected Yucca Mountain Project and Other Boreholes Extracted from ANL-NBS-HS-000021, Geochemical and Isotopic Constraints on Groundwater Flow Directions, Mixing, and Recharge at Yucca Mountain, Nevada. Submittal date: 07/27/2000. Submit to RPC, URN-0522.

MO0012BRLI25C2.000. Bromide Abundance and Lithium Abundance Data of Crushed Tuff Column Studies with Filtered J-13 Water from UE-25 C #2 at 2406 FT., from DTN LA9909PR831231.004, Table S99488_006. Submittal date: 12/04/2000. Submit to RPC, URN-0758.

MO0012CATECHOL.000. Cation Exchange Capacity Data of C-Well Tuff from UE-25 C #1 and UE-25 C #2, from DTN LA9909PR831231.004, Table S99488_004. Submittal date: 12/05/2000. Submit to RPC, URN-0760.

MO0012MINLCHOL.000. Mineral Abundance Data using X-ray Diffraction Analyses of C-Well Tuffs from UE-25 C #1, and UE-25 C #2 from DTN LA9909PR831231.004, Table S99488_003. Submittal date:12/05/2000. Submit to RPC, URN-0759.

MO0012PERMCHOL.000. Permeability Data (using Filtered J-13 Water) from UE-25 C #1, UE-25 C #2, and UE-25 C #3, from DTN LA9909PR831231.004, Table S99488_001. Submittal date: 12/05/2000. Submit to RPC, URN-0757.

MO0012POROCHOL.000. Porosity Data (using Deionized Water) from UE-25 C #1, UE-25 C #2, and UE-25 C #3 from DTN LA9909PR831231.004, Table S99488_002. Submittal date: 12/05/2000. Submit to RPC, URN-0762.

MO0012SORBCHOL.000. Sorbing Element Concentration Data of J-13 and C-3 Well Water from UE-25 C #1 and UE-25 C #2, from DTN LA9909PR831231.004, Table S99488_007. Submittal date: 12/05/2000. Submit to RPC, URN-0761.

MO9906GPS98410.000. Yucca Mountain Project Borehole Locations. Submittal date: 06/23/1999.

8.5 OUTPUT DATA, LISTED BY DATA TRACKING NUMBER

LA0003AM831341.001. Preliminary Revision of Probability Distributions for Sorption Coefficients (K_ds). Submittal date: 03/29/2000.

LA0003JC831362.001. Preliminary Matrix Diffusion Coefficients for Yucca Mountain Tuffs. Submittal date: 04/10/2000.

LA9909WS831372.019. Busted Butte Simulation Results 3-D Model. Submittal date: 04/11/2000.

LA9909WS831372.020. Summary of Monte Carlo Cases Including Correlation Length of Heterogeneities. Submittal date: 04/12/2000.

LA9909WS831372.021. Busted Butte Phase 1-A Modeling Results for Stochastic Model. Submittal date: 04/11/2000.

LA9909WS831372.022. Fracture and Matrix Property Sets Used in Simulations for the Phase-2 Test. Submittal date: 04/11/2000.